

# **Foam Engineering**

# Foam Engineering

Fundamentals and Applications

Edited by

Paul Stevenson

*Department of Chemical and Materials Engineering,  
Faculty of Engineering, University of Auckland, New Zealand*

 WILEY-BLACKWELL

A John Wiley & Sons, Ltd., Publication

This edition first published 2012  
© 2012 John Wiley & Sons, Ltd

*Registered Office*

John Wiley & Sons, Ltd, The Atrium, Southern Gate, Chichester, West Sussex, PO19 8SQ, United Kingdom

For details of our global editorial offices, for customer services and for information about how to apply for permission to reuse the copyright material in this book please see our website at [www.wiley.com](http://www.wiley.com).

The right of the author to be identified as the author of this work has been asserted in accordance with the Copyright, Designs and Patents Act 1988.

All rights reserved. No part of this publication may be reproduced, stored in a retrieval system, or transmitted, in any form or by any means, electronic, mechanical, photocopying, recording or otherwise, except as permitted by the UK Copyright, Designs and Patents Act 1988, without the prior permission of the publisher.

Wiley also publishes its books in a variety of electronic formats. Some content that appears in print may not be available in electronic books.

Designations used by companies to distinguish their products are often claimed as trademarks. All brand names and product names used in this book are trade names, service marks, trademarks or registered trademarks of their respective owners. The publisher is not associated with any product or vendor mentioned in this book. This publication is designed to provide accurate and authoritative information in regard to the subject matter covered. It is sold on the understanding that the publisher is not engaged in rendering professional services. If professional advice or other expert assistance is required, the services of a competent professional should be sought.

The publisher and the author make no representations or warranties with respect to the accuracy or completeness of the contents of this work and specifically disclaim all warranties, including without limitation any implied warranties of fitness for a particular purpose. This work is sold with the understanding that the publisher is not engaged in rendering professional services. The advice and strategies contained herein may not be suitable for every situation. In view of ongoing research, equipment modifications, changes in governmental regulations, and the constant flow of information relating to the use of experimental reagents, equipment, and devices, the reader is urged to review and evaluate the information provided in the package insert or instructions for each chemical, piece of equipment, reagent, or device for, among other things, any changes in the instructions or indication of usage and for added warnings and precautions. The fact that an organization or Website is referred to in this work as a citation and/or a potential source of further information does not mean that the author or the publisher endorses the information the organization or Website may provide or recommendations it may make. Further, readers should be aware that Internet Websites listed in this work may have changed or disappeared between when this work was written and when it is read. No warranty may be created or extended by any promotional statements for this work. Neither the publisher nor the author shall be liable for any damages arising herefrom.

*Library of Congress Cataloging-in-Publication Data*

Foam engineering : fundamentals and applications / [edited by] Paul Stevenson. – 1st ed.

p. cm.

Includes bibliographical references and index.

ISBN 978-0-470-66080-5 (hardback)

1. Foam. 2. Foam—Industrial applications. 3. Foam—Technological innovations. 4. Foamed materials.

I. Stevenson, Paul, 1973—

QD549.F59 2012

620.1—dc23

2011037211

A catalogue record for this book is available from the British Library.

Print ISBN: 9780470660805

Set in 10/12pt Times by SPi Publisher Services, Pondicherry, India

# Contents

<i>About the Editor</i>	xiii
<i>List of Contributors</i>	xv
<i>Preface</i>	xvii
<b>1 Introduction</b>	<b>1</b>
<i>Paul Stevenson</i>	
1.1 Gas–Liquid Foam in Products and Processes	1
1.2 Content of This Volume	2
1.3 A Personal View of Collaboration in Foam Research	3
<b>Part I Fundamentals</b>	<b>5</b>
<b>2 Foam Morphology</b>	<b>7</b>
<i>Denis Weaire, Steven T. Tobin, Aaron J. Meagher and Stefan Hutzler</i>	
2.1 Introduction	7
2.2 Basic Rules of Foam Morphology	7
2.2.1 Foams, Wet and Dry	7
2.2.2 The Dry Limit	9
2.2.3 The Wet Limit	11
2.2.4 Between the Two Limits	11
2.3 Two-dimensional Foams	11
2.3.1 The Dry Limit in 2D	11
2.3.2 The Wet Limit in 2D	12
2.3.3 Between the Two Limits in 2D	12
2.4 Ordered Foams	15
2.4.1 Two Dimensions	15
2.4.2 Three Dimensions	16
2.5 Disordered Foams	19
2.6 Statistics of 3D Foams	20
2.7 Structures in Transition: Instabilities and Topological Changes	21
2.8 Other Types of Foams	22
2.8.1 Emulsions	22
2.8.2 Biological Cells	22
2.8.3 Solid Foams	23
2.9 Conclusions	24
Acknowledgements	24
References	25

<b>3 Foam Drainage</b>	<b>27</b>
<i>Stephan A. Koehler</i>	
3.1 Introduction	27
3.2 Geometric Considerations	29
3.3 A Drained Foam	33
3.4 The Continuity Equation	35
3.5 Interstitial Flow	36
3.6 Forced Drainage	38
3.7 Rigid Interfaces and Neglecting Nodes: The Original Foam Drainage Equation	41
3.8 Mobile Interfaces and Neglecting Nodes	43
3.9 Neglecting Channels: The Node-dominated Model	46
3.10 The Network Model: Combining Nodes and Channels	48
3.11 The Carman – Kozeny Approach	50
3.12 Interpreting Forced Drainage Experiments: A Detailed Look	51
3.13 Unresolved Issues	53
3.14 A Brief History of Foam Drainage	54
References	55
<b>4 Foam Ripening</b>	<b>59</b>
<i>Olivier Pitois</i>	
4.1 Introduction	59
4.2 The Very Wet Limit	59
4.3 The Very Dry Limit	61
4.3.1 Inter-bubble Gas Diffusion through Thin Films	61
4.3.2 von Neumann Ripening for 2D Foams	62
4.3.3 3D Coarsening	64
4.4 Wet Foams	65
4.5 Controlling the Coarsening Rate	69
4.5.1 Gas Solubility	69
4.5.2 Resistance to Gas Permeation	70
4.5.3 Shell Mechanical Strength	70
4.5.4 Bulk Modulus	71
References	72
<b>5 Coalescence in Foams</b>	<b>75</b>
<i>Annie Colin</i>	
5.1 Introduction	75
5.2 Stability of Isolated Thin Films	76
5.2.1 Experimental Studies Dealing with Isolated Thin Liquid Films	76
5.2.2 Theoretical Description of the Rupture of an Isolated Thin Liquid Film	77
5.3 Structure and Dynamics of Foam Rupture	78
5.4 What Are the Key Parameters in the Coalescence Process?	81

5.5 How Do We Explain the Existence of a Critical Liquid Fraction?	86
5.6 Conclusion	89
References	89
<b>6 Foam Rheology</b>	<b>91</b>
<i>Nikolai D. Denkov, Slavka S. Tcholakova, Reinhart Höhler and Sylvie Cohen-Addad</i>	
6.1 Introduction	91
6.2 Main Experimental and Theoretical Approaches	93
6.3 Foam Visco-elasticity	95
6.3.1 Linear Elasticity	95
6.3.2 Non-linear Elasticity	98
6.3.3 Linear Relaxations	99
6.3.4 Shear Modulus of Particle-laden Foams	102
6.4 Yielding	103
6.5 Plastic Flow	105
6.6 Viscous Dissipation in Steadily Sheared Foams	106
6.6.1 Predominant Viscous Friction in the Foam Films	108
6.6.2 Predominant Viscous Friction in the Surfactant Adsorption Layer	111
6.7 Foam-Wall Viscous Friction	112
6.8 Conclusions	114
Abbreviations	115
Acknowledgement	115
References	116
<b>7 Particle Stabilized Foams</b>	<b>121</b>
<i>G. Kaptay and N. Babcsán</i>	
7.1 Introduction	121
7.2 A Summary of Some Empirical Observations	123
7.3 On the Thermodynamic Stability of Particle Stabilized Foams	125
7.4 On the Ability of Particles to Stabilize Foams during Their Production	131
7.5 Design Rules for Particle Stabilized Foams	135
7.6 Conclusions	138
Acknowledgement	138
References	138
<b>8 Pneumatic Foam</b>	<b>145</b>
<i>Paul Stevenson and Xueliang Li</i>	
8.1 Preamble	145
8.2 Vertical Pneumatic Foam	145
8.2.1 Introduction	145
8.2.2 The Hydrodynamics of Vertical Pneumatic Foam	147

8.2.3	The ‘Vertical Foam Misapprehension’	152
8.2.4	Bubble Size Distributions in Foam	153
8.2.5	Non-overflowing Pneumatic Foam	153
8.2.6	The Influence of Humidity upon Pneumatic Foam with a Free Surface	155
8.2.7	Wet Pneumatic Foam and Flooding	155
8.2.8	Shear Stress Imparted by the Column Wall	157
8.2.9	Changes in Flow Cross-sectional Area	158
8.3	Horizontal Flow of Pneumatic Foam	158
8.3.1	Introduction	158
8.3.2	Lemlich’s Observations	159
8.3.3	Wall-slip and Velocity Profiles	160
8.3.4	Horizontal Flow Regimes	161
8.4	Pneumatic Foam in Inclined Channels	162
8.5	Methods of Pneumatic Foam Production	162
	Nomenclature	164
	References	165
<b>9</b>	<b>Non-aqueous Foams: Formation and Stability</b>	<b>169</b>
	<i>Lok Kumar Shrestha and Kenji Aramaki</i>	
9.1	Introduction	169
9.1.1	Foam Formation and Structures	169
9.1.2	Foam Stability	170
9.2	Phase Behavior of Diglycerol Fatty Acid Esters in Oils	173
9.3	Non-aqueous Foaming Properties	174
9.3.1	Effect of Solvent Molecular Structure	174
9.3.2	Effect of Surfactant Concentration	177
9.3.3	Effect of Hydrophobic Chain Length of Surfactant	181
9.3.4	Effect of Headgroup Size of Surfactant	187
9.3.5	Effect of Temperature	189
9.3.6	Effect of Water Addition	191
9.3.7	Non-aqueous Foam Stabilization Mechanism	201
9.4	Conclusion	203
	Acknowledgements	203
	References	204
<b>10</b>	<b>Suprafroth: Ageless Two-dimensional Electronic Froth</b>	<b>207</b>
	<i>Ruslan Prozorov and Paul C. Canfield</i>	
10.1	Introduction	207
10.2	The Intermediate State in Type-I Superconductors	208
10.3	Observation and Study of the Tubular Intermediate State Patterns	211
10.4	Structural Statistical Analysis of the Suprafroth	215
	Acknowledgements	224
	References	224

<b>Part II Applications</b>	<b>227</b>
<b>11 Froth Phase Phenomena in Flotation</b>	<b>229</b>
<i>Paul Stevenson and Noel W.A. Lambert</i>	
11.1 Introduction	229
11.2 Froth Stability	233
11.3 Hydrodynamic Condition of the Froth	235
11.4 Detachment of Particles from Bubbles	236
11.5 Gangue Recovery	238
11.6 The Velocity Field of Froth Bubbles	241
11.7 Plant Experience of Froth Flotation	242
11.7.1 Introduction	242
11.7.2 Frother-constrained Plant	242
11.7.3 Sampling, Data Manipulation and Data Presentation	244
11.7.4 Process Control	245
11.7.5 The Assessment of Newly Proposed Flotation Equipment	246
11.7.6 Conclusions about Froth Flotation Drawn from Plant Experience	246
Nomenclature	246
References	247
<b>12 Froth Flotation of Oil Sand Bitumen</b>	<b>251</b>
<i>Laurier L. Schramm and Randy J. Mikula</i>	
12.1 Introduction	251
12.2 Oil Sands	251
12.3 Mining and Slurrying	253
12.4 Froth Structure	265
12.5 Physical Properties of Froths	272
12.6 Froth Treatment	274
12.7 Conclusion	278
Acknowledgements	278
References	278
<b>13 Foams in Enhancing Petroleum Recovery</b>	<b>283</b>
<i>Laurier L. Schramm and E. Eddy Isaacs</i>	
13.1 Introduction	283
13.2 Foam Applications for the Upstream Petroleum Industry	284
13.2.1 Selection of Foam-Forming Surfactants	284
13.3 Foam Applications in Wells and Near Wells	287
13.3.1 Drilling and Completion Foams	287
13.3.2 Well Stimulation Foams: Fracturing, Acidizing, and Unloading	288
13.4 Foam Applications in Reservoir Processes	289
13.4.1 Reservoir Recovery Background	289
13.4.2 Foam Applications in Primary and Secondary Oil Recovery	292
13.4.3 Foam Applications in Enhanced (Tertiary) Oil Recovery	293

13.5 Occurrences of Foams at the Surface and Downstream	298
13.6 Conclusion	299
References	299
<b>14 Foam Fractionation</b>	<b>307</b>
<i>Xueliang Li and Paul Stevenson</i>	
14.1 Introduction	307
14.2 Adsorption in Foam Fractionation	310
14.2.1 Adsorption Kinetics at Quiescent Interface	311
14.2.2 Adsorption at Dynamic Interfaces	314
14.3 Foam Drainage	315
14.4 Coarsening and Foam Stability	316
14.5 Foam Fractionation Devices and Process Intensification	317
14.5.1 Limitations of Conventional Columns	317
14.5.2 Process Intensification Devices	319
14.6 Concluding Remarks about Industrial Practice	324
Nomenclature	325
References	326
<b>15 Gas–Liquid Mass Transfer in Foam</b>	<b>331</b>
<i>Paul Stevenson</i>	
15.1 Introduction	331
15.2 Non-overflowing Pneumatic Foam Devices	334
15.3 Overflowing Pneumatic Foam Devices	336
15.4 The Waldhof Fermentor	338
15.5 Induced Air Methods	340
15.6 Horizontal Foam Contacting	341
15.7 Calculation of Specific Interfacial Area in Foam	342
15.8 Hydrodynamics of Pneumatic Foam	343
15.9 Mass Transfer and Equilibrium Considerations	345
15.9.1 Gas–Liquid Equilibrium	345
15.9.2 Rate of Mass Transfer	345
15.9.3 Estimation of Mass Transfer Coefficient	346
15.10 Towards an Integrated Model of Foam Gas–Liquid Contactors	347
15.11 Discussion and Future Directions	349
Nomenclature	351
Acknowledgements	351
References	352
<b>16 Foams in Glass Manufacturing</b>	<b>355</b>
<i>Laurent Pilon</i>	
16.1 Introduction	355
16.1.1 The Glass Melting Process	356
16.1.2 Melting Chemistry and Refining	359
16.1.3 Motivations	362

16.2	Glass Foams in Glass Melting Furnaces	363
16.2.1	Primary Foam	363
16.2.2	Secondary Foam	363
16.2.3	Reboil	364
16.2.4	Parameters Affecting Glass Foaming	365
16.3	Physical Phenomena	365
16.3.1	Glass Foam Physics	365
16.3.2	Surface Active Agents and Surface Tension of Gas/Melt Interface	368
16.3.3	Drainage and Stability of a Single Molten Glass Film	369
16.3.4	Gas Bubbles in Molten Glass	370
16.4	Experimental Studies	373
16.4.1	Introduction	373
16.4.2	Transient Primary and Secondary Glass Foams	374
16.4.3	Steady-state Glass Foaming by Gas Injection	384
16.5	Modeling	386
16.5.1	Introduction	386
16.5.2	Dynamic Foam Growth and Decay	387
16.5.3	Steady-state Glass Foams	389
16.5.4	Experiments and Model Limitations	395
16.6	Measures for Reducing Glass Foaming in Glass Melting Furnaces	396
16.6.1	Batch Composition	396
16.6.2	Batch Conditioning and Heating	397
16.6.3	Furnace Temperature	397
16.6.4	External and Temporary Actions	397
16.6.5	Atmosphere Composition and Flame Luminosity	399
16.6.6	Control Foaming in Reduced-pressure Refining	400
16.7	Perspective and Future Research Directions	401
	Acknowledgements	402
	References	402
17	<b>Fire-fighting Foam Technology</b>	411
	<i>Thomas J. Martin</i>	
17.1	Introduction	411
17.2	History	413
17.3	Applications	415
17.3.1	Foam Market	415
17.3.2	Hardware	415
17.4	Physical Properties	416
17.4.1	Mechanism of Action	417
17.4.2	Class A Foams	422
17.4.3	Class B Foams	422
17.5	Chemical Properties	430
17.5.1	Ingredients and Purpose	430
17.5.2	Example Recipes	447
17.6	Testing	448
17.6.1	Lab Test Methods	449
17.6.2	Fire Test Standards	452

17.7	The Future	453
	Acknowledgements	454
	References	454
<b>18</b>	<b>Foams in Consumer Products</b>	<b>459</b>
	<i>Peter J. Martin</i>	
18.1	Introduction	459
18.1.1	Foams and Consumer Appeal	459
18.1.2	Market Descriptions and Directions	461
18.1.3	The Scope of This Chapter	463
18.2	Creation and Structure	463
18.2.1	Surfactants and Their Application	464
18.2.2	Creation	466
18.2.3	Growth	468
18.2.4	Application of Structure	469
18.2.5	Maintenance of Structure	469
18.2.6	Summary	470
18.3	Sensory Appeal	470
18.3.1	Visual	471
18.3.2	Auditory	472
18.3.3	Mouth Feel	473
18.3.4	Summary	473
18.4	Conclusions	473
	References	473
<b>19</b>	<b>Foams for Blast Mitigation</b>	<b>477</b>
	<i>A. Britan, H. Shapiro and G. Ben-Dor</i>	
19.1	Introduction	477
19.2	Free Field Tests	478
19.2.1	Compressibility	478
19.2.2	Typical Test Rigs	480
19.2.3	Decay of the Foam Barrier	482
19.2.4	Effect of Foam Density	485
19.2.5	Foam Impedance and the Barrier Thickness	488
19.3	Shock Tube Testing	493
19.3.1	Main Restrictions	493
19.3.2	Foam Shattering	494
19.4	Theoretical Approaches	497
19.4.1	Governing Processes	497
19.4.2	Hierarchy of the Process	498
19.5	Conclusions	508
	Acknowledgements	509
	References	509
	<b>Index</b>	<b>513</b>

# About the Editor

Paul Stevenson is a senior lecturer in the Chemical and Materials Engineering Department of the University of Auckland, New Zealand. He took BA (Hons) and MEng degrees in chemical engineering from the University of Cambridge, UK, where he completed doctoral studies in multiphase flow in oil flowlines. After post-doctoral research with the 2nd Consortium on Transient Multiphase Flow at Cambridge, he took a position at the University of Newcastle, Australia, to investigate froth flotation and foam fractionation. He has worked as a process chemist for Allied Colloids and as a chemical engineer for Croda Hydrocarbons and British Steel Technical, all in the UK. In addition he has spent periods as a Japanese convertible bond dealer for the US investment bank D.E. Shaw Securities International and a racecourse bookmaker for his family's business.

# List of Contributors

## **Kenji Aramaki**

Graduate School of Environment and Information Sciences, Yokohama National University, Yokohama, Japan

## **N. Babcsán**

BAY-ZOLTAN Foundation for Applied Research, Miskolc-Tapolca, Iglói, Hungary

## **G. Ben-Dor**

Protective Technologies R&D Center, Faculty of Engineering Sciences, Ben-Gurion University of the Negev, Beer Sheva, Israel

## **A. Britan**

Protective Technologies R&D Center, Faculty of Engineering Sciences, Ben-Gurion University of the Negev, Beer Sheva, Israel

## **Paul C. Canfield**

Department of Physics and Astronomy, Ames Laboratory, Iowa State University, Ames, IA, USA

## **Sylvie Cohen-Addad**

Université Paris 6, Paris, France, and Université Paris-Est, Marne-la-Vallée, France

## **Annie Colin**

Université Bordeaux, Pessac, France

## **Nikolai D. Denkov**

Department of Chemical Engineering, Faculty of Chemistry, Sofia University, Sofia, Bulgaria

## **Reinhard Höller**

Université Paris 6, Paris, France, and Université Paris-Est, Marne-la-Vallée, France

## **S. Hutzler**

School of Physics, Trinity College, Dublin, Ireland

## **E. Eddy Isaacs**

Alberta Innovates – Energy and Environment Solutions, Calgary, AB, Canada

## **G. Kaptay**

BAY-ZOLTAN Foundation for Applied Research, Miskolc-Tapolca, Iglói, Hungary, and University of Miskolc, Egyetemváros, Miskolc, Hungary

## **Stephan A. Koehler**

Physics Department, Worcester Polytechnic Institute, Worcester, MA, USA

## **Noel W.A. Lambert**

Clean Process Technologies Pty Ltd, Lower Belford, NSW, Australia

## **Xueliang Li**

Centre for Advanced Particle Processing, University of Newcastle, Callaghan, Australia

## **Peter J. Martin**

School of Chemical Engineering and Analytical Science, The University of Manchester, Manchester, UK

**Thomas J. Martin**

Chemical Technology and Quality Assurance,  
Research & Development,  
Chemguard, Inc.,  
Mansfield, TX, USA

**A.J. Meagher**

School of Physics, Trinity College,  
Dublin, Ireland

**Randy J. Mikula**

Natural Resources Canada, Devon, AB,  
Canada

**Laurent Pilon**

Henry Samueli School of Engineering and Applied Science, Mechanical and Aerospace Engineering Department,  
University of California Los Angeles,  
Los Angeles, CA, USA

**Olivier Pitois**

Université Paris-Est, Laboratoire Navier,  
IFSTTAR, France

**Ruslan Prozorov**

Department of Physics and Astronomy,  
Ames Laboratory, Iowa State University,  
Ames, IA, USA

**Laurier L. Schramm**

Saskatchewan Research Council,  
Saskatoon, SK, Canada

**H. Shapiro**

Protective Technologies R&D Center,  
Faculty of Engineering Sciences,  
Ben-Gurion University of the Negev,  
Beer Sheva, Israel

**Lok Kumar Shrestha**

International Center for Young Scientists,  
WPI Center for Materials  
Nanoarchitectonics, National Institute  
for Materials Science, Tsukuba Ibaraki,  
Japan

**Paul Stevenson**

Department of Chemical and Materials Engineering, Faculty of Engineering,  
University of Auckland, New Zealand

**Slavka S. Tcholakova**

Department of Chemical Engineering,  
Faculty of Chemistry, Sofia University,  
Sofia, Bulgaria

**S.T. Tobin**

School of Physics, Trinity College, Dublin,  
Ireland

**D. Weaire**

School of Physics, Trinity College, Dublin,  
Ireland

# Preface

I am enormously grateful to all of authors who have contributed to this volume on gas–liquid foam. One of the great pleasures of working with such accomplished scientists and engineers from industry and academia is that everybody has known the level at which to pitch their contributions.

Special thanks are due to Laurie Schramm who, along with co-authors, has contributed two chapters on foams in enhanced oil recovery and flotation of oil sands, and to Thomas Martin who endured initial confusion upon my part to produce a first class chapter on fire-fighting foams. I'd like to express my gratitude to Stephan Koehler for giving me sound advice about the selection of authors for various chapters, and to Denis Weaire who advised upon how to engender more coherence in the volume. Cat Chimney gave sterling assistance in formatting referencing styles of a number of chapters. My former colleague Noel Lambert delivered excellent copy at tremendously short notice despite being in enormous demand by others. Gratitude is due to Sven Schröter (of Schroeter Imagery) for his excellent photography and production of the image on the cover of this volume. I could not have completed this project without the constant and faithful assistance of my doctoral student and friend Xueliang (Bruce) Li. Bruce co-wrote two chapters with me, reviewed other chapters and developed ideas for cover art. He is truly a gentleman and scholar.

Thanks should also go to the staff at Wiley (Chichester), in particular Rebecca Stubbs, Sarah Tilley and Amie Marshall, who first envisaged this project and gave excellent support as the volume developed.

Last but not least I'd like to thank my second daughter, Charlotte, for being born at a perfect time to enable me to claim my nine weeks paternity leave from the University of Auckland, during which I worked upon this volume, as well as my wife Tracey for giving birth to her and my first daughter Emily for being cute.

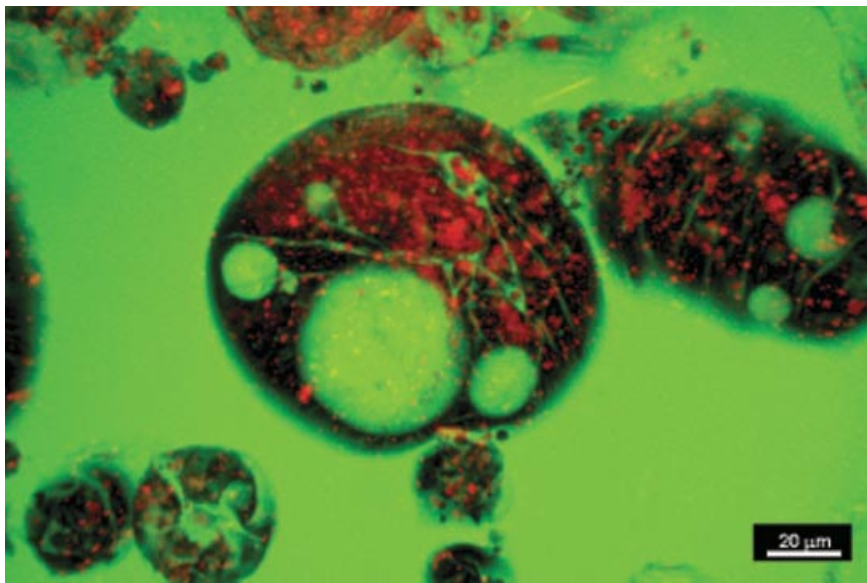


**Plate 1: Fig. 12.10** Confocal micrograph of a bitumen froth (deaerated) from an easily processed ore. The mineral is colored red and the bitumen is green. Most of the mineral is associated with the water phase that has been trapped as the bitumen bubbles collapsed at the top of the separation cell. Photomicrograph by V. Muñoz.

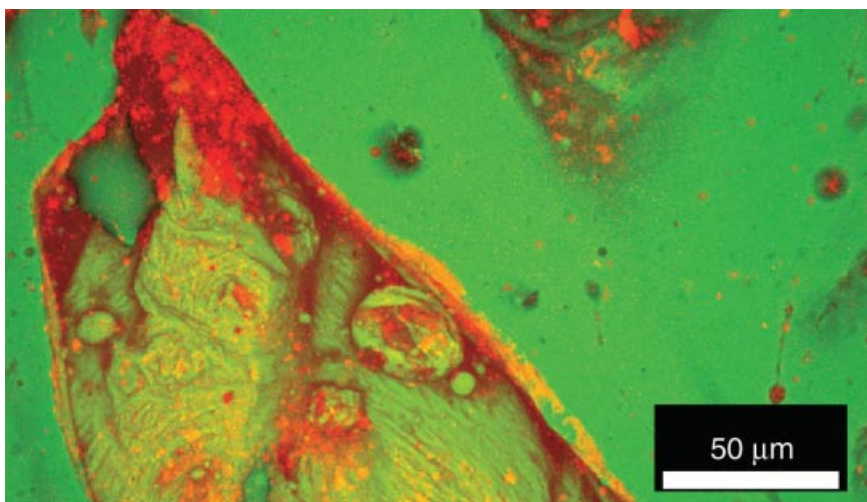


**Plate 2: Fig. 12.12** Confocal micrograph of a bitumen froth (deaerated) from a difficult to process ore. The mineral is colored red and the bitumen is green. Most of the mineral in this case is closely associated with the bitumen (oil wet solids) and a very complex emulsified froth structure is observed due to the high surfactant concentration in the bitumen. The bitumen component is imaged in a fluorescent mode and the decreased brightness in this image relative to Fig. 12.11 is indicative of a different bitumen chemistry in the bitumen component. Photomicrograph by V. Muñoz.

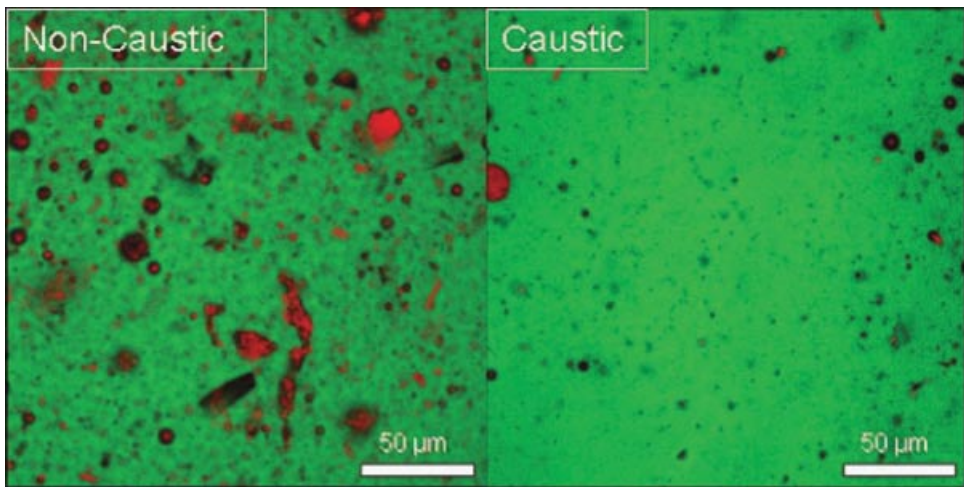


**Plate 3: Fig. 12.14** The loose froth (left) is from the same oil sand as the coalesced froth (right). The use of sodium hydroxide in the extraction process changes the nature of the bitumen, resulting in a froth that has significantly less mineral and water. In these confocal microscope images, the red colors are mineral components, the green are hydrocarbon, and the dark areas are water. Photomicrographs by V. Muñoz.

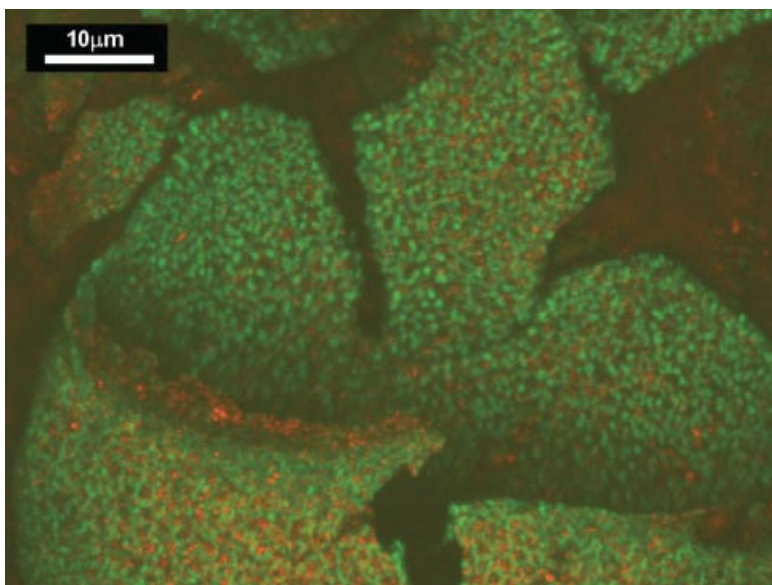


**Plate 4: Fig. 12.17** A detail of a similar membranous sac at higher magnification showing both mineral (red) and organic phases (green). The stronger the association between the mineral and organic components, the greater is the proportion of yellow in this image. Photomicrograph by V. Muñoz.



**Plate 5: Fig. 19.3** (a-c) Typical arrangements of the foam barrier for internal explosion case; (d and e) the effect on the van of a blast from an explosion of a 44 kg charge of C4 (d: not protected; e: protected).

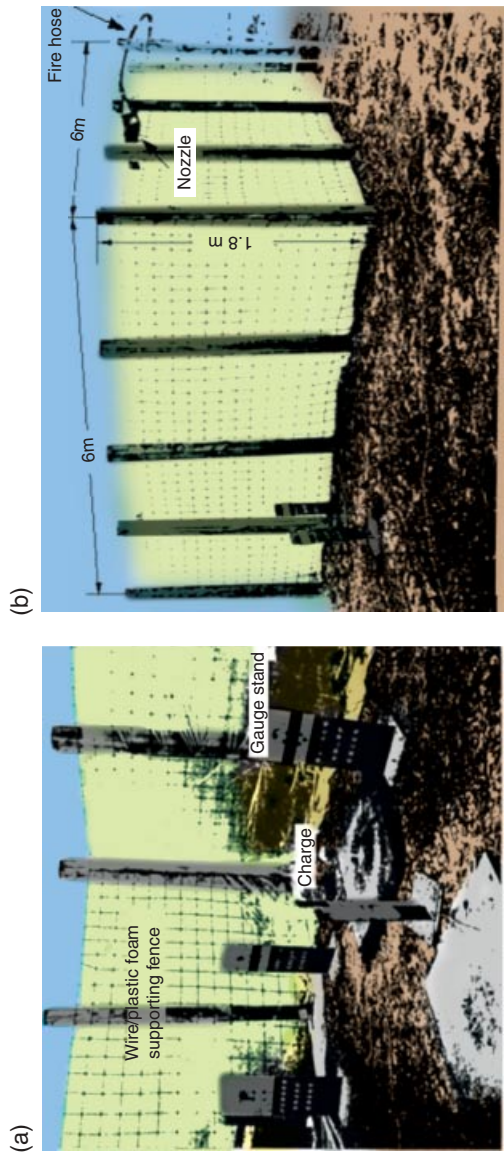


*Plate 6: Fig. 19.4 (a) Layout and (b) typical dimensions of a rig used for testing the close field of an internal explosion [19].*

# 1

## Introduction

*Paul Stevenson*

### 1.1 Gas–Liquid Foam in Products and Processes

A gas–liquid foam, such as those found on the top of one’s bath or one’s beer, is a multiphase mixture that generally exhibits several physical properties that make it amenable to be used in multifarious industrial applications:

- 1. High specific surface area.** The amount of gas–liquid surface area per unit volume of material that is attainable in a foam is greater than that in comparable two-phase systems. This property makes gas–liquid foam particularly attractive for interphase mass transfer operations. Examples of such processes are froth flotation, in which valuable hydrophobic particles are recovered from a slurry, the recovery of oil sands, and the stripping of gases from effluent by absorption into the liquid phase.
- 2. Low interphase slip velocity.** The slip velocity between gas and liquid phases is the absolute velocity of the liquid phase relative to the gas phase, and this is typically much smaller in a foam than in a bubbly gas–liquid mixture. This is because the large specific surface area is able to impart a relatively large amount of shear stress on the liquid phase, thereby limiting the relative slip velocity between phases. A high contact time between gas and liquid phases can be engendered, which can also enhance the amount of mass transfer from liquid to gas, gas to liquid, or liquid to interface.
- 3. Large expansion ratio.** Because the volumetric liquid fraction of a foam can be very low, the expansion ratio (i.e. the quotient of total volume and the volume of liquid used to create that foam) can be very high. This property is harnessed in the use of the material for fighting fires and to displace hydrocarbons from reservoirs.

**4. A finite yield stress.** Because gas–liquid foams can support a finite shear stress before exhibiting strain, they are very effective for use in delivering active agents contained in liquids in household and personal care products (such as bathroom cleaner and shaving foam), as well as in topical pharmaceutical treatments.

Thus, the geometrical, hydrodynamical and rheological properties of gas–liquid foam can be harnessed to make it a uniquely versatile multiphase mixture for a variety of process applications and product designs. It is therefore a material that is of broad interest to chemical engineers.

However, these physical properties of gas–liquid foam are determined by the underlying physics of the material. The rheology of foam is dependent upon, *inter alia*, the liquid fraction in the foam, which is in turn dependent of the rate of liquid drainage. This is a function of the rate at which bubbles coalesce and how the bubble size distribution evolves because of inter-bubble gas diffusion. The performance of a froth flotation column is dependent upon the stability of the foam, but the very attachment of particles to interfaces can have a profound influence upon this stability. In fact, the underlying physical processes that dictate the performance of a foam in a process or product application are generally highly interdependent.

It is precisely because of this interdependency, and how the interdependent fundamental physical processes impact upon the applications of foam, that it is hoped that this volume will have utility, for it seems axiomatic that those motivated by applications of foam would need to know about the underlying physics, and *vice versa*.

## 1.2 Content of This Volume

This volume is split into two major sections, within which the chapters broadly:

1. Give a treatment of one or another aspect of the **fundamental** physical nature or behaviour of gas–liquid foam
2. Consider a process or product **application** of foam

The first part provides a chapter in which the topology of gas–liquid foam is described followed by expositions of how this can change through liquid drainage, inter-bubble gas diffusion and coalescence, although these processes are highly mutually interdependent. Further, there are chapters on the rheology of foam and how particles can enhance stability, since these topics are rooted in fundamental physics, but have an important impact upon applications of foam. There is a chapter on the hydrodynamics of pneumatic foam, which underpins the processes of froth flotation, foam fractionation and gas–liquid mass transfer, and one on the formation and stability of non-aqueous foams. Finally in the ‘Fundamentals’ section there is a chapter on ‘Suprafroth’, which is a novel class of magnetic froth in which coarsening is promoted by the application of a magnetic field and therefore is reversible.

In the second part, ‘Applications’, there are chapters on processes and products that exploit the properties of foam. Froth flotation, foam fractionation and foam gas absorption are unit operations for different types of separation processes that rely upon pneumatic gas–liquid foam for their operation, and each is treated in an individual chapter. In addition

there is a dedicated chapter on the flotation of oil sands because the technical challenges of this process are dissimilar to those of phase froth flotation of minerals and coal and because the supply of hydrocarbon resources from this source is likely to become increasingly important over the next century. However, foams also find utility in the enhanced recovery from oil reservoirs and this is described in a chapter. Foams manifest in a variety of manufacturing processes, and there is a description of foam behaviour and control in the production of glass. One of the most common applications of foam is in firefighting, as is discussed in a dedicated chapter. There is an important chapter on the creation and application of foams in consumer products; such products are typically of high added-value and therefore this field is rich with opportunities for innovation and development. Finally, a chapter on blast-mitigation using foam is given.

### 1.3 A Personal View of Collaboration in Foam Research

I had been doing postdoctoral work in the UK into multiphase flow through subsea oil flowlines when, in 2002, I travelled to Newcastle, Australia, to commence research on froth flotation of coal. I confess to not knowing what flotation was, but when I was travelling to work by train on my first morning I saw a coal train pass that seemed to be at least one mile long, so I thought it must be a field worthy of engagement. I had never considered foams beyond those encountered in domestic life.

However, once in Australia, it soon became clear to me that there was nothing specific for me to do, so I was left to my own devices from the outset. I inherited a pneumatic foam column that lived in a dingy dark-room, and for six months I would go there each morning and watch foam rise up a column and collect the overflow in a bucket. When it got too hot, I went to the excellent and well-air-conditioned library to read about foam drainage. I especially remember reading articles on drainage of Denis Weaire's (co-author of Chapter 2 herein) group from Trinity College Dublin, and the work that Stephan Koehler (author of Chapter 3) carried out at Harvard. Despite having had a relatively rigorous education in a good chemical engineering department, I felt totally out of my depth when trying to get to grips with this work. I'd come across vector notation as an undergraduate, but it still daunted me. One afternoon I read the words 'self-similar ansatz', and immediately retired for the day. During this time, I shared an office with Noel Lambert (joint author of Chapter 11), now Chief Process Engineer of CleanProTech, who would come into the office coated in coal dust and issue instructions down the telephone to organise the next day's flotation plant trials. I found the mathematical approach of Denis and Stephan difficult to comprehend, but Noel's world was completely alien to me. And yet we were all working on one or another aspect of foam.

I learnt enough from Noel to realise that flotation was an incredibly physically complicated process and that plant experience was of paramount importance when trying to improve and innovate. In this context, methods that claimed to be able to simulate the entire flotation process by numerical solutions of sets of equations based upon oversimplified physics seemed particularly contrived. Similarly, there was a plethora of dimensionally inconsistent data fits in the flotation literature that were by their very nature only relevant to the experiments from which they were developed, but upon which general predictive capability was claimed. It is not surprising that some physicists appear to view some work of engineers with caution.

#### **4** *Foam Engineering*

However, it was a chemical engineer who, arguably, was the first researcher to make significant process in both the fundamental science of gas–liquid foam and the process applications. Among his many achievements, Robert Lemlich of the University of Cincinnati proposed what is often now known as the ‘channel-dominated foam drainage model’, and he used this to propose a preliminary mechanistic model for the process of foam fractionation. Thus, the desire for a better understanding of a process technology for the separation of surface-active molecules from aqueous solution was the driver for the development of what some regard as the ‘standard model’ of foam drainage. Robert Lemlich’s career was characterised by trying to describe and innovate process technologies that harnessed foam by building a better understanding of the underlying physics. Lemlich’s contributions, which are often not given the credit that they deserve, demonstrate the value of a combined approach of physical understanding and practical application. Lemlich, and his co-workers, were able to effect these developments within their own research group. Those of us who do not possess Lemlich’s skill and insight may not be able to make similar progress single-handedly, but can still benefit from cross-disciplinary collaboration to achieve similar goals.

As a chemical engineer working on the fundamentals of gas–liquid foam and its process applications, I have collaborated with physicists and have found that the biggest impediments to interdisciplinary research in foam are caused by semantic problems. For example, as a former student of chemical engineering, I learnt about Wallis’s models of one-dimensional two-phase flow, and I therefore frequently invoke the concept of a ‘superficial velocity’ (i.e. the volumetric flowrate of a particular phase divided by the cross-sectional area of the pipe or channel). However, I have discovered that this is not a term universally known by the scientific community, and its use by me has caused some consternation in the past. Equally, I am quite sure that I have inadvertently disregarded research studies because I have failed to understand the language and methods correctly. However, I have recently found that perseverance, an open mind and a willingness to ask and to answer what may superficially appear to be trivial questions can overcome some difficulties.

The contributors to this volume may be from differing disciplines of science and engineering, but all are leading experts in their fields and all are active in developing the science and technology of foam fundamentals and applications. It is very much hoped that, in bringing together this diverse cohort of authors into a single volume, genuine cross-disciplinary research will be stimulated that can effectively address problems in the fundamental nature of gas–liquid foam as well as innovate new processes that can harness its unique properties. In addition, it is anticipated that engineering practitioners who design products and processes that rely on gas–liquid foam will benefit from gaining an insight into the physics of the material.

# **Part I**

## Fundamentals

# 2

## Foam Morphology

*Denis Weaire, Steven T. Tobin, Aaron J. Meagher and Stefan Hutzler*

### 2.1 Introduction

When bubbles congregate together to form a foam, they create fascinating structures that change and evolve as they age [1], are deformed [2], or lose liquid [3]. Foams are usually disordered mixtures of bubbles of many sizes, but they may also be monodisperse, in which case ordered structures may also be found. They may be relatively wet or dry, i.e. contain a greater or lesser amount of liquid.

While the familiar foams of industry and everyday life are three-dimensional, laboratory experiments create two-dimensional foams of various kinds, offering attractive possibilities of easy experiments, computer simulations and visualizations, and more elementary theory. One form of 2D foam consists of a thin sandwich of bubbles between two glass plates. Let us begin with the 3D case, recognizing its greater practical importance.

### 2.2 Basic Rules of Foam Morphology

#### 2.2.1 Foams, Wet and Dry

Foams may be classified as dry or wet according to liquid content, which may be represented by liquid volume fraction  $\phi$ . This ranges from much less than 1% to about 30%. Engineers call the gas fraction (i.e.  $1 - \phi$ ) the *foam quality*. Foams used in firefighting are classified by their *expansion ratio*, which is defined by  $\phi^{-1}$ . At each extreme (the dry and wet limits)

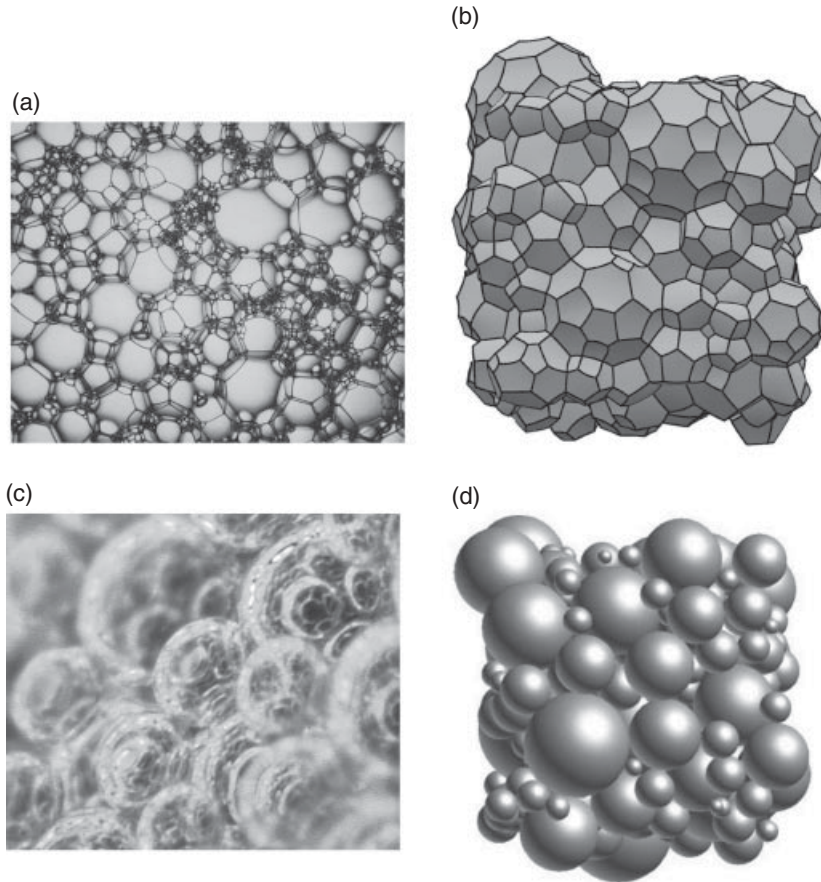


**Fig. 2.1** Shown are examples of 3D dry and wet foams, as obtained from experiment (a and c) and computer simulations (b and d). Typical 3D foams are polydisperse, consisting of bubbles of many different sizes. (a) Reproduced with kind permission of M. Boran. (d) Reproduced with permission from Wiley-VCH Verlag GmbH & Co. KGaA. (b) and (d) are simulations carried out by A. Kraynik [4].

the bubbles come together to form a structure which resembles one of the classic idealized paradigms of nature's morphology: the division of space into cells in the dry limit and the close-packing of spheres in the wet limit (see Fig. 2.1).

Bubble size is important in determining which picture is more relevant in equilibrium under gravity. If the average bubble diameter is less than the capillary length  $l_0$ , defined as

$$l_0^2 = \frac{\gamma}{\Delta\rho g} \quad (2.1)$$

where  $\gamma$  is the surface tension of the liquid,  $g$  is acceleration due to gravity and  $\Delta\rho$  is the density difference of the gas and liquid, a thin layer of foam consisting of small bubbles will be wet (i.e. have a liquid fraction larger than about 20%). Larger bubbles in equilibrium under gravity form a dry foam.

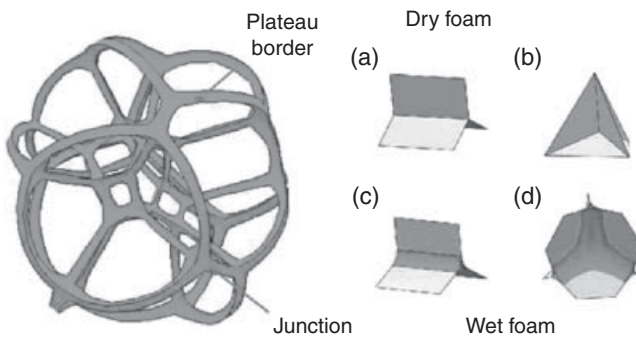


**Fig. 2.2** Plateau's rules of equilibrium require tetrahedral junctions for dry foams. They are prevalent for small values of liquid fraction, but wet foams can contain junctions of more than four edges (or six cells) [7].

### 2.2.2 The Dry Limit

In the dry limit the soap films that constitute the interface between bubbles may be idealized as infinitesimally thin curved surfaces, which are generally not simply spherical. These surfaces constitute the faces of polyhedral cells. Many varieties of polyhedra are found in equilibrated dry foams, as enumerated, for example, in the classic observations of Matzke [5] (see Fig. 2.21). But they are subject to important geometrical and topological restrictions, first stated by Plateau [6],<sup>1</sup> foam morphologist *par excellence*. His rules, illustrated in Fig. 2.2, are as follows.

- Faces (films) must meet three at a time. The angles at which they meet must everywhere be 120 degrees, so that three cells are joined symmetrically at a cell edge.
- Edges must meet four at a time. The angles between edges are  $\arccos(-1/3) \approx 109.43$  degrees, the Maraldi angle, where six cells meet symmetrically at every corner.

It may seem intuitively reasonable that such rules follow somehow from local equilibrium of surface tension forces at the points in question. In part this is indeed true, but it is not obvious upon naive consideration why conjunctions of more than six cells are not possible. Plateau observed only tetrahedral junctions in the soap film configurations that he created in wire frames; in due course a colleague, Lamarle [8], supplied a very longwinded mathematical proof. We still await something more expeditious. Taylor [9] has provided a more refined and rigorous modern proof, but it is even less transparent.

Returning to the surfaces that constitute the cell faces, there is a further rule, well known as the Laplace–Young law in the general context of fluid interfaces. It expresses the balance of forces on a small element of soap film in terms of a pressure difference  $\Delta p$ ,

$$\Delta p = \frac{4\gamma}{r} \quad (2.2)$$

<sup>1</sup>Both the original text and an English translation of the work may be found at <http://www.susqu.edu/brakke/PlateauBook/PlateauBook.html>



**Fig. 2.3** A photograph of the surface of a foam. The curvatures of the films are made visible by the reflections of light on the surface.

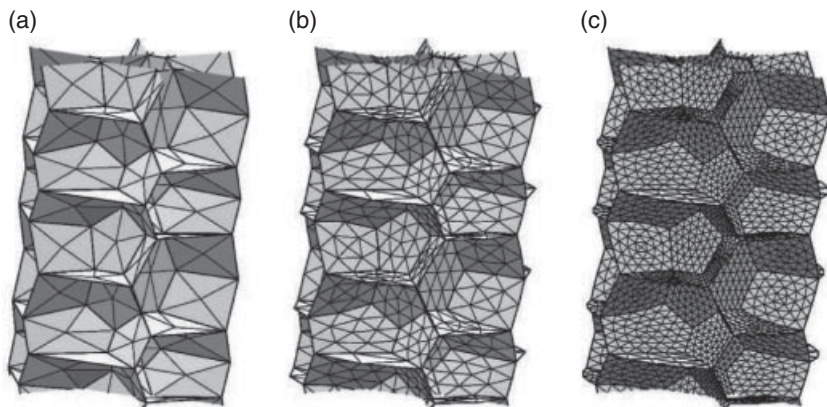


**Fig. 2.4** Simulations of foams are usually carried out with K. Brakke's Surface Evolver [10]. This software approximates surfaces with a triangulated mesh or tessellation. This mesh can be refined (i.e. the number of triangles used can be increased) to improve the accuracy of the approximation. (a) to (c) show the same surfaces as the refinement of the tessellation is increased. Note how the curvature of the surfaces becomes much smoother.

Here  $\gamma$  is surface tension and  $r$  is the mean radius of curvature. It is related to the two principal radii of curvature,  $R_1$  and  $R_2$ , by the expression

$$\frac{1}{r} = \frac{1}{2} \left( \frac{1}{R_1} + \frac{1}{R_2} \right) \quad (2.3)$$

In the general case  $R_1$  differs from  $R_2$ ; for the case of a sphere  $R_1 = R_2$ .

The surface is therefore free to have a complicated form, difficult to formulate mathematically; see Fig. 2.3. It is for this reason that almost all detailed descriptions of

dry foam structures are numerical in character, consisting of some sort of tessellation, as shown in Fig. 2.4. In modern times they are usually carried out with the freely available Surface Evolver software of Ken Brakke [10].<sup>2</sup>

### 2.2.3 The Wet Limit

In the wet limit, the bubbles are spherical (see Fig. 2.1c, d). There are some restrictions on the possibilities for such a packing of hard spheres, familiar in the idealized models used in the field of granular materials. Each sphere must be in contact with at least three others (with the rare exception of ‘rattlers’, small spheres trapped in large cages). The average number of these contacts is six in disordered packings. The latter result, from the elementary theory of mechanical constraints that was originated by James Clerk Maxwell, is not to be considered exact, but is generally valid in practice (at least approximately).

### 2.2.4 Between the Two Limits

A real foam must lie somewhere between these two idealized limiting cases. Let us start from the dry end, first considering the addition of an amount of liquid that is large enough that we may still neglect the liquid content of the films, but nevertheless still close to the dry limit. The liquid occupies the interstitial space associated with the cell edges. These swell to form what are called Plateau borders.

For a small enough liquid fraction, Plateau’s rules should still apply in some approximate sense. They are progressively violated as the liquid fraction is increased, and our understanding of this intermediate regime is limited. Progressing towards the wet limit we reach a regime in which the cells are slightly deformed spheres, but these are not easy to describe, other than by simulation or rather over-idealized models. For example, the bubbles are sometimes represented by overlapping spheres [4] (or circles in 2D [11]).

## 2.3 Two-dimensional Foams

The merits of the much simpler 2D foam may now be obvious. Its structure may be modelled using only circular arcs, with curvatures consistent with local gas and liquid pressures. It was C.S. Smith [12] who did most to promote this system as an object of study, although many before him, including Lord Kelvin, had occasional recourse to it.

### 2.3.1 The Dry Limit in 2D

In the dry limit the 2D foam consists of polygonal cells, as in Fig. 2.5. Since the vertices can only be threefold (a Plateau condition), it follows easily that the average number of sides of a cell is exactly six (Euler’s theorem) [13].

---

<sup>2</sup><http://www.susqu.edu/brakke/>

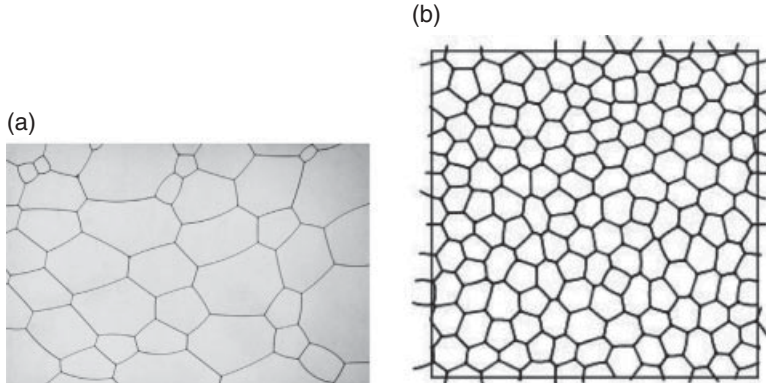


**Fig. 2.5** Examples of experimental and simulation images of 2D dry foam. Recently there has been renewed interest in experiments with various types of 2D foam, in particular with regard to their rheological properties [14–17].

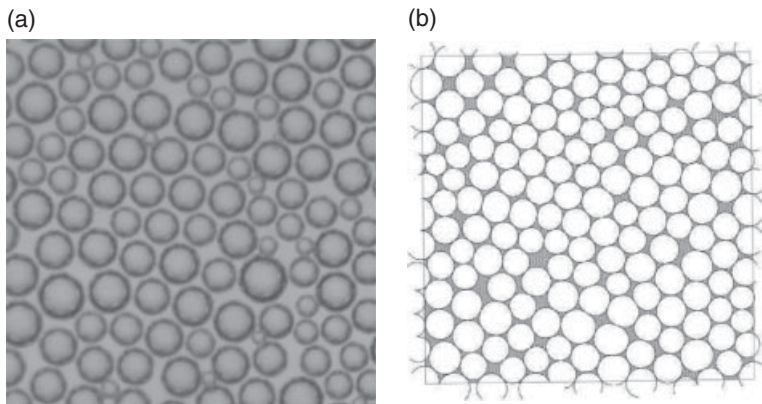


**Fig. 2.6** Examples of experimental and simulation images of a 2D wet foam. In contrast to the dry system shown in Fig. 2.5, the Plateau borders between bubbles can touch four or more bubbles. As with Fig. 2.5(b), the simulation was carried out with the PLAT [18] software, and includes periodic boundary conditions.

### 2.3.2 The Wet Limit in 2D

In the wet limit, the cells are touching circular disks, as shown in Fig. 2.6. Just as in the 3D case, we make contact with close-packed structures and hence with the theory of granular materials [19]. Bubbles, the epitome of soft particles, become effectively hard particles in this limit.

### 2.3.3 Between the Two Limits in 2D

As in 3D, it is not so obvious what happens in the intermediate regime, as Plateau's requirement of threefold vertices is relaxed, so that stable vertices (in reality liquid-filled junctions) of higher order can appear, as shown in Figs 2.7 and 2.8.

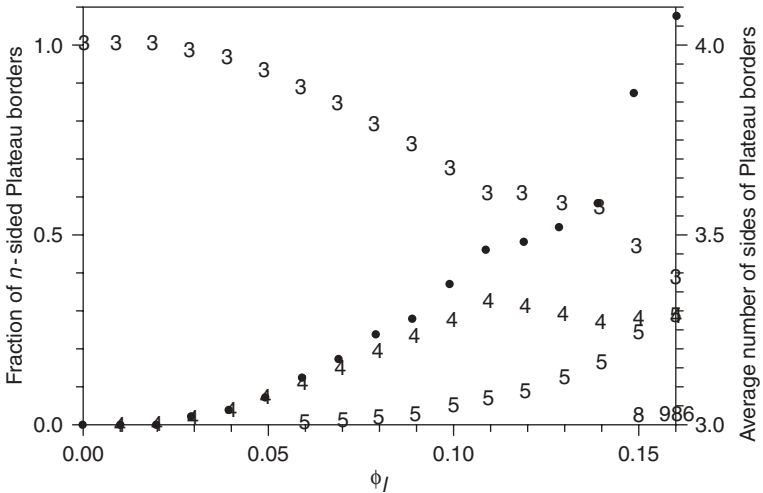


**Fig. 2.7** In a 2D foam the fraction of  $n$ -sided Plateau borders (left  $y$ -axis) varies with liquid fraction  $\phi$ . In the dry case (i.e.  $\phi = 0$ ) all Plateau borders have three sides. As  $\phi$  is increased, the fraction of Plateau borders with four sides begins to increase, and eventually five and more sided Plateau borders begin to appear. The dots represent the average number of sides of Plateau borders (right scale).

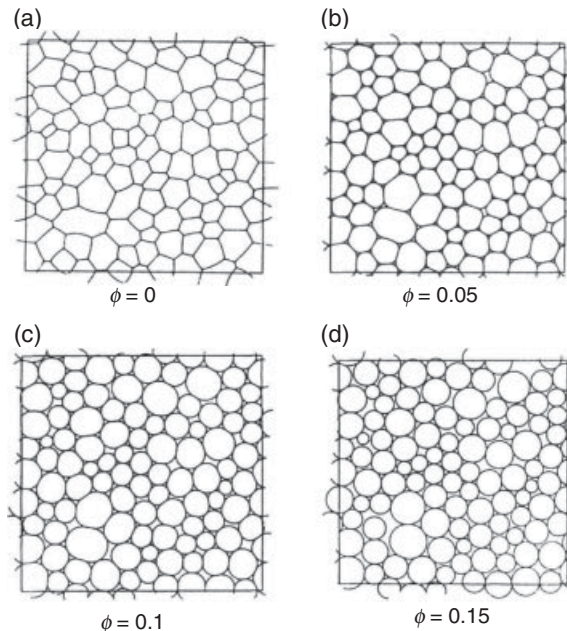


**Fig. 2.8** Examples of 2D foams with varying liquid fraction  $\phi$ . The average number of contact per cell is seen to vary smoothly from six (for dry foams) to four (for wet foams). These images result from early computer simulations, demonstrating the rigidity loss of the foam at  $\phi \approx 0.16$  [20] (the structure loses mechanical stability as the bubbles come apart at this value of  $\phi$ ).

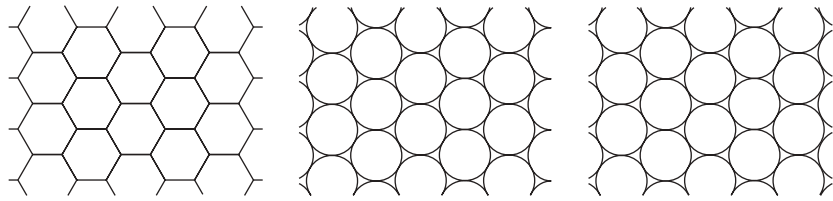


**Fig. 2.9** Simulation of 2D hexagonal foam with liquid fraction increasing from left to right (simulations carried out with the PLAT software) [18, 21, 24]. The dry (leftmost) honeycomb is the structure that optimally partitions 2D space. Note that for the honeycomb, the average contact number remains six even as  $\phi$  is varied, in contrast to the 2D foam shown in Fig. 2.8.

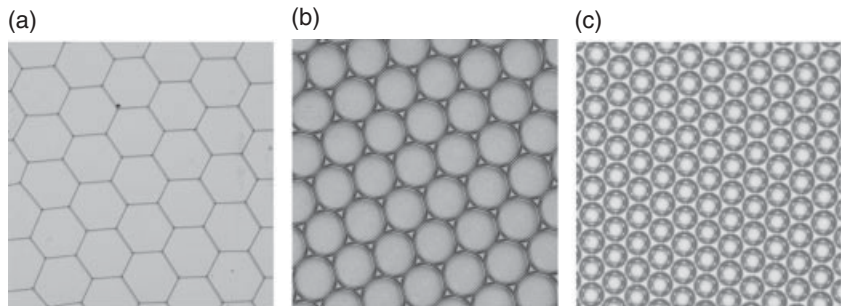


**Fig. 2.10** Experimental packing of bubbles into the honeycomb configuration for the case of a dry foam, an intermediate foam and the wet case (the dry foam is confined between two glass plates, while the intermediate and wet cases are free-floating Bragg rafts). This progression is approximately equivalent to that shown for the simulations in Fig. 2.9. Note that in the wet (rightmost) case the bubbles appear separated due to an optical effect.

The following relation connects the average number  $z$  of sides of Plateau borders with the average number  $n$  of sides (i.e. films) of the cells.

$$n = \frac{2z}{z - 2} \quad (2.4)$$

As seen in Figs 2.7 and 2.8, these quantities vary continuously over the full range of  $\phi$  in the case of a typical disordered foam. Contrast this behaviour with that of the ordered honeycomb (see Figs 2.9 and 2.10) for which there is no such variation ( $z = 3$ ,  $n = 6$ ). For this reason, early models of the mechanical properties of foams (which were based on the honeycomb) were misleading.

For liquid fractions small enough that no such higher order vertices appear, a useful theorem is available. The Decoration Theorem [21] states that such a 2D foam has a skeleton that is a dry foam in equilibrium, whose vertices may be decorated with Plateau borders to recover exactly the original structure.

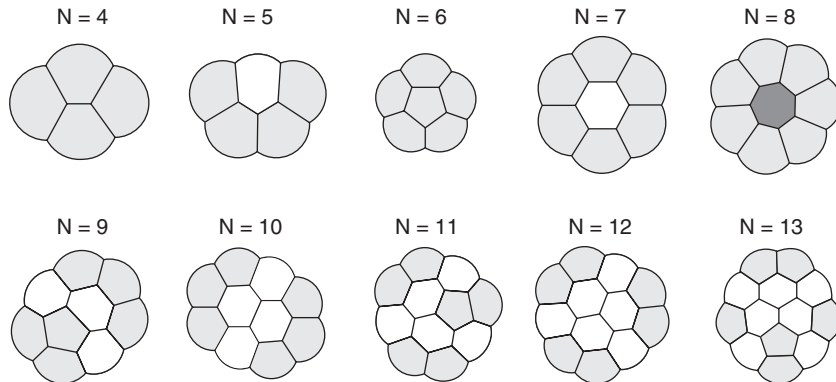


**Fig. 2.11** Examples of 2D finite clusters for varying numbers of bubbles. Each cluster has minimal perimeter length (equivalent to surface area of a 3D foam). Such calculations were carried out for clusters with up to 200 bubbles [26]. The authors would like to thank S. Cox for providing the above figure.

## 2.4 Ordered Foams

### 2.4.1 Two Dimensions

#### 2.4.1.1 The 2D Honeycomb Structure

The paragon of perfection of foam structure is surely the 2D hexagonal honeycomb (see Fig. 2.9, leftmost). It may be made by trapping monodisperse bubbles between two glass plates (see Fig. 2.10 for examples). It has been presumed for centuries that this structure minimizes line length (for given bubble size). The proof of this was a long time in coming [22, 23]; it is nevertheless elementary. Plateau borders may be added, the Decoration Theorem being entirely trivial in this case, up to the point where the bubbles form touching circles – the wet limit. See Fig. 2.9.

#### 2.4.1.2 2D Dry Cluster

Finite 2D clusters display an interesting sequence of minimal structures (see Fig. 2.11), and have been studied both experimentally and in simulations in recent years [25, 26].

#### 2.4.1.3 2D Confinement

Ordered 2D foams confined in narrow channels are of particular importance to what has been termed *discrete microfluidics* [27, 28]. Here, trains of bubbles are pushed through networks of channels, the design of which allows for a number of tightly controlled manipulations. Fig. 2.12 shows how neighbouring bubbles may be separated in a simple U-bend; other geometries allow for the controlled injection of bubbles into a moving train, or the separation of a double row of bubbles into two single rows. Dynamic simulation methods are on hand to help interpretation of such processes [27].

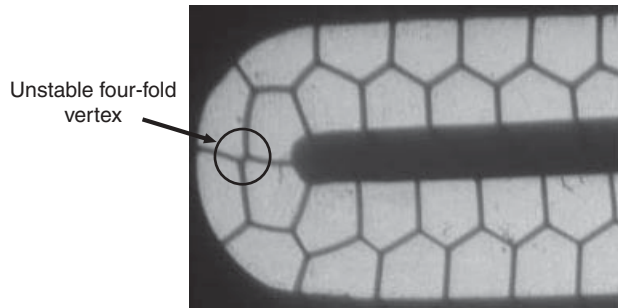


**Fig. 2.12** Example of a 2D dry foam in a U-bend. The foam is being pushed through the tube. Note the (temporary) formation of an unstable fourfold vertex occurring in the bubbles in the U-bend. This leads to a topological T1 or neighbour-switching, which is discussed in Section 2.7.

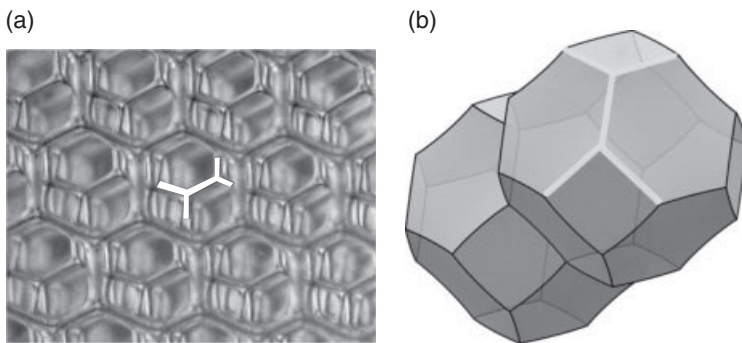


**Fig. 2.13** Experimental and simulated examples of a 3D crystalline dry foam. The simulation image is two cells of a bulk Kelvin foam (Lord Kelvin's conjectured space-partitioning structure). The experimental structure contains this bulk Kelvin structure, but the bubbles in contact with the walls are deformed.

## 2.4.2 Three Dimensions

### 2.4.2.1 3D Dry Foam

What is the counterpart of the honeycomb in 3D; that is, how can we partition space into cells of equal volume and minimum area? This question was first asked by Lord Kelvin in 1887 [29]. His conjectured answer consisted of identical cells in a body-centred cubic arrangement, as shown in Fig. 2.13. After a hundred years of consideration of this proposition, Weaire and Phelan computed a structure of lower surface area [30, 31]. This structure is shown in Fig. 2.14.

This remains the undisputed, but rigorously unconfirmed, champion. It has proven practically impossible to create experimentally, while Kelvin's simpler structure can be made in various ways.

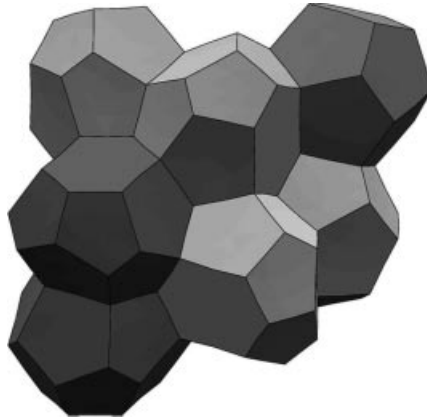


**Fig. 2.14** A simulation of the Weaire–Phelan structure. The structure consists of two different (but equal-volume) bubble types: an irregular dodecahedron with pentagonal faces, and a tetrakaidecahedron with two hexagonal faces and twelve pentagonal faces (All pentagonal faces are slightly curved). The structure achieves a surface area 0.3% less than the Kelvin structure. Although the Weaire–Phelan structure has not been mathematically proven to be optimal, no better structure has yet been found.

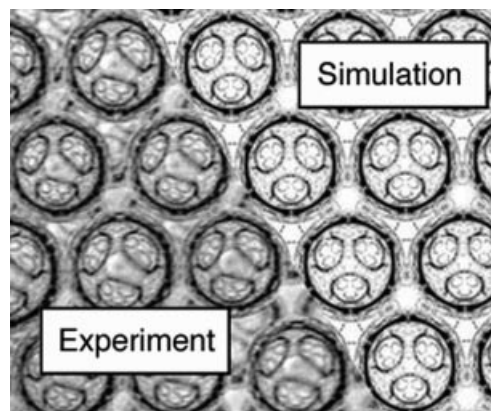


**Fig. 2.15** Comparison between an experimental crystalline wet foam (left) and a simulation (right). The simulation involved the application of ray-tracing to the fcc arrangement of glass spheres [33].

#### 2.4.2.2 3D Wet Foam

In the wet limit a 3D monodisperse foam should form a close packing of spherical bubbles, with no obvious discrimination between fcc and other possibilities. It was first observed by Bragg and Nye [32] that wet foams of small bubbles do in fact readily crystallize, perhaps too readily for our understanding. Experiments [33] suggest that the fcc structure predominates; see Fig. 2.15. Recent X-ray tomography experiments [34] have shown that ordering might be restricted to the bubble layers close to confining boundaries of the sample (Fig. 2.16), but further experiments are required to settle the issue.

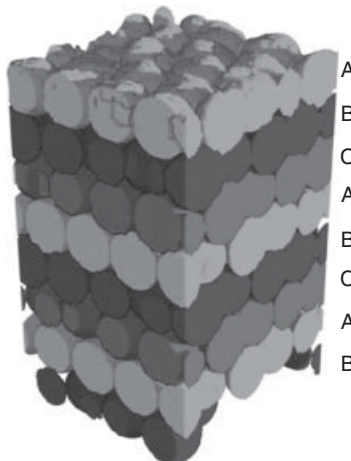


**Fig. 2.16** X-ray tomographic image of an ordered microfoam showing the ABC arrangement of bubbles associated with fcc crystallization. The image shows the foam as it has ordered between a flat surface (top) and a liquid interface (bottom). On increasing the number of layers in such a sample, it is found that fcc crystallization no longer extends through the bulk [34] (see Section 2.5).

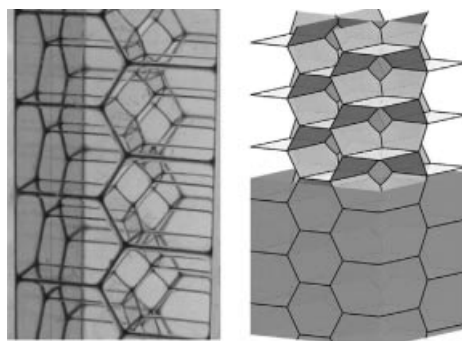


**Fig. 2.17** A comparison between experimental imagery and simulation for a dry structure, confined in a tube with square cross-section. The structure has six bubbles in its unit cell. The simulation image on the right is rotated 90 degrees about the vertical compared to the photograph on the right.

Again, the scenario is more complicated and largely unexplored between the two extremes of wet and dry. The ‘phase diagram’ of monodisperse foam is still unknown.

#### 2.4.2.3 Ordered Columnar Foams

We have seen that 2D confinement induces ordering. The same is true of confinement in a narrow column or channel. The structural variations observed as the column width is changed are fascinating [35–38], and have taken on some practical importance in microfluidics and other contexts. Examples are shown in Figs 2.17, 2.18 and 2.19.

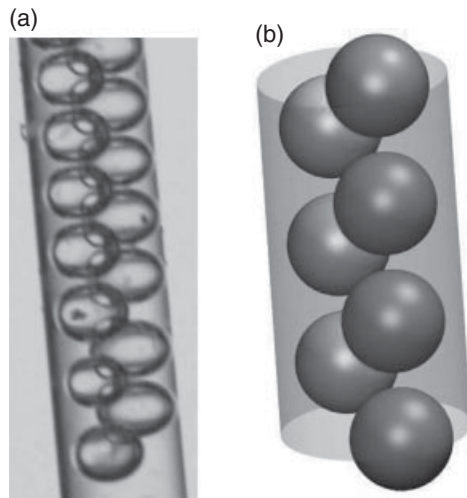


**Fig. 2.18** Example of experimental and simulation images for an ordered wet foam confined in a cylinder. Bubbles of size 0.5 mm are seen to order in the same configuration as predicted by simulations of the packing of hard spheres in a similar cylindrical confinement [39].

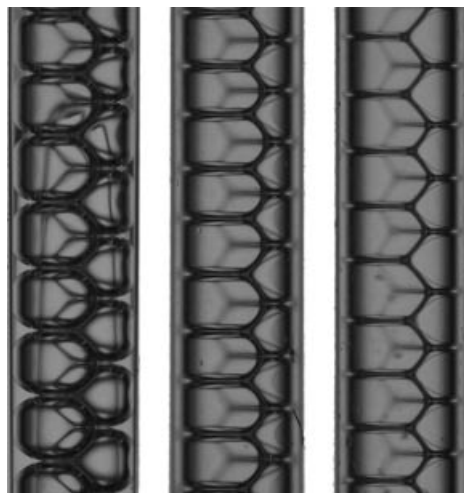


**Fig. 2.19** A progression from a wet to a dry foam (left to right), demonstrated for a simple ordered foam structure with only two bubbles in the periodic cell. The tube diameter is roughly 1 mm.

## 2.5 Disordered Foams

Only specially prepared laboratory foams are monodisperse, and hence perhaps ordered; see Figs 2.15–2.19. However, monodispersity does not guarantee order. X-ray tomography of the interior of large foam samples (20,000 bubbles) show that the bubbles are

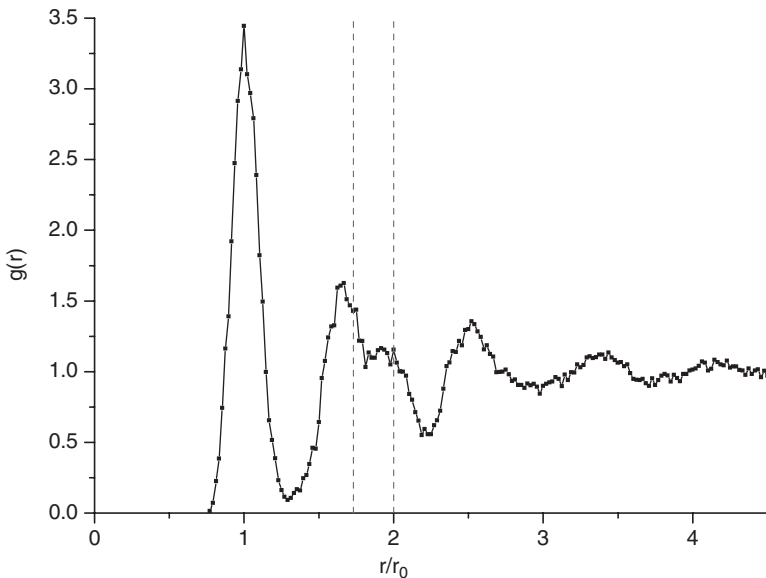


**Fig. 2.20** Radial distribution function  $g(r)$  – a measure of local arrangements within a sample – calculated for the bulk of a monodisperse foam composed of 20,000 bubbles of diameter  $800\text{ }\mu\text{m} \pm 40$  [34]. The distribution exhibits a split second peak at values of  $r/r_0 = \sqrt{2}$  and 2 (shown with dashed vertical lines), but  $g(r)$  quickly approaches one, corresponding to the absence of long-range order [40].

random-closed-packed, featuring the characteristic radial distribution function of the Bernal packing of hard spheres, first investigated by Bernal in his study of the structure of liquids, see Fig. 2.20 [40].

Generally, foams made by ordinary methods (e.g. shaking, sparging or gas evolution) consist of a wide range of bubbles sizes as shown in Fig. 2.1, and are *inevitably* disordered. Their morphology is necessarily a matter of statistics with a number of interesting regularities emerging [13].

## 2.6 Statistics of 3D Foams

The description of disordered foams is framed in terms of averages and distributions. They may firstly be characterized by the distribution  $p(V)$  or  $p(A)$  of cell sizes (in 3D, the cell volume  $V$ , in 2D the cell area  $A$ ).

A second characteristic is the distribution  $p(n)$  of the number of faces belonging to each cell, or of sides (edges) in two dimensions. This can vary according to the preparation and treatment of the sample, even though the size distribution is unaltered. In 2D its mean (for an infinite sample) is exactly six for dry foam, by Euler's theorem, and its second moment  $\mu_2$  is a traditional measure of (topological) disorder. One may also define a second moment for  $p(V)$  or  $p(A)$ , which may be used as the measure of polydispersity. Often  $\mu_2$  is of order unity, but its value depends on how the foam was prepared and its subsequent history.



**Fig. 2.21** Some exemplary polyhedral cells with 12, 13, and 16 faces, as identified by Matzke in 1946 in a disordered foam [5]. Matzke's findings have recently been reproduced in a study by Kraynik et al. [43], which identified all 36 of his reported polyhedra in a monodisperse foam sample that was produced using computer simulations. Images courtesy of R. Gabbielli, created with 3dt software.

There is no corresponding exact result for the mean number of faces  $N$  in the 3D case, although it is commonly found to lie between 13 and 14. An interesting hypothetical design for the ideal 3D cell has flat faces and obeys Plateau's rules: it would comprise 13.39 faces [42] so it cannot, of course, be realized. Nevertheless this mathematical chimera has played a role in thinking about 3D foam cells, and the Kelvin problem in particular.

In an early experimental study of monodisperse disordered foam comprising 600 bulk bubbles [5] (see Fig. 2.21), Matzke obtained  $N \approx 13.70$ , which is very close to the hypothetical value above. Matzke's result was confirmed by computer simulations involving up to 1000 bubbles [43].

## 2.7 Structures in Transition: Instabilities and Topological Changes

The topological structure of a foam can be characterized precisely in terms of the construction of its cells in terms of discrete elements (faces, edges, etc.), and this will usually not be changed by a small perturbation. However, when it is varied (e.g. by an imposed strain), it may be brought to a configuration in which there is a violation of Plateau's rules by the introduction of a forbidden vertex. This dissociates rapidly and a new structure is formed.

In 2D, the possibilities are rather simple: the so-called T1 process eliminates a fourfold vertex and forms two threefold ones, as shown in Fig. 2.22.

In 3D, the most elementary possibility involves the disappearance of a triangular face or the inverse process in which a line (Plateau border) is reduced to zero length, see Fig. 2.23. But in reality, the disappearance of one triangle generally causes a neighbouring triangle to vanish too. Indeed, topological changes often come in cascades, particularly for wet foams [44, 45]. The details of their dynamics are still under investigation [46, 47].

For both dry and wet foams the processes of phase change in ordered foams (for example, from bcc to fcc) are largely unexplored. This may be of little direct importance, but the close analogy with some metallurgical phase transformations should add interest.

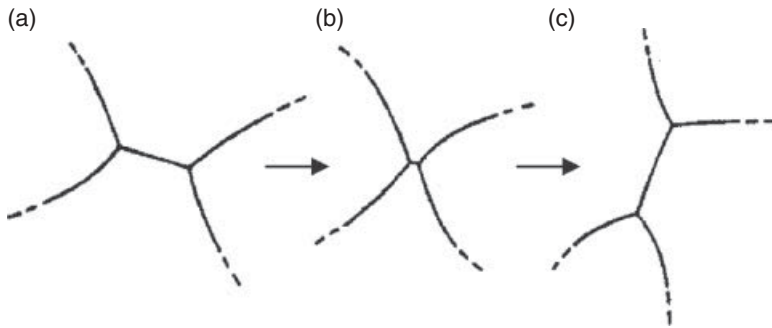


**Fig. 2.22** Rearrangement in 2D foam. If conditions are varied in such a way that the length of one of the cell sides goes to zero resulting in a fourfold vertex, we necessarily encounter an instability and the system jumps to a different configuration that is in accord with Plateau's rules. This is called the 'T1 process' or neighbour-swapping event.

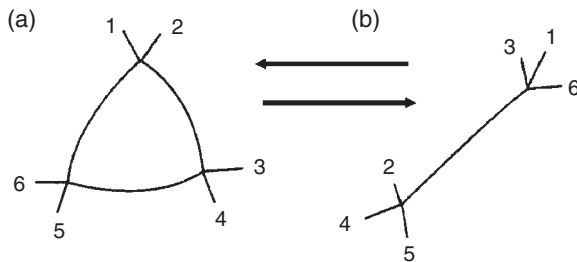


**Fig. 2.23** A T1 event in 3D involves the shrinkage and disappearance of a triangular face, followed by the formation of a Plateau border (or the reverse process).

## 2.8 Other Types of Foams

### 2.8.1 Emulsions

While microemulsions may bring into play additional forces, emulsions which have droplets with diameter on the order of  $100\text{ }\mu\text{m}$  or more are closely analogous to foams (see the example shown in Fig. 2.24). All of the above applies, except that close matching of the densities of the two constituent liquids is possible. It follows that the emulsion is likely to be 'wet' if there is an excess of the continuous phase lying below or above it. That is, the droplets will be nearly spherical. By ensuring that there is less of the continuous phase, a dry emulsion of polyhedral cells may be prepared.

### 2.8.2 Biological Cells

Ever since the microscope was first applied to biological tissue, its foam-like cellular nature has been generally evident. As part of his eloquent case for the introduction of mathematics

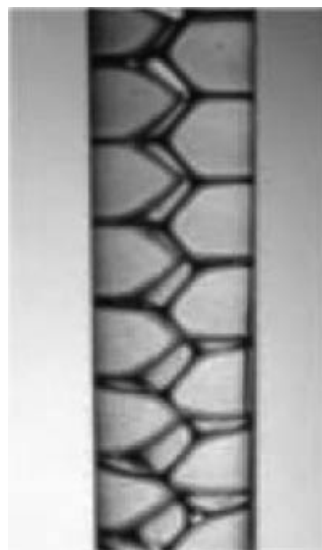


**Fig. 2.24** An example of a monodisperse ordered emulsion of silicone oil in water [48]. Note that this structure is the same as that displayed in Fig. 2.19 for monodisperse foam.

into biological morphology and morphogenesis, D'Arcy Wentworth Thompson envisaged a theory that was based on surface tension [50, 51]. Succeeding generations of biologists were at first intrigued by this notion, and sought to find Kelvin cells in particular. They are prevalent only in epithelial layers, so scepticism prevailed [5, 51].

Today Thompson's vision is enjoying a revival, as attempts are made to frame models of cell arrangements that are based largely on surface tension [52].

Is this a real (i.e. physical) surface tension, or do more biological principles somehow mimic its effects? Remarkably, evidence is at last appearing for the role of the physical force. Of course there will be complications, but it seems that the insights gained from foam physics will extend into biological science and medicine at this level.

### 2.8.3 Solid Foams

Solid foams generally have a solidifying liquid foam as a precursor. The solidification may occur due to a change in temperature, as is the case for metal foams, which may be formed by foaming a liquid melt, followed by rapid cooling [53, 54].

An interesting recent development is the formation of threads of hydrogel polymer with a crystalline cellular structure [55]. In this case, air and two different chemical solutions (one containing monomers, cross-linker, an accelerator, a surfactant, and water; the other only the initiator, a surfactant, and water) are brought together in a flow-focusing device. As soon as the ordered liquid foam emerges, it begins to solidify due to chemical reactions between its liquid components (see Fig. 2.25 for examples).

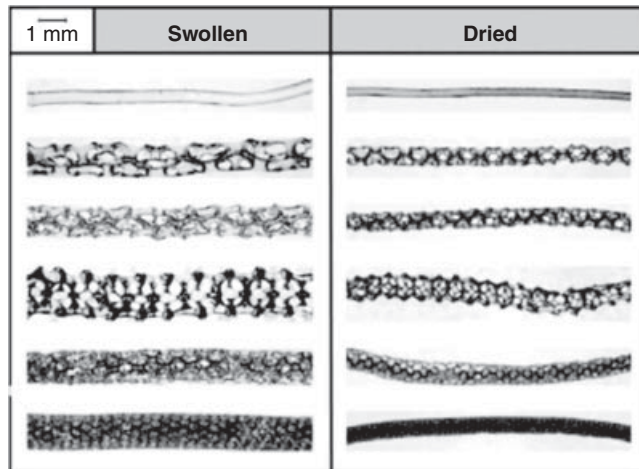


**Fig. 2.25** Examples of ordered polymerized foam threads, in both swollen and dried states. The different ordered structures are created by varying the cross-section of the tube used to confine the initially liquid foam. Drying and swelling of the structures is completely reversible [55].

## 2.9 Conclusions

We have seen that the morphology of foams presents a variety of geometrical patterns in 2D and 3D, which we can today simulate and analyse in great detail (in particular, by using the Surface Evolver).

We have not pursued the observational side of the subject. In the case of 3D foams it presents some challenges; the multiple light scattering that gives foam its white appearance obscures its interior from view.

Nevertheless, Matzke [5] was able to use stereoscopic microscopy to record the details of thousands of large 3D bubbles, half a century ago, so perhaps we have made too many excuses in that regard, at least for dry foams. But today new techniques promise much more powerful and efficient probes of morphology, including X-ray tomography and MRI. Increasingly they can even observe changing structures, opening up the role of morphology in dynamics.

That is where the cutting edge of the subject is to be found at present. The truly complex processes that underlie common phenomena of foam physics need to be understood at the local level. Modern probes and modern simulations may soon make this feasible.

## Acknowledgements

This publication has emanated from research conducted with the financial support of Science Foundation Ireland (08/RFP/MTR1083). Research supported by the European Space Agency (MAP AO-99-108:C14914/02/NL/SH and AO-99-075:C14308/00/NL/SH), the Irish Research Council for Science, Engineering & Technology (IRCSET), and the SFI SURE

Summer Undergraduate Research Experience programme. D. Weaire would like to thank the University of Hyderabad for graciously hosting him while this work was being completed.

## References

- [1] O. Pitois. Foam ripening. In *Foam Engineering: Fundamentals and Applications*, P. Stevenson (ed.). John Wiley & Sons, Ltd, Chichester, 2012, pp. 59–74, chapter 4.
- [2] N.D. Denkov, S.S. Tcholakova, R. Höhler and S. Cohen-Addad. Foam rheology. In *Foam Engineering: Fundamentals and Applications*, P. Stevenson (ed.). John Wiley & Sons, Ltd, Chichester, 2012, pp. 91–120, chapter 6.
- [3] S.A. Koehler. Foam drainage. In *Foam Engineering: Fundamentals and Applications*, P. Stevenson (ed.). John Wiley & Sons, Ltd, Chichester, 2012, pp. 27–58, chapter 3.
- [4] A. Kraynik. The structure of random foam. *Advanced Eng. Mater.*, **8**(9): 900–6, 2006.
- [5] E.B. Matzke. Volume-shape relationships in variant foams. A further study of the role of surface forces in three-dimensional cell shape determination. *Am. J. Botany*, **33**: 58, 1946.
- [6] J.A.F. Plateau. *Statique Expérimentale et Théorique des Liquides soumis aux seules Forces Moléculaires*. Gauthier-Villars, Paris, 1873.
- [7] D. Barrett, E.J. Daly, M. Dolan, S. Kelly, W. Drenckhan, D. Weaire and S. Hutzler. Taking plateau into microgravity: the formation of an eight-fold vertex in a system of soap films. *Microgravity – Sci. Tech.*, **20**: 17–22, 2008.
- [8] E.E. Lamarle. Sur la stabilité des systèmes liquides en lames minces. *Mem. Acad. R. Belg.*, **35/6**, 1864–7.
- [9] J. Taylor. The structure of singularities in soap-bubble-like and soap-film-like minimal surfaces. *Ann. Math.*, **103**: 489–539, 1976.
- [10] K.A. Brakke. The surface evolver. *Exp. Math.*, **1**: 141–65, 1992.
- [11] D.J. Durian. Bubble-scale model of foam mechanics: melting, nonlinear behavior, and avalanches. *Phys. Rev. E*, **55**: 1739–51, 1997.
- [12] C.S. Smith. The shapes of metal grains, with some other metallurgical applications of topology. *Metal Interfaces (ASM Cleveland)*, 1952.
- [13] D. Weaire and S. Hutzler. *The Physics of Foams*. Oxford University Press, Oxford, 1999.
- [14] G. Debrégeas, H. Tabuteau and J.-M. di Meglio. Deformation and flow of a two-dimensional foam under continuous shear. *Phys. Rev. Lett.*, **87**: 178305, 2001.
- [15] Y. Wang, K. Krishnan and M. Dennin. Impact of boundaries on velocity profiles in bubble rafts. *Phys. Rev. E*, **73**: 031401, 2006.
- [16] K. Krishnan and M. Dennin. Viscous shear banding in foam. *Phys. Rev. E*, **78**: 051504, 2008.
- [17] G. Katgert, M.E. Möbius, and M. van Hecke. Rate dependence and role of disorder in linearly sheared twodimensional foams. *Phys. Rev. Lett.*, **101**: 058301, 2008.
- [18] F. Bolton. Software PLAT: a computer code for simulating two-dimensional liquid foams. <http://www.tcd.ie/Physics/Foams/plat.php>, 1996.
- [19] D. Weaire, V. Lanlgois, M. Saadatfar, S. Hutzler. Foam as granular matter. *Granular and Complex Materials, World Scientific Lecture Notes in Complex Systems*, T. Aste, T. Di Matteo and A. Tordesillas (eds), **8**: 1–26, <http://www.worldscibooks.com/physics/6616.html>, 2007.
- [20] F. Bolton and D. Weaire. Rigidity loss transition in a disordered 2D froth. *Phys. Rev. Lett.*, **65**: 3449, 1990.
- [21] F. Bolton and D. Weaire. The effects of Plateau borders in the two-dimensional soap froth. I. Decoration lemma and diffusion theorem. *Phil. Mag. B*, **63**: 795–809, 1991.
- [22] T.C. Hales. The Honeycomb Conjecture. *ArXiv Mathematics e-prints*, June 1999.
- [23] T. Aste and D. Weaire. *The Pursuit of Perfect Packing*. Institute of Physics Publishing, Bristol and Philadelphia, 2000.
- [24] F. Bolton and D. Weaire. The effects of Plateau borders in the two-dimensional soap froth. II. General simulation and analysis of rigidity loss transition. *Phil. Mag. B*, **65**: 473–87, 1992.
- [25] M.F. Vaz and M.A. Fortes. Two-dimensional clusters of identical bubbles. *J. Phys. Condens. Matter*, **13**: 1395–411, 2001.

- [26] S. Cox, F. Graner, M. Vaz, C. Monnereau-Pittet and N. Pittet. Minimal perimeter for N identical bubbles in two dimensions: calculations and simulations. *Phil. Mag.*, **83**(11): 1393–406, 2003.
- [27] W. Drenckhan, S.J. Cox, G. Delaney, H. Holste, D. Weaire and N. Kern. Rheology of ordered foams – on the way to discrete microfluidics. *Coll. Surf.: Physicochem. Eng. Aspects*, **263**(1–3): 52–64, 2005.
- [28] G.M. Whitesides. The origins and the future of microfluidics. *Nature*, **442**(7101): 368–73, 2006.
- [29] W. Thomson. On the Division of Space with Minimum Partition Area. *Phil. Mag.*, **24**: 503, 1887.
- [30] D. Weaire and R. Phelan. A counterexample to kelvin conjecture on minimal-surfaces. *Phil. Mag. Lett.*, **69**(2): 107–10, 1994.
- [31] D. Weaire, editor. *The Kelvin Problem*. Taylor and Francis, London, 1997.
- [32] L. Bragg and J.F. Nye. A dynamical model of a crystal structure. *Proc. R. Soc. Lond. A*, **190**: 474–81, 1947.
- [33] A. van der Net, W. Drenckhan, D. Weaire and S. Hutzler. The crystal structure of bubbles in the wet foam limit. *Soft Matter*, **2**(2): 129–34, 2006.
- [34] A.J. Meagher, M. Mukherjee, D. Weaire, S. Hutzler, J. Banhart and F. Garcia-Moreno. Analysis of the internal structure of a monodisperse liquid foam by X-ray tomography. *Soft Matter*, in press, 2011.
- [35] N. Pittet, N. Rivier and D. Weaire. Cylindrical packing of foam cells. *Forma*, **10**: 65–73, 1995.
- [36] M. Saadatfar, J. Barry, D. Weaire and S. Hutzler. Ordered cylindrical foam structures with internal bubbles. *Phil. Mag. Lett.*, **88**: 661–8, 2008.
- [37] S.T. Tobin, J.D. Barry, A. Meagher, B. Bulfin, C. O’Rathaille and S. Hutzler. Ordered polyhedral foams in tubes with circular, triangular, and square cross-section. *Coll. Surf. A*, **382**(1–3): 24–31, 2011.
- [38] D. Weaire, S. Hutzler and N. Pittet. Cylindrical packings of foam cells. *Forma*, **7**(3): 259, <http://www.scipress.org/journals/forma/abstract/07030259.html>, 1992.
- [39] A. Meagher *et al.* The structures of wet foams in capillary tubes. In preparation.
- [40] J.D. Bernal. A geometrical approach to the structure of liquids. *Nature*, **183**: Jan. 1959.
- [41] J.L. Finney. Random packings and the structure of simple liquids. ii. the molecular geometry of simple liquids. *Proc. R. Soc. Lond. A*, **319**(1539): 495–507, 1970.
- [42] C. Isenberg. *The Science of Soap Films and Bubbles*. Dover Publications Inc., 1992.
- [43] A.M. Kraynik, D.A. Reinelt and F. van Swol. Structure of random monodisperse foam. *Phys. Rev. E*, **67**(3): 031403, 2003.
- [44] S. Hutzler, D. Weaire and F. Bolton. The effects of Plateau borders in the two-dimensional soap froth, III. Further results. *Phil. Mag. B*, **71**: 277, 1995.
- [45] D. Weaire, M.F. Vaz, P.I.C. Teixeira and M.A. Fortes. Instabilities in liquid foams. *Soft Matter*, **3**: 47–57, 2007.
- [46] M. Durand and H.A. Stone. Relaxation time of the topological T1 process in a two-dimensional foam. *Phys. Rev. Lett.*, **97**: 226101, 2006.
- [47] S. Hutzler, M. Saadatfar, A. van der Net, D. Weaire and S.J. Cox. The dynamics of a topological change in a system of soap films. *Coll. Surf. A*, **323**: 123–31, 2008.
- [48] S. Hutzler, N. Péron, D. Weaire and W. Drenckhan. The foam/emulsion analogy in structure and drainage. *Eur. Phys. J. E*, **14**: 381–6, 2004.
- [49] D.W. Thompson. *On Growth and Form*, 2nd edn. Cambridge University Press, Cambridge, 1942.
- [50] K. Guevorkian, M.-J. Colbert, M. Durth, S. Dufour and F. Brochard-Wyart. Aspiration of biological viscoelastic drops. *Phys. Rev. Lett.*, **104**(21): 218101, 2010.
- [51] K.J. Dorner. *Fundamental Tissue Geometry for Biologists*. Cambridge University Press, Cambridge, 1980.
- [52] J. Käfer, T. Hayashi, A.F.M. Marée, R. Carthew and F. Graner. Cell adhesion and cortex contractility determine cell patterning in the drosophila retina. *Proc. Natl Acad. Sci.*, **104**: 18549–54, 2007.
- [53] J. Banhart and D. Weaire. On the road again: metal foams find favor. *Phys. Today*, 37–42, July 2002.
- [54] J. Banhart. Metal foams: Production and Stability. *Advanced Eng. Mater.*, **8**(9): 781–94, 2006.
- [55] A. van der Net, A. Gryson, M. Ranft, F. Elias, C. Stubenrauch and W. Drenckhan. Highly structured porous solids from liquid foam templates. *Coll. Surf. A: Physicochemical and Engineering Aspects*, **346**: 5–10, 2009.

# 3

## Foam Drainage

*Stephan A. Koehler*

### 3.1 Introduction

The term foam drainage originally described the process by which fluid flows out of a foam, such as liquid draining out of a soap froth [1, 2], or the draining head on freshly poured beer (see Fig. 3.1a). Since then many technological applications have been developed for foams, which include cleansing, water purification, and minerals extraction as well as production of cushions, food stuffs, and ultra-lightweight structural materials [3–7]. Consequently they have received much attention by the scientific community, and foam drainage has taken on a broader meaning of just fluid flow between compressed bubbles. Fig. 3.1(b) shows a close-up of a soap foam in a forced-drainage experiment, where the fluid is fluorescent and the drainage front traveling between the bubbles is clearly visible. As instrumentation and techniques have advanced, more detailed microscopic studies of fluid flow in foams have been performed on the level of individual bubbles and smaller, which are also considered to be foam drainage. For example, Fig. 3.1(c) shows a 3D image of the continuous phase of a liquid – liquid foam (oil in water emulsion) obtained by confocal microscopy. Only the channel-like network is seen because the films separating bubbles (oil droplets) are too thin to be resolved by the microscope. Using confocal microscopy with greater magnification and seeding the flow with micron-sized particles makes it possible to determine the flow fields. But as with most materials studies, an increased level of understanding leads to an increased number of unanswered questions. Thus at first glance foam drainage may appear to be a relatively straightforward fluids problem dealing with the flow between bubbles, but instead is a multifaceted process with

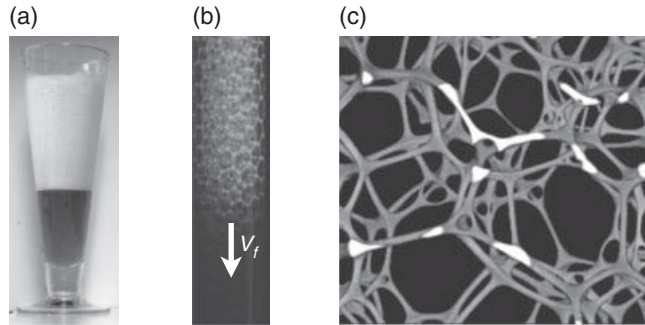


**Fig. 3.1** (a) The draining head on a freshly poured beer. (b) A forced drainage experiment, where continuous perfusion of a dry foam column from above results in a downwards-flowing drainage front, velocity  $V_f$ , followed by a uniformly wet region. (c) 3D confocal image of an emulsion with average bubble size  $200\text{ }\mu\text{m}$  and continuous fraction  $\epsilon \approx 0.005$ .

length scales ranging from nanometers for surfactant molecules, to micrometers for films, to millimeters for bubbles, to centimeters for bulk foams.

Foams are metastable dispersions of gas in liquid that are evolving in time, which complicates precise measurements and obfuscates experimental trends. Despite their having a very simple composition (merely gas bubbles, highly concentrated in a fluid with small amounts of surfactants), achieving the current level of understanding has taken over a century of considerable effort by the scientific community, which includes chemical engineers, food scientists, surfactant chemists, and soft matter physicists. To date there are only semi-empirical models. Several key questions remain unanswered, such as the role of surfactants on interfacial stresses, which were posed by chemical engineers as early as the 1940s [8].

There are two main dynamic processes, which are (i) the redistribution of liquid, also known as foam drainage or syneresis [8, 9], and (ii) the redistribution of gas between bubbles, also known as coarsening or Ostwald ripening [10, 11]. Unless appropriate precautions are taken, it is often difficult to disentangle these dynamic processes and perform systematic studies [12, 13]. For example, the shrinking head on a beer freshly poured into a glass is a complicated process that simultaneously involves the drainage of fluid as well as bubble rupture and inter-bubble gas diffusion. For certain surfactants another undesirable process is chemical degradation, such as the conversion of SDS (sodium dodecyl sulfate) to DOH (dodecanol) by hydrolysis, which can significantly impact foam properties [14]. A more tractable drainage scenario is the “forced drainage” experiment where a continuous perfusion from above creates a uniformly wet region that drains downwards at constant velocity (see Fig. 3.1b) [15]. Foam stability is optimized by using a surfactant with minimal chemical degradation and film rupture, as well as gas with a low diffusion rate.

Models for foam drainage deal with the flow and liquid distribution from a mean-field perspective, where the resolving length scale is over many bubbles. These theories are quite similar in spirit to fluid flow through porous solids, such as sands, soils, and packed beds, which are well described by Darcy’s law

$$Q = \frac{K}{\mu}(\nabla p - \rho g), \quad (3.1)$$

where  $K$  is the porous medium's permeability (in units of area), and  $Q$  is the fluid's volumetric flux (in units of length/time),  $\rho$  the (volumetric) density,  $\mu$  the viscosity,  $p$  the pressure and  $g$  gravitational acceleration. The key property is the medium's permeability, which depends on the pore structure and generally is determined experimentally. The main difference between foams and porous media is that for foams the pores are elastic and vary with flow rate. This is illustrated by the forced drainage experiment, where a constant fluid flux is poured onto the foam, which results in the drainage wave shown in Fig. 3.1(b). The foam can accommodate a large range of perfusion fluxes because the pores self-adjust such that the permeability is proportional to the flux  $K = (\mu Q) = (\rho g)$ . In contrast, performing a similar experiment by replacing the foam with a plug of porous material would result in accumulation of a puddle above if the flux exceeds  $q > K\rho g = \mu$ . Another important difference between porous materials and foams is the boundary condition of the flow: for solids the no-slip boundary condition holds at the pores' walls, whereas for foams the walls are surfactant-laden liquid – gas interfaces, which generally are also flowing. Therefore foam drainage theories must take into account how the structure is modified by flow as well as flow of the liquid – gas interfaces, which contributes to a rich phenomenology of behaviors.

## 3.2 Geometric Considerations

It turns out that dry foams with liquid fraction  $\varepsilon \leq 0.02$  have distinctive geometric features that greatly facilitate understanding and analysis. In particular, the continuous network is dominated by straight, slender channels that are easy to understand (see Fig. 3.1c). However, as the liquid fraction increases the channels swell and are difficult to distinguish from other geometric elements. But for the sake of tractability the analysis and approximations made for dry foams in many situations can be extended to monodisperse wet foams without sacrificing too much rigor.

Although real foams often have polydisperse disordered bubbles, it is conceptually useful to simplify the structure to an idealized monodisperse foam. A convenient idealization for dry foams is a bcc packing of regular octahedra whose six corners have been truncated to create square faces. This results in a total number of fourteen faces. Moreover, every edge has the same length,  $L$ , and hence this polygon is a special type of tetrakaidecahedron that tessellates space. A commonly used name for this shape is the Kelvin bubble in honor of Lord Kelvin, who considered minimal surface area tilings of 3D space [16]. Figure 3.2(a) shows a Kelvin bubble decorated by the neighboring channel-like network. This can be classified into three geometric components that are: (i) films, which separate two compressed bubbles (Fig. 3.2b); (ii) channels, which are regions between three compressed bubbles and the intersections of three films (Fig. 3.2c); and (iii) nodes, which are regions between four compressed bubbles and the intersections of four channels (Fig. 3.2d). Alternative designations for films are lamellae (taken from the biological term for thin layers or membranes), channels are Plateau borders (named after the famous nineteenth-century Belgian physicist), and nodes are junctions (because they serve as flow junctions between channels). The bubble from Fig. 3.2(a) is decorated by channels that are shared with two adjacent bubbles and nodes that are shared with three adjacent bubbles. The tetrakaidecahedron contains a rounded bubble that is surrounded by thirds of channels and

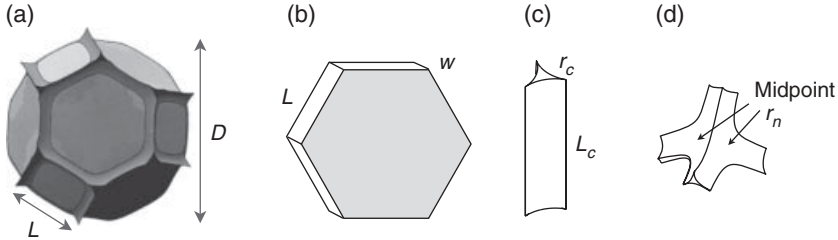


**Fig. 3.2** Foam geometry: (a) Kelvin bubble,  $\varepsilon = 0.01$ , where the channels and nodes from other bubbles are included (courtesy of Andrew Kraynik); (b) film of thickness  $w$ ; (c) idealized channel with transverse radius of curvature  $r_c = r$ ; (d) node. At the surface's midpoint the principle radii of curvature are equal and  $r_n = 2r$ .

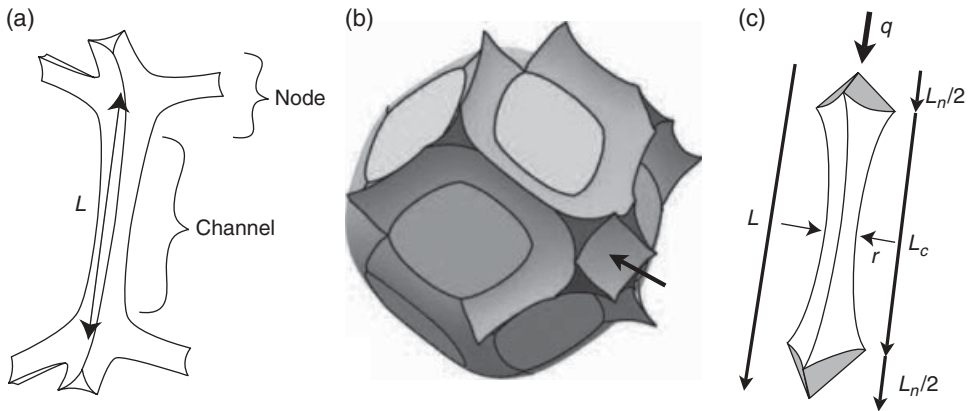


**Fig. 3.3** (a) A portion of the channel-like network, with node-to-node separation  $L$ . (b) A rhombic dodecahedral bubble decorated by interstitial fluid at  $\varepsilon = 0.05$ . The arrow indicates an eight-way node (courtesy of Andrew Kraynik). (c) The network unit for flow, which consists of a channel and two quarter nodes.

quarters of nodes. Fig. 3.3(a) is an illustration of a portion of the channel-like network that consists of a channel and the two adjoining nodes. Note that the separation between nodes also is the edge length.

As the liquid fraction increases the six square faces of the Kelvin bubble, which resulted from truncation of the octahedron, shrink and disappear at  $\varepsilon^* \approx 0.1$  [17]. The four nodes of each of the square faces merge into a single node, which becomes the junction between eight channels. This foam is no longer stable to shearing, and rearranges to a fcc packing where the unit cell is a rhombic dodecahedron consisting of twelve faces – see Fig. 3.3(b). The arrow shows a node with an eightfold coordinated node, i.e., the junction of eight channels. (Plateau's rule for fourfold nodes only applies to dry foams.) The number of nodes has dropped from 24 to only 14, of which six are eightfold coordinated and the remaining eight nodes are fourfold coordinated. With increasing liquid fraction the bubbles become more spherical and at  $\varepsilon_{\text{fcc}} = 1 - \pi/\sqrt{18} \approx 0.26$  the foam is a fcc hexagonal close pack of spheres. In most situations the foam is unconfined, and thus will expand as liquid

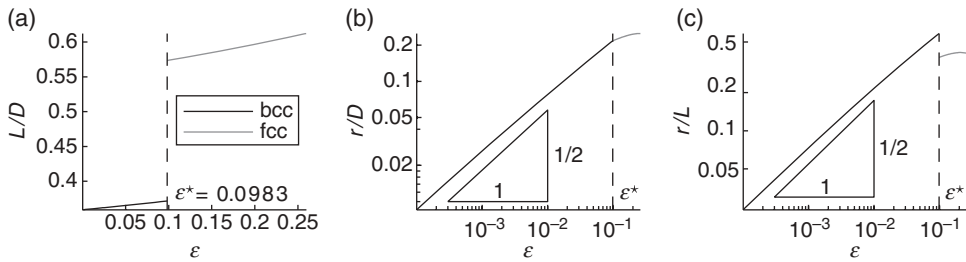


**Fig. 3.4** The liquid fraction dependence of: (a) edge length,  $L/D$ ; and the channel's aspect ratios in terms of (b)  $r/L$  and (c)  $r/D$ .

is introduced. Under normal conditions the compressibility of gas is negligible because the overpressure caused by the foam's weight is small compared with atmospheric pressure. Therefore as liquid is introduced the gas volume,  $V_g$ , stays constant and the extra liquid causes the unit cell to grow. The volume of the unit cell is the sum of the liquid and gas,  $V_t = V_g + V_l$ , and is proportional to the edge length  $L^3$ . Denoting the edge length of a completely dry foam  $L_0$ , and realizing the liquid volume is  $\epsilon V_t$ , the increasing liquid fraction causes the edge length to grow  $L = L_0(1 - \epsilon)^{1/3}$ . The volume of the tetrakaidecahedron is  $2^{7/2}L^3$ , and that of the dodecahedron is  $2^{43-3/2}L^3$ . Denoting  $D$  as the equivalent diameter of the gas bubble,  $V_g = \pi D^3/6$ , the edge length dependence on liquid fraction is

$$\frac{L}{D} = \frac{L_0}{D}(1 - \epsilon)^{-1/3} = (1 - \epsilon)^{-1/3} \times \begin{cases} 2^{-3/2}3^{-1/3}\pi^{1/3} & \text{for bcc packing, } \epsilon \leq \epsilon^* \\ 2^{-5/3}3^{1/6}\pi^{1/3} & \text{for fcc packing, } \epsilon \geq \epsilon^* \end{cases} \quad (3.2)$$

Fig. 3.4(a) shows how the edge length increases with liquid fraction, and is discontinuous at  $\epsilon^*$  where structural rearrangement occurs. The decrease in the number of edges is from 36 for bcc to 24 for fcc, which equals the increase in the length of the fcc edges compared with the bcc edges.

The relationship between the interfacial curvature and the gas pressure of the bubbles,  $p_b$ , and the liquid pressure,  $p$ , is given by Young – Laplace's law. The interfacial curvature can be parameterized by the inverse radius of the (total) curvature,  $1/r$ . Recall a surface has two principle radii of curvature which are in orthogonal planes and  $r^{-1} = r_1^{-1} + r_2^{-1}$ . Young – Laplace's law states

$$p = p_b - \gamma/r, \quad (3.3)$$

where  $\gamma$  is the surface tension. (Note that the liquid pressure inside films is an exception to this rule because films are so thin that short-range disjoining forces between opposing interfaces come into play, which is discussed later.) Films are essentially flat, which means the local variations in the gas pressure between nearby bubbles are small. Consequently Young – Laplace's law results in a locally uniform interfacial curvature, because any variations in  $r$  result in liquid pressure variations, which lead to fluid flow that removes non-uniformities.

The smallest geometric length is the film thickness,  $w$ , which is determined by the disjoining pressure of the surfactants lining the interfaces and the pressure compressing the bubbles. The disjoining pressures are molecular in nature and due to repulsion between different

regions of the surfactant molecules, such as the electrostatic repulsion among tail groups of ionic surfactants. The fluid inside the films is shielded from the gas pressure by the interface's disjoining forces, and essentially is the same pressure as that of the adjoining channels. Since these forces have range, the films are generally very thin,  $w \leq 0.1 \mu\text{m}$ . But for certain foams experimental studies have documented increases of film thickness with drainage rate [18, 19]. Hereafter it is assumed that the films contain a negligible amount of liquid and can be ignored.

For dry foams,  $\varepsilon \leq 0.01$ , the channels are long and slender and can be idealized as the volume between three cylinders having transverse radius of curvature  $r_c$  (cf. Fig. 3.2c) [20]. A channel's cross-sectional area is

$$A_c = \delta_c r_c^2 \text{ where } \delta_c = \sqrt{3} - \pi / 2. \quad (3.4)$$

Since the axial curvature of the channels is small, the transverse curvature is close to the total curvature:  $r_c \approx r$ . Also the length of the channels is that of the node-to-node separation,  $L_c \approx L$ , because the nodes are tiny. But as the liquid fraction increases the channel length shortens and approaches zero for spherical bubbles.

The arrows of Fig. 3.2(d) show the symmetry points of the node where both principle radii of curvature are the same. Here the node's radii of curvature are  $r_n = 2r$ , which in the limit of dry foams are twice those of the channels,  $r_n \approx 2r_c$ .

For a Kelvin foam the relationship between edge length, radius of curvature and liquid volume fraction is calculated using the Surface Evolver [21, 22]. A second order polynomial provides a good approximation for  $\varepsilon < \varepsilon^*$ , where  $\varepsilon^* \approx 0.1$ :

$$\varepsilon \approx \delta_1 \left( \frac{r}{L} \right)^2 + \delta_2 \left( \frac{r}{L} \right)^3, \text{ with } \delta_1 \approx 0.171, \delta_2 \approx 0.20. \quad (3.5)$$

It is important to take into account foam expansion with liquid fraction, and thus using  $L$  in eqn (3.5) leads to errors, even though in practice it is often assumed that  $L = L_0$  regardless of  $\varepsilon$ . For example, the node-to-node separation of the wettest unconfined Kelvin foam is  $L = 1.06L_0$ , and assuming  $L = L_0$  results in a 10% over-prediction of the liquid volume fraction.

At  $\varepsilon^*$  the packing transitions from bcc to fcc, and the bubble shape changes from tetrakaidecahedra to dodecahedra, which invalidates the above expression for liquid fraction. Recent work by Höhler *et al.* [23] on emulsions and foams has provided a semi-empirical relationship between liquid fraction and the interfaces' radius of curvature. The authors measured the osmotic pressure of foams and emulsions, which is directly related to the pressure drop across curved interfaces given by the Young – Laplace law, eqn (3.3). Unlike Kelvin foams, the relationship is implicit in  $\varepsilon$ ,

$$\frac{r}{D} \left( 4 + \delta_3 \frac{(\varepsilon - \varepsilon_{\text{fcc}})^2}{\sqrt{\varepsilon}} \right)^{-1} \text{ with } \delta_3 = 7.3. \quad (3.6)$$

It is noteworthy that in the limit of dry fcc packings the above relationship is not in exact agreement with geometric considerations based upon the volume in Plateau borders and the volume of the unit cell: The dodecahedron has 24/3 complete Plateau borders, containing  $8\delta_c r^2 L$  volume of fluid, and its total volume is  $2^{4/3} 3^{-3/2} L^3$ . Accordingly the liquid fraction is  $\varepsilon = (8\delta_c r^2 L) / (2^{4/3} 3^{-3/2} L^3) \approx 0.114(r/L)^2$ , whereas the dry limit of eqn (3.6) is

$\varepsilon = \delta_3 \varepsilon_{\text{fcc}}^2 (L/D)(r/L)^2 \approx 0.0742(r/L)^2$ . The discrepancy of 40% indicates the semi-empirical nature of the fcc approximation, eqn (3.6), which, however, is irrelevant here because at low liquid fractions the bcc approximation, eqn (3.5), is used. It is also noteworthy that Höhler *et al.* [23] provide a similar relationship for random close packings that are used elsewhere [24]; however, in keeping with the spirit of idealizing dry foams as bcc packings of Kelvin bubbles it makes more sense to idealize wet foams as fcc packings of dodecahedra.

Figure 3.4(b) shows the dependence of the ratio  $r/D$  on liquid fraction for a dry bcc (Kelvin) foam from eqns (3.5) and (3.2), as well as for a wet fcc foam from eqn (3.6). The two expressions intersect at  $\varepsilon^* = 0.0983$ , which is between the values for the liquid fraction where the interfacial energy of the bcc foam equals that of the fcc foam, 0.063 [23], and the Kelvin foam loses structural stability,  $\approx 0.11$  [25]. This will serve as a value for  $\varepsilon^*$ , which serves as the demarcation between bcc and fcc for the idealized foam geometry. The relationship between liquid fraction and curvature shown in Fig. 3.4(b) is discontinuous in its first derivate, thereby exhibiting a first-order phase transition. But in reality, hysteresis in the packing is expected as the liquid fraction varies across the range  $0.05 \leq \varepsilon \leq 0.12$ .

Figure 3.4(c) shows the discontinuity of the channel's aspect ratio  $r/L$ . At  $\varepsilon = \varepsilon^*$  the structural rearrangement results in a drop in the aspect ratio of 40%, which is due to an increase of the edge length. This large change in the channel's aspect ratio will affect flow through the channels, which can affect foam drainage.

Equation (3.5) can be understood geometrically in terms of contributions from channels and nodes. Figure 3.3(a) shows a portion of the channel-like network, which is a channel with a node at either end. Figure 3.3(c) shows a network unit, which is a channel and two quarter nodes at either end. The size of the node scales with  $r$ , and its extent can be approximated as  $L_n \approx \xi r$ , leaving the channel length  $L_c = L - \xi r$ . At the critical value  $\varepsilon^*$ , the radius of curvature is  $r = 0.584L$ , the nodes merge and choosing  $\xi = 1.71$  results in zero channel length. The entire channel-like network can be composed of such network units. The Kelvin cell has 12 complete channels and 6 complete nodes; thus its volume fraction can be expressed as

$$\varepsilon = \frac{12}{L^{7/2}} (\delta_c r^2 (L - \xi r) + \xi r A_n / 2), \text{ where } \xi = 1.71 \quad (3.7)$$

and  $A_n = \delta_n r^2$  is the average cross-sectional area of a node. Comparing with eqn (3.5) it follows

$$\delta_n = \frac{2^{9/2} \delta_2}{12 \xi} + 2 \delta_c \approx 0.543. \quad (3.8)$$

Note that the value for  $\delta_n$  is not unreasonable, when considering the cross-sectional area through a node's midpoint (cf. Fig. 3.2d), which roughly is  $\delta_c (2r)^2 \approx 0.645r^2$ .

### 3.3 A Drained Foam

It is instructive to consider the case of an unconfined drained foam, where the liquid flow is negligible. The liquid content is set by a balance of Young – Laplace's law and gravitational forces. Since there is no flow, the liquid pressure is entirely hydrostatic,  $p = p_0 + \rho g z$ ,

where  $z = 0$  is the top of the foam and the  $z$ -axis is orientated downwards (in the direction of gravity). At first glance, this scenario may appear trivial, but it is informative to provide a rigorous solution because many of the techniques will be used in subsequent sections dealing with drainage.

A quick approximation can be obtained by assuming that the node-to-node separation remains constant,  $L = L_0$ , and the pressure inside the bubbles also is unchanged. From Young – Laplace's law, eqn (3.3), it follows that

$$\frac{\gamma}{r} = \frac{\gamma}{D/4} + \rho g H, \quad (3.9)$$

where  $H$  is the height. At the bottom the bubbles are spherical in a fcc packing and their radius of curvature is  $D/4$ . Natural choices for the length and pressure scales are  $D$  and  $\gamma/D$  respectively, which transforms eqn (3.9) into

$$\frac{r}{D} = \left( 4 + C \frac{H}{D} \right)^{-1}, \text{ where } C = \frac{\rho g D^2}{\gamma}. \quad (3.10)$$

The dimensionless parameter  $C$  relates the capillary and gravitational forces, and is the square of the ratio of the bubble diameter,  $D$ , and the capillary length  $\sqrt{\gamma/\rho g}$ . At the bottom of the drained foam, in the region where  $\varepsilon \geq \varepsilon^*$ , comparison with eqn (3.6) shows that the osmotic pressure equals the hydrostatic pressure, which provides an implicit relationship for  $\varepsilon$ ,

$$\delta_3 \frac{(\varepsilon - \varepsilon_{\text{fcc}})^2}{\sqrt{\varepsilon}} = C \frac{H}{D},$$

that is valid over the interval  $0 \leq H \leq H^*$ , where  $H^* = \delta_3 (\varepsilon^* - \varepsilon_{\text{fcc}})^2 \gamma / (\rho g D \sqrt{\varepsilon^*}) \approx 0.6053 \gamma / (\rho g D)$ . Above this point the idealized foam has bcc packing for which eqn (3.5) applies. Far above the foam's bottom, the liquid fraction is low, so the liquid fraction can be approximated to lowest-order from eqn (3.5), and the liquid fraction's asymptotic dependence on the height is  $\varepsilon \approx \delta_1 C^{-2} L_0^{-2} D^4 H^2$ .

Generally for atmospheric conditions variations of the bubbles' gas pressure is negligible, because the compression due to the foam's weight is small. However, for other situations, such as forced drainage discussed below in Section 3.12, the total amount of liquid in the foam can be substantial and can lead to compression of the bubbles at the bottom of the foam. Here it is reasonable to assume that the bubble diameter does not vary. Figure 3.5 shows the dependence of the liquid fraction on the height above the bottom of the foam. Eqn (3.6), which is the fcc expression for the liquid fraction, is plotted for the entire range of heights to show the contrast with the bcc expression, eqn (3.5). The liquid fraction based upon the bcc approximation is 2.5 times greater than that of the fcc approximation, which is due to the greater osmotic pressure of the bcc packing.

The assertion that the bubbles' compression due to the foam's weight is negligible deserves justification. The weight of the foam column is distributed horizontally across the foam's cross-section and causes an overpressure at height  $H$  which is  $\int_H^\infty \rho g e dH$ . Compared with atmospheric pressure this overpressure is very small. For a standard surface tension  $\gamma = 20 \text{ dyn/cm}^2$  and very small bubbles,  $D = 100 \mu\text{m}$ , the ratio of the overpressure to atmospheric pressure is  $\sim 10^{-3}$ . If the gas is isothermal and ideal, this results in a reduction of the

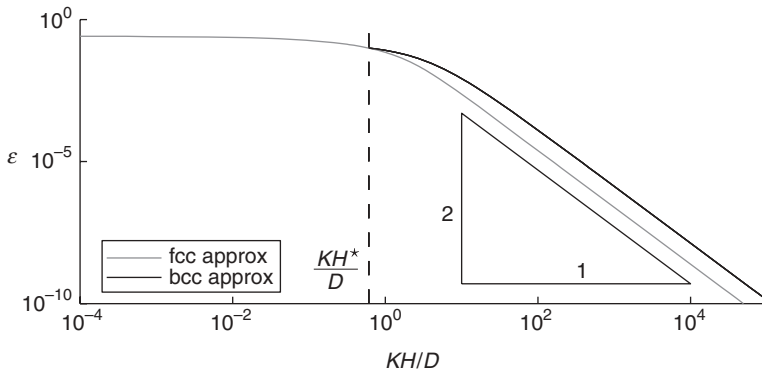


**Fig. 3.5** The liquid fraction of drained foam. For  $H \leq H^*$  the fcc approximation given by eqn (3.6) is applicable, and for  $H \geq H^*$  the bcc approximation given by eqn (3.5) is applicable. The inset triangle shows the power-law relation  $\varepsilon \propto (CH/D)^{-2}$ .

bubble's volume by  $\sim 10^{-3}$  and indeed is negligible as asserted above. In most situations the bubbles are larger, making the amount of liquid in the drained foam less and the bubbles' compression less.

### 3.4 The Continuity Equation

The foam drainage equation describes the spatio-temporal evolution of the liquid fraction on the mesoscale of several bubbles. It is based upon the continuity equation, which is a relationship between the liquid fraction and the liquid velocity. Several semi-empirical models have been developed for interstitial flow, which are addressed in some detail in subsequent sections.

From the continuum viewpoint, the foam's liquid fraction is changed by the divergence of the liquid flux,  $\psi$ . Assuming that the foam is confined, i.e. the volume of the unit cell is unchanged, then conservation of liquid requires

$$\frac{\partial \varepsilon}{\partial t} = -\nabla \cdot \psi = -\nabla \cdot (\mathbf{u}\varepsilon), \quad (3.11)$$

where  $\mathbf{u}$  is the mean-field liquid velocity.

In the case of unconfined foams the continuity equation, eqn (3.11), has to be modified to account for foam expansion. Consider a mesoscale control volume composed of gas and liquid  $V_t = V_g + V_l$ . An inflow of an infinitesimal amount of fluid  $dV_l$  increases the total volume to  $V_t + dV_l$ . The liquid fraction becomes

$$\varepsilon + d\varepsilon = \frac{V_l + dV_l}{V_t + dV_l} = \frac{V_l}{V_t} + \frac{dV_l}{V_t} - \frac{V_l dV_l}{V_t^2} + O\left(\frac{dV_l}{V_t}\right)^2. \quad (3.12)$$

Using  $V_t/V_t = \varepsilon$  and  $dV_t = -V_t \nabla \cdot \psi dt$  gives the unconfined continuity equation:

$$\frac{\partial \varepsilon}{\partial t} = -\nabla \cdot \psi + \frac{V_t}{V_t} \nabla \cdot \psi = -(1-\varepsilon) \nabla \cdot \psi = -(1-\varepsilon) \nabla \cdot (\varepsilon \mathbf{u}), \quad (3.13)$$

which for small liquid fractions is the same as the original continuity equation, eqn (3.11). In summary, the factor  $(1 - \varepsilon)$  for unconfined foams arises from the fact that introducing liquid into a region of foam causes that region to expand, which consequently lowers the liquid fraction.

Once the average liquid velocity  $\mathbf{u}$  is determined, insertion into the continuity equation results in a partial differential equation describing the spatio-temporal evolution of the liquid fraction, which is known as the foam drainage equation. The foam drainage equation was independently developed by two groups [26, 27], and the velocity had a simple dependence on the liquid fraction and its gradient (and of course material parameters such as  $\rho$ ,  $g$ ,  $\mu$ ,  $L_0$  or  $D$ ). In fact, the original foam drainage equation was a non-linear advective diffusion equation that is quite similar to the heat (flow) equation. However, the liquid velocity has a complex dependence on parameters not accounted for in the original formulation, such as surface viscosity and possibly other surface stresses such as Marangoni forces. To date there is no complete theory for foam drainage, and so far only semi-empirical approaches have been developed [22, 24, 28–32].

### 3.5 Interstitial Flow

Only a few foam studies have dealt with non-Newtonian fluids, such as polymer solutions (PEG) [33, 34] or liquid crystals [35], and the vast majority of research involves Newtonian fluids, such as water, glycerin or oil. For these fluids the velocity field,  $\mathbf{u}$ , obeys the Navier – Stokes equation

$$\rho \left[ \frac{\partial \mathbf{u}}{\partial t} + (\mathbf{u} \cdot \nabla) \mathbf{u} \right] = \mu \nabla^2 \mathbf{u} - \nabla p + \rho \mathbf{g}, \quad (3.14)$$

where  $\rho$  is the density,  $\mu$  the viscosity and  $\rho \mathbf{g}$  is the gravitational body force. In addition, the compressibility of standard fluids can be neglected, so  $\nabla \cdot \mathbf{u} = 0$ .

As a general rule, the Reynolds number of draining foams never is large and inertial effects are negligible. The forced drainage experiment shown in Fig. 3.8(b) is of unusually large bubbles and the downwards liquid flow is unusually fast (the average liquid speed is about 7 mm/s). Shearing occurs transversely to the flow, which is on the scale of the radius of curvature. Here  $r \approx 10 \mu\text{m}$ , making the Reynolds number

$$Re = \frac{\rho u r}{\mu} \approx 5, \quad (3.15)$$

which serves as a loose upper bound, because in most cases the bubble sizes are smaller and the flows are slower. Moreover, the gravitational term on the right-hand side of eqn (3.14) dominates over the inertial term,

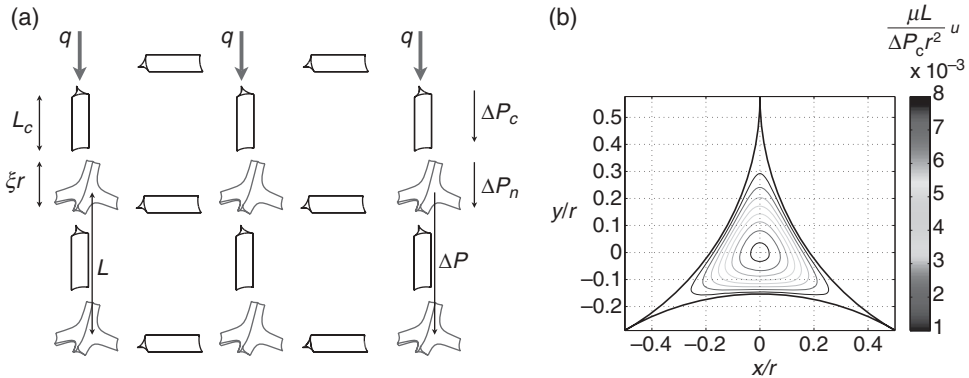


**Fig. 3.6** (a) Schematic of uniform flow through the network composed of channels and nodes. The pressure drop across nodes and channels is  $\Delta P_n$  and  $\Delta P_c$ . The pressure drop between adjacent node centers is  $\Delta P$ . (b) Contour plot of the axial flow,  $u$ , through a Plateau border with rigid walls.

$$\frac{|(\mathbf{u} \cdot \nabla) \mathbf{u}|}{\rho g} \sim \frac{u^2}{r \rho g} \sim 10^{-2}, \quad (3.16)$$

which shows that predominant forces are viscous drag and gravitational attraction and that in general inertial terms are negligible. However, for the case of large bubbles and high liquid fractions inertial terms may in fact become important [36].

Dropping the inertial term, subsuming the liquid pressure into the effective pressure  $P = p - \rho g \cdot x$  and making use of Young – Laplace’s law, eqn (3.3), gives Stokes’s equation

$$\mu \nabla^2 \mathbf{u} = \nabla P, \text{ where } P = p_b - \gamma / r - \rho \mathbf{g} \cdot \mathbf{x}. \quad (3.17)$$

Flow through the continuous network can be considered as a collection of pipes and junctions, which are channels and nodes. Figure 3.6(a) schematically shows the flow passing from node to channel. The pressure drop across the nodes and channels adds up to the pressure drop across adjacent node centers,  $\Delta P_c + \Delta P_n = \Delta P$ . Flow in the channels is essentially unidirectional, whereas in nodes it bends and the difference between entering and exiting flow directions is  $\sim 109^\circ$ . Accordingly, solving eqn (3.17) in channels is far easier. For dry foams these are the predominant fluid structure and may reasonably model foam drainage for certain situations.

Figure 3.6(b) shows the contour lines of liquid flowing through an infinite Plateau border with rigid walls, which is an example of a Haagen – Poiseuille flow. For pipes of arbitrary cross-sectional shape the relationship between flow rate,  $q$ , and pressure drop,  $\Delta P$ , can be characterized by a hydraulic resistance  $R$

$$q = \Delta P / R. \quad (3.18)$$

**Table 3.1** Flow resistance factors for different pipe geometries (with rigid boundaries). An exterior Plateau border is the interstitial area between two bubbles pressed onto a flat wall.

Circle	Square	Equilateral triangle	(Interior) Plateau border	Exterior Plateau border
$8\pi \approx 25.13$	$\approx 28.46$	$20\sqrt{3} \approx 34.64$	$\approx 50$	$\approx 51$

By dimensional analysis, the hydraulic resistance is of the form

$$R = \alpha \frac{\mu L}{A^2}, \quad (3.19)$$

where  $L$  is the pipe length,  $A$  the cross-sectional area and  $\alpha$  the dimensionless resistance factor that depends on geometry. The flow resistances have been calculated for a variety of different shapes [29, 37], and are given in Table 3.1. Determining the flow through a channel-like network is equivalent to a resistor network problem, which can be solved using Kirchhoff's circuit laws.

Achieving an accurate understanding of the physical processes at play in foam drainage requires detailed measurements of the liquid flow between bubbles. Mapping out the flow field between bubbles is difficult, and so far the only successful technique has been tracking micro-particles using confocal microscopy [38, 39]. Figure 3.7(a) schematically shows the experimental configuration where a confocal microscope obtains a thin imaging slice at depths up to a few millimeters inside a foam. If the liquid fraction is low, the optical distortions due to refraction from films are small enough not to interfere with tracking of micron-sized latex spheres that have been added to the flow. The figure schematically also shows the two types of channel flows that might be expected, which are either rigid or mobile liquid – gas interfaces. The former produces a parabolic profile, whereas the latter produces a plug-like profile; they are discussed later in Sections 7 and 9 respectively.

Figure 3.7(b–d) shows the tracks left by particles passing through the channel-like network. The flows are highly laminar, and as highlighted by the transverse separation the flow lines stay segregated without any indication of mixing in either channels or nodes. This microscopic observation has been further confirmed by flow-mixing experiments on the macroscopic level [40]. Figure 3.7(d) shows liquid flow through a node, where the upstream channel at the left sources flow for the remaining three downstream channels. Two of these are visible towards the right, while the third is directed out of the page. However, many other configurations are possible where two or three channels source the flow into the node. (Fig. 3.6(a) assumes one particular configuration: the flow is sourced from one upstream channel, exits the downstream channel and the remaining other two channels lie in the horizontal plane and do not carry any fluid.) Thus the flow through a node depends on both the orientation and how flows enter and exit.

### 3.6 Forced Drainage

Another steady-state situation is forced drainage, where a foam is continuously perfused with constant liquid fraction. Here the force balance essentially is between gravity and

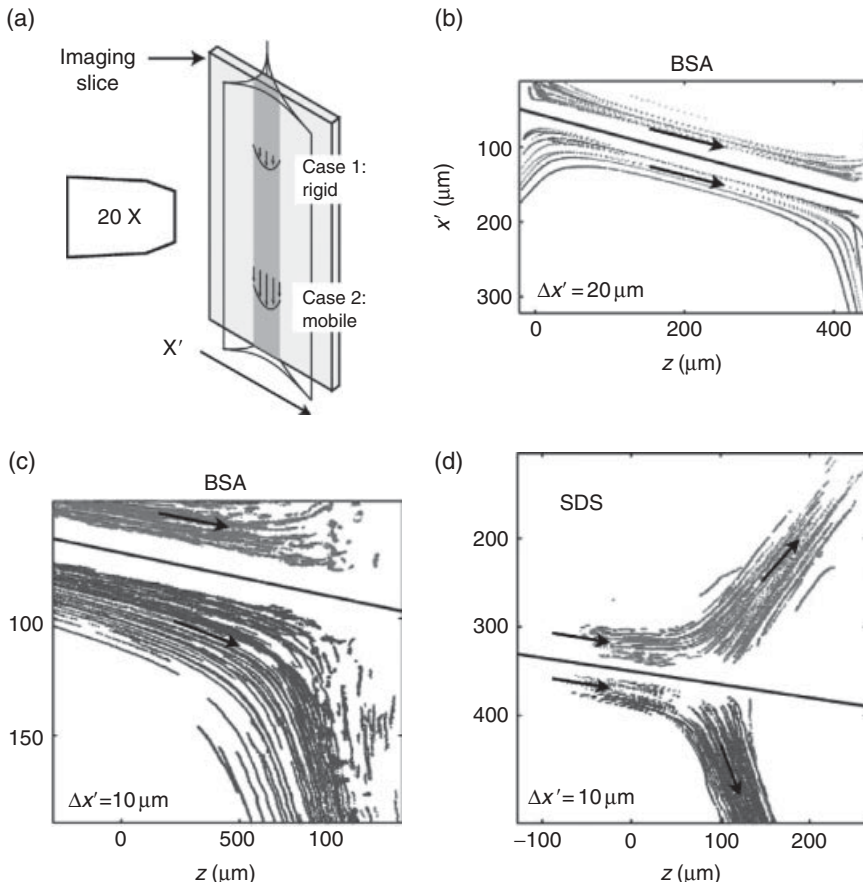


**Fig. 3.7** Confocal imaging. (a) Sketch of the channel and the imaging slice in the  $x' \times z$  plane (gravity is pointing to the right). Two scenarios of the velocity field are drawn for rigid and mobile interfaces. (b–d) Particle tracks of  $1 \mu\text{m}$  latex microspheres showing flow streamlines; flow is indicated by the arrows and gravity is directed to the right. The tracks are offset in the transverse direction by  $\Delta x'$  in order to emphasize that streamlines do not mix.

viscous drag, whereas for the drained foam discussed previously the force balance is between gravity and capillarity. This scenario is useful for industrial applications as well as for research, and has been studied at least since the 1940s [8]. More recently Weaire *et al.* [15] developed a variant of the forced drainage experiment, which is optically measuring the growing region of wet foam that moves downwards to the bottom. This experiment is easy to perform and interpret, and the measurable range of liquid fractions and drainage velocities can extend over several decades. Figure 3.8(a) schematically shows a modified version of Weaire's forced drainage experiment. A vertical cylinder is filled with a monodisperse foam and injected in the top region with the foaming solution at a constant flux  $\psi$ . The foam is illuminated with UV light, which causes the dye in the solution to fluoresce that is imaged by a camera. Continuous perfusion produces a traveling wave

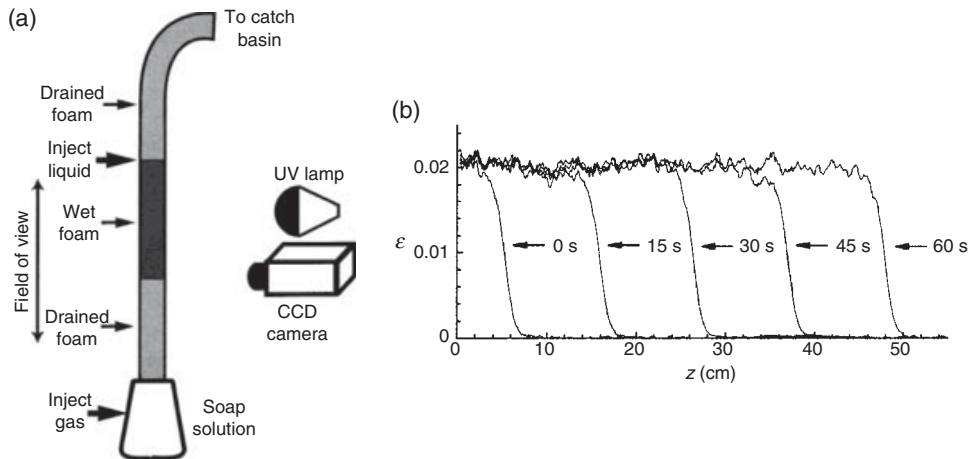


**Fig. 3.8** (a) Schematic of the forced drainage experiment taken from [22]. A constant flux of liquid perfuses the foam, whose liquid fraction is determined from the fluorescence intensity. (b) Snapshots of the liquid fraction profiles, which are traveling waves. The bubble diameter is 4 mm, and the surfactant is SDS.

(see Fig. 3.1b), which moves downwards with constant velocity  $V_f$ . The liquid fraction can be determined from the fluorescence intensity, and Fig. 3.8(b) shows the liquid fraction profiles at five successive snapshots as the fluid drains downwards between the bubbles. Behind the front the liquid fraction has a plateau value, whose value is  $\varepsilon = \psi/V_f$ . The traveling wave can be expressed as  $\varepsilon(z, t) = f(z - Vf)$ , which in the limit of small liquid fractions satisfies eqn (3.13). Note that the foam is unconfined because the top of the tube opens to a catch basin.

In the plateau region the curvature of the channel-like network is uniform and there are no variations in the channel's curvature. Hence according to Laplace's law, eqn (3.3), there are no pressure gradients. Therefore in the plateau region the viscous drag is balanced by the gravitational body force and resembles the situation of gravity-driven flow in capillary tubes. Although the viscous drag in the front region is greater because the channel-like network is narrower, capillary suction provides the additional force necessary so that fluid in the front has the same average speed as that in the plateau region.

In summary, Weaire's version of the forced drainage experiment is an effective way to determine viscous dissipation of drainage flow for three reasons: (i) the average fluid velocity is the same as that of the front and is therefore easily determined; (ii) the liquid fraction is determined from  $\varepsilon = \psi/V_f$ ; and (iii) in the plateau region there is no capillarity so the viscous drag equals the gravitational pull. However, for wet drainage waves some care has to be taken in the interpretation because the foam is unconfined, gas in the bubbles is compressed and bubbles travel up the tube during the perfusion. Section 3.12 provides a more detailed analysis of the forced drainage experiment.

### 3.7 Rigid Interfaces and Neglecting Nodes: The Original Foam Drainage Equation

The original foam drainage equation, proposed independently by two groups [26, 27], is based upon the assumptions that liquid – gas interfaces do not flow (i.e., are rigid) and nodes do not affect drainage. Accordingly this approach is known as the channel dominated model or the rigid channel model.

The starting point is considering the flow through a single channel inside the foam, which is idealized as the non-aligning pipe with three curved faces shown in Fig. 3.2(c). The average velocity of the channel depends on the pressure drop,  $\Delta P_c$ , and is directed along the channel from high to low pressure. From eqns (3.18) and (3.19), this can be expressed as

$$\mathbf{v}_c = \frac{\Delta P_c A_c}{\alpha_r \mu L_c} \hat{\mathbf{L}}_c \quad (3.20)$$

where  $\alpha = 50$  is the flow resistance for the interior channel with rigid interfaces (cf. Table 3.1), and  $\hat{\mathbf{L}}_c$  is the tangent vector along the channel's axis in the flow direction.

To determine the average macroscopic drainage velocity  $\mathbf{V}$ , define  $P_{\text{macro}}$  as the macroscopic driving pressure, which is an average of the local driving pressure  $P$  from eqn (3.17) taken over several bubbles. Because inertial effects are negligible, the average flow direction is aligned with the pressure gradient:  $\mathbf{V} \parallel \nabla P_{\text{macro}}$ . Substituting  $\hat{\mathbf{L}}_c \cdot \nabla P_{\text{macro}}$  for  $\Delta P_c = L_c$  in eqn (3.20) makes the average drainage velocity

$$\mathbf{V} = \hat{\mathbf{V}} \langle \hat{\mathbf{V}} \cdot \mathbf{v}_c \rangle = -\hat{\mathbf{V}} \langle (\hat{\mathbf{V}} \cdot \hat{\mathbf{L}}_c)(\hat{\mathbf{L}}_c \cdot \nabla P_{\text{macro}}) \rangle = -\frac{A_c}{3\alpha_r \mu} \nabla P_{\text{macro}}, \quad (3.21)$$

where the last equality follows from averaging over  $2\pi$  steradians:  $\langle \cos(\theta)^2 \rangle = \int \cos(\theta)^2 \sin(\theta) d\theta / \int \sin(\theta) d\theta = 1/3$ . The above arguments hold for averaging the flow along randomly oriented channels to obtain the macroscopic drainage velocity, which is one third of the maximum individual channel velocity that occurs when it is aligned with the pressure gradient.

Verbist *et al.* [27] worked out a simple form of the drainage velocity for the limit of dry foams,  $\epsilon \leq 0.05$ . The channel's radius approaches the radius of curvature,  $r_c \approx r$ , and the liquid fraction, eqn (3.5), simplifies to  $\epsilon \approx \delta_l (r_c/L)^2$ , which makes eqn (3.21)

$$\mathbf{V} = -\frac{\delta_c / \delta_l}{3\alpha_c \mu} L^2 \epsilon \nabla P_{\text{macro}} \approx -6.3 \times 10^{-3} \frac{L^2 \epsilon}{\mu} \nabla P_{\text{macro}}. \quad (3.22)$$

For the case of forced drainage there are no capillary forces in the plateau region and  $\nabla P_{\text{macro}} = -\rho g$ . Verbist's approximation gives a simple dependence of the front velocity:  $V_f \approx 6.3 \times 10^{-3} \rho g L^2 \epsilon / \mu$ .

For the general case capillarity has to be included in for the driving pressure gradient,  $-\nabla P_{\text{macro}} = \nabla(\gamma/r) + \rho g$ . Substituting for  $r$  in the dry limit and using the continuity equation, eqn (3.11), gives Verbist's foam drainage equation

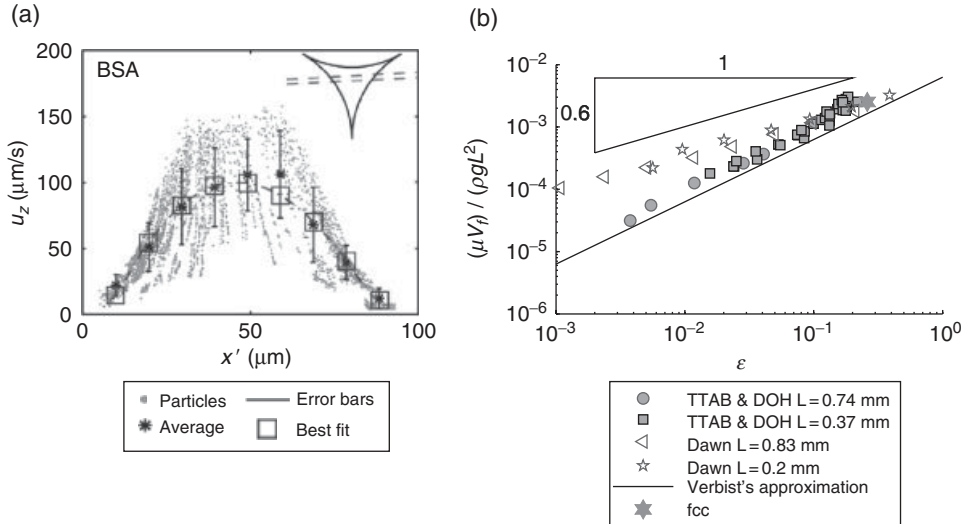


**Fig. 3.9** (a) Profile of the axial velocity of slice through the channel of a foam made with BSA and co-surfactant PGA determined by confocal tracking of  $1 \mu\text{m}$  latex particles [39]. (b) Dependence of the rescaled front velocity on liquid fraction for a TTAB & DOH foam [24] and a foam made with the commercial dish detergent Dawn [45]. The continuous line is the rigid interface prediction, eqn (3.22), and the large filled star indicates the drainage velocity through a fcc packing of spheres [46].

$$\mu \frac{d}{dt} \varepsilon + \left( \frac{\delta_c}{3\alpha_c \delta_1} \right) \nabla \cdot \left\{ \varepsilon^2 \left[ \rho g L^2 + \sqrt{\delta_c} \gamma \nabla (L \varepsilon^{-1/2}) \right] \right\} = 0, \quad (3.23)$$

which is a non-linear advective diffusive equation. For unidirectional drainage along the  $z$ , which is the direction of gravity, and uniform channel lengths natural choices for the length and time scales are  $(\sqrt{\delta_c} \gamma) / (2\rho g L)$  and  $(3\mu\gamma\alpha_c\delta_1) / (2\sqrt{\delta_c} \rho^2 g^2 L^3)$ , which give a dimensionless version of Verbiest's foam drainage equation

$$\frac{d}{dt} \varepsilon + \frac{\partial}{\partial z} \varepsilon^2 \left( \varepsilon^{1/2} \frac{\partial}{\partial z} \varepsilon \right) = 0, \quad (3.24)$$

where the  $\sim$  indicates dimensionless variables. The dynamics and asymptotic behavior of this partial differential equation have been worked out for several cases [41, 42].

It is known that proteins adsorbed onto interfaces create a semi-rigid layer that resists shearing, and therefore protein foams should conform to the rigid-channel model. Confocal particle tracking experiments of the flow fields in channels of protein foams confirm this picture. Figure 3.9(a) shows the distribution of axial velocities across a channel, which is parabolic and zero at the edges and conforms to the rigid scenario from Fig. 3.7(a). The pair of dashed red lines in the inset of Fig. 3.9(a) indicate the imaging slice of the confocal microscope (the imaging layer thickness is about  $20 \mu\text{m}$ ). The stars and squares show the average velocity for the flow field generated from Stokes's equation, eqn (3.17), for a rigid

interface. The agreement between theory and measurements is satisfactory, confirming the rigid channel picture and establishing the reliability of flow field mapping using particle tracking and confocal microscopy.

So far no systematic detailed forced drainage studies have been performed for protein foams, because they do not easily form large volumes of foam and are more difficult to work with. The surfactant behavior of proteins depends on pH and ionic concentration, and proteins degrade over time. Therefore datasets spanning a large range of liquid fractions and drainage velocities for protein foams are difficult to obtain. Instead experimentalists have used different surfactant systems to investigate the macroscopic drainage behavior of foams with (semi-)rigid interfaces, such as the combination of SDS with DOH or TTAB with DOH [24, 28, 43, 44].

Figure 3.9(b) shows the dependence of the front velocity on liquid fraction for forced drainage experiments. (With a minor caveat mentioned in Section 3.12 the front velocity equals the same as upstream velocity inside the plateau region.) The filled-in symbols are for TTAB and DOH foams with two different bubble sizes taken from Lorenceau *et al.* [24]. The solid line is for Verbist's rigid-channel approximation, eqn (3.22), which consistently is a factor of two below the actual measurements. In fact, Stevenson points out that the rigid channel model chronically underpredicts measured drainage velocities [31].

The open symbols of Fig. 3.9(b) show forced drainage data for a common dish washing detergent, which at low liquid fractions drains much faster than TTAB and DOH foam. The data also displays power-law behavior; however, the exponent is closer to 0.6 than 1 as predicted by the rigid interface model. Generally most experiments follow power-law behavior [31],

$$V = \frac{\rho g L^2}{\mu} K \varepsilon^\chi. \quad (3.25)$$

The range of the measured exponents is  $0.5 \leq \chi \leq 1$ , and in some cases the exponents vary with liquid fraction. For example Carrier *et al.* [19] observed that for low liquid fractions,  $\varepsilon \leq 0.05$ , the local exponent is  $\chi \sim 1$ , and for greater liquid fractions the exponent decreases to  $\chi \sim 0.7$ .

In summary, the rigid channel model predicts the drainage behavior of certain types of foams reasonably well (within a factor of two). For other foams the agreement is poor: the observed power-law is significantly smaller, and the predictions intersect with measurements only for very wet foams. Interestingly, Fig. 3.9(b) shows the normalized drainage velocities all coincide at the maximum liquid fraction,  $\varepsilon_{\text{fc}}$ . Moreover, these velocities also agree with the normalized drainage velocity through a packed fcc bed of spheres, which is represented by a large filled-in star. Experiments by Rouyer *et al.* [47] for drainage through bubbly fluids,  $\varepsilon \sim 60\%$ , show that the drag on bubbles approaches that of rigid spheres regardless of the type surfactant (mobile or not).

### 3.8 Mobile Interfaces and Neglecting Nodes

The influence of surface viscosity on the mobility of liquid gas interfaces has been well established: many types of soap films on wire frames display swirls and show advection, whereas protein films do not. Similarly, the motion of films inside foams depends on the surface viscosity [18, 19]. These considerations prompted Leonard and Lemlich to develop

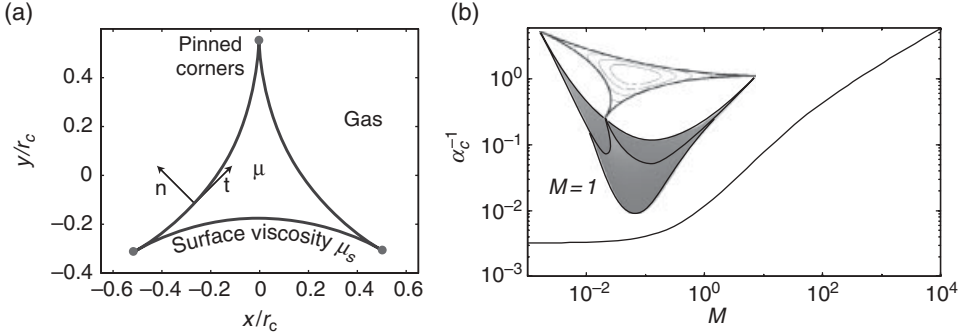


**Fig. 3.10** (a) Cross-section of the channel showing the interfacial boundary conditions and the unit normal and tangent,  $\hat{n}$  and  $\hat{t}$ . (b) Dependence of the inverse flow resistance on interfacial mobility. The inset shows a surface plot superimposed on to a contour plot of the velocity field for the case  $M = 1$ .

a model for flow through channels taking into account the interfacial mobility [9], which shall be called the mobile channel model. In a follow-up to this theoretical study, they measured foam drainage for one type of surfactant and obtained fair agreement [18]. A later experimental study performed by Desai and Kumar [48] on foams with different types of surfactants confirmed that drainage rates decrease with increase surface viscosity.

The surface velocity field depends on surface viscosity, surface stresses, and shear stresses from the bulk sublayer. The in-plane stress on a free surface is  $\mu_s \nabla_{\parallel}^2 \mathbf{u}$ , where  $\nabla_{\parallel}$  is the 2D Laplacian in the plane of the interface and the velocity field  $\mathbf{u}$  is evaluated at the surface. Surface shear stresses can be caused by variations in the surface tension, known as Marangoni forces, which arise from variations in the surfactant's surface density. The latter are given by  $\nabla_{\parallel} \gamma$ , where  $\nabla_{\parallel}$  is the 2D gradient in the plane of the interface. Additionally, shearing of the surface from the bulk sublayer leads to stresses on the surface,  $\mu(\hat{n} \cdot \nabla) \mathbf{u}$ , where  $\hat{n}$  is the surface normal. The resulting force balance at the surface is

$$(\mu(\hat{n} \cdot \nabla) - \mu_s \nabla_{\parallel}^2) \mathbf{u} = \nabla_{\parallel} \gamma, \quad (3.26)$$

where the term on the right-hand side is due to Marangoni stresses. Leonard and Lemlich made three simplifying assumptions in their treatment of flow through channels, which are (i) the three corners are pinned, (ii) Marangoni forces are negligible, hence the left-hand side of eqn (3.26) equals zero, and (iii) the channels do not flare and have constant width as shown in Fig. 3.2(c). Figure 3.10(a) provides a schematic representation of the channel's cross-section and the boundary conditions.

The dimensionless number characterizing the influence of the surface on the flow is the interfacial mobility,

$$M = \frac{\mu r}{\mu_s}, \quad (3.27)$$

which relates the bulk and surface viscosities. The ratio  $\mu_s/\mu$  is a length scale for the region of influence of the pinned corners, which in the case of small-molecule surfactant like SDS

is about 1–10 microns [43]. For channels narrower than  $\mu_s/\mu$  the interfaces are essentially pinned, whereas for wider channels ( $M \gg 1$ ) the interfaces offer little resistance and flow with the bulk. The inset to Fig. 3.10(b) shows an intermediate case, where the largest interfacial velocity is halfway between the pinned corners and is about half the peak bulk velocity.

The inverse of the flow resistance for the mobile channel model has been calculated analytically [29]:

$$\alpha_m^{-1} = \frac{1}{50} + \sqrt{\frac{M}{18}} \arctan \sqrt{\frac{M}{18}} - \frac{1}{6} \arctan \left( \frac{M}{2\pi} \right). \quad (3.28)$$

Note that in the limit of rigid interfaces the value  $\alpha_r \rightarrow 50$  is recovered (cf. Table 3.1). As shown in Fig. 3.10(b) for  $M \leq 0.1$  the flow resistance is that of a rigid interfaces, and for values  $M \geq 1$  the flow resistance approaches zero as  $\sim M^{-1/2}$ .

The forced drainage velocity for the mobile interface model is given by eqn (3.21), substituting  $\nabla P = \rho g$  and replacing the flow resistance for rigid interfaces with that for mobile interfaces,  $\alpha_r \rightarrow \alpha_m$ , gives

$$V_f = \frac{A_c}{3\alpha_m \mu} \rho g, \quad (3.29)$$

where  $A_c$  is the average channel cross-sectional area defined in eqn (3.4).

Simulations of the mobile channel model are shown in Fig. 3.11(a) for a range of surface viscosities, which in dimensionless form are expressed as  $\mu D/\mu_s$ . The curves appear almost straight and can be characterized by their local power-law behaviors, which are given in terms of the local logarithmic slopes that are included in the figure. The trend is that the logarithmic slopes diminish with increasing liquid fraction and this is due to a leveling off of  $r$  at  $\varepsilon \geq \varepsilon^*$  (cf. Fig. 3.4b). In the limit of rigid interfaces,  $\mu_s \rightarrow \infty$ , the logarithmic slopes vary from 1 for dry foams to 0.8 for wet foams. For the lowest surface viscosity shown here,  $\mu_s = 10^3 \mu D$ , the logarithmic slopes are 1.4 for dry foams and diminish to 1 at  $\varepsilon$ . Superimposed is forced drainage data for the TTAB and also TTAB & DOH foams [24]. The agreement with the TTAB foams is poor; the logarithmic slope of the measurements is about half that of the model. But the agreement with the TTAB & DOH foams is good for  $\mu D/\mu_s = 4.4$ , which corresponds to  $\mu_s \approx 2.2 \times 10^{-4}$ ,  $4.5 \times 10^{-4}$  g/s for the  $D = 1$  mm and  $D = 2$  mm foams respectively. These values are in reasonable agreement with those from literature [43, 44, 49]. But measurements of the surface viscosity are difficult and typically values reported by different groups can vary by an order of magnitude. Moreover, the surface viscosity is very sensitive to the DOH concentration, and it is questionable whether the interfacial concentration (and hence the surface viscosity) inside the draining foam is the same as that of the bulk.

In Fig. 3.11(b) the forced drainage measurements are fitted to the only free parameter of the Leonard and Lemlich model, which is the surface viscosity. The agreement for the TTAB & DOH foams is reasonable, and the best fit value for the surface viscosity is  $\mu_s \approx 2.5 \times 10^{-4}$  g/s. (Note that the  $D = 1$  mm foam measurements far outnumber those of the  $D = 2$  mm foam, and thus the best fit value is skewed towards fitting the finer foam.) But the agreement with the TTAB foams is poor, and for the worst case the discrepancies exceed a factor of five! Additionally the best fit value for the surface viscosity is  $\mu_s \approx 10^{-4}$  g/s, which is more than a factor of ten greater than that expected from other works [43, 44, 49].

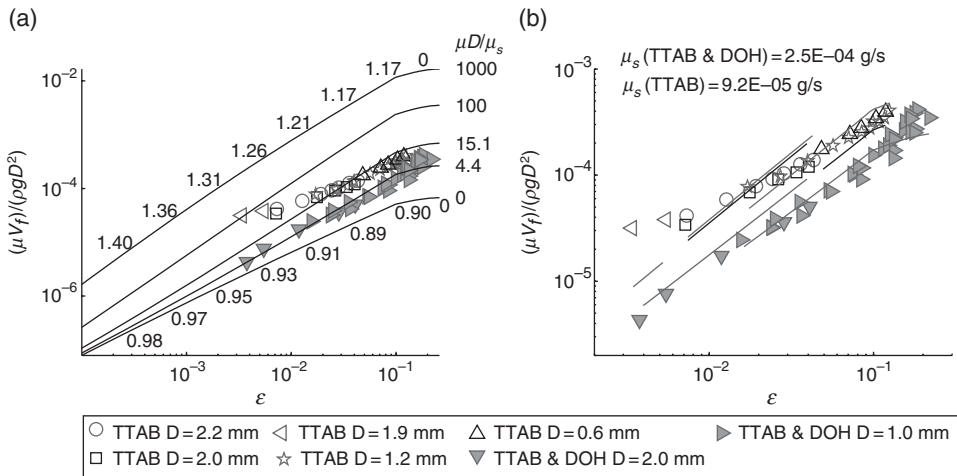


**Fig. 3.11** The mobile channel model. (a) Comparing the mobile model with forced drainage experiments for a range of dimensionless surface viscosities,  $\mu D/\mu_s$ . The numbers along the curves are the local logarithmic slopes. (b) Optimal fit to the data where the surface viscosity is given in the figure.

It is interesting that the Verbist approximation, eqn (3.22), is in better agreement with the data than the more rigorous Leonard and Lemlich theory for  $\mu_s = \infty$ . The values for the Verbist approximation are somewhat higher than those for the Leonard and Lemlich model because the liquid fraction for Verbist's model does not include the node contribution. Therefore the plotted liquid fractions are underestimates of the real liquid fraction, which in effect increases the values of the drainage velocity.

In summary, the success of the mobile channel model does not extend from TTAB & DOH foams to TTAB or Dawn foams. Rather than having logarithmic slopes  $\chi \sim 2/3$  for large interfacial mobilities, Figure 3.11(a) shows that the logarithmic slopes exceed unity with increasing  $M$  for  $\epsilon \leq \epsilon^*$ . This discrepancy indicates that the presence of additional dissipation mechanisms missed by the Leonard and Lemlich approach becomes increasingly important for mobile interfaces.

### 3.9 Neglecting Channels: The Node-dominated Model

A main assumption of the Leonard and Lemlich approach is that nodes do not contribute to the viscous dissipation and merely provide mechanisms for creating a random distribution of channel directions and evening out the distribution of liquid velocities. An alternative approach therefore is to neglect viscous dissipation in the channels and instead assume that the fluid velocity is set by dissipation inside the nodes. Figure 3.12(a) shows the axial velocity across a channel, which is a parabolic profile where the boundaries are flowing with a velocity that is about half the peak velocity. Compared with a channel of the same size, same flow rate, and no-slip boundaries, the dissipation is about one-third.

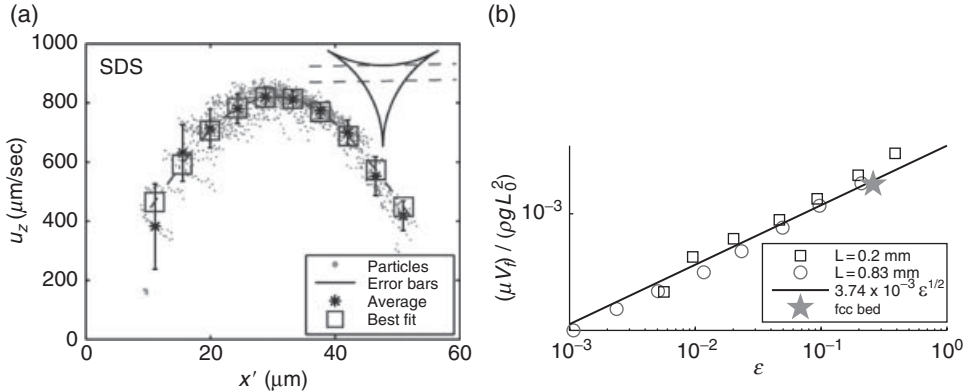


**Fig. 3.12** Mobile interfaces. (a) Profile of the axial velocity of slice through the channel of a SDS foam determined by tracking 1  $\mu\text{m}$  latex particles. (b) Applying the node-dominated model, eqn (3.30), to forced drainage data for Dawn soap foam taken from [45]. The large filled-in pentagram indicates the equivalent drainage velocity for a fcc packing of spheres [46].

However the flow field of the nodes is far more complex than in the channels, which is apparent when considering the confocal experiments (Fig. 3.7c, d). Each node is the junction of four channels, and depending on its orientation the flow into the node can be sourced by one, two, or three upstream channels. Similarly, the flow out of the node can exit through two or three downstream channels. Figure 3.7(d) shows a scenario where the flow from one upstream channel exits three downstream channels. (The void in the center is because particles flowing into the channel directed out of the page leave the focal plane.) Consequently calculating flow in nodes is a complex problem that requires considering all orientations and taking ensemble averages, which to date has not been done.

A qualitative argument for the viscous losses in a node can be made using a simple scaling argument. The length of the node is  $\xi r$  and the average cross-sectional area is  $\delta_n r^2$ , see eqn (3.7) and Fig. 3.3(c) for the network unit. For an average flow speed through the network unit,  $v$ , the viscous losses in the node scale with  $\mu v/r^2$ . Since the losses in the channel portion are assumed negligible, the pressure drop from the top to the bottom of the network unit is  $\mathbf{L} \cdot \nabla P_{\text{macro}}$  and equals the viscous dissipation  $\mu v/r$ . The macroscopic pressure gradient for forced drainage is  $\rho g$ , and averaging over all orientations gives an estimate for the average liquid velocity  $\mu v/r \sim \rho g L$ . For dry foams the lowest-order expression for liquid fraction, eqn (3.5), is sufficient, and the velocity dependence becomes

$$\mathbf{V} \approx K L_0^2 \epsilon^{1/2} \nabla P_{\text{macro}} / \mu, \quad (3.30)$$

where the dimensionless prefactor  $K$  adsorbs much ignorance.

Insertion of the velocity in the continuity equation, eqn (3.11), gives the so-called node-dominated foam drainage equation, which in the limit of dry foams is

$$\mu \frac{d}{dt} \epsilon + K \rho g \frac{d}{dz} (L^2 \epsilon^{3/2}) - K \sqrt{\delta_c} \gamma \nabla \cdot (L \nabla \epsilon) = 0. \quad (3.31)$$

This is the heat equation with a non-linear advective term.

Forced drainage experiments for two Dawn soap foams are shown in Fig. 3.12(b); the coarsest foam with the largest bubbles has been omitted because they do not scale with bubble size in a similar way, which may be due to Marangoni effects [24, 50]. The normalized drainage velocity for a fcc packed bed of spheres [46] is in agreement with the trends of the foams. The best fit to eqn (3.30) is for  $K = 3.7 \times 10^{-3}$ , which is shown by the straight line and runs almost exactly through the data point for the fcc bed of spheres. Indeed, the fcc bed has served as an estimate for the prefactor  $K$  [22].

There are several shortcomings of the node-dominated model. The observed exponential slopes are closer to  $\chi = 2/3$  rather than  $\chi = 1/2$ . There is no flow-field calculation for nodes. The flow in the channels is not plug-like, as evidenced by the confocal measurements of Fig. 3.12(a), and likely the dissipation in the channels cannot be entirely ignored, especially when the foam is dry and the nodes become tiny. Finally, the above estimates did not account for the fact that the average velocity in the nodes is about one-third that of the channels and that the average velocity of the entire network unit is a weighted average of the velocity of the node and the channel portions.

### 3.10 The Network Model: Combining Nodes and Channels

Drainage of foams with low interfacial mobility is reasonably well described by the Leonard and Lemlich model, but for mobile interfaces experimental agreement is poor, which calls for a re-examination of their assumptions. A reasonable explanation is that the dissipation in the nodes has to be accounted for when the interfaces are mobile and the dissipation in channels is small. But the complexity of flow in the nodes has so far hampered flow-field calculations and limited modeling. The approach combining both nodes and channels as presented here stems from earlier work by Koehler *et al.* [22, 29] and has been discussed by Carrier *et al.* [19], as well as Lorenceau *et al.* [24] among others.

The network unit shown in Fig. 3.3(c) consists of a channel with quarter nodes at both ends. These elements are in series, so the hydraulic resistance is the sum  $R_c + R_n/2$ . The pressure drop across the network unit is  $\mathbf{L} \cdot \nabla P$ . The resistance of the channel and node are given by eqn (3.19), and are proportional to their lengths, which are  $L - \xi r$  and  $\xi r$  respectively, and inversely proportional to the square of the cross-sectional areas. Denoting the flow factors  $\alpha_c$  and  $\alpha_n$  respectively, the flow resistances are  $R_c = \mu \alpha_m (L - \xi r) = A_c^2$  and  $R_n = \mu \alpha_n \xi r = A_n^2$ . These preliminaries result in an expression for the flow through a network unit

$$q = -\frac{\mathbf{L} \cdot \nabla P}{R_c + R_n/2} = -\left(\frac{\mathbf{L} \cdot \nabla P}{\mu}\right) A_c^2 \left[ \alpha_m (L - \xi r) + \alpha_n \frac{\xi r \delta_c^2}{2 \delta_n^2} \right]^{-1}, \quad (3.32)$$

where the last equality comes from the substitution  $A_n = \delta_n A_c / \delta_c$ .

The average velocity through a unit is due to the time for the flow to pass through the node sections and also the channel. This is a weighted average of the average channel velocity  $v_c = q/A_c$ , and the node velocity  $v_n = q/A_n$ , which can be expressed as

$$v = L \left( \frac{\xi r}{v_n} + \frac{L - \xi r}{v_c} \right)^{-1} = v_c \left[ \xi \left( \frac{\delta_n}{\delta_c} - 1 \right) \frac{r}{L} + 1 \right]^{-1}, \quad (3.33)$$

where the last equality follows from  $v_n/v_c = A_c/A_n = \delta_c/\delta_n$ .

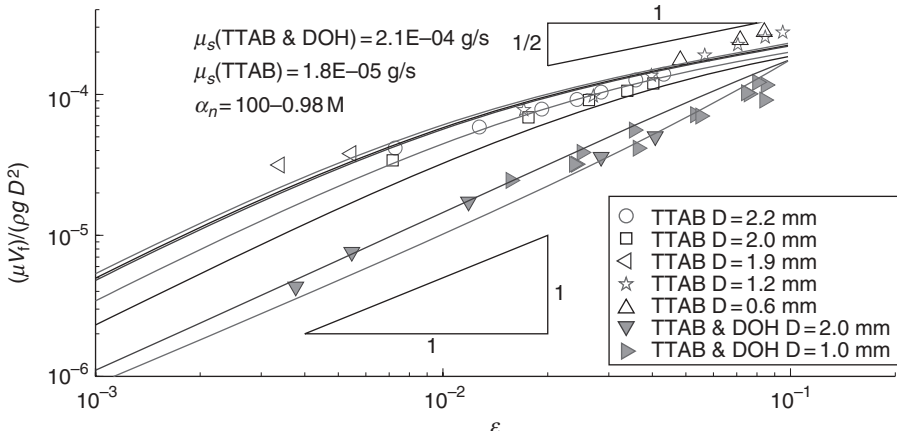


**Fig. 3.13** Dependence of the dimensionless forced drainage velocity on liquid fraction for the network model compared with measurements from [24]. The best-fit values for the surface viscosity and first-order polynomial form of  $\alpha_n(M)$  are shown.

Combining eqns (3.32) and (3.33) gives an expression for the average velocity through a network. Taking the average velocity over all orientations as for the development of eqn (3.21) yields the average macroscopic velocity

$$\mathbf{V} = -\frac{\nabla P}{3\mu} A_c \left[ \alpha_m \left( 1 - \xi \frac{r}{L} \right) + \alpha_n \frac{\xi \delta_c^2 r}{2\delta_n^2 L} \right]^{-1} \left[ \xi \left( \frac{\delta_n}{\delta_c} - 1 \right) \frac{r}{L} + 1 \right]^{-1} \quad \text{for } \epsilon \leq \epsilon^*. \quad (3.34)$$

This expression is intended for bcc foams, because the structural rearrangement about  $\epsilon^*$  increases the node to node separation and results in an abrupt increase of the channel length from  $L = 0$  to  $L = 0.2D$ . The jump in channel length causes a discontinuity in the velocity, which is an unphysical limitation of the network model.

In the limit of low liquid fractions, the portion of the hydraulic resistance due to nodes diminishes with  $r/L$  and becomes negligible. Moreover, the average velocity approaches that of the channel,  $v \rightarrow v_c$ . Therefore the flow through the network unit is dominated by the channel,  $\mathbf{V} = -A_c \nabla P / (3\alpha_m \mu)$ . When the channel's width is small compared with the effective interfacial thickness,  $r \ll \mu/\mu$ , the flow factor of the channel approaches  $\alpha_m = 1/50$ . Altogether this results in the network velocity approaching that of a rigid channel, and has a local power-law  $\chi \approx 1$ .

Conversely, in the limit of wetter foams, the channel length approaches zero, and therefore the node's hydraulic resistance dominates. To lowest order the average network velocity is proportional to  $\mathbf{V} \propto r L \alpha_n \nabla P / \mu$ , which results in a local power-law  $\chi \approx 1/2$  and in fact is the node-dominated velocity, eqn (3.30).

Figure 3.13 shows that the network model is capable of capturing the trends of forced drainage for  $\epsilon \leq \epsilon^*$  far better than the previous models. Even the worst discrepancies, which are for the  $D = 1.9$  mm TTAB foam, still fall within a factor of two of the model. The network

model transitions from the channel-dominated model for either rigid interfaces or low liquid fractions to the node-dominated model for mobile interfaces at higher liquid fractions.

The best-fit values for the surface viscosities of TTAB and TTAB & DOH are  $1.8 \times 10^{-5}$  and  $2.1 \times 10^{-4}$  g/s respectively, which are in reasonable agreement with literature values [43, 44]. The flow factor of the node is approximated by a first-order polynomial,  $\alpha_n = 100 - 0.98M$ , which follows the expectation that the hydraulic resistabce flow factor diminishes with increasing interfacial mobility. The node's flow factor is twice that of the channel, and diminishes with increasing  $M$  at half the rate. This observation indicates that the branching in the nodes essentially doubles the dissipation in the nodes, which remains even as the interfacial mobility increases. However, the experimentally determined value for the node's flow factor needs to compared with future theoretical work.

### 3.11 The Carman – Kozeny Approach

Recently a different approach towards describing foam drainage based upon porous media studies was proposed by Pitois et al. [51] and further expanded by Rouyer et al. [47]. Their starting point is the Carman – Kozeny equation which is a semi-empirical relation between the flux, liquid fraction, geometry, viscosity and pressure gradients. In terms of the notation adopted here, it is

$$\mathbf{V} = \frac{1}{C} \left( \frac{\varepsilon V_t}{S} \right)^2 \frac{\nabla P}{\mu}, \quad (3.35)$$

where  $C$  is a geometric factor,  $S$  is the surface area of the walls in contact with the flow within the unit cell volume  $V_t$ . Typically films are not included, because they are too thin to contribute to the flow. The commonly accepted geometric factor for packed spheres is  $C = 5$  [52].

To calculate the specific surface area consider the Kelvin cell, which has edge length  $L$ . The edges and corners are lined on the inside with fluid, which are quarters of nodes and thirds of channels. In the limit of dry foams, most of the liquid is contained in the 36 channels that are shared among three unit cells. The surface area of each partial channel is  $\pi r L / 3$ , and the volume of the Kelvin cell is  $2^{7/2} L^3$ . Thus the specific surface area is

$$\frac{S}{V_t} = \frac{36\pi r L}{2^{7/2} 3 L^3} = \frac{12\pi r}{2^{7/2} L^2} = 8.058 \varepsilon^{1/2} / L, \quad (3.36)$$

where the last approximation is from  $\approx 0.171(r/L)^2$ . Insertion into eqn (3.35) yields

$$\mathbf{V}_{bcc} = \frac{\varepsilon^2}{C} \left( \frac{2^3 L^4}{9\pi^2 r^2} \right) \frac{\nabla P}{\mu} \approx \frac{0.0154 \varepsilon}{C} \frac{\nabla P}{\mu}, \quad (3.37)$$

where the approximation is for the limit of dry foams. For packed spheres the commonly used value is  $C = 5$ , which gives  $\mathbf{V} \approx 3.1 \times 10^{-3} \varepsilon \nabla P / \mu$  which is about half the drainage velocity of Verbist's estimate eqn (3.22). This discrepancy may well be due to the differences

of a dry foam's interstitial geometry compared with that of a packed bed of spheres. But with increasing liquid fraction the foam geometry approaches that of a packed bed of spheres, and indeed as discussed in Section 3.7 their drainage rates are similar. A natural resolution would be for the factor to vary with increasing liquid fraction from  $C \approx 2$  for non-spherical bubbles to  $C \approx 5$  for spherical bubbles.

A similar calculation can be performed using fcc packing of rhombic dodecahedra. Although the fcc configuration is unstable for  $\varepsilon \leq 0.06$ , it has been used as an idealized foam geometry and therefore it still is informative to examine the low liquid fraction limit. The unit cell has eight complete channels, and in the limit of low liquid fractions the specific surface area is  $S/V_r = (9/2)\pi 3^{-1/2} \delta^{1/2} \varepsilon^{1/2} L^{-1}$ . Insertion into eqn (3.35) gives

$$V_{\text{fcc}} = \left( \frac{4\delta_l L^2 \varepsilon}{27\pi^2 C} \right) \frac{\nabla P}{\mu} = \left( \frac{2.57 \times 10^{-3}}{C} \right) \frac{\nabla P}{\mu}, \quad (3.38)$$

which is five times smaller than the above bcc calculation eqn (3.37) and ten times smaller than Verbiest's approximation (3.22). It remains to be seen whether the Carman – Kozeny approach continues to give unphysical small predictions for the drainage velocity at liquid fractions  $\varepsilon \geq \varepsilon^*$  where the fcc packing is actually realized.

The Carman – Kozeny approach has been extended to foams with mobile interfaces by Rouyer *et al.* [47]. They propose a semi-empirical modification for the specific surface area to account for the mobility,  $A_s \approx \varepsilon^{3/4} g(\varepsilon)/L$ , where  $g(\varepsilon) = 6.63(1 - 2.7\varepsilon + 2.2\varepsilon^2)$ . But it is unclear when to use the mobile or rigid version of the specific area, or how the transition between these two limits depends on interfacial mobility.

### 3.12 Interpreting Forced Drainage Experiments: A Detailed Look

It is necessary to re-examine the interpretation of forced drainage results. At low liquid fractions, the liquid flow is a small perturbation of the foam structure and merely swells the nodes and channels. However, at larger liquid fractions,  $\varepsilon \sim 0.1$ , structural transitions can occur. Moreover, the liquid introduced between the bubbles can non-negligibly increase their separation, which affects the observed drainage velocity,  $V_f$ , obtained from experiments. The physically relevant quantity is not the liquid velocity relative to the lab frame, but the liquid velocity relative to the bubbles.

In this treatment of determining the liquid velocity relative to the bubbles from forced drainage experiments three assumptions will be made. First, the liquid content of the initially dry foam is very small. Second, assume all of the fluid drains downwards from the point of injection, which is not entirely the case because capillarity will suck some of the liquid into the dry region above the point of injection. But for long foam columns this amount of fluid is negligible. Finally, inertial effects are assumed negligible so that the system is in quasi-static equilibrium, which generally is the case for foams at atmospheric pressures.

Define  $\psi$  as the perfusing flux,  $H_0$  as the point of injection, and  $H$  as the location of the forced drainage front relative to the foam bottom (see Fig. 3.14a). The pressure of the gas in the dry region increases due to the weight of the wet region, which is  $(H_0 - H)\rho g \varepsilon$ , where  $\varepsilon$  is the average liquid fraction of the wet region. Accordingly the gas pressure of the dry region is

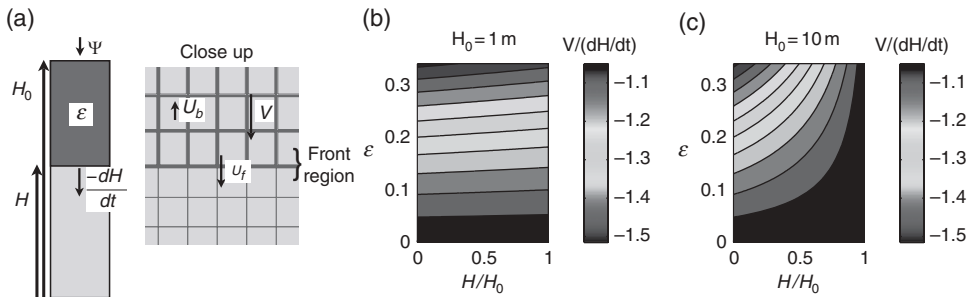


**Fig. 3.14** (a) Schematic of forced drainage experiment, where the wet region extends from \$H\_0\$ to \$H\$. Correction factors for the liquid velocity of a forced drainage experiment relative to the changing front position for (b) 1 m and (c) 2 m columns at atmospheric pressure.

$$p = p_0 + \rho g(H_0 - H)\epsilon, \quad (3.39)$$

where \$p\_0\$ is the ambient (atmospheric) pressure. Since the gas is isothermal it follows ideal gas law behavior \$dH/H = -dp/p\$, where \$dp = \rho g \psi dt\$. Thus the rate of gas compression is \$-(H\rho g \psi)/(p\_0 + \rho g(H\_0 - H)\epsilon)\$. Now consider the region of foam in the vicinity of the front, as shown schematically in the close-up of Fig. 3.14(a). In the reference frame of the dry bubbles below the front, denote the velocity of the front as \$U\_f\$. Accordingly the downwards velocity of the front is

$$-\frac{dH}{dt} = \frac{H\rho g \psi}{p_0 + \rho g(H_0 - H)\epsilon} + U_f. \quad (3.40)$$

The perfusing flux equals the *average* wet liquid fraction times the rate at which the wet region is growing, \$\psi = \epsilon dH/dt\$. Combining with eqn (3.40) gives

$$U_f = \left( \frac{H\rho g \epsilon}{p_0 + \rho g(H_0 - H)\epsilon} - 1 \right) \frac{dH}{dt}. \quad (3.41)$$

The last step is relating the the front velocity relative to the dry bubbles to the liquid velocity relative to the wet bubbles above the front \$u\$. In the frame of the dry bubbles just below the front (which is moving downwards due to compression of the dry foam region below) the influx of fluid is \$\epsilon U\_f\$, which displaces the bubbles upwards with velocity \$U\_b\$. Because the bubbles behind the front region do not compress any more, the liquid influx is compensated by an upwards flux of the gas, \$\epsilon U\_f + (1 - \epsilon)U\_b = 0\$. The liquid velocity relative to the wet bubbles is \$U = U\_f - U\_b = U\_f/(1 - \epsilon)\$. Combining with eqn (3.41) results in a relationship for the liquid velocity relative to the wet bubbles

$$V = \left( \frac{dH}{dt} \right) \left( \frac{\rho g(2H - H_0)\epsilon - p_0}{\rho g(H_0 - H)\epsilon + p_0} \right) / (1 - \epsilon). \quad (3.42)$$

Note that the quasi-static assumption implies that the ambient pressure,  $p_0$ , is large because otherwise addition of liquid causes non-negligible acceleration of the wet region as the column of dry bubbles compresses. Also, it has been assumed that the friction of the bubbles against the tube walls is negligible; experiments show that friction increases with diminishing liquid fraction [53, 54], which would slow the compression of the lower, dry foam region.

Figure 3.14 shows two examples of forced drainage: one is 1 m tall, and the second is 10 m tall. The contour plots show the correction factor,  $u/(dH/dt)$ , as a function of the front position,  $H$ , and liquid fraction. For the short column the correction factor is predominantly due to the foam expansion effect,  $\sim(1 - \varepsilon)^{-1}$ , which results in an upwards flow of bubbles. In comparison the compression of the dry foam at the bottom is small. But for the 10 m tall tube compression is important unless the front is close to the bottom, just as for the short column. Interestingly, at the beginning of the experiment, the front velocity is close to that of drainage flow,  $-dH/dt \sim V$ , which is from opposing effects of foam expansion and bubble compression. As the front moves downwards, however, the compression effect diminishes and hence the errors again increase, which for wet foams can approach 50%. Here, however, most of the focus has been for foams with  $\varepsilon \leq \varepsilon^*$ , and the estimated errors do not exceed 10%.

### 3.13 Unresolved Issues

There are still several outstanding issues, many of which have been pointed out in the literature [19, 29, 30, 36, 50, 55]. These can roughly be categorized according to uncertainties regarding (i) network geometry, (ii) boundary conditions, and (iii) the role of films in general.

Drainage models of monodisperse foams are based on the idealization of Kelvin's foam structure. But the geometric elements that the foam drainage model makes use of are minimal: channels have uniform length, are randomly oriented, and there is a second order polynomial relationship between curvature and liquid fraction. The drainage process is not sensitive to particular details of bubble packing. So even if the geometry is different, such as fcc packing, the drainage should not vary much as long as the network unit shape is maintained. However, little is known for the case of polydisperse foams, especially regarding how a range of channel lengths affects drainage. Consider the disappearance of channels as the interfacial curvature grows,  $\xi r \geq L$ , for monodisperse foams. For a polydisperse foam there is a range of channels with different lengths, of which the shortest will disappear when  $L \leq \xi r$ . Their disappearance will reduce the number of channels and nodes, thereby decreasing the resistance and increasing drainage. Thus one might expect local power-laws exceeding unity, i.e.  $\chi > 1$  in eqn (3.25). Another consideration is that very small bubbles of a polydisperse foam,  $D \leq r$ , can get lodged inside channels or nodes, which results in blockage and reduces the drainage rates.

It has long been known that surfactants affect boundary conditions, which in turn affects drainage [9]. An important surfactant property is the surface viscosity, which can lead to mobile or rigid interfaces. However, there is a range of physicochemical properties such as Marangoni stresses, solubility, equilibrium or dynamic surface tension, surface elasticity, and surface diffusion coefficient [47, 56]. In particular the behaviors of protein-stabilized

foams are sensitive to a large range of physicochemical parameters such as pH, ionic strength, concentration of cosurfactants, and temperature [5, 57, 58]. Recently foams have been stabilized with colloidal particles [35, 59–61]. Their drainage behavior should be completely different because, unlike molecular surfactants, surfactant particles are stuck at interfaces, which impedes dilation and contraction of the surfaces with varying flow rate. Therefore these foams would behave more like solid porous materials and their drainage should resemble Darcy's law 1.

There are two types of questions regarding the role of films in foam drainage, which are (i) their contribution to drainage, and (ii) their effect on flow in channels and nodes. Because films generally are thin, their contribution to foam drainage is limited [29, 50]. But experiments show that film thickness increases with liquid fraction [18, 19], and that films of protein-stabilized foams can be quite thick [57]. If the film flow is indeed non-negligible foam drainage theories would require modification. However, the second question regarding the affects of films on channels and nodes is truly fascinating. Particle-tracking experiments using confocal microscopy confirm the Leonard and Lemlich picture [9] that films pin the velocity in the channel corners to zero [39]. But the mechanism responsible for pinning the velocity has not been investigated in detail. One plausible mechanism is Marangoni stresses that are created by circulatory flow of the interfaces. The downwards flow of the channel walls causes a depletion of surfactant molecules at the top, which likely causes an upward flow in the films that replenishes surfactants at the top. But it is unclear how the Marangoni stresses vary with surfactant composition, and whether the Leonard and Lemlich assumption of pinned corners in some cases is wrong.

### 3.14 A Brief History of Foam Drainage

Foams play an important technical and industrial role, and have been part of everyday life ever since early civilizations. The ancient Egyptians and Israelites made bread and beer in large quantities. In modern times many applications for foams have been developed, such as personal hygiene, water purification, minerals extraction, structural materials, and food products. One of the main properties of foams is the relative density (another is the distribution of bubble sizes). This is a dynamic property that is determined by the drainage process whereby liquid flows downwards between bubbles due to gravitation. Consequently there has been considerable engineering interest in understanding and controlling drainage. Moreover, foams are appealing to physicists because they serve as a simple model system for soft materials that exhibit a wide range of interesting phenomena, such as packing, crystallization, yield-stresses, jamming, and microfluidics to name a few.

Early studies focused on characterizing surfactants in terms of the ability to create large volumes of foam and their stability as applicable for industrial settings. Numerous different tests were developed to assess these properties, but as pointed out long ago by Ross and Miles [62], extracting any detailed understanding regarding different physical mechanisms from these tests is very difficult.

One of the first studies specifically dealing with foam drainage was performed by Miles *et al.* [8]. They were careful to avoid effects from other processes, such as film rupture and bubble coarsening, which complicate data interpretation. In their experimental procedure

they perfused a stable monodisperse foam with a continuous liquid flux until the liquid volume fraction of the foam was uniform. Thereupon the liquid fraction was determined by weighing the foam and comparing with its volume. Plotting the relationship between the liquid content and the flow rate through the foam on log-log paper they found power-law behavior, which is in agreement with experiments performed by Weaire *et al.* [15] 50 years later. Thus arguably Miles *et al.* was the first group to study forced drainage, although the term was coined much later by Weaire *et al.* [63]. Moreover, they determined the liquid fraction from electrical conductivity measurements, which in recent studies have been frequently used [63–65]. It should be pointed out that this early study did not consider the dynamics of the liquid fraction, known as the foam drainage equation, which is a pioneering contribution of Weaire's study.

An important series of drainage studies was performed by Leonard and Lemlich [9, 18]. The authors investigated in detail how liquid flows between bubbles. They used Stokes's equations to model the fluid through Plateau borders, which are the interstitial spaces between three compressed bubbles. The boundary condition of the Plateau border's liquid – gas interface was set by pinning the corners and assuming a free-surface flow with a surface viscosity. Their experimental verification was foam fractionation, the process by which a continuously generated foam removes surface-active particles from a solution, which is more difficult to analyze.

Several decades later two independent studies of foam drainage dynamics were performed. The earlier study, performed by Goldfarb *et al.* [26], is a theoretical calculation of the spatiotemporal evolution of a foam's liquid fraction. The later study, performed by Verbist and Weaire [27], is a similar theoretical treatment and was followed up a year later with experimental confirmation [63]. It is noteworthy that unlike the earlier work by Leonard and Lemlich [9] both models assumed fixed boundaries at the liquid – gas interface. This was precisely the point of departure for the next study of foam drainage performed by Koehler *et al.* [45], who found for their particular surfactant system that the dynamics of foam drainage differed from the theories based upon rigid interfaces. Instead they proposed that the interfaces are mobile, causing the dissipation to shift from Plateau borders to nodes. A follow-up study was performed where foam drainage with different starting conditions was carefully compared with theory [22]. In several subsequent studies the surfactants were altered to investigate the role of interfacial mobility on the drainage dynamics, generally confirming the two limits, which are rigid and mobile interfaces [24, 28, 32]. However, as pointed out by Stevenson [31], the models in general are not robust and *a priori* quantitative agreement in many cases is less than desirable.

## References

- [1] J.J. Bikerman. *Foams*. Springer, New York, 1973.
- [2] D. Weaire and S. Hutzler. *The Physics of Foam*. Oxford University Press, New York, 2000.
- [3] R. Lemlich and E. Lavi. Foam fractionation with reux. *Science*, **134**(3473): 191, 1961.
- [4] R. Leonard. Adsorptive bubble separation techniques: foam fractionation and allied techniques. *Ind. Eng. Chem.*, **39**: 16–29, 1968.
- [5] F.A. Husband, D.B. Sarney, M.J. Barnard and P.J. Wilde. Comparison of foaming and interfacial properties of pure sucrose monolaurates, dilaurate and commercial preparations. *Food Hydrocoll.*, **12**(2): 237–44, 1998.

- [6] J. Banhart. Properties and applications of cast aluminum sponges. *Adv. Eng. Mater.*, **2**: 188–91, 2000.
- [7] P. Stevenson and G. J. Jameson. Modeling continuous foam fractionation with reux. *Chem. Eng. Process.*, **39**: 590, 2007.
- [8] G.D. Miles, L. Shedlovsky and J. Ross. Foam drainage. *J. Phys. Chem.*, **49**(2): 93–107, 1945.
- [9] R.A. Leonard and R. Lemlich. A study of interstitial liquid flow in foam, part 1. *AIChE J.*, **11**: 18–24, 1965.
- [10] W. Ostwald. *Lehrbuch der Allgemeinen Chemie*, vol. 2. W. Engelmann, Leipzig, 1896.
- [11] D.J. Durian, D.A. Weitz and D.J. Pine. Dynamics and coarsening in three-dimensional foams. *J. Phys.: Condensed Matter*, **2**: SA433–6, 1990.
- [12] S. Hutzler and D. Weaire. Foam coarsening under forced drainage. *Phil. Mag. Lett.*, **80**(6): 419–25, 2000.
- [13] S. Hilgenfeldt, S.A. Koehler and H.A. Stone. Dynamics of coarsening foams: accelerated and self-limiting drainage. *Phys. Rev. Lett.*, **86**: 4704–7, 2001.
- [14] J.K. Angarska, K.D. Tachev and N.D. Denkov. Composition of mixed adsorption layers and micelles in solutions of sodium dodecyl sulfate and dodecyl acid diethanol amide. *Coll. Surf. A: Physicochem. Eng. Aspects*, **233**: 193–201, 2004.
- [15] D. Weaire, N. Pittet and S. Hutzler. Steady-state drainage of an aqueous foam. *Phys. Rev. Lett.*, **71**(16): 2670–3, 1993.
- [16] W. Thomson. On the division of space with minimum partitional area. *Phil. Mag.*, **24**(151): 504, 1887.
- [17] R. Phelan, D. Weaire and K. Brakke. Computation of equilibrium foam structures using the surface evolver. *Exp. Math.*, **4**(3): 181, 1995.
- [18] R.A. Leonard and R. Lemlich. Part ii. Experimental verification and observations. *AIChE J.*, **11**: 25–9, 1965.
- [19] V. Carrier, S. Destouesse and A. Colin. Foam drainage: a film contribution? *Phys. Rev. E*, **65**: 061404, 2002.
- [20] A.M. Kraynik. Foam structure: from soap froth to solid foams. *MRS Bull.*, **28**(4): 275–8, 2003.
- [21] K. Brakke. Surface Evolver Program, Mathematics Department, Susquehanna University. [www.susqu.edu/brakke/evolver/evolver.html](http://susqu.edu/brakke/evolver/evolver.html).
- [22] S.A. Koehler, S. Hilgenfeldt and H.A. Stone. A generalized view of foam drainage: experiment and theory. *Langmuir*, **16**: 6327–41, 2000.
- [23] R. Hohler, Y.Y.C. Sang, E. Lorenceau and S. Cohen-Addad. Osmotic pressure and structures of monodisperse ordered foam. *Langmuir*, **24**: 418–25, 2008.
- [24] E. Lorenceau, N. Louvet, F. Rouyer and O. Pitois. Permeability of aqueous foams. *Eur. Phys. J. E*, **28**(3): 293–304, 2009.
- [25] D. Weaire. Structural transformations in foams. *Phil. Mag. Lett.*, **69**(2): 99–105, 1994.
- [26] I.I. Gol'dfarb, K.B. Kann and I.R. Shreiber. Liquid flow in foams. *Fluid Dynamics*, **23**: 244–9, 1988.
- [27] G. Verbist and D. Weaire. A soluble model for foam drainage. *Europhys. Lett.*, **26**: 631, 1994.
- [28] M. Durand, G. Martinoty and D. Langevin. Liquid flow through aqueous foams: from the plateau border-dominated regime to the node-dominated regime. *Phys. Rev. E*, **60**: R6307, 1999.
- [29] S.A. Koehler, S. Hilgenfeldt and H.A. Stone. Foam drainage on the microscale. part 1: Modelling flow through single plateau borders. *J. Coll. Interface Sci.*, **276**: 420–38, 2004.
- [30] A. Saint-Jalmes. Physical chemistry in foam drainage and coarsening. *Soft Matter*, **2**(10): 836–49, 2006.
- [31] P. Stevenson. On forced drainage of foam. *Coll. Surf. A: Physicochem. Eng. Aspects*, **305**: 1–9, 2007.
- [32] O. Pitois, N. Louvet, E. Lorenceau and F. Rouyer. Node contribution to the permeability of liquid foams. *J. Coll. Interface Sci.*, **322**(2): 675–7, 2008.
- [33] M. Safouane, M. Durand, A. Saint-Jalmes, D. Langevin and V. Bergeron. Aqueous foam drainage. role of the rheology of the foaming fluid. *J. de Physique IV*, **11**: 275–80, 2001.
- [34] M. Safouane, A. Saint-Jalmes, V. Bergeron and D. Langevin. Viscosity effects in foam drainage: Newtonian and non-newtonian foaming fluids. *Eur. Phys. J. E*, **19**: 195–202, 2006.

- [35] S. Fujii, P.D. Iddon, A.J. Ryan and S.P. Armes. Aqueous particulate foams stabilized solely with polymer latex particles. *Langmuir*, **22**(18): 7512–20, 2006.
- [36] P. Stevenson and X. Li. A viscous – inertial model of foam drainage. *Chem. Eng. Res. Des.*, **88**: 928–35, 2010.
- [37] N.A.Mortensen, F. Okkels and H. Bruus. Reexamination of hagen-poiseuille flow: Shape dependence of the hydraulic resistance in microchannels. *Phys. Rev. E*, **71**: 057301, 2005.
- [38] S.A. Koehler, S. Hilgenfeldt, E.R. Weeks and H.A. Stone. Drainage of single plateau borders: Direct observation of rigid and mobile interfaces. *Phys. Rev. E*, **66**: 040601–4, 2002.
- [39] S.A. Koehler, E.R. Weeks, S. Hilgenfeldt and H.A. Stone. Foam drainage on the microscale. Part 2: Imaging flow through single plateau borders. *J. Coll. Interface Sci.*, **276**: 439–49, 2004.
- [40] S.A. Koehler. Flow streamlines in uniform draining foams. *J. Stat. Mech., Theory Exp.*, **3**: L03002, 1–8, 2007.
- [41] G. Verbist, D. Weaire and A. Kraynik. The foam drainage equation. *J. Phys.: Condensed Matter*, **8**: 3715–31, 1996.
- [42] S.A. Koehler, H.A. Stone, M.P. Brenner and J. Eggers. Dynamics of foam drainage. *Phys. Rev. E*, **58**: 2097, 1998.
- [43] N.F. Djabbarah and D.T. Wasan. Dilational viscoelastic properties of fluid interfaces. 3. Mixed surfactant systems. *Chem. Eng. Sci.*, **37**(2): 175–84, 1982.
- [44] W. Drenckhan, H. Ritacco, A. Saint-Jalmes, A. Saugey, P. McGuinness, A. van der Net, D. Langevin and D. Weaire. Fluid dynamics of rivulet flow between plates. *Phys. Fluids*, **19**(10), 2007.
- [45] S.A. Koehler, S. Hilgenfeldt and H.A. Stone. Liquid flow through aqueous foams: the node-dominated foam drainage equation. *Phys. Rev. Lett.*, **82**: 4232, 1999.
- [46] A.A. Zick and G.M. Homsy. Stokes flow through periodic arrays of spheres. *J. Fluid Mech.*, **115**(1): 13–26, 1982.
- [47] F. Rouyer, O. Pitois, E. Lorenceau and N. Louvet. Permeability of a bubble assembly: From the very dry to the wet limit. *Phys. Fluids*, **22**(4): 2010.
- [48] D. Desai and R. Kumar. Flow through a plateau border of cellular foam. *Chem. Eng. Sci.*, **37**(9): 1361–70, 1982.
- [49] M. Joly. *Recent Progress in Surface Science*, vol. 1, p. 45. Academic Press, New York, 1964.
- [50] F. Rouyer, E. Lorenceau and O. Pitois. Film junction effect on foam drainage. *Coll. Surf. A: Physicochem. Eng. Aspects*, **324**(1–3): 234–6, 2008.
- [51] O. Pitois, E. Lorenceau, N. Louvet and F. Rouyer. Specific surface area model for foam permeability. *Langmuir*, **25**(1): 97–100 2009.
- [52] F.A.L. Dullien. *Porous Media: Fluid Transport and Pore Structure*. Academic Press, New York, 1992.
- [53] R. Soller and S.A. Koehler. Rheology of steady-state draining foams. *Phys. Rev. Lett.*, **100**: 208301, 2008.
- [54] N.D. Denkov, S. Tcholakova, K. Golemanov, K.P. Ananthapadmanabhan and A. Lips. Viscous friction in foams and concentrated emulsions under steady shear. *Phys. Rev. Lett.*, **100**: 138301, 2008.
- [55] V. Carrier and A. Colin. Anisotropy of draining foams. *Langmuir*, **18**: 7564–70, 2002.
- [56] M. Durand and D. Langevin. Physicochemical approach to the theory of foam drainage. *Eur. Phys. J. E*, **7**: 35–44, 2002.
- [57] J.M.R. Patino, M.D.N. Delgado and J.A.L. Fernandez. Stability and mechanical strength of aqueous foams containing food protein. *Coll. Surf. A: Physicochem. Eng. Aspects*, **99**(1): 65–78, 1995.
- [58] K.G. Marinova, E.S. Basheva, B. Nenova, M. Temelska, A.Y. Mirarefi, B. Campbell and I.B. Ivanov. Physico-chemical factors controlling the foamability and foam stability of milk proteins: sodium caseinate and whey protein concentrates. *Food Hydrocoll.*, **23**: 1864–76, 2009.
- [59] R. Aveyard, B.P. Binks and J.H. Clint. Emulsions stabilised solely by colloidal particles. *Adv. Coll. Interface Sci.*, **100**: 503–46, 2003.
- [60] Z.P. Du, M.P. Bilbao-Montoya, B.P. Binks, E. Dickinson, R. Ettelaie and B.S. Murray. Outstanding stability of particle-stabilized bubbles. *Langmuir*, **19**(8): 3106–8, 2003.
- [61] T.S. Horozov. Foams and foam films stabilised by solid particles. *Curr. Opinion Coll. Interface Sci.*, **13**(3): 134–40, 2008.

- [62] J. Ross and G.D. Miles. An apparatus for comparison of foaming properties of soaps and detergents. *J. Am. Oil Chemists' Soc.*, **18**(5): 99–102, 1941.
- [63] D. Weaire, S. Findlay and G. Verbist. Measurement of foam ac conductivity. *J. Phys., Condensed Matter*, **7**: L217–22, 1995.
- [64] R. Garcia-Gonzales, C. Monnereau, J.F. Thovert, P.M. Adler and M. Vignes-Adler. Conductivity of real foams. *Coll. Surfaces A: Physicochem. Eng. Aspects*, **151**(3): 497–503, 1999.
- [65] K. Feitosa, S. Marze, A. Saint-Jalme and D.J. Durian. Electrical conductivity of dispersions: from dry foams to dilute suspensions. *J. Phys.: Condensed Matter*, **17**(41): 6301–5, 2005.

# 4

## Foam Ripening

*Olivier Pitois*

### 4.1 Introduction

The diffusion of gas between bubbles is an important phenomenon by which liquid foam evolves towards thermodynamic equilibrium. By this process, bubbles smaller than the average size shrink, whereas larger bubbles grow, resulting in a growing of the average size of the bubbles over time, and a spontaneous evolution of the radii distribution towards a statistically invariant one. This coarsening, or disproportionation, is analogous to the ripening or aging of emulsions and crystals. This process is strongly coupled with drainage, and rheological and optical foam properties. This is mainly due to the increase of the average bubble size, but note also that ripening induces internal dynamics that are central in the complex rheological behaviour of foams.

Here I present fundamentals for describing ripening in dilute suspensions of spherical bubbles, in dry and wet foams. In each case, kinetics for bubble growth are given as a function of the relevant parameters. Finally, several strategies for controlling bubble ripening are suggested.

### 4.2 The Very Wet Limit

We consider here a suspension of well-separated spherical bubbles with radius  $R$ . The concentration of gas  $c = c(r, t)$  diffusing in the liquid surrounding each bubble is spherically symmetric and described by Fick's second law of diffusion:  $\partial c / \partial t = D \cdot \Delta c$ , where  $D$  is the

diffusion coefficient of the gas in the liquid. Assuming that the time to reach a fully developed concentration profile is sufficiently small compared to the time of evolution of the bubble radius, i.e.  $\partial c/\partial t \approx 0$ , the expected concentration profile is:

$$c(r) = c_{\infty} + R(c(R) - c_{\infty})/r \quad (4.1)$$

where  $c_{\infty}$  and  $c(R)$  are gas concentrations at  $r \approx \infty$  and  $r = R$  respectively. Using Fick's first law, the flux of gas across the bubble surface is determined and the resulting change in bubble volume is given by:

$$\frac{dV}{dt} = 4\pi R^2 D v_m (\partial c / \partial r)_{r=R} \quad (4.2)$$

where  $v_m$  is the ideal gas molar volume and  $(\partial c / \partial r)_{r=R} = (c_{\infty} - c(R))/R$  is obtained from eqn (4.1). The gas concentration at the bubble's surface,  $c(R)$ , is in equilibrium with bubble gas pressure:  $P = P_0 + 2\sigma/R$ , where  $\sigma$  is the surface tension and  $P_0$  is the reference pressure. It can be determined from Henry's law:

$$c(R) = H(P_0 + 2\sigma/R) \quad (4.3)$$

where  $H$  is Henry's law constant. From eqns (4.2) and (4.3), the time evolution for bubble radius is:

$$\frac{dR}{dt} = \frac{1}{4\pi R^2} \frac{dV}{dt} = \frac{HDP_0 v_m}{R} \left( s - \frac{2\sigma}{P_0 R} \right) \quad (4.4)$$

where  $s = (c_{\infty} - c_0)/c_0$  is the saturation parameter. Thus, for every value of  $s > 0$ , there exists a critical radius  $R_s = 2\sigma/sP_0$  with which a gas bubble is in equilibrium with the solution, i.e.  $dR/dt = 0$ . In other words, the bubble grows if  $R > R_s$  and it dissolves if  $R < R_s$ . The liquid surrounding bubbles acts as a reservoir in which small bubbles supply gas and large bubbles remove it (see Fig. 4.1). The coarsening of the bubble assembly is analogous to Ostwald ripening as considered by Lifshitz and Slyosov [1] and by Wagner [2] (LSW). The authors have shown that the average size  $\langle R \rangle \equiv R_s$ , so that eqn (4.4) can be rewritten:

$$\frac{dR}{dt} = \frac{K_1}{R} \left( \frac{1}{\langle R \rangle} - \frac{1}{R} \right) \quad (4.5)$$

with  $K_1 = 2\sigma HDv_m$ . From eqn (4.5), it is obvious that large bubbles grow at the expense of small ones, so that the average bubble size increases as a function of time. Lifshitz and Slyosov were also able to show that the growth  $\langle R(t) \rangle$  will asymptotically approach the following expression:

$$\langle R \rangle = \left( \frac{4}{9} K_1 t \right)^{1/3} \quad (4.6)$$

This asymptotic growth rate is applicable to dilute systems, in which bubble–bubble interactions are not important. As shown in the following, foam ripening generally exhibits a different scaling law due to these interactions.

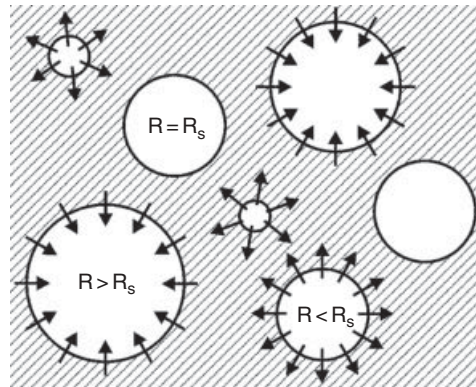


**Fig. 4.1** Ripening of a very wet bubbly system (Ostwald ripening). Liquid surrounding bubbles acts as a reservoir in which bubbles with radius smaller than the mean radius  $\langle R \rangle \equiv R_s$  supply gas and large bubbles remove it. The average bubble growth is characterized by the scaling law:  $\langle R \rangle \sim t^{1/3}$ .

### 4.3 The Very Dry Limit

In the dry foam limit, gas bubbles resemble closely packed polyhedra. Gas diffusion takes place through the thin liquid films separating neighbouring bubbles. First, I describe the gas diffusion process through liquid films. Then I present the theory of von Neumann for the ripening of foams in two dimensions, as well as extensions of his analysis in three dimensions.

#### 4.3.1 Inter-bubble Gas Diffusion through Thin Films

Consider such a film of thickness  $h$ , with a wall in contact with the gas of a bubble at pressure  $P_1$  and the other at pressure  $P_2$ . Gas concentration in liquid at film walls is respectively  $c_1$  and  $c_2$ . The volume gas flow rate per unit area through the film is related to both Fickian diffusion through the central liquid layer (bulk) and permeation through the two monolayers. The permeability of the complete film,  $k_f$ , can be written as follows [3]:

$$\frac{1}{k_f} = \frac{1}{k_{bulk}} + \frac{2}{k'_{ml}} \quad (4.7)$$

The volume gas flow rate per unit area through the central liquid layer is obtained by applying Fick's first law:

$$\vec{q}_{bulk} = -Dv_m \frac{dc}{dx} \vec{e}_x = k_{bulk} (P_1 - P_2) \vec{e}_x \quad (4.8)$$

where  $x$  is the coordinate along the axis  $\vec{e}_x$ , normal to the film, and where  $k_{bulk} = DHv_m/h$  (Henry's law has been used to relate gas concentrations in liquid to gas pressures). Gas

flow rate corresponding to the monolayers is  $\bar{q}_{ml} = (Hv_m k_{ml}/2)(P_1 - P_2)\bar{e}_x$ , where  $k_{ml}$  is defined by  $k'_{ml} = Hv_m k_{ml}$ . The resulting gas flow rate per unit area for the complete film is thus given by:

$$\bar{q}_f = k_f(P_1 - P_2)\bar{e}_x = \left[ \frac{DHv_m}{h + 2D/k_{ml}} \right] (P_1 - P_2)\bar{e}_x \quad (4.9)$$

The gas flow rate through a face of a polyhedral bubble in dry foam is given by eqn (4.9). It is strongly dependent on film thickness and its direction is determined by the gas pressure difference between the two bubbles sharing the same face. But whereas the gas pressure in a spherical bubble is given by the Laplace law, the pressure in a polyhedral bubble depends in a complex way upon its size and its shape. An analysis of this problem has been proposed by von Neumann for two-dimensional foams. It is presented in the next part.

#### 4.3.2 von Neumann Ripening for 2D Foams

Consider a 2D dry foam satisfying Plateau's rules, such as that presented in Fig. 4.2. Thin films of length  $l_{ij}$  separate neighbouring bubbles  $i$  and  $j$ , and join symmetrically three by three, with an angle equal to  $2\pi/3$ . As presented above, gas diffuses between neighbouring bubbles  $i$  and  $j$  with a gas flow rate (per unit length) given by  $q_{ij} = -k_f(P_i - P_j)l_{ij}$ . Laplace law is used to express the pressure difference as a function of the radius of curvature  $R_{ij}$  of the film ( $ij$ ), which is counted positively if the centre of the circle is inside bubble  $i$ :  $P_i - P_j = 2\sigma/R_{ij}$  (the coefficient 2 accounts for the two interfaces of the film). The change in area  $A_i$  of bubble  $i$  is then obtained by summing  $q_{ij}$  over the  $n$  neighbouring bubbles:

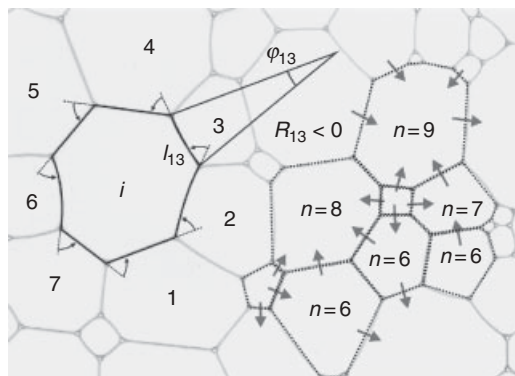


**Fig. 4.2** Picture of 2D foam (bubbles are squeezed between two glass plates): lines correspond to liquid films separating bubbles. The bubble noted by  $i$  has  $n = 7$  sides of length  $l_{ij}$ . The total angle covered by films' curvatures along the perimeter of bubble  $i$  is equal to  $\sum_{j=1}^n \varphi_{ij} = \sum_{j=1}^n l_{ij}/R_{ij} = \pi(6 - n)/3$ . Arrows illustrate the exchange of gas between  $n$ -sides bubbles.

$$\frac{dA_i}{dt} = -k_f \sum_{j=1}^n (P_i - P_j) l_{ij} = -2\sigma k_f \sum_{j=1}^n \frac{l_{ij}}{R_{ij}} \quad (4.10)$$

Defining the angle  $\varphi_{ij} = l_{ij}/R_{ij}$  (see Fig. 4.2), it can be easily shown that  $\sum_{j=1}^n \varphi_{ij}$ , which is the angle covered by films' curvatures along the perimeter of the bubble, verifies the following relation:

$$\sum_{j=1}^n \varphi_{ij} = 2\pi - n \frac{\pi}{3} = \frac{\pi}{3}(6 - n) \quad (4.11)$$

The rate of size evolution for bubble  $i$  is then deduced from eqns (4.10) and (4.11):

$$\frac{dA_i}{dt} = \frac{2\pi\sigma}{3} k_f (n - 6) = D_{2d} (n - 6) \quad (4.12)$$

Thus, a two-dimensional bubble with  $n$  sides grows at a rate proportional to  $n - 6$  and is not dependent on the bubble size. This remarkable result is due to von Neumann in 1952 [4]. Experiments performed by enclosing foam in a thin glass cell showed that eqn (4.12) holds on the average (Fig. 4.3a). Thus, at a given time, bubbles with  $n < 6$  get smaller and bubbles with  $n > 6$  grow. Bubbles with hexagonal shape, with  $n = 6$ , do not evolve. Moreover, note that these latter can have both concave and convex sides, because this is compatible with  $\sum_{j=1}^n \varphi_{ij} = \sum_{j=1}^n l_{ij}/R_{ij} = 0$ . Examples of gas transfers between  $n$ -sided bubbles are also presented in Fig. 4.2.

Equation (4.12) implies that bubbles with  $n < 6$  disappear within a characteristic time  $\tau_n \sim \langle A \rangle / D_{2d} (6 - n)$ , where  $\langle A \rangle_n$  is the mean area of  $n$ -sides bubbles, so that the mean bubble

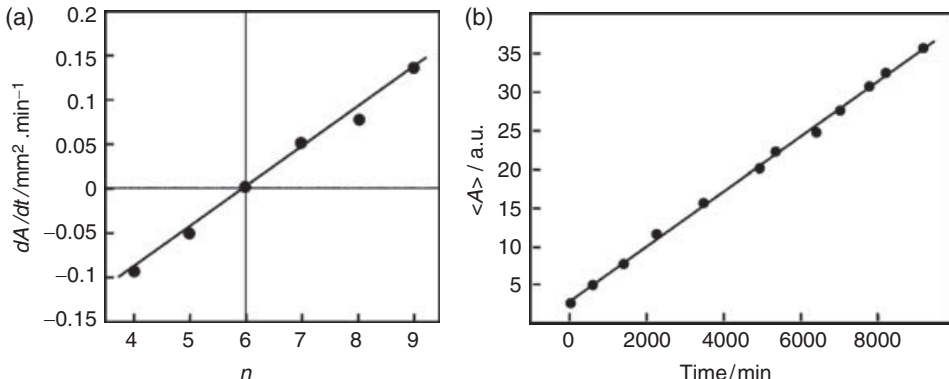


**Fig. 4.3** Growth rate of bubbles in 2D foams. (a) Average rate of size evolution of  $n$ -sides bubbles (from [5]). At each time, bubbles with  $n < 6$  shrink, bubbles with  $n > 6$  grow, bubbles with  $n = 6$  do not evolve. Data verify eqn (4.12) with  $D_{2d} \approx 0.046 \text{ mm}^2/\text{min}$ . (b) Average bubble area as a function of time (from [6]), illustrating eqn (4.13).

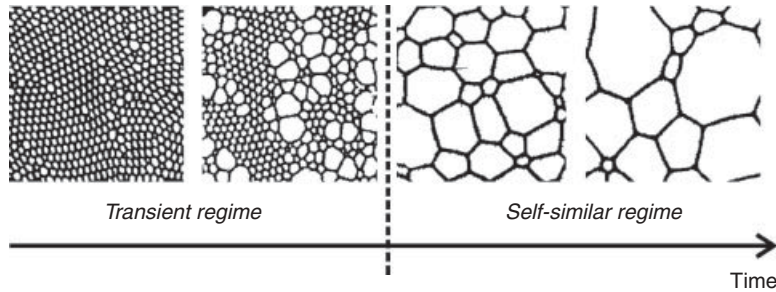


**Fig. 4.4** Pictures of 2D foam (lines correspond to liquid films separating bubbles) as a function of time. In the transient regime, coarsening initiates in areas containing topological defects and spreads to ordered areas. Then the self-similar regime begins, where successive pictures look alike, except that the average bubble size increases as  $\langle R \rangle \sim t^{1/2}$ .

area,  $\langle A \rangle$ , increases as a function of time. The decrease of the total number of bubbles per unit time can be written  $dN/dt = -\sum_{n<6} N(n)/\tau_n$ , where  $N(n)$  is the number of  $n$ -sides bubbles. If we assume that a self-similar regime is reached for the bubble growth, where  $N(n)/N$  and  $\langle A \rangle / \langle A \rangle_0$  are invariant quantities, it implies that  $dN/dt \sim -N^2$  or equivalently  $N \sim t^{-1}$ . As a consequence, the growth rate of the mean bubble area is expected to be [7]:

$$\langle A(t) \rangle - \langle A_0 \rangle \propto t - t_0 \quad (4.13)$$

where  $t_0$  is the time corresponding to the beginning of the self-similar regime. The validity of eqn (4.13) can be checked in Fig. 4.3b. Note that this scaling behaviour is restricted to the self-similar regime, which is observed after a transient regime. The duration of this latter depends on the initial foam disorder, which can be measured through the second moment  $\mu_2 = \sum_n (n - \bar{n})^2 p(n)$  of the distribution  $p(n)$ . In the self-similar regime,  $\mu_2 \approx 1.5$ . If a disordered two-dimensional foam is created, with a value of  $\mu_2$  of order unity, it will rapidly settle into its asymptotic state. In contrast, a long transient regime with a different scaling behaviour is observed for initially ordered foams, i.e.  $\mu_2 \approx 0$ . In particular, coarsening initiates in areas containing topological defects and spreads to ordered areas. An illustration of both behaviours is presented in Fig. 4.4. Note also that whereas a perfect crystal of hexagons is not expected to coarsen, topological defects induce the coarsening at boundaries.

### 4.3.3 3D Coarsening

The growth law for a bubble in dry three-dimensional foams can be written by analogy with eqn (4.10):

$$\frac{dV_i}{dt} = -k_f \sum_{j=1}^n (P_i - P_j) S_{ij} = -2\sigma k_f \sum_{j=1}^n S_{ij} \left( \frac{1}{R_{1,ij}} + \frac{1}{R_{2,ij}} \right) \quad (4.14)$$

Here, gas diffuses through films  $(i,j)$ .  $S_{ij}$ ,  $R_{1,ij}$  and  $R_{2,ij}$  are respectively the area and the two principal radii of curvature of a film  $(i,j)$  between two neighbouring bubbles  $i$  and  $j$ . The analogue of von Neumann's rule has been proposed only very recently by MacPherson and Srolovitz [8]:

$$\sum_{j=1}^n S_{ij} \left( \frac{1}{R_{1,ij}} + \frac{1}{R_{2,ij}} \right) = 2\pi \ell_i - \frac{\pi}{3} E_i \quad (4.15)$$

where  $\ell_i$  and  $E_i$  are respectively the linear size and the total length of edges of bubble  $i$ . The validity of this three-dimensional version of von Neumann's law has not yet been established experimentally, although in principle, high speed X-ray tomography studies, such as those of Lambert et al. [9], could allow the comparison. Until now, experiments on 3D foams have attempted to relate bubble growth rate to the number of faces per bubble [10, 11]. Eqns (4.14) and (4.15) indicate that in three dimensions, bubbles' growth law depends on both bubble size and bubble shape. This is in contrast with results obtained for both well separated bubbles (eqn 4.5), where the growth rate is determined only by bubble size, and 2D dry foams (eqn 4.12), where the growth rate is determined only by bubble shape. As for 2D dry foams, assuming that a self-similar regime is reached provides the growth rate of the mean bubble volume:

$$\langle V(t) \rangle^{2/3} - \langle V_0 \rangle^{2/3} \propto t - t_0 \quad (4.16)$$

Thus, for dry foams, the increase in mean bubble radius is described by the power-law growth  $\langle R \rangle \sim t^{1/2}$ , which differs from the growth law given by eqn (4.6). Experimental evidence for such growth behaviour for dry foams has been found using X-ray tomography. Note that this behaviour has been unambiguously attributed to the existence of the self-similar regime, in which the bubble size distribution does not change with time [9].

#### 4.4 Wet Foams

In dry foam, the growth rate for a given bubble has been shown to be determined by both bubble size and bubble shape. In wet foam, bubble shape is expected to be more spherical, so that the influence of the shape parameter is not as crucial as in dry foam. More precisely, X-ray tomography experiments on wet foams have shown that a reasonably well defined curve exists when plotting the average bubble growth rate as a function of the bubble volume [10]. Thus, on average, it makes sense to describe the growth rate of bubbles with volume  $V$  by the following form:

$$\frac{dV}{dt} = V^{1/3} \cdot G_V \quad (4.17)$$

where  $G_V$  is an average value over bubbles with volume  $V$  and has dimensions of diffusivity, including the physico-chemical characteristics of the liquid, gas and surfactant.  $G_V$  is presented in Fig. 4.5. as a function of  $V/\langle V \rangle$ , where  $\langle V \rangle$  is mean bubble volume. Bubbles

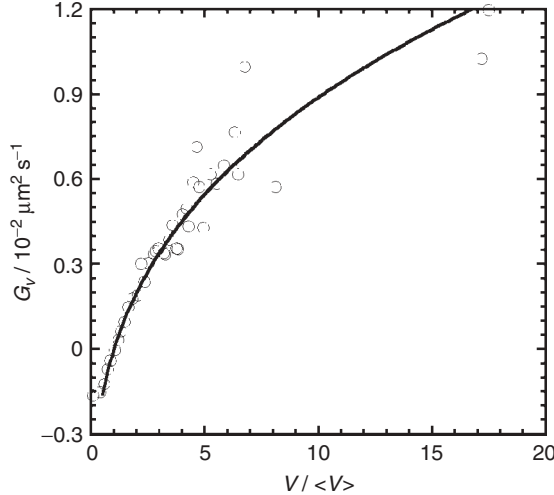


**Fig. 4.5** Average bubble growth rate as a function of the bubble volume (data from [9]) for a wet foam with liquid fraction 20%. The solid line corresponds to eqn (4.19) with  $K'_2$  equal to  $7.7 \times 10^{-3} \mu\text{m}^2/\text{s}$ .

with a volume larger than  $\langle V \rangle$  grow, i.e.  $G_V > 0$ , whereas bubbles with a volume lower than  $\langle V \rangle$  shrink, i.e.  $G_V < 0$ . At each time, everything happens as if bubbles with mean volume  $\langle V \rangle$  serve as a reservoir, in which smaller bubbles supply gas and larger bubbles remove it. This picture is similar to the ripening of very wet bubble assemblies, except that here gas diffuses between neighbouring bubbles according to a rate given by eqn (4.9). The gas pressure of bubbles is assumed to be that of volume-equivalent spherical bubbles, i.e.  $P \approx P_0 + 2\sigma/R$ . Thus, the average rate of change of bubbles with radius  $R$  is given by:

$$\frac{dR}{dt} = -q_f = 2\sigma\bar{k}_f \left[ \frac{1}{\langle R \rangle} - \frac{1}{R} \right] = K_2 \left[ \frac{1}{\langle R \rangle} - \frac{1}{R} \right] \quad (4.18)$$

where  $\bar{k}_f$  is an effective film permeability accounting for the non-uniform film thickness in wet foam. Alternatively, eqn (4.18) can be written with respect to the bubble volume, allowing for the function  $G_V$  to be expressed by:

$$G_V = K'_2 \left[ \left( \frac{V}{\langle V \rangle} \right)^{1/3} - 1 \right] \quad (4.19)$$

with  $K'_2 = 3^{1/3} (4\pi)^{2/3} K_2$ . Eqn (4.19) is plotted in Fig. 4.5, showing good agreement with experimental data. Note that eqns (4.18) and (4.19) make sense on average only, and cannot be applied to predict the growth rate of a given bubble. This was anticipated by Lemlich in 1978 [12] and appears to be useful to describe the ripening of wet foams. It can be shown that  $\langle R \rangle \equiv \langle R \rangle_{21} = \int_0^\infty R^2 F(R) dR / \int_0^\infty R F(R) dR$ , where  $F(R)$  is the bubble size distribution

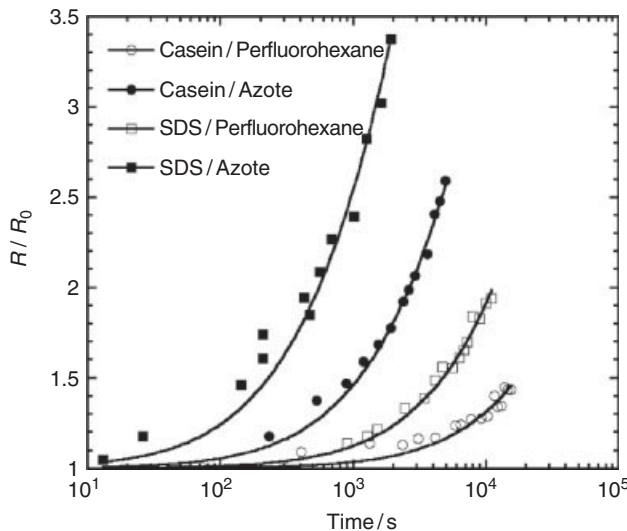


**Fig. 4.6** Relative growth of bubble radius as a function of time (data from [15]) in foams made with SDS or casein surfactants and azote or perfluorohexane gases, at constant liquid fraction  $\varepsilon = 0.15$ . The initial bubble size is  $R_0 = 60 \mu\text{m}$ . Solid lines correspond to eqn (4.22) with  $K_2 = 37.9, 7.35, 1.72$  and  $0.37 \mu\text{m/s}$  for SDS/azote, casein/azote, SDS/perfluorohexane and casein/perfluorohexane respectively.

function. Eqn (4.18) has similarity solutions, and the asymptotic size distribution function, for  $R/\langle R \rangle = w < 2$ , takes the form:

$$F(R) \sim \frac{w}{(2-w)^5} t^{-2} \exp\left(\frac{-3w}{2-w}\right) \quad (4.20)$$

and the explicit dependence of  $\langle R \rangle$  on time is given by:

$$\langle R \rangle = \left( \frac{K_2}{2} t \right)^{1/2} \quad (4.21)$$

Thus, the coarsening of wet foams is expected to be described by the same scaling behaviour as for dry foams (eqn 4.13). For practical use, the evolution for the bubble size can be written:

$$\frac{R(t)}{R_0} = \left[ 1 + \frac{K_2}{2R_0^2} t \right]^{1/2} \quad (4.22)$$

$2R_0^2/K_2 \equiv t_C$  is sometimes referred to as the coarsening time. This scaling behaviour is in satisfactory agreement with available experimental data [13–15]. An example is presented in Fig. 4.6, where the increase in bubble size was measured at constant foam liquid fraction.

Fig. 4.6 highlights the strong influence of the physico-chemical characteristics of gas and surfactant. Note that the value of foam liquid fraction also has a significant influence on  $K_2$ . The primary effect is to modify the bubble shape as well as the resulting contact geometry between bubbles. Whereas thin liquid films occupy the total surface of polyhedral bubbles in dry foams, as liquid fraction increases, the thin film area decreases at the expense of Plateau borders, which are generally assumed to not participate to gas transfer. We define the mean fraction of the total surface area of a bubble covered by thin films as  $\alpha(\varepsilon) = S_f / 4\pi CR^2$ , where the constant  $C \approx 1.1$  accounts the bubble surface area in the foam. If the thin film thickness  $h$  is known, and the interfacial resistance to gas transfer is negligible, an expression for  $K_2$  is obtained:

$$K_2 = 2\sigma \frac{DHv_m C\alpha(\varepsilon)}{h} \quad (4.23)$$

The fraction  $\alpha(\varepsilon)$  is not known in the general case, but approximate expressions can be found. For example, Surface Evolver simulations have provided the following relation [16]:

$$\alpha(\varepsilon) = (1 - 1.52\varepsilon^{1/2})^2 \quad (4.24)$$

It is generally assumed that the appropriate value for  $h$  is that of the common black film, which is expected to be of the order of  $10^{-7}$  m. A more pragmatic approach has been proposed earlier by Lemlich [12, 17]. He proposed to determine an average film thickness,  $\bar{h}$ , by dividing the volume of liquid contained in foam lamellae, i.e. a fraction  $\varphi$  of the global liquid fraction  $\varepsilon$ , by the total bubble surface area. The average number of bubbles per unit volume of foam is  $(1 - \varepsilon)/\langle V \rangle$ , and the corresponding bubble surface area is  $4\pi\langle R^2 \rangle \cdot (1 - \varepsilon)/\langle V \rangle$ , so that:

$$\bar{h} = \frac{1}{2} \frac{\varphi\varepsilon}{3C(1-\varepsilon)} \frac{\int_0^\infty R^3 F(R) dR}{\int_0^\infty R^2 F(R) dR} \equiv \frac{\varphi\varepsilon \langle R \rangle_{32}}{6C(1-\varepsilon)} \quad (4.25)$$

where the coefficient 1/2 has been introduced because each film is between two bubble surfaces.  $\varphi$  is expected to be of the order of 10%. Lemlich proposed to relate  $\varphi$  to the formation factor  $\Gamma$  (the ratio of electrical liquid conductivity to foam conductivity) and liquid fraction by:  $\varphi = 1.3125/\varepsilon\Gamma - 0.3125 \cdot \varepsilon\Gamma + 0.5$  [18]. Moreover, Lemlich also proposed a relation between  $\varepsilon$  and  $\Gamma$ :  $\varepsilon = 3/\Gamma - 5/2\Gamma^{4/3} + 1/2\Gamma^2$  [19], so that in principle,  $\varphi$  can be deduced from measurements of electrical conductivity in foam. The corresponding expression for  $K_2$  can be written:

$$K_2 = 2\sigma \frac{6CDHv_m(1-\varepsilon)}{\varphi\varepsilon \langle R \rangle_{32}} \quad (4.26)$$

It is still difficult to draw conclusions regarding the most appropriate form between (4.23) and (4.26). Note also that recently an empirical law has been found to capture correctly the dependence of coarsening on liquid fraction for foams continuously generated in a column [20]. In that case,  $K_2 \sim \varepsilon^{-1/2}$  for liquid fractions in the range 0.03–0.2. This might

indicate that the constant film thickness assumption is not fully justified, all the more so given that several studies have reported film swelling phenomena under drainage [21, 22]. Although the effective film thickness is a crucial parameter for predicting coarsening rate, the equilibrium thickness of foam lamellae under drainage conditions is far from being well understood.

## 4.5 Controlling the Coarsening Rate

The description of disproportionation given above allows for several strategies to be proposed to reduce the disproportionation rate. Some strategies are based on gas solubility. Others take advantage of the thin shell that coats the gaseous core to reduce gas permeation or to develop surface stresses that can counter surface tension effects. In that case, the shell may be composed of proteins, polymers, lipids or solid particles. Finally, bulk elasticity of the material suspending bubbles can be a possible way to delay or stop the ripening of bubble assemblies.

### 4.5.1 Gas Solubility

The bubble growth rate is proportional to the gas solubility that is given by Henry's law constant. Respectively for CO<sub>2</sub>, N<sub>2</sub> and C<sub>6</sub>F<sub>14</sub> (Perfluorohexane),  $H = 3.4 \times 10^{-4}$ ,  $6.4 \times 10^{-6}$  and  $5.5 \times 10^{-7}$  mol/m<sup>3</sup>/Pa. Thus, changing gas from N<sub>2</sub> to C<sub>6</sub>F<sub>14</sub> results in a disproportionation rate divided by one order of magnitude, as presented in Fig. 4.6, for both casein and SDS surfactants [15].

The effect of less soluble gases or entirely immiscible gases can be used in mixtures with soluble gases. Consider that  $v$  molecules of a species which are immiscible with the continuous phase are present within bubbles. Such molecules are effectively trapped. In this case an additional term that corresponds physically to the osmotic pressure of the trapped phase will contribute to bubble equilibrium. The rate of change in bubble radius given by eqn (4.4) thus becomes:

$$\frac{dR}{dt} = \frac{HDP_0v_m}{R} \left( s - \frac{2\sigma}{P_0 R} + \frac{v v_{mi}}{N_A 4\pi R^3 / 3} \right) \quad (4.27)$$

where  $v_{mi}$  and  $N_A$  are respectively the molar volume of the immiscible species and the Avogadro number. We may define another equilibrium bubble radius  $R_S^*$  as that at which the osmotic and Laplace pressures are in balance, which gives:

$$R_S^* = \left( \frac{3v v_{mi} P_0}{8\pi\sigma N_A} \right)^{1/2} \quad (4.28)$$

The osmotic stabilization of foams (as well as emulsions) is subjected to a minimum amount of trapped species in each bubble [23, 24].

### 4.5.2 Resistance to Gas Permeation

The basic influence of surfactant on disproportionation is to set the value of surface tension, and thus it affects the driving force for gas exchange. Note also that other effects are not directly related to the surface tension value. For example, the disproportionation rate of foam made with casein is smaller than that of foam made with SDS (as presented in Fig. 4.6), whereas surface tension of casein solution is larger than that of SDS solution. This was attributed to the larger thickness of casein foam lamellae due to the presence of casein aggregates [15]. Note that this mechanism is expected to be relevant for any kind of aggregates or small (colloidal) particles confined in foam lamellae.

The increase of the resistance of the surfactant shell to gas transport ( $1/k_m$  in eqn 4.9) is a possible strategy to reduce the rate of change in bubble radius. As measured by Borden and Longo [25], the resistance to air permeation induced by a lipid monolayer shell results in a significant reduction of bubble dissolution rate. The resistance of the shell was found to increase monotonically with lipid hydrophobic chain length. Note that this effect superimposes on that presented in the next paragraph.

### 4.5.3 Shell Mechanical Strength

The effect of interfacial elasticity on bubble dissolution was first treated by Gibbs [26, 27]. For an elastic interface, surface stress increases due to surface compression during bubble shrinking, which in turn reduces the effective surface tension. The reduction in surface tension as the bubble surface area  $A$  decreases is described by the Gibbs elastic modulus  $E_G = d\sigma/(dA/A) = R/2 \cdot d\sigma/dR$ . Gas exchange between bubbles of equal size is prevented as soon as:

$$\frac{d}{dR} \left( \frac{2\sigma}{R} \right) = \frac{-2\sigma}{R^2} + \frac{2}{R} \frac{d\sigma}{dR} > 0 \quad (4.29)$$

or equivalently if  $E_G$  is larger than half of the surface tension, i.e.  $E_G > \sigma/2$ .

Kloek et al. [28] have shown that for a completely elastic interface, every spherical bubble will become stable during shrinkage. For small values of  $E_G/\sigma$  the bubble has to shrink considerably before it becomes stable. For saturated solutions, the relative bubble size at which bubble shrinkage stops is given by:

$$\frac{R}{R_0} = \exp \left( -\frac{\sigma}{2E_G} \right) \quad (4.30)$$

Note that this expression holds for purely elastic interfaces. Such a stabilization mechanism has been observed with class II (water soluble) hydrophobins [29]. The ratio  $2E_G/\sigma$  of surfaces covered with such highly surface-active proteins is larger than 5 and can effectively stop disproportionation over time scales of months. This behaviour is different from that of other proteins (such as casein), which may be molecularly compressed or even detached from the surface. From a surface rheological point of view, these latter are characterized

by a significant amount of viscous dissipation. Note that interfacial dilatational viscosity,  $\eta_d$ , which accounts for the exchange of surfactant molecules between surface and bulk, can, however, delay bubble shrinkage if interfacial viscous stress counters interfacial tension, i.e.  $-2\eta_d/R \cdot dR/dt \sim \sigma$  [30].

A particular type of shell is composed of irreversibly attached particles with appropriate contact angle. As expected, monolayers of such particles exhibit high surface elasticity under compression,  $E_G \sim 100 \text{ mN/m}$ . Similarly to the so-called Pickering emulsions, on a bubble surface, these monolayers form some kind of armour [31] able to counteract the disproportionation process [32].

#### 4.5.4 Bulk Modulus

Bulk rheology can have a significant effect on the rate of change in bubble radius. Bulk viscosity can retard bubble dissolution according to two basic mechanisms: first, in reducing liquid drainage and thus in maintaining a high liquid fraction (see the dependence of the ripening coefficient  $K_2$  on  $\epsilon$  in eqns 23 and 26); and second, if bulk viscous stress at the bubble boundary becomes comparable to capillary pressure (this is expected at viscosities larger than about  $10^7 \text{ Pa/s}$  for a spherical bubble [28]). Bulk elasticity can stabilize bubbles against dissolution. The pressure in a bubble is given by  $P = P_0 + 2\sigma/R - \tau_{rr}$ , where  $\tau_{rr}$  is the excess radial bulk stress tensor at the bubble boundary for a single spherical bubble in an infinite elastic medium with shear modulus,  $G$  [33]:

$$\tau_{rr} = 2G \frac{R_0}{R} + \frac{G}{2} \left( \frac{R_0}{R} \right)^4 - \frac{5}{2} G \quad (4.31)$$

For a shrinking bubble,  $\tau_{rr}$  is larger than zero and therefore the total bubble pressure decreases due to the bulk elastic contribution. In saturated conditions, the bubble stability criterion is obtained as  $2\sigma/R = \tau_{rr}$  [28]. For a significant degree of shrinkage, i.e.  $R/R_0 \leq 0.95$ , the stability criterion is given by:

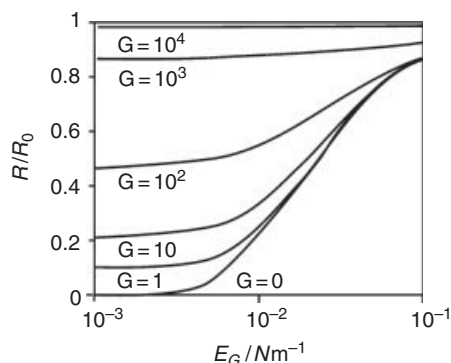


**Fig. 4.7** Effect of interfacial elasticity ( $E_G$ ) and bulk modulus  $G$  on bubble dissolution (from [28]). The lines indicate the relative radius at which a bubble becomes stabilized. Indicated bulk moduli are in Pa.

$$\frac{R}{R_0} \approx 0.7 \times 0.875^{\frac{GR_0}{\sigma}} \times \left( \frac{GR_0}{\sigma} \right)^{0.36} + 0.053 \frac{GR_0}{\sigma} \quad (4.32)$$

This shows that for a larger initial bubble size or a lower interfacial tension the bubble shrinks less. Kloek *et al.* [28] have studied the combined effects of both bulk and interfacial elasticities on bubble dissolution (see Fig. 4.7). This illustrates very well that both bulk and interfacial effects can be used to advantage to stabilize bubbles against disproportionation.

## References

- [1] I.M. Lifshitz and V.V. Slyozov. The kinetics of precipitation from supersaturated solid solutions. *J. Phys. Chem. Solids*, **19**: 35–50, 1961.
- [2] C. Wagner. Theorie der Altering von Niederschlägen durch Umlösen (Ostwald–Reifung). *Z. Elektrochem.*, **65**: 581–91, 1961.
- [3] H.M. Princen, J.Th.G. Overbeek and S.G. Mason. The permeability of soap films to gases II. *J. Coll. Interface Sci.*, **24**: 125–30, 1967.
- [4] J. von Neumann. Discussion – shape of metal grains, in *Metal Interfaces*, C. Herring (ed.). American Society for Metals, Cleveland, 1952.
- [5] J.A. Glazier, S.P. Gross and J. Stavans. Dynamics of two-dimensional soap froths. *Phys. Rev. A*, **36**: 306–12, 1987.
- [6] J. Stavans. Temporal evolution of two-dimensional drained soap froths. *Phys. Rev. A*, **42**: 5049–51, 1990.
- [7] J.A. Glazier and B. Prause. In *Foams, Emulsion and Their Application*, P. Zitha *et al.* (eds). Verlag MIT, Bremen, 2000.
- [8] R. Mc Pherson and D. Srolovitz. An exact generalisation to higher dimensions of von Neumann's theory of two-dimensional grain growth. *Nature*, **446**: 1053, 2007.
- [9] J. Lambert, R. Mokso, I. Cantat, P. Cloetens, J. Glazier, F. Graner and R. Delannay. Coarsening foams robustly reach a self similar growth regime. *Phys. Rev. Lett.*, **104**: 248304, 2010.
- [10] J. Lambert, I. Cantat, R. Delannay, R. Mokso, P. Cloetens, J. Glazier and F. Graner. Experimental growth law for bubbles in a moderately “wet” 3D liquid foam. *Phys. Rev. Lett.*, **99**: 058304, 2007.
- [11] C. Monnereau and M. Vignes-Adler. Dynamics of 3D real foam coarsening. *Phys. Rev. Lett.*, **80**: 5228–31, 1998.
- [12] R. Lemlich. Prediction of changes in bubble-size distribution due to interbubble gas diffusion in foam. *Ind. Eng. Chem. Fundam.*, **17**: 89–93, 1978.
- [13] D.J. Durian, D.A. Weitz and D.J. Pine. Scaling behavior in shaving cream. *Phys. Rev. A*, **44**: R7902–5, 1991.
- [14] S.A. Magrabi, B.Z. Dlugogorski and G.J. Jameson. Bubble size distribution and coarsening of aqueous foams. *Chem. Eng. Sci.*, **54**: 4007–22, 1999.
- [15] A. Saint-Jalmes, M.-L. Peugeot, H. Ferraz and D. Langevin. Differences between protein and surfactant foams: microscopic properties, stability and coarsening. *Coll. Surf. A*, **263**: 219–25, 2005.
- [16] S. Hilgenfeldt, S.A. Koehler and H.A. Stone. Dynamics of coarsening foams: accelerated and self-limiting drainage. *Phys. Rev. Lett.*, **86**: 4704–7, 2001.
- [17] H.C. Cheng and R. Lemlich. Theory and experiment for interbubble gas diffusion in foam. *Ind. Eng. Chem. Fundam.*, **24**: 44–9, 1985.
- [18] A.K. Agnihotri and R. Lemlich. Electrical conductivity and the distribution of liquid in polyedral foam. *J. Coll. Interface Sci.*, **84**: 42–6, 1981.
- [19] R. Lemlich. Semitheoretical equation to relate conductivity to volumetric foam density. *Ind. Eng. Chem. Process Des. Dev.*, **24**: 686–7, 1985.

- [20] M.J. Vera and D.J. Durian. Enhanced drainage and coarsening in aqueous foams. *Phys. Rev. Lett.*, **88**: 088304, 2002.
- [21] V. Carrier, S. Destouesse and A. Colin. *Phys. Rev. E*, **65**: 061404, 2002.
- [22] N. Louvet, F. Rouyer and O. Pitois. Ripening of a draining foam bubble. *J. Coll. Interface Sci.*, **334**: 82–6, 2009.
- [23] A.S. Kabalnov and E.D. Schukin. Ostwald ripening theory: applications to fluorocarbon emulsion stability. *Adv. Coll. Interface Sci.*, **38**: 69, 1992.
- [24] A.J. Webster and M.E. Cates. Osmotic stabilization of concentrated emulsions and foams. *Langmuir*, **17**: 595–608, 2001.
- [25] M.A. Borden and M.L. Longo. Dissolution behavior of lipid monolayer-coated, air-filled microbubbles: effect of lipid hydrophobic chain length. *Langmuir*, **18**: 9225–33, 2002.
- [26] J.W. Gibbs. *Collected Works: Volume I Thermodynamics*. Yale University Press, New Haven, CT, 1957.
- [27] E.H. Lucassen-Reynders. In *Anionic Surfactants: Physical Chemistry of Surfactant Action*, E.H. Lucassen-Reynders (ed.). Dekker, New York, 1981.
- [28] W. Kloek, T. Van Vliet and M. Meinders. Effect of bulk and interfacial rheological properties on bubble dissolution. *J. Coll. Interface Sci.*, **237**: 158–66, 2001.
- [29] T.B.J. Blijdenstein, P.W.N. De Groot and S.D. Stoyanov. On the link between foam coarsening and surface rheology: why hydrophobins are so different. *Soft Matter*, **6**: 1799–808, 2010.
- [30] A.D. Ronteltap and A. Prins. The role of surface viscosity in gas diffusion in aqueous foams. II. Experimental. *Coll. Surf.*, **47**: 285–98, 1990.
- [31] M. Abkarian, A.B. Subramaniam, S.-H. Kim, R.J. Larsen, S.-M. Yang and H.A. Stone. Dissolution arrest and stability of particle-covered bubbles. *Phys. Rev. Lett.*, **99**: 188301, 2007.
- [32] A. Cervantes Martinez, E. Rio, G. Delon, A. Saint-Jalmes, D. Langevin and B.P. Binks. On the origin of the remarkable stability of aqueous foams stabilized by nanoparticles: link with microscopic surface properties. *Soft Matter*, **4**: 1531–5, 2008.
- [33] M.M. Fyrillas, W. Kloek, T. van Vliet and J. Mellema. Factors determining the stability of a gas cell in an elastic medium. *Langmuir*, **16**: 1014, 2000.

# 5

## Coalescence in Foams

*Annie Colin*

### 5.1 Introduction

Foams are a mixture of gas and liquid stabilized by surfactant, consisting of gas bubbles dispersed in a liquid. They are metastable, so that the mean size of the bubbles tends to increase with time. They belong to a wide class of nonequilibrium systems such as emulsions or off-critical decomposing mixtures that rearrange and coarsen with time. The characteristic time for coarsening of foams spans a remarkably wide range, from a few seconds to a few months. Foams are extremely important for a variety of applications such as detergency, food processing, and cosmetology, and their stability is a key factor for all applications.

Two limiting mechanisms are responsible for their evolution. One, Ostwald ripening, is due to the diffusion of the dispersed phase out of the smaller bubbles into the bigger ones through the continuous phase driven by the higher Laplace pressure in the smaller droplets. The second mechanism, coalescence, is due to the rupturing of the thin liquid film that separates two adjacent cells.

In this chapter, I deal with coalescence. I do not characterize the foaming properties. I instead focus on the destruction of foams. At the opposite of the Ostwald ripening process, the mechanisms in charge of coalescence remain at this stage unclear. A fundamental question concerns the determination of the critical parameters that govern the destruction of foams.

Coalescence involves the rupturing of a thin liquid film. The study of isolated thin liquid films has thus motivated many theoretical and experimental studies in the past century. I refer to these works in Section 5.2.

I then move towards foam in Section 5.3. I present experimental studies that deal with the characterization of the structure of foam evolving coalescence events. I compare this evolution with Ostwald ripening process.

In Section 5.4 I describe the parameters in charge of coalescence. I point out the crucial role of the liquid fraction.

Section 5.5 deals with a discussion of the possible mechanism in charge of coalescence in draining foams. It focuses on the fact that rupture of isolated films is very different from rupture of foam. Coalescence in foam is a cooperative process proceeding through a cascade of breaking events. It involves stretching, dilatations of films that are not present in the studies of isolated thin liquid films.

## 5.2 Stability of Isolated Thin Films

Aqueous foam is a system of gas bubbles dispersed in a liquid and stabilized by surfactants adsorbed at the gas–liquid interfaces. Liquid films are formed between two adjacent gas bubbles, and channels (Plateau borders) are formed where three neighboring films meet. Breaking of the foam comes from the rupturing of the liquid films. In the past century, many experimental and theoretical studies have been devoted to the study of isolated thin liquid films.

### 5.2.1 Experimental Studies Dealing with Isolated Thin Liquid Films

Liquid films formed between two adjacent gas bubbles in a foam are composed of two surfactant monolayers separated by a thin layer of water. The overlap of interaction between the two layers induces the apparition of a force normal to the interface. This pressure can be either positive or negative and its value depends upon the thickness of the film.

Such disjoining pressure curves have been measured experimentally by Mysels and Jones [1] who have developed a device operating by maintaining a balance between capillary and thin film forces. This initial set up, called a thin-film balance, has been greatly improved by Scheludko, by Claesson and by Bergeron [2–10]. In the cell developed by Bergeron, single thin-liquid films are formed in a hole drilled through a solution saturated fritted glass disk that is fused to a capillary tube. This film holder is enclosed in a hermetically sealed Plexiglas cell with the capillary tube exposed to a constant reference pressure. The solution under investigation is placed in a glass container within the cell to prevent contact and possible contamination with the Plexiglas chamber. Manipulation of the cell pressure with a precise screw-driven syringe pump alters the imposed capillary pressure,  $P_c$ , on the film and sets the disjoining pressure. Once equilibrium is established, the aqueous core film thickness,  $h$ , is measured using an optical interferometer. Film with a thickness greater than 8 nm can be measured with a precision higher than 2%. Disjoining pressure ranging between 80 Pa and a few atmospheres can be measured with a precision of 5%.

The disjoining curve obtained can be described by using the Derjaguin–Landau–Verwey–Overbeek (DLVO) theory [11, 12]. This theory combines two types of interaction forces: electrostatic repulsive forces, which tend to stabilize the films, and van der Waals

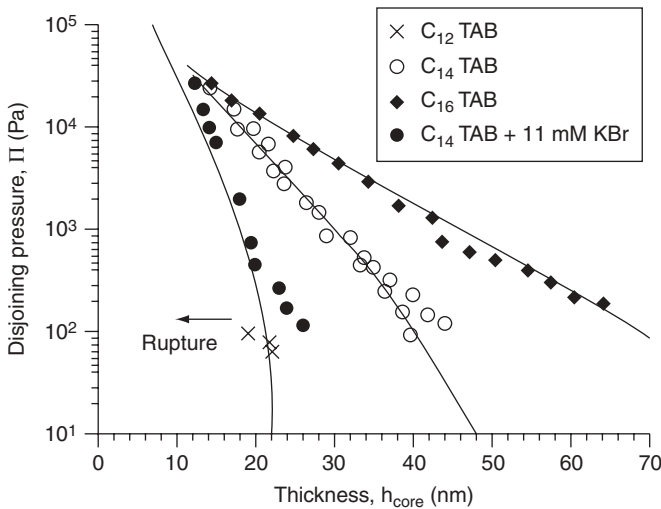


**Fig. 5.1** Example of disjoining pressure measurements for  $CnTAB$  surfactant solutions [10].

forces, which are responsible for foam film destabilization. The thickness of the film is then determined by the balance between the external pressure applied on the film and the disjoining pressure. A typical DLVO isotherm, where steric repulsions occurring at short distances have been superimposed, is shown in Fig. 5.1. Three regions can be defined. At low (region 1) and large (region 2) thickness, the disjoining pressure decreases with the thickness. The thicker state (typically 20–30 nm) is called the Common Black Film state, the thinner one is the Newton Black Film state (smaller than 10 nm, as a reference to the original work of Newton). Note that the branch corresponding to the NBF does not exist in the absence of short repulsive interactions. In the intermediate region (region 3), the disjoining pressure increases with the thickness of the film. The classical DLVO approach, which simply balances repulsive and attractive interactions across the film, cannot explain the film stability. An analysis of the variation of the film thickness towards thickness fluctuations or towards surfactant density fluctuations is required and is the purpose of the next section [13–15].

### 5.2.2 Theoretical Description of the Rupture of an Isolated Thin Liquid Film

The general idea is that thin films break by spontaneous growth of thermal fluctuations of film thickness. Vrij [13, 14] proposed a model for the amplification of thermal thickness fluctuations. These fluctuations are controlled by two contributions to the free energy of the film. The first one is always positive due to the increase of the film surface area (the surface energy is the product of surface area by the surface tension  $\gamma$ ) and the second one may be positive or negative depending on the sign of  $d\Pi/dh$ ,  $\Pi(h)$  being the disjoining pressure (force between film surfaces per unit area) and  $h$  the film thickness. The film thickness can be written as

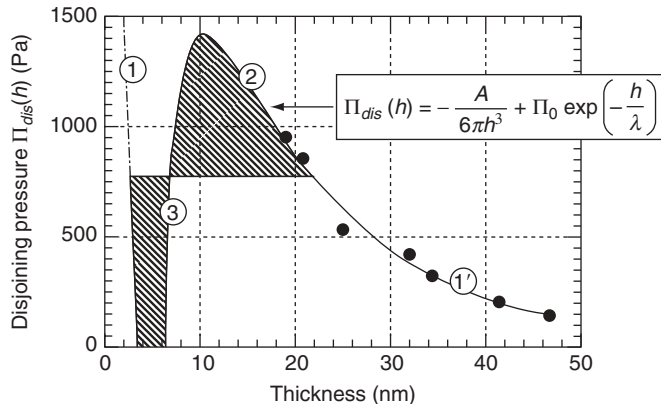


**Fig. 5.2** Typical DLVO isotherm, with steric repulsions occurring at short distances superimposed.

$$h = h_o + \sum_q A_q \exp(i(q_x x + q_y y))$$

where  $h_o$  is the average thickness of the film and  $A_q$  is the amplitude of the fluctuation of wave vector  $q$ ,  $A_q(t) = A_o \exp(t/\tau)$ .

When  $d\Pi/dh > 0$ , the characteristic time is positive. This point suggests that the region 2 of Fig. 5.2 is an unstable region. In the absence of short repulsive forces, applying an external force greater than the barrier on the film will thus lead to rupture.

This model allows understanding of the metastable character of CBF but does not explain why NBF may rupture. In order to do so, surfactant density fluctuations are required. The creation of a bare zone of surfactants induces the disappearance of forces and thus the collapse of the film. Their amplitude is ruled by the Gibbs elasticity of the monolayer [16]. Such fluctuations may also explain why CBF breaks at external applied pressure lower than the barrier.

In this section, I have summarized the main mechanism in charge of the stability of isolated thin films. We will see in the following that the link between the stability of isolated films and foams is not obvious. Clearly stable isolated thin liquid films are required to form stable foams. However, the situations encountered by the thin liquid films in foams are dynamic. In foams, thin liquid films are stretched and dilated. These deformations have not been taken into account in the previous studies and thus reduce their conclusions.

### 5.3 Structure and Dynamics of Foam Rupture

In order to study coalescence in foams it is very important to differentiate coalescence and Oswald ripening. They are the major mechanisms in charge of the evolution of a foam.

As explained in the introduction, they are due to two different processes. Oswald ripening is due to the diffusion of the gas from the smallest bubbles to the biggest ones. The basic

dynamics is driven by the pressure difference across the bubbles. Coalescence is due to film rupture. These two different processes induce different structure evolutions. Let us first focus on the case of Ostwald ripening.

For 2D foams, the bubble area evolves following the von Newman equation. Bubbles of five or less sides shrink and those of seven or more sides grow. Mean cell area  $\langle a \rangle$  grows as  $t$ . Most significantly, in the case of Ostwald ripening, after a transient regime, the evolution is characterized by a steady regime where the normalized volume distribution ( $P(v/\langle v \rangle, t)$  in 3D) or area distribution ( $P(a/\langle a \rangle, t)$  in 2D) is steady. Moreover, the steady state distribution is rather monodisperse.

Numerical simulations for 3D foams point out that the conventional measure of volume polydispersity,  $\sigma_R/R$ , defined as

$$\frac{\sigma_R}{R} = \sqrt{\frac{\langle (R - \langle R \rangle)^2 \rangle}{\langle R \rangle}}$$

is equal to 0.38 for steady state. In the previous equation  $R$  is the radius of the bubble defined as  $R = (3V/4\Pi)^{1/3}$  where  $V$  is the volume of the bubble [17].

The evolution of breaking foams is significantly different. The mechanism of foam rupture by coalescence is rather particular. For 2D foam, Burnett *et al.* [18] have broken the process into three reasonably distinct phases. Foam is generated in a cell by vigorous shaking of a sodium dodecyl sulphate solution. The liquid fraction of the foam can be controlled by removing some part of the liquid. In these experiments, coalescence is induced by the effect of gentle heating, provided by the heat generated by the light box used to illuminate the cell containing the foam. The authors first note that coalescence is a rapid process in comparison with Ostwald ripening. The destruction of the foam is completed in less than 10 min, whereas Ostwald ripening relaxation proceeds over a time scale of 10 h.

During the first few minutes, there are a few rearrangements due to the breakage of tiny three-dimensional bubbles, nestled in the Plateau borders, which triggers some T1 transitions in the immediate neighbourhood. After this induction period, wall rupture takes over a major mechanism. The breakdown is characterized by a cascade of wall rupture. The latter stages of the foam are characterized by narrow, isthmus-like regions of small bubbles into which the main part of the liquid has been drained.

After the induction period, the mean cell area  $\langle a \rangle$  grows as  $t^\beta$  with  $\beta$  depending upon the ramping rate of heating and greater than 3. No steady regime in the normalized area distribution ( $P(a/\langle a \rangle, t)$ ) is evidenced. In the breaking period, it shows a long tail corresponding to large  $a/\langle a \rangle$  values. In later times, a shift towards the small bubbles is evidenced. It corresponds to the regions remaining after the cascade events. The mean feature of coalescence for 2D foam is thus the coexistence of very large bubbles with small ones in the latter stages of evolution.

More recently Ritacco and coworkers [19] have studied coalescence on bubble rafts. As in the study of Burnett, the collapse process follows a sequence with two steps. A first bubble ruptures due to thermal fluctuations and induces a cascade of bursting bubbles. The authors studied the size distribution of the avalanches. The distribution form depends upon the viscosity of the liquid. For solutions of low bulk viscosity a power-law distribution was observed only for small avalanches in a limited range. These systems exhibit a peak for  $n$

close to the initial number of bubbles in the raft. The exponents found for the regions with power-laws vary from 2.2 to 0.8. For intermediate viscosities the authors found power-laws with an exponent of 1 for a wide range of  $s$  values. For high viscosities the distribution of avalanche sizes seems to be exponential. In this later case, the process is thus not correlated. The same catastrophic behaviour has been evidenced in 3D foams.

Using acoustic experiments on foams Müller and di Meglio [20] observed non-Poissonian distributions of popping events by counting the number of pops at various time intervals. They confirmed the existence of cascade events and the cooperative behaviour of coalescence events. The authors also note that the events are mainly localized at the top of the foam. Following the same approach, Vandewalle *et al.* [21] show that the dynamics of a collapsing foam is discontinuous and evolves by sudden bursts of activity separated by periods of stasis.

In these experiments, foams have been created by continuously injecting air at the base of a water/soap mixture in a cylindrical vessel. With this method, the bubbles are roughly monodisperse and spherical at the bottom of the foam layer (typically a diameter of 2.5 mm). However, bubbles grow and shrink inside the layer due to classical coarsening. At the top of the foam, large polyhedral bubbles can be observed (typically with a diameter of 8 or 10 mm). Different commercial soaps have been tested.

To analyse the coalescence process, the authors captured bubble pops using a high quality microphone placed above the top of the foam. Recording of the (dimensionless) acoustic activity  $A(t)$  presents successive pops. Each pop looks like a “wave packet” made of 8 kHz oscillations modulated by a Gaussian-like envelope. Oscillations correspond to a sound wavelength of 40 mm, i.e. four times the typical size of surface bubbles such as those in organ tubes. The characteristic duration of a pop is typically 1 ms. The acoustic energy  $E$  dissipated within each pop (occurring at  $t_0$ ) is then calculated. It is equal to the integral of the square of the amplitude during the pop. This dissipated energy  $E$  is given in arbitrary units and is attributed to the rupture of the bubble membrane, i.e. to be proportional to the surface area of the disappearing bubble (and not especially the volume of the bubble).

The histogram  $h(E)$  of the frequency of peak occurrence as a function of the peak intensity  $E$  is a power law. In other words, no sharp cutoff is observed in  $h(E)$  for high  $E$  values. This implies that a wide variety of membrane areas is exploding.

The histogram  $h(t)$  of the interpeak durations  $t$ , i.e. the time intervals  $t$  separating successive bubble explosions, also behaves like a power-law. For a homogeneous (random) occurrence of bubble explosions, one expects an exponential decay for  $h(t)$ .

These experimental data allow the authors to conclude that the avalanching process is a catastrophic and correlated process. The power-law behaviour indicates that bubble explosions are correlated events. Moreover, they point out that a wide variety of bubble sizes participate in the phenomenon. In other words, small and large bubbles are involved in the avalanche process during the dynamics of collapsing foam. This experimental result is in contrast with the widely accepted and intuitive argument that only large membranes are more curved and are fragile, exploding at the air–foam interface (an argument used in some simulations [22]). The authors conclude that the radii of the bubbles do not govern the stability of the draining foam. There is no rupture threshold in the size of the bubble membrane.

These studies clearly point out the differences between Ostwald ripening and coalescence. Coalescence occurs via cascade events. In 3D foams, events are localized at the top of the

foam. In 2D systems, in the latter stage of evolution of the foam, small bubbles coexist with very large ones. The evolution for Oswald ripening is less catastrophic and leads to rather monodisperse foams.

## 5.4 What Are the Key Parameters in the Coalescence Process?

After having characterized the foam evolution it is important to know what the parameters in charge of the coalescence process are. In order to probe this point, Carrier *et al.* [22] analysed the role of the size of the bubbles and of the liquid fraction in the coalescence process.

To better understand the role of the film size in the destruction of the foam, the authors studied draining foams comprised of initially monodisperse bubbles. They performed dielectric experiments and visual observations, and they measured the evolution of the liquid fraction of the foam during the collapsing process. In this study, great care was brought to the preparation and to the characterization of the foam.

Foams of sodium dodecylbenzenesulfonate (SDBS), poly(ethylene glycol) surfactant (C10E10), and tetradecyltrimethylammoniumbromide (TTAB) were made; SDBS and TTAB were purchased at Aldrich and used as received. C10E10 was provided by AtoFina Company. The foaming solutions were prepared with deionized water. Various concentrations and mixtures of surfactants above and below the critical micellar concentration were used. By choosing a mixture of gas that has a very low diffusivity in water, they eliminated on the time scale of the experiment one class of destabilizing phenomena, that of Ostwald ripening. This allowed the authors to study the evolution of the coalescence process only.

The size of the bubbles and the initial liquid fraction and were set using the following procedures. Foams were created by continuously bubbling perfluorohexane-saturated nitrogen through a capillary (hole diameter: 1, 0.5, 0.2 and 0.1 mm) or a porous glass disk (porosity: 150–200, 90–150 and 40–90 µm) into the foaming solution, inside a Plexiglas column (25 cm × 25 cm × 60 cm high) equipped with 25 electrodes and counter electrodes (Fig. 5.5). Determination of the bubble size was made by image analysis of the plateau borders on the border of the column.

To set the liquid fraction in the foam, the authors used the following procedure. During the bubbling, they wetted the foam from above with the foaming solution at a constant rate by using a peristaltic pump. Before reaching the foam, the foaming solution fell on the wall of the column. This avoided wetting to induce coalescence. The column had an overflow pipe at its bottom. This method allowed the authors to produce monodisperse foam with an initial liquid fraction homogeneous in the entire column. By tuning the flow rate, the authors could change the initial liquid fraction. The liquid fraction was measured using dielectric experiments.

After this period of sample preparation, the experiment began. Bubbling was stopped and the pump was turned off. The column was hermetically closed with a Plexiglas cover and a polymer film in order to avoid evaporation. The foam was left to coalesce and collapse freely. Three successive regimes were observed. First, the height of the foam remained constant. Due to gravity, liquid flowed and the foam dried. Second, the foam continued to dry but the bubbles present at the air/foam interface ruptured. A rupture front propagated in

the foam, and the height of the foam decreased. This evolution was discontinuous; it evolved by avalanches separated by periods of stasis. Visual observations suggested that coalescence events occurred only at the top of the foam.

In order to check this point, the authors rewetted the foam from above with the flow used for the preparation of the sample. They then measured the liquid fraction and compared this value to the one initially measured. As the two values were the same, they concluded that the number of bubbles was unchanged before the arrival of the rupture front.

The third regime corresponds to the end of the experiments. In the lower part of the column, a residual height of bubbles persisted. This foam was stable and did not evolve or coalesce further.

This first analysis of the experiment demonstrates a key point: coalescence events occur only at the top of the foam.

To determine the parameters that govern the stability of the foam, the authors recorded the evolution of the liquid fraction as a function of time for various positions in the column. Figure 5.2 presents the evolution of the liquid fraction versus time for a fixed position in the column. The soapy solution used to make the foam is a mixture of 70% SDBS and 30% C10E10. The concentration of surfactant is 1% in weight. The length of the plateau borders is 2 mm, and the standard deviation is 0.5 mm. First, liquid drains in the foam. When the drying front reaches the position where the measurement is made, the liquid fraction begins to decrease. The discontinuous drop of the liquid fraction that occurs at a longer time corresponds to the breaking of the foam. A non-zero signal is measured after rupture because some water is expelled on the walls and builds a wetting film that drives the electrical current. By comparing the signals at different positions, the authors note (Fig. 5.6) that rupture arises nearly always at the same liquid fraction. More precisely, destruction occurs in a narrow field of liquid fraction ranging from 0.0005 to 0.0007 (Fig. 5.3).

At the end of the experiment, a residual height of foam persists in the lower part of the column. No coalescence events occur in this residual foam. In this part of the foam, the liquid fraction has reached an equilibrium value corresponding to the balance between the capillary and gravity forces. This equilibrium value is higher than the critical liquid fraction involved in the rupture front. This shows that the top of the foam is not a particular place for coalescence. All these points suggest the existence of a sharp threshold controlled by the liquid fraction.

To support this point, I carried out a forced drainage measurement. The soapy solution used to make the foam is a mixture of 70% SDBS and 30% C10E10. The concentration of surfactant is 1% in weight. The length of the plateau borders is 2 mm, and the standard deviation is 0.5 mm. The foam is continuously wetted from above with a high enough continuous flow that the liquid fraction remains higher than the threshold value. The flow rate is equal to 0.0004 mm/s. In this case, no coalescence events are recorded (Fig. 5.4). At the opposite, when the flow at the top of the foam is decreased to 0.0001 mm/s and reaches the value of the flow necessary to establish a liquid fraction near the threshold value, the foam breaks in the entire column in a very catastrophic way. Due to gravity, the first events are recorded at the top of the foam but some parts of the foam break simultaneously at the middle and at the bottom of the column. As previously, this shows that the top of the foam is not a particular place for coalescence.

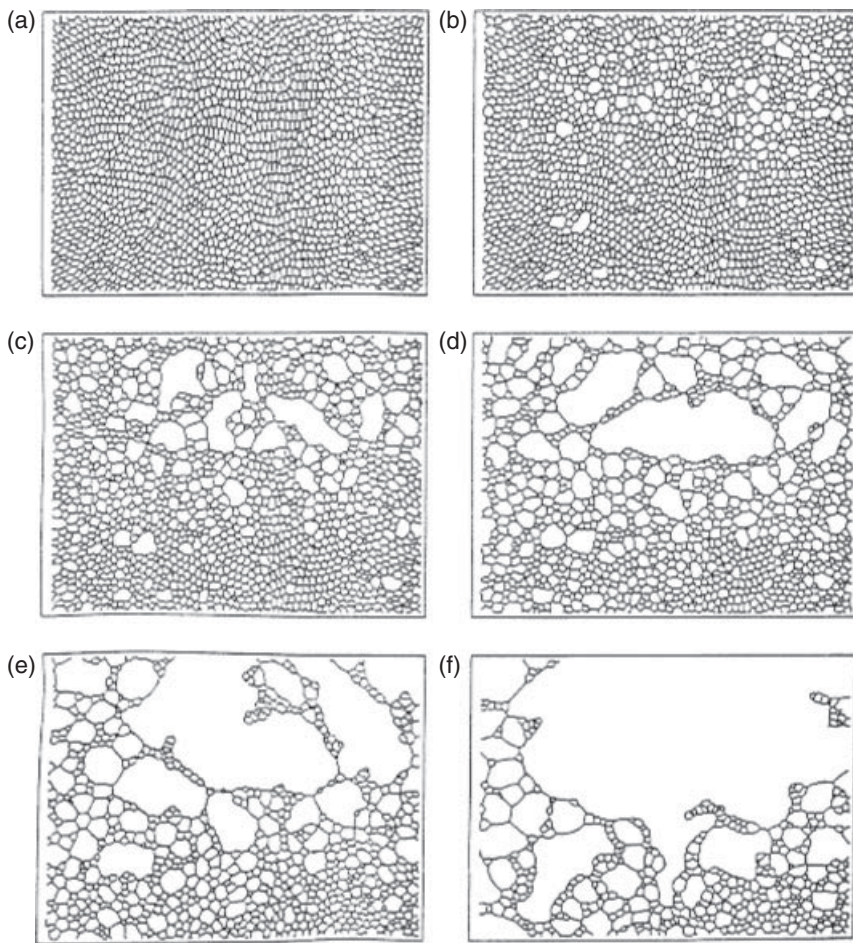


**Fig. 5.3** Sequence of images of a 2D breaking foam. (a)  $t = 290\text{s}$ , (b)  $t = 590\text{s}$ , (c)  $t = 690\text{s}$ , (d)  $t = 750\text{s}$ , (e)  $t = 790\text{s}$ , (f)  $t = 850\text{s}$  [18].

These experiments point out a very important feature of coalescence. Coalescence in foams occurs at a critical liquid fraction. Liquid fraction is a key parameter.

One may wonder what the role of the size of the bubbles is. To understand this point, I performed experiments as a function of the radii of the bubbles. Figure 5.5 presents the evolution of the liquid fraction for various bubble sizes at a fixed position in the column. The length of the Plateau borders varies between 0.24 and 2 mm. The soapy solution used to make the foam is a mixture of 70% SDDBS and 30% C10E10. The total concentration of surfactant is 1% in weight. The initial liquid fraction is nearly the same for all the foams. We can note three major points. First, the decrease as a function of time of the liquid fraction is slower when the bubbles of the foam are smaller. This is a classical result obtained in the drainage experiments. The velocity of the fluid in the drainage process is slowed by viscous processes that occur in the plateau borders or in the nodes of the foams.

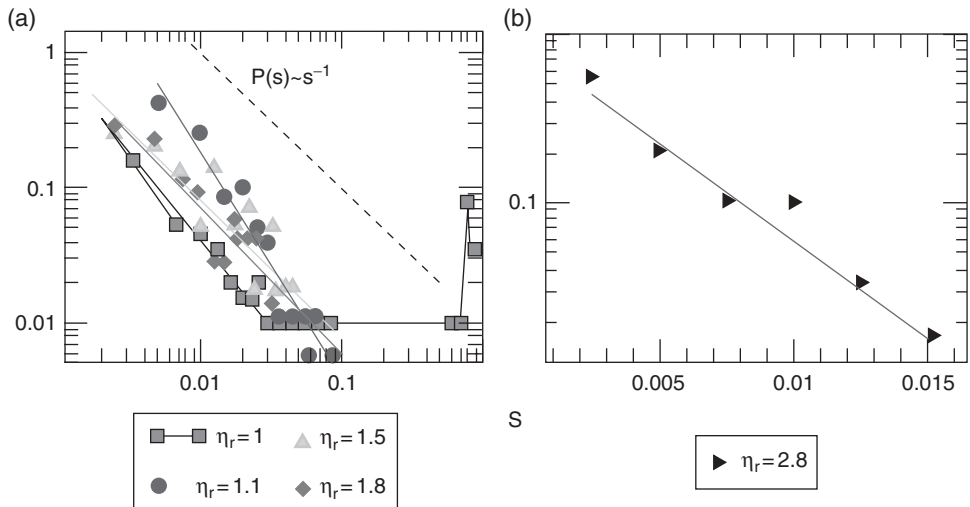


**Fig. 5.4** (a) Size distribution of the first avalanche for different viscosities (power-law behavior). (b) Experiment: size distribution for large viscosity (exponential behavior) [19].

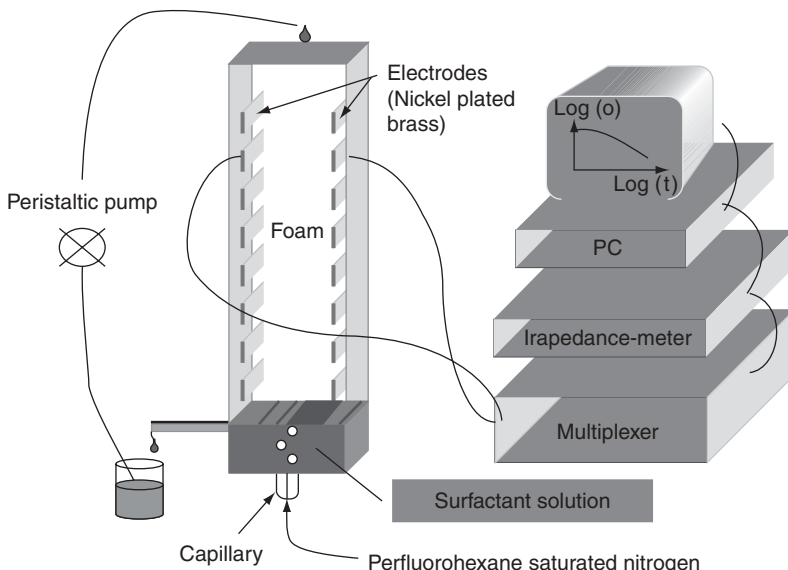


**Fig. 5.5** Experimental set up [22].

The nodes are the regions where four plateau borders meet. These processes are more efficient when the sizes of the nodes or of the plateau borders are smaller. For a fixed value of the liquid fraction, these flows are thus slower when the bubble radius is smaller. Second, the jump of liquid fraction at the end of the experiments that corresponds to the arrival of the rupture front is more important for big bubbles than for small ones. This

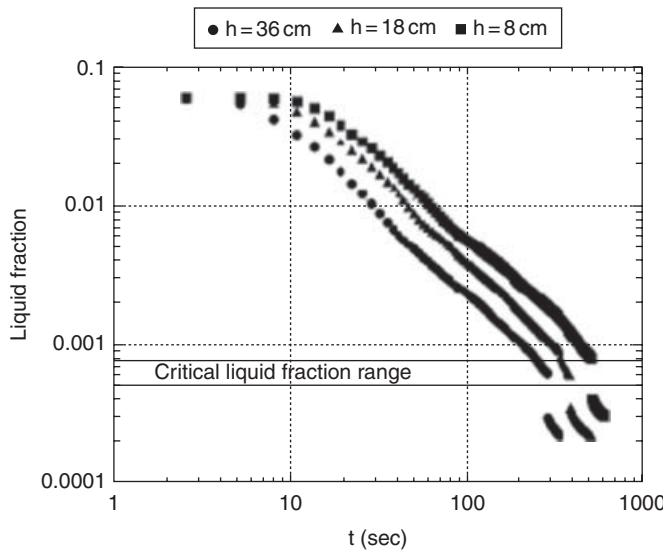


**Fig. 5.6** Evolution of the liquid fraction versus time for various fixed positions in the column. The measurements are recorded at the heights 36, 18, and 8 cm. The soapy solution used to make the foam is a mixture of 70% SDBS and 30% C10E10. The total concentration of surfactant is 1% in weight. The length of the plateau borders is 2 mm, and the standard deviation is 0.5 mm. The discontinuous drop down of the liquid fraction that occurs at longer time corresponds to the breaking of the foam. A critical liquid fraction is evidenced [22].

suggests that the evolution of liquid fraction is more discontinuous in the case of large bubbles than in the case of smaller ones. Visual observations confirm this point. In the case of large bubbles, coalescence events evolve large avalanches, whereas the decrease of the height of fine foams is nearly continuous. Third, the main result brought by these experiments is to show that the threshold in liquid fraction is independent of the size of the bubbles. The coalescence process occurs, then, at a critical liquid fraction. More precisely, destruction occurs in a narrow field of liquid fraction ranging from 0.0005 to 0.0007 (Fig. 5.7).

These experiments clearly demonstrate the role of the liquid fraction. Coalescence events are dramatically enhanced below a critical liquid fraction. This critical liquid fraction does not depend on the size of the bubbles. Same results have been shown recently by Biance and co-workers [23]. All these measurements thus confirm the results obtained by Vandewalle [4, 5] and point out that the radius of the bubbles does not govern the stability of draining foams. However, these results suggest that the lifetime of a foam is enhanced when the bubbles are smaller because it takes more time for a fine foam to drain and to reach the critical liquid fraction. This fact may explain the widely accepted idea that foams with small bubbles are more stable.

The critical liquid fraction is a function of the nature of the surfactant and of its concentration. Various surfactants have been tested. For each surfactant, the critical liquid fraction depends upon the concentration of surfactant. The critical liquid fraction decreases as a function of the concentration and reaches a plateau at high concentration. For TTAB,

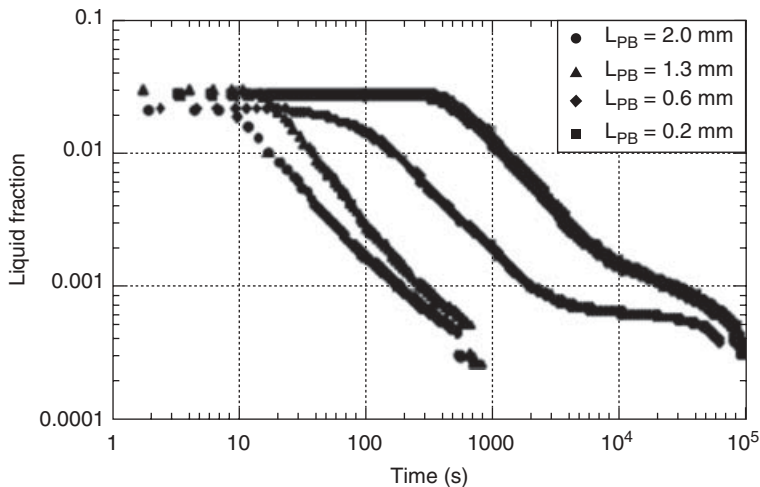


**Fig. 5.7** Evolution of the liquid fraction versus time for a fixed position in the column. The soapy solution used to make the foam was a mixture of 70% SDBS and 30% C10E10. The total concentration of surfactant was 1% in weight. The curves correspond to foams with various lengths of Plateau borders. Respectively from right to left, the length of the plateau borders is 0.2 mm (std 0.06 mm), 0.6 mm (std 0.13 mm), 1.3 mm (std 0.3 mm), and 2 mm (std 0.5 mm) [22].

the critical liquid fraction is equal to 0.0008 near the critical micellar concentration and decreases to 0.0002 for ten times the critical micellar concentration.

## 5.5 How Do We Explain the Existence of a Critical Liquid Fraction?

The previous results are striking: they point out the fundamental role of the liquid fraction and the second order role of the size of the film. This evidence rules out many mechanisms classically evoked to explain the stability of isolated films.

The previous results demonstrate that coalescence in foam is not governed by a disjoining pressure criterion. Hence, if it were the case, then the critical liquid fraction measured for a monodisperse foam would vary as the square of the inverse of the radius of the bubbles. We recall that  $\pi_d = \gamma/r = 0.6\gamma/L_{PB}\sqrt{\varphi}$  where  $\gamma$  is the surface tension,  $r$  is the radius of curvature of the plateau borders, and  $L_{PB}$  is the length of the Plateau borders, which is proportional to the radius of the bubbles.

Moreover, the value of the disjoining pressure exerted on the films in the foam when coalescence occurs is very small compared to the disjoining pressure that isolated films are able to support before breaking. Indeed, in the case of the TTAB solution, the critical liquid fraction, for a surfactant solution near the critical micellar concentration, is equal to 0.0008. In this experiment, the length of the plateau borders is 1.5 mm, and the surface tension is  $39 \times 10^{-3}$  N/m. The disjoining pressure applied to the films in the foam just

before coalescence events is thus equal to 351 Pa. This value is two orders of magnitude smaller than the values that isolated films are able to support without breaking for the same solution.

These two points suggest that another mechanism must be responsible for coalescence in draining foams. Coalescence in foams is a cooperative process. It proceeds via dynamic conditions that do not exist for isolated thin films. One needs to take into account the dynamic conditions induced by the drainage. Once the foam dries, elementary movements are still observed. These movements resemble what is known as T1 in 2D foams. These movements are very rapid and are induced by a change in liquid fraction and are a surface minimization process. During these T1 events, films are stretched and dilated. Some disappear and others appear. These large amplitude dilatations do not exist for isolated thin films.

At this stage two different explanations have been given to capture the breaking of thin films during T1 events. Carrier and co-workers proposed a mechanism based upon dilatation. This mechanism considers the existing thin film, which is stretched before its disappearance. Following Princen, they recall that the strain borne by a liquid film during a T1 event strongly increases with foam dryness, noticeably for liquid fractions as low as 0.3%. This maximum strain, from a dimensional analysis, is not dependent on bubble size but instead depends only on the liquid fraction. It can thus be conceived that when the liquid fraction becomes too low, the fast relative surface area increase produced by an elementary movement will be too high to be stabilized by the surfactants.

The stretched film will thus become unstable. In this picture, the critical liquid fraction could then correspond to a critical relative dilation. From a formulation point of view, surfactant developing strong repulsive forces, moving quickly towards the interface and inducing slow T1 events will be an efficient stabilizing agent towards coalescence.

Very recently, another possible mechanism has been proposed by Biance and co-workers [23]. They focus on the creation of the new film. They suggest that T1 events require a critical volume of liquid available in Plateau borders to create an entirely new film in dynamic conditions. Using fast video they point out a strong thickening of the film during rearrangement. Before and after rearrangement the films are thin and appear black. During rearrangement the newly created film is coloured and thick (see Fig. 5.8).

This behaviour is close to the one involved in the classical Landau Levich [24] experiment. Let us describe this process classically encountered in coating technology, because it is one of the simplest ways to deposit a thin film of liquid on a substrate.

When a solid object is pulled out of a liquid reservoir, a thin layer of liquid is entrained by viscous drag. According to the pioneering work of Landau and Levich and Derjaguin (LLD), a film of unique thickness  $h_{LLD}$  is selected by the speed of withdrawal  $U$ . This film results from a balance between the effects of viscosity, which causes a macroscopic entrainment of liquid by the solid, and surface tension, which resists the film entrainment, so that the film thickness is proportional to the capillary number  $Ca = U/\gamma$  raised to the 2/3 power, where  $\eta$  is the viscosity,  $\gamma$  is the surface tension.

During a T1 event a liquid film is entrained between the two new neighbouring bubbles and the competition between capillary and viscous forces will select its thickness. Biance and co-workers assume that the order of magnitude of the film thickness  $h$  can be estimated

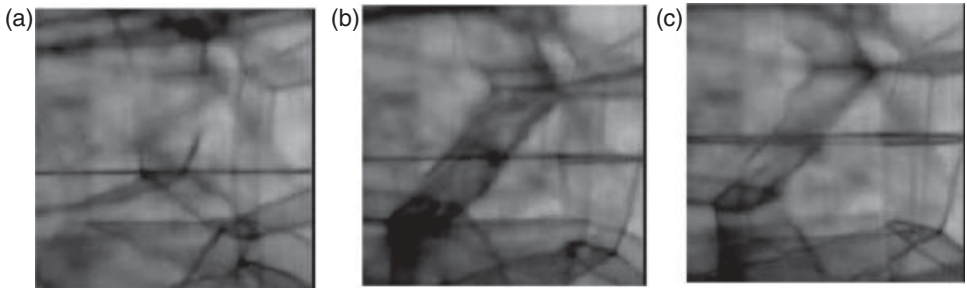


**Fig. 5.8** Sequence of images showing one T1 event in 3D foams made of TTAB at a liquid fraction greater than the critical one. Images (a), (b), and (c) correspond to situations respectively before, during, and after bubble rearrangement. The pattern in (b) reveals the thickening of the new film formed by T1. The size of images is approximately 1.5 mm [23].

from Frankel's law with constant receding velocity,  $L/\tau$ , where  $\tau$  is a characteristic time for bubble rearrangement and is expected to depend on the foaming solution. Thus, one can write

$$h \approx r \left( \frac{\eta L}{\tau \gamma} \right)^{2/3}$$

where  $r$  is the Plateau border radius and  $L$  the size of the bubble. This amount of water corresponds to a critical liquid fraction

$$\phi \approx \left( \frac{\eta R}{\gamma \tau} \right)^{4/3}$$

Typical values calculated from these equations are in agreement with the measured one.

However, the accordance of this model with measured values is not satisfactory with respect to bubble radius dependence. Indeed,  $\tau$  is only weakly dependent on the bubble radius, involving  $\phi \approx R^{4/3}$ . Obviously, this reflects the poor relevance of Frankel's law to account for the complex interfacial phenomena in T1 events. As recently highlighted by Van Nierop et al. [25], the dependence of the film thickness on meniscus size involves coupling terms with surface parameters that remain to be understood thoroughly. However that may be, this mechanism opens a new way for the understanding of the existence of a critical liquid fraction.

From a formulation point of view, as in the previous mechanism, surfactant-inducing slow T1 events will be an efficient stabilizing agent.

Recent work on the dynamics of T1 events indicates that  $\tau \propto \kappa/\gamma$ , where  $\kappa$  is the dilatational viscosity of the interface [25]. This point may allow us to understand the key role of dynamic properties of the interfaces (elasticity and surface viscosity) on foam stability, reported in many experiments since the 1950s [26–28].

## 5.6 Conclusion

In this chapter, I have given an overview of the experimental and theoretical studies dealing with coalescence in foams. I have focused on stable foams and have not discussed the case of foams in the presence of antifoams. I have shown that the parameter in charge of coalescence in foams differs from the one involved in the stability of thin liquid films.

Coalescence in foams is a catastrophic process. It occurs at a critical liquid fraction. The reason for this remains at this stage still unclear. It is, however, clearly related to the T1 events occurring when the foam is drying or is ageing. Experiments at the level of a few bubbles in movement are required in order to better understand this point.

From an applied point of view, the existence of a criterion on the liquid fraction has some consequences. Avoiding drainage will increase dramatically the lifetime of foam. Foams with small bubbles, surfactants with high surface viscosity, and jellified systems are thus likely to be more stable.

## References

- [1] K.J. Mysels and M.N. Jones. Direct measurement of the variation of double-layer repulsion with distance. *Discuss. Faraday Soc.*, **42**: 42, 1966.
- [2] A. Scheludko, D. Platikan and E. Manev. Disjoining pressure in thin liquid films and electro-magnetic retardation effect of molecule dispersion interactions. *Discuss. Faraday Soc.*, **40**: 253, 1965.
- [3] P.M. Claesson, T. Ederth, V. Bergeron and M.W. Rutland. Techniques for measuring surface forces. *Adv. Coll. Interface Sci.*, **67**: 119, 1996.
- [4] P.M. Claesson, T. Ederth, V. Bergeron and M.W. Rutland. *Trends Phys. Chem.*, **5**: 161, 1995.
- [5] D. Exerowa, T. Kolarov and Khr. Khristov. *Coll. Surf.*, **22**: 171, 1987.
- [6] V. Bergeron and C.J. Radke. Equilibrium measurements of oscillatory disjoining pressures in aqueous foam films. *Langmuir*, **8**: 3020, 1992.
- [7] V. Bergeron, M.E. Fagan and C.J. Radke. The influence of disjoining pressure on foam stability and flow in porous media. *Langmuir*, **9**: 1704, 1993.
- [8] V. Bergeron and C.J. Radke. Disjoining pressure and stratification in asymmetric thin-liquid films. *Coll. Polymer Sci.*, **273**: 165, 1995.
- [9] V. Bergeron, A. Waltermo and P.M. Claesson. Disjoining pressure measurements for foam films stabilized by a nonionic sugar-based surfactant. *Langmuir*, **1996**: 12, 1336.
- [10] V. Bergeron. Microtubes created in thin liquid films during bilayer adhesion and fusion. *Langmuir*, **12**: 5751, 1996.
- [11] B. Derjaguin and L. Landau. Theory of stability of highly charged liophobic sols and adhesion of highly charged particles in solutions of electrolytes. *Zhurnal Eksperimentalnoi i Teoreticheskoi Fiziki*, **15**(11): 663–82, 1945.
- [12] E.J.W. Verwey and J.T.G. Overbeek. *Theory of Stability of Lyophobic Colloids*. Elsevier, Amsterdam, 1948.
- [13] A. Vrij. Possible mechanism for the spontaneous rupture of thin, free liquid films. *Discuss. Faraday Soc.*, **42**: 23, 1966.
- [14] A. Vrij and J.T.G. Overbeek. Rupture of thin liquid films due to spontaneous fluctuations in thickness. *J. Am. Chem. Soc.*, **90**: 3074, 1968.
- [15] A. De Vries. Foam stability: Part IV. Kinetics and activation energy of film rupture. *J. Recl. Trav. Chim. Pays-Bas*, **77**: 383, 441, 1958.

- [16] V. Bergeron. Disjoining pressures and film stability of alkyltrimethylammonium bromide foam films. *Langmuir*, **13**: 3473–82, 1997.
- [17] L. Gilberto, R. Thomas, M.C. de Almeida and F. Gruner. Coarsening of three-dimensional grains in crystals, or bubbles in dry foams, tends towards a universal, statistically scale-invariant regime. *Phys. Rev. E*, **74**: 021407, 2006.
- [18] G.D. Burnett, J.J. Chae, W.Y. Tam, M.C. de Almeida and M. Tabor. Structure and dynamics of breaking foams. *Phys. Rev. E*, **51**: 6, 1995.
- [19] H. Ritacco, F. Kiefer and D. Langevin. Lifetime of bubble rafts: cooperativity and avalanches. *Phys. Rev. Lett.*, **98**: 244501, 2007.
- [20] N. Vandewalle, J.F. Lentz, S. Dobolo and F. Brisbois. Avalanche of draining foams. *Phys. Rev. Lett.*, **86**(1): 179–82, 2001.
- [21] J.J. Chae and M. Tabor. Avalanches of popping bubbles in collapsing foams. *Phys. Rev. E*, **55**: 598, 1997.
- [22] V. Carrier and A. Colin. Coalescence in draining foams. *Langmuir*, **19**(11): 4535–8, 2003.
- [23] A. Biance and O. Pitois. Accepted by *Phys. Rev. Lett.*, 2011.
- [24] V. Levich. Physicochemical hydrodynamics. Prentice-Hall, NJ, 1962.
- [25] E.A. van Nierop, B. Scheid and H. A. Stone. On the thickness of soap films: an alternative to Frankel's law. *J. Fluid Mech.*, **602**: 119–27, 2008.
- [26] V. Craig. Bubble coalescence and specific-ion effects. *Curr. Op. Coll. Interface Sci.*, **9**(1/2): 178–84, 2004.
- [27] D. Langevin. Influence of interfacial rheology on foam and emulsion properties. *Adv. Coll. Interface Sci.*, **88**(1/2): 209–22, 2000.
- [28] L. Scriven. Dynamics of a fluid interface: equation of motion for Newtonian surface fluids. *Chem. Eng. Sci.*, **12**(2): 98–108, 1960.

# 6

## Foam Rheology

*Nikolai D. Denkov, Slavka S. Tcholakova, Reinhard Höhler  
and Sylvie Cohen-Addad*

### 6.1 Introduction

Rheological properties of foams, such as elasticity, plasticity, and viscosity, play a major role in foam production, transportation, and applications [1–8]. Obvious examples are foam extrusion through nozzles and slits (used in cosmetic and food applications, and in plastic foam production), transportation through pipes (e.g. for compartment cleaning in nuclear plants and in foam-aided natural gas production), flow through porous media (in enhanced oil recovery), foam perception in personal and home care applications (shaving and styling foams, facial cleansers, shampoos), and many others – see Chapter 18 in this book for further examples.

Understanding foam rheology is a challenging scientific problem, mainly due to the complexity of the interactions and processes involved [4–14]. By definition, foams are bubble dispersions with gas volume fraction,  $\Phi = V_{\text{gas}} / V_{\text{foam}}$ , higher than that of closely packed spheres ( $\Phi_{CP} \approx 0.64$  for disordered foam). Therefore, neighbouring bubbles are squeezed against each other and separated by thin films and Plateau borders, whose liquid–gas interfaces are stabilized by surfactants, proteins, polymers or solid particles [1–4]. If foam is subjected to a small shear stress, it deforms like a soft solid. This response can be characterized by visco-elastic moduli [2, 4, 8, 12]. For applied stresses beyond a threshold, called ‘yield stress’, visco-plastic flow sets in. In this regime, foams behave like shear-thinning fluids, which means that their effective viscosity is a decreasing function of shear rate [4, 7, 8, 12, 14]. Additional rheological phenomena arise at the contact between foams and confining solid walls: If the surface of the solid wall is smooth on the scale of the bubble

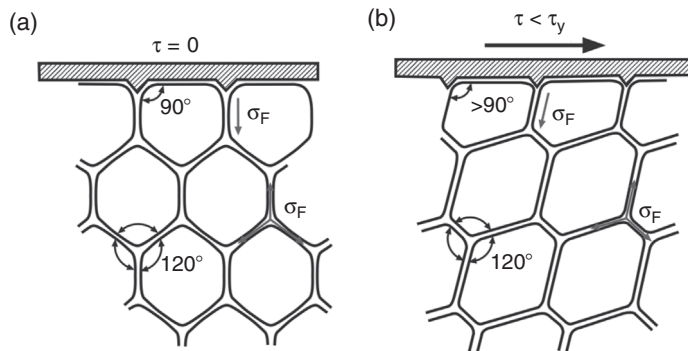


**Fig. 6.1** Schematic presentation of the origin of elastic response of foam, subject to shear stress,  $\tau$ , lower than the foam yield stress,  $\tau_y$ . (a) In the absence of external stress, the bubbles are symmetrical and the tensions of the foam films,  $\sigma_F$ , are balanced both inside the foam and at the confining solid wall. (b) At low external stress, the bubbles deform and the resulting slope of the foam films creates elastic shear stress inside the foam and in the contact zone foam–wall. Due to the preserved static angles between the foam films,  $120^\circ$ , the forces acting on each bubble are again balanced, despite bubble deformation.

size, the foam tends to slip on the wall. In this case, the velocity of the first layer of bubbles in contact with the wall and the wall velocity do not match, in contrast to what is observed with simple liquids [4, 5, 14–20]. If this wall slip is not accounted for properly, it can lead to artefacts in rheological measurements aimed at determining bulk foam properties. Wall slip can also be useful, e.g. for foam transportation through pipes and for foam extrusion through orifices. The rheological properties of foams are complex not only because both the elastic and the viscous responses are nonlinear functions of the applied stress, but also because shear localization (coexistence of moving and non-moving regions) may occur under certain conditions [21–26].

Foam rheology is of practical as well as of fundamental interest, because of its observed similarities with the behaviour of other concentrated dispersions of soft ‘particles’, such as emulsion droplets, microgel beads, or lipid vesicles [4, 8, 27–29]. These similarities could be the result of generic physico-chemical mechanisms, which are currently under active investigation.

Significant progress has been made towards the physical understanding of the rheological properties of foams [4, 7, 8, 12, 14, 30, 31]. The elastic response is due to surface tension effects: each foam film bears a mechanical tension,  $\sigma_F$ , approximately equal to twice the surface tension of the liquid,  $\sigma$ , from which the foam is generated. If shear stress is applied externally, the bubbles are deformed, as illustrated in Fig. 6.1. As a consequence, the average orientation of the films is biased in the direction of the applied shear. This gives rise to an elastic stress inside the foam, which balances the applied stress (see Fig. 6.1(b)). As long as the external stress is smaller than the foam yield stress,  $\tau_y$ , the films meeting at the Plateau borders are in static mechanical equilibrium and the bubbles are trapped in a self-supporting structure.

If the applied stress is strong enough to separate neighbouring bubbles, the foam structure yields, a steady shear flow sets in, and the bubbles slide along each other (see Fig. 6.2). The

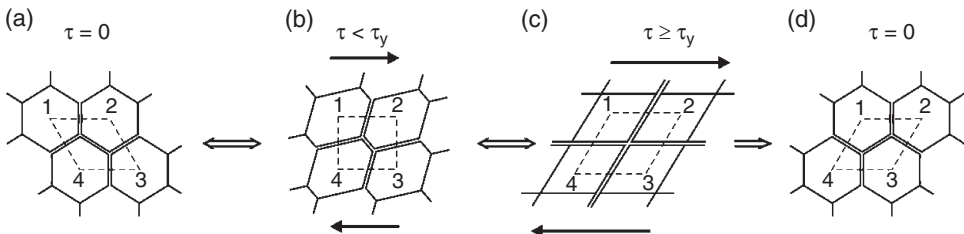


**Fig. 6.2** Schematic illustration of foam yielding and plastic deformation, under applied shear stress, which increases from (a) to (c) [4, 30]. The structure shown on image (c) illustrates the largest possible elastic deformation of the foam structure (presented here for 2D foam). This structure can relax either elastically, by returning to structure (a), or by a bubble rearrangement, leading to structure (d). This latter configuration is similar to structure (a), but the top bubble layer is shifted irreversibly with respect to the bottom layer, thus changing the bubble packing topology. Note the neighbour switching between bubbles 1 and 3, which became neighbours instead of 2 and 4. This topological change is called a ‘T1 event’ in dry foam. The viscous friction in the sheared foam films and Plateau borders between the moving neighbouring bubbles leads to energy dissipation and, hence, to viscous contribution to the shear stress.

bubble rearrangements lead to local shear flow of the liquid inside the foam films and Plateau borders, resulting in dissipation of energy and a shear-rate-dependent (viscous) contribution to the macroscopic stress. If the applied stress is decreased back to zero, the flow stops and the bubbles relax towards a new equilibrium (see Fig. 6.2(d)). The macroscopic deformation, realized with respect to the initial stress-free structure, is called ‘plastic strain’.

This review aims to present briefly our current understanding of the main phenomena involved in foam flow under steady and oscillatory shear deformation, and the main factors that control these phenomena. In addition, we track the links between the macroscopic rheological foam properties and the underlying processes at the microscopic scale. Only the simplest theoretical expressions are presented where available, to avoid mathematical complexity. The structure of the review is as follows: in Section 6.2 we outline the main experimental and theoretical approaches used to study foam rheology; in Sections 6.3–6.6 we discuss consecutively the foam visco-elasticity, yielding, plasticity, and steady viscous flow; in Section 6.7 we consider the foam-wall friction.

## 6.2 Main Experimental and Theoretical Approaches

Various experimental techniques are employed to characterize and analyse foam deformation and flow [4, 12, 14–16, 18, 32–34]. The macroscopic response to applied oscillatory or steady shear stress can be measured by rotational rheometers. Parallel plate, cone-plate and Couette cylinders have all been successfully used as shear geometries. However, several precautions must be taken to obtain physically interpretable rheological results. The surfaces of the confining walls must be roughened to avoid wall slip. Alternatively, one can use smooth surfaces and, in such cases, the foam-wall slip must be explicitly considered in

data analysis [31]. In addition, measures must be taken to ensure foam stability during the experiment, with respect to liquid drainage, bubble coarsening and liquid evaporation at the contact with ambient atmosphere. Only under such conditions are the gas volume fraction, mean bubble size, and bubble polydispersity well defined. These characteristics, along with surface tension and viscosity of the foaming solution (and sometimes the surface dilatational modulus; see Sections 6.6 and 6.7 below), must all be controlled to analyse quantitatively the rheological data and to compare the results for different systems. Alternatively, one can study the coupling between foam aging (due to bubble coarsening) and the rheological foam properties. In this case, the ageing process must be characterized for a foam sample, identical to that studied in the rheometer. For all these reasons, the rheological foam measurements are far from straightforward and the experimental protocols should be designed carefully, depending on the specific system and aim of the study.

Several complementary methods have been used to characterize the bubble velocity profiles and structural rearrangement dynamics in flowing foams. Magnetic resonance imaging (MRI) detects the velocity distribution inside sheared foam, while diffusing wave spectroscopy (DWS) provides statistical information about the rate of bubble rearrangements in strained and in flowing foams [18, 33, 35–38]. Direct optical observations of bubble monolayers (2D foams) have provided rich information about the bubble shape and dynamics in flowing foams [23, 24, 39–47]. Direct observations of dynamics inside dry 3D foams have been carried out using optical tomography [21]. Optical observations of isolated small bubble clusters have also provided valuable information about the bubble deformation and rearrangement in foams [48–50].

The experimental studies have clearly evidenced that the rheological response of foam involves processes in a wide range of length-scales. As already mentioned in Section 6.1, the deformation of individual bubbles creates the elastic stress of foams, while the yielding and plastic flow are the consequence of rearrangements in the bubble packing, and the viscous friction in the liquid films between neighbouring bubbles is a source of energy dissipation. At an even smaller structural scale, the stability and the mechanical response of the liquid–gas interfaces are governed by the adsorption of the foam stabilizers (surfactants, polymers, particles) [13, 16, 51–57]. At present, one of the most challenging and exciting research problems in foam rheology is to explain and predict the links between the macroscopically observed foam behaviour and the microscopic processes that govern this behaviour.

With this aim in view, the experimental results have stimulated the development of many theoretical models [4, 7, 11, 12, 17, 23, 24, 51, 52, 55, 58–68]. Two types of approaches are distinguished: continuum descriptions on a macroscopic scale, and physical models considering explicitly the foam microstructure. In the continuum models, the mechanical foam properties, such as elastic and viscous moduli, effective viscosity and yield stress, are incorporated phenomenologically in constitutive laws, which relate the stress, strain and rate of strain. Such constitutive laws are very useful to describe the macroscopic flow behaviour of foams, under various conditions. The physical models aim not only to construct constitutive laws, but also to predict foam rheological properties on the basis of the foam microstructure and local dynamics [23, 24, 46, 50–52, 63–66]. Additional insight has been gained by numerical simulations: the Surface Evolver software [69] has been used to determine foam equilibrium structures [70], as well as the stress in strained or flowing foams under quasistatic conditions [71, 72]. In this kind of numerical simulation, the interplay of rheology and coarsening can also be studied [73]. The viscous friction in foams is

currently simulated numerically by either the so-called ‘bubble model’ [63, 64] or the ‘soft disk model’ [61], which postulate linear dependence between the viscous stress and the relative velocity of the bubbles. For 2D foams confined by solid walls, the so-called ‘viscous froth model’ [74–76] is applied, which accounts explicitly for the viscous friction between the bubbles and the wall.

The following presentation briefly describes our current understanding of the main foam rheological properties, achieved by combining experimental and numerical work, as well as the theoretical approaches outlined above.

## 6.3 Foam Visco-elasticity

### 6.3.1 Linear Elasticity

Subjected to a sufficiently small shear strain, foam behaves like an elastic material and the stress  $\tau$  varies linearly with the strain  $\gamma$ . In this linear regime, the bubbles are deformed, but the applied strain is too small to modify the topology of their packing. The specific surface area of the foam increases with the applied strain, and so does the volume density of bubble surface energy. The latter quantity scales as the tension of the gas–liquid interface,  $\sigma$ , divided by the average bubble size. Moreover, dimensional arguments show that the foam shear modulus,  $G = \tau/\gamma$ , scales as the surface energy density, multiplied by a prefactor, which depends on foam structure, polydispersity and liquid content [4]. The effects of these foam characteristics on the foam elastic modulus are considered below.

#### 6.3.1.1 Monodisperse Dry Foam

We first consider ordered monodisperse dry foam, whose bubbles are assembled in a body-centred cubic structure (see Fig. 6.3). For this model system, called ‘Kelvin foam’ (see Chapter 3), the static shear modulus, averaged over all orientations of the sample,

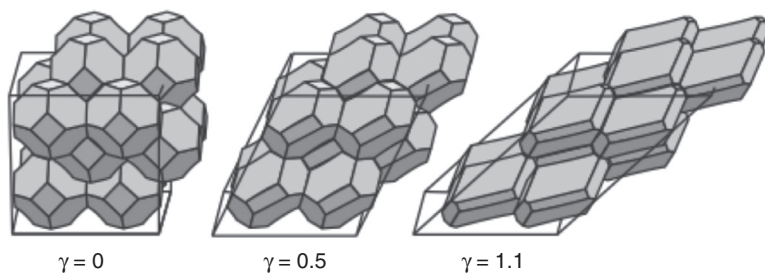


**Fig. 6.3** Dry Kelvin foam, subjected to a quasi-static shear strain  $\gamma$ , applied in the (100) direction. Each bubble has eight hexagonal films and six square films. Upon the deformation, the angles between the foam films, joining at a Plateau border, remain equal to  $120^\circ$ , and the angles between Plateau borders that join at a vertex are  $109.5^\circ$ , as required by Plateau’s rules. The bubble deformation leads to an increase of the density of the surface energy in the foam (due to the increased bubble surface area) and to a resulting elastic response, characterized by the shear elastic modulus,  $G$ . Reproduced from [77], Editions Belin, Paris, 2010.

has been determined in numerical simulations using the surface minimization code ‘Surface Evolver’ [69, 78]:

$$G = 0.51 \frac{\sigma}{R} \quad (6.1)$$

$R = (3V/4\pi)^{1/3}$  is the radius of a bubble of volume  $V$ . For a typical foaming solution with  $\sigma = 30\text{ mN/m}$  and bubble radius  $R = 100\text{ }\mu\text{m}$ , eqn (6.1) predicts a shear modulus  $G = 150\text{ Pa}$ , illustrating that foams are soft materials.

Simulations of disordered monodisperse dry 3D foams yield a shear modulus close to that of a Kelvin foam. To analyse the physical origin of the prefactor in eqn (6.1), the structure of a disordered dry foam has been described as an ensemble of randomly oriented tetrahedral vertices, each connecting four Plateau borders. When these structures are sheared, their geometry evolves in agreement with Plateau’s rules. A geometric calculation on this basis yields the relative change of interfacial area, as a function of the applied strain [65]. Using the specific surface area of random disordered monodisperse foams,  $3.3/R$ , obtained in numerical simulations [70], this model predicts a shear modulus  $G = 0.55\sigma/R$ , in good agreement with eqn (6.1) for ordered foam.

### 6.3.1.2 Effects of Bubble Polydispersity and Liquid Content

The volume to surface ratio of the bubbles sets a characteristic length scale in the foam (corresponding to the specific surface area of the bubbles) that governs foam elasticity. For polydisperse foam, this average ratio is conveniently represented by the so-called Sauter mean radius,  $R_{32} = \langle R^3 \rangle / \langle R^2 \rangle$ , which is determined by dividing the third moment of the bubble size distribution by its second moment. The Sauter radius is larger than the cubic mean bubble radius  $R_o$ , defined as  $R_o = (3\langle V \rangle / 4\pi)^{1/3} = \langle R^3 \rangle^{1/3}$ . The ratio  $R_{32}/R_o$  can be used as a quantitative measure of foam polydispersity. For a given mean bubble radius  $R_o$ , the elastic shear modulus decreases with increasing bubble polydispersity, as demonstrated in Fig. 6.4 by the simulation results for dry foams. In real foams, an increase of polydispersity with time arises, for instance, when an initially (almost) monodisperse foam ages by bubble coarsening. In this case, at long coarsening times, the ratio of the various mean radii typically converge towards  $R_{32}/\langle R \rangle \approx 1.3$  and  $R_o/\langle R \rangle \approx 1.1$  [79], where  $\langle R \rangle$  is the arithmetic mean radius of the bubbles. Note that the ratio  $GR_{32}/\sigma \approx 0.51$  does not depend on bubble polydispersity – therefore,  $R_{32}$  is a convenient bubble size scale for the elastic foam properties.

Let us discuss now the impact of gas volume fraction  $\Phi$  on the elasticity of disordered foams. For a given mean bubble size, wet foams are softer than dry ones – as  $\Phi$  decreases, the shear modulus  $G$  also decreases. The latter tends towards zero as  $\Phi$  approaches the random close packing volume fraction,  $\Phi_{CP}$ , which is a weakly increasing function of polydispersity. The loss of rigidity occurs when the packing reaches an isostatic mechanical equilibrium, where the bubbles are spherical and neighbours barely touch each other [80]. At  $\Phi = \Phi_{CP}$ , the foam can be sheared slowly without any interfacial energy ‘cost’. Figure 6.5 shows experimental results for the dependence of the shear modulus of polydisperse foam on  $\Phi$ , which are well described by the empirical relation [81]:

$$G = 1.4\Phi(\Phi - \Phi_{CP}) \frac{\sigma}{R_{32}} \quad (6.2)$$

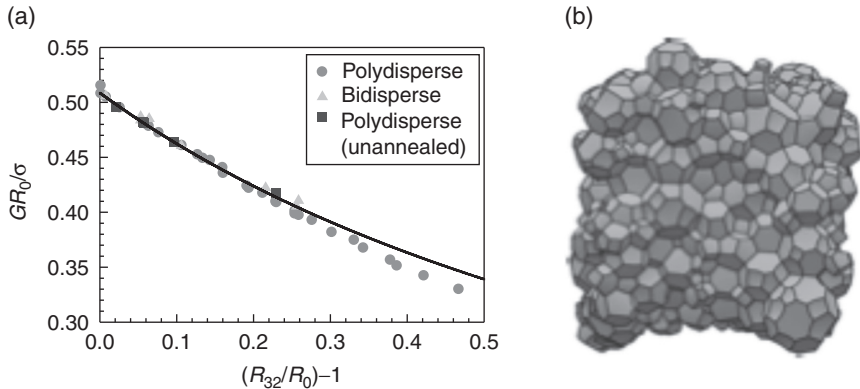


**Fig. 6.4** (a) Variation of the shear modulus  $G$  of disordered 3D dry foams, normalized by  $\sigma/R_o$ , with increasing foam polydispersity, characterized by the parameter  $(R_{32}/R_o - 1)$ . The mean radius  $R_o$  is defined as  $R_o = (3\langle V \rangle / 4\pi)^{1/3}$  where  $V$  is the volume of a bubble in the foam.  $R_{32}$  is the mean volume-surface radius (Sauter radius). The continuous line is  $GR_o/\sigma = 0.51R_o/(R_{32})$ . For monodisperse foam with  $R_{32} = R_o = R$ , the intercept with the ordinate axis corresponds to  $G = 0.51\sigma/R$ , in agreement with eqn (6.1). Data from [71]. (b) Structure of a dry polydisperse foam with  $R_{32}/R_o = 1.15$ , simulated using Surface Evolver software. Courtesy of A. Kraynik.

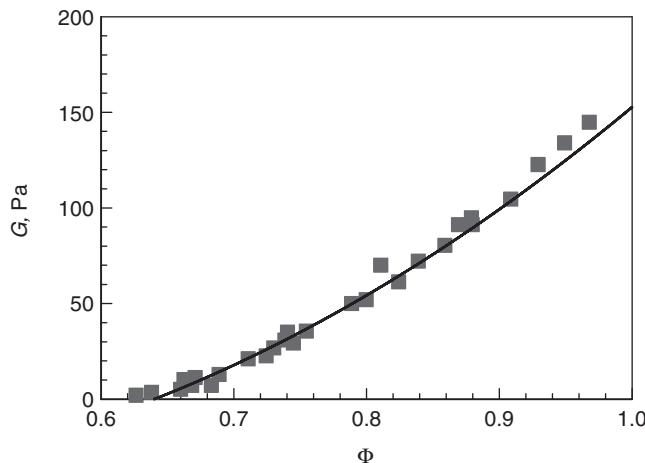


**Fig. 6.5** Shear modulus,  $G$ , versus gas volume fraction  $\Phi$ , measured for 3D disordered polydisperse foams with  $R_{32} = 66 \mu\text{m}$ ,  $\sigma = 20 \text{ mN/m}$ , and  $\Phi_{CP} \approx 0.64$ . The continuous curve represents eqn (6.2). The Sauter mean radius  $R_{32}$  is determined from videomicroscopy measurements of the bubble diameter at the sample surface. Data from [81].

with  $\Phi_{CP} = 0.64$ . For a dry foam ( $\Phi = 1$ ), eqn (6.2) yields a numerical pre-factor of 0.50, similar to that predicted for monodisperse foam (cf. eqn (6.1)).

Foams are much harder to compress than to shear, and their Poisson ratio is very close to 0.5. Neglecting the water compressibility and the interfacial contribution, the foam compression modulus is given by the ratio  $K_T/\Phi$ , where  $K_T$  is the compression modulus of the gas

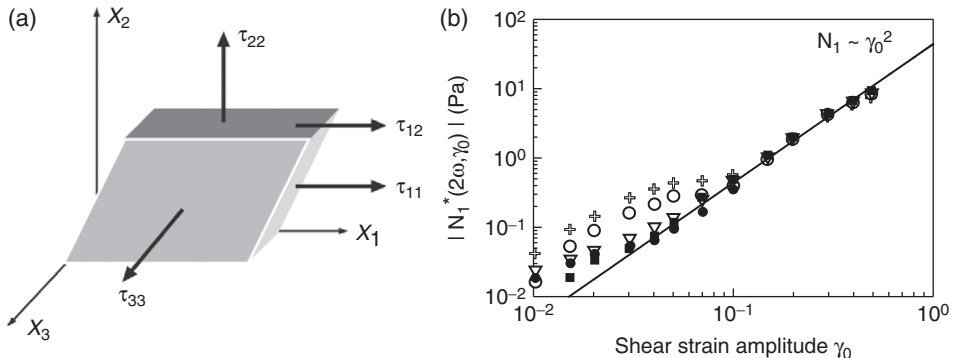


**Fig. 6.6** (a) A cube of foam is sheared in the  $X_1$  direction. The arrows illustrate the components of the induced stress. (b) Amplitude of the first normal stress difference,  $N_1$ , induced by an applied oscillatory strain of amplitude  $\gamma_0$ , in a dry foam ( $\Phi = 0.97$ , average bubble radius  $R = 80 \mu\text{m}$ , surface tension  $\sigma = 27 \text{ mN/m}$ , yield strain  $\gamma_y = 0.4$ ). The foam is sheared in the gap of cone-plate geometry, with angle equal to  $10^\circ$  (open symbols) or  $15^\circ$  (filled symbols) at a frequency of 2 Hz. Note the quadratic dependence of  $N_1$  on  $\gamma_0$ , except at low amplitudes, where deviations are seen due to residual trapped stresses. See more details in ref. [82], where these data are taken from.

confined in the bubbles. The magnitude of  $K_T$  is of the order of the gas pressure outside the foam. Taking realistic values, one obtains  $K_T/\Phi \gg G$ . Therefore, the bubble volume, in foam undergoing shear flow, is constant to a very good approximation. On the other hand, foam flows related to significant variations of the applied pressure (e.g. pumped flow or release from pressurized containers) may lead to significant changes of the bubble volume and of the air volume fraction in the foam. In such (more complex) cases, the dependence of the foam properties on the local values of the bubble size and volume fraction should be explicitly considered. In addition, the visco-elastic foam properties upon foam compression and expansion could become important [6].

### 6.3.2 Non-linear Elasticity

For larger strains, which are still too small to induce bubble rearrangements, foam film rotations and stretching lead to nonlinear mechanical response. For instance, shear deformation of a foam in the  $X_1$  direction, as shown in Fig. 6.6(a), induces the shear stress component,  $\tau_{12}$  (proportional to  $\gamma$ ) and two normal stress differences,  $N_1 = (\tau_{11} - \tau_{22})$  and  $N_2 = (\tau_{22} - \tau_{33})$ , which are observed to scale as  $\gamma^2$ . These differences arise because, with increasing strain, the foam films become predominantly oriented perpendicularly to the direction  $X_2$ . As a result, the surface tension of the foam films contributes more to the normal stresses  $\tau_{11}$  and  $\tau_{33}$ , and less to  $\tau_{22}$ , thus leading to the normal stress differences  $N_1$  and  $N_2$  (see Fig. 6.6(a)).

A quantitative model of this effect, in quasistatically strained dry disordered 3D foams, was developed using the formalism of large deformation continuum mechanics. It predicts

a constitutive law of the Mooney–Rivlin form [66], in a good agreement with the results from the numerical simulations (cf. Fig. 6.12(a) below):

$$\tau_{12} = G \gamma \text{ (a)} \quad N_1 = G \gamma^2 \text{ (b)} \quad N_2 = -\frac{6}{7}G \gamma^2 \text{ (c)} \quad (6.3)$$

The results from oscillatory shear experiments, shown in Fig. 6.6(b), confirm that the amplitude of  $N_1$  indeed scales with the square of strain amplitude, in agreement with eqn (6.3b). In addition, these data show that, at low strain amplitudes, internal stresses can remain trapped in the foam structure and modify the foam nonlinear response to strain – see the open symbols at strain amplitude  $\gamma < 0.1$ , which deviate from eqn (6.3b). These trapped stresses, which are enhanced with a small cone angle of the rheometer geometry, relax as the foam coarsens with time.

### 6.3.3 Linear Relaxations

Aqueous foams, subject to mechanical stress, not only store elastic energy – they can also dissipate energy, via viscous friction in the liquid contained in the foam films and Plateau borders, intrinsic viscous friction on the bubble surfaces and/or diffusive exchange of surfactant molecules between the solution and the air–water interface [55]. Here we focus on the regime where stresses and strains are so small that the viscoelastic response is linear and bubble rearrangements are not induced. For an applied oscillatory shear strain of amplitude  $\gamma_0$  and angular frequency  $\omega$ ,  $\gamma(t) = \gamma_0 \text{Re}[e^{i\omega t}]$ , the shear stress varies as  $\tau(t) = \gamma_0 \text{Re}[G^*(\omega)e^{i\omega t}]$ , where  $G^*(\omega) = G'(\omega) + iG''(\omega)$  is the complex shear modulus. The real part of the complex modulus accounts for the elastic foam response, whereas  $G''$  accounts for the energy dissipation.

Figure 6.7 presents an example of the foam viscoelastic response over six decades in frequency. In the entire range of frequencies studied  $G' > G''$ , which reflects the predominant elastic behaviour of the foams. The data for  $G''$  plotted in Fig. 6.7 show two relaxation processes, related to different mechanisms of energy dissipation. At low frequency (around  $10^{-3}$  rad/s) a peak of  $G''$  reveals a slow relaxation process with a characteristic time-scale of the order of  $1/\omega \sim 10^3$  s. At high frequency (above 1 rad/s), there is a rapid increase of  $G''$  with the frequency as  $G'' \propto \omega^{1/2}$ , in contrast to the expected behaviour for Newtonian viscous fluids,  $G'' \propto \omega$ . The physico-chemical origin of these two relaxation mechanisms is discussed below.

#### 6.3.3.1 Slow Relaxation

Slow relaxations can be additionally probed by a creep experiment, where a stress step with amplitude  $\tau_0 \ll \tau_y$  is applied to the sample, and the resulting strain  $\gamma(t)$  is measured as a function of time. A typical creep response is illustrated in Fig. 6.8(a). After an instantaneous initial elastic response, steady flow sets in, even if the applied stress is very small. The strain evolution with time  $\gamma(t) \equiv \tau_0(1/G + t/\eta)$  is reminiscent of Maxwell fluid behaviour [84], with static shear modulus  $G$  and viscosity  $\eta$ . The ratio  $t_0 = \eta/G$  gives the characteristic time of the slow relaxation process, which is of the order of several minutes for the data shown in Fig. 6.8. The peak of  $G''(\omega)$  for such system is expected at a frequency  $\omega_0 = 1/t_0 \approx 10^{-3}$  rad/s, in agreement with the results shown in Fig. 6.7.

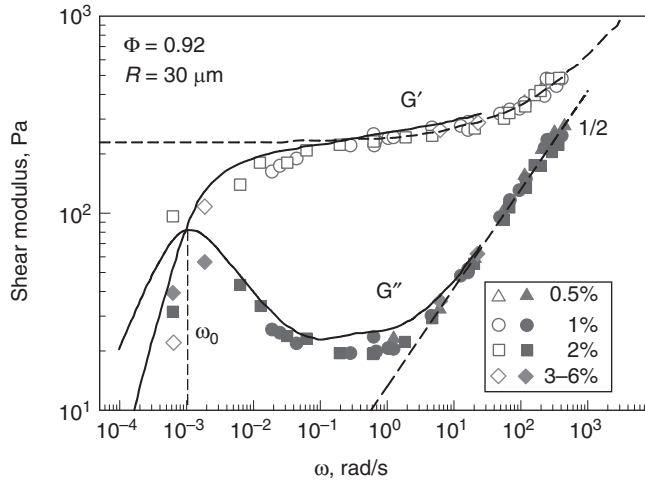


**Fig. 6.7** Dependence of the elastic  $G'$  and loss  $G''$  shear moduli on oscillation frequency. The symbols correspond to different strain amplitudes as indicated in the legend. The dashed lines are a fit to  $G^*(\omega) = G(1 + (i\omega/\omega_c)^{1/2})$ , with  $G = 230 \text{ Pa}$  and  $\omega_c = 156 \text{ rad/s}$ . The sample is Gillette shaving foam. Data from [83].

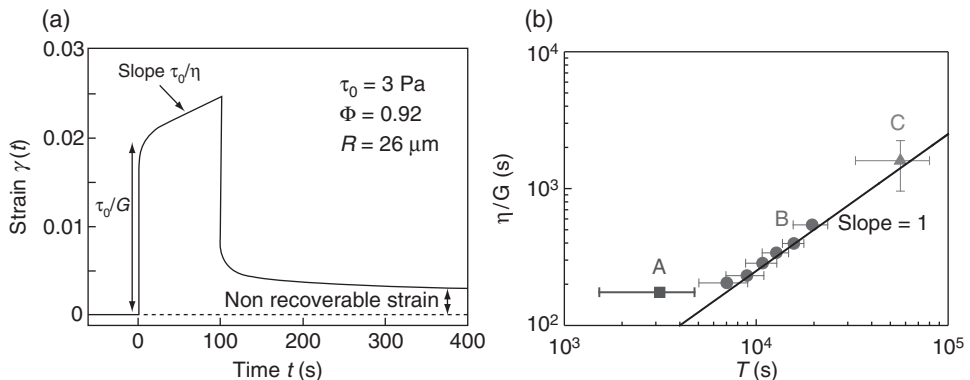


**Fig. 6.8** (a) Time evolution of the shear strain during a creep experiment with foam. A step stress,  $\tau_0$ , is applied at  $t = 0 \text{ s}$ , during a time interval  $\Delta t = 100 \text{ s}$ . This stress is released at  $t = 100 \text{ s}$ , so that no stress is applied beyond this time.  $\Delta t$  is chosen short enough so that the average bubble size does not vary significantly during  $\Delta t$ , but long enough for numerous coarsening-induced bubble rearrangements to occur. The sample is Gillette (normal) shaving foam, sheared in a Couette cell with rough surfaces. Its steady creep behaviour is characterized by the parameters  $G = (150 \pm 10) \text{ Pa}$  and  $\eta = (66 \pm 6) \cdot 10^3 \text{ Pa s}$ . (b) Characteristic time of the steady creep  $t_0 = \eta/G$ , as a function of the average time interval,  $T$ , between coarsening-induced rearrangements in a volume  $(2R)^3$ , for different foams with the same gas volume fraction,  $\Phi = 0.92$ . From A to C, the solubility of the gas in the foaming solution and, hence, the rate of coarsening-induced rearrangements decreases. The straight line is a linear fit:  $t_0 = T(2R)^3/V_r$ , with the foam volume affected by a rearrangement being  $V_r = (6R)^3$ , i.e. about 50 bubbles. See details in [85].

The low frequency response is related to the foam ageing, as the bubbles coarsen due to diffusive gas exchange between neighbouring bubbles (Ostwald ripening). This effect leads to intermittent local bubble rearrangements, which induce small random jumps of the macroscopic strain  $\gamma(t)$  [83]. If shear stress is applied to the foam, the orientation of these jumps is biased towards the direction of the stress [73] and the foam flows steadily with a creep rate  $\dot{\gamma}/\tau_o = 1/\eta$ , given by the scaling law [72, 85]:

$$\frac{1}{\eta} \equiv \alpha \frac{r V_r}{G} \quad (6.4)$$

Here  $r$  is the average number of coarsening-induced bubble rearrangements per unit time and unit volume,  $V_r$  is the typical foam volume affected by single rearrangement event, and  $\alpha$  is constant of the order of unity. The time interval between coarsening-induced bubble rearrangements in a volume  $V_r$  is given by  $T = 1/(rV_r)$ . Using multiple light scattering, combined *in situ* with rheological creep measurements, eqn (6.4) has been validated [85]. Fig. 6.8(b) shows indeed good agreement between the data and eqn (6.4) with  $V_r = (6.6 <R>)^3$ . Therefore, eqn (6.4) links the slow rheological response of foams, expressed by the time  $t_o = h/G = 1/\omega_o$ , to their coarsening dynamics which sets the time  $T$ . As the foam coarsens, its rearrangement dynamics slows down and  $T$  increases with foam age  $t_w$  as  $t_w^{0.66}$  [86, 87]. As a consequence, the relaxation frequency  $\omega_o$  decreases as  $t_w^{-0.66}$  [85]. Note that along the coarsening, the foam softens and its elastic modulus  $G$  decreases as described by eqn (6.2), due to the increase of the average bubble size.

### 6.3.3.2 Fast Relaxation

The anomalous non-Newtonian dissipation, observed at frequency higher than 1 rad/s in Fig. 6.7, is due to fast relaxations, coupled to the viscoelastic properties of the bubble surfaces that can promote either adhesion or sliding between adjacent bubbles [50]. In this range of frequencies, the complex foam modulus varies as:

$$G^*(\omega) = G (1 + (i\omega/\omega_c)^{1/2}) + i\eta_\infty \omega \quad (6.5)$$

in agreement with a theoretical model, based on randomly oriented weak zones in the foam [67]. In these weak zones, the bubbles slide with respect to each other when a macroscopic shear strain is applied, instead of undergoing affine deformation. This collective relaxation process exhibits a characteristic relaxation frequency,  $\omega_c$ , set by the interplay between an elastic storage modulus and a viscous dissipation, and depending on the interface ‘rigidity’ [55] (the latter can be characterized by the surface dilatational modulus of the foaming solution, see section 6.6 below and Refs. [16, 54]). The Newtonian viscosity  $\eta_\infty$  (eqn 6.5) is expected to dominate  $G^*$  at very high frequencies, and should scale with the viscosity of the foaming solution  $\eta_0$ .

As illustrated in Fig. 6.9, experiments with a series of different foaming solutions show that  $\omega_c$  exhibits different scaling laws with shear modulus  $G$ , or equivalently with the bubble size  $R$ , depending on the rigidity of the liquid–gas interfaces. Theoretical modelling of these processes predicts that the energy dissipation is dominated by Marangoni flow in the foam films between the bubbles for foams with ‘rigid interfaces’ (i.e. those having high surface dilatational elastic modulus), whereas for mobile interfaces (low surface modulus) the dissipation

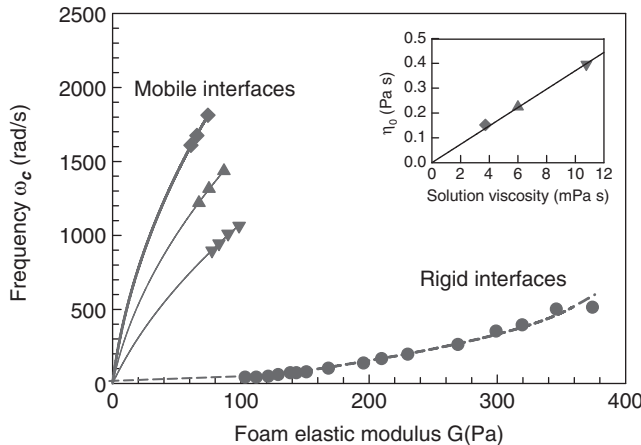


**Fig. 6.9** Characteristic frequency  $\omega_c$  of the fast collective relaxation process versus shear modulus  $G$ , for foams with (●) rigid interfaces (Gillette shaving foam) and with mobile interfaces (SLES/CAPB) containing Glycerol of (◆) 40 wt%, (▲) 50 wt%, and (▼) 60 wt%. The gas volume fraction is the same for all of these foams:  $\Phi = 93\%$ . We recall that  $G \propto \sigma/R$  according to eqn (6.1). The dashed line represents the scaling law,  $\omega_c \propto Eh/\eta_0 R^2$ , whereas the continuous lines correspond to the law,  $\omega_c \propto \sigma/(\eta_0 R + \kappa)$ , with  $E$  and  $\kappa$  being the dilatational surface elasticity and viscosity respectively, and  $h$  being the film thickness. See details in [56]. The insert shows the solution viscosity deduced from the fits of the SLES/CAPB data to the scaling law (b), compared to the viscosity measured independently. The error bars are comparable to the size of the symbols.

is dominated by marginal flow of liquid withdrawn from or receding into the Plateau borders [56]. The model predicts also that the foam loss modulus is independent of the bubble size in the case of rigid surfaces,  $G''_{\text{rigid}} \propto (\eta_0/Eh)^{1/2}$ , where  $E$  is the dilatational surface modulus and  $h$  is the foam film thickness. In contrast, the foam loss modulus decreases with  $R$  for mobile surfaces as  $G''_{\text{mobile}} \propto (\eta_0/\sigma R)^{1/2}$  (after neglecting the contribution of interfacial viscosity).

Therefore, to formulate foam with maximal dissipation of mechanical energy upon oscillatory shear, one should increase the solution viscosity and the interfacial rigidity, since we generally have  $Eh \ll \sigma R$  for a given bubble size and gas volume fraction. This prediction may be of practical relevance for foams used as mechanical attenuators.

### 6.3.4 Shear Modulus of Particle-laden Foams

The experiments with particle-laden foams [88] showed that solid particles, comparable in size to the foam bubbles, enhance strongly the linear foam elasticity – much more than homogenization arguments in the framework of continuum mechanics would predict. This is due to the capillary interactions between the particles captured within the foam structure [88]. In contrast, the yield stress of the foam does not exhibit such an anomalously large enhancement. The rheology of foams, stabilized by particles that are much smaller than the bubble size, has not been investigated systematically so far, but it may be expected to be similar to that of particle stabilized emulsions [89].

## 6.4 Yielding

When foams are subjected to increasing shear stress or strain, they exhibit a transition from solid-like to fluid-like behaviour, called ‘yielding’ [90]. Figure 6.10(a) shows a typical stress response to steadily increasing applied shear strain. As described in the previous section, the stress first increases, as in an elastic solid. Afterwards, the stress passes through weak maximum and finally settles at a plateau. In this latter regime, the stress (the height of the plateau) is an increasing function of the applied shear rate,  $\dot{\gamma}$ . The stress threshold, beyond which the flow sets in, is called ‘yield stress’ and is denoted by  $\tau_y$ . The corresponding strain threshold is the yield strain, denoted by  $\gamma_y$  (see Fig. 6.10(a)).

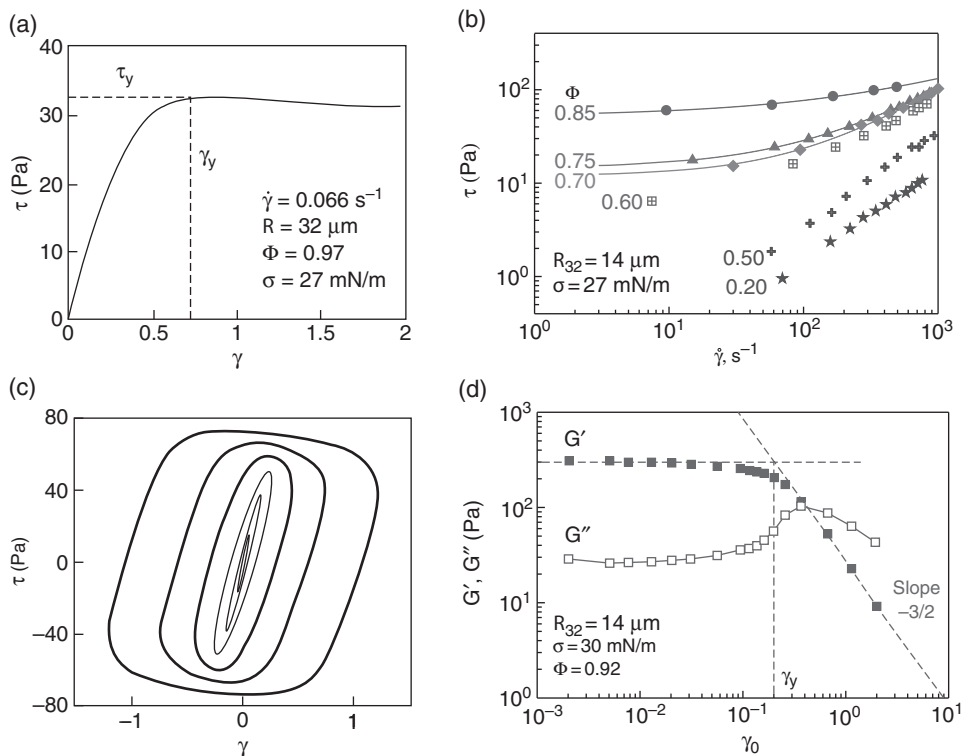


**Fig. 6.10** (a) Shear stress, induced by an applied shear strain,  $\gamma$ , that increases with time at constant rate [94]. (b) Shear stress, as a function of the strain rate, for several gas volume fractions. The data for  $\Phi > 0.64$  exhibit a plateau at low shear rates, indicating yield stress behaviour. The continuous lines are fits to the data using the Herschel-Bulkley law, eqn (6.7) [95]. (c) Shear stress versus strain, measured in an oscillatory experiment, at a frequency of 1 Hz [93]. The six curves correspond to increasing strain amplitudes of 0.055, 0.15, 0.25, 0.43, 0.72 and 1.2, respectively, and are drawn using lines of increasing thickness. The sample is the same as in (d), where its properties are specified. (d) Oscillatory response, represented as the dependency of the storage and loss moduli,  $G'$  and  $G''$ , with the oscillation amplitude,  $\gamma_0$ . The angular frequency is  $\omega = 2 \text{ rad/s}$ . For  $\gamma_0 > 0.5$ , localized flow was observed in this experiment.

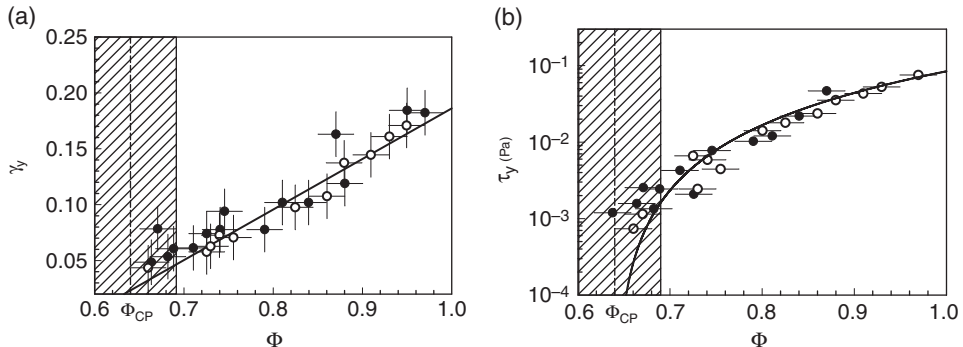


**Fig. 6.11** Yield strain (a) and yield stress (b), as a function of the volume fraction, measured in an oscillatory measurement at a frequency of 1 rad/s. The average bubble size is  $\langle R \rangle = 55\text{ }\mu\text{m}$ , the surface tension is  $\sigma = 17\text{ mN/m}$ . In the shaded region, the water drainage from the foam could not be avoided, making these data unreliable. The vertical lines in the shaded region indicate  $\Phi_{CP} = 0.64$ . Data from [81].

Several experimental protocols are used in practice to determine  $\gamma_y$  and  $\tau_y$ . The measurement of stress versus strain, at a fixed strain rate (as illustrated in Fig. 6.10(a)) is called a ‘shear start-up’ experiment. Measuring stress versus strain rate is another widely used protocol (see Fig. 6.10(b)). Here  $\tau_y$  is estimated as the stress at which the flow curve approximately converges to a plateau, at low shear rates – the value of  $\tau_y$  in this protocol is usually determined by fitting the experimental data by the Herschel–Bulkley model, eqn (6.7).

Large amplitude oscillatory experiments (LAOS) are a third option, illustrated in Fig. 6.10(c) by a parametric plot of stress versus strain. For an elastic material, such a Lissajous plot yields a straight line, whose slope gives the shear modulus  $G$  (Section 6.3.1). Viscoelastic relaxations introduce a phase shift between stress and strain, leading to an elliptic contour. This is the behaviour observed for foams in the linear viscoelastic regime, at small strain amplitudes (Section 6.3.3). For progressively increasing strain amplitudes, the response becomes non-linear, because the stress is bound by the yield stress of the foam, as seen in Fig. 6.10(c). This feature is analysed quantitatively by calculating the fundamental Fourier component of the stress oscillation, as a function of the strain amplitude  $\gamma_0$ . By normalizing this stress component by the strain amplitude, one obtains the complex shear modulus  $G^* = G' + iG''$ . The decrease of  $G'$  with the increase of  $\gamma_0$  is used to detect the yield strain,  $\gamma_y$ , at the intercept between the linear regime and the asymptotic power law  $G' \propto \gamma_0^{-3/2}$  [81, 91, 92] (see Fig. 6.10(d)). The yield stress is deduced as  $\tau_y = |G^*(\gamma_y)|\gamma_y$ . Since the variations of  $G^*$  with strain amplitude describe only the fundamental component of the stress response, they capture only partially the complete stress–strain relation shown in Fig. 6.10(c). Thus to be conclusive, a test of any non-linear rheological model requires a measurement of the full Fourier spectrum of the stress [93].

The dependence of the yield strain and yield stress on liquid volume fraction is illustrated in Fig. 6.11. Dimensional arguments suggest that the yield stress should scale with the bubble capillary pressure,  $\sigma/R$ , in agreement with the experimental results. Such scaling can be used also to compare the yielding properties of foams and emulsions, which turn out to be similar [4, 14, 92]. Technically, experiments with foams are rather difficult at  $\Phi < 0.8$ ,

due to the water drainage from the foam, which destabilizes the samples. Experiments with emulsions, which are less prompt to drainage in this range of volume fractions, showed that the yield stress and strain both tend to zero as  $\Phi$  approaches  $\Phi_{CP} \approx 0.64$  [92]. For  $\Phi < \Phi_{CP}$ , the number of contacts between neighbouring bubbles (or drops) becomes too small to sustain static mechanical equilibrium, and an arbitrarily small stress induces steady flow. The dependence of the yield stress on bubble size, surface tension and dispersed volume fraction in foams and emulsions is described well by the following empirical law [81, 92]:

$$\tau_y = \beta \frac{\sigma}{\langle R \rangle} (\Phi - \Phi_{CP})^2 \quad (6.6)$$

where  $\beta$  is a dimensionless coefficient close to 0.50 [12].

As illustrated schematically in Fig. 6.2 for a 2D foam, the foam yielding occurs at the scale of the individual bubbles when the applied macroscopic stress or strain is large enough to induce rearrangements in the bubble packing. For real polydisperse 3D foams, the bubble structure is more complex, but similar irreversible bubble rearrangements (called ‘T1 events’ for dry foam) lead to yielding and plastic flow of the foam.

So far, we have discussed the transition from solid-like to liquid-like behaviour only as a function of gas volume fraction and applied stress or strain. However, the experimental time scale, over which the mechanical response is probed, is another control parameter of the foam response. This time scale is set by the inverse frequency of an applied oscillatory strain or by the inverse strain rate for a steady flow. For sufficiently long time scales, so that the bubble coarsening induces a significant number of bubble rearrangements, foam flows like a highly viscous liquid even at very low stress,  $\tau < \tau_y$  (cf. Section 6.3.3). Even if the experimental time scale is so short that coarsening is negligible, the time scale can still affect the yielding behaviour – shear start-up experiments showed that the critical strain and stress, at which the shear-induced bubble rearrangements are triggered, are increasing functions of the applied strain rate [21]. This dependence is related to the duration of the individual rearrangement events, which in turn is affected strongly by the visco-elastic properties of the gas–liquid interfaces [39, 48].

## 6.5 Plastic Flow

Plastic strain is defined as the irreversible deformation that occurs when a material is sheared beyond its yield strain. For a very slow plastic shear flow, one may expect the sample to relax almost instantaneously towards static equilibrium whenever the applied shear rate is released suddenly. Such behaviour is called ‘quasi-static’. In practice, even very slow foam flows are quasi-static only approximately, due to the slow viscoelastic relaxations discussed in Section 6.3.

As an illustration of the plastic properties of a foam, Fig. 6.12 shows the evolution of several components of the stress tensor, as a function of the applied shear strain, obtained in a 3D numerical simulation of dry foam [71]. The stress–strain relationship is similar to the experimental results shown in Fig. 6.10(a), except for the abrupt small jumps, which are due to rearrangement events of the individual bubbles. These jumps cannot be resolved in

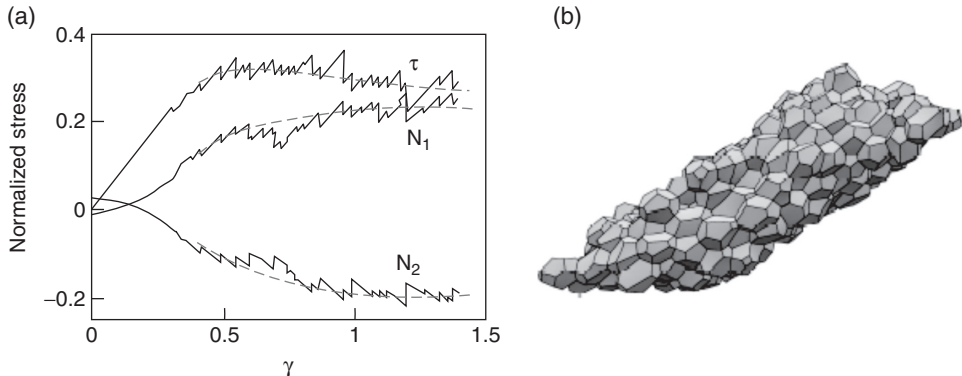


**Fig. 6.12** (a) Shear stress and normal stress differences versus shear strain, obtained in a quasi-static simulation using the Surface Evolver software. The sample is 3D disordered monodisperse dry foam containing 216 bubbles. The dashed curves, drawn at  $\gamma > 0.4$ , are guides to the eye. The quantities  $\tau$ ,  $N_1$ , and  $N_2$  are normalized by  $\sigma/V^{1/3}$  where  $V$  is the volume of a bubble. (b) Structure of the sheared foam. Data from [64].

the experimental measurements with a macroscopic foam sample, because the latter contains a much larger number of bubbles than those used in the numerical simulation. Figure 6.12 shows also that the normal stress differences are similar in magnitude to the shear stress in the steady flow regime. This is in agreement with the theoretical predictions [82]. Normal stress differences arise in many flowing visco-elastic materials, and they are of practical importance in extrusion flows, for instance [84]. However, in contrast to many polymeric liquids, the normal stress differences  $N_1$  and  $N_2$  in flowing foams are of similar magnitude and opposite signs.

As a first step towards a general constitutive law, relating stress and strain in rearrangement-driven plastic flow, the elementary plastic events have been modelled as force dipoles acting on an elastic continuum [68], in a good agreement with numerical simulations [42]. In another approach, so far limited to 2D foams, the anisotropy of the foam microstructure is captured by a texture tensor related to the macroscopic stress [45]. The striking similarity between the rheology of glasses and many complex fluids, including foams, has stimulated the development of another general model (called the ‘soft glassy rheology’ model), which captures the non-linear elastic and plastic response of yielding foams [93]. In addition, several phenomenological models have been proposed, which extend the elasto-plastic constitutive laws by including relaxation terms describing the visco-elastic foam behaviour [96].

## 6.6 Viscous Dissipation in Steadily Sheared Foams

The stress in steadily sheared foam depends on the applied shear rate. Experiments have shown [4, 16, 18, 31, 52] that this behaviour is usually represented well by the Herschel–Bulkley equation (see Fig. 6.13a):

$$\tau(\dot{\gamma}) = \tau_y + \tau_V(\dot{\gamma}) = \tau_y + k\dot{\gamma}^n \quad (6.7)$$

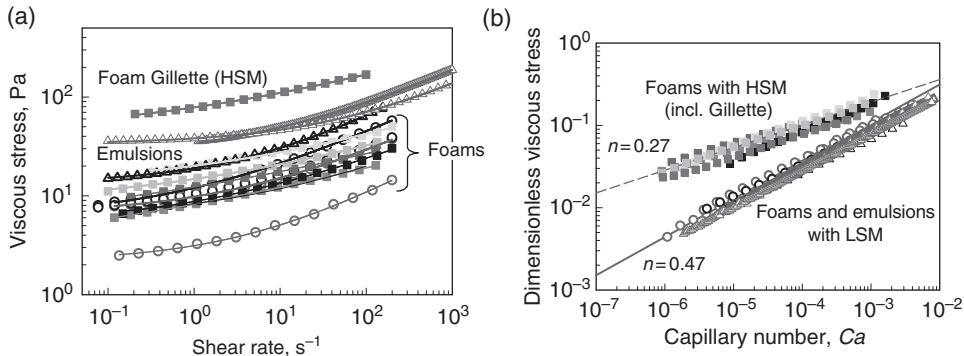


**Fig. 6.13** (a) Experimental results for the dependence of shear stress,  $\tau$ , on shear rate,  $\dot{\gamma}$ , for steadily sheared foams and emulsions. The open circles denote foams with low surface modulus, the filled squares foams with high surface modulus and the open triangles emulsions with low surface modulus. For the foams, the bubble radius varies between 20 and 300  $\mu\text{m}$ , surface tension varies between 22 and 30 mN/m, and viscosity of the continuous phase is varied between 1 and 11 mPa.s by adding glycerol in the aqueous phase. For the emulsions, the drop radius varies between 2 and 40  $\mu\text{m}$ , interfacial tension varies between 2 and 10 mN/m, and viscosity of the drop phase varies between 2 and 5 mPa.s. For all systems, the bubble (drop) volume fraction is  $0.90 \pm 0.01$ . The curves are fits by the Herschel–Bulkley model, eqn (6.7). (b) Dimensionless viscous stress,  $\tilde{\tau}_v$ , v. capillary number,  $\text{Ca}$ , for the same systems. Two different types of flow behaviour are evidenced, characterized by different values of the power-law index,  $n$ .

which contains three characteristic parameters: the yield stress  $\tau_y$ , the power-law index  $n$  and the consistency  $k$ . Here,  $\tau_y(\dot{\gamma})$  is the rate-dependent part of the total stress, determined by subtracting  $\tau_y$  from the total stress,  $\tau(\dot{\gamma})$ . For foams and concentrated emulsions with  $\Phi > \Phi_{cp}$ , the power-law index,  $n$ , is typically between 0.2 and 0.5, reflecting the strong shear-thinning behaviour of these systems [16, 18, 31, 52]. The dimension of the consistency  $k$  is Pa.s<sup>n</sup> and it is, therefore, dependent on the specific value of  $n$ . The flow behaviour of Herschel–Bulkley fluids in different geometries (through pipes, between Couette cylinders, etc.) is described in rheology textbooks [84, 97] and will not be recalled here.

When comparing experimental results for various systems and with theoretical predictions, it is convenient to use appropriate dimensionless quantities. The viscous stress is scaled by the mean capillary pressure of the bubbles,  $\tilde{\tau}_v = \tau_v R_{32}/\sigma$ . The shear rate is scaled by the ratio of the viscous stress and bubble capillary pressure, leading to the so-called ‘capillary number’,  $Ca = (\eta\dot{\gamma}R_{32})/\sigma$ . This number plays the role of a dimensionless shear rate in this context. Comparing shear flow data for different systems, plotted in terms of the dimensionless quantities  $\tilde{\tau}_v$  and  $Ca$ , eliminates the generic effects of  $R_{32}$ ,  $\sigma$ , and  $\eta$ . Such a representation highlights the specific influence of the type of dispersion (foam or emulsion), surfactant type [14–16] or other specific features, if present.

As an example, we show in Fig. 6.13(b) experimental data  $\tilde{\tau}_v(Ca)$ , for a variety of foams and concentrated emulsions with different values of  $R_{32}$ ,  $\sigma$  and  $\eta$ . The requirements met by all the experimental data compiled on this graph are: (i) the continuous phase of the foam or the emulsion is Newtonian; (ii) wall slip was suppressed so that the true foam flow curve

was measured; (iii) data about the mean bubble or droplet size, interfacial tension and solution viscosity are available, so that the final results can be presented in dimensionless form; (iv) the mean radius of the drops and bubbles is larger than about  $2\text{ }\mu\text{m}$  to avoid possible effects of surface forces acting in the foam and emulsion films (see [52] for numerical estimates about the effect of surface forces). Remarkably, all these data collapse onto two master curves, when plotted in this dimensionless representation. Thus we can distinguish two qualitatively different cases:

1. Systems in which the power-law index is  $n \approx 0.45 \pm 0.03$  [16, 18, 31, 33, 51, 52, 54, 98].
2. Systems where  $n$  is close to  $0.25 \pm 0.05$  [16, 18, 51, 52, 54, 99].

For similar characteristics  $\Phi$ ,  $\eta$ ,  $\sigma$  and  $R_{32}$ , type 2 systems exhibit much higher viscous friction compared to those of type 1 [14, 16, 52]. Moreover, local velocity measurements using MRI techniques showed that the foams of both types exhibit flow that is described well by the Herschel–Bulkley law (eqn 6.7), without observable indications of shear banding [35] for gas volume fractions in the range 0.88–0.95. Similar findings were reported for emulsions [33].

Experiments comparing the interfacial properties of the foaming solutions [16, 52] showed that the principal difference between systems of type 1 and 2 is the magnitude of their surface dilatational modulus,  $E$ . This parameter characterizes the amplitude of surface tension variation, induced by a sinusoidal perturbation of the solution surface area. For all systems of the first type (with  $n \approx 1/2$ ) the surface modulus, measured at frequencies of the order of 0.1 Hz, is low,  $E < 10\text{ mN/m}$  [16, 52]. In contrast, the surface modulus is much higher for the systems of the second type,  $E > 100\text{ mN/m}$  [16, 18, 52]. These results show that the predominant mechanisms of viscous dissipation in foams, stabilized by surfactants with low surface modulus (LSM) and by surfactants with high surface modulus (HSM), are different. Therefore, to compare and discuss experimental data obtained with different foaming solutions, the solution surface properties (including its surface modulus) must be characterized and taken into account. It is worth noting that some commercial foams used widely in rheological studies (e.g. Gillette shaving foam) are formulated to have HSM, whereas other foaming systems (e.g. dishwashing liquids) usually have LSM.

Theoretical modelling showed that the experimental data could be described by considering two principal mechanisms of viscous dissipation of energy in sheared foams: (i) in the foam films, formed between two neighbouring bubbles, and (ii) in the surfactant adsorption layers on the bubble surfaces [51, 52]. These two mechanisms are considered consecutively below.

### **6.6.1 Predominant Viscous Friction in the Foam Films**

Let us consider first the viscous dissipation of energy in the foam films, which is due to the relative motion of the bubbles with respect to each other, and which is the prevailing mechanism of energy dissipation for foams stabilized by LSM surfactants. The relative bubble motion creates local velocity gradients in the fluid confined in the foam films; see Fig. 6.14. The theoretical modelling showed [52] that the liquid motion inside the sheared foam films could be decomposed into two coexisting ‘elementary’ processes:

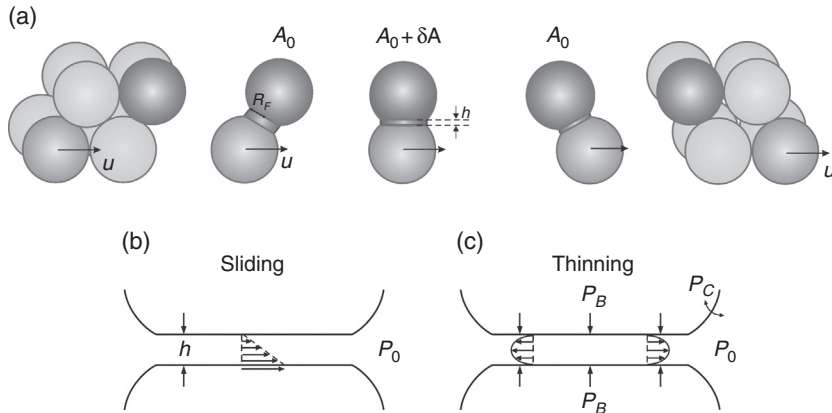


**Fig. 6.14** (a) Schematic presentation of the processes of formation, thinning, and disappearance of a foam film between two bubbles in sheared foam [51, 52]. Note that the process of formation and expansion, and the subsequent shrinking and disappearance of the foam film, is accompanied by a change in the total surface area of the colliding bubbles. (b) Schematic presentation of the process of sliding: opposite film surfaces move at different velocities, driven by the relative motion of neighbouring bubbles in flowing foam. The film thickness  $h$  determines the local shear rate of the liquid in the film. (c) Schematic presentation of film thinning. This process is driven by the excess of pressure in the bubbles,  $P_B$ , as compared to the pressure in the liquid outside the film,  $P_0$ . The viscous dissipation is predominantly due to the sliding motion.

(i) sliding motion of the opposite film surfaces, driven by the relative motion of the neighbouring bubbles in sheared foam (Fig. 6.14(b)); (ii) thinning of the foam film, which is due to the higher dynamic pressure inside the film (imposed by the capillary pressure of the bubbles,  $P_C$ ), as compared to the pressure in the surrounding Plateau channels; see Fig. 6.14(c).

The numerical estimates showed that the main dissipation of energy in the foam films is due to the sliding motion of the bubbles, i.e. to process (i) [52]. However, the film thinning process (ii) should be also considered explicitly, because it determines the instantaneous film thickness and the resulting velocity gradient inside the foam film. Using a standard hydrodynamic approach and reasonable assumptions, the rate of energy dissipation inside the foam films was calculated and used to derive an approximate formula for the viscous stress in sheared foams [51, 52],

$$\tilde{\tau}_{VF} \approx 1.16 Ca^{0.47} \Phi^{5/6} (\Phi - 0.74)^{0.1} / (1 - \Phi)^{0.5} \quad (6.8)$$

$\tilde{\tau}_{VF} = \tau_{VF} R_0 / \sigma$  is the dimensionless shear stress, related to the friction in the foam films (the subscript VF denotes viscous friction inside the films). This model predicts  $n \approx 0.47$ , which is in a very good agreement with the experimental results for LSM systems. Despite the fact that the theoretical model assumes ordered and monodisperse foam structure, it was verified experimentally that eqn (6.8) is applicable to both disordered monodisperse and polydisperse foams and emulsions, if the assumptions used to derive eqn (6.8) are satisfied (e.g. the surface forces between the foam film surfaces are negligible [52]). These

experimental tests were carried out in the range of volume fractions  $0.8 < \Phi < 0.98$ . In addition, for eqn (6.8) to be valid, the shear rate must be sufficiently high, as discussed below.

In recent studies of 2D foams (sheared monolayers of bubbles), a conceptually different explanation of the power-law index  $n \approx 1/2$  was proposed [46, 47, 61]. This explanation is based on the results from the numerical simulations of the viscous friction in disordered 2D foams using the ‘bubble model’ [63, 64]. This model assumes that the friction force between neighbouring bubbles depends linearly on their relative velocity, and that the friction coefficient is independent of the shear rate [62] (in contrast to the model leading to eqn (6.8)). For the macroscopic stress induced by steady shear of the foam, a power-law index  $n=0.54$  was obtained from the numerical simulations, made under these assumptions. Thus, friction forces depending linearly on the relative velocity of neighbouring bubbles can give rise to macroscopic non-Newtonian viscous behaviour. The simulations showed also that the bubble trajectories are highly irregular in the investigated range of low shear rates. The link between local and macroscopic viscous dissipation in 2D foams was also investigated experimentally, using bubble rafts floating on a liquid surface [46, 100]. The local viscous interaction between neighbouring bubbles was in this case found to be a non-linear function of the relative bubble velocity, with a power-law index that was again different from the one deduced from the macroscopic foam flow data. Both the experimental and the simulation work led to the suggestion that the disorder of the foam structure may have a strong impact on foam rheology, and that the highly irregular bubble motion observed in flowing 2D foams can be the origin of the observed difference between the macroscopic and the local friction laws.

These findings raise the question whether irregular bubble motion in disordered 3D foams may also have a strong impact on the non-linear macroscopic viscous dissipation, or whether the mechanism leading to eqn (6.8), which does not take into account the bubble disorder, is dominant. As evidenced by the experimental results and theoretical analysis, the answer may depend on the foam shear rate: light scattering experiments with sheared 3D Gillette foam showed that the bubble dynamics was intermittent at rates below  $0.5 \text{ s}^{-1}$ , suggesting irregular motion reminiscent of the one discussed above for 2D foams. In contrast, the flow was found to be approximately laminar at higher shear rates [37], in qualitative agreement with the observations of bubble trajectories at the surface of rapidly sheared foams, as reported in [14]. As discussed in ref. [14] (see eqn (6.14) and the related discussion therein) this transitional shear rate might be explained by comparing the characteristic time for film thinning with the contact time of the bubbles (the latter is approximately equal to the inverse shear rate of the foam) – in slowly sheared foams, the foam films have enough time to thin down to their equilibrium thickness,  $h_{EQ}$ . In contrast, the bubbles are in contact very shortly in rapidly sheared foams, so that the transient foam films formed between colliding bubbles have no time to thin down to  $h_{EQ}$ . In this regime, the theoretical model predicts [52] that the thickness of the transient foam film scales with  $Ca^{1/2}$ , i.e. it significantly increases with the shear rate. Depending on the system parameters, the threshold shear rate, separating these two different regimes of foam flow, is expected to be of the order of 0.01 to  $1 \text{ s}^{-1}$  [14]. These results suggest that the assumptions used to derive eqn (6.8) are best verified at high shear rates. Indeed, most of the published flow curves for 3D foams were measured at high shear rates, whereas 2D foams have been studied mostly at low shear rates. Data where the viscous contribution to the shear stress

in 3D or 2D foam is resolved well enough to establish accurately the power law exponents in *both* regimes would clearly be of interest. We recall that in the limit of very low shear rates, coarsening-induced creep flow becomes the dominant flow mechanism (see Section 6.3.3). In this regime, the flow index is equal to 1 and the foam flows like a very viscous Newtonian fluid.

### 6.6.2 Predominant Viscous Friction in the Surfactant Adsorption Layer

The viscous stress, measured under the same conditions for foams stabilized by HSM surfactants, is much higher than in foams stabilized by LSM surfactants. This result shows that an additional contribution into the viscous stress must exist for these systems. Theoretical arguments show that the bubble collisions in sheared foams lead to oscillations of the bubble surface areas around their mean value,  $A_0$ . This variation of the bubble surface area leads to viscous dissipation of energy in the surfactant adsorption layer, due to the surface dilatational viscosity. The following expression was derived theoretically for this contribution (denoted as  $\tau_{vs}$ ) to the total viscous stress [52]:

$$\tilde{\tau}_{vs} \equiv \tau_{vs} R_0 / \sigma \approx 9.8 \Phi (E_{LD} / \sigma) \Phi a_0^2 \quad (6.9)$$

$E_{LD}$  is the surface dilatational loss modulus of the adsorption layer (viscous surface modulus) and  $a_0$  is the relative amplitude of the bubble area oscillations. In general, the viscous stress in sheared foams includes contributions from the energy dissipation in both the foam films and adsorption layers:  $\tau_v = \tau_{vf} + \tau_{vs}$ . However, the second contribution is important for HSM systems only [52].

Two series of experimental results, obtained with different types of foam samples, deserve additional discussion.

Soller and Koehler [32] studied the rheological properties of draining foams, maintained in a stationary state by continuous perfusion of surfactant solution at the top of the foam. The measured flow curves were incompatible with the Herschel–Bulkley model, in contrast to other results obtained under conditions where drainage is insignificant. The most probable reason for this difference is that the film thickness is modified in the presence of liquid drainage in the foam, as previously reported [101]. Since the friction between neighbouring bubbles depends on film thickness, liquid drainage is indeed expected to affect the bubble–bubble friction and the resulting foam viscous stress. The results obtained in [32], concerning the specific rheological properties of draining foams, could be of specific interest in several practical applications.

Pilon and co-workers studied foam rheology at lower volume fractions experimentally ( $\Phi$  varied between 0.54 and 0.70) [102, 103]. The foam viscous stress was determined by pipe-flow rheometry and the power-law index  $n$  was found to be in the range between 0.60 and 0.66 for all foams studied. The authors interpreted these data as a dependence  $\tau_v \propto Ca^{2/3}$  (i.e.  $n \approx 2/3$ ), which was assumed to be a result of predominant friction in curved meniscus regions [103]. Firmly established theoretical models for foam viscosity at low volume fractions are not yet available. Moreover, the authors' claim that there was no wall slip in their experiments deserves more convincing verification. An interesting observation in this study was that the viscous friction depended strongly on bubble polydispersity,

most probably, because  $\Phi$  was around the value of  $\Phi_{cp}$ . In contrast, the experimental results obtained by other authors at  $\Phi \geq 0.80$  did not indicate a strong dependence of the viscous stress on bubble or drop polydispersity [16, 31, 52].

## 6.7 Foam–Wall Viscous Friction

If foam is in contact with a smooth solid wall, the application of external stress often leads to sliding of the boundary bubbles along the wall surface, thus violating the common ‘non-slip’ boundary condition for fluid flow at solid surfaces, see Fig. 6.15 [4, 7–9, 15–18]. This ‘foam-wall slip’ phenomenon may affect strongly the rheological measurements because, in its presence, the actual shear rate inside the foam cannot be deduced directly from the motion of the walls bounding the sample.

Foam-wall slip is conveniently studied by placing the foam in contact with a smooth solid surface in the rheometer (e.g. with the wall of a Couette cylinder, plate, or cone) and applying an external stress that is lower than the yield stress of the foam [15–18]. Under these conditions, foam-wall slip with controlled slip velocity is obtained, and the measured shear stress is entirely due to the viscous friction of the boundary layer of bubbles with the wall surface. A similar type of viscous friction is observed when bubbles or drops travel along a narrow capillary tube (so-called ‘Bretherton problem’). The latter configuration is relevant to several important applications, such as enhanced oil recovery by surfactant solutions and microfluidics [5, 7, 9, 19, 106–110].

The measured foam-wall stress,  $\tilde{\tau}_w$ , is conveniently scaled by the bubble capillary pressure,  $\tilde{\tau}_w = \tau_w R_{32}/\sigma$ , while the relative foam-wall velocity,  $V_0$ , is represented in dimensionless form by the wall capillary number,  $Ca^* = \eta V_0/\sigma$ . The experimental results for  $\tilde{\tau}_w$  v.  $Ca^*$  are well represented by a power law,  $\tilde{\tau}_w = k_w (Ca^*)^m$ , see Fig. 6.16. These experimental results also provide evidence that the foam-wall yield stress is usually negligible in

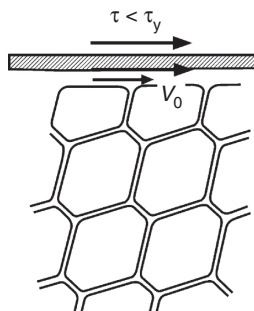


**Fig. 6.15** If the boundary bubbles slide with respect to the confining solid wall (relative velocity  $V_0$ ), viscous friction appears in the wetting films, formed between the boundary bubbles and the wall surface. If the applied stress is lower than the foam yield stress,  $\tau < \tau_y$ , the foam is deformed elastically, without bubble rearrangements occurring. In contrast, when  $\tau > \tau_y$ , the foam also flows and the actual shear rate inside the foam depends on the wall-slip velocity,  $V_0$ .

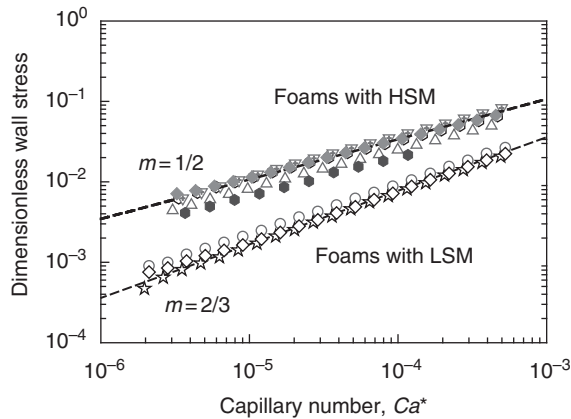


**Fig. 6.16** Dimensionless foam-wall friction stress,  $\tau_w/(\sigma/R_{32})$ , versus capillary number,  $Ca^* = \mu V_0/\sigma$ . The foams were prepared from different surfactant solutions whose viscosity was varied between 1 and 11 mPa.s by adding glycerol. In the various foams studied, the mean bubble radius varies between 100 and 300  $\mu\text{m}$ , and the surface tension varies between 22 and 30 mN/m. The lines are drawn as guides to the eye with slopes corresponding to the indicated flow index,  $m$ . The air volume fraction is  $\Phi = 0.90 \pm 0.01$ .

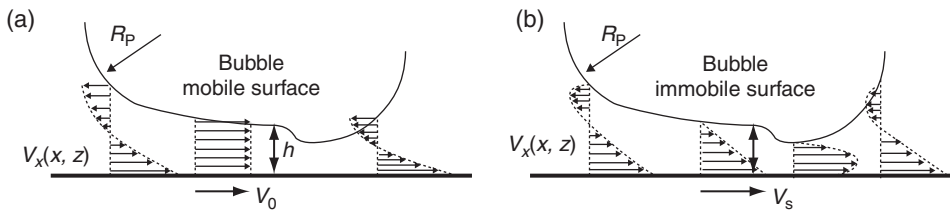


**Fig. 6.17** Schematic presentation of the zone of bubble–wall contact with the profile of the fluid velocity [17]. (a) In the case of tangentially mobile bubble surface, there is no velocity gradient in the wetting film, so that the bubble–wall friction originates in the meniscus zones around the film only. (b) In the case of tangentially immobile bubble surface, the friction occurs in both zones – of the film and in the surrounding meniscus regions. The theoretical models show that the friction in meniscus regions scales as  $(Ca^*)^{2/3}$  for both mobile and immobile bubble surfaces, whereas the friction in the film region scales as  $(Ca^*)^{1/2}$  (for immobile surface) [16, 17, 104, 105, 109].

comparison with the foam-wall viscous stress. As illustrated in Fig. 6.16, the experimental results obtained with many different foam systems merge around two master lines, depending on the surface modulus of the foaming solutions: (i) systems with LSM give power-law index  $m \approx 2/3$ ; (ii) systems with HSM give  $m \approx 1/2$  [16–18, 54].

Several detailed theoretical models of the viscous friction between bubbles and smooth solid wall have been proposed [5, 16, 17, 104–109]. All of them are based on calculations of the fluid velocity profile in the wetting films, formed in the bubble–wall contact zone; see Fig. 6.17. In these calculations, a ‘non-slip’ boundary condition is used for the liquid flow at the surface of the solid wall, whereas different boundary conditions are considered

for the gas–liquid interface. For bubbles with tangentially mobile surfaces (those with LSM) one can assume a stress-free boundary condition, which results in a plug flow of the liquid inside the wetting films (i.e. flow without velocity gradient; see Fig. 6.17(a)). In contrast, solutions with HSM give bubbles with tangentially immobile surfaces; the usual non-slip boundary condition for the liquid flow can be applied and a velocity profile with a gradient is established in the wetting films (Fig. 6.17(b)). Once this velocity profile has been calculated, one can determine the resulting viscous stresses acting on the wall surface,  $\tau_w$  [16, 17]. In most theoretical models, the numerical calculations are made for idealized, infinitely long cylindrical bubbles (2D bubbles) [5, 16, 17, 104–106]. In [16, 17] it is shown how the results for such model 2D bubbles could be extended to estimate  $\tau_w$  for real 3D bubbles in foam slipping on a solid wall.

The theoretical models predict  $\tau_w \propto (Ca^*)^{2/3}$  for the systems, in which the bubble–wall friction is dominated by the viscous stress in the curved menisci regions surrounding the wetting film [104, 105, 109]. In contrast,  $\tau_w \propto (Ca^*)^{1/2}$  is predicted for bubbles in which the bubble–wall friction is dominated by the viscous stress inside the wetting film, which is possible only if the bubble surface is tangentially immobile [16, 17]. These predictions are in good agreement with the experimental results [14–16]: the solutions with high surface modulus yield bubbles with tangentially immobile surface and  $m \approx 1/2$ , whereas solutions with low surface modulus lead to bubbles with tangentially mobile surface and  $m \approx 2/3$  is measured; see Fig. 6.16.

It is worth mentioning that the surfactants that give mobile bubble surfaces in the foam–wall experiments were shown to behave as with immobile bubble surfaces in the inside-foam friction experiments [53, 110, 111]. Most probably, the reason for this non-trivial result is the qualitatively different dynamics of the bubbles and of the respective thin films in the two types of experiments. In the foam–wall friction experiments, the bubbles have stationary shape and the films have constant radius and thickness at given velocity of the wall. In contrast, the foam films between colliding bubbles in sheared foams have a limited lifetime, and continuously change their thickness and radius during this lifetime; see Fig. 4 in ref. [52]. Therefore, the viscous stresses exerted on the film surfaces, and the mass-transfer of surfactant towards/from the bubble surface, are qualitatively different in both types of experiments – steady state configuration is realized in the foam–wall friction experiments, whereas oscillations of the film and bubble surface areas are realized in sheared foams, with a frequency  $\approx \dot{\gamma}$ . Further model experiments with single bubbles or more detailed theoretical models, accounting for the dynamics of surfactant adsorption, could be very useful in clarifying this issue.

## 6.8 Conclusions

In recent years, significant progress towards a physical understanding of the multi-scale processes that govern the mechanical properties of liquid foams has been made. It has been demonstrated that foam rheology is controlled by a coupling between elastic and viscous effects: surface tension forces give rise to an elastic mechanical response, depending on bubble deformations, whereas viscous friction inside the films and Plateau channels, and/or in the surfactant adsorption layers, leads to viscous dissipation of energy.

Depending on the choice of surfactants, shear rate and foam ageing (bubble coarsening), one among several possible mechanisms of dissipation may prevail. To rationalize this complexity, it is necessary to identify experimentally the dominant physico-chemical processes at the scale of the bubbles and foam films, and to define adequate theoretical models.

The dependencies of foam viscosity, elasticity and yield stress on the bubble size, surface tension, solution viscosity and coarsening rate have been established experimentally and explained theoretically. The respective scaling laws have been used to describe conveniently a large variety of experimental data in terms of appropriate dimensionless quantities. This approach has provided much insight about the strong effects of the visco-elastic surface modulus of the foaming solution on several phenomena related to foam rheology – foam–wall friction, bulk viscous stress in flowing foam, and energy dissipation during fast visco-elastic relaxations. In addition, the influence of foam ageing (via bubble coarsening) on foam rheology has been clarified.

Many interesting questions in the field of foam rheology are still open and call for further investigation. What local mechanisms and macroscopic laws govern the flow of very wet or very dry foams? How can physico-chemical tools be used to control most efficiently the foam rheological properties? How deep is the analogy between foam, emulsion, paste and suspension rheology? A current direction of active research is the foam rheology in very short time scales. Sound propagation in foams [112], the mechanical impact of solid objects on foams [113] and blast mitigation by foams [114] all fall into this category. Another active field of research is the coupling between foam structure and flow. Examples are bubble break-up induced by shear flow [53], and the coupling between osmotic pressure and shear flow [2], called also ‘dilatancy’. This non-exhaustive list of open questions clearly demonstrates how attractive this area currently is for fundamental research studies, with important practical implications.

## Abbreviations

2D, 3D	two dimensional and three dimensional, respectively
CAPB	cocoamidopropyl betaine (amphoteric surfactant)
DWS	diffusing wave spectroscopy
HSM	high surface modulus
LAOS	large amplitude oscillation
LSM	low surface modulus
MRI	magnetic resonance imaging
SLES	sodium lauryl-trioxyethylene sulfate (anionic surfactant)

## Acknowledgement

The authors are grateful for the support of this study to the bilateral research program ‘Rila-4’, funded by the French foundation ‘EGIDE’ and the National Science Fund of Bulgaria (project no. 202).

## References

- [1] R.K. Prud'homme and S.A. Khan (eds). *Foams: Theory, Measurements, and Applications*, Surfactant Science Series, Vol. 57. Marcel Dekker, New York, 1996.
- [2] D. Weaire and S. Hutzler. *The Physics of Foams*. Oxford University Press, Oxford, 2001.
- [3] D. Exerowa and P.M. Kruglyakov. *Foams and Foam Films: Theory, Experiment, Application*. Elsevier, Amsterdam, 1998.
- [4] H.M. Princen. The structure, mechanics, and rheology of concentrated emulsions and fluid foams. In *Encyclopedia of Emulsion Technology*, J. Sjöblom (ed.). Marcel Dekker, New York, 2001.
- [5] G.J. Hirasaki and J.B. Lawson. Mechanisms of foam flow in porous media: apparent viscosity in smooth capillaries. *Soc. Petroleum Eng. J.*, **25**: 176, 1985.
- [6] D.A. Edwards, D.T. Wasan and H. Brenner. *Interfacial Transport Processes and Rheology*. Butterworth-Heinemann, Boston, 1991.
- [7] A.M. Kraynik. Foam flows. *Ann. Rev. Fluid Mech.*, **20**: 325, 1988.
- [8] D. Weaire. The rheology of foam. *Curr. Opin. Coll. Interface Sci.*, **13**: 171, 2008.
- [9] D. Weaire and W. Drenckhan. Structure and dynamics of confined foams: A review of recent progress. *Adv. Coll. Interface Sci.*, **137**: 20, 2008.
- [10] D. Weaire and S. Hutzler. Foam as a complex system. *J. Phys: Condens. Matter*, **21**: 474227, 2009.
- [11] D. Weaire, J.D. Barry and S. Hutzler. The continuum theory of shear localization in two-dimensional foam. *J. Phys: Condens. Matter*, **22**: 193101, 2010.
- [12] R. Höhler and S. Cohen-Addad. Rheology of liquid foam. *J. Phys: Condens. Matter*, **17**: R1041, 2005.
- [13] D. Langevin. Aqueous foams: A field of investigation at the Frontier between chemistry and physics. *ChemPhysChem*, **9**: 510, 2008.
- [14] N. Denkov, S. Tcholakova, K. Golemanov, K.P. Ananthpadmanabhan and A. Lips. Role of surfactant type and bubble surface mobility in foam rheology. *Soft Matter*, **7**: 3389, 2009.
- [15] H.M. Princen. Rheology of foams and highly concentrated emulsions. II. Experimental study of the yield stress and wall effects for concentrated oil-in-water emulsions. *J. Coll. Interface Sci.*, **105**: 150, 1985.
- [16] N.D. Denkov, V. Subramanian, D. Gurovich and A. Lips. Wall slip and viscous dissipation in sheared foams: Effect of surface mobility. *Coll. Surf. A*, **263**: 129, 2005.
- [17] N.D. Denkov, S. Tcholakova, K. Golemanov, V. Subramanian and A. Lips. Foam–wall friction: Effect of air volume fraction for tangentially immobile bubble surface. *Coll. Surf. A*, **282/283**: 329, 2006.
- [18] S. Marze, D. Langevin and A. Saint-Jalmes. Aqueous foam slip and shear regimes determined by rheometry and multiple light scattering. *J. Rheol.*, **52**: 1091, 2008.
- [19] I. Cantat, N. Kern and R. Delannay. Dissipation in foam flowing through narrow channels. *Europhysics Lett.*, **65**: 726, 2004.
- [20] C. Raufaste, A. Foulon and B. Dollet. Dissipation in quasi-two-dimensional flowing foams. *Phys. Fluids*, **21**: 053102, 2009.
- [21] F. Rouyer, S. Cohen-Addad, M. Vignes-Adler and R. Höhler. Dynamics of yielding observed in a three-dimensional aqueous dry foam. *Phys. Rev. E*, **67**: 021405–7, 2003.
- [22] P. Coussot and G. Ovarlez. Physical origin of shear-banding in jammed systems. *Europhys. J. E*, **33**: 183, 2010.
- [23] G. Katgert and M. Van Hecke. Jamming and geometry of two-dimensional foams. *Europhys. Lett.*, **92**: 34002, 2010.
- [24] P. Schall and M. Van Hecke. Shear bands in matter with granularity. *Annual Rev. Fluid Mech.*, **42**: 67, 2010.
- [25] M. Dennin. Discontinuous jamming transitions in soft materials: Coexistence of flowing and jammed states. *J. Phys: Condens. Matter*, **20**: 283103, 2008.
- [26] N.D. Denkov, S. Tcholakova, K. Golemanov and A. Lips. Jamming in sheared foams and emulsions, explained by critical instability of the films between neighbouring bubbles and drops. *Phys. Rev. Lett.*, **103**: 118302, 2009.

- [27] S. Meeker, R.T. Bonnecaze and M. Cloitre. Slip and flow in pastes of soft particles: direct observations and rheology. *J. Rheol.*, **48**: 1295, 2004.
- [28] J.R. Seth, M. Cloitre and R.T. Bonnecaze. Influence of short-range forces on wall-slip in microgel pastes. *J. Rheol.*, **52**: 1241, 2008.
- [29] U. Seifert. Hydrodynamic lift on bound vesicles. *Phys. Rev. Lett.*, **83**: 876, 1999.
- [30] H.M. Princen. Rheology of foams and highly concentrated emulsions: I. Elastic properties and yield stress of a cylindrical model system. *J. Coll. Interface Sci.*, **91**: 160, 1983.
- [31] H.M. Princen and A.D. Kiss. Rheology of foams and highly concentrated emulsions: IV. An experimental study of the shear viscosity and yield stress of concentrated emulsions. *J. Coll. Interface Sci.*, **128**: 176, 1989.
- [32] R. Soller and S.A. Koehler. Rheology of steady-state draining foams. *Phys. Rev. Lett.*, **100**: 208301, 2008.
- [33] G. Ovarlez, S. Rodts, A. Ragouilliaux, P. Coussot, J. Goyon and A. Colin. Wide-gap Couette flows of dense emulsions: local concentration measurements, and comparison between macroscopic and local constitutive law measurements through magnetic resonance imaging. *Rheol. Rev. E*, **78**: 036307, 2008.
- [34] C. Enzendorfer, R.A. Harris, P. Valko, M.J. Economides, P.A. Fokker and D.D. Davies. Pipe viscometry of foams. *J. Rheol.*, **39**: 345, 1995.
- [35] G. Ovarlez, K. Krishan and S. Cohen-Addad. Investigation of shear banding in three-dimensional foams. *Europhys. Lett.*, **91**: 68005, 2010.
- [36] A.D. Gopal and D.J. Durian. Nonlinear bubble dynamics in a slowly driven foam. *Phys. Rev. Lett.*, **75**: 2610, 1995.
- [37] A.D. Gopal and D.J. Durian. Shear-induced ‘melting’ of an aqueous foam. *J. Colloid Interface Sci.*, **213**: 169, 1999.
- [38] R. Höhler, S. Cohen-Addad and H. Hoballah. Periodic nonlinear bubble motion in aqueous foam under oscillating shear strain. *Phys. Rev. Lett.*, **79**: 1154, 1997.
- [39] M. Durand and H.A. Stone. Relaxation time of the topological T1 process in a two-dimensional foam. *Phys. Rev. Lett.*, **97**: 226101, 2006.
- [40] J. Lauridsen, G. Chanhan and M. Dennin. Velocity profiles in slowly sheared bubble rafts. *Phys. Rev. Lett.*, **93**: 018303, 2004.
- [41] C. Gilbreth, S. Sullivan and M. Dennin. Flow transitions in two-dimensional foams. *Phys. Rev. E*, **74**: 051406, 2006.
- [42] G. Debregeas, H. Tabuteau and J.-M di Meglio. Deformation and flow of a two-dimensional foam under continuous shear. *Phys. Rev. Lett.*, **87**: 178305, 2001.
- [43] B. Dollet and F. Graner. Two-dimensional flow of foam around a circular obstacle: local measurements of elasticity, plasticity and flow. *J. Fluid Mech.*, **585**: 181, 2007.
- [44] B. Dollet, M. Aubouy and F. Graner. Anti-inertial lift in foams: a signature of the elasticity of complex fluids. *Phys. Rev. Lett.*, **95**: 168303, 2005.
- [45] C. Raufaste, S.J. Cox, P. Marmottant and F. Graner. Discrete rearranging disordered patterns: Prediction of elastic and plastic behaviour, and application to two-dimensional foams. *Phys. Rev. E*, **81**: 031404, 2010.
- [46] G. Katgert, M.E. Möbius and M. van Hecke. Rate dependence and role of disorder in linearly sheared two-dimensional foams. *Phys. Rev. Lett.*, **101**: 058301, 2008.
- [47] M.E. Möbius, G. Katgert and Martin van Hecke. Relaxation and flow in linearly sheared two-dimensional foams. *Europhys. Lett.*, **90**: 44003, 2010.
- [48] A.-L. Biance, S. Cohen-Addad and R. Höhler. Topological transition dynamics in a strained bubble cluster. *Soft Matter*, **5**: 4672, 2009.
- [49] S. Hutzler, M. Saadatfar, A. van der Net, D. Weaire and S.J. Cox. The dynamics of a topological change in a system of soap films. *Coll. Surf. A*, **323**: 123, 2008.
- [50] S. Besson and G. Debrégeas. Statics and dynamics of adhesion between two soap bubbles. *European Phys. J. E*, **24**: 109, 2007.
- [51] N.D. Denkov, S. Tcholakova, K. Golemanov, K.P. Ananthapadmanabhan and A. Lips. Viscous friction in foams and concentrated emulsions under steady shear. *Phys. Rev. Lett.*, **100**: 138301, 2008.
- [52] S. Tcholakova, N.D. Denkov, K. Golemanov, K.P. Ananthapadmanabhan and A. Lips. Theoretical model of viscous friction inside steadily sheared foams and concentrated emulsions. *Phys. Rev. E*, **78**: 011405, 2008.

- [53] K. Golemanov, S. Tcholakova, N.D. Denkov, K.P. Ananthapadmanabhan and A. Lips. Breakup of bubbles and drops in steadily sheared foams and concentrated emulsions. *Phys. Rev. E*, **78**: 051405, 2008.
- [54] K. Golemanov, N.D. Denkov, S. Tcholakova, M. Vethamuthu and A. Lips. Surfactant mixtures for control of bubble surface mobility in foam studies. *Langmuir*, **24**: 9956, 2008.
- [55] D.M.A. Buzzac, C.-Y.D. Lu and M.E. Cates. Linear shear rheology of incompressible foams. *J. Physique II France*, **5**: 37, 1995.
- [56] K. Krishan, A. Helal, R. Höhler and S. Cohen-Addad. Fast relaxations in foam. *Phys. Rev. E*, **82**: 011405, 2010.
- [57] S. Marze, R.M. Guillermic and A. Saint-Jalmes. Oscillatory rheology of aqueous foams: surfactant, liquid fraction, experimental protocol and aging effects. *Soft Matter*, **5**: 1937, 2009.
- [58] L.W. Schwartz and H.M. Princen. A theory of extensional viscosity for flowing foams and concentrated emulsions. *J. Coll. Interface Sci.*, **118**: 201, 1987.
- [59] D.A. Reinelt and A.M. Kraynik. Viscous effects in the rheology of foams and concentrated emulsions. *J. Coll. Interface Sci.*, **132**: 491, 1989.
- [60] E. Janiaud, D. Weaire and S. Hutzler. Two-dimensional foam rheology with viscous drag. *Phys. Rev. Lett.*, **97**: 038302, 2006.
- [61] V.J. Langlois, S. Hutzler and D. Weaire. Rheological properties of the soft-disk model of two-dimensional foams. *Phys. Rev. E*, **78**: 021401, 2008.
- [62] D. Weaire, S. Hutzler, V.J. Langlois and R.J. Clancy. Velocity dependence of shear localisation in a 2D foam. *Philos. Mag. Lett.*, **88**: 387, 2008.
- [63] D.J. Durian. Foam mechanics at the bubble scale. *Phys. Rev. Lett.*, **75**: 4780, 1995.
- [64] D.J. Durian. Bubble-scale model of foam mechanics: Melting nonlinear behaviour, and avalanches. *Phys. Rev. E*, **55**: 1739, 1997.
- [65] D. Stamenovic. A model of foam elasticity based upon the laws of Plateau. *J. Colloid Interface Sci.*, **145**: 255, 1991.
- [66] R. Höhler, S. Cohen-Addad and V. Labiausse. A constitutive equation describing the nonlinear elastic response of aqueous foams and concentrated emulsions. *J. Rheol.*, **48**: 679, 2004.
- [67] A.J. Liu, S. Ramaswamy, TG. Mason, H. Gang and D.A. Weitz. Anomalous viscous loss in emulsions. *Phys. Rev. Lett.*, **76**: 3017, 1996.
- [68] G. Picard, A. Ajdari, F. Lequeux and L. Bocquet. Elastic consequences of a single plastic event: A step towards the microscopic modeling of the flow of yield stress fluids. *European Phys. J. E*, **15**: 371, 2004.
- [69] <http://www.susqu.edu/brakke/evolver>.
- [70] A.M. Kraynik, D.A. Reinelt and F.V. Swol. Structure of random monodisperse foam. *Phys. Rev. E*, **67**: 031403–11, 2003.
- [71] A.M. Kraynik and D.A. Reinelt. Microrheology of random polydisperse foam. *Proc. XIVth Int. Congr. on Rheology*, 2004.
- [72] S. Vincent-Bonnieu, R. Höhler and S. Cohen-Addad. Slow viscoelastic relaxation and aging in aqueous foam. *Europhysics Lett.*, **74**: 533, 2006.
- [73] S. Vincent-Bonnieu. *Multiscale simulation and modelling of 2D foam rheology*. PhD thesis, 2006, University Marne-la-Vallée, Champs-sur-Marne.
- [74] N. Kern, D. Weaire, A. Martin, S. Hutzler and S.J. Cox. Two-dimensional viscous froth model for foam dynamics. *Phys. Rev. E*, **70**: 041411, 2004.
- [75] S.J. Cox. A viscous froth model for dry foams in the Surface Evolver. *Coll. Surf. A*, **263**: 81, 2005.
- [76] P. Grassia, G. Montes-Atenas, L. Lue and T.E. Green. A foam film propagating in a confined geometry: analysis via the viscous froth model. *European Phys. J. E*, **25**: 39, 2008.
- [77] I. Cantat, S. Cohen-Addad, F. Elias *et al.* *Les Mousses: Structure et Dynamique*. Belin, Paris, 2010.
- [78] A.M. Kraynik and D.A. Reinelt. Linear elastic behaviour of dry soap foams. *J. Colloid Interface Sci.*, **181**: 511, 1996.
- [79] K. Feitosa and D.J. Durian. Gas and liquid transport in steady-state aqueous foam. *European Phys. J. E*, **26**: 309, 2008.
- [80] M. van Hecke. Topical review: Jamming of soft particles: geometry, mechanics, scaling and isostaticity. *J. Phys.: Condens. Matter*, **22**: 033101, 2010.

- [81] A. Saint-Jalmes and D.J. Durian. Vanishing elasticity for wet foams: equivalence with emulsions and role of polydispersity. *J. Rheol.*, **43**: 1411, 1999.
- [82] V. Labiausse, R. Hohler and S. Cohen-Addad. Shear induced normal stress differences in aqueous foams. *J. Rheol.*, **51**: 492, 2007.
- [83] A.D. Gopal and D.J. Durian. Relaxing in foam. *Phys. Rev. Lett.*, **91**: 188303–4, 2003.
- [84] C. Macosko. *Rheology, Principles, Measurements and Applications*. Wiley-VCH, New York, 1994.
- [85] S. Cohen-Addad, R. Höhler and Y. Khidas. Origin of the slow linear viscoelastic response of aqueous foams. *Phys. Rev. Lett.*, **93**: 028302–4, 2004.
- [86] D.J. Durian, D.A. Weitz and D.J. Pine. Scaling behaviour in shaving cream. *Phys. Rev. A*, **44**: R7902–5, 1991.
- [87] S. Cohen-Addad and R. Höhler. Bubble dynamics relaxation in aqueous foam probed by multispeckle diffusing-wave spectroscopy. *Phys. Rev. Lett.*, **86**: 4700–3, 2001.
- [88] S. Cohen-Addad, M. Krzan, R. Höhler and B. Herzhaft. Rigidity percolation in particle-laden foams. *Phys. Rev. Lett.*, **99**: 168001, 2007.
- [89] S. Arditty, V. Schmitt, F. Lequeux and F. Leal-Calderon. Interfacial properties in solid-stabilized emulsions. *European Phys. J. B*, **44**: 381, 2005.
- [90] R.G. Larson. *The Structure and Rheology of Complex Fluids*. Oxford University Press, New York, 1999.
- [91] F. Rouyer, S. Cohen-Addad and R. Höhler. Is the yield stress of aqueous foam a well-defined quantity? *Colloids Surf. A*, **263**: 111, 2005.
- [92] T.G. Mason, J. Bibette and D.A. Weitz. Yielding and flow of monodisperse emulsions. *J. Colloid Interface Sci.*, **179**: 439–48, 1996.
- [93] F. Rouyer, S. Cohen-Addad, R. Höhler, P. Sollich and S.M. Fielding. The large amplitude oscillatory strain response of aqueous foam: Strain localization and full stress Fourier spectrum. *European Phys. J. E*, **27**: 309–21, 2008.
- [94] S.A. Khan, C.A. Schnepper and R.C. Armstrong. Foam rheology: III. Measurement of shear flow properties. *J. Rheol.*, **32**: 69–92, 1988.
- [95] B. Herzhaft, S. Kakadjian and M. Moan. Measurement and modeling of the flow behaviour of aqueous foams using a recirculating pipe rheometer. *Colloids Surf. A*, **263**: 153–64, 2005.
- [96] P. Marmottant and F. Graner. An elastic, plastic, viscous model for slow shear of a liquid foam. *European Phys. J. E*, **23**: 337–47, 2007.
- [97] S.M. Peker and S.S. Helvacı. *Solid–Liquid Two Phase Flow*. Elsevier, Amsterdam, 2008.
- [98] L. Becu, S. Manneville and A. Colin. Yielding and flow in adhesive and nonadhesive concentrated emulsions. *Rheol. Rev. Lett.*, **96**: 138302, 2006.
- [99] S. Rodts, J.C. Baudez and P. Coussot. From ‘discrete’ to ‘continuum’ flow in foams. *Europhys. Lett.*, **69**: 636, 2005.
- [100] G. Katgert. PhD thesis, Leiden University, 2008.
- [101] V. Carrier, S. Destouesse and A. Colin. Foam drainage: A film contribution? *Rheol Rev E*, **65**: 061404, 2002.
- [102] S. Larmignat, D. Vanderpool, H.K. Lai and L. Pilon. Rheology of colloidal gas aphrons (microfoams). *Colloid Surf. A*, **322**: 199, 2008.
- [103] J. Zhao, S. Pillai and L. Pilon. Rheology of microfoams made from ionic and non-ionic surfactant solutions. *Colloid Surf. A*, **348**: 93, 2009.
- [104] F.P. Bretherton. The motion of long bubbles in tubes. *J. Fluid Mech.*, **10**: 166–188, 1961.
- [105] L.W. Schwartz, H.M. Princen and A.D. Kiss. On the motion of bubbles in capillary tubes. *J. Fluid Mech.*, **172**: 259–75, 1986.
- [106] J. Ratulowski and H.C. Chang. Marangoni effects of trace impurities on the motion of long gas bubbles in capillaries. *J. Fluid Mech.*, **210**: 303–28, 1990.
- [107] H. Wong, C.J. Radke and S. Morris. Motion of long bubbles in polygonal capillaries. Part 1. Thin films. *J. Fluid Mech.*, **292**: 71, 1995.
- [108] H. Wong, C.J. Radke and S. Morris. Motion of long bubbles in polygonal capillaries. Part 2. Drag, fluid pressure and fluid flow. *J. Fluid Mech.*, **292**: 95, 1995.
- [109] A. Saugey, W. Drenkhan and D. Weaire. Wall slip of bubbles in foams. *Phys. Fluids*, **18**: 053101, 2006.
- [110] A. Prins and F. van Voorst Vader. *Proc. 6th Int. Congr. Surf. Act. Subst. (Zurich)*, 1972, 441.

- [111] J. Lucassen. In *Anionic Surfactants: Physical Chemistry of Surfactant Action*, Lucassen and E. H. Reynders (Eds). Dekker, New York, 1981; pp 11.
- [112] M. Erpelding, R.M. Guillermic, B. Dollet, A. Saint-Jalmes and J. Crassous. Investigating acoustic-induced deformations in a foam using multiple light scattering. *Rhys. Rev. E*, **82**: 021409, 2010.
- [113] A. Le Goff, L. Courbin, H.A. Stone and D. Quéré. Energy absorption in a bamboo foam. *Europhys. Lett.*, **84**: 36001, 2008.
- [114] Britan, M. Liverts and G. Ben-Dor. Mitigation of sound waves by wet aqueous foams. *Colloid Surf. A*, **344**: 48, 2009.

# 7

## Particle Stabilized Foams

*G. Kaptay and N. Babcsán*

### 7.1 Introduction

Foams are bubbles dispersed in liquids. However, bubbles in one-component liquids are unstable both thermodynamically and kinetically. Thus, to prepare foams, bubbles should be separated from each other and from the outer surface. The separation of bubbles in liquids is called ‘foam stabilization’.

Foams can be stabilized in two ways: either by surfactants (i.e. by atomically/molecularly dissolved components in the liquid phase) or by solid particles (i.e. by small solid phases dispersed in the liquid phase). Historically, foam stabilization by surfactants has priority (see other chapters of this book).

It was probably Ramsden who wrote the first paper on stabilizing foams and emulsions by solid particles more than a century ago [1]. Four years later Pickering described emulsion stabilization in more details [2], and as a result, a name, ‘Pickering emulsions’, became widespread. Sometimes it is extrapolated to the term ‘Pickering foams’. In this chapter the term particles stabilized foams (PSFs) is used.

The subject of PSFs had a sleeping period before 1990 (see Fig. 7.1). Papers on PSFs suddenly appeared around 1990 and their number gradually increased in the 1990s, mainly thanks to colloid chemists. However, the slope of the increase in number of papers jumped considerably around the year 2000 (see Fig. 7.1). Since then, PSFs have emerged from the colloid chemists labs and are used widely to synthesize new materials. It is approximated that the total number of written scientific papers, books and theses (highly visible and almost invisible considered together) with subjects related to PSFs is around 10,000.

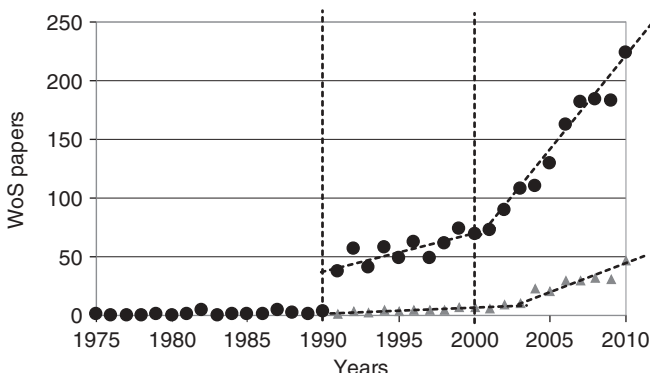


**Fig. 7.1** Number of papers published in each year since 1975 with the keywords 'particle\* AND foam' (large circles) and with keywords 'particle\* AND foam AND metal\*' (small triangles). Found by the search engine of ISI Web of Knowledge in March, 2011.



**Fig. 7.2** A piece of metallic foam floating on the surface of water (an unusual behaviour from a metallic material), demonstrating its low density.

Fortunately in the past 15 years at least 10 good reviews have been published and are easily available [3–13]. The largest number of papers is published in the area of aqueous foams (for details see some recent papers [14–31]), while the subject of non-aqueous foams is being developed mostly by one group [32–36]. Synthesis of special materials based on PSFs is a new and emerging area [37–40].

Metallic foams are a special class of PSFs (see Fig. 7.2, reviews [41–43] and recent papers [44–68]). This is partly due to their high economic potential, partly to the high temperature environment of their production. Metallic foams are also special as they present a unique opportunity to study the effect of particles solely on the stabilization of

foams. Room-temperature foams are stabilized by surfactants and/or by particles. It is more an exception than a rule that aqueous foams are stabilized by particles alone. However, the high temperatures required to melt metals ensure the dissociation of any long-chain molecule that might be responsible for foam stabilization. Thus, the only way to stabilize metallic foams is to use solid particles. This is true even if it is not always realized by the metallurgists. For example, there are technologies where liquid Al alloys are ‘thickened’ (before bubbling for foam production) through oxidation and tiny oxide particles form, leading to foam stabilization due to capillary pressure (see below). However, the ‘level of thickening’ is measured through the effective viscosity of the suspension and therefore it might seem that viscosity increase is the primary reason of foam stabilization.

As a large number of original and review papers exist in the literature, it is not considered necessary to describe the high variety of technical details in this chapter. Instead, the evergreen question of foam stabilization is discussed here, based on [69–103]. However, before this, let us summarize some of the empirical observations about PSFs.

## 7.2 A Summary of Some Empirical Observations

The stabilizing effect of solid particles in both aqueous and liquid metal foams depends on the foaming method. During static foaming (such as baking) the system can be stabilized by less strong stabilisers (particles network, fat crystals in ice cream or gel structures). During foaming under dynamic conditions (continuous bubble generation such as in froth flotation of minerals or boiling suspensions or gas injection metal foaming) the surface segregation of particles is required for foam stabilization. During static foaming a somewhat larger particle size and lower particle volume fraction is sufficient for foam stabilization, compared to dynamic foaming (for an explanation see Section 7.5).

The stabilizing particles are ceramic particles in metal foams and protein-based nanoparticles in beer foams. Silica particles with a size of 10–20 nm (usually agglomerated to 100–200 nm clusters) stabilize Pickering emulsions. Emulsions can also be stabilized by heteroaggregation of positively charged nanoparticles. Amphiphilic – so-called ‘Janus’ particles (two different contact angle sides of one particle) can also be applied to stabilize foams and emulsions.

Foam and emulsion stability depends also on the particle aspect ratio, with elongated particles showing better foam stability compared to less elongated particles of similar wettability [104]. Polymer rodlike particles (0.2–2.2 wt%) with an average length of 23.5 µm and an average diameter of 0.6 µm are good foam stabilizers even if simple shaking is applied. By the control of the contact angle Binks [5] produced long lasting foams using silica nanoparticles without any surfactants. Gozenbach *et al.* [23] were the first to prepare ceramic foams using slurry foams by simple design of the appropriate contact angle on the particles. Stable colloidal systems have also been obtained by the formation of a weak gel-like particle network called ‘colloidal armour’.

To stabilize foams by particles, a minimum critical amount (volume fraction) of solid particles is needed [76]. Particles act in foams in different ways depending on their size,

**Table 7.1** The classification of solid particles used for metal foam stabilization.

Particle type	Colloid class	Description	Shape of particles	Size range of particles
Added particles	Liquid–metal <i>suspensions</i> → can sediment → no true colloids	Liquid MMC (metal matrix composite with liquid matrix)	Smooth or angular polyhedron	0.1–50 µm
In situ generated particles		Solid (endogenous) particles in melt	Spherical	10–100 µm
	Liquid–metal <i>sols</i> → no sedimentation → true colloids	Bi-films in melt	Complex shaped	≈ 0.5–10 µm
Oxide remnants	Liquid–metal <i>gels</i> → no sedimentation → true colloids	Melted powder compacts	Irregular filaments	20 nm thick 50 µm wide

shape and wettability. Stability maps giving limits for the particle volume fraction and particle size required for foam stabilisation are due to Jin et al. [105] (see also [79]).

If they are nanometric and of equal size, hydrophilic particles form layers that remain trapped inside the films, preventing excessive film thinning and rupture. Eventually, partly hydrophobic particles remain attached at the bubble surface just as surfactants do, as shown in [56]. It was also observed that particle addition to liquid-aluminium alloy can significantly decrease the apparent surface tension of the liquid-metal dispersions [45].

Metal foaming technologies demonstrate that the stabilizing particles can be quite different in nature (see Table 7.1):

1. Added ceramic particles.
2. In-situ created particles.
3. Oxides originating from powder particles used in processing.
4. Solid particles which are a natural component of any semi-solid melt.

On the phenomenological level the necessity of the presence of particles for foam stability is evident although the way they act needs further clarification. While traditional aqueous foams can be considered colloidal systems because the diameter of the stabilizing elements is usually well below 1 µm, liquid-metal foams are stabilized by particles which cover a wider size range. Mixing particles with liquid metals of high surface tension and achieving a uniform mixture is more difficult for small particles. Therefore, such systems only exist above 100 nm particle size although in metals 10 µm particles are still good foam stabilizers. In situ oxidation techniques also help in stabilizing metallic foams. Oxide remnants of powders used for processing are even smaller at least in one direction.

Analysing the literature data on liquid metal foams, one can conclude that metallic foams can be stabilized with a relatively small amount of particles (less than 0.1 wt%) if

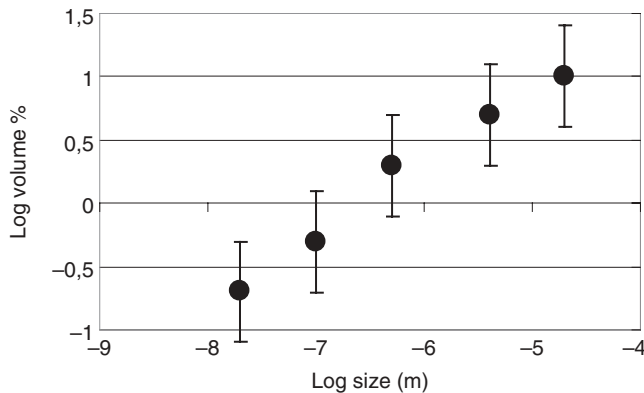


**Fig. 7.3** The minimal volume percentage of particles required to stabilize metallic foams as a function of their size (based on different measurements, for details see [43]).

their size is kept small (20 nm). Since there are problems with introducing such small particles into liquid metals, only *in situ* or remnant particles can be applied in this size range, such as oxide filaments. Up to the sedimentation limit (50  $\mu\text{m}$  or so) larger particles can also be used. However, larger particles are needed in a higher volume fraction compared to smaller ones to achieve similar foam stabilization. The volume fraction of particles needed for foam stabilization as function of their size is shown in Fig. 7.3.

### 7.3 On the Thermodynamic Stability of Particle Stabilized Foams

In Fig. 7.4 four different thermodynamic states of the three-phase solid/liquid/gas system is schematically shown (the solid phase means the particles, the wall of the vessel is ignored from the analysis). Figure 7.4(a) shows the initial state, a one-component liquid with gas and solid particles outside. Figure 7.4(b) shows a foam without particles. Figure 7.4(c) shows the particles within the liquid, without bubbles. Finally, Figure 7.4(d) shows the particle stabilized foam. The states presented in Fig. 7.4 will be called states A, B, C and D, respectively, hereafter. In this simplified analysis the following conditions are supposed to be valid:

1. All particles are spherical, rigid, solid particles, with equal radii of  $r$  (m).
2. The phases do not dissolve in each other, and do not influence the bulk Gibbs energy of each other, i.e. only the interfacial part of the Gibbs energy will be different in different situations of Fig. 7.4.
3. All interfaces (solid/gas, liquid/gas and solid/liquid) are stable, i.e. all the corresponding interfacial energies have positive values, considered here material constants.
4. The contact between the particles has a negligible influence (i.e. particle agglomeration is ignored in both gaseous and liquid phases).

5. The liquid has a contact angle  $\Theta$  on the particles in the environment of the gas inside the bubbles.
6. The particles are very small in size and so the effect of gravity is neglected compared to the effect of the interfacial force. Thus the particles occupy their equilibrium positions at the liquid/gas interface, dictated only by their size and contact angle.
7. The bubbles are much larger compared to particles, so all particles experience a large, flat liquid/gas interface.
8. The contact angle of the liquid on the wall of the vessel is  $90^\circ$  (to exclude the influence of the wall).
9. The total surface area of bubbles (see Fig. 7.4b, d) is denoted by  $A_g$ , while the total surface area of all particles (see Fig. 7.4) is denoted by  $A_s$  ( $\text{m}^2$ ). The ratio of these two values is defined as:  $a \equiv A_s/A_g$ .
10. Particles with a total maximum cross sectional area of  $fA_g$  are in touch with the liquid/gas interface of bubbles ( $0 < f < 0.906$ ) where  $f$  is called ‘bubble coverage’ by particles. The value of 0.906 is the maximum theoretical coverage of a flat surface by a closely packed layer of equal spheres.
11. The top liquid/gas surface area is negligible compared to both  $A_s$  and  $A_g$ .

Based on the above conditions the Gibbs energy ( $G_i$ , in J) of states I = A, B or C in Fig. 7.4 is written as:

$$G_A = G^o + A_s \cdot \sigma_{sg} \quad (7.1)$$

$$G_B = G^o + A_s \cdot \sigma_{sg} + A_g \cdot \sigma_{lg} \quad (7.2)$$

$$G_C = G^o + A_s \cdot \sigma_{sl} \quad (7.3)$$

with  $G^o$  being the bulk Gibbs energy of the system (J);  $\sigma_{sg}$ ,  $\sigma_{sl}$  and  $\sigma_{lg}$  are the solid/gas, solid/liquid and liquid/gas interfacial energies, respectively ( $\text{J/m}^2$ ). Let us consider state A (Fig. 7.4a) as the initial state, and let us define the Gibbs energy change (per a unit liquid/gas surface area) experienced by the system while it is transferred from state A to state B as  $\Delta G_{A-B} \equiv (G_B - G_A)/A_g$  ( $\text{J/m}^2$ ). The Gibbs energy change accompanying the transfer of the system from state A into state C or D is defined accordingly as:  $\Delta G_{A-C} \equiv (G_C - G_A)/A_g$  and  $\Delta G_{A-D} \equiv (G_D - G_A)/A_g$ . Substituting eqns (7.1–7.3) into these definitions, the following equations follow:

$$\Delta G_{A-B} = \sigma_{lg} \quad (7.4)$$

$$\Delta G_{A-C} = -a \cdot \sigma_{lg} \cdot \cos \Theta \quad (7.5)$$

Equations (7.5) was written taking into account the Young equation:

$$\cos \Theta = \frac{\sigma_{sg} - \sigma_{sl}}{\sigma_{lg}} \quad (7.6)$$

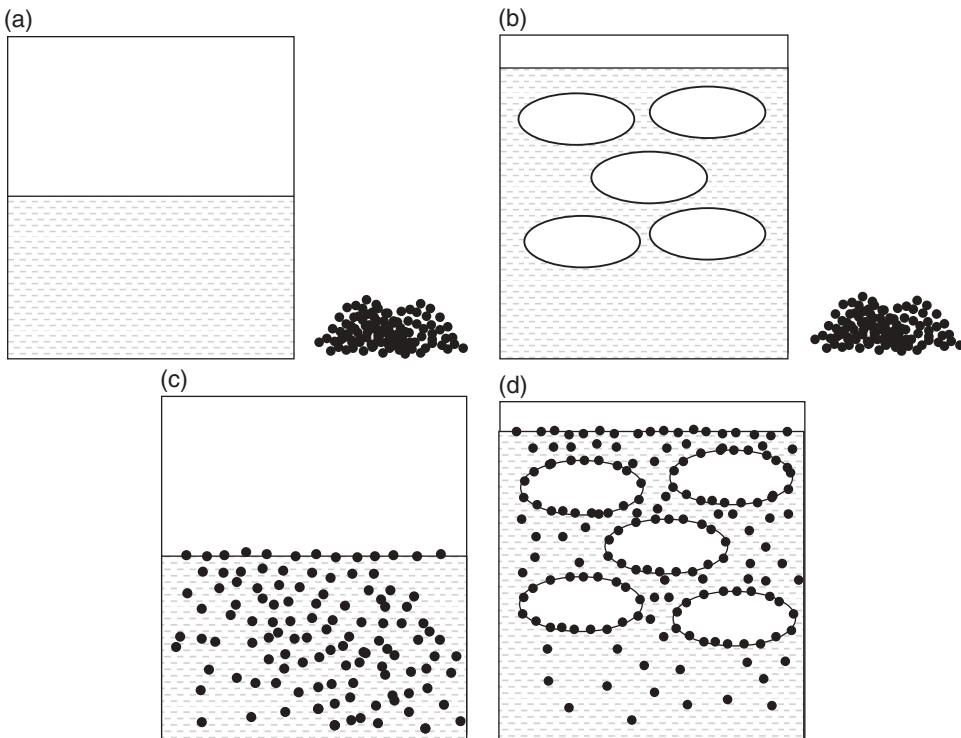


**Fig. 7.4** Schematic of different thermodynamic states of a three-phase (liquid, solid, gas) system.

As follows from eqn (7.4), the process to transfer the system from state A into state B is always accompanied with a positive change in Gibbs energy, as all interfacial energies have positive values, by definition. Thus, foams without particles are never in equilibrium state, even in the presence of surfactants, which can ensure temporary stability of foams.

As follows from eqn (7.5), state C is preferred compared to state A, if the liquid wets the particles ( $\Theta < 90^\circ$ ), and vice versa. It should be mentioned that the role of the top liquid/gas surface is neglected here, i.e. eqn (7.5) does not take into account the process of transferring the particles through the top liquid/gas interface (for details see [106]).

Now, let us consider the Gibbs energy of state D (Fig. 7.4d). First, let us write an equation for the total surface area of the particles:  $A_s = N \cdot 4 \cdot \pi \cdot r^2$ . From here, the number of particles:

$$N = \frac{A_s}{4 \cdot \pi \cdot r^2} \quad (7.7a)$$

In Fig. 7.4(d) the particles are in two positions: some are in contact with the gas bubbles ( $N_g$ ), the others are dispersed in the liquid ( $N_l$ ), with the obvious relationship:

$$N_g + N_l = N \quad (7.7b)$$

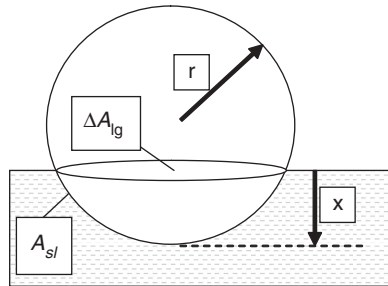


**Fig. 7.5** Schematic of a single solid spherical particle at the liquid–gas interface, partially immersed into the liquid to the depth of  $x$ .

The total cross-sectional area of the particles can be written through parameter  $f$  as:  $f \cdot A_g = N_g \cdot \pi \cdot r^2$ . From here the number of particles attached to bubbles can be expressed as:

$$N_g = \frac{f \cdot A_g}{\pi \cdot r^2} \quad (7.7c)$$

Substituting eqns (7.7a, c) into eqn (7.7b), the number of particles dispersed in the liquid is obtained:

$$N_l = \frac{A_g}{4 \cdot \pi \cdot r^2} \cdot (a - 4 \cdot f) \quad (7.7d)$$

Equation (7.7d) puts an important limitation to the model parameters. To keep the number of particles dispersed in the liquid a non-negative number, the following condition must be fulfilled:

$$a \geq 4 \cdot f \quad (7.7e)$$

Using the above variables, the Gibbs energy of state D can be written as:

$$G_D = G^o + N_l \cdot 4 \cdot \pi \cdot r^2 \cdot \sigma_{sl} + N_g \cdot A_{sl} \cdot \sigma_{sl} + N_g \cdot (4 \cdot \pi \cdot r^2 - A_{sl}) \cdot \sigma_{sg} + (A_g - N_g \cdot \Delta A_{lg}) \cdot \sigma_{lg} \quad (7.7f)$$

where  $A_{sl}$  and  $\Delta A_{lg}$  are surface areas defined by a single particle, as shown in Fig. 7.5. From the geometry of Fig. 7.5:

$$A_{sl} = 2 \cdot r \cdot \pi \cdot x \quad (7.7g)$$

$$\Delta A_{lg} = 2 \cdot r \cdot \pi \cdot x - \pi \cdot x^2 \quad (7.7h)$$

When the particle is in equilibrium at the liquid/gas interface (with the influence of other particles and gravity neglected), its equilibrium depth of immersion equals (see also [107]):

$$x = r \cdot (1 + \cos \Theta) \quad (7.7i)$$

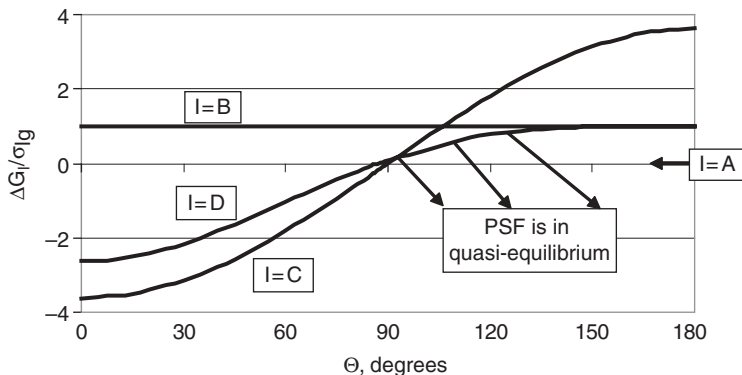


**Fig. 7.6** The dependence of the dimensionless ratio  $\Delta G_i/\sigma_{lg}$  (with  $i = A, B, C, D$ ) on the contact angle for parameters:  $f = 0.906$ ,  $a = 4 \cdot f$ .

Let us substitute eqn (7.7i) into eqns (7.7g, h), and let us substitute the resulting equations together with eqns (7.7c, d) into eqn (7.7f):

$$G_D = G^o + A_g \cdot a \cdot \sigma_{sl} + 2 \cdot f \cdot A_g \cdot (1 - \cos \Theta) \cdot \sigma_{lg} \cdot \cos \Theta + A_g \cdot [1 - f \cdot (1 - \cos^2 \Theta)] \cdot \sigma_{lg} \quad (7.7j)$$

Now, let us substitute eqns (7.1, 7.7i) into the definition  $\Delta G_{A-D} \equiv (G_D - G_A)/A_g$ :

$$\Delta G_{A-D} = \sigma_{lg} \cdot [1 - a \cdot \cos \Theta - f \cdot (1 - \cos \Theta)^2] \quad (7.7k)$$

The first two terms of eqn (7.7k) coincide with eqns (7.4 and 7.5). This is understandable, as Fig. 7.4(d) is the combination of Fig. 7.4(b, c). Now, let us analyse eqns (7.4, 7.5, 7.7k) together as function of contact angle. In Fig. 7.6 the most favourable situation for state D is shown, with the maximum value of parameter  $f = 0.906$  and with the minimum value of parameter  $a = 4 \cdot f$ , as follows from eqn (7.7e). One can see that the state of particle stabilized foam is less favourable compared to other possible states. When  $\Theta \leq 93^\circ$ , the dispersion of particles without bubbles (state C) is energetically more favourable compared to the state of PSF (state D). On the other hand, when  $\Theta \geq 87^\circ$ , the state when both particles and bubbles are outside of the liquid (state A) is energetically more favourable compared to the state of PSF (state D). No such combination of parameter values of  $f$ ,  $a$  and  $\Theta$  exist (within the set limits of  $f \leq 0.906$ ,  $a \geq 4 \cdot f$ ,  $0^\circ \leq \Theta \leq 180^\circ$ ), for which PSFs (state D) would have the most negative Gibbs energy compared to other possibilities shown in Fig. 7.4(a, c). Thus, we can conclude that PSF can never be in thermodynamic equilibrium.

This is what we expected based on the widespread opinion in the literature. Such a long derivation of this well known conclusion would be useless without noting that there is an interesting range of contact angles at  $\Theta > 93^\circ$  in Fig. 7.6. One can see that PSF is energetically more favourable compared to the dispersion of particles in the liquid. Although the state when the particles are out of the liquid is even more favourable, the process  $D \rightarrow A$  is not easy to realize. If the outer liquid/gas surface (with a negligible surface area compared to that of the particles) is fully covered by some of the particles, the rest of the particles

dispersed within the bulk of the liquid cannot spontaneously jump out of the liquid, especially because the particles covering the outer surface are in equilibrium at the liquid/gas interface at any value of  $0^\circ < \Theta < 180^\circ$  [108]. Thus, if one introduces bubbles into state C (this is how PSFs are actually produced) at  $93^\circ < \Theta < 180^\circ$ , the system will experience a negative change in its total Gibbs energy, i.e. the  $C \rightarrow D$  process becomes energetically favourable. This makes PSF a quasi-equilibrium state at  $93^\circ < \Theta < 180^\circ$  (within the conditions of Fig. 7.6). Of course, one can claim that it is difficult to introduce the particles into liquids when  $\Theta > 93^\circ$ . That is certainly true. However, there are ways around it. For example, non-wettable particles can be precipitated *in situ* in the liquid from over-saturated solutions, especially if sites for heterogeneous nucleation are used.

Now, let us have a closer look at the  $C \rightarrow D$  process, and let us define the Gibbs energy change of this process in a similar way as above:  $\Delta G_{C-D} \equiv (G_D - G_C)/A_g$ . Substituting eqns (7.3 and 7.7k) into this equation, the following expression is obtained:

$$\Delta G_{C-D} = \sigma_{lg} \cdot \left[ 1 - f \cdot (1 - \cos \Theta)^2 \right] \quad (7.7l)$$

Parameter  $a$  is fallen out from eqn (7.7l), i.e. the condition of quasi-equilibrium depends only on two parameters (on the bubble coverage and on the contact angle). The Gibbs energy change of eqn (7.7l) will be negative if the expression in its parenthesis is negative. This can be expressed by two identical inequalities:

$$f \geq \frac{1}{(1 - \cos \Theta)^2} \quad (7.7m)$$

$$\Theta \geq \arccos\left(1 - \frac{1}{\sqrt{f}}\right) \quad (7.7n)$$

The contact angle–bubble coverage diagram is shown in Fig. 7.7, with the curved line calculated by eqn (7.7n). The vertical line at  $f=0.906$  in Fig. 7.7 shows the limit of possible

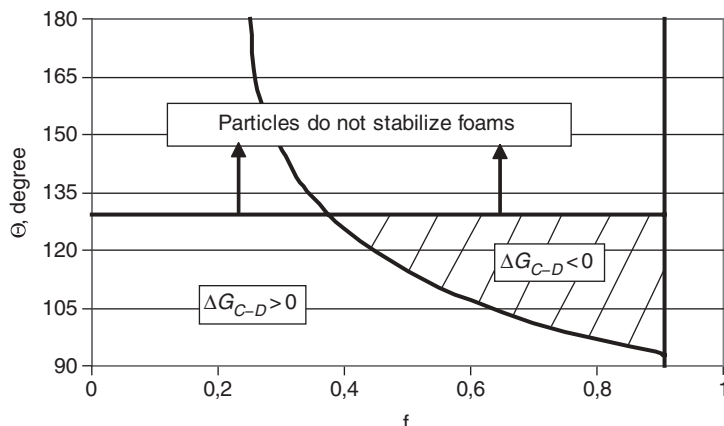


**Fig. 7.7** The contact angle–bubble coverage diagram with a dashed area of parameters when PSFs are quasi-stable.

values of the bubble coverage. The horizontal line at  $\Theta = 129^\circ$  shows a theoretical limit, above which particles cannot stabilize foams (see below and [83, 93]). The hatched area of Fig. 7.7 shows parameter combinations under which PSFs are quasi-stable.

Thus, we have shown that a thermodynamic difference exists between foams stabilized by surfactants and particle stabilized foams, the latter being more stable.

## 7.4 On the Ability of Particles to Stabilize Foams during Their Production

The first condition to stabilize foams by particles is that they are stable at the surface of the bubbles. The Gibbs energy needed to remove a spherical particle of radius  $r$  from a large and flat liquid/gas interface is written as:

$$\Delta G_{\text{rem}} = \pi \cdot r^2 \cdot \sigma_{\text{lg}} \cdot (1 \pm \cos \Theta)^2 \quad (7.8a)$$

where sign ‘+’ refers to the removal of the particle into the gas phase, and sign ‘−’ refers to the removal of the particle into the liquid phase. Eqn (7.8a) was derived independently several times in the literature, the first derivation being probably due to Koretzki and Kruglyakov [108] (for further historical details see [93]). For particles of the same size and for liquids of the same surface tension, the probability of the particle remaining stable at the bubble surface is a function of contact angle. From eqn (7.8a) the probability of particle stability at the bubble surface ( $\varepsilon$ ) can be written as:

$$\varepsilon = (1 \pm \cos \Theta)^2 \quad (7.8b)$$

The probability of the particles being stable at the interface of the bubbles as a function of contact angle is shown in Fig. 7.8. One can see that the particles are most stable at the bubble surfaces if  $\Theta = 90^\circ$  and loose their stability below  $30^\circ$  and above  $150^\circ$ . However,

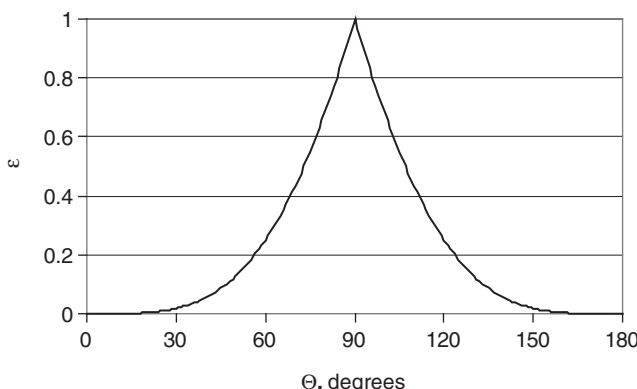


**Fig. 7.8** The probability of the particles remaining at the surface of the bubbles as a function of the contact angle.

claiming that the stability of the particles at the surface of bubbles is identical to the stability of the foams by particles is an over-simplification.

Foams become stable when two bubbles covered by particles approach each other and the liquid film between them remains stable even when the bubble/liquid film/bubble system reaches steady state (the term ‘equilibrium’ is not used here – see the previous section). The two bubbles are separated from each other due to the ‘capillary pressure’, caused by the particles. For the stability of foams, the maximum capillary pressure is important, introduced first by Denkov *et al.* [71] as:

$$P_c \propto \frac{2 \cdot \sigma_{lg}}{r} \quad (7.9a)$$

One can see that the maximum capillary pressure is proportional to the Laplace pressure. Thus, the dimensionless capillary pressure is introduced here as:

$$P_c^* \equiv \frac{P_c \cdot r}{2 \cdot \sigma_{lg}} \quad (7.9b)$$

The numerical coefficient of eqn (7.9a) was not determined as a functional relationship of other variables in [71]. However, this relationship is needed for practical applications of eqn (7.9.a). Such a relationship was derived in [93], with the results summarized in terms of the dimensionless maximum capillary pressure as:

$$P_c^* = b \cdot (\cos \Theta + c) \quad (7.9c)$$

where parameters  $b$  and  $c$  depend on the configuration of the particles between the bubbles and on the bubble coverage (see Table 7.2; for details of derivation see [93]). The dependence of the dimensionless maximum capillary pressure on the contact angle is shown in Fig. 7.9 for a given value of  $f$ . In Table 7.2 and Fig. 7.9 single layer and double (and more) layer models are compared. The double (and more) layer model means that both bubbles are covered by particles, and additionally the liquid film between these two bubbles consists of some additional particles dispersed in it. In this case, foam stabilisation takes place only if the particles in the liquid film form a mechanically stable 3D structure that ensures the transfer of any load from one bubble to another.

From Fig. 7.9 one can see that at  $\Theta=0^\circ$  the two models provide the same, largest value for any value of parameter  $f$ . The model of a single layer of particles predicts that the maximum capillary pressure stabilizing the thin liquid film between the bubbles diminishes at  $\Theta=90^\circ$ , while it takes place for the double (or more) layer model at  $\Theta=129^\circ$ . This value is the same as shown in Fig. 7.7 as the ultimate contact angle, above which foams cannot be stabilized by particles.

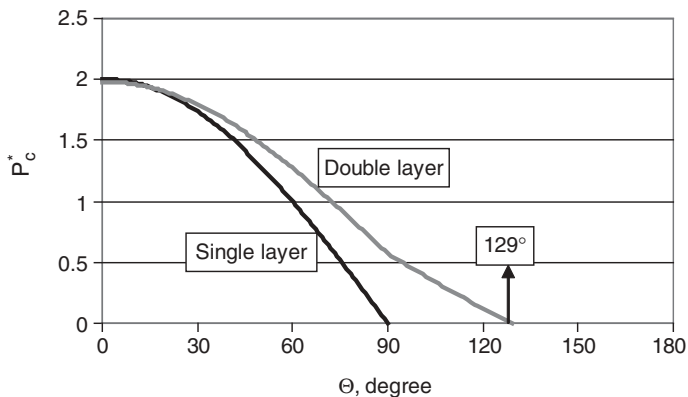
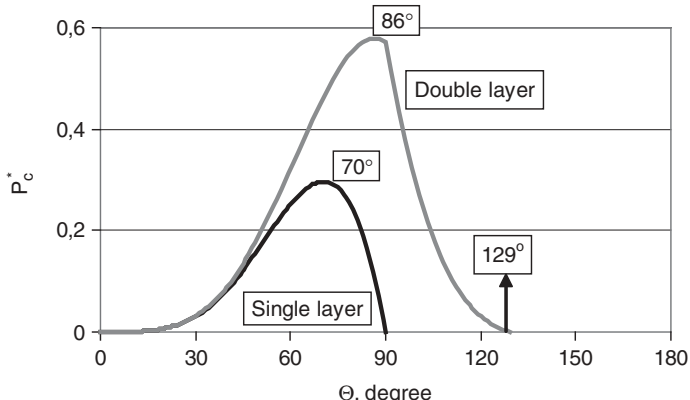
Now, it is time to compare Figs 7.8 and 7.9. Figure 7.8 predicts the probability of particle stabilization on bubble surfaces, while Fig. 7.9 predicts the maximum capillary pressure stabilizing the liquid film between the two bubbles covered by particles. The latter does not exist without the former. Thus, the ‘effective’ dimensionless maximum capillary pressure is obtained as the product of eqns (7.8b, 7.9c):

$$P_c^* = b \cdot (\cos \Theta + c) \cdot (1 \pm \cos \Theta)^2 \quad (7.9d)$$

Equation (7.9d) is shown graphically in Fig. 7.10 for the two cases as a function of the contact angle. One can see that in each case the maximum capillary pressure goes through

**Table 7.2** The values of parameters b and c of eqns (7.9c, 7.9d, 7.10).

Particle layers	$\Theta$	Parameter b	Parameter c
Single	$\Theta \leq 90^\circ$	$b \approx 2f + 6.2f^4$	0
Double or more	$\Theta \leq 90^\circ$	$b \approx 1.4f + 4.4f^4$	0.405
Double or more	$\Theta \geq 90^\circ$	$b \approx 0.9f + 2.8f^4$	0.633

**Fig. 7.9** The dimensionless maximum capillary pressure as function of contact angle for  $f = 0.6$  and two different configurations of particles (see text on curves), calculated by eqn (7.9c) and Table 7.2.**Fig. 7.10** The effective dimensionless maximum capillary pressure as a function of the contact angle for  $f = 0.6$  and two different configurations of particles (see text on curves), calculated by eqn (7.9d) and Table 7.2.

a maximum as a function of the contact angle. This maximum corresponds to the optimum contact angle for foam stabilization. For a single layer of particles this maximum is situated around  $70^\circ$ . The foam preserves at least 10 % of its maximum stability in the contact angle interval of  $30^\circ \leq \Theta \leq 89^\circ$ . Outside of this contact angle interval foams cannot be stabilized by a single layer of particles between the two bubbles.

For foams stabilized by the double (or more) layers of particles, maximum foam stability corresponds to the contact angle of  $86^\circ$ . The foam preserves at least 10% of its maximum stability in the contact angle interval of  $35^\circ \leq \Theta \leq 116^\circ$ . Outside of this contact angle interval foams cannot be effectively stabilized by the double (or more) layers of particles between the bubbles. It is important to mention that foams stabilized by a double (or more) layer of particles appear to be twice more stable compared to foams stabilized by a single layer of particles (if compared at their optimum contact angles).

One can see that the two cases provide similar results in terms of the optimum contact angle value, appearing in a narrow interval between  $70^\circ$  and  $86^\circ$ . This is in good agreement with experimental data [72, 76, 80].

For clarity, the final equation for the absolute value of the effective maximum capillary pressure stabilizing foams is written by substituting eqn (7.9d) into eqn (7.9b) and expressing the value of  $P_c$  from the resulting equation:

$$P_c = \frac{2 \cdot b \cdot \sigma_{lg}}{r} \cdot (\cos \Theta + c) \cdot (1 \pm \cos \Theta)^2 \quad (7.10)$$

where sign ‘+’ refers to  $\Theta \geq 90^\circ$ , sign ‘-’ refers to  $\Theta \leq 90^\circ$ ; the values of parameters  $b$  and  $c$  are given in Table 7.2. As parameter  $b$  increases monotonically with the bubble coverage by particles ( $f$ ), we can conclude that foams stabilized by particles are more stable, if:

- the bubbles are covered by a higher ratio by particles;
- the surface tension of the liquid is higher;
- the particle size is smaller;
- the contact angle of the liquid on the particles is closer to the optimum interval, being between  $70^\circ$  and  $86^\circ$ ;
- the ratio of the volume fraction of the particles in the initial suspension to the total surface area of bubbles is higher (as in this case the formation of double (or more) layers of particles is more probable, compared to a single layer of particles);
- the aspect ratio of the particles is higher (this has an influence only for low values of particle volume fraction and bubble coverage).

The only difference between aqueous, non-aqueous and metallic foams in terms of eqn (7.10) is in the surface tension values of their corresponding liquids, changing from about 30 mN/m (non-aqueous foams) through about 70 mN/m (aqueous foams) to about 1000 mN/m (aluminium foams). The higher surface tension of liquid metals allows the use of larger particles for the same foam stabilization effect compared to non-metallic foams. Thus, metallic foams are stable with particles of 10 micron size, while non-metallic foams are rarely stable with micron-sized particles (for details, see below).

## 7.5 Design Rules for Particle Stabilized Foams

To produce PSFs, the following engineering parameters need to be addressed:

- the chemical composition of the liquid to be foamed;
- the chemical composition of the foaming gas;
- the chemical surface composition, size, aspect ratio and volume fraction of the particles;
- the temperature.

The chemical composition of the three phases and temperature determine the surface properties of the system, such as contact angle and surface tension. They can both be tailored using surfactants. The first question is whether stable foam is obtained or not applying the given combination of the above engineering parameters. Another question is how high the foam can be to withstand its own weight in gravity, and what dynamic actions the foam can withstand during production or service. These questions can be answered if all actions are summed in pressure terms and if the resulting pressure is compared to the capillary pressure calculated by eqn (7.10). The foam will be stable if the capillary pressure will be higher than the sum of all pressures destroying the foam, i.e. if the following condition is fulfilled:

$$P_c \geq P_{dyn} + \rho_f \cdot g \cdot h_f \quad (7.11a)$$

where  $P_{dyn}$  (Pa) is the maximum dynamic pressure acting on foam during its production or service,  $\rho_f$  is the density of the foam ( $\text{kg}/\text{m}^3$ ),  $g = 9.81 \text{ m}/\text{s}^2$  acceleration due to gravity,  $h_f$  is the height of the foam. Let us consider an example how to apply eqns (7.10) and (7.11). Suppose the density and the height of the foam are:  $\rho_f = 200 \text{ kg}/\text{m}^3$ ,  $h_f = 1 \text{ m}$ . Then, the second term of eqn (7.11a) provides a static pressure due to gravity:  $P_{stat} = 2 \text{ kPa}$ . It is usually a small value compared to the dynamic pressure term, which can reach the value of 100 kPa even without extreme production methods or service conditions. Thus, the static pressure due to the effect of gravity can usually be neglected.

Let us calculate further with a requirement that the foam should withstand the dynamic pressure term. Let us consider a foam stabilized by a double (or more) layer of particles, with a contact angle below  $90^\circ$ . Then, parameter values  $b$  and  $c$  of eqn (7.10) become more specified, and for this particular case eqn (7.11a) can be written in a more particular form as (see Table 7.2):

$$P_c = \frac{(2.8 \cdot f + 8.8 \cdot f^4) \cdot \sigma_{lg}}{r} \cdot (\cos \Theta + 0.405) \cdot (1 - \cos \Theta)^2 \geq P_{dyn} \quad (7.11b)$$

Let us consider first an aqueous foam with surface tension of about  $\sigma_{lg} = 0.05 \text{ N}/\text{m}$  (decreased from the usual value of  $0.072 \text{ N}/\text{m}$  due to surfactants added to push the contact angle value into the right interval). Suppose there is a sufficient amount of particles to ensure a double (or more) particle layer between the bubbles. Suppose the contact angle is shifted close to the optimum value of  $86^\circ$  and it has a value of  $\Theta = 80^\circ$ . Suppose each bubble is covered by the particles with a bubble coverage of  $f = 0.5$ . Let

us also suppose that the dynamic pressure is:  $P_{dyn} = 100 \text{ kPa} = 1 \text{ bar}$ . Now, we can use eqn (7.11b) to estimate the largest radius of the stabilizing particle, ensuring foam stabilization, even under the influence of the above dynamic pressure:  $r \leq 385 \text{ nm}$ . If the foam is prepared from an organic liquid with  $\sigma_{lg} = 0.03 \text{ N/m}$  and with other parameters kept constant, the result would be:  $r \leq 230 \text{ nm}$ . If the foam is prepared from liquid aluminium with  $\sigma_{lg} = 1 \text{ N/m}$  and with other parameters kept constant, the result would be:  $r \leq 7.7 \mu\text{m}$ . This example shows again that metallic foams can be stabilized by particles of about  $10 \mu\text{m}$  in diameter, while non-metallic foams can be stabilized only by sub-micron particles to withstand the same load. Now it has become clear why ‘static’ and ‘dynamic’ conditions of foam preparation require different technological parameters (see Section 2). Dynamic conditions lead to higher  $P_{dyn}$ , requiring smaller particles or higher bubble coverage in accordance with eqn (7.11b), if other parameters are kept constant.

We have supposed above that the bubbles have a relatively high coverage by particles. However, this should also be ensured by the experimental design, particularly by the volume fraction of particles. Let us derive an equation connecting the volume fraction of particles in the initial suspension and the bubble coverage by particles. For that, let us consider the liquid of volume  $V_l (\text{m}^3)$  and the bubbles with total volume of  $V_g (\text{m}^3)$  with a dimensionless ratio  $v$  defined as:  $v \equiv V_g/V_l$ . Foams usually have the order of magnitude  $v = 10$ . Let us suppose that the foam is composed of spherical bubbles of equal radii  $r_g (\text{m})$ , stabilized by spherical particles of equal radii  $r (\text{m})$ . The bubble size has an order of magnitude of  $r_g = 1 \text{ mm}$  (changing less than an order of magnitude from foam to foam), while the particle size can vary much more, usually in the interval of  $10 \text{ nm} \leq r \leq 10 \mu\text{m}$ . The total volume of the gas bubbles is written as:  $V_g = v \cdot V_l = N_g \cdot 4 \cdot \pi \cdot r_g^3 / 3$ . Expressing from here the number of bubbles ( $N_g$ ), and substituting it into the equation for the total surface area of the bubbles ( $A_g = N_g \cdot 4 \cdot \pi \cdot r_g^2$ ), the latter is written as:

$$A_g = \frac{3 \cdot v \cdot V_l}{r_g} \quad (7.12a)$$

Repeating a similar procedure for particles, their total largest cross-sectional area is written as:

$$A_p = \frac{3 \cdot \phi \cdot V_l}{4 \cdot r} \quad (7.12b)$$

where  $\phi$  is the volume ratio of the solid particles in the initial suspension (before bubbling). By definition, the coverage of the bubbles by particles is defined as:  $f \equiv A_p/(z \cdot A_g)$ , with  $z$  being the ratio of the total number of particles to the number of particles attached to the bubble surface (if all particles are attached to the bubble surface, then  $z = 1$ , and if some of them remain dispersed in the cell walls, then  $z > 1$ ). Substituting eqns (7.12a, b) into this equation, the requested relationship between the volume ratio of the particles and their size is obtained:

$$\phi = \frac{4 \cdot z \cdot v \cdot f}{r_g} \cdot r \quad (7.12c)$$

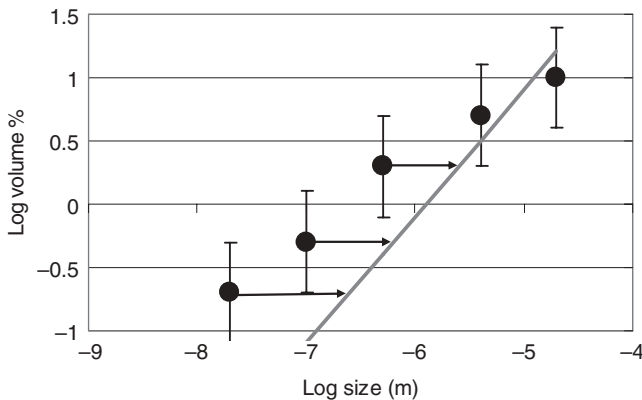


**Fig. 7.11** The same as Fig. 7.3 with the theoretical line calculated by eqn (7.12d) using parameters  $f_{cr} = 0.1$ ,  $r_g = 10^{-3}$  m,  $z = 2$ ,  $v = 10$ . Arrows show the correction to experimental points due to agglomeration of nanoparticles. 1

Thus, if ‘structural parameters’ of the foam ( $z, v, f, r_g$ ) are fixed, the requested volume fraction of particles appears to be proportional to the radius of the particles. Let us take the following characteristic values:  $r_g = 10^{-3}$  m,  $z = 2$ ,  $v = 10$ ,  $f = 0.5$ . Then, eqn (7.12c) simplifies to:  $\phi = 4 \times 10^4 r$ . For  $r = 200$  nm,  $\phi = 8 \times 10^{-3} = 0.8$  vol%. On the other hand, if  $r = 5\text{ }\mu\text{m}$ , then  $\phi = 0.2 = 20$  vol%. Thus, indeed, for the same structural parameters of the foam one needs a much smaller volume fraction of sub-micron particles compared to larger particles. The application of larger particles for metallic foams is actually limited by settling and also by the viscosity of the liquid. Indeed, the percolation threshold for equal sized spheres is 18 vol%, leading to high effective viscosity of the suspension. Thus, the size and the volume fraction of the particles should also be optimized from this point of view.

Equation (7.12c) can be used to derive the critical volume fraction ( $\phi_{cr}$ ) of particles needed for foam stabilisation. For that, a critical bubble coverage ( $f_{cr}$ ) should be defined, and its value should be substituted into eqn (7.12c):

$$\phi_{cr} = \frac{4 \cdot z \cdot v \cdot f_{cr}}{r_g} \cdot r \quad (7.12d)$$

As follows from eqn (7.11b), the capillary pressure reduced by 7 times, when the bubble coverage is reduced from  $f = 0.5$  to  $f = 0.1$ . That is why we suppose  $f_{cr} = 0.1$ . Substituting this value together with previous parameter values ( $r_g = 10^{-3}$  m,  $z = 2$ ,  $v = 10$ ) into eqn (7.12d), the following simplified equation is found:  $\phi_{cr} = 8 \times 10^3 r$ . This theoretical equation is shown in Fig. 7.11 together with the experimental points of Fig. 7.3. One can see a good agreement for large (above micron) particles. However, data points differ considerably for nanoparticles from the theoretical values. It is probably due to the agglomeration of nanoparticles. In other words, the nominal size of nanoparticles seems to increase by almost an order of magnitude during foaming, reducing their stabilizing efficiency.

## 7.6 Conclusions

Particle stabilized foams (PSFs) are reviewed in this chapter. In the introduction the history of the subject is shown through statistics from the Web of Knowledge, and a classification of PSFs is given.

In Section 7.2 the influence of the production method (static or dynamic), particle size, particle aspect ratio and particle volume ratio is discussed on foam stabilisation.

In Section 7.3 it is shown that although PSFs are not in thermodynamic equilibrium, they are in a quasi-equilibrium state within a certain interval of parameters (contact angle and bubble coverage). This quasi-equilibrium state means that PSFs are more stable than the suspensions to be bubbled. This thermodynamic analysis shows a superiority of PSFs to foams stabilized by surfactants.

In Section 7.4 the way particles can stabilize foams is explained through the concept of the maximum capillary pressure. It is shown that the optimal contact angle range for foam stabilization is between 70° and 86°. It is also shown that foams stabilized by a double (or more) layer of particles are stronger (by a coefficient of about 2) compared to foams stabilized by a single layer of particles, if both are compared at their own optimal contact angle values.

In Section 7.5 design rules for PSFs are given. PSFs are designed to withstand a given static and dynamic pressure during their production and service. The capillary pressure stabilizing the foam should be stronger than the destroying pressure for the foam to remain stable. The capillary pressure is a function of contact angle, surface tension, particle radius, bubble coverage and particle arrangement (a single or a double layer of particles). Trial calculations are conducted to show characteristic values of particle sizes, being able to stabilize aqueous and metallic foams.

In Section 7.5, a theoretical relationship is derived to connect the minimal initial volume fraction of particles in the suspension needed for foam stabilisation as function of particle size. Comparison with experimental data shows good agreement for micron-sized particles. The agreement for nanometre-sized particles becomes acceptable only if particle agglomeration is taken into account.

## Acknowledgement

This work was carried out as part of the TAMOP-4.2.1.B-10/2/KONV-2010-0001 project with support by the European Union and the European Social Fund.

## References

- [1] W. Ramsden. Separation of solids in the surface layers of solutions and suspensions (observations on surface-membranes, bubbles, emulsions, and mechanical coagulation): preliminary account. *Proc. Roy. Soc.*, **72**: 156–64, 1903.
- [2] S.U. Pickering. Emulsions. *J. Chem. Soc.*, **91**: 2001–21, 1907.
- [3] R.J. Pugh. Foaming, foam films, antifoaming and defoaming. *Adv. Coll. Interface Sci.*, **64**: 67–142, 1996.

- [4] H.D. Goff. Colloidal aspects of ice cream: a review. *Int. Dairy J.*, **7**: 363–73, 1997.
- [5] B.P. Binks. Particles as surfactants: similarities and differences. *Curr. Opinion Coll. Interface Sci.*, **7**: 21–42, 2002.
- [6] B.S. Murray and R. Ettelaie. Foam stability: proteins and nanoparticles. *Curr. Opinion Coll. Interface Sci.*, **2004**, **9**: 314–20, 2004.
- [7] N.D. Denkov. Mechanism of foam destruction by oil-based antifoams. *Langmuir*, **20**: 9463–505, 2004.
- [8] T.S. Horozov. Foams and foam films stabilized by solid particles. *Curr. Opinion Coll. Interface Sci.*, **13**: 134–40, 2008.
- [9] M. Vignes-Adler. New foams: fresh challenges and opportunities. *Curr. Opinion Coll. Interface Sci.*, **13**: 141–9, 2008.
- [10] T.N. Hunter, R.J. Pugh, G.V. Franks and G.J. Jameson. The role of particles in stabilizing foams and emulsions. *Adv. Coll. Interface Sci.*, **137**: 57–1, 2008.
- [11] S.E. Frieberg. Foams from non-aqueous systems. *Curr. Opinion Coll. Interface Sci.*, **15**: 359–64, 2010.
- [12] P.A. Wierenga and H. Gruppen. New views on foams from protein solutions. *Curr. Opinion Coll. Interface Sci.*, **15**: 365–73, 2010.
- [13] P. Stevenson. Inter-bubble gas diffusion in liquid foam. *Curr. Opinion Coll. Interface Sci.*, **15**: 374–81, 2010.
- [14] R.G. Alargova, D.S. Warhadpande, V.N. Paunov and O.D. Velev. Foam superstabilization by polymer microrods. *Langmuir*, **20**: 10371–4, 2004.
- [15] T. Kostakis, R. Ettelaie and B.S. Murray. Effect of high salt concentrations on the stabilization of bubbles by silica particles. *Langmuir*, **22**: 1273–80, 2006.
- [16] U.T. Gonzenbach, A.R. Studart, E. Tervoort and L.J. Gauckler. Ultrastable particle-stabilized foams. *Ang. Chem.: Int. Ed.*, **45**: 3526–30, 2006.
- [17] L.K. Shrestha, D.P. Acharya, S.C. Sharma, K. Aramaki, H. Asaoka, K. Ihara, T. Tsunehiro and H. Kunieda. Aqueous foam stabilized by dispersed surfactant solid and lamellar liquid crystalline phase. *J. Coll. Interface Sci.*, **301**: 274–81, 2006.
- [18] U.T. Gonzenbach, A.R. Studart, E. Tervoort and L.J. Gauckler. Tailoring the microstructure of particle-stabilized wet foams. *Langmuir*, **23**: 1025–32, 2007.
- [19] L.K. Shrestha, E. Saito, R.G. Shrestha, H. Kato, Y. Takase and K. Aramaki. Foam stabilized by dispersed surfactant solid and lamellar liquid crystal in aqueous systems of diglycerol fatty acid esters. *Coll. Surf. A*, **293**: 262–71, 2007.
- [20] R.J. Pugh. Foaming in chemical surfactant free aqueous dispersions of anatase (Titanium dioxide) particles. *Langmuir*, **23**: 7972–80, 2007.
- [21] I. Blute, R.J. Pugh, J. van de Pas and I. Callaghan. Silica nanoparticle sols 1. Surface chemical characterization and evaluation of the foam generation (foamability). *J. Coll. Interface Sci.*, **313**: 645–655, 2007.
- [22] B.M. Somosvari, N. Babcsan, P. Barczy and A. Berthold. PVC particles stabilized water-ethanol compound foams. *Coll. Surf. A*, **309**: 240–5, 2007.
- [23] U.T. Gozenbach, A.R. Studart, E. Tervoort and L.J. Gauckler. Tailoring the microstructure of particle-stabilized wet foams. *Langmuir*, **23**: 1025–32, 2007.
- [24] H.A. Wege, S. Kim, V.N. Paunov, Q.X. Zhong and O.D. Velev. Long-term stabilization of foams and emulsions with in-situ formed microparticles from hydrophobic cellulose. *Langmuir*, **24**: 9245–53, 2008.
- [25] S. Zhang, Q. Lan, Q. Liu, J. Xu and D. Sun. Aqueous foams stabilized by Laponite and CTAB. *Coll. Surf. A*, **317**: 406–13, 2008.
- [26] S. Zhang, D. Sun, X. Dong, C. Li and J. Xu. Aqueous foams stabilized with particles and ionic surfactants. *Coll. Surf. A*, **324**: 1–8, 2008.
- [27] R.J. Davenport, R.L. Pickering, A.K. Goodhead and T.P. Curtis. A universal threshold concept for hydrophobic mycolata in activated sludge foaming. *Water Res.*, **42**: 3446–54, 2008.
- [28] T.N. Hunter, E.J. Wanless and G.J. Jameson. Effect of esterically bonded agents on the monolayer structure and foamability of nano-silica. *Coll. Surf. A*, **334**: 181–90, 2009.

- [29] T.N. Hunter, G.J. Jameson, E.J. Wanless, D. Dupin and S.P. Armes. Adsorption of submicrometer-sized cationic sterically stabilized polystyrene latex at the air–water interface: contact angle determination by ellipsometry. *Langmuir*, **25**: 3440–9, 2009.
- [30] Á. Detrich, A. Deák, E. Hild, A.L. Kovács and Z. Hórvölgyi. Langmuir and Langmuir-Blodgett films of bidisperse silica nanoparticles. *Langmuir*, **26**: 2694–9, 2010.
- [31] D.N.H. Tran, C.P. Whitby, D. Fornasiero and J. Ralston. Foamability of aqueous suspensions of fine graphite and quartz particles with a triblock copolymer. *J. Coll. Int. Sci.*, **348**: 460–8, 2010.
- [32] L.K. Shrestha, K. Aramaki, H. Kato, Y. Takase and H. Kunieda. Foaming properties of monoglycerol fatty acid esters in nonpolar oil systems. *Langmuir*, **22**: 8337–45, 2006.
- [33] L.K. Shrestha, R.G. Shrestha, C. Solans and K. Aramaki. Effect of water on foaming properties of diglycerol fatty acid ester-oil systems. *Langmuir*, **23**: 6918–26, 2007.
- [34] H. Kunieda, L.K. Shrestha, D.P. Acharya, H. Kato, Y. Takase and J.M. Gutierrez. Super-stable nonaqueous foams in diglycerol fatty acid esters: non polar oil systems. *J. Dispers. Sci. Technol.*, **28**: 133–42, 2007.
- [35] L.K. Shrestha, R.G. Shrestha, S.C. Sharma and K. Aramaki. Stabilization of nonaqueous foam with lamellar liquid crystal particles in diglycerol monolaurate/olive oil system. *J. Coll. Interface Sci.*, **328**: 172–9, 2008.
- [36] R.G. Shrestha, L.K. Shrestha, C. Solans, C. Gonzalez and K. Aramaki. Nonaqueous foam with outstanding stability in diglycerol monomyristate/olive oil system. *Coll. Surf. A*, **353**: 157–65, 2010.
- [37] A.R. Studart, U.T. Gonzenbach, I. Akartuna, E. Tervoort and L.J. Gauckler. Materials from foams and emulsions stabilized by colloidal particles. *J. Mater. Chem.*, **17**: 3283–9, 2007.
- [38] J.C.H. Wong, E. Tervoort, S. Busano, U.T. Gozenbach, A.R. Studart, P. Ermanni and L.J. Gauckler. Macroporous polymers from particle-stabilized foams. *J. Mater. Chem.*, **19**: 5129–33, 2009.
- [39] J.C.H. Wong, E. Tervoort, S. Busato, U.T. Gozenbach, A.R. Studart, P. Ermanni and L.J. Gauckler. Designing macroporous polymers from particle-stabilized foams. *J. Mater. Chem.*, **20**: 5628–40, 2010.
- [40] J.C.H. Wong, E. Tervoort, S. Busato, L.J. Gauckler and P. Ermanni. Controlling phase distributions in macroporous composite materials through particles stabilized foams. *Langmuir*, **27**: 3254–260, 2011.
- [41] J. Banhart. Manufacture, characteristaion and application of cellular metals and metallic foams. *Prog. Mater. Sci.*, **46**: 559–632, 2001.
- [42] J. Banhart. Metal foams: production and stability. *Adv. Eng. Mater.*, **8**: 781–94, 2006.
- [43] N. Babcsán and J. Banhart. Metal foams: towards high-temperature colloid chemistry. In *Colloidal Particles at Liquid Interfaces*, B.P. Binks and T.S. Horozov (eds). Cambridge University Press, Cambridge, 2006.
- [44] T. Nakamura, S.V. Gnyloskurenko, K. Sakamoto, A.V. Byakova and R. Ishikawa. Development of new foaming agent for metal foam. *Mater. Trans.*, **43**: 1191–6, 2002.
- [45] N. Babcsán, D. Leitlmeier and H.P. Degischer. Foamability of particle reinforced aluminum melt. *Mat.-wiss. U. Werkstofftech.*, **34**: 1–8, 2003.
- [46] C.C. Yang and H. Nakae. The effects of viscosity and cooling conditions on the foamability of aluminium alloy. *J. Mater. Process. Technol.*, **141**: 202–6, 2003.
- [47] F. Garcia Moreno, M. Fromme and J. Banhart. Real-time X-ray radioscopy on metallic foams using a compact micro-focus source. *Adv. Eng. Mater.*, **6**: 416–20, 2004.
- [48] N. Babcsán, D. Leitlmeier, H.P. Degischer and J. Banhart. The role of oxidation in blowing particle-stabilized aluminium foams. *Adv Eng Mater*, **6**: 421–8, 2004.
- [49] V. Gergely and T.W. Clyne. Drainage in standing liquid metal foams: modelling and experimental observations. *Acta mater.*, **52**: 3047–58, 2004.
- [50] C. Körner, M. Arnold and R.F. Singer. Metal foam stabilization by oxide network particles. *Mater. Sci. Eng. A*, **A396**: 28–40, 2005.
- [51] F. Garcia Moreno, N. Babcsán and J. Banhart. X-ray radioscopy of liquid metallic foams: influence of heating profile, atmosphere and pressure. *Coll. Surf. A*, **263**: 2990–4, 2005.
- [52] N. Babcsán, D. Leitlmeier and J. Banhart. Metal foams – high temperature colloids. Part I. Ex situ analysis of metal foams. *Coll. Surf. A*, **261**: 123–30, 2005.

- [53] T. Wübben and S. Odenbach. Stabilization of liquid metallic foams by solid particles. *Coll. Surf. A.*, **266**: 207–13, 2005.
- [54] A. Irretier and J. Banhart. Lead and lead alloy foams. *Acta Mater.*, **53**: 4903–17, 2005.
- [55] B. Matijasevic and J. Banhart. Improvement of aluminium foam technology by tailoring of blowing agent. *Scr. Mater.*, **54**: 503–8, 2006.
- [56] N. Babcsán, G.S. Vinod Kumar, B.S. Murty and J. Banhart. Grain refiners as liquid foam stabilizers. *Trans. Indian Inst. Met.*, **60**: 127–32, 2007.
- [57] A.A. Gokhale, S.N. Sahu, V.K.W.R. Kulkarni, B. Sudhakar and N.R. Rao. Effect of titanium hydride powder characteristics and aluminium alloy composition on foaming. *High Temp. Mater. Process.*, **26**: 247–56, 2007.
- [58] K. Kadoi and H. Nakae. Effect of particle addition to liquid metal on fabrication of aluminum foam. *High Temp. Mater. Process.*, **26**: 275–83, 2007.
- [59] C. Körner. Foam formation mechanism in particle suspensions applied to metallic foams. *Mater. Sci. Eng. A*, **495**: 227–35, 2008.
- [60] Z.K. Cao, B. Li, G.C. Yao and Y. Wang. Fabrication of aluminum foam stabilized by copper-coated carbon fibers. *Mater. Sci. Eng. A*, **486**: 350–6, 2008.
- [61] A. Dudka, F. Garcia-Moreno, N. Wanderka and J. Banhart. Structure and distribution of oxides in aluminium foam. *Acta Mater.*, **56**: 3990–4001, 2008.
- [62] A.J. Klinter, C.A. Leon and R.A.L. Drew. The optimum contact angle range for metal foam stabilization: an experimental comparison with the theory. *J. Mater. Sci.*, **45**: 2174–80, 2010.
- [63] Y.H. Song, M. Tane, T. Ide, Y. Seimiya, B.Y. Hur and H. Nakajima. Fabrication of Al-3.7 pct Si-0.18 pct Mg foam strengthened by AlN particle dispersion and its compressive properties. *Metall. Mater. Trans. A*, **41A**: 2104–11, 2010.
- [64] X.N. Liu, Y.X. Li, X. Chen, Y. Kiu and X.L. Fan. Foam stability in gas injection foaming process. *J. Mater. Sci.*, **45**: 6481–93, 2010.
- [65] Y.H. Song, M. Tane, T. Ide, Y. Seimiya, B.Y. Hur and H. Nakajima. Fabrication of Al-3.7 pCt Si-0.18 pct Mg foam strengthened by AlN particle dispersion and its compressive properties. *Metall. Mater. Trans. A*, **41A**: 2104–11, 2010.
- [66] V. Kevorkijan, S.D. Skapin, I. Paulin, B. Sustarsic and M. Jenko. Synthesis and characterisation of closed cells aluminium foams containing dolomite powder as foaming agent. *Mater. Technol.*, **44**: 363–71, 2010.
- [67] M. Golestanipour, H.A. Mashhadi, M.S. Abravi, M.M. Malekjafarian and M.F. Sadeghian. Manufacturing of Al/SiC composite foams using calcium carbonate as foaming agent. *Mater. Sci. Technol.*, **27**: 923–7, 2011.
- [68] S. Barg, C. Soltmann, A. Schwab, D. Koch, W. Schwieger and G. Grathwohl. Novel open cell aluminum foams and their use as reactive support for zeolite crystallization. *J. Porous Mater.*, **18**: 89–98, 2011.
- [69] A. Dippenaar. The destabilization of froth by solids. I. The mechanism of film rupture. *Int. J. Miner. Process.*, **9**: 1–14, 1982.
- [70] F.Q. Tang, Z. Xiao, J.A. Tang and J.A. Long. The effect of SiO<sub>2</sub> particles upon stabilization of foam. *J. Coll. Interface Sci.*, **131**: 498–502, 1989.
- [71] N.D. Denkov, I.B. Ivanov, P.A. Kralchevsky and D.T. Wasan. A possible mechanism of stabilization of emulsions by solid particles. *J. Coll. Interf. Sci.*, **150**: 589–93, 1992.
- [72] G. Johansson and R.J. Pugh. The influence of particle size and hydrophobicity on the stability of mineralized froths. *Int. J. Miner. Process.*, **34**: 1–21, 1992.
- [73] D.T. Wasan, A.D. Nikolov, L.A. Lobo, K. Koczo and D.A. Edwards. Foams, thin film and surface rheological properties. *Progr. Surf. Sci.*, **39**: 119–54, 1992.
- [74] M.V. Ramani, R. Kumar and K.S. Gandhi. A model for static foam drainage. *Chem. Eng. Sci.*, **48**: 455–65, 1993.
- [75] R. Aveyard, B.P. Binks, P.D.I. Fletcher and C.E. Rutherford. Contact angle in relation to the effects of solids on film and foam stability. *J. Disp. Sci. Technol.*, **15**: 251–71, 1994.
- [76] S.W. Ip, Y. Wang and J.M. Toguri. Aluminum foam stabilization by solid particles. *Can. Metall. Q.*, **38**: 81–92, 1999.
- [77] R. Sedev, Z. Németh, R. Ivanova and D. Exerowa. Surface force measurement in foam films from mixtures of protein and polymeric surfactants. *Coll. Surf. A*, **149**: 141–4, 1999.

- [78] S.A. Ali, P.A. Gauglitz and W.R. Rossen. Stability of solids-coated liquid layers between bubbles. *Int. Eng. Chem. Res.*, **39**: 2742–5, 2000.
- [79] G. Kapitay. A generalised stability diagram of production of metallic foams by the melt route. In *Cellular Metals and Metal Foaming Technology*, J. Banhart, M.F. Ashby and N.A. Fleck (eds). MIT Verlag, Bremen, 2001; pp 117–122.
- [80] Y.Q. Sun and T. Gao. The optimum wetting angle for the stabilization of liquid-metal foams by ceramic particles: experimental simulations. *Metall. Mater. Trans.*, **33A**: 3285–92, 2002.
- [81] E. Dickinson, R. Ettelaie, B.S. Murray and Z. Du. Kinetics of disproportionation of air bubbles beneath a planar air–water interface stabilized by food proteins. *J. Coll. Interface Sci.*, **252**: 202–13, 2002.
- [82] K.G. Marinova, N.K. Denkov, P. Branlard, Y. Giraud and M. Deruelle. Optimal hydrophobicity of silica in mixed oil-silica antifoams. *Langmuir*, **18**: 3399–403, 2002.
- [83] G. Kapitay. Interfacial criteria for stabilization of liquid foams by solid particles. *Coll. Surf. A*, **230**: 67–80, 2003.
- [84] Z. Du, M.P. Bilbao-Montoya, B.P. Binks, E. Dickinson, R. Ettelaie and B.S. Murray. Outstanding stability of particle-stabilized bubbles. *Langmuir*, **19**: 3106–8, 2003.
- [85] D. Wang and Z. Shi. Effect of ceramic particles on cell size and wall thickness of aluminium foam. *Mater. Sci. Eng. A*, **A361**: 45–9, 2003.
- [86] T. Wübben, H. Stanzick, J. Banhart and S. Odenbach. Stability of metallic foams studied under microgravity. *J. Phys. C: Solid State Phys.*, **15**: S427–33, 2003.
- [87] G. Sethumadhavan, A. Nikolov and D. Wasan. Stability of films with nanoparticles. *J. Coll. Interface Sci.*, **272**: 167–71, 2004.
- [88] T.S. Horozov and B.P. Binks. Stability of suspensions, emulsions, and foams studied by a novel automated analyzer. *Langmuir*, **20**: 9007–13, 2004.
- [89] C. Körner, M. Hirschmann, V. Brautigam and R.F. Singer. Endogenous particle stabilization during magnesium integral foam production. *Adv. Eng. Mater.*, **6**: 1–6, 2004.
- [90] E. Dickinson, R. Ettelaie, T. Kostakis and Murray. Factors controlling the formation and stability of air bubbles stabilized by partially hydrophobic silica nanoparticles. *Langmuir*, **20**: 8517–25, 2004.
- [91] P.M. Kruglyakov and A.V. Nushtayeva. Investigation of the influence of capillary pressure on stability of a thin layer emulsion stabilized by solid particles. *Coll. Surf. A*, **263**: 330–5, 2005.
- [92] R.S. Subramanian, R.J. Larsen and H.A. Stone. Stability of flat gas-liquid interface containing nonidentical spheres to gas transport: toward an explanation of particle stabilization of gas bubbles. *Langmuir*, **21**: 4526–31, 2005.
- [93] G. Kapitay. On the equation of the maximum capillary pressure induced by solid particles to stabilize emulsions and foams and on the emulsion stability diagrams. *Coll. Surf. A*, **282/283**: 387–401, 2006.
- [94] A. Haibel, A. Rack and J. Banhart. Why are metal foams stable? *Appl. Phys. Lett.*, **89**: 154102, 2006.
- [95] B.S. Murray. Stabilization of bubbles and foams. *J. Coll. Interface Sci.*, **12**: 232–41, 2007.
- [96] S. Ata. Coalescence of bubbles covered by particles. *Langmuir*, **24**: 6085–91, 2008.
- [97] G. Morris, M.R. Pursell, S.J. Neethling and J.J. Cilliers. The effect of particle hydrophobicity, separation distance and packing patterns on the stability of a thin film. *J. Coll. Interface Sci.*, **327**: 138–44, 2008.
- [98] S. Ata, E.S. Davis, D. Dupin, S.P. Armes, E.J. Wanless and J. Erica. Direct observation of pH-induced coalescence of latex-stabilized bubbles using high-speed video imaging. *Langmuir*, **26**: 7865–74, 2010.
- [99] B.M. Somosvári, P. Bárczy, P. Szirovicza, J. Szőke and T. Bárczy. Foam evolution and stability at elevated gravity levels. *Mater. Sci. Forum*, **649**: 391–7, 2010.
- [100] G. Morris, S.J. Neethling and J.J. Cilliers. The effects of hydrophobicity and orientation of cubic particles on the stability of thin films. *Miner. Eng.*, **23**: 979–84, 2010.
- [101] K.E. Cole, G.D.M. Morris and J.J. Cilliers. Froth touch samples viewed with scanning electron microscopy. *Miner. Eng.*, **23**: 1018–22, 2010.
- [102] S.N. Tan, Y. Yang and R.G. Horn. Thinning of a vertical free-draining aqueous film incorporating colloidal particles. *Langmuir*, **26**: 63–73, 2010.

- [103] G. Morris, S.J. Neethling and J.J. Cilliers. A model for investigating the behaviour of non-spherical particles at interfaces. *J. Coll. Interface Sci.*, **354**: 380–5, 2011.
- [104] B. Madivala, S. Vandebril, J. Fransaer and J. Vermant. Exploiting particle shape in solid stabilized emulsions. *Soft Matter*, **5**: 1717–27, 2009.
- [105] I. Jin, L.D. Kenny and H. Sang. US Patent 5,112,697, 1992.
- [106] G. Kaptay. Interfacial phenomena during melt processing of ceramic particle-reinforced metal matrix composites. Part I. Introduction (incorporation) of solid particles into melts. *Mater. Sci. Forum*, **215/216**: 459–66, 1996.
- [107] G. Kaptay. Classification and general derivation of interfacial forces, acting on phases, situated in the bulk, or at the interface of other phases. *J. Mater. Sci.*, **40**: 2125–31, 2005.
- [108] A.F. Koretzki and P.M. Kruglyakov. Emulgiruiushee deistvie tvordich chastic I energetika ich smachivaniia na granice razdela voda-maslo. *Izv. Sib. Otd. AN SSSR, Seriya him. nauk*, **2**(1): 139–41, 1971.

# 8

## Pneumatic Foam

*Paul Stevenson and Xueliang Li*

### 8.1 Preamble

We define a pneumatic foam as one in which gas is continuously sparged into a pool of surfactant-containing solution thereby enabling continuous production of gas–liquid foam. The applications of such foams are multifarious, but pneumatic foams that climb vertical columns form the basis of froth flotation (see Chapter 11) for the recovery of mineral products and coal, foam fractionation proteins and peptides (see Chapter 14), and gas absorption processes (see Chapter 15). Because of their relative importance to the minerals processing, chemical process and biotechnology industries, a fundamental treatment of vertical pneumatic foams makes up the bulk of this chapter in Section 8.2, before horizontal foams, which are used for cutting transport in oil wells and are found in the dispense of fire-fighting foams, are discussed in Section 8.3.

### 8.2 Vertical Pneumatic Foam

#### 8.2.1 Introduction

The motivation for studying vertical pneumatic foams is that they are used extensively in minerals processing in froth flotation columns that are a workhorse of the industry. Although froth flotation is described elsewhere in this volume (Chapter 11), it is pertinent

to consider the features of pneumatic foam that enable the flotation process. Firstly, the foam presents a very large specific surface area (i.e. area of gas–liquid interface per unit volume of foam). This means that there is a large surface area onto which valuable mineral particles attach, and the flux of surface area is large, whilst the flux of interstitial liquid is generally low. Secondly, because the process is in a vertical orientation, the unattached gangue material (i.e. the unwanted products) falls through the column and is rejected to the ‘tailings stream’, whereas the attached valuable mineral particles report to the ‘concentrate stream’ at the top of the column.

Another process that takes advantage of these two features of pneumatic foam is ‘foam fractionation’ (described in detail in Chapter 14), which is closely related to froth flotation. Rather than mineral particles attaching to the gas–liquid interface, amphiphilic molecules adsorb. However, the features of high specific surface area and vertical orientation, so that the foam layer moves upwards from the bubbly liquid pool at the bottom, are crucial to the operation of a foam fractionator. Although foam fractionation currently has much less industrial significance than froth flotation, its potential for providing a simple and cost-effective upstream separation method in biotechnology is great. Other applications of horizontal pneumatic foam include mass transfer operations, for example, the absorption of CO<sub>2</sub> into water (see Chapter 15).

Figure 8.1 shows a schematic representation of a generic pneumatic foam that is formed in a vertical column, and there will be a discussion of the features of this before a mechanistic description of pneumatic foam is undertaken. Gas bubbles are sparged to the bottom of the column via a perforated plate, glass frit or ‘air stone’ into a surfactant containing solution to produce a bubbly liquid. The gas bubbles rise up through the bubbly liquid into the ‘foam phase’ where they continue their journey up the column. Thus, a foam layer is found on top of the bubbly liquid. An everyday example of this situation is the layer of foam ‘head’ on the top of the bubbly liquid in a pint of Irish stout. In the generic system shown in Fig. 8.1, foam rises up the column and is discharged from the column at the top. Because there is interstitial liquid carried up the column with gas bubbles in the foam, the pneumatic foam gives rise to a flux of liquid that travels up the column and is discharged at the top. Surfactant solution is fed to the bubbly liquid via a pump and, at steady-state, the liquid that does not travel in the foam up the column leaves in the tailings via a vented underflow, the elevation of which sets the location of the interface between bubbly liquid and rising foam.

In both froth flotation and foam fractionation, it is often important to understand what governs the volumetric liquid fraction of the foam phase as well as the liquid flux up the column. It is therefore more than surprising that only five years ago, there was no mechanistic understanding of how such properties of the foam were influenced by system parameters. (Note that we consider only gas–liquid systems here rather than mineralised flotation froths, even though the treatment has broad generality.) Leonard and Lemlich [1] and Haas and Johnson [2] made attempts to describe the liquid flux in a foam fraction column, but this was only done as a function of liquid fraction in the foam.

In fact, such was the lack of mechanistic understanding of vertical pneumatic foam columns that a description we refer to as the ‘Vertical Foam Misapprehension’ has entered into the canon of foam fractionation literature that introduces a serious misunderstanding of the physics that underpin the process. This misapprehension, which holds that the

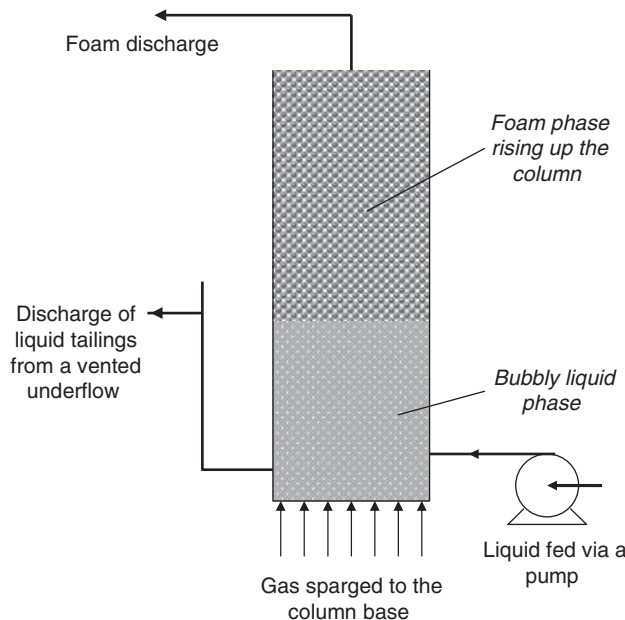


**Fig. 8.1** A schematic representation of a generic vertical pneumatic foam column.

liquid fraction in a foam decreases with height because the foam at the top of the column has had longer to drain, is described in Section 8.2.3.

Before commencing the analysis, it is appropriate to explain one piece of terminology that is commonly used by chemical engineers, but appears to be less well known amongst physicists and mathematicians: the *superficial velocity* is the volumetric flow rate of one phase of matter divided by the flow cross-sectional area. This term is interchangeable with the ‘volumetric flux’. The use of the superficial velocity is useful in one-dimensional problems, where the properties of the foam might change axially along the column, but not radially as a function of position on the flow cross-section. In this chapter, we largely make a one-dimensional assumption. The implication of this is that wall effects are neglected, and therefore there is no need to consider the rheology of the foam itself, although this assumption is discussed later in this chapter. In columns of low cross-sectional area, wall effects are likely to become significant, as is the rheology of the foam itself (see Chapter 6).

### 8.2.2 The Hydrodynamics of Vertical Pneumatic Foam

In this section, a mechanistic description of vertical pneumatic foam is developed that, to a large extent, follows the analysis of Stevenson [3]. Initially, a very simple system with isotropic bubble size distribution and no capillarity is considered, before simplifying assumptions are progressively relaxed.

### 8.2.2.1 Pneumatic Foam with Constant Bubble Size Distribution

Consider a pneumatic foam that is created by sparging gas at a superficial velocity of  $j_g$  so that bubbles of uniform radius of  $r_b$  are formed. By writing a simple mass balance, it is possible to relate the liquid superficial velocity up the column,  $j_f$ , with the volumetric liquid fraction in the foam,  $\varepsilon$ . Thus:

$$j_f = \frac{\varepsilon j_g}{1 - \varepsilon} - j_d \quad (8.1)$$

where  $j_d$  is the liquid drainage superficial velocity in the Lagrangian reference frame moving with the bubbles. There are several commonly used models of foam drainage, but we choose to use the drainage expression proposed by Stevenson [4], which holds when capillarity effects are insignificant and losses due to drainage are entirely viscous:

$$j_d = \frac{\rho g r_b^2}{\mu} m \varepsilon^n \quad (8.2)$$

where  $m$  and  $n$  are dimensionless adjustable constants that can be measured by the method of forced drainage that was established by Weaire *et al.* [5] or by a magnetic resonance imaging technique proposed by Stevenson *et al.* [6]. Thus, equation (8.3) gives a locus of liquid flux versus liquid fraction:

$$j_f = \frac{\varepsilon j_g}{1 - \varepsilon} - \frac{\rho g r_b^2}{\mu} m \varepsilon^n \quad (8.3)$$

However, the locus does not give a unique operating condition that provides an estimate of both liquid flux and volumetric liquid fraction. This can be demonstrated in Fig. 8.2 by plotting eqn (8.3) for  $\mu = 1.0 \text{ mPa.s}$ ,  $\rho = 1000 \text{ kg.m}^{-3}$ ,  $j_g = 8 \text{ mm/s}$ ,  $r_b = 0.5 \text{ mm}$ ,  $m = 0.016$  and  $n = 2$ , which are those measured by Stevenson *et al.* [6] for foam stabilised by 2.92 g/l of sodium dodecyl sulphate. It is seen that the plot of liquid flux versus liquid fraction exhibits a maximum, and Stevenson [7] showed, by invoking a simple stability argument, that this maximum gives the equilibrium condition of the foam. A pneumatic foam adjusts its liquid fraction to maximise the liquid flux. The equilibrium liquid fraction that the foam attains may be calculated by the numerical solution of:

$$\frac{\mu j_g}{m n \rho g r_b^2} = \varepsilon^{n-1} (1 - \varepsilon)^2 \quad (8.4)$$

It should be reiterated that the above analysis is only valid if capillary effects are negligible, and the bubble size distribution is constant from the very bottom (at the interface with the bubbly liquid) to the very top (where the foam is removed to a sink). We do not claim any general validity of this theory for all pneumatic foam (although it has been experimentally verified by Stevenson [7] for systems in which there is little change in bubble size distribution with height), and these assumptions have caused some consternation in the subsequent literature. For instance, Kruglyakov [8] has dismissed the above analysis because the liquid

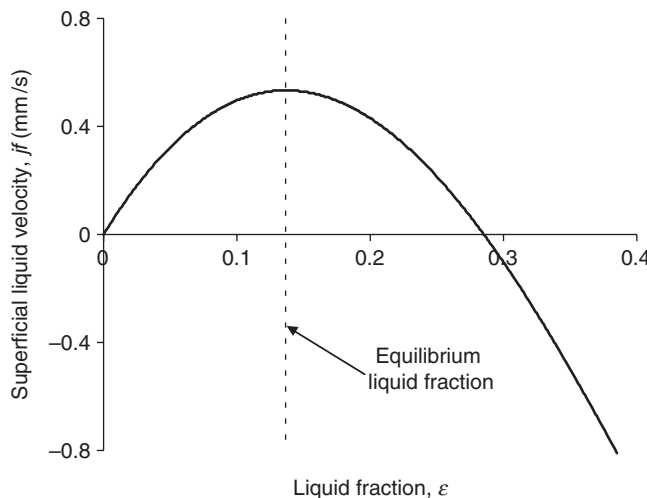


**Fig. 8.2** Liquid superficial velocity versus liquid fraction, with the dotted line indicating the equilibrium condition.

fraction in pneumatic foams is often observed to decrease with height. Thus, we will restate the validity and utility of this analysis.

In a vertical pneumatic foam in which capillary effects are insignificant and no change in the bubble size distribution and acceleration due to gravity is constant at all positions in the column, the liquid fraction is constant as a function of height and is given by the numerical solution of eqn (8.4). The corollary is that changes in liquid fraction with height in pneumatic foam columns, beyond the zone in which capillary effects are significant, are entirely due to changes in bubble size distribution.

We believe that many authors have conflated the liquid fraction profiles in free draining stationary columns of foam with liquid fraction profiles in vertical pneumatic foam. In a free draining stationary foam, the liquid fraction does indeed decrease with height, but the physics of the two situations are dissimilar. In the vertical pneumatic foam, a liquid fraction is attained such that the force due to the self-weight of the interstitial liquid is exactly opposed by the force due to bubbles exerting a shear stress on the interstitial liquid. Once this balance of forces is achieved, the liquid fraction of the column of the foam could be maintained to an infinite height from the interface of the bubbly liquid if there were no change in bubble size distribution.

In fact, in the following sections we demonstrate how this analysis can be extended to account for capillary effects and changes in bubble size distribution.

#### 8.2.2.2 The Introduction of Capillary Forces to Give a Liquid Fraction Profile

Implicit in the drainage term of eqn (8.1) is that the liquid fraction is constant throughout the foam column and that the weight of the interstitial liquid is exactly opposed by the shear stress imparted by the gas–liquid surface upon the liquid. In fact, capillary forces must also be taken into account. If the assumption of constant bubble size distribution is

retained, the liquid fraction of the foam is seen to vary with height near the interface with the bubbly liquid; the liquid fraction right at the interface exhibits a relatively high value, and the liquid fraction asymptotically relaxes with height over typically 5–30 cm to the value given by eqn (8.4). The liquid flux is constant with height, however. Stevenson [3] gave the following ODE, which can be solved to give the liquid fraction profile near the interface with the bubbly liquid:

$$\frac{\partial \varepsilon}{\partial x} = \frac{p \rho g r_b \varepsilon^{1+q}}{q \sigma} \left[ \left( \frac{\varepsilon j_g}{1-\varepsilon} - j_f \right) \frac{\mu}{\rho g r_b^2 m \varepsilon^n} - 1 \right] \quad (8.5)$$

where  $x$  is the vertical dimension in the froth measured positive upwards from the interface with the bubbly liquid and  $\sigma$  is the surface tension. The pre-factor  $p$  and index  $q$  originate from a power-law relationship that approximates the radius of curvature of the Plateau border wall or foam,  $r$ , to  $r_b$  and  $\varepsilon$ . Thus:

$$r = r_b p \varepsilon^q \quad (8.6)$$

Stevenson and Stevanov [9] give values of  $p = 1.28$  and  $q = 0.46$  for a wide range of  $\varepsilon$ .

### 8.2.2.3 Liquid Fraction Profile with Changing Bubble Size Distribution with Height

We now relax the assumption that bubble size is independent of height in the column. Bubble size distribution can change with time (and therefore height) by the process of (i) disproportionation caused by inter-bubble gas-diffusion (see Chapter 4), and (ii) coalescence both within the bulk of the foam and on the surface (see Chapter 5).

As the bubbles coalesce and disproportionate, the foam gets coarser and therefore the ‘mean bubble size’, the definition of which is described below, increases. As the bubbles get bigger, the capacity for supporting liquid transport up the column is diminished. At steady-state, the net liquid flux up the column is constant, so it is the size of the bubbles at the very top of the column that determine the liquid flux.

Consider a vertical pneumatic foam that has a monodispersive bubble radius of 0.5 mm throughout the column, but some of the bubbles burst at the free surface to give a monodispersive bubble size of 0.7 mm at the very top. The liquid superficial velocity is determined by drawing the curve given by eqn (8.3) that is pertinent to a bubble radius of 0.7 mm and locating its maximum as described above. However, the hydrodynamic condition of the bulk of the foam in this contrived example must lie on the operating curve pertinent to bubbles of radius 0.5 mm. As the bubbles burst at the surface, liquid that cannot be supported by the foam made up of larger bubbles is liberated to flow down the column (effectively, as if washwater was added to the top of the column). Thus, the foam beneath the surface experiences an enhanced liquid fraction as demonstrated in Fig. 8.3.

Figure 8.3 demonstrates how the liquid fraction can respond to a sudden change in bubble size in the column. However, if there is a gradual change in bubble size with height due to inter-bubble gas diffusion and a stochastic coalescence process, then there will be a gradual decrease in liquid fraction with height, even in the zone in which capillary forces are insignificant.

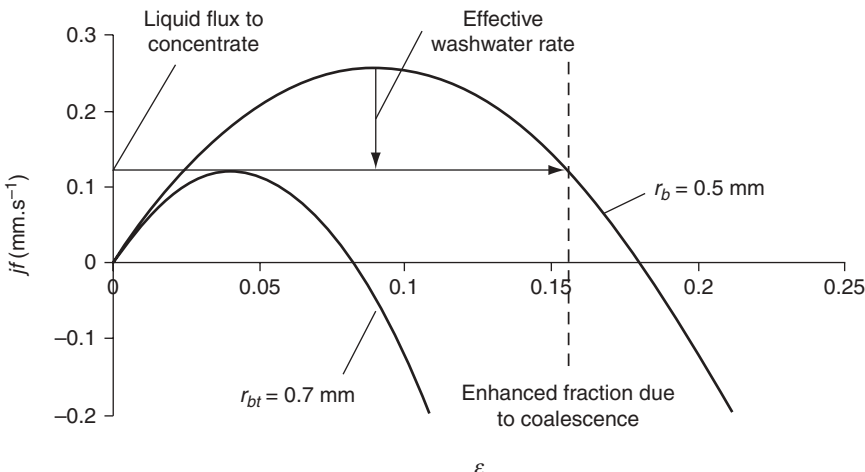


**Fig. 8.3** Calculation of liquid fraction enhancement due to coalescence of surface bubbles. The properties assumed are  $\mu = 1 \text{ mPa.s}$ ,  $\rho = 1000 \text{ kg.m}^{-3}$ ,  $m = 0.016$ ,  $n = 2$ ,  $j_g = 5.8 \text{ mm.s}^{-1}$ .

#### 8.2.2.4 Addition of Washwater to a Pneumatic Foam

Washwater is routinely added to the top of a column flotation process in order to add the rejection of unwanted ‘gangue’ particles from the overhead ‘concentrate steam’ [10]. If the washwater rate is sufficient to create a net downwards flux of liquid within the foam, then the column is said to be operating under ‘positive bias’, and such an operation is generally thought to be important for effective washing. The question therefore arises as to how much washwater is required to achieve positive bias. This will be answered by invoking the theory of vertical pneumatic foam presented above. However, the addition of liquid to the top of a foam also has applications in the provision of an external reflux stream to the top of a foam fractionation device, and the comments in this section will have utility for this unit operation as well.

Consider a vertical pneumatic foam flowing at steady-state such that it operates at the maximum of the liquid flux–liquid fraction curve as described above. Now consider a steady flow of liquid added to a point within the flowing foam. Due to stability arguments, all of the added liquid travels down the column. Thus, the liquid fraction of the foam below the washwater addition point is enhanced, whereas there is no change in liquid fraction above [3]. If capillary forces are insignificant then there is a step change in liquid fraction, but in reality there is a smooth transition between the original liquid fraction above and the enhanced liquid fraction below [11]. By the same stability argument, if washwater is added to an ‘immature’ pneumatic foam (i.e. one that is yet to attain the steady-state given by the peak of the flux curve), then the situation is reversed and the liquid fraction of the foam above the washwater addition point is instead enhanced.

The extent to which the liquid fraction of a mature foam is enhanced by the addition of washwater can be readily ascertained graphically. Recall that when bubbles burst, liquid is liberated and this travels down the column as shown in Fig. 8.3. When washwater is added, the new net flux of liquid can be calculated, and the location of the operating point

on the flux curve that corresponds to this reduced liquid flux gives the enhanced liquid fraction. Positive bias is incipiently achieved when the rate of washwater addition is precisely that of the original overflow rate, thereby giving zero net flux of liquid in the foam. The enhanced liquid fraction is given by the point of the flux curve where it crosses the abscissa. Note that this condition is referred to as ‘total reflux’ in the context of foam fractionation [12].

In column flotation, gangue particles travel through the foam via a convection–dispersion mechanism [13]. Positive bias prevents gangue particles reporting to the concentrate at the top of the column because it ensures that the convection component of the transport of gangue is downwards, making it very difficult for the gangue particle to reach the concentrate by dispersion alone.

### 8.2.3 The ‘Vertical Foam Misapprehension’

An implication of the theory presented above is that if the bubble size distribution is constant as a function of height in the column, then, beyond the zone at the very bottom of the foam over which capillary forces relax, the liquid fraction is constant up the column. However, it is commonly observed that the foam gets drier with height in the column. This has important implications to the process of foam fractionation (see Chapter 14) and so has become a phenomenon of interest to foam fractionation researchers. The cause of the monotonically decreasing liquid fraction with height is the coarsening of the bubbles, but foam fractionation researchers have almost universally laboured under the misapprehension that the cause of the diminution of liquid fraction with height is that the higher the foam, the longer the residence time for the foam to drain, and therefore the drier the foam. This assertion has been repeated as if like a mantra by many foam fractionation researchers. For example, Boonyasuwat *et al.* [14] stated that ‘An increase in foam height leads to a longer foam residence time, which allows more drainage’ and Saleh *et al.* [15] say that ‘Increasing the gas-flow rates resulted in higher volume of wet foam due to the short residence time for the foam to drain the liquid, leading to increase in recovery but decreased enrichment ratios.’ Numerous others have adopted similar flawed reasoning [16–25]. In a review of foam separations, Kruglyakov [8] used observations that liquid fraction was a function of height to incorrectly infer that foam drainage expressions used by others are incorrect.

Because what we have come to refer to as the ‘vertical foam misapprehension’ is so entrenched in the literature, it is worthwhile showing, by *reductio ad absurdum*, that the commonly observed decrease in liquid fraction with height is not due to residence time effects.

Consider a vertical pneumatic foam, somewhere away from the interface with the bubbly liquid so that capillary forces can be neglected. The foam is running at steady-state (i.e. there is no temporal change in liquid fraction). The foam exhibits a uniform bubble size throughout its height, but it also exhibits a monotonically decreasing liquid fraction with height. It can be shown that this situation cannot exist by reference to Fig. 8.2, which gives a typical dependency of liquid superficial velocity upon liquid fraction. If the bubble sizes stay constant, then the hydrodynamic condition of the foam must lie upon the locus pertinent to that bubble radius. Thus, if the liquid fraction changes with height but the bubble size stays constant, then the liquid superficial velocity will also vary as a function of height.

The consequence of this would be that there would be accumulation within the column and the foam would not, in fact, be at steady-state. It is shown that a pneumatic foam, in which capillary forces are insignificant, cannot experience change in liquid fraction whilst maintaining a constant bubble size as a function of height, and therefore changes in liquid fraction must be caused by changes in bubble size.

### 8.2.4 Bubble Size Distributions in Foam

It has been demonstrated above that the hydrodynamic condition of a pneumatic foam is crucially dependent upon the ‘bubble size’, but this raises two important questions:

1. How does one measure the bubble size distribution within the bulk of a pneumatic foam?
2. What representative bubble size should one extract from the measured distribution to describe foam drainage behaviour?

Cheng and Lemlich [26] argued that bubble size distributions obtained by analysing two-dimensional images of foam taken through a transparent column wall were not representative of the bulk of the foam because of planar sampling bias and that small bubbles could wedge big ones away from the wall. Methods of measuring bubble size distribution have been reviewed by Stevenson [27] and include X-ray tomography [28] and pulsed-field gradient nuclear magnetic resonance (PFG-NMR) [29]. It is acknowledged that neither of these techniques is readily accessible in the general laboratory.

Some studies on the forced drainage of foam (e.g. the experiments of Neethling *et al.* [30]) have claimed to have produced foam with a completely uniform bubble size from a single capillary tube, but those produced by sparging gas through a glass frit, air stone or perforated plate always exhibit a greater or lesser degree of polydispersity with respect to bubble size. The bubble size distributions of pneumatic foam measured by PFG-NMR [29] exhibited Weibull distributions, but other workers have reported Gaussian and log-normal statistics.

Whatever the bubble size distribution, eqn (8.3) for liquid flux in the column demands a single bubble size (i.e. a single parameter descriptor). Our current opinion is that the root-mean square bubble radius is used [29], although this assertion has yet to be experimentally verified.

### 8.2.5 Non-overflowing Pneumatic Foam

A non-overflowing vertical pneumatic foam is one in which gas bubbles are sparged into a reservoir of surfactant solution as described above. However, rather than the foam reaching the top of the column and overflowing, thereby creating a steady flow of liquid up the column, a non-overflowing foam collapses somewhere within the column due to the bursting of all of the bubbles on the free surface. Thus, the foam eventually reaches a steady height within the column and the net liquid superficial velocity up the column is zero. Non-overflowing foams have been used to measure the stability of foam (see below), and are commonly found as a ‘head’ on the top of a glass of beer, where nucleated carbon dioxide bubbles continuously arrive at the bottom of the foam layer, but, because of bubble rupture at the free surface, there is no net liquid flux.

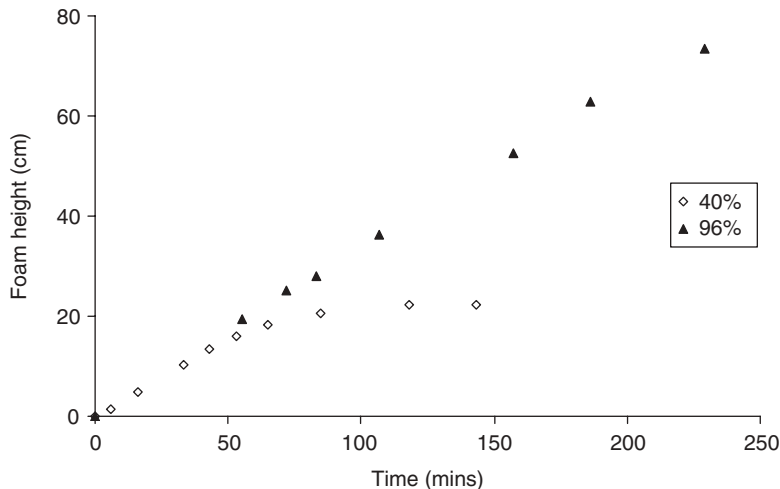


**Fig. 8.4** The growth of a foam made from a lower SDS concentration (0.292 g/l),  $j_g = 0.053 \text{ mm/s}$ . The legend indicates relative humidity [33].

The construction shown in Fig. 8.2 for the relationship between liquid flux and liquid fraction in a pneumatic foam is still valid in this case. The operating point is where the curve crosses the abscissa, since the net liquid superficial velocity is zero.

For the special case of  $n = 2$  in the region where capillary forces are insignificant, there exists an analytical solution [29] for the liquid fraction as a function of the representative bubble size, which is here taken to be the RMS radius,  $r_M$ :

$$\varepsilon = \frac{1}{2} - \sqrt{\frac{1}{4} - \frac{\mu j_g}{m \rho g r_M^2}} \quad (8.7)$$

Non-overflowing foam forms the basis for the Bikerman ‘foamability’ test [31]. The foam layer is allowed to grow under the action of a gas superficial velocity of  $j_g$ , and when it reaches equilibrium, the height of the foam layer is measured as  $h_0$ . Bikerman defined the foamability of a foam as the quotient of foam height and gas superficial velocity, i.e.:

$$\Sigma = \frac{h_0}{j_g} \quad (8.8)$$

The Bikerman test is a widely used method of measuring the stability of foam, and has been adapted to provide a description of the stability of flotation froth [32]. However, it has recently been demonstrated [33] that the equilibrium height that a non-overflowing foam can achieve is dependent upon the humidity gradient in the empty part of the top of the column. Figure 8.4 shows the evolution of the height of a layer of foam stabilised by SDS, with the top of the column being maintained at relative humidities of 40% and 96%. When the relative humidity was set at 40% an equilibrium foam height of around 20 cm

was achieved, whereas when the air was nearly saturated (relative humidity 96%) the foam layer grew with constant velocity until it reached the top of the column. Thus, it is clear that the height of the foam layer, and therefore the value of Bikerman's unit of foamability, is dependent upon environmental humidity and cannot give an intrinsic measure of foam stability. It is therefore apparent that the height a non-overflowing foam can attain, and therefore the stability of the foam, is governed by the rate of evaporation from the free surface.

### 8.2.6 The Influence of Humidity upon Pneumatic Foam with a Free Surface

Neethling and Cilliers [34] recognised that the liquid flux in an overflowing foam was dependent upon the degree of bubble rupture at the free surface of the foam. However, their approach appears to be unphysical. Neethling [35] defined  $\alpha$  as the fraction of bubbles at the free surface of an overflowing foam that do not burst, and gave the following relationship for the liquid fraction:

$$\varepsilon = \frac{255.6 j_g (1-\alpha) \mu}{\rho g r_b^2} \quad (8.9)$$

and this expression has been used in models of column flotation [36]. However, this expression suggests that if no bubbles burst at the surface of the foam (i.e.  $\alpha = 1$ ) then the liquid fraction is zero and there can be no foam. Clearly this is unphysical and incorrect. Neethling and Cilliers [34] gave a mechanistic description of the surface bursting rate as a preliminary to modelling the rate of an overflowing foam. Their model did not propose dependency upon environmental humidity or evaporation rate, and was not experimentally verified.

The observation that the stability of a non-overflowing pneumatic foam was dependent upon humidity, as discussed above, suggested that humidity might also govern the bursting rate on the free surface of a foam overflowing into a launder, such as those commonly found on flotation columns. Thus, we measured the liquid flux in a pneumatic foam whilst controlling the head-space in the launder vessel [37]. It was found that, in general, as humidity was increased (so evaporation from the free surface was diminished) the liquid flux increased. Therefore, it is apparent that reducing the evaporation rate increases the stability of the free surface, which results in increased liquid flux. Environmental humidity is thus seen as an important parameter in determining the behaviour of an overflowing foam with a free surface, but ours appears to be the only study to investigate this phenomenon.

### 8.2.7 Wet Pneumatic Foam and Flooding

Equation (8.2) was adopted to describe the liquid drainage superficial velocity in a reference frame travelling with bubbles as they rise up the column. This expression is obtained through dimensional analysis [4] and assumes that pressure losses due to drainage are entirely viscous. The assumption is usually good when considering, say, the free-drainage

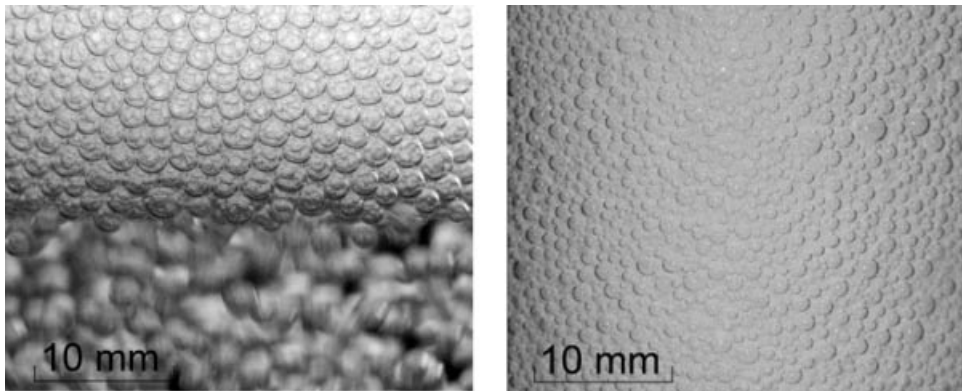


**Fig. 8.5** The interface between foam and bubbly liquid before the flooding point (left) and the foam with no interface after flooding (right).

of stationary foams, because they are typically very dry. Pneumatic foams exhibit a liquid fraction that increases monotonically with gas rate. Thus two questions are raised:

1. Is there a maximum liquid fraction that a pneumatic foam can attain as gas rate is increased, and what happens when the gas rate is increased still further?
2. How good is the assumption that pressure losses due to foam drainage are entirely viscous?

The analysis given thus far has assumed that the pneumatic foam moves in ‘plug flow’, i.e. all the bubbles move vertically with a uniform velocity, and this is observed when the foam is relatively dry. However, Hoffer and Rubin [38] described two further flow regimes as the foam becomes progressively wetter: (i) ‘turbulent flow’, and (ii) bubble column. The term ‘turbulent’ is used loosely and describes the condition in which there is significant convection currents of bubbles established; the bubbles no longer have a vertical trajectory but instead exhibit a wavering path, and even circulation. A mechanism for the onset of convection has, by balancing capillary and gravitational forces, been proposed by Embley and Grassia [39].

At relatively low gas rates, there exists a distinct interface between the bubbly liquid and the rising foam as shown in Fig. 8.1. Rubin and Hoffer described a condition, the ‘bubble column’, in which the interface is impossible to locate and occasional bubbles much larger than in the foam rise quickly through the column. This phenomenon is also described elsewhere [3] and an analogy was drawn to Davidson and Harrison’s ‘Two-Phase Theory of Fluidisation’ [40] in which air over and above that required to cause incipient fluidisation manifests as gross bubbles.

The mechanism for the onset of the ‘bubble column’ regime can be explained [41] by invoking Wallis’s [42] model of one-dimensional two-phase flow. As the gas rate increases, the liquid fraction of the bubbly liquid decreases and the liquid fraction of the foam increases until they converge, and the interface disappears as shown in Fig. 8.5. This condition has also been described as ‘flooding’ [41]. After the flooding point is exceeded, the excess gas does indeed rise through the column as gross bubbles causing the global liquid

fraction within the foam to decrease, whilst significant convection within the column continues to occur.

In the context of the gas-flux versus liquid fraction plot of Figs 8.2 and 8.3, the onset of flooding occurs when the curve no longer exhibits a maximum. Thus, if the pressure losses due to drainage are assumed to be only viscous, the maximum liquid fraction that can be maintained by a pneumatic foam is:

$$\varepsilon^* = \frac{n-1}{n+1} \quad (8.10)$$

This condition occurs at a maximum gas rate:

$$j_g^* = \frac{\rho g r_b^2}{\mu} m n \left( \frac{2}{n+1} \right)^2 \left( \frac{n-1}{n+1} \right)^{n-1} \quad (8.11)$$

However, when the liquid fraction is large causing a large slip velocity between phases, the assumption that only viscous losses occur is worthy of question. We have recently proposed a drainage equation that assumes that viscous and inertial losses are additive in the same way as in the Ergun [43] equation for viscous-inertial flow through a packed bed:

$$j_d = \frac{\varepsilon \left( \sqrt{(K_1 \mu)^2 + 4 K_2 g r_b^3 \varepsilon \rho^2 (1 + \Pi)} - K_1 \mu \right)}{2 K_2 r_b \rho} \quad (8.12)$$

where  $K_1$  and  $K_2$  are adjustable constants that reflect viscous and inertial losses, respectively.

The criterion for the validity of the viscous-only approach is given by:

$$\frac{K_2}{K_1 \varepsilon} \frac{\rho j_d r_b}{\mu} \ll 1 \quad (8.13)$$

For most cases of foam drainage, this criterion is comfortably met and the inertial losses are insignificant. However, because a pneumatic foam close to the flooding point is very wet, inertial losses become significant, and must be accounted for.

### 8.2.8 Shear Stress Imparted by the Column Wall

The pressure gradient in a vertical pneumatic foam is made up of two components:

1. The liquid mass of the foam, which, if the mass of gas is neglected, gives a pressure gradient of  $-\rho g \varepsilon$ .
2. The shear stress,  $\tau$ , imparted by the column wall upon the foam. If the column has a circular cross-section for a diameter  $D$  the pressure gradient is  $4\tau/D$ .

Deshpande and Barigou [44] measured the pressure differential in a vertical pneumatic foam of  $\varepsilon < 0.18$ , and suggested expressions for the friction factor. However, crucially, they attributed all of the pressure gradient to the shear stress, and neglected to account for the contribution to the pressure differential of the mass of the foam.

We have recently developed a method to decouple the two components so that the contribution due to shear stress can be isolated [45]. The pressure differential was measured in a pneumatic foam that was abruptly stopped. Thus, there was a step change in measured pressure differential that was equal to the contribution due to the shear stress. Typically, for an aqueous foam flowing in a Perspex column of a diameter that is 100 times bigger than the diameter of the bubbles, the contribution of shear stress on the total pressure gradient is insignificant if the liquid fraction is greater than 0.1 but below the flooding condition. Certainly, in typical industrial froth flotation devices, for instance, the shear stress contribution to the pressure gradient is insignificant.

The shear stress will be a function of many factors, including the wetting properties of the column wall; we intend to perform an experimental campaign to yield comprehensive expressions for friction factor in the future.

### **8.2.9 Changes in Flow Cross-sectional Area**

The description of the hydrodynamics of pneumatic foam has thus far only considered a vertical column with constant cross-sectional area. In such vertical columns, the liquid fraction and liquid flux are determined by system properties such as the gas superficial velocity, liquid properties and bubble size profile. However, we have shown [45], experimentally and theoretically by adapting Wallis's drift flux method, that a sudden contraction in the column causes a reduction in the liquid fraction whilst maintaining an unchanged liquid volumetric flow rate, whereas a sudden expansion reduces both the liquid fraction and the liquid flow rate. This phenomenon is exploited in the process intensification of foam fractionation [46].

## **8.3 Horizontal Flow of Pneumatic Foam**

### **8.3.1 Introduction**

The study of vertical pneumatic foam has, to a large extent, been encouraged by a desire to develop a mechanistic understanding of the processes of froth flotation and foam fractionation. The study of pneumatic foam flowing through horizontal pipes or channels has, instead, been motivated by a desire to understand the flow of fire-fighting foams (see Chapter 17) and the transport of cuttings by foam in oil wells. Because gravity acts in the direction of the flow, there exists a slip velocity between the gas and liquid phases in vertical pneumatic foam, but this feature is absent in horizontal systems, making them arguably less challenging, and less interesting to investigate. The foam is a non-Newtonian fluid (see Chapter 6 on foam rheology) flowing along a channel and can exhibit a boundary condition with slip. Whereas in the vertical flow of foam we rather dismissed wall shear stress because, at least for large diameter columns, it is insignificant compared to the weight of foam, for horizontal flow the wall shear stress contributes the entire pressure gradient.

The first modern thorough study of the flow of foam through a horizontal pipe was conducted by the omnipresent Robert Lemlich [47], and it is to his work that we first turn. As in other fields of foam research, Lemlich's excellent study has tended to be overlooked by more recent researchers.

### 8.3.2 Lemlich's Observations

Lemlich [47] measured the pressure gradient caused by foam stabilised by the surfactant EDHA through pipes made of both acrylic (Perspex) and galvanised steel. For foam flow in acrylic tubes, Lemlich observed the foam to exhibit almost perfect plug flow with the foam exhibiting a slip velocity on a liquid film layer at the wall. The slip velocity was obtained using Mooney's formalism [48] and the film thickness, which is discussed in Section 8.3.3. However, for the same foam flowing along a horizontal tube made of galvanised steel (of roughness 100–500 µm) Mooney's formalism indicated that the foam exhibited a shear-thinning power-law rheology with zero wall slip.

Lemlich stated that the 'acrylic surface is not (or is at best poorly) wetted by the foam', but that, for the galvanised steel, a 'tactile examination of the wall indicated that the metal surface was well wetted'. To investigate this, we have measured the static contact angle, at 20°C, of a droplet of deionised water on both Perspex and galvanised steel using a contact angle goniometer, and found them to be 77.0° and 77.8°, respectively. Thus, our measurements indicate that the surface wettability of Perspex is very similar to that of galvanised steel, so that differences in the inherent hydrophobicity of Lemlich's pipe walls cannot explain the difference in Lemlich's results. The only relevant property that could possibly explain the difference is the surface roughness of the pipe wall, which might affect the surface boundary condition by either:

1. Surface roughness disrupting the liquid film as the pipe wall and thereby promoting no-slip there.
2. Surface roughness modifying the wettability of the wall via the 'Wenzel Effect' [49], which enhances the hydrophilicity of hydrophilic surfaces.

The latter mechanism is unlikely to be the reason for the no-slip condition at the wall because, if anything, increased hydrophilicity will promote the formation of a liquid layer at the wall. Thus, it seems likely that the transition from plug flow to the no-slip condition observed by Lemlich was due to surface roughness disrupting the liquid layer at the pipe wall upon which the foam could slip when the pipe wall was smooth. This is, of course, not to say that pressure gradient due to, and velocity profile of, foam flow in a horizontal tube is independent of the wettability of the pipe surface.

Although the rheology of foam is discussed in detail in Chapter 6, it is appropriate to discuss the circumstances under which the velocity profile inferred by Lemlich would arise. If the pressure gradient in the horizontal tube is  $dp/dx$  the shear stress in the fluid as a function of the radial distance,  $r$ , from the tube axis,  $\tau$ , is  $0.5r dp/dx$ . Thus, the maximum shear stress experienced by the foam is either at the wall (in the absence of a liquid wall layer) or at the interface between the liquid layer, if it exists, and the foam. Clearly, the foam flowing through the Perspex tube in Lemlich's experiments does not experience a shear stress in excess of a yield stress at the interface between the foam and the liquid layer, and therefore the foam exhibits plug flow. Crucially, the observation of plug flow necessitates the existence of a yield stress. However, application of the Mooney formulation for the data obtained for foam flowing through the galvanised steel pipe yields a constitutive equation that has no yield stress, and this is inconsistent with the plug flow observation. It should, however, be noted that the flow curve that gives the constitutive equation is a fit to data obtained via the Mooney formalisation, and does not directly preclude a yield stress.

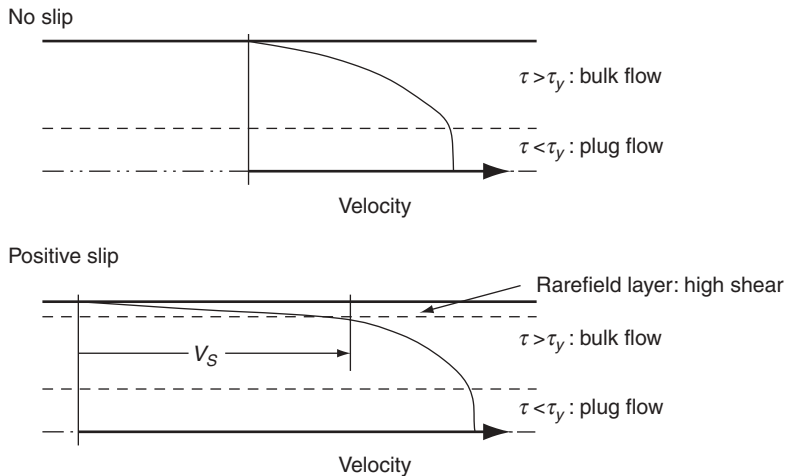


**Fig. 8.6** Generic velocity profiles in a foam showing the plug flow region (where the shear stress  $\tau$  is less than the yield stress  $\tau_y$ ), after Martin and Wilson [51].

Lemlich also gave a Newtonian constitutive relationship for foam through the Perspex pipe. Because a particular foam must exhibit a unique constitutive relationship that is independent of the nature of the pipe wall, the inferences of Lemlich represent a dichotomy, and show that a fit obtained from capillary rheometry does not necessarily accurately yield the rheological features of a material.

In addition, Lemlich performed experiments on foams containing coal and sand particles that were contained within the Plateau borders, indicating that they were hydrophilic. He observed that the presence of the solids did not significantly change pressure gradient or velocity profile.

### 8.3.3 Wall-slip and Velocity Profiles

Just as in the flow of pastes in tubes, liquid can segregate from the foam to form a thin layer at the wall. This provides decreased resistance to shear, and can engender ‘slip’ at the wall as in Lemlich’s experiments using a Perspex tube. Figure 8.6 shows typical velocity profiles of capillary flow with (i) no slip, (ii) positive slip over a rarefied layer of liquid at the pipe wall where the foam exceeds the yield stress in an annulus and (iii) positive slip where the yield stress is nowhere exceeded. Notably Blondin and Doubliez [50] have employed particle imaging velocimetry to visualise velocity profiles in horizontal flows of foam.

A Weissenberg–Rabinowitsch method can be used to translate data for the pressure differential of a non-Newtonian fluid flowing in a tube, with a no-slip wall condition, as a function of flow rate into a constitutive equation (i.e. shear stress as a function of strain rate). This method was extended by Mooney [48] to accommodate a slip velocity at the

wall, as introduced above, because Lemlich used the method to obtain constitutive relationships for a foam. Once the slip velocity,  $V_s$ , has been estimated, the thickness of the liquid layer,  $\delta$ , can be estimated as a function of the wall shear stress:

$$V_s = \frac{\delta}{\mu} \tau_w \quad (8.14)$$

where  $\mu$  is the liquid viscosity.

Some years before Lemlich's work, Jastrzebski [52] investigated the flow of pastes through a capillary. The data did not produce linear Mooney plots, which was reconciled by suggesting that the slip velocity was inversely proportional to the capillary radius. This suggestion has been adopted for the interpretation of foam data [51]. However, Yeow *et al.* [53] suggested that Tikhonov regularisation [54] is used to analyse capillary rheometry data, and have shown that Jastrzebski has limited support and that the Mooney formalism with Tikhonov regularisation is successful for the interpretation of foam data.

### 8.3.4 Horizontal Flow Regimes

Briceño and Joseph [55] have codified seven different flow regimes that can be exhibited by a pneumatic foam in a smooth horizontal tube, which represents the most detailed qualitative description, and provides an excellent platform to develop future mechanistic models.

*Pattern 1.* When the foam is very wet with a *delivered* liquid fraction of above about 27%, a liquid stratum forms at the invert of the pipe, and the foam layer moves on top of this.

*Pattern 2.* At a liquid fraction of 21–27%, the liquid layer becomes thinner and bubbles can exhibit limited shear past one another. There is also some bubble size segregation with the bigger bubbles tending to locate near the soffit of the pipe.

*Pattern 3.* At a liquid fraction of 11–21%, there is churning of bubbles that causes the size classification observed in pattern 2 to disappear. The visible liquid layer (but not necessarily the microscopic layer described by Lemlich) vanishes, and there is a distinct velocity profile in the foam.

*Pattern 4.* At a liquid fraction of 3–11%, the foam exhibits plug flow, which corresponds to Lemlich's observations in the Perspex tube. The authors refer to the foam as a 'wispy solid'.

*Pattern 5.* At a liquid fraction of 2–3%, the large bubbles start to segregate towards the top of the column once more.

*Pattern 6.* At a liquid fraction 1–2%, the foam forms into distinct plugs separated by pockets of gas as shown by the Briceño photograph in Fig. 8.7.

*Pattern 7.* The gas rate becomes so great that it can break through the foam plugs and the foam becomes incoherently dispersed in the tube. This has analogy with the phenomenon of 'gas pull-through' observed in gas–liquid oil flow lines.

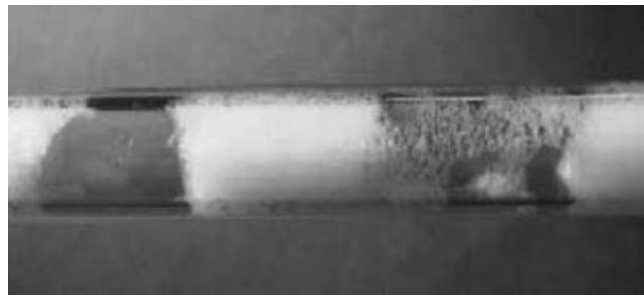


**Fig. 8.7** Briceño's photograph [55] of flow pattern 6 showing successive plugs of gas and foam.

## 8.4 Pneumatic Foam in Inclined Channels

It should briefly be mentioned that pneumatic foam through inclined channels has an application in the process intensification of the foam fractionation process. The Boycott effect [56] has been used to increase phase segregation between liquid and gas in foam fractionation [57].

## 8.5 Methods of Pneumatic Foam Production

The generation of aqueous foam is a process of incorporating gas into a liquid, during which a gas–liquid interface is created. The work,  $W$ , required to generate a certain amount of surface area ( $\Delta A$ ) can be calculated by:

$$W = \sigma \Delta A \quad (8.15)$$

where  $\sigma$  ( $\text{J/m}^2$ ) is the surface energy of the gas–liquid interface. From eqn (8.15) it can be seen that it is easier to generate a foam when the surface energy density is lower. In practical applications, the surface tension is generally reduced to  $0.02\text{--}0.035 \text{ J.m}^{-2}$  by the presence of surface active material.

Pneumatic foams used in foam fractionation or froth flotation and related research are normally generated by (i) injection of gas through orifices, i.e. sparging, (ii) mechanical agitation, (iii) entrainment by high speed liquid jet and (iv) cavitation.

1. Sparging methods. In the simplest case, a single needle is used to create monodisperse foam, i.e. a foam consisting of equal-size bubbles [58–60]. In most practical cases such as foam fractionation and column flotation, however, a porous medium such as sintered glass, air stone or perforated stainless steel plate is used to generate a large amount of polydisperse foam. In the industrial scale foam fractionation of Nisin (see Chapter 14), stainless steel plates with laser burnt pores are used, due to their mechanical strength, chemical stability and relatively uniform pore size. The bubbles generated from a porous

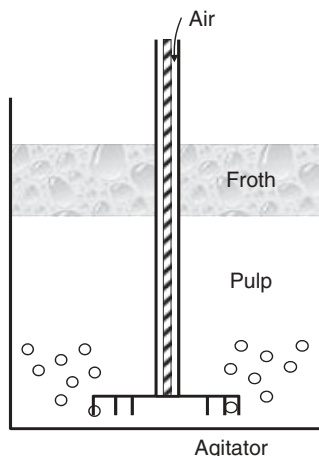


**Fig. 8.8** A mechanical flotation cell, after [62].

medium always have a polydisperse size distribution, due to the non-uniformity of pore sizes. Unlike single orifice spargers from which the bubble size generally increases with gas velocity, the average bubble size generated from a porous medium may decrease with increasing gas velocity. This is because, at lower gas rates, only those bigger pores are active, resulting in mostly big bubbles. At high gas flow rates, more and more small pores become active, and thus the number of smaller bubbles increases, resulting in a smaller average bubble size.

2. Agitation. Figure 8.8 shows a schematic diagram of a mechanical flotation cell. Turbulent flow is produced by the rapid rotation of the impeller at the bottom of the cell. The air stream is broken down and dispersed into small bubbles due to the turbulent flow of the liquid phase and the relative velocity between the air and liquid phases. The bubbles rise to the top of the liquid and a froth layer is formed. The bubble size generated by this method is determined by the energy input and the interfacial tension. Generally speaking, the higher the mixing rate, the more the energy input, and according to eqn (8.1), the smaller the bubbles. Reduction of gas–liquid surface tension also results in smaller bubbles [61]. Different types of impellers may be used to improve the performance of the agitator.
3. Entrainment by plunging liquid jet. Air entrainment by liquid jets does not require a mechanical impeller or a porous medium. It happens naturally at waterfalls, in mountain streams, etc. [63]. It is also frequently met during the pouring and filling of containers with liquids. Studies on gas entrainment by contrived high-speed liquid jet have gained interest since the 1970s and a few comprehensive reviews are available [64]. The bubble size generated by a plunging liquid jet is determined by the combined effects of jet velocity, jet length, air/liquid flow rate ratio, etc. [65].
4. Cavitation. When a liquid containing dissolved gas is throttled to a reduced pressure, very small bubbles can form when the gas comes out of solution. The phenomenon is known as hydrodynamic cavitation, and is harnessed in both fine and coarse particle

flotation, oil agglomeration of fine particles of coal, and the processing of oil sand [66], and used in dissolved bubble flotation. Bubble sizes produced by cavitation of down to about  $15\text{ }\mu\text{m}$  have been measured using laser diffraction [67] but smaller bubbles produced by this method have been reported elsewhere [66]. Proprietary devices are available, known as cavitation tubes, through which the throttling process causes cavitation, such as the range developed by Canadian Process Technologies for the flotation of a range of minerals, including iron ore, phosphate, fluorite, feldspar, mica and molybdenum. In this context, it is appropriate to mention that electroflotation is another mineral processing technology capable of forming very small bubbles [68] and therefore a fine foam.

## Nomenclature

### Roman

$A$	Bubble surface area	[ $\text{m}^2$ ]
$g$	Acceleration due to gravity	[ $\text{m.s}^{-2}$ ]
$h_0$	Equilibrium height of foam layer	[m]
$j_d$	Superficial drainage velocity	[ $\text{m.s}^{-1}$ ]
$j_f$	Superficial liquid velocity	[ $\text{m.s}^{-1}$ ]
$j_g$	Superficial gas velocity	[ $\text{m.s}^{-1}$ ]
$j_g^*$	Superficial gas velocity at flooding	[ $\text{m.s}^{-1}$ ]
$K_1$	Viscous loss coefficient	[–]
$K_2$	Inertial loss coefficient	[–]
$m$	Dimensionless number used in eqn (8.2)	[–]
$n$	Dimensionless index used in eqn (8.2)	[–]
$p$	Dimensionless number used in eqn (8.6)	[–]
$q$	Dimensionless index used in eqn (8.6)	[–]
$r$	Radius of curvature of a Plateau border wall	[m]
$r_b$	Characteristic mean bubble radius	[m]
$r_M$	RMS bubble radius	[m]
$V_s$	Slip velocity at the wall	[ $\text{m.s}^{-1}$ ]
$W$	Work expended in forming a bubble	[J]
$x$	Vertical dimension in direction of the flow	[m]

### Greek

$\alpha$	Air fraction overflowing as unburst bubbles	[–]
$\delta$	Liquid film thickness	[m]
$\varepsilon$	Volumetric liquid fraction in the foam	[–]
$\varepsilon^*$	Maximum volumetric liquid fraction in the foam	[–]
$\mu$	Interstitial liquid dynamic viscosity	[ $\text{Pa.s}$ ]
$\Pi$	Dimensionless number accounting for capillary forces	[–]

$\rho$	Interstitial liquid density	[kg.m <sup>-3</sup> ]
$\sigma$	Equilibrium surface tension	[N.m <sup>-1</sup> ]
$\Sigma$	Bikerman's unit of foaminess	[s]
$\tau_w$	Wall shear stress	[N.m <sup>-2</sup> ]

## References

- [1] R.A. Leonard and R. Lemlich. A study of interstitial liquid flow in foam. I. Theoretical model and application to foam fractionation. *AIChE J.*, **11**: 18–25, 1965.
- [2] P.A. Haas and H.F. Johnson. Foam columns for the countercurrent surface-liquid extraction of surface-active solutes. *AIChE J.*, **11**: 319–24, 1965.
- [3] P. Stevenson. Hydrodynamic theory of rising foam. *Miner. Eng.*, **20**: 282–9, 2007.
- [4] P. Stevenson. Dimensional analysis of foam drainage. *Chem. Eng. Sci.*, **61**: 4503–10, 2006.
- [5] D. Weaire, N. Pittet and S. Hutzler. Steady state drainage of an aqueous foam. *Phys. Rev. Lett.*, **71**: 2670–3, 1993.
- [6] P. Stevenson, M.D. Mantle, A.J. Sederman and L.F. Gladden. Quantitative measurements of liquid holdup and drainage in foam using NMRI. *AIChE J.*, **53**: 290–6, 2007.
- [7] P. Stevenson. The wetness of a rising foam. *Indust. Eng. Chem. Res.*, **45**: 803–7, 2006.
- [8] P.M. Kruglyakov. Adsorption accumulation and separation of dissolved substances in dry foams. *Curr. Opinion Coll. Interface Sci.*, **15**: 382–91, 2010.
- [9] P. Stevenson and C. Stevanov. Effect of rheology and interfacial rigidity on liquid recovery from rising froth. *Indust. Eng. Chem. Res.*, **43**: 6187–94, 2004.
- [10] B.V. Clingan and D.R. McGregor Column flotation experience at Magma Copper Co. *Miner. Metall. Process.*, **3**: 121–5, 1987.
- [11] P. Stevenson, M.D. Mantle, A.B. Tayler and A.J. Sederman. Quantitative NMRI studies of transient washwater addition to rising foam. *Chem. Eng. Sci.*, **64**: 1001–9, 2009.
- [12] P. Stevenson and G.J. Jameson, Modelling continuous foam fractionation with reflux. *Chem. Eng. Process.*, **46**: 1286–91, 2007.
- [13] P. Stevenson, S. Ata and G.M. Evans. Convective-dispersive transport of gangue through flotation froth. *Chem. Eng. Sci.*, **62**: 5736–44, 2007.
- [14] S. Boonyasuwat, S. Chavadej, P. Malakul and J.F. Scamehorn. Anionic and cationic surfactant recovery from water using a multistage foam fractionator. *Chem. Eng. J.*, **93**: 241–52, 2003.
- [15] Z. Saleh, R. Stanley, and M. Nigam. Extraction of polyphenolics from apple juice by foam fractionation. *Int. J. Food. Eng.*, **2**: Art. 2, 2006.
- [16] C. Crofcheck and K. Gillette. Evaluation of foam fractionation column scale-up for recovering bovine serum albumin. *Trans. ASAE*, **46**: 1759–64, 2003.
- [17] A.K. Brown, A. Kaul and J. Varley. Continuous foaming for protein recovery: part I. Recovery of beta-casein. *Biotech. Bioeng.*, **62**: 278–90, 1999.
- [18] H. Maruyama, A. Suzuki, H. Seiki and N. Inoue. Enrichment in axial direction of aqueous foam in continuous foam separation. *Biochem. Eng. J.*, **30**: 253–9, 2006.
- [19] C.E. Lockwood, S.H. Kim, P.M. Bummer and M. Jay. Scintigraphic measurement of liquid holdup in foam fractionation columns. *J. Coll. Interface Sci.*, **227**: 24–31, 2000.
- [20] S.D. Webb, R.C. Page, M. Jay and P.M. Bummer. Characterization and validation of the gamma-scintigraphic method for determining liquid holdup in foam. *Appl. Radiat. Isotopes*, **57**: 243–55, 2002.
- [21] Y.-H. Qu, G.M. Zeng, J.H. Huang *et al.* Recovery of surfactant SDS and Cd<sup>2+</sup> from permeate in MEUF using a continuous foam fractionator. *J. Hazardous Mater.*, **155**: 32–8, 2008.
- [22] Z.-D. Chang, H.-Z. Liu and J.-Y. Chen. Foam separation of tributyl phosphate from aqueous solutions: Part II: simulation. *Separation and Purification Tech.*, **19**: 137–44, 2000.
- [23] J. Zhang, Y. Jing, Z. Wu and Q. Li. Removal of trace Cu<sup>2+</sup> from aqueous solution by foam fractionation. *Desalination*, **249**: 503–6, 2009.

- [24] T. Sarachat, O. Pornsunthorntawee, S. Chavadej and R. Rujiravanit. Purification and concentration of a rhamnolipid biosurfactant produced by *Pseudomonas aeruginosa* SP4 using foam fractionation. *Bioresource Tech.*, **101**: 324–30, 2010.
- [25] D. Linke and R.G. Berger. Foaming of proteins: new prospects for enzyme purification processes. *J. Biotech.*, in press.
- [26] H.C. Cheng and R. Lemlich. Errors in the measurement of bubble-size distribution in foam. *Indus. Eng. Chem. Fundament.*, **22**: 105–9, 1983.
- [27] P. Stevenson. Inter-bubble gas diffusion in liquid foam. *Curr. Opinion Coll. Interface Sci.*, **15**: 374–81, 2010.
- [28] J. Lambert, I. Canat, R. Delannay *et al.* Experimental growth law for bubbles in a moderately ‘wet’ 3D liquid foam. *Phys. Rev. Lett.*, **99**: 058304, 2007.
- [29] P. Stevenson, A.J. Sederman, M.D. Mantle *et al.* Measurement of bubble size distribution in a gas-liquid foam using pulsed-field gradient nuclear magnetic resonance. *J. Coll. Interface Sci.*, **352**: 114–20, 2010.
- [30] S.J. Neethling, H.T. Lee and J.J. Cilliers. A foam drainage equation generalised for all liquid contents. *J. Phys. Condensed Matter*, **14**: 331–42, 2002.
- [31] J.J. Bikerman. The unit of foaminess. *Trans. Faraday Soc.*, **34**: 634–8, 1938.
- [32] B.B. Triffett and J.J. Cilliers. Measuring froth stability. International Patent Application Number PCT/AU2004/000331, 2004.
- [33] X. Li, R. Shaw and P. Stevenson. Effect of humidity on dynamic foam stability. *Int. J. Miner. Process.*, **94**: 14–19, 2010.
- [34] S.J. Neethling and J.J. Cilliers. Modelling flotation froths. *Int. J. Miner. Process.*, **72**: 267–87, 2003.
- [35] S.J. Neethling. A mathematical model of flowing foams and froths. PhD thesis, University of Manchester Institute of Science and Technology, 1999.
- [36] X. Zheng, J.P. Franzidis and N.W. Johnson. An evaluation of different models of water recovery in flotation, **19**: 871–82, 2006.
- [37] R. Shaw, G.M. Evans and P. Stevenson. Dependency of liquid overflow rate upon humidity of a pneumatic foam. **97**: 26–30, 2010.
- [38] M.S. Hoffer and E. Rubin. Flow regimes of stable foams. *Indus. Eng. Chem. Fundament.*, **8**: 483–90, 1969.
- [39] B. Embley and P. Grassia. Mechanisms for the onset of convective instability in foams. *Phil. Magazine Lett.*, **86**: 385–94, 2006.
- [40] J.F. Davidson and D. Harrison. The behaviour of a continuously bubbling fluidised bed. *Chem. Eng. Sci.*, **21**: 731–8, 1966.
- [41] X. Wang *et al.* The maximum volumetric liquid fraction in a vertical pneumatic foam. In preparation.
- [42] G.B. Wallis. *One-Dimensional Two-Phase Flow*. McGraw-Hill Book Company, New York, 1969.
- [43] S. Ergun. Fluid flow through packed columns. *Chem. Eng. Prog.*, **48**: 9–94, 1952.
- [44] N.S. Deshpande and M. Barigou. Foam flow phenomena in sudden expansions and contractions. *Int. J. Multiphase Flow*, **27**: 1462–77, 2001.
- [45] X. Li, X. Wang, G.M. Evans and P. Stevenson. Foam flowing vertically upwards in pipes through expansions and contractions. *Int. J. Multiphase Flow*, **37**: 802–11, 2011.
- [46] X. Li, G.M. Evans and P. Stevenson. Process intensification of foam fractionation by successive contraction and expansion. *Chem. Eng. Res. Design*, **89**: 2298–308, 2011.
- [47] N.N. Thondavadl and R. Lemlich. Flow properties of foam with and without solid particles. *Indus. Eng. Chem. Process Design Devel.*, **24**: 748–53, 1985.
- [48] M. Mooney. Explicit formulas for slip and fluidity. *J. Rheol.*, **2**: 210–22, 1931.
- [49] R.N. Wenzel. Surface roughness and contact angle. *J. Phys. Coll. Chem.*, **53**: 1466–7, 1949.
- [50] E. Blondin and L. Doubliez. Particle imaging velocimetry of a wet aqueous foam with an underlying liquid film. *Experiments in Fluids*, **32**: 294–301, 2002.
- [51] P.J. Martin and D.I. Wilson. A critical assessment of the Jastrzebski interface condition for the capillary flow of pastes, foams and polymers. *Chem. Eng. Sci.*, **60**: 493–502, 2005.

- [52] Z.D. Jastrzebski. Entrance effects and wall effects in an extrusion rheometer during the flow of concentrated suspensions. *Indus. Eng. Chem. Fundament.*, **6**: 445–54, 1967.
- [53] Y.L. Yeow, H.L. Lee, A.R. Melvani and G.C. Mifsud. A new method of processing capillary viscometry data in the presence of wall slip. *J. Rheol.*, **47**: 337–48, 2003.
- [54] A.N. Tychonoff and V.Y. Arsenin. *Solution of Ill-Posed Problems*. Winston & Sons, Washington, DC.
- [55] M.I. Briceño and D.D. Joseph. Self-lubricated transport of aqueous foams in horizontal conduits. *Int. J. Multiphase Flow*, **29**: 1817–31, 2003.
- [56] A.E. Boycott. Sedimentation of blood corpuscles. *Nature*, **104**: 532, 2002.
- [57] J.E. Dickinson, D. Laskovski, P. Stevenson and K.P. Galvin. Enhanced foam drainage using parallel inclined channels in a single-stage foam fractionation column. *Chem. Eng. Sci.*, **65**: 2481–90, 2010.
- [58] E. Lorenceau, N. Louvet, F. Rouyer and O. Pitois. Permeability of aqueous foams. *Eur. Phys. J. E*, **28**: 293–304, 2009.
- [59] F. Rouyer, O. Pitois, E. Lorenceau and N. Louvet. Permeability of a bubble assembly: From the very dry to the wet limit. *Phys. Fluids*, **22**: 043302, 2010.
- [60] M.J. Lockett and R.D. Kirkpatrick. Ideal bubbly flow and actual flow in bubble columns. *Trans. Inst. Chem. Eng.*, **53**: 267–73, 1975.
- [61] R.J.P. Shouci Lu and F. Eric (eds). Gas/liquid interfacial separation. In *Studies in Interface Science*. Elsevier, Amsterdam, 2005.
- [62] B.A. Wills and T. Napier-Munn. Froth flotation. In *Wills' Mineral Processing Technology*, 7th edn. Butterworth-Heinemann: Oxford, 2005.
- [63] M.J. Kenn and K.J. Zanker. Aspects of similarity for air-entraining water flows. *Nature*, **213**: 59–60, 1967.
- [64] A.K. Bin. Gas entrainment by plunging liquid jets. *Chem. Eng. Sci.*, **48**: 3585–630, 1993.
- [65] G.M. Evans, G.J. Jameson and C.D. Rielly. Free jet expansion and gas entrainment characteristics of a plunging liquid jet. *Exp. Thermal and Fluid Sci.*, **12**: 142–9, 1996.
- [66] Z.A. Zhou, Z.H. Zu, J.A. Finch, J.H. Masliyah and R.S. Chow. On the role of cavitation in particle collection in flotation – a critical review. *Minerals Eng.*, **22**: 419–33, 2009.
- [67] H.J.B. Couto, D.G. Nunes, R. Neumann and S.C.A. Franca. Micro-bubble size distribution measurements by laser diffraction technique. *Minerals Eng.*, **22**: 330–5, 2009.
- [68] M.S.K.A. Sarkar, G.M. Evans and S.W. Donne. Bubble size measurement in electroflotation. *Minerals Eng.*, **23**: 1058–65, 2010.

# 9

## Non-aqueous Foams: Formation and Stability

*Lok Kumar Shrestha and Kenji Aramaki*

### 9.1 Introduction

Foaming is an important issue in the application of series of personal care products, mineral separation, food manufacturing, cosmetic formulations, and several industrial processes such as enhanced oil recovery, drilling operations in the oil industry, benefaction of ores by foam floatation, polymer foam insulation, construction materials, textile and also in the synthesis of porous materials [1–5]. Applications involving foams in modern industrial processes have grown significantly. Consumers expect many of the personal care products they use to produce foam, and therefore, the acceptability of many consumer products is closely linked to the quality and texture of the foam they produce. Many cosmetics and toiletries are formulated to provide foam in accordance with the wishes of the consumers [6]. Therefore an understanding of foams and foaming is of wide-ranging technological importance.

#### 9.1.1 Foam Formation and Structures

Liquid-based foams are non-equilibrium dispersions of gas bubbles in a relatively smaller volume of liquid generally containing surface-active agents [7, 8]. The surface of bubbles dispersed within a pure liquid possesses a strong tendency to minimize the surface area. Therefore stable foam cannot be produced in pure liquids unless the liquid possesses very high viscosity. When surface-active molecules (surfactants or polymers) are solubilized

within the liquid phase, they adsorb at the gas–liquid interface and are responsible for both the ability of a liquid to foam (foamability) and the stability of the resulting foams [9, 10]. Adsorption of surface-active molecules to the bubble surfaces reduces the surface tension of the liquid, which is a measure of the tendency of the surface to minimize its area as low as possible [1]. The decrease in the surface tension enhances the foam stability because the increase in the free energy associated with the increase in the surface area is low. Generation of foam, at the beginning, leads to the formation of wet foam, which consists of spherical gas bubbles surrounded by a liquid [2]. Due to liquid drainage, the structure of foam gradually changes and the spherical foam bubbles are eventually transformed into polyhedral shape bubbles separated by a thin liquid film, often called dry foams. Owing to the high volume fraction of gas, the bubbles in the foams are distorted in the form of polyhedra separated by thin liquid films, which are stabilized by surface-active molecules adsorbed at the gas–liquid interface. When the volume fraction of the dispersed phase in foam exceeds 0.74, the gas bubbles deform from the spherical shape and the foam films are formed at the contacts between the deformed droplets. With further increasing volume fraction of the dispersed phase, the area occupied by the thin films increases due to further deformation of the foam bubbles. Thus the structure of foam depends on the volume fraction of the dispersed phase. The three adjacent thin films meet at a point called the Plateau border. It is well known that the pressure of the liquid is proportional to the interfacial curvature of the interface and, hence, the pressure at the Plateau border is less than in the adjoining thin films, and as a consequence, the liquid drains out of the thin films to the border followed by the drainage of the liquid through the network of Plateau borders due to gravity. Drainage of the liquid phase leads to profiles of volume fraction of the gas phase from top to bottom of the foam column, with the higher volume fraction at the top [11]. When the foam becomes dry (after drainage), the foam film thickness enters the range of a few hundred angstroms and can be stabilized by (i) steric forces in the case of an amphiphilic polymer, (ii) structural forces in the case of surfactant and polyelectrolyte mixtures, and (iii) long-range electrostatic forces [7, 11, 12]. One can easily distinguish the foam film stabilization mechanism by measuring disjoining pressure as a function of the film thickness [13, 14]. One can obtain additional information on maximum pressure sustainable by the film by measuring disjoining pressure. This pressure is a measure of the film's stability [15].

### 9.1.2 Foam Stability

Foams are thermodynamically unstable systems and undergo self-destruction processes due to liquid drainage, Ostwald ripening and coalescence [7, 11, 12, 16, 17]. However, stable foams can be achieved if one has control over these processes. Liquid drainage can be slowed down either by increasing the bulk viscosity of the liquid or by increasing the surface elasticity and viscosity, respectively. The Ostwald ripening can be slowed down by reducing the polydispersity of the gas bubbles. Increasing the resistance of the foam films to rupture can slow down bubble coalescence. It has been shown that a stable foam film requires both a high disjoining pressure and a high surface visco-elasticity [18–23]. Foam stability of dilute aqueous surfactant solutions can also be explained by the Gibbs–Marangoni mechanism. Similarly, dynamic interfacial properties (dynamic surface tension and surface dilatational elasticity) are considered to have a significant contribution to the foamability and foam stability [24–29].

Low molecular weight ionic or non-ionic surfactants, polymers or proteins have been known to stabilize aqueous foams. These days foams or emulsions stabilized by colloidal particles in the presence or absence of surfactants or proteins are drawing considerable attention [30–38]. In several foaming studies, solid particles have been used in combination with surfactants or polymers. The stability of such foams is influenced by the particle size, concentration, hydrophobicity and particle–surfactant interactions [30, 39–43]. Factors controlling the formation and stability of aqueous foams stabilized by partially hydrophobic silica nanoparticles have been well described [44].

The stability mechanism of aqueous (water-based) and non-aqueous (oil-based) foams is basically the same; however, it is difficult to get stable non-aqueous foams, as the surfactants are less surface-active in non-aqueous solvents. The value of surface tension of most of the oils is already so low that there is only a little adsorption of hydrocarbon surfactants to the surface. This could be the reason why non-aqueous foams have been sparsely studied [45, 46]. Nearly a decade back Sirota and co-workers demonstrated that surface crystallization of *n*-alkanes can significantly improves the stability of foam bubbles [47]. They showed that microscopically observable foam stability can be related to the crystallization of a microscopic monolayer at the liquid–vapour interface at a temperature above the bulk melting temperature. Recently, Ichinose and co-workers have introduced a novel method for the preparation of non-aqueous thin films, in which they replaced water by ionic liquid [48]. A major contribution on non-aqueous foaming came from Stig E. Friberg quite some time ago. Friberg and his co-workers studied the stability of foams in two-phase regions consisting of hydrocarbon solution and a lamellar liquid crystal ( $L_\alpha$ ) phase [49–52]. The  $L_\alpha$  showed surface activity with regard to the hydrocarbon solution due to higher frequency of methyl groups at the surface of the liquid crystalline state compared to the liquid state. The weaker intermolecular forces from the methyl groups were assumed to result in a lower surface tension of the  $L_\alpha$  phase in comparison to the liquid. The lower surface tension of the liquid crystal caused it to be located at the liquid–air interface and, hence, stabilized the foams. Similarly, Friberg and co-workers have shown the influence of liquid crystalline phases on foam stability [53]. It has been shown that foams with excellent stability can be observed with compositions that contained both a liquid crystalline phase and a liquid phase in comparison to those where only liquid phase is present. Although Friberg and co-workers has indicated a direction for non-aqueous foam science, not many studies were carried out until the late Professor Hironobu Kunieda realized the necessity of and demand for non-aqueous foaming. In his laboratory, we have carried out systematic studies of oil-based non-aqueous foam stability properties depending on various outer conditions.

The present chapter describes the stabilization of non-aqueous foams by  $L_\alpha$  or solid ( $\alpha$  or  $\beta$ -form) or their mixtures. Biodegradable and biocompatible non-ionic surfactants; homologous series of mono- and diglycerol fatty acid esters and different nonpolar oils; liquid paraffine, squalane, squalene, hexadecane and olive oil were used. The molecular structures of non-ionic surfactants and some of the non-polar oils mentioned in this chapter are given in Fig. 9.1.

Non-aqueous foam formation capacity and the stability of the resulting foams depending on the solvent and surfactant molecular architecture, surfactant concentration, temperature and water addition were investigated systematically. We have found super-stable non-aqueous foams from the dispersions of  $\alpha$  or  $\beta$ -crystals and a link between

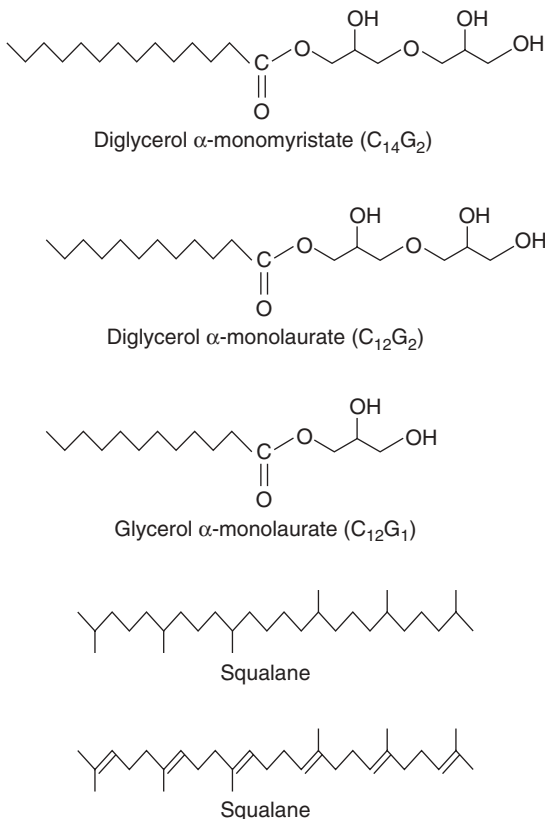


**Fig. 9.1** Molecular structures of glycerol-based nonionic surfactants: diglycerol  $\alpha$ -monomyristate ( $C_{14}G_2$ ), diglycerol  $\alpha$ -monolaurate ( $C_{12}G_2$ ), glycerol  $\alpha$ -monolaurate ( $C_{12}G_1$ ), and non-polar oils squalane and squalene.

foam stability and the particle size, namely the smaller the particle size the higher the foam stability. The foam stability was largely influenced by the molecular structure of oils. For example, dilute systems of diglycerol monomyristate in liquid paraffin, and squalene gave highly stable foams with foam stability more than 12 h [54]. However, the dilute systems of the same surfactant in other oils, squalane and hexadecane could not produce stable foams. Foam collapsed soon after the foam production. It was found that, in such non-foaming systems, the dispersed  $\alpha$ -crystals or  $L_\alpha$  particles are coagulated, forming clusters [54]. Addition of a small amount of water shattered these clusters and improved the foaming properties dramatically, resulting in the formation of stable foams [55]. From the studies of non-aqueous foaming from diglycerol monolaurate/oil systems, it was found that the dispersions of  $L_\alpha$  particles stabilize non-aqueous foam for a few minutes to several hours depending on the particle concentration and their size [56]. Interestingly, from the foaming experiments in monoglycerol fatty acid esters/oil systems, it was found that in addition to the particle size, the shape of the particles plays a crucial role in the foam stability [57].

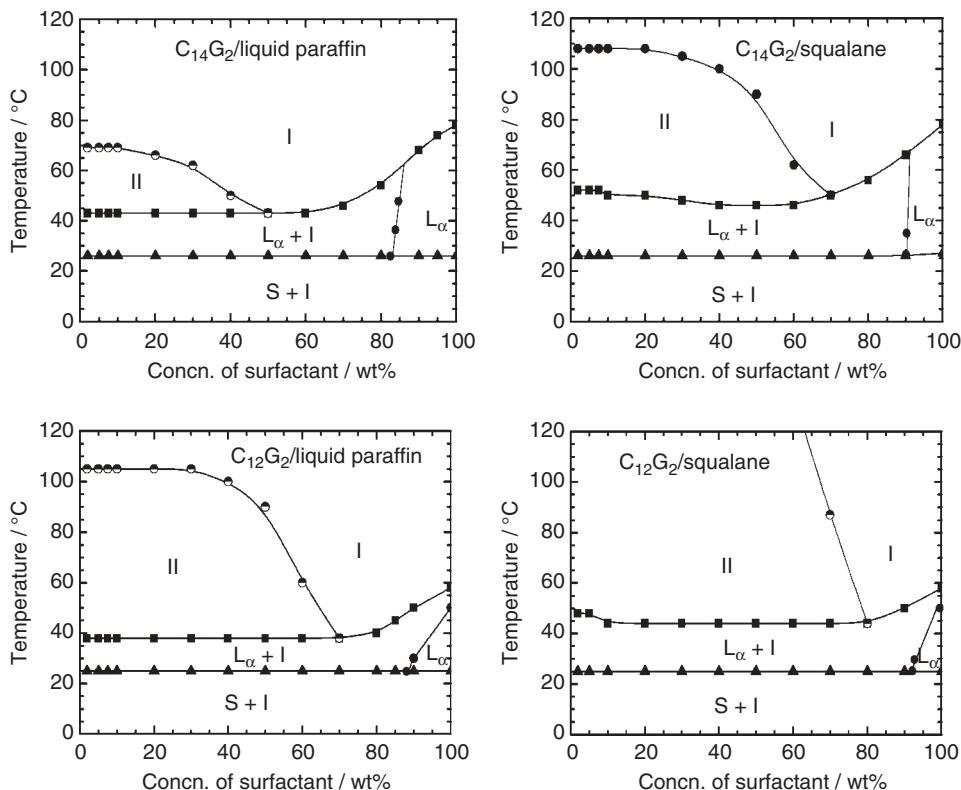


**Fig. 9.2** Phase diagrams of  $C_{14}G_2$  and  $C_{12}G_2$  in liquid paraffin and squalane over a wide range of temperatures and concentrations at atmospheric pressure ( $S$  = solid,  $L_\alpha$  = lamellar liquid crystal,  $I$  = isotropic solution, and  $II$  = isotropic two-liquid phases). Adapted from ref. [58].

## 9.2 Phase Behavior of Diglycerol Fatty Acid Esters in Oils

This section describes the non-aqueous phase behavior of diglycerol fatty acid esters in different solvents. When these surfactants are added into organic solvents such as liquid paraffin or squalane, they spontaneously undergo a self-assembly process and form a variety of self-assembled structures [58]. In Fig. 9.2, we present binary phase diagrams of diglycerol monomyristate ( $C_{14}G_2$ ) and diglycerol monolaurate ( $C_{12}G_2$ ) in liquid paraffin and squalane as typical examples. The data are adopted from Shrestha et al. [58].

One can see a surfactant solid phase at lower temperatures, which does not swell with oil, and its melting temperature is practically the same at all mixing fractions of surfactant and oil. We also note that in each surfactant system, the solid melting temperature is practically the same upon changing oil from liquid paraffin to squalane. The melting behavior of the pure surfactant was observed in WAXS patterns, in which there appeared one sharp peak in a wide-angle regime at lower temperatures whose position ( $q$ -value)

corresponds to the characteristic distance  $\sim 0.42$  nm in real space (see [58]). This high- $q$  peak is the signature of solid state of surfactant that arises from the crystalline structure of the hydrophobic tail. It diminished at a temperature between 25 and 35°C. The solid showed a lamellar structure in the SAXS region, whereas a strong single peak was observed in the WAXS region [58]. Hence this crystal is considered to be  $\alpha$ -solid or  $L_\beta$  crystal [59–62]. After disappearance of the WAXS peak at and above 35°C, an equidistant sharp reflection in the small-angle region ( $q < 2$ ) was observed. This indicates solid to liquid crystal phase transition.

After the solid surfactant is melted, a liquid crystal is formed, whose structure was identified as a lamellar liquid crystal ( $L_\alpha$ ), as confirmed by SAXS. It was found that the  $L_\alpha$  phase solubilizes some amount of oil and gets swollen, but with successive addition of oil, a two-phase region consisting of excess oil and the  $L_\alpha$  phase is obtained. In the two-phase region, the interlayer spacing was unchanged with oil concentration [58]. In all the systems, the  $L_\alpha$  phase is formed in a concentrated region after melting of the solid phase and vesicular dispersions in the dilute regions at temperatures between the solid melting temperature and isotropic two-or single-phase regions (see Fig. 9.2). With further increasing temperature, isotropic solutions of reverse micellar phase are observed.

### 9.3 Non-aqueous Foaming Properties

Non-aqueous foaming properties of the dilute systems of mono- and diglycerol fatty acid esters in different oils is discussed here. The foam formation capacity (foamability) and the foam life after the foam formation (foam stability) were measured in different surfactant/oil systems depending on the solvent and surfactant molecular structure, surfactant concentration and temperature. Furthermore, the effect of trace water addition on the non-aqueous foaming properties was investigated. The foam stability was determined in the following way. Around 20 g of surfactant dispersion in oils was placed into a special glass bottle and made airtight. Liquid petroleum gas to  $\sim 20$  wt% was then added, shaken and the content extruded into a measuring cylinder. The variations in foam height and the drained liquid were measured against time at different temperatures.

#### 9.3.1 Effect of Solvent Molecular Structure

In order to investigate the effect of solvent molecular structure on the non-aqueous foaming properties, diglycerol monomyristate ( $C_{14}G_2$ ) was chosen and oils were varied from liquid paraffin to squalene via squalane. Additionally, foaming of the  $C_{14}G_2$ /olive oil system was studied. Liquid paraffin is a blend of hydrocarbons with average carbon number 23. Squalene and squalane are branched unsaturated and saturated oils. The dilute system of  $C_{14}G_2$  in liquid paraffin formed highly stable foams at 25°C. Foam produced by the 5 wt%  $C_{14}G_2$ /liquid paraffin system was stable for more than 12 h [54]. As can be seen in Fig. 9.3a, the system has the ability to produce a huge volume of foams. This indicates that the system can be a potential candidate for practical applications, where high foam volume is required. Next, the foam height appears to be unchanged even after 12 h, i.e. foams are super-stable. Close inspection of the foams after 12 h reveals that foam cavities are formed in the bulk but the original outer structure is retained even for several days. It

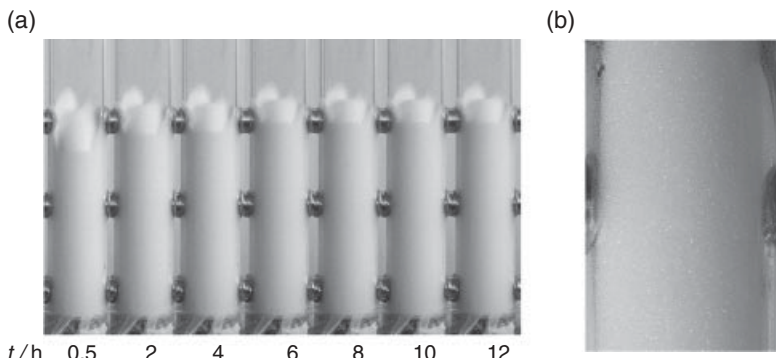


**Fig. 9.3** (a) Evolution of foam volume with time in 5 wt%  $C_{14}G_2$ /liquid paraffin system, and (b) enlarged picture of the foam taken after 11.5 h. Adapted with permission from Ref. [54], Taylor & Francis.

can be said that the foam lamella has high rigidity. Figure 9.3b shows a closer view of the foam observed after 11.5 h of foam formation. We note that a narrow distribution of the bubble size remains even after a long time.

Foam stability of the 5 wt%  $C_{14}G_2$ /squalene system was comparable with that of the  $C_{14}G_2$ /liquid paraffin system. Here again foam was stable for ~12 h. From visual observation we found a similar quality of foams in both the systems. Narrow distributions of foams continued to exist for several hours and the foam bubbles were less polydispersed. Thus the results showed that changing oil from liquid paraffin to squalene does not change the foaming property. However, surprisingly, when these oils are replaced with squalane, the foaming property is dramatically changed. The 5 wt%  $C_{14}G_2$ /squalane system could not produce stable foams. The foams collapsed soon after the foam was produced. Visually, it was found that the foam bubble sizes are very big with no use in practical applications. Thus from these results, it can be inferred that solvent molecular structure plays a dominant role in non-aqueous foaming properties.

A question then arose: why the  $C_{14}G_2$  surfactant could not produce stable foam in squalane? Since the foaming properties can generally be explained by interfacial properties, we anticipated that the interfacial properties of this system might be different from the stable foaming systems. However, as described earlier, the values of surface tension of organic solvents are already very low and the addition of surfactants did not change the surface tension of oils significantly. So, the surface tension properties may not explain the foaming properties of the present systems. Therefore anticipating that the phase behavior might have some contribution, we compared the phase behavior of the  $C_{14}G_2$  in the foaming and non-foaming oil. Nevertheless, the phase behaviours of the highly stable foaming ( $C_{14}G_2$ /liquid paraffin and  $C_{14}G_2$ /squalene) and non-foaming ( $C_{14}G_2$ /squalane) systems are quite similar. Both the foaming and non-foaming systems are essentially the dispersions of  $\alpha$ -solid at 25°C (see Fig. 9.2). Thus the phase behaviour also could not explain the discrepancy in the foaming behaviour of the  $C_{14}G_2$  in liquid paraffin and squalane. Then we took optical micro images of the solid dispersions in liquid paraffin, squalene and squalane, and also measured the average particle size. With this, we end up with a conclusion that particle size is very important in the particle-stabilized foaming systems. Figure 9.4 shows

the optical micrographs of 5 wt%  $C_{14}G_2$ /oil systems at 25°C and also a micro image of foam stabilized by  $\alpha$ -solid particle.

The optical photomicrographs clearly show the dispersions of the small micron size  $\alpha$ -solid and  $L_\alpha$  particles in highly foaming systems. The length and diameter of the individual micro-rods are less than 20 and 5  $\mu\text{m}$ , respectively. On the other hand, in the non-foaming  $C_{14}G_2$ /squalane system, the micro-rods and  $L_\alpha$  particles are coagulated, forming giant clusters; the cluster size is much larger than particles in the foaming systems. These clusters tend to settle down and it is difficult to produce stable foams.

As mentioned earlier, 5 wt%  $C_{14}G_2$ /oil systems are essentially the dispersion of  $\alpha$ -solid or  $L_\alpha$  particles. It was found that when the samples are undisturbed for a few hours, most or all the particles settle down and there is no foaming from the supernatant phases, which are pure oils. This observation highlights the fact that the systems must contain particles ( $\alpha$ -solid or  $L_\alpha$  particles) to make stable foams. These particles tend to adsorb at the gas–liquid interface and stabilize the foams. As can be seen in Fig. 9.4, the foam bubble is encircled by the particles and the particles are also dispersed in the continuous medium. The adsorption of these particles at the surface makes the gas–oil interface rigid and avoids bubble coalescence when the bubbles approach each other due to the liquid drainage. This may also reduce the gas diffusion and avoid Ostwald's ripening effect. Besides,

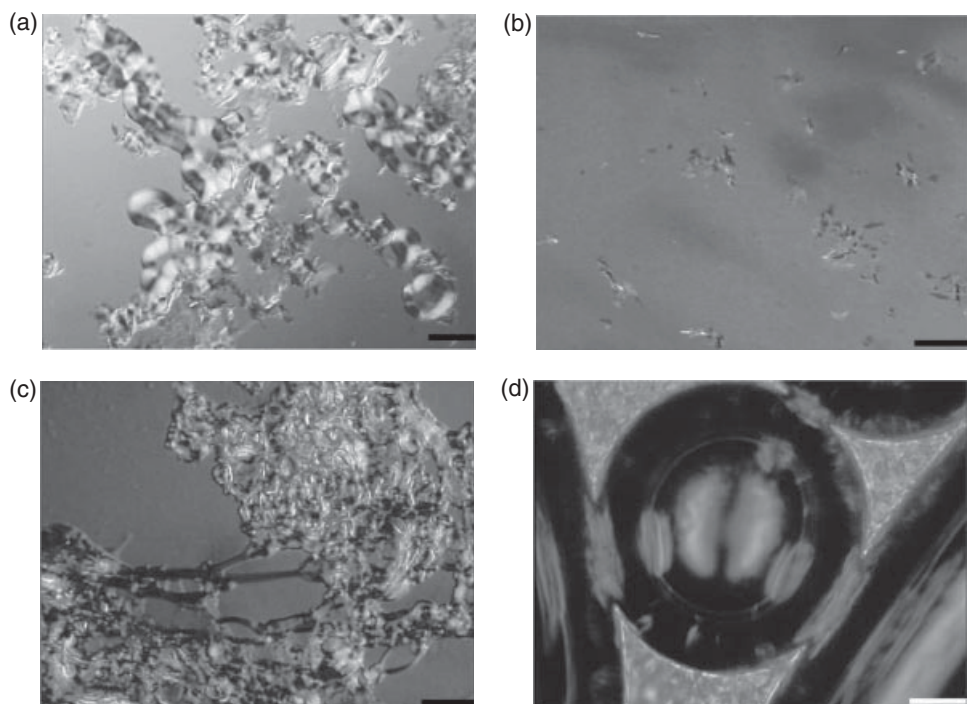


**Fig. 9.4** Micrographs of dispersed surfactant solid in different oils: (a) 5 wt%  $C_{14}G_2$ /liquid paraffin, (b) 5 wt%  $C_{14}G_2$ /squalene, (c) 5 wt%  $C_{14}G_2$ /squalane, and (d) non-aqueous foam stabilized by  $\alpha$ -solid. The scale bar is 20  $\mu\text{m}$ . Adapted with permission from Ref. [54], Taylor & Francis.

as naturally expected, dispersion of particles in any liquid increases the viscosity. As a result, the liquid drainage decreases, and foams are stable.

### 9.3.2 Effect of Surfactant Concentration

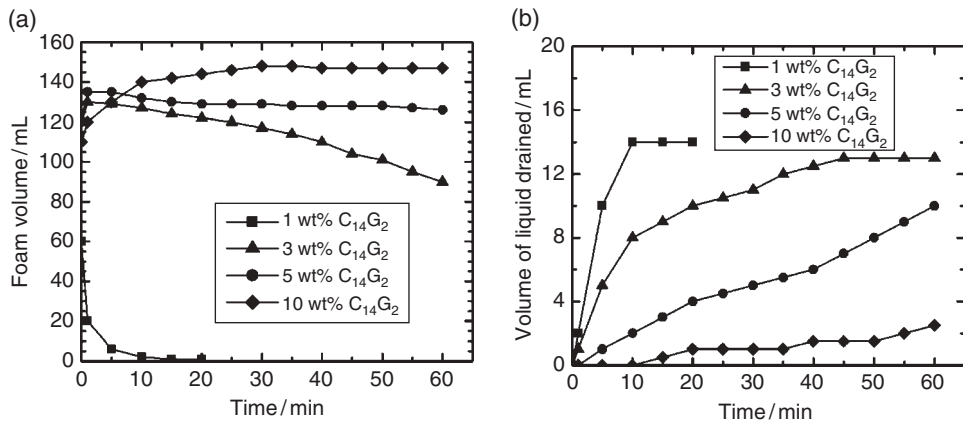
The effect of surfactant concentration on the foamability and foam stability of  $C_{14}G_2$  in olive oil at 25°C is discussed. The effect of surfactant concentration on the foaming properties of the  $C_{12}G_2$ /olive oil and  $C_{12}G_1$ /squalane systems are discussed in section 9.3.3.2 and 9.3.4 respectively. Olive oil is a triglyceride oil and used in the formulation of food and cosmetics products. Therefore foaming from this system would offer various practical applications. First we discuss the foam formation capacity of the  $C_{14}G_2$ /olive oil system at different surfactant concentrations. Table 9.1 shows the concentration dependence of foamability in the dilute regions (1–10 wt%).

Table 9.1 shows that foamability increases with increasing surfactant concentration from 1 to 3 wt% and then levels off [63]. The improved foamability may be due to the action of surfactant molecules (molecular adsorption to the interface) or adsorption of the  $\alpha$ -solid particles at the surface or both. The systems are the dispersions of the  $\alpha$ -solid in the dilute regions [64] and, due to the complexity of the system, it was difficult to distinguish the action of molecular adsorption or adsorption of particles. We will come to this point later on in the equilibrium surface tension section. From visual observation, better quality of foam (monodispersed spherical bubbles) were observed at higher concentrations. At lower concentration, say in a 1 wt%  $C_{14}G_2$ /olive oil system, foam bubble size was bigger and polydispersed with polyhedral shape.

Now we discuss the effect of surfactant concentration on the foam stability studied at 25°C. Figure 9.5 shows the results of foam stability: changes in foam volume and liquid drained versus time, at different surfactant concentrations. As can be seen in Fig. 9.5a, foam stability depends on surfactant concentration, showing an outstanding stability at higher concentrations. Although the data up to 60 min are shown in Fig. 9.5a, at higher concentrations (> 5 wt%) the foams were stable for several weeks without affecting the foam structure. At lower concentration (1 wt%  $C_{14}G_2$ ), random foam breakage started immediately after the formation of foam, and all the foams collapsed after 20 min. We noted that at and above 3 wt% surfactant, foam height increases after the foam generation, attains equilibrium value, and then decreases. It seems that the foam formation process continued even if we stopped foam generation. It is also possible that the foam bubbles grow with time.

**Table 9.1** Effect of surfactant concentration on the foamability of  $C_{14}G_2$ /olive oil systems at 25°C: the total foam volume produced by the systems at time  $t = 0$  min (directly after the foam generation) at different surfactant concentrations.

Systems	Foam volume (ml)
1 wt% $C_{14}G_2$ /olive oil	$60 \pm 5$
3 wt% $C_{14}G_2$ /olive oil	$120 \pm 6$
5 wt% $C_{14}G_2$ /olive oil	$120 \pm 5$
10 wt% $C_{14}G_2$ /olive oil	$110 \pm 6$



**Fig. 9.5** (a) Foam volume and (b) volume of liquid drained versus time for  $C_{14}G_2$ /olive oil system at different surfactant concentrations at 25°C. In the figure, foam volume up to 1 h is presented; however, foams produced by the 10 wt%  $C_{14}G_2$ /olive oil system are stable for more than a month. Adapted with permission from Ref. [63], Elsevier.

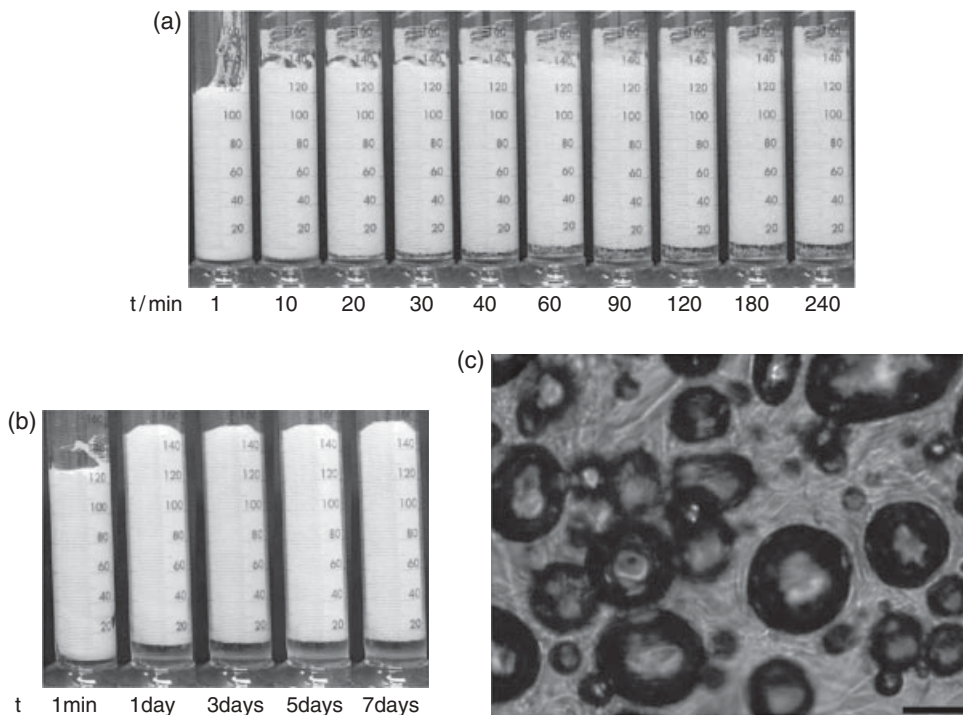


**Fig. 9.6** Evolution of foam volume with time for  $C_{14}G_2$ /olive oil systems at 25°C: (a) 5 wt%  $C_{14}G_2$ /olive oil, (b) 10 wt%  $C_{14}G_2$ /olive oil system, and (c) optical micrograph of 10 wt%  $C_{14}G_2$ /olive oil system foams taken after 24 h. In (c), the scale bar represents 20  $\mu\text{m}$ . Adapted with permission from Ref. [63], Elsevier.

Coming to the liquid drainage, it was found that the drainage decreases with increasing surfactant concentration. As can be seen in Fig. 9.5b, ~95% of liquid has drained off within 20 min in the 1 wt%  $C_{14}G_2$  system; however, it took ~1 h for the 80% liquid to drain off in the 3 wt%  $C_{14}G_2$  system. Interestingly, only 20% liquid has drained off in 1 h in the 10 wt%  $C_{14}G_2$  system. This indicates that the liquid holding capacity of the foams increases with increasing surfactant concentration and due to the higher volume fraction of liquid in the foams; the wet foams persist for a long period of time.

Figure 9.6 shows the digital images of foams versus time for the 5 and 10 wt%  $C_{14}G_2$  systems in different time scales. There is not a significant change in foam volume even after 4 h in the 5 wt%  $C_{14}G_2$ /olive oil system (see Fig. 9.6a). Minute observation reveals that ~95% of liquid drains off after 3 h and foams become dry and rigid. As the time passes by, foams at the bottom of the cylinder contain relatively a large amount of liquid (wet foams) and possess nearly spherical shape. On the other hand, foams at the top of cylinder are relatively dry with polyhedral foam cells and are polydispersed.

Foams with a narrow bubble size distribution can be seen in the 10 wt%  $C_{14}G_2$ /olive oil system. Most of the liquid drains off after 24 h and after that there is no net change in the foam height even after a week. Visual inspections showed that although the foams become dry, a less polydispersed foam bubble continues to persist for several weeks. In Fig. 9.6b, we show images up to one week, but the foam was stable for more than a month. As mentioned earlier, a dilute system of  $C_{14}G_2$ /olive oil is essentially a dispersion of solid at 25°C [64] and hence appears as a turbid solution, but we can see a clear solution in the drained liquid. This indicates that the solid particles remain in the foam and are responsible for the foam stabilization. Wide-angle X-ray scattering confirmed the structure of solid as  $\alpha$ -crystal.

The optical micrograph of the foam stabilized solid particles in 10 wt%  $C_{14}G_2$ /olive oil was taken after 24 h and presented in Fig. 9.6c, which shows that the foam structure is retained by the system. We can still see the spherical shape of the foam bubbles with some polydispersity in size. Of course, this may not be the true shape and size of the foams as we put the foams on microscopic slides mounted by a thin glass plate. The process may change the structure of the foams. We can see the dispersion of small particles around the bubbles and also in the continuous phase.

### 9.3.2.1 Particle Size Distribution

We have also measured particle size versus surfactant concentration using laser diffraction technique. Figure 9.7 shows the average particle size and distribution of solid particles at different surfactant concentrations. One can see a broad distribution in the size of the particles in the studied systems. Minute observation reveals that with increasing surfactant concentration the average particle diameter decreases. In the best foaming system (10 wt%  $C_{14}G_2$ ), the average particle diameter was found to be ~20  $\mu\text{m}$ . On the other hand, in the poor foaming system (1 wt%  $C_{14}G_2$ ), the average particle diameter was higher than 50  $\mu\text{m}$ . Judging from the foam stability and particle size distribution, a correlation between foam stability and particle size can be established namely, the smaller the particles the better the foam stability.

### 9.3.2.2 Rheological Properties of Particle Dispersion

The dynamic oscillatory-shear rheology of the solid particle dispersions were carried out at 25°C. Figure 9.8 shows the variation of elastic modulus ( $G'$ ) and viscous modulus ( $G''$ ) as

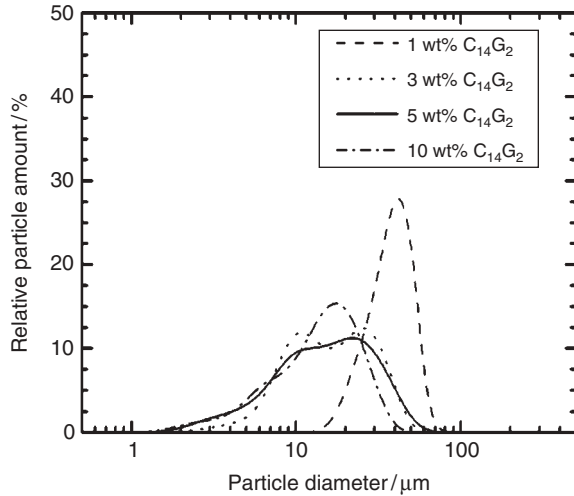


**Fig. 9.7** Particle size distribution of  $C_{14}G_2$ /olive oil systems at different surfactant concentrations at 25°C. Adapted with permission from Ref. [63], Elsevier.

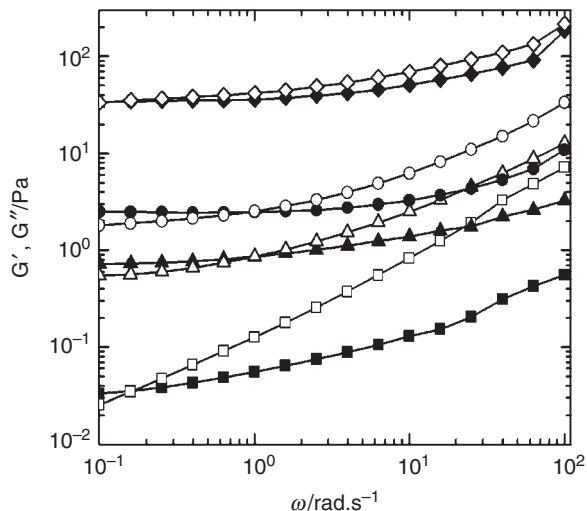


**Fig. 9.8** The effect of surfactant concentration on the dynamic oscillatory-shear rheological behavior of  $C_{14}G_2$ /olive oil systems at 25°C: variation of  $G'$  (filled symbols) and  $G''$  (open symbols) as a function of  $\omega$  at different surfactant concentrations. Squares, 1 wt%  $C_{14}G_2$ ; triangles, 3 wt%  $C_{14}G_2$ ; circles, 5 wt%  $C_{14}G_2$ ; diamonds, 7 wt%  $C_{14}G_2$ ; inverted triangles, 10 wt%  $C_{14}G_2$ . Adapted with permission from Ref. [63], Elsevier.

a function of oscillation frequency ( $\omega$ ) at different surfactant concentrations. As can be seen in Fig. 9.8, all the samples show a typical gel-like behavior, i.e., the samples show both elastic and viscous properties with  $G' > G''$  at lower  $\omega$  and  $G'' > G'$  at higher  $\omega$ . At a fixed surfactant concentration, both the elastic and the viscous modulus increases with increasing  $\omega$  with a cross over of  $G'$  and  $G''$ . We note that increasing surfactant concentration

**Table 9.2** Equilibrium surface tension and equilibrium phase as a function of surfactant concentration for  $C_{14}G_2$ /olive oil system. The surface tension of measurements was carried out at 25°C.

System	$\gamma_{25^\circ\text{C}}$ (mN/m)	Equilibrium phase
Olive oil	32.1	I phase
0.2 wt% $C_{14}G_2$ /olive oil	30.1	I phase
0.3 wt% $C_{14}G_2$ /olive oil	26.9	I phase
0.4 wt% $C_{14}G_2$ /olive oil	26.6	I phase
0.5 wt% $C_{14}G_2$ /olive oil	26.4	I phase
1 wt% $C_{14}G_2$ /olive oil	26.4	II phase (solid dispersion)
2 wt% $C_{14}G_2$ /olive oil	25.8	II phase (solid dispersion)
3 wt% $C_{14}G_2$ /olive oil	24.4	II phase (solid dispersion)
5 wt% $C_{14}G_2$ /olive oil	24.1	II phase (solid dispersion)
10 wt% $C_{14}G_2$ /olive oil	24.2	II phase (solid dispersion)

increases  $G'$  and  $G''$ , i.e. both the elastic and viscous properties of the system increase with particle concentration. This is in a good agreement with the foaming properties that the drainage is too slow and foams are super-stable at higher concentrations. From these results it can be concluded that increasing surfactant concentration decreases the particle size, which in effect increases elastic and viscous properties of the systems and stabilizes foams.

### 9.3.2.3 Equilibrium Surface Tension

We have measured equilibrium surface tension of the  $C_{14}G_2$ /olive oil systems as a function of surfactant concentration at 25°C and the results are summarized in Table 9.2. It was found that the decreasing in surface tension value with increasing surfactant concentration is not a straightforward mechanism. As can be seen in Table 9.2, surface tension decreases with increasing surfactant concentration from 0.2 to 0.5 wt%, and then remains constant up to 1 wt%. With further increasing concentration, surface tension decreases up to 5 wt% and then attains a constant value. A detailed phase behaviour study showed a miscibility gap at 0.5 wt%. An isotropic single-phase solution appeared up to 0.5 wt% surfactant and then a dispersion of solid particles above this concentration. We note that the decrease of surface tension value up to 0.5 wt% surfactant is caused by the molecular adsorption of the soluble surfactant to the surface. The constant surface tension value with increasing concentration from 0.5 to 1 wt% is the result of phase separation to the solid phase. A further decrease of surface tension above 1 wt% surfactant can be attributed to adsorption of solid particles to the surface to form an insoluble monolayer at the surface. Note that the solid particles could reduce the surface tension of oil by ~25%. From these observations it is obvious that the solid particles have a strong tendency to adsorb at the surface and stabilize foams.

### 9.3.3 Effect of Hydrophobic Chain Length of Surfactant

The effect of surfactant molecular structure on the non-aqueous foaming properties was studied in different oils. First we discuss the foaming in liquid paraffin, squalene and squalane, and then we discuss foaming in olive oil.

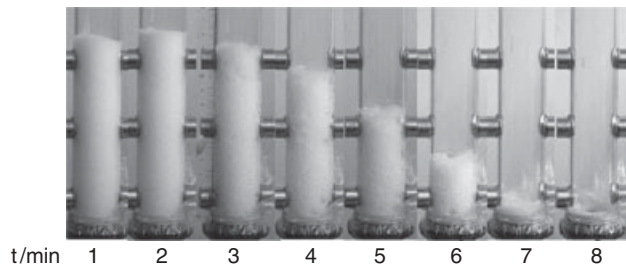


**Fig. 9.9** Evolution of foam volume with time for the 5 wt%  $C_{12}G_2$ /liquid paraffin system at 25°C. Adapted with permission from Ref. [54], Taylor & Francis.

### 9.3.3.1 Foaming of $C_{12}G_2$ in Liquid Paraffin, Squalene, and Squalane

Foaming properties of diglycerol monolaurate ( $C_{12}G_2$ ) in liquid paraffin, squalene and squalane were studied at 25°C and the results were compared with the  $C_{14}G_2$  oil systems. Non-aqueous foam stability was found to decrease with decreasing hydrocarbon chain of the surfactant. Figure 9.9 shows the digital images of foam versus time for 5 wt%  $C_{12}G_2$ /liquid paraffin system.

Foam produced by the  $C_{12}G_2$ /oil systems was stable only for few minutes. On the other hand, foams with the  $C_{14}G_2$ /oil systems were stable for several hours. As can be seen in Fig. 9.9, foam produced by the  $C_{12}G_2$ /liquid paraffin system coarsened quickly, leading to progressive destruction, and almost all the foams are destroyed within 8 min [54]. Similarly, in the  $C_{12}G_2$ /squalene system, the coarsening and foam destruction occurred even more rapidly than in the  $C_{12}G_2$ /liquid paraffin system. Unlike in  $C_{14}G_2$ , the  $C_{12}G_2$  produced foam with squalane and the foam was stable for ~30 min. However, foamability of this system was low compared to other two systems:  $C_{12}G_2$ /liquid paraffin and  $C_{12}G_2$ /squalene systems. The difference in the foam stability depending on the hydrocarbon chain length of surfactant can be attributed to the phase transition of solid to lamellar liquid crystal particle.

### 9.3.3.2 Foaming of $C_{12}G_2$ in Olive Oil

Here, first, we describe the foamability of the  $C_{12}G_2$ /olive oil system at different surfactant concentrations in dilute region (1–10 wt%  $C_{12}G_2$ ) at 25°C and then we describe the foam stability. In aqueous systems, foamability depends on the ability of a surfactant to attain a low surface tension in a short time, i.e. the faster the adsorption of the surfactant to the newly created interface, the better the foamability. Moreover, it has been observed that the maximum foamability occurs at concentrations  $\geq$  critical micelle concentration (*cmc*) and that the foamability is the larger the lower the *cmc* of the surfactant [29]. Thus the foamability depends on the nature and the concentration of the surfactant. However, the present systems are essentially the dispersion of liquid crystal and thus the basic theory of aqueous system may be applied. It was found that foamability increases with increasing surfactant concentration up to 3 wt%, which is in agreement with the generally accepted trends in aqueous systems, but with further increasing surfactant concentration, it tends to decrease (see Table 9.3). Visually, better qualities of foams were observed at higher concentrations. At 1 wt%  $C_{12}G_2$  system, the foam's bubble sizes were bigger and polydispersed with

**Table 9.3** Effect of surfactant concentration on the foamability of  $C_{12}G_2$ /olive oil systems at 25°C: the total foam volume produced by the systems at time  $t = 0\text{ min}$  (directly after the foam generation) at different surfactant concentrations.

Systems	Foam volume (ml)
1 wt% $C_{12}G_2$ /olive oil	30 ± 4
3 wt% $C_{12}G_2$ /olive oil	200 ± 6
5 wt% $C_{12}G_2$ /olive oil	180 ± 5
10 wt% $C_{12}G_2$ /olive oil	120 ± 5

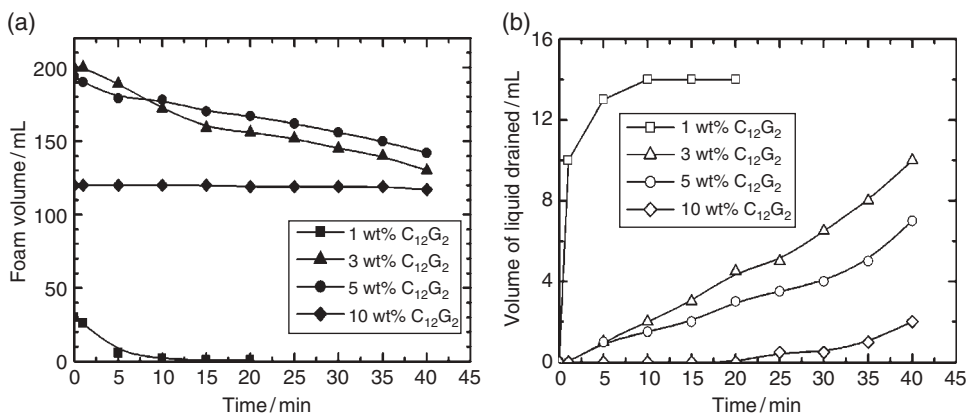


**Fig. 9.10** (a) Foam volume and (b) volume of liquid drained versus time for the  $C_{12}G_2$ /olive oil system at different surfactant concentrations at 25°C. Adapted with permission from Ref. [56], Elsevier.

polyhedral shape. As the surfactant concentration was increased, the polydispersity decreased and viscous foams with almost spherical foam bubbles were observed. Such foams can have a significant practical application in food and cosmetic industries.

Now we describe the effect of surfactant concentration on the foam stability of the  $C_{12}G_2$ /olive oil system. Figure 9.10 shows the changes in foam volume and drained liquid versus time at different concentrations at 25°C. Foams with olive oil were stable for a few minutes to several hours depending on the  $C_{12}G_2$  concentrations. In the 1 wt%  $C_{12}G_2$ /olive oil system, foam breakage started immediate after foam formation and since the drainage rate was high, all the foams were collapsed after 20 min. Foam stability was improved with increasing  $C_{12}G_2$  concentration. Foams produced by the 10 wt%  $C_{12}G_2$  system were stable for more than 6 h.

The decreasing liquid drainage with increasing  $C_{12}G_2$  can be clearly seen in Fig. 9.10b. Approximately 95% liquid drained off within 10 min in the 1 wt%  $C_{12}G_2$  system; however, it took ~30 min for 50% liquid to drain off in the 3 wt%  $C_{12}G_2$  system. Interestingly, no liquid was drained off within 20 min in the 10 wt%  $C_{12}G_2$  system. This indicates that the liquid holding capacity of the foams increases with  $C_{12}G_2$  concentration, as a result, wet foams persist for a long period of time in concentrated systems.

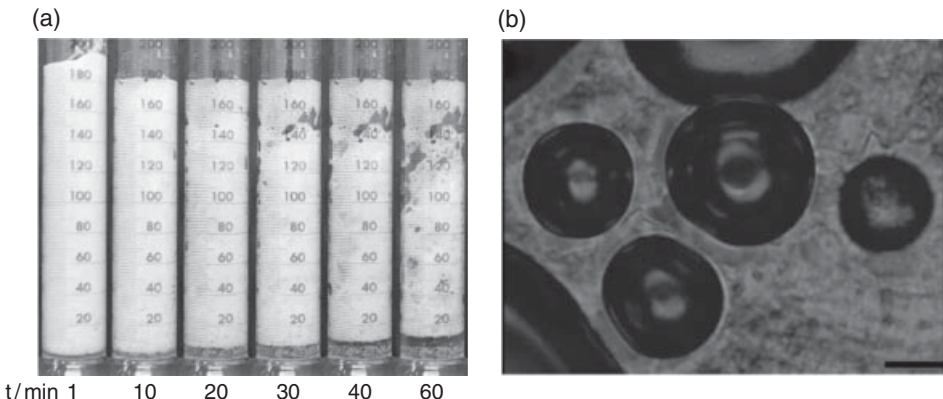


**Fig. 9.11** (a) The evolution of foam volume with time for the 5 wt%  $C_{12}G_2$ /olive oil systems at 25°C and (b) an optical micrograph of 10 wt%  $C_{12}G_2$ /olive oil foams stabilized by  $L_\alpha$  particles. In (b), the scale bar represents 20  $\mu\text{m}$ . Adapted with permission from Ref. [56], Elsevier.

In Fig. 9.11, we present digital images of foams taken at different intervals of time for the 5 wt%  $C_{12}G_2$  system. As can be seen in the images, as time passes by, wet foam appears only at the bottom of the cylinder. Foams at the top of cylinder are relatively dry, with polyhedral foam cells. Due to thin foam films, random foam breakage started after 30 min. Although complete foam breakage took nearly 3 h the image up to 1 h is shown in Fig. 9.11a.

Visually, viscous foams with a narrow distribution in the foam bubbles were observed with a 10 wt%  $C_{12}G_2$ /olive oil system. The foam bubbles were almost homo-dispersed with a uniform polyhedral size. Phase behavior study has shown that the  $C_{12}G_2$  forms  $L_\alpha$  dispersion in olive oil in the dilute region at 25°C [64]. Previously, it has been shown that the liquid crystal phase adsorb at the gas–liquid interface due to its low surface tension than the corresponding solution of similar composition and stabilizes the foams [49–52]. Highly stable non-aqueous foams observed in the present systems are the contribution of the liquid crystal particles, which tend to adsorb at the interface and stabilize the foams by increasing mechanical rigidity of the interface. Besides, the viscosity of the continuous phase increases, which consequently decreases the liquid drainage and increases the foam life.

Figure 9.11b shows the optical micrographs of the non-aqueous foams stabilized by  $L_\alpha$  particles in the 10 wt%  $C_{12}G_2$ /olive oil system. Foam bubbles are surrounded by the  $L_\alpha$  particles, showing the tendency of the  $L_\alpha$  particles to adsorb at the gas–liquid interface, which in turn increase the mechanical rigidity of the interface increases; as a result, the bubble coalescence is less likely to occur. Besides, the collection of the particles at the Plateau border increases the viscosity, controls the liquid drainage and stabilizes the foams.

**Average size of the  $L_\alpha$  particles.** Figure 9.12 shows the particle size distribution of the  $C_{12}G_2$ /olive oil system as a function of surfactant concentration. Similar to the monomyristate/oil systems, the average particle size of the dispersed  $L_\alpha$  particles decreased with increasing

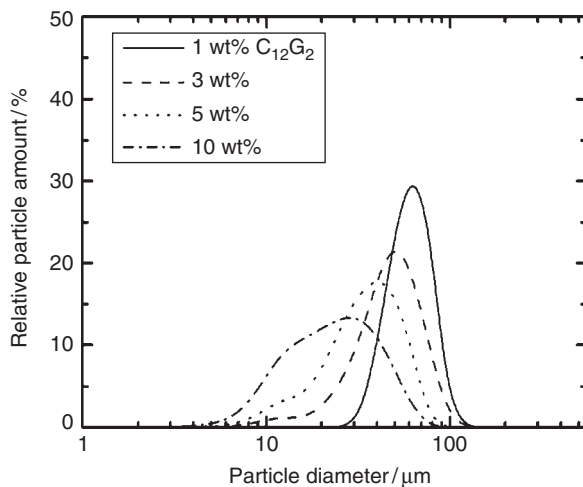


**Fig. 9.12** Particle size distribution of the  $C_{12}G_2$ /olive oil system at different surfactant concentrations at 25°C. Adapted with permission from Ref. [56], Elsevier.

surfactant concentration, again indicating that the dispersion of smaller particles would give better stable foams. The average particle diameter was found to be  $\sim 25\text{ }\mu\text{m}$  in the best foaming system, i.e. the 10 wt%  $C_{12}G_2$ /olive oil system.

**Rheological behavior of  $L_\alpha$  particle dispersion.** Figure 9.13 shows the variation of elastic modulus ( $G'$ ) and viscous modulus ( $G''$ ) as a function of oscillation frequency ( $\omega$ ) for  $C_{12}G_2$ /olive oil systems at different surfactant concentrations at 25°C. At 1 wt% surfactant, the system shows viscous properties with  $G''$  higher than  $G'$  throughout the studied  $\omega$  region. At higher surfactant concentrations at and above 3 wt% surfactant, the systems show viscoelastic properties with a crossover of  $G'$  and  $G''$  at lower  $\omega$  ( $<1\text{ rad/s}$ ). As can be seen from Fig. 9.13, both  $G'$  and  $G''$  increase with increasing surfactant concentration from 1 to 3 wt% and then decrease with further increasing concentration from 3 to 10 wt%. A similar result was obtained in the viscosity ( $\eta$ ) versus shear rate ( $\gamma$ ) curves [56]. All the samples exhibit shear-thinning behaviour with plateau values at lower shear rate. The viscosity value in the Plateau region followed a discontinuous trend with surfactant concentration; first it was increased but afterwards decreased. However, foam stability was increased continuously. This shows that only viscosity does not play a major role in the foam stabilization mechanism, at least in the studied systems.

**Equilibrium surface tension.** The equilibrium surface tension of olive oil and the liquid crystal dispersion as a function of surfactant concentrations were measured at 25°C and the results are presented in Table 9.4. We noted that the addition of the  $C_{12}G_2$  (1–10 wt%) reduces the surface tension of olive oil only to a small extent. Since the difference in the surface

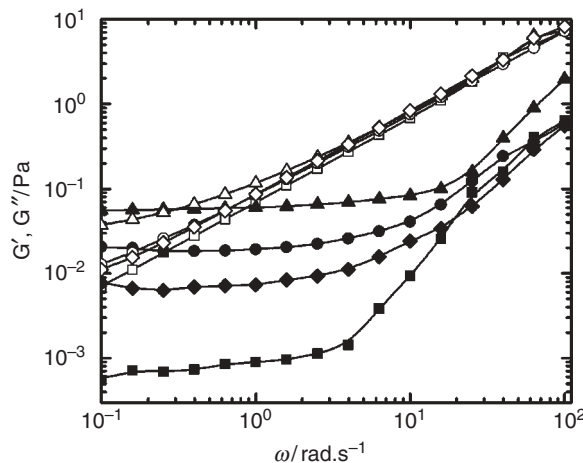


**Fig. 9.13** Variation of elastic modulus ( $G'$ ) and viscous modulus ( $G''$ ) as a function of frequency ( $\omega$ ) for the  $C_{12}G_2$ /olive oil system at different surfactant concentrations at  $25^\circ\text{C}$ .  $G'$ , closed symbols;  $G''$ , open symbols. Squares, 1 wt%  $C_{12}G_2$ ; triangles, 3 wt%  $C_{12}G_2$ ; circles, 5 wt%  $C_{12}G_2$ ; diamonds, 10 wt%  $C_{12}G_2$ . Adapted with permission from Ref. [56], Elsevier.

**Table 9.4** Equilibrium surface tensions of olive oil and  $C_{12}G_2$  dispersion at different surfactant concentration. All the measurements were carried out at  $25^\circ\text{C}$ . Adapted with permission from Ref. [56], Elsevier.

System	$\gamma_{25^\circ\text{C}}$ (mN/m)
Olive oil	32.1
1 wt% $C_{12}G_2$ /olive oil	26.9
3 wt% $C_{12}G_2$ /olive oil	26.2
5 wt% $C_{12}G_2$ /olive oil	26.4
10 wt% $C_{12}G_2$ /olive oil	26.4

**Table 9.5** Summary of the stability of non-aqueous foam in 5% surfactant/oil systems.

Surfactants	Oils			
	Liquid paraffin	Squalene	Squalane	Olive oil
$C_{14}G_2$	Super stable > 12 h	Super stable > 12 h	Unstable	Stable > 4 h
$C_{12}G_2$	Meta stable < 8 min	Meta stable < 5 min	Stable ~ 30 min	Stable ~ 1 h

tension value is low, there might be a little or no Gibbs–Marangoni foam stabilization mechanism in this system. However, a slight decrease in the surface tension value unambiguously shows that the  $L_\alpha$  particles have a tendency to adsorb at the gas–liquid interface and are responsible for stabilizing the foams. Table 9.5 summarizes the foam stability of  $C_{14}G_2$  and  $C_{12}G_2$  in variety of oils at  $25^\circ\text{C}$ .

### 9.3.4 Effect of Headgroup Size of Surfactant

In this section, we discuss the effect of the hydrophilic headgroup size of the surfactant on the non-aqueous foaming properties. The hydrocarbon chain length of surfactant was fixed and the headgroup size was reduced from diglycerol to monoglycerol. Foam stability of monolaurin ( $C_{12}G_1$ ) in liquid paraffin, squalane and squalene was dramatically increased compared to the  $C_{12}G_2$  systems. Foams were stable for more than 12–14 h depending on the oils [57]. Dilute systems of  $C_{12}G_1$  in the aforementioned oils are the dispersions of solid as confirmed by phase behaviour [65]. WAXS measurements have confirmed the structure of solid to be  $\beta$ -crystal [57]. Note that in the  $C_{12}G_2$ /oil systems foam was stabilized by  $L_\alpha$  particles and the foams were stable only for a few minutes. Judging from phase and foaming results, it can be concluded that reducing the headgroup size of the surfactant from di- to monoglycerol causes structural transition of  $L_\alpha$  to  $\beta$ -solid and foams are super-stable in the latter systems. Optical microscopy has shown that the shape of the dispersed  $\beta$ -solid particle also plays a crucial role in the non-aqueous foaming properties. We will come to this point later on.

Figure 9.14 shows the changes in foam volume and drained liquid as a function of time for the 5 wt%  $C_{12}G_1$ /oil systems at 25°C. The normalized foam volume versus time at different surfactant concentrations in a particular oil system is also presented. Although the complete destruction of foams took more than 12 h, the foam volume only up to 6 h is presented. After 6 h of foam formation, the foam became dry and there was a wide distribution in shape and size of the foam bubbles. Moreover, due to the formation of cavities inside the foams, the foam volume could not be measured accurately. Foam stability was increased upon changing oil from squalene to squalane via liquid paraffin. The rate of decrease of foam volume was high in squalene compared to other oils. As can be seen in Fig. 9.14, foam volume decreases rapidly until the volume of the liquid drained reaches its maximum and afterwards slow down. We note that the decrease in the foam volume at the initial stage is due to bubble compaction, not due to bubble coalescence. It was observed that the drainage rate was high and reached its plateau value within 1 h in the  $C_{12}G_1$ /squalene system, in which foam life was relatively low compared to the other two systems. However, the liquid drainage was slow and took nearly 4 h to reach its plateau value in the  $C_{12}G_1$ /liquid paraffin and the  $C_{12}G_1$ /squalane systems. After 6 h, drained liquid volume in the  $C_{12}G_1$ /squalene system was double of the  $C_{12}G_1$ /squalane system (see Fig. 9.14b). This indicates that the liquid holding capacity of the foam in the latter system is higher than that in the former system. Due to high volume fraction of the liquid thick foam film lamellae persist for a long time and foams are stable.

The effect of surfactant concentration on the non-aqueous foam stability was also studied in the  $C_{12}G_1$ /squalane system at 25°C. Foam stability was increased with increasing surfactant concentration. For example, in the 1 wt%  $C_{12}G_1$ /squalane system foam collapsed within 1 h; however, as the surfactant concentration was increased foam stability was improved and the foams produced from the 5 wt% and above surfactant systems are stable for more than 12 h.

Now we describe the effect of the hydrocarbon chain length of the surfactant on the non-aqueous foaming properties in monoglycerol fatty acid ester/oil systems. Similarly to the diglycerol systems, reducing hydrocarbon chain of the surfactant decreases the

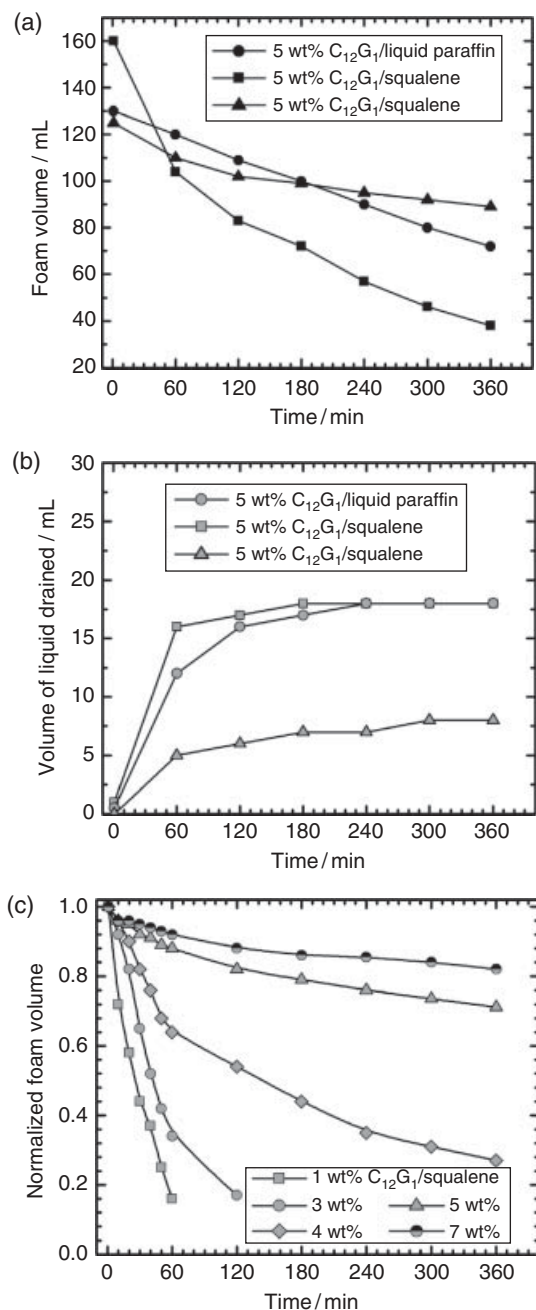


**Fig. 9.14** (a) Foam volume, (b) the volume of liquid drained versus time for the  $C_{12}G_1$ /oil systems at 25°C, and (c) normalized foam volume versus time at different surfactant concentrations for the  $C_{12}G_1$ /squalane system at 25°C. Adapted with permission from Ref. [57], American Chemical Society.

foam stability of the monoglycerol systems. For example, the foam stability of the  $C_{10}G_1$ /oil systems was reduced to 3–4 h depending on the oil [57]. With further reduction of the chain length, namely in the  $C_8G_1$ /oil systems, foams were stable for only a few minutes. Foams collapsed within 2 min. Phase behaviour studies have shown that there is dispersion of solid particles in the dilute regions of the monoglycerol fatty acid ester/oil systems [67]. However, as described, the foam stability was decreased with decreasing hydrocarbon chain of the surfactant or also dependent on the oil's molecular geometry. This phenomenon can be explained in terms of the structure of the solid particles. We took optical micrographs of the particle dispersions in different surfactant/oil systems. It was found that there is dispersion of a small micron-sized needle-shaped or rod-like solid crystal in the best foaming system, i.e.  $C_{12}G_1$ /squalane. On the other hand, there are dispersions of disk-like, flat and bulky crystals in the poor foaming systems, e.g. in  $C_{10}G_1$ /oil systems. It is possible that these bulky crystals may not be perfectly and tightly packed at the gas–liquid interface compared to the fine needle-shaped crystals; as a result foams are less stable. Figure 9.15 shows the optical micrographs of the particle dispersions in monoglycerol fatty acid esters of two different alkyl chain lengths in liquid paraffin, squalane and squalene at 25°C and also non-aqueous foam stabilized by dispersion of needle-shaped  $\beta$ -crystals.

### 9.3.5 Effect of Temperature

Phase behaviour studies of diglycerol surfactants in different oils have shown the presence of different phases depending on temperature. Therefore, we anticipate different foam stability at different temperature. Besides, as mentioned earlier, the  $C_{14}G_2$  could not produce stable foam with squalane at 25°C due to coagulation of  $\alpha$ -solid particles, which transforms into  $L_\alpha$  and micellar phases upon heating. Note that there are  $L_\alpha$  and micellar phases at 40 and 60°C, respectively [58, 66]. If the non-foaming behavior of this system at 25°C is caused due to coagulation of solid particles, then there must be foaming at higher temperatures from the dispersions of liquid crystal or reverse micellar phase. In order to quantify this anticipation, we have tested the foaminess of the  $C_{14}G_2$  in squalane and hexadecane at higher temperatures. Note that the  $C_{14}G_2$ /hexadecane system also could not produce stable foam at 25°C. Foams were produced following a similar method as was mentioned earlier, but at higher temperatures. As expected,  $C_{14}G_2$  produced a large volume of foams in both the oils at higher temperatures of 40 and 60°C. Therefore, the good foamability at higher temperatures can be attributed to the dispersion of smaller size  $L_\alpha$  particles or micellar solutions. This confirms that the non-foaming behaviour of these systems at lower temperature is indeed caused by the solid clusters. From the foam stability tests, it was found that the foams are stable for approximately 50 min in the 5 wt%  $C_{14}G_2$ /squalane system and about 30 min in the 5 wt%  $C_{14}G_2$ /hexadecane system at 40°C [55]. With further increasing temperature, say at 60°C, the foam stability was reduced to ~20 min. The changes in foam volume versus time for 5 wt%  $C_{14}G_2$ /squalane and 5 wt%  $C_{14}G_2$ /hexadecane systems at 40 and 60°C are presented in Fig. 9.16. At 40°C, stable foams could be achieved due to the dispersion of  $L_\alpha$  particles. On the other hand, the poor foam stability at 60°C is mainly caused due to the absence of liquid crystal particles.

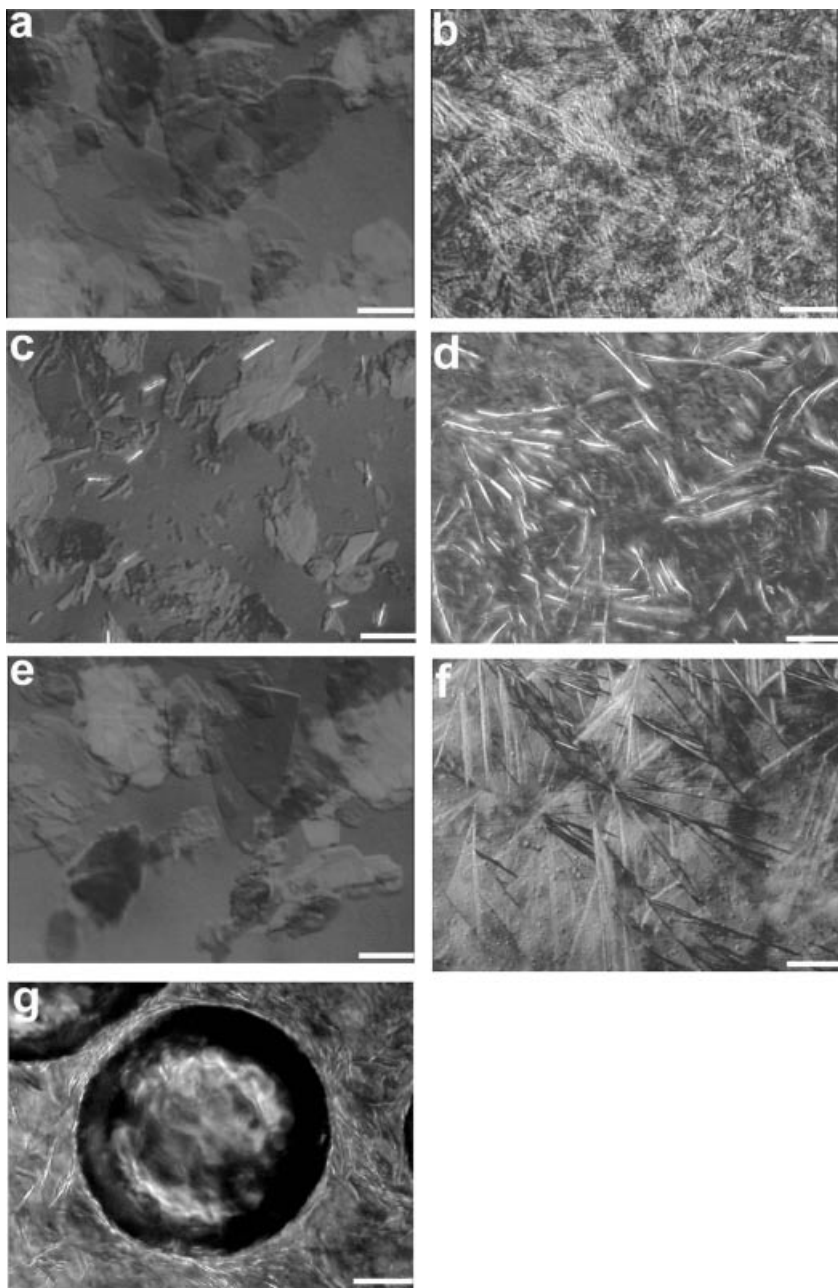


**Fig. 9.15** Optical micrographs of 5 wt% monoglycerol fatty acid ester/oil systems at 25°C: (a)  $C_{10}G_1$ /liquid paraffin, (b)  $C_{12}G_1$ /liquid paraffin, (c)  $C_{10}G_1$ /squalane, (d)  $C_{12}G_1$ /squalane, (e)  $C_{10}G_1$ /squalene, (f)  $C_{12}G_1$ /squalene, and (g) optical micrograph of 5 wt%  $C_{12}G_1$ /squalane foam stabilized by rod-like surfactant solid particles. The scale bar is 20  $\mu\text{m}$  for all of these images. Adapted with permission from Ref. [57], American Chemical Society.

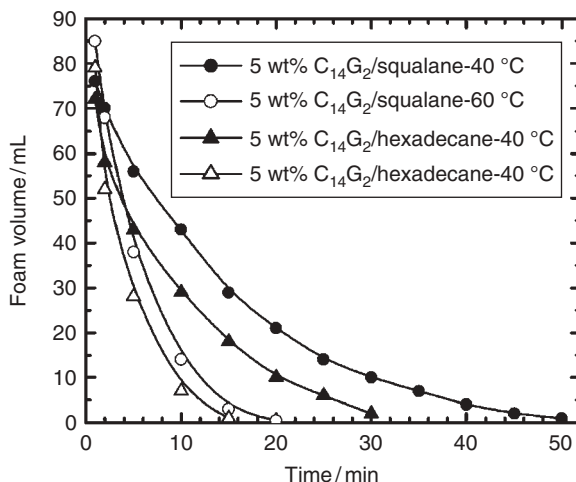


**Fig. 9.16** Foam volume versus time for the 5 wt%  $C_{14}G_2$ /oil systems at higher temperatures (40 and 60°C). Adapted with permission from Ref. [55], American Chemical Society.

### 9.3.6 Effect of Water Addition

The effect of water addition on foamability and foam stability was tested for different systems. We basically selected two types of systems: those that do not have ability to produce foams without water; and those that produce foams without water. In the following sections, we first discuss the effect of water addition on foamability and then on foam stability for different surfactant/oil systems.

#### 9.3.6.1 Effect of Water on Foamability

We have mentioned that  $C_{14}G_2$  could not produce foams in squalane and hexadecane at 25°C due to the formation of clusters of solid particles. On the other hand, although foam was stable for 30 min, foamability of the  $C_{12}G_2$ /squalane system was very low. We have tested the effect of water addition on the foam formation capacity of these systems and found that water improves the foamability system; the foamability increases with increase in the water concentration [55]. For example, the addition of 1% water in the 5 wt%  $C_{14}G_2$ /squalane system produced a very small volume of foam but the foam volume increased to 100 ml upon addition of 3% water. The effects of added water on the foamability of the 5 wt%  $C_{12}G_2$ /squalane, 5 wt%  $C_{14}G_2$ /squalane and 5 wt%  $C_{14}G_2$ /hexadecane systems are summarized in Table 9.6.

As can be seen in Table 9.6, foamability of the 5 wt%  $C_{14}G_2$ /hexadecane system increases with water concentration. Approximately 80 ml of foam is produced by the addition of 3% water, while there is less than 3 ml of foam without water. As it was described previously, dilute systems of  $C_{14}G_2$  in squalane and hexadecane are the dispersions of  $\alpha$ -solid and the non-foaming behaviour is caused due to the coagulation of the solid forming giant clusters. It was found that added water inhibits the coagulation and instead breaks the clusters into the smaller size particles. Moreover, WAXS measurements showed that water

**Table 9.6** Effect of added water on the foamability of 5 wt%  $C_{12}G_2$ /squalane, 5 wt%  $C_{14}G_2$ /squalane, and 5 wt%  $C_{14}G_2$ /hexadecane systems at 25°C.

System	Foam volume (ml)				
	0% water	1% water	2% water	3% water	5% water
5 wt% $C_{12}G_2$ /squalane	6 ± 2	10 ± 2	120 ± 7	140 ± 8	—
5 wt% $C_{14}G_2$ /squalane	<2 ml	<2 ml	10 ± 2	100 ± 6	170 ± 10
5 wt% $C_{14}G_2$ /hexadecane	<3 ml	<4 ml	60 ± 5	80 ± 6	—

may causes structural transformation from  $\alpha$ -solid to  $L_\alpha$  phase, which behaves differently at the interface and improve the foaminess of the systems. The effect of water on the particle size distribution and on the structure of the dispersed phase is described in the following section.

Water improved the foamability of the  $C_{12}G_2$ /squalane system and a nearly double volume of foam was produced upon addition of 1% water. Foamability continued to increase with water concentration (see Table 9.6). Since the  $C_{12}G_2$ /squalane system consists of  $L_\alpha$  dispersion without water, the enhanced foamability is caused by the dispersion of smaller size  $L_\alpha$  particles.

We have also studied the effect of added water on the foam formation capacity of  $C_{14}G_2$  and  $C_{12}G_2$  in olive oil. Note that these systems produce foams without water addition. Water addition gave a mixed results. In  $C_{12}G_2$  system, foamability was first decreased and then increased with increase in the water concentration [56]. As can be seen in Table 9.7, addition of 1% water decreased the total foam volume of the 5 wt%  $C_{12}G_2$ /olive oil system from 180 to 85 ml, but with further increasing water the foam volume was increased and eventually reached 200 ml foams in a 10% water added system. Foamability of the 5 wt%  $C_{14}G_2$ /olive oil system was increased in parallel to the water concentration (see Table 9.7). The water-added systems are complex than the systems without water. However, judging from the data it seems that water promotes the adsorption of surfactant to the interface and increases the foamability.

### 9.3.6.2 Effect of Water on Foam Stability

**$C_{14}G_2$ /squalane and  $C_{12}G_2$ /squalane systems.** Here we discuss the effect of water on the foam stability of the  $C_{14}G_2$ /squalane and  $C_{14}G_2$ /squalane systems. First we describe the  $C_{14}G_2$ /squalane system. It was found that at lower concentrations of water (~2%) foam life is very short: all the foams formed collapsed within 1 h. However, the foam stability increased with water concentration; foam was stable for approximately 4 h in the 5% water-added system. In Fig. 9.17, we present the digital images of the foams taken at different intervals of time for the 5 wt%  $C_{14}G_2$ /squalane + 3% water as a typical example. There is not a substantial change in the net foam volume up to 2 h. It was observed that immediately after the foam production, the foam films are very thick due to the presence of excess liquid in the lamellae so that film break-up is hindered temporarily. Due to liquid drainage, foam became dry and there was a wide distribution of bubbles after 50 min.

**Table 9.7** Effect of added water on the foamability of 5 wt%  $C_{12}G_2$ /olive oil and 5 wt%  $C_{14}G_2$ /olive oil systems at 25°C.

System	Foam volume (ml)			
	0% water	1% water	5% water	10% water
5 wt% $C_{12}G_2$ /olive oil	180 ± 8	85 ± 5	135 ± 8	200 ± 12
5 wt% $C_{14}G_2$ /olive oil	120 ± 8	122 ± 7	132 ± 10	210 ± 12

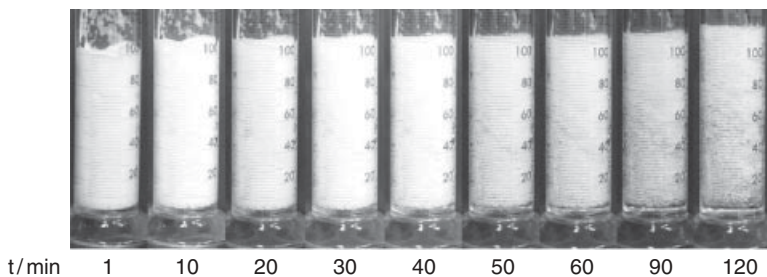


**Fig. 9.17** Digital images of the foams versus time for the 5 wt%  $C_{14}G_2$ /squalane + 3% water system at 25°C. Adapted with permission from Ref. [55], American Chemical Society.

We have also performed foam stability tests at higher water concentrations (10 and 20%). Addition of 10% water to the 5 wt%  $C_{14}G_2$ /squalane system resulted in the formation of emulsion, which was stable for a few hours and then phase separated to  $L_\alpha$  and isotropic liquid phase. Emulsion stability was increased with water concentration; emulsion was stable for several months in the 20% water-added system. It is interesting to note that the foam stability from these emulsions was better compared to the  $L_\alpha$  particle dispersions at lower water content systems. The foam was stable for more than 6 h in the 5 wt%  $C_{14}G_2$ /squalane + 20% water system. Besides a better quality of foam; viscous, monodispersed and relatively smaller bubbles, were observed. A narrow distribution of bubbles persisted for a long time. It was found that the drainage rate is very slow in the foam produced by the emulsion systems, indicating the higher liquid-holding capacity of the foams. Wet foams continued to exist for a several hours.

Now we discuss the effect of water on the foam stability of  $C_{12}G_2$ /squalane system, which produced a small volume of foam without water and was stable for ~30 min. Foam stability was increased significantly upon the addition of water and was stable for 2–3 h depending on the amount of water added. Digital image of the foams versus time for the 5 wt%  $C_{12}G_2$ /squalane + 2% water system is shown in Fig. 9.18.

Note that the 5 wt%  $C_{12}G_2$ /squalane + 2% water system is essentially the dispersion of smaller  $L_\alpha$  particles and appears as a turbid solution. But the drained liquid is a clear and

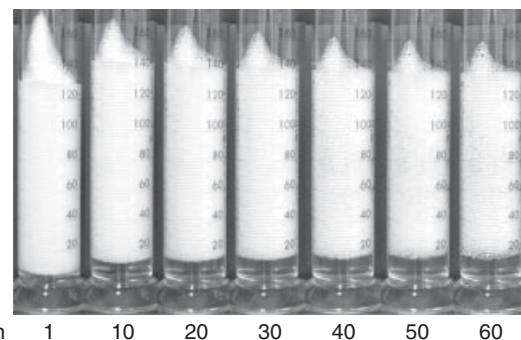


**Fig. 9.18** Digital image of foams taken at different intervals of time for the 5 wt%  $C_{12}G_2$ /squalane + 2% water system at 25°C. Adapted with permission from Ref. [55], American Chemical Society.

transparent solution. This indicates that the particles are either adsorbed at the gas–liquid interface or dispersed in the bulk liquid and stabilize the foams by increasing the mechanical rigidity of the interface or increasing the viscosity of the continuous phase.

**1. Optical micrographs of particle dispersions.** Qualitative information regarding the shape and size of the dispersed solid or liquid crystal particles can be observed from the microscopic analysis. Figure 9.19 shows the optical micrographs of the 5 wt%  $C_{14}G_2$ /squalane system at different concentrations of water.

As can be seen in Fig. 9.19a, solid and liquid crystal particles are coagulated, forming a giant cluster in the 5 wt%  $C_{14}G_2$ /squalane system. The addition of water broke the cluster and also caused structural transition from  $\alpha$ -solid to  $L_\alpha$  phases. As can be seen in the micro image, the clustered structure totally disappears and there is a dispersion of smaller  $L_\alpha$  particles at 3% water. The concentration of the smaller particles seems to increase with further increasing water concentration in, say, the 5% water system. Thus, the optical micrographs unambiguously show that water shatters the coagulated cluster and causes the transition to the  $L_\alpha$  phase. As mentioned before, at higher concentrations of water there is a tendency of emulsion formation. Addition of 10% water produced emulsion with an average droplet size  $\sim 15\text{ }\mu\text{m}$  (see Fig. 9.19e). At this concentration the emulsion droplets are polydisperse and are not very stable. Stable emulsion could be observed at higher water concentration. The 5 wt%  $C_{14}G_2$ /squalane + 20% water system created stable emulsion with low polydispersity in the droplet size (see Fig. 9.19f). The average size of the particle in this system is found to be around  $1\text{ }\mu\text{m}$  by laser diffraction measurements. To sum up, the micrographs show the dispersion of  $L_\alpha$  particles at higher water concentrations. Therefore the better foam stability at higher water content may possibly be due to the better packing of the smaller liquid crystal particles at the gas–liquid interface. Besides, these particles are dispersed in the solvent, thus increasing the viscosity of the continuous phase. Due to higher viscosity, the liquid drainage can be controlled and it is possible to obtain stable foams. Nevertheless, we cannot avoid the possibility of particles impacting on the rheological behaviour and, hence, the foaming properties.

**2. Particle size distribution.** In the particle stabilized liquid foam systems, the shape and size of the particle play a vital role in foaming properties. Foam stability may increase

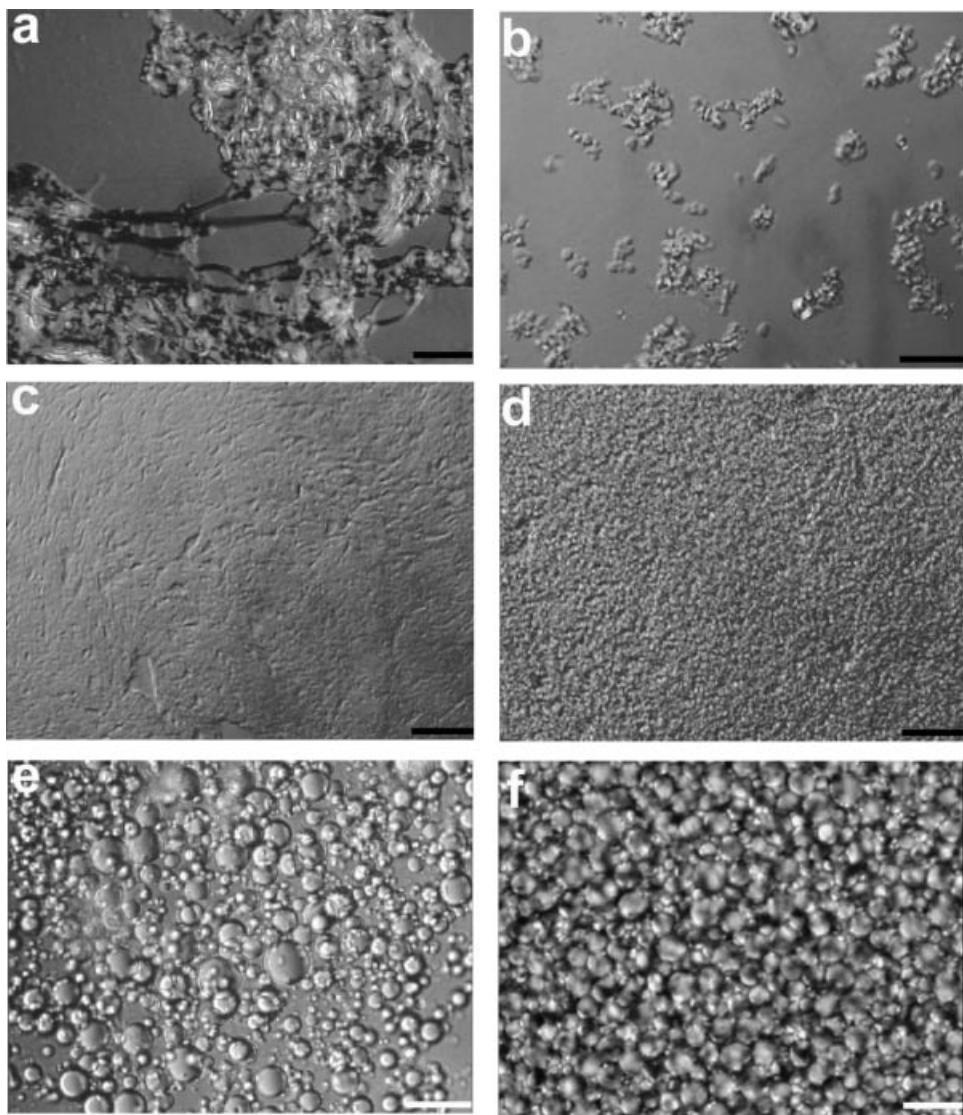


**Fig. 9.19** Optical micrographs of 5 wt%  $C_{14}C_2$ /squalane + water systems at different concentrations of water at 25°C: (a) 0%, (b) 2%, (c) 3%, (d) 5%, (e) 10%, and (f) 20%. The scale bar is 20  $\mu\text{m}$  for all of these images. Adapted with permission from Ref. [55], American Chemical Society.

or decrease depending on the size and shape of the particle in both the aqueous and non-aqueous systems [11, 30, 36, 39, 67, 68]. Therefore the knowledge of particle size distribution is very important. The particle size distributions of the present systems were determined using laser diffraction technique and the data are presented in Fig. 9.20. As can be seen from Fig. 9.20, there is a wide distribution of the particle size in the systems

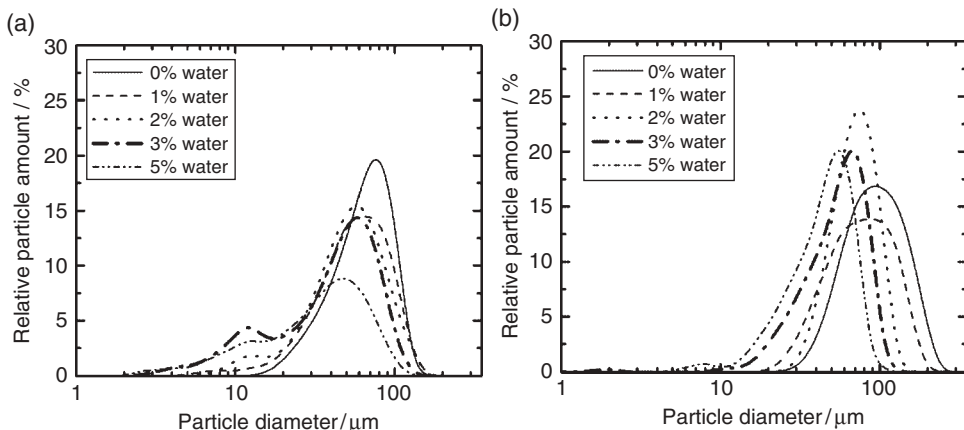


**Fig. 9.20** Effect of added water on the particle size distribution: (a) 5 wt%  $C_{14}G_2$ /squalane, and (b) 5 wt%  $C_{12}G_2$ /squalane at 25°C. Adapted with permission from Ref. [55], American Chemical Society.

studied. The particle size of the dispersed  $\alpha$ -solid or liquid crystal phase is very big in the water free systems. However, average particle diameter decreased with the concentration of the added water. When the amount of water is much higher (above 10%), the particle size is much smaller (~20  $\mu\text{m}$  in 10% water and ~1  $\mu\text{m}$  in 20% water data not shown here) [55].

**$C_{14}G_2$ /hexadecane system.**  $C_{14}G_2$ /hexadecane is a system that could not produce stable foams without water addition at room temperature due to the coagulation of solid particles. The addition of water improved the foam stability as water could break the coagulated solid into smaller particles and it was found that the stability increases with water concentration. For example, the addition of 2% water produced foams with a life time of ~3 h, and at 3% water the foams were stable for more than 4 h [55]. The enhanced foam stability at higher water concentration is caused by the adsorption of smaller particles at the surface.

**$C_{14}G_2$  and  $C_{12}G_2$  in olive oil systems.** So far we have discussed the effect of water on the foaming of those systems that could not produce stable foams or at least less stable foams without water addition. In this section, we discuss the water effect on the systems that produce stable foams without water.

Figure 9.21 shows the effect of water on foam stability of the 5 wt%  $C_{14}G_2$ /olive oil system. As can be seen in Fig. 9.21, addition of 1% water drastically reduces the foam stability of the 5 wt%  $C_{14}G_2$ /olive oil system. Although the foam stability increases with the increasing amount of water, the overall foam stability of the water-added systems is much less than that of the water-free system. For the complete destruction of foams it took ~3–4 h, depending on the amount of water; the data only up to 1 h are presented in Fig. 9.21a. This is because after 1 h, foams became dry and, due to a wide distribution of bubbles, the foam volume measurement was not very reliable. Figure 9.21b shows the corresponding liquid drainage as a function of time. One can see the higher drainage rate in water-added systems compared to the system without water. This shows that the viscosity of water-added systems is less than that of the water-free system. At the beginning, liquid drainage is higher, which

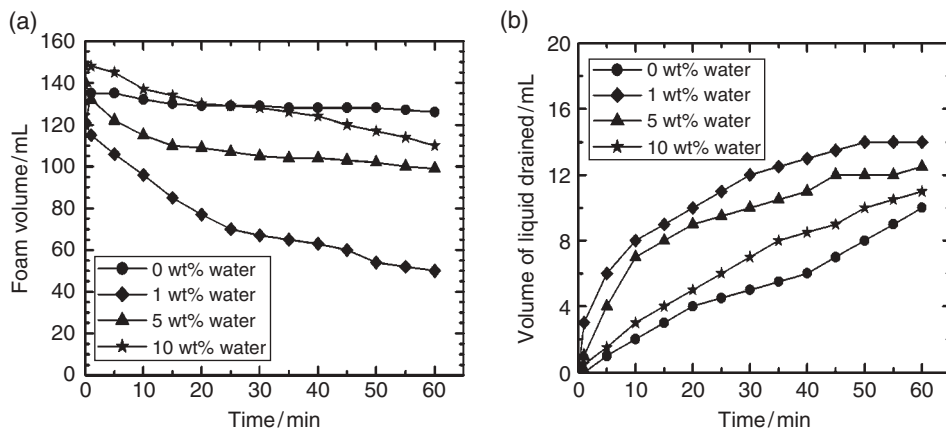


**Fig. 9.21** Effects of added water on foam stability of 5 wt%  $C_{14}G_2$ /olive oil system at 25°C: (a) foam volume versus time at different concentrations of water, and (b) the corresponding volume of liquid drained versus time. Adapted with permission from Ref. [63], Elsevier.

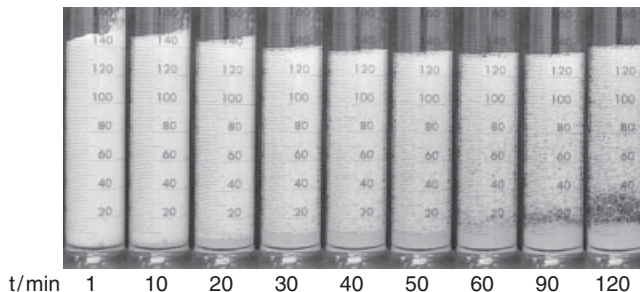


**Fig. 9.22** Evolution of foam volume and structure with time for 5 wt%  $C_{14}G_2$ /olive oil + 5% water systems at 25°C. Adapted with permission from Ref. [63], Elsevier.

is accompanied by the rapid decrease in the foam volume. However, with time, the drainage rate becomes slow, as does the change in foam volume. These observations reveal that the rapid decrease in the foam volume in the initial stage is mainly caused by the liquid drainage. Minute observation showed that ~55% liquid drained off after 10 min in the 1% water-added system, whereas only ~15% liquid drained off after 10 min in the water-free system. By increasing the amount of water, the liquid drainage is controlled (see Fig. 9.21b).

The evolution of foam structure as a function of time for the 5 wt%  $C_{14}G_2$ /olive oil + 5% water system is shown in Fig. 9.22 as a typical example. Immediately after foam generation, the foam contains a substantial amount of liquid, i.e. foams are wet and, hence, foam destruction is unlikely to occur. However, as time passes the foam volume decreases due to liquid drainage. The drained liquid can be seen at the bottom of the cylinder after 10 min. The volume of liquid drained increases with time but the overall structure of the foams

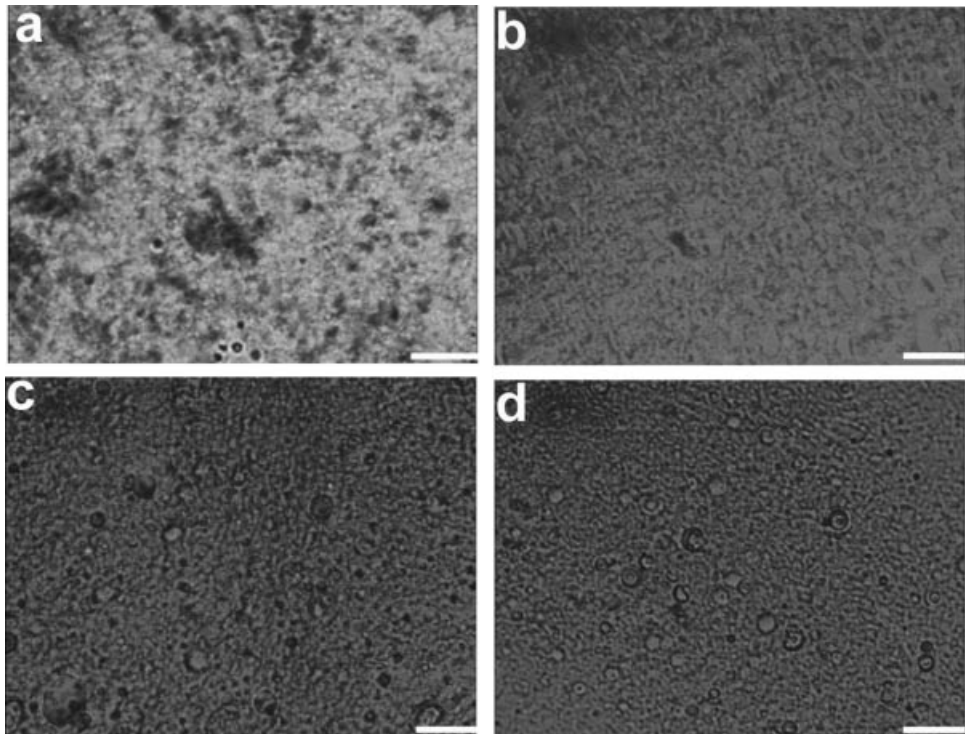


**Fig. 9.23** Optical micrographs of 5 wt%  $C_{14}G_2$ /olive oil systems at different concentration of added water at 25°C: (a) 0% water, (b) 1% water, (c) 5% water, and (d) 10% water. The scale bars represent 20  $\mu\text{m}$ . Adapted with permission from Ref. [63], Elsevier.

(mostly spherical and less polydispersed) is retained until, say, 50 min, when bubbles grow randomly and polydispersity increases. Foams with a polyhedral shape can be seen in the digital images taken after 60 min. Note that after 60 min more than 95% of liquid has drained off and, certainly, foams at this stage are very dry.

**1. Optical micrographs.** Figure 9.23 shows the micrographs of 5 wt%  $C_{14}G_2$ /olive oil + water systems at different concentrations of water. The texture of solid particle disappears and that of lamellar liquid crystal appears upon the addition of 1% water in the 5 wt%  $C_{14}G_2$ /olive oil system, showing the water-induced transition from solid to  $L_\alpha$  phases. Further addition of water leads not to any structural changes, but to a dispersion of smaller liquid crystals (see Fig. 9.23b–d). Judging from the foaming test and micrographs, one can say that the drastic change in the foam stability of water-added systems is caused by a structural transition of the dispersed solid particles to lamellar liquid crystal particles.

**2. Particle size distribution.** Particle size distribution of the 5 wt%  $C_{14}G_2$ /olive oil system versus water concentration was measured by laser diffraction particle size analysis. It was found that the water, depending on the concentration, increases and decreases the particle size. Surprisingly, the addition of 1% water increases the average particle size,

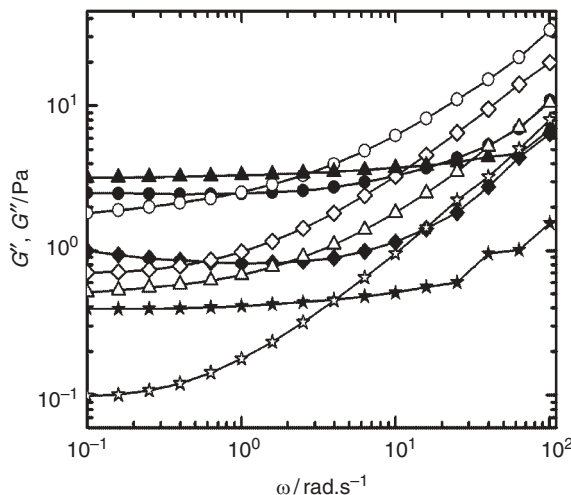


**Fig. 9.24** Dynamic oscillatory rheological behavior 5 wt%  $C_{14}G_2$ /olive oil + water systems at different concentrations of water at 25°C.  $G'$ , closed symbols;  $G''$ , open symbols. Circles, 0% water; diamonds, 1% water; triangles, 5% water; stars, 10% water. Adapted with permission from Ref. [63], Elsevier.

which may be a possible reason for the reduced foam stability of the 1% water-added system compared to the system without water. On the other hand, with further increasing water, the average particle diameter decreased (data not shown [56]), which well supports the foaming data. That is, an increase in foam stability with water concentration above 1% is caused by the decrease in the particle size. Note that the effect of water on the particle size does not seem to be a straight forward mechanism. It might be possible that the alpha-solid swells with water until 1% water, and then phase transform into the lamellar liquid crystal phase.

**3. Rheological behavior.** The addition of water causes a drastic change in the rheological behaviour of the system (see Fig. 9.24, which shows the effect of added water on the rheology of the 5 wt%  $C_{14}G_2$ /olive oil system). Both the elastic ( $G'$ ) and the viscous modulus ( $G''$ ) decreases with increasing concentration of water demonstrating a solid to liquid crystal phase transition, which is in a good agreement with the foaming data that lower foam stability of the water-added systems is caused by the decrease in the viscosity of the systems.

Coming to the  $C_{12}G_2$ /olive oil system, it was found that water first decreased the foam stability and then increased. Figure 9.25 shows changes in foam volume and drained liquid versus time at different concentrations of water. The foam stability of the 5 wt%  $C_{12}G_2$ /olive oil system decreased upon addition of 1% water. All the foams collapsed within ~1 h, but with further increasing water the foam stability was increased. Note that foams produced with a 10% water system were stable for ~4 h.

The changes in foam volume, drained liquid and foam structure versus time for the 5 wt%  $C_{12}G_2$ /olive oil + 10% water system are shown in Fig. 9.26. Due to the presence of a substantial amount of liquid in the foam, foam was stable in the initial stage. Foam film

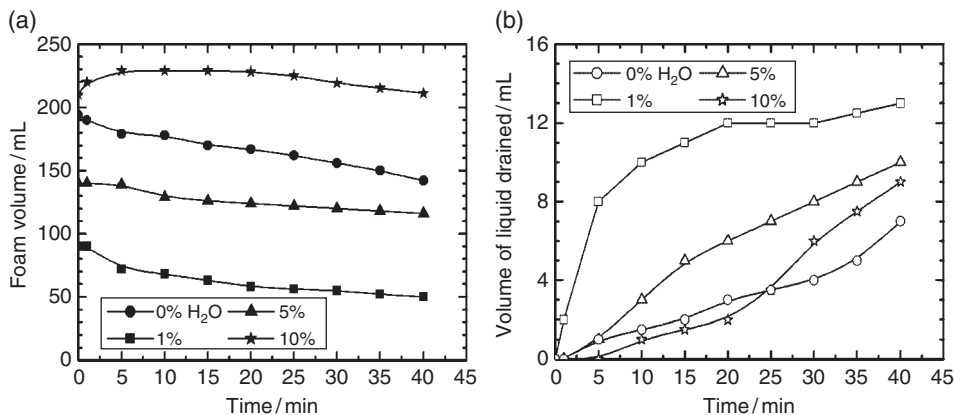


**Fig. 9.25** Effects of added water on foam stability of the 5 wt%  $C_{12}G_2$ /olive oil system. (a) Foam volume versus time at different concentration of water and (b) the corresponding volume of liquid drained at 25°C. Adapted with permission from Ref. [56], Elsevier.

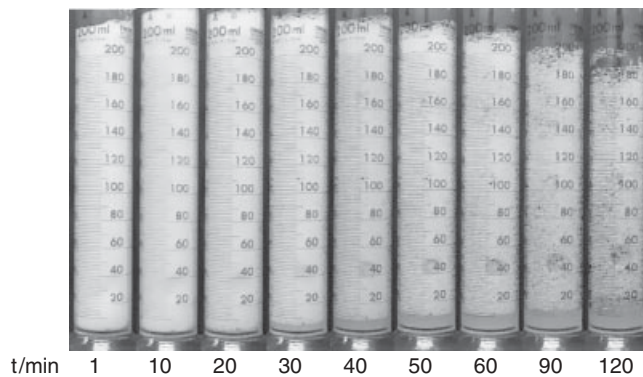


**Fig. 9.26** Digital images of the foams taken at different intervals of time for 5 wt%  $C_{12}G_2$ /olive oil + 10% water systems at 25°C. Adapted with permission from Ref. [56], Elsevier.

thickness decreased with time due to liquid drainage and ultimately a random foam breakage started. Bubble size was increased, resulting in polydispersed foams with polyhedral shape after  $\sim 1$  h. Foams at this stage were very dry and foam film lamellae had less liquid.

Particle size measurements have shown a slight increase in the average particle diameter upon the addition of 1% water, but with further increasing water concentration the particle size decreases (data not shown [56]). Steady-shear rheology measurements have shown that viscosity increases with water concentration up to a certain point and then decreases. However, foam stability measurements showed that above 1% water, foam stability increases continuously with water concentration. Thus, judging from foaming and viscosity data it can be concluded that only viscosity does not play a major role in the foam stabilization mechanism.

### 9.3.7 Non-aqueous Foam Stabilization Mechanism

We have presented evidence on the formation of stable non-aqueous foams in surfactant/oil and surfactant/oil/water systems. Foams were stable for from a few minutes to several weeks. Foam stability was found to depend on the surfactant and solvent molecular structure, surfactant concentration and water addition. As mentioned in the results section, foam obtained from higher surfactant concentrations consists of small spherical and less polydisperse bubbles and contains a substantial amount of liquid, which would reduce the area of contact between the bubbles and increase the foam film thickness. Moreover, due to narrow distributions of foam bubbles, diffusion of entrapped gas, and the Ostwald ripening effect are less likely to occur. These factors may contribute to the enhanced foam stability; however, the main factor for foam stability is the dispersion of small solid particles, which tend to adsorb at the gas–liquid interface. Microscopic studies have clearly shown the adsorption of these particles at the gas–liquid interface. Because each foam bubble is surrounded by the particles, the mechanical rigidity of the interface is increased. WAXS measurements have confirmed the structure of the particles to be  $\alpha$ - or  $\beta$ -solid depending on the surfactant molecular structure. The  $\beta$ -solid is found in monoglycerol fatty acid ester/oil systems, and the  $\alpha$ -solid in diglycerol fatty acid ester/oil systems.

The adsorption of particles at an air–water interface depends on the hydrophobicity of the particle, which can be quantified by contact angle [69–71]. The contact angle increases with the hydrophobicity of the particle. Previous experiments have shown that maximum foam stability can be obtained if the contact angle of the particle is close to 90° [30]. Presently, we could not measure the contact angle of the particles due to the complexity of the systems, and to quantify their hydrophobicity. Nevertheless, surface tension data have shown their ability to adsorb to the air–liquid (oil) interface. With regard to the  $C_{14}G_2$ /olive oil system, it was found that the surface tension of oil decreases with increasing  $C_{14}G_2$  concentration, attains a plateau value and then again decreases and finally regains the plateau value (see Table 9.2). The initial decrease of surface tension can be attributed to the adsorption of soluble surfactant molecules to the surface. We note a phase separation into solid crystals in the first plateau region and with further increasing  $C_{14}G_2$  concentration the surface tension further decreases, which could be attributed to the adsorption of solid particles to the air–liquid interface. After a while, the interface becomes saturated with the insoluble solid and surface tension becomes constant. From these observations, one can conclude that the solid particles have a strong tendency to adsorb at the air–liquid interface and, hence, stabilize the oil-based non-aqueous foams. This is further confirmed by the fact that at higher temperatures where the solid phase melts to a reverse micellar phase, foam stability is dramatically reduced. In some systems, where particles are too big, the particles settled at the bottom of the vial when undisturbed for a few hours and there are no foaming from the supernatant phases, which are almost pure solvents. All these observations have confirmed the importance of the presence of particles in the system to obtain stable non-aqueous foams.

In the case of particle-stabilized foaming systems, the foaming properties are highly influenced by the characteristics of the colloidal dispersion. Foaming depends on the tendency of the particles to adsorb at the gas–liquid interface, their size and their concentrations [4, 30, 31, 36, 39, 42]. Silica or polymer latex particles with particle size up

to hundreds nanometres are known to stabilize aqueous foams [36, 72–4]. Similarly to the aqueous foams, non-aqueous foams could be stabilized by the dispersions of solid crystals ( $\alpha$  and  $\beta$ -solid) and/or lamellar liquid crystal (see a recent review by Friberg [75], in which he has mentioned oil foam stability from fundamentals to current developments). The stability of particle stabilized foams has been found to depend on the concentration and size of the particles. In the case of giant clusters or coagulated solids, foams are unstable. Foam stability increases with decreasing average particle size, which could be understood in terms of better packing at the air–liquid interface. Experiments have shown that the foam stability increases with increasing concentration of surfactant. Moreover, it is found that particle size decreases with the surfactant concentration. So the enhanced foam stability at higher surfactant concentration is the result of a dual contribution: adsorption of smaller particles at the interface, and the increased number of particles at the interface. Under these conditions, the air–liquid interface becomes more rigid, which in turn inhibits foam bubble coalescence and gas diffusion may also be reduced. Dynamic oscillatory-shear rheology data have shown that elastic and viscous modulus increase with increasing surfactant concentration (see Fig. 9.8). Thus one can expect lower liquid drainage at higher particle concentration and as a result wet foam persists for a long time, and foams are stable. In the studies on foaming from monoglycerol fatty acid ester/oil systems, it has found that foaming also largely depends on the shape of the solid particles, with higher foam stability from the dispersion of needle-shaped fine crystals and poor foam stability from disk-like or flat crystal dispersions. It is expected that the fine needle-shaped micro-crystals adsorb at the air–liquid interface and have better packing, forming a rigid network structure. However, this may not be possible with the disk-like or flat 2D crystal. The 2D crystals may not have better packing as needle-shaped 1D crystals do. Since the average particle sizes of needle-shaped 1D and flat disk-like 2D crystals are apparently the same, the difference in the foam stability could only be due to the difference in their shape. Optical microscopic observation of foams showed that the particles are also collected at the Plateau border. This increases the bulk viscosity of liquid and consequently controls the liquid drainage.

Foaming with liquid crystal particle dispersions is very different from that with solid dispersions. Relatively the foam stability decreases with liquid crystal dispersion. A similar result was found in the case of aqueous systems. Aqueous foam stability is much higher with the dispersion of  $\alpha$ -solid compared to the  $L_\alpha$  particles [67, 68]. It is possible that solid particles make more rigid interface compared to liquid crystals, and since the viscosity of solid dispersion is higher than that of liquid crystal dispersion, the drainage is controlled and, hence, foams obtained from solid dispersions are more stable.

As mentioned above, when the systems consist of giant clusters of solid or liquid crystal – for example, in  $C_{14}G_2$ /squalane or  $C_{14}G_2$ /hexadecane systems – stable foam could not be observed. The clusters tend to settle at the bottom of the vial. The addition of trace water could improve the foaming of such systems by breaking the cluster into smaller particles. At relatively higher water concentrations, there is a phase transition to the lamellar phase and foams are stable for a few hours. Note that liquid crystal stabilized forms are always less stable than solid stabilized foams. For example, when we add water to the  $\alpha$ -solid stabilized forming system  $C_{14}G_2$ /olive oil, foam stability decreases. Relatively poor foaming with the water-added systems can be attributed to the transformation of  $\alpha$ -solid to lamellar  $L_\alpha$  particle.

We have mentioned that the solid and liquid crystal particles have tendency to adsorb at the air–liquid interface. As confirmed by surface tension measurements, the  $\alpha$ -solid adsorbs at the interface and reduces the equilibrium surface tension of olive oil by ~25% in the  $C_{14}G_2$ /olive oil system. Phase behavior study shows the formation of solid dispersion above 0.5 wt%  $C_{14}G_2$ /olive oil. Similarly in the  $C_{12}G_2$ /olive oil system, where there is a dispersion of  $L_\alpha$  particles, the surface tension of the oil is reduced by ~18% showing the adsorption of  $L_\alpha$  particles at the air–liquid interface. Thus one can say that these solid and liquid crystal particles have strong tendency to move to the interface and to stabilize the non-aqueous foams for hours to days depending on their particle size and concentration.

#### 9.4 Conclusion

Stable non-aqueous foams could be achieved by taking advantage of surfactant self-assemblies with environmentally friendly, biocompatible and biodegradable non-ionic surfactant/oil systems. The systems are composed of olive oil, liquid paraffin, squalene and mono- and diglycerol fatty acid esters. Since these surfactants and oils are edible and also mild on the skin, non-aqueous foams produced with these systems could offer various practical applications in the food and cosmetic industries. This chapter mainly shows the non-aqueous foams stabilized by the dispersed surfactant solid particles and a link of the foam stability to the size distribution of the solid particulates (the smaller the particle, the better the foam stability). In addition to the size, the importance of the shape of the dispersed solid particles is also highlighted. Foams are relatively more stable from the needle-shaped 1D crystal dispersions compared to flat disk-like 2D solid crystals. Furthermore, it has shown that dispersions of crystalline solids (obtained in the absence of water) are more effective at stabilizing foam than dispersions of a lamellar liquid crystalline phase (obtained in the presence of water). Both solid and liquid crystal particles reduce the surface tension of oils (up to ~25% in some system), showing that these particles adsorb at the surface and contribute to the formation of stable non-aqueous foams. We believe that this chapter has both fundamental and practical implications and highlights the mechanism of particle stabilized non-aqueous foams.

#### Acknowledgements

L.K.S. thanks the International Center for Young Scientists (ICYs), National Institute for Materials Science (NIMS) and International Center for Materials Nanoarchitectonics (MANA) for partial support. The authors are thankful to Taiyo Kagaku Co., Ltd, Yokkaichi, Japan, for supplying the diglycerol fatty acid ester surfactants. We are grateful to Prof. Conxita Solans, CSIC, Barcelona, Prof. Stig E. Friberg, Clarkson University, USA, and Prof. Cosima Stubenrauch, University of Stuttgart, Germany, for fruitful discussion, comments and advice. The technical assistance of Dr Rekha G. Shrestha, Tokyo University Science, Japan, is highly acknowledged.

## References

- [1] A.J. Wilson. *Foams: Physics, Chemistry and Structure*. In Springer Series in Applied Biology, A.W. Robards (ed.), Springer, Berlin, 1989.
- [2] D.L. Schmidt. Nonaqueous foams. In *Foams: Theory, Measurements and Application*, R.K. Prud'homme and S.A. Khan (eds). Surfactant Science Series 57, Marcel Dekker, New York, 1996.
- [3] S.E. Friberg and J.-H. Fang. Foams from aqueous systems of polymerisable surfactants. *J. Coll. Interface Sci.*, **118**: 543–52, 1987.
- [4] R. Aveyard, B.P. Binks, P.D.I. Fletcher, T.G. Peck and C.E. Rutherford. Aspects of aqueous foam stability in the presence of hydrocarbon oils and solid particles. *Adv. Coll. Interface Sci.*, **48**: 93–120, 1994.
- [5] A. V-d. Net, A. Gryson, M. Ranft, F. Elias, C. Stubenrauch and W. Drenckhan. Highly structured porous solids from liquid foam templates. *Coll. Surfaces A*, **346**: 5–10, 2009.
- [6] A. Arzhavitsina and H. Steckel. Foams for pharmaceutical and cosmetic application. *Int. J. Pharmaceutics*, **394**: 1–17, 2010.
- [7] J.F. Sodac and N. Rivier. *Foams and Emulsion*. Kluwer Academic, Dordrecht, 1999.
- [8] M. J. Rosen, *Surfactants and Interfacial Phenomena*. John Wiley & Sons, Inc., New York, 1989.
- [9] D.J. Durian and D.A. Weitz. Foams. In *Kirk-Othmer Encyclopedia of Chemical Technology*, 4th edn, vol. 11, 1994.
- [10] C. Stubenrauch and R. Klitzing. Disjoining pressure in thin liquid foam and emulsion films. *J. Phys.: Condens. Matter*, **15**: R1197–232, 2003.
- [11] R.J. Pugh. Foaming, foam films, antifoaming and defoaming. *Adv. Coll. Interface Sci.*, **64**: 67–142, 1996.
- [12] D. Exerowa and P.M. Kruglyakov. *Foam and Foam Films: Theory Experiment, Application*. Elsevier, New York, vol. 5, 1998.
- [13] C. Stubenrauch. On foam stability and disjoining pressure isotherms. *Tenside Surf. Det.*, **38**: 350–5, 2001.
- [14] C. Stubenrauch, J. Schlaremann and R. Strey. A disjoining pressure study of *n*-dodecyl-β-D-maltoside films. *Phys. Chem. Chem. Phys.*, **4**: 4504–13, 2002; and *Phys. Chem. Chem. Phys.*, **5**: 2736–7, 2003 (erratum).
- [15] C. Stubenrauch and B.R. Blomqvist. Foam films, foams and surface rheology of non-ionic surfactants: amphiphilic block copolymers compared with low molecular weight surfactants. In *Colloid Stability: The Role of Surface Forces, Part 1*, T. Tadros (ed.). Wiley-VCH, Weinheim, 2006.
- [16] A. Scheludko and E. Manev. Critical thickness of rupture of chlorbenzene and aniline films. *Trans. Faraday Soc.*, **64**: 1123–34, 1968.
- [17] A. Scheludko. Thin liquid films. *Adv. Coll. Interface Sci.*, **1**: 391–464, 1967.
- [18] L. Ting, D.T. Wasan, K. Miyano and S.Q. Xu. Longitudinal surface waves for the study of dynamic properties of surfactant systems. II. Air–solution interface. *J. Coll. Interface Sci.*, **102**: 248–59, 1984.
- [19] E.H. Lucassen-Reynders. Relaxation effects in monolayers and their contribution to water wave damping: a comment. *J. Coll. Interface Sci.*, **117**: 589–90, 1987.
- [20] T. Tamura, Y. Kaneko and M. Ohayama. Dynamic surface tension and foaming properties of aqueous polyoxyethylene *n*-dodecyl ether solutions. *J. Coll. Interface Sci.*, **173**: 493–9, 1995.
- [21] K. Wantke, K. Malysa and K. Lunkenheimer. A relation between dynamic foam stability and surface elasticity. *Coll. Surf. A*, **82**: 183–91, 1994.
- [22] Y.H. Kim, K. Koczo and D.T. Wasan. Dynamic film and interfacial tensions in emulsion and foam systems. *J. Coll. Interface Sci.*, **187**: 29–44, 1997.
- [23] C. Stubenrauch and R. Miller. Stability of foam films and surface rheology: an oscillating bubble study at low frequencies. *J. Phys. Chem. B*, **108**: 6412–21, 2004.
- [24] K. Malysa, R. Miller and K. Lunkenheimer. Relationship between foam stability and surface elasticity forces: fatty acid solutions. *Coll. Surf.*, **53**: 47–62, 1991.

- [25] A. Patist, T. Axelberd and D.O. Shah. Effect of long chain alcohols on micellar relaxation time and foaming properties of sodium dodecyl sulphate solutions. *J. Coll. Interface Sci.*, **208**: 259–65, 1998.
- [26] L. Arnaudov, N.D. Denkov, I. Surcheva, P. Durbut, G. Broze and A. Mehreteab. Effect of oily additives on foamability and foam stability. 1. Role of interfacial properties. *Langmuir*, **17**: 6999–7010, 2001.
- [27] D. Beneventi, R.J. Pugh, B. Carre and A. Gandini. Surface rheology and foaming properties of sodium oleate and  $C_{12}(EO)_6$  aqueous solutions. *J. Coll. Interface Sci.*, **268**: 221–9, 2003.
- [28] D.P. Acharya, J.M. Gutiérrez, K. Aramaki, K. Aratani and H. Kunieda. Interfacial properties and foam stability effect of novel Gemini-type surfactants in aqueous solutions. *J. Coll. Interface Sci.*, **291**: 236–43, 2005.
- [29] C. Stubenrauch, L.K. Shrestha, D. Varade, I. Johansson, G. Olanya, K. Aramaki and P. Claesson. Aqueous foams stabilized by *n*-dodecyl- $\beta$ -D-maltoside, hexaethyleneglycol monododecyl ether, and their 1:1 mixture. *Soft Matter*, **5**: 3070–80, 2009.
- [30] B.P. Binks. Particles as surfactants-similarities and differences. *Curr. Opin. Coll. Interface Sci.*, **7**: 21–41, 2002.
- [31] Z. Du, M.P. Bilbao-Montoya, B.P. Binks, E. Dickinson, R. Ettelaie and B.S. Murray. Outstanding stability of particle-stabilized bubbles. *Langmuir*, **19**: 3106–8, 2003.
- [32] N.D. Denkov, I.B. Ivanov, P.A. Kralchevsky and D.T. Wasan. A possible mechanism of stabilization of emulsions by solid particles. *J. Coll. Interface Sci.*, **150**: 589–93, 1992.
- [33] S.E. Friberg. Emulsion stabilization by solid particles. A two layer approach: spherical particles, *J. Dispers. Sci. Technol.*, **26**: 647–54, 2005.
- [34] G. Kapitay. On the equation of the maximum capillary pressure induced by solid particles to stabilize emulsions and foams and on the emulsion stability diagrams. *Coll. Surf. A*, **282/283**: 387–401, 2006.
- [35] G.N. Sethumadhavan, A.D. Nikolov and D.T. Wasan. Stability of liquid films containing monodisperse colloidal particles. *J. Coll. Interface Sci.*, **240**: 105–12, 2001.
- [36] B.P. Binks and T.S. Horozov. Aqueous foams stabilized solely by silica nanoparticles. *Angew. Chem. Int. Ed.*, **44**: 3722–5, 2005.
- [37] U.T. Gonzenbach, A.R. Studart, E. Tervoort and L.J. Gauckler. Stabilization of foams with inorganic colloidal particles. *Langmuir*, **22**: 10983–8, 2006.
- [38] U.T. Gonzenbach, A.R. Studart, E. Tervoort and L.J. Gauckler. Ultrastable particle-stabilized foams. *Angew. Chem. Int. Ed.*, **45**: 3526–3530, 2006.
- [39] F.Q. Tang, F. Tang, Z. Xiao, J. Tang and L. Jiang. The effect of  $SiO_2$  particles upon stabilization of foam. *J. Coll. Interface Sci.*, **131**: 498–502, 1989.
- [40] D.T. Wasan, A. Nikolov, P. Kralchevsky and I. Ivanov. Universality in film stratification due to colloid crystal formation. *Coll. Surf.*, **67**: 139–45, 1992.
- [41] B.S. Murray and R. Ettelaie. Foam stability: proteins and nanoparticles. *Curr. Opin. Coll. Interface Sci.*, **9**: 314–20, 2004.
- [42] R.G. Alargova, D.S. Warhadpande, V.N. Paunov and O.D. Velev. Foam superstabilization by polymer microrods. *Langmuir*, **20**: 10371–4, 2004.
- [43] T.N. Hunter, E.J. Wanless, G.J. Jameson and R.J. Pugh. Non-ionic surfactant interactions with hydrophobic nanoparticles: impact on foam stability. *Coll. Surf. A*, **347**: 81–9, 2009.
- [44] E. Dickinson, R. Ettelaie, T. Kostakis and B.S. Murray. Factors controlling the formation and stability of air bubbles stabilized by partially hydrophobic silica nanoparticles. *Langmuir*, **20**: 8517–25, 2004.
- [45] I.B. Ivanov, B. Radoev, E. Manev and A. Scheludko. Theory of the critical thickness of rupture of thin liquid films. *Trans. Faraday Soc.*, **66**: 1262–73, 1970.
- [46] R.J. Mannheimer and R.S. Schechter. Shear-dependent surface rheological measurements of foam stabilizers in nonaqueous liquids. *J. Coll. Interface Sci.*, **32**: 212–24, 1970.
- [47] H. Gang, J. Patel, X. Z. Wu, M. Deutsch, O. Gang, B. M. Ocko and E.B. Sirota. Macroscopic manifestations of surface crystallization. *Europhys. Lett.*, **43**: 314–19, 1998.
- [48] W. Bu, J. Jin and I. Ichinose. Foam films obtained with ionic liquid. *Angew. Chem. Int. Ed.*, **47**: 902–5, 2008.

- [49] S.E. Friberg and S.I. Ahmad. Liquid crystals and the foaming capacity of an amine dissolved in water and p-xylene. *J. Coll. Interface Sci.*, **35**: 175, 1971.
- [50] S.E. Friberg, S. Chang, W.B. Greene and R.V. Gilder. A nonaqueous foam with excellent stability. *J. Coll. Interface Sci.*, **101**: 593–4, 1984.
- [51] S.E. Friberg, I. Blute, H. Kunieda and P. Stenius. Stability of hydrophobic foams. *Langmuir*, **2**: 659–64, 1986.
- [52] S.E. Friberg, I. Blute and P. Stenius. Foam stability in a glycerol system. *J. Coll. Interface Sci.*, **127**: 573–81, 1989.
- [53] G. Jederström, L. Rydhag and S. Friberg. Liquid crystalline phases in aerosol formation II: Influence of liquid crystalline phases on foam stability. *J. Pharm. Sci.*, **62**: 1973–82, 1973.
- [54] H. Kunieda, L.K. Shrestha, D.P. Acharya, H. Kato, Y. Takase and J.M. Gutiérrez. Superstable nonaqueous foams in diglycerol fatty acid esters-nonpolar oil systems. *J. Dispers. Sci. Technol.*, **28**: 133–42, 2007.
- [55] L.K. Shrestha, R.G. Shrestha, C. Solans and K. Aramaki. Effect of added water on the foaming properties of diglycerol fatty acid esters-oil systems. *Langmuir*, **23**: 6918–26, 2007.
- [56] L.K. Shrestha, R.G. Shrestha, S.C. Sharma and K. Aramaki. Stabilization of nonaqueous foam with lamellar liquid crystal particles in diglycerol monolaurate/olive oil system. *J. Coll. Interface Sci.*, **328**: 172–9, 2008.
- [57] L.K. Shrestha, K. Aramaki, H. Kato, Y. Takase and H. Kunieda. Foaming properties of monoglycerol fatty acid esters in nonpolar oil system. *Langmuir*, **22**: 8337–45, 2006.
- [58] L.K. Shrestha, M. Kaneko, T. Sato, D.P. Acharya, T. Iwanaga and H. Kunieda. Phase behavior of diglycerol fatty acid esters-nonpolar oil systems. *Langmuir*, **22**: 1449–54, 2006.
- [59] N. J. Krog. Food emulsifiers and their chemical and physical properties. In *Food Emulsion*, K. Larsson and S.E. Friberg (eds). Marcel Dekker, New York, 1990.
- [60] K. Larsson and P. Dejmek. Milk and dairy-type emulsions. In *Food Emulsion*, K. Larsson and S.E. Friberg (eds). Marcel Dekker, New York, 1990.
- [61] L. Hernqvist. Crystal structures of fats and fatty acids. In *Crystallization and Polymorphism of Fats and Fatty Acids*, N. Garti and K. Sato (eds). Marcel Dekker, New York, 1988.
- [62] K. Larsson. Arrangement of rotating molecules in the high-temperature form of normal paraffins. *Nature*, **213**: 383–4, 1967.
- [63] R.G. Shrestha, L.K. Shrestha, C. Solans, C. Gonzalez and K. Aramaki. Nonaqueous foam with outstanding stability in diglycerol monomyristate/olive oil system. *Coll. Surfaces A.*, **353**: 157–65, 2010.
- [64] L.K. Shrestha, R.G. Shrestha and K. Aramaki. Self-assembled structures of diglycerol monolaurate-and monomyristate in olive oil. *J. Dispers. Sci. Technol.*, **30**: 1552–32, 2009.
- [65] L.K. Shrestha, T. Sato, D.P. Acharya, T. Iwanaga, K. Aramaki and H. Kunieda. Phase behavior of monoglycerol fatty acid esters in nonpolar oils: reverse rodlike micelles at elevated temperatures. *J. Phys. Chem. B*, **110**: 12266–73, 2006.
- [66] L.K. Shrestha and K. Aramaki. Phase behavior of diglycerol monomyristate in different nonpolar organic solvent systems. *J. Dispers. Sci. Technol.*, **28**: 1236–41, 2007.

# 10

## Suprafroth: Ageless Two-dimensional Electronic Froth

*Ruslan Prozorov and Paul C. Canfield*

### 10.1 Introduction

The fundamental physics and chemistry of complex systems, including practical issues related to the stability of froths (e.g., insulating foams, ultra-light alloys, fire extinguishers) have made them a topic of broad basic and applied interest [1]. In particular, the structure and dynamics of froths have been subjects of intense interest due to the desire to understand the behavior of complex systems where topological intricacy prohibits exact evaluation of the ground state. Though precise solutions are difficult, general laws, that take into account both the topological constraints and the physics and chemistry of the froth matter, have been developed. Two-dimensional froths consist of arrays of polygonal shaped cells with three edges per vertex and the mathematics developed for describing the cellular evolution of the system as a whole, neglecting the detailed evolution of a particular cell, has proven to be surprisingly simple in form. This gives rise to the hope that, whereas the behavior of individual cells may be unpredictable, the overall system can be described by relatively simple ensemble rules.

Various froths have been studied, and in most cases the coarsening parameter has been time and the microscopic mechanism has been diffusion of vapour molecules between the cells as well as drainage of the liquid from the cell walls. Although the dynamics of a traditional froth involves mass transport and is irreversible, magnetic froths offer a substantial range of reversible control parameters: specifically, magnetic field and

temperature. In the case of magnetic froth, however, the coarsening is promoted by the applied magnetic field. Two types of magnetic froths have been known: (i) a ferrofluid, in an immiscible liquid, stimulated by an applied alternating magnetic field [2]; and (ii) the magnetic domain structure observed in transparent ferromagnetic garnets [1, 3]. However, in both cases, only limited analysis exploring the analogy of time-dependent coarsening of the conventional froth and magnetic field-induced coarsening in the magnetic froth was performed.

Here we describe an entirely new type of two-dimensional magnetic froth, formed in bulk clean, type-I superconductors. Specifically, in this froth the cell boundaries consist of a superconducting phase, whereas cell interiors are normal state metal filled with magnetic flux. Unlike any froth studied before, this superconducting froth involves only electrons – normal and paired in Cooper pairs and a magnetic field. We call this new topological phase “**suprafroth**” [4] in the spirit of early discoveries when superconductors were called “**supraconductors**” (in French, “**supraconducteur**”). The coarsening of the suprafroth is promoted either by increasing applied magnetic field or increasing temperature. It is very important that, unlike in all previous cases, here we know macroscopic laws governing the behavior of clean superconductors. Thus we are able to check the compatibility of the statistical laws of cellular evolution with the macroscopic behavior as a function of magnetic field and temperature. The dynamic evolution of this suprafroth does not involve mass transport and allows for the study of the topological hysteresis decoupled from the hysteresis of the “aging” of the froth matter. Despite a very different microscopic origin, topological analysis of the structure of the suprafroth shows that von Neumann’s and Lewis’s laws apply. Furthermore, for the first time in the analysis of froths there is a global measurable property, the magnetic moment, which can be directly related to the suprafroth structure. We show that the statistical laws are in a good agreement with the predicted macroscopic response. We propose that this suprafroth is a new, close to ideal, model system for the analysis of the complex physics of two-dimensional froths – with magnetic field and temperature as external (reversible) control parameters.

## 10.2 The Intermediate State in Type-I Superconductors

Here we briefly summarize the phenomenon of superconductivity necessary for the understanding of the suprafroth formation and behavior described in this chapter. When some materials are cooled below a characteristic, magnetic field-dependent, critical temperature,  $T_c(H)$ , their electrical resistance drops to zero and currents (up to the critical value) can flow (circulate) indefinitely without loss due to resistance. This new thermodynamic phase is different from the normal state (even of a hypothetically perfect metal with zero resistance) in many respects, most notably in the ability to expel weak magnetic fields from the sample interior [5]. Electrons form so called Cooper pairs, which obey Bose statistics and therefore can condense into a unique ground-state quantum energy level all having the same macroscopic wave-function as described by the Bardeen–Cooper–Schrieffer (BCS) theory [6]. When a superconductor is subject to a magnetic field,  $H$ , the energy of an expelled field,  $H^2/8\pi$  is added to the energy of a superconductor and a transition to the normal state will formally occur at a so-called thermodynamic critical field,

$$H_c = \frac{\phi_0}{2\sqrt{2}\pi\lambda\xi} \quad (10.1)$$

Where flux quantum  $\phi_0 = hc/2e \approx 2 \times 10^{-7}$  G.cm<sup>2</sup>, (here  $h$  is Planck's constant,  $c$  is the speed of light in vacuum and  $e$  is the electron charge),  $\xi$  is the coherence length (the spatial extent of a Cooper pair or the length at which the superconducting order parameter changes) and  $\lambda$  is the London penetration depth (the depth to which a weak magnetic field penetrates a superconductor). For larger magnetic fields, however, different superconductors exhibit different behavior and are divided into two types [7]. So-called type-II superconductors have a region on the magnetic field–temperature phase diagram, bound by lower,

$$H_{c1}(T) = \frac{\phi_0}{4\pi\lambda^2} \ln \frac{\lambda}{\xi},$$

and upper,

$$H_{c2}(T) = \frac{\phi_0}{2\pi\xi^2},$$

critical fields, in which the magnetic field exists in the form of Abrikosov vortices embedded into the superconducting matrix [7, 8]. Each Abrikosov vortex carries exactly one flux quantum,  $\phi_0$ , and behaves as an elastic tube. This **mixed** (or Shubnikov) state is a true thermodynamic phase and persists up to the upper critical field,  $H_{c2}(T)$ , above which it undergoes a second-order phase transition into the normal state. This is possible because the energy of the interface between normal and superconducting phases is negative, and thus between  $H_{c1}(T)$  and  $H_{c2}(T)$  it is possible to compensate for an increase of free energy due to the conversion of the superconducting phase to normal (so-called condensation energy). The absolute majority of materials, including those used in superconducting magnets and other power-related applications, are type-II superconductors.

In stark contrast, a small fraction of materials, all of them elemental metals, are type-I superconductors in which the superconductor–normal phase (S/N) interface energy is positive and the abrupt first order transition into the normal state occurs at the thermodynamic critical field,  $H_c$ . However, if the sample is finite then this thermodynamic limit is lifted due to the demagnetizing effects. Specifically, the magnetic field,  $H_e$ , on the edge of a finite sample is larger than the applied magnetic field,  $H_e = H/(1 - N)$ , where  $N$  is the demagnetization factor determined by the sample shape [9]. When  $H_e$  exceeds the critical field,  $H_c$ , magnetic flux penetrates the specimen and an unhomogeneous **intermediate state** is formed. Because the S/N energy is positive, the system is trying to minimize the total surface area. However, conditions imposed on the distribution of the magnetic induction and macroscopic shielding currents force the system to develop a macroscopic pattern of embedded normal phase. In the language of superconductivity research one refers to domains of superconducting and normal phases separated by the interface boundary that, due to proximity effects, has positive surface energy,

$$\sigma \left[ \frac{\text{erg}}{\text{cm}^2} \right] = \delta[\text{cm}] \frac{H_c^2}{8\pi} \left[ \frac{\text{erg}}{\text{cm}^3} \right] \quad (10.2)$$

conventionally parameterized by the “wall thickness  $\delta$ ” as a fraction of the condensation energy per unit volume,  $H_c^2/8\pi$ .

The theoretical description of the intermediate state problem dates back to the 1930s when Lev Landau suggested a simple stripe model, which was possible to analyse analytically [10–12]. Landau’s one dimensional analysis led to the conclusion that the intermediate state forms a pattern of alternating stripes or laminae. In two dimensions it was believed that a labyrinth-like (laminar) pattern of wriggling domains (laminae) represented the equilibrium state. Later refinements of the original Landau model (such as domain widening and/or branching) tried to address apparent inconsistencies between the model and various experiments, with the main problem being multiple observations of the closed-topology structures (flux “tubes” or “spots”) in the best samples [5, 13–15]. Still, until recently, the labyrinth pattern has been widely viewed as the equilibrium topology of the intermediate state. However, even a well known book by Shoenberg [16] shows one of the first visualizations of the intermediate state patterns by Meshkovsky and Shalnikov [17] where flux spots are clearly seen. Later, Goren and Tinkham questioned the Landau model, stating that: “It turns out that this ‘spot model’ of the intermediate state has approximately the same free energy as the laminar model (within the accuracy of our rather simple calculation), which implies that either flux spots, laminae, or both could exist in the intermediate state” [15]. Such energetics degeneracy, of course, gives rise to a rich array of patterns. A recent movie produced by the authors is available as supplementary material in refs [4, 21]. Realizing the difficulties of the simplified laminar picture, experimental and theoretical effort has never stopped [22–29]. An earlier video recording produced by Solomon and Harris under their contract with United Aircraft Research Laboratories in 1970–1 clearly shows the mobile tubular pattern of the intermediate state,<sup>1</sup> in agreement with the above predictions. Unfortunately, this tape has never been made widely available (probably due to the difficulty in distributing research video material) and published papers do not contain the important physics related to the observed pattern formation, its dynamics and evolution [18–20]. A very similar unpublished movie was produced by Dutoit and Renderer (Université de Lausanne) in 1988–92.<sup>2</sup> Focusing on the topology and pattern formation and dynamics, it has been finally shown that the equilibrium, intermediate state in a type-I superconductor consists of flux tubes at least for certain experimental conditions [4, 21, 27–31]. At high enough densities the tubes evolve into a well defined superconducting froth as shown in Figs 10.4 and 10.7 below. The fundamental problem is that in a finite system it is impossible to predict 2D and moreover 3D pattern based solely on the energy minimization arguments [24]. The topology of the pattern has to be assumed and then its geometrical parameters are determined from the minimization. It is interesting to entertain the idea of the possibility of minimizing free energy working with the parameters of pattern generators, such as iterated function systems [32], and then generating and “revealing” the best pattern.

---

<sup>1</sup>We thank Nigel Goldenfeld (University of Illinois at Urbana-Champaign, USA) for sharing this video tape with us.

<sup>2</sup>We thank Michael Indenbom (University of Brest, France) for sharing this video tape with us.

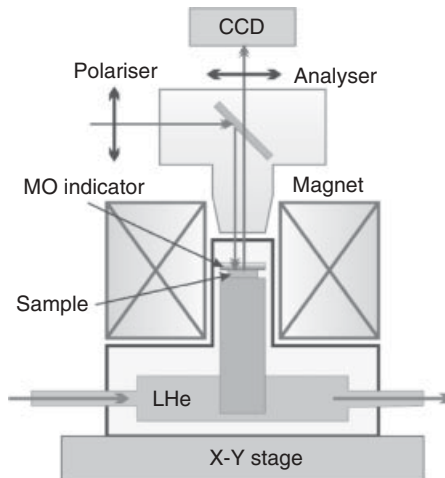


**Fig. 10.1** Magneto-optical setup for low-temperature measurements.

### 10.3 Observation and Study of the Tubular Intermediate State Patterns

To observe and study the behavior of suprafroth, we used low temperature magneto-optical imaging [4, 13, 21, 28–31]. Single crystals of lead (Pb) with (001) orientation were grown, cut and polished by Mateck GmbH (<http://www.mateck.de>). The samples were in the form of bulk discs, 5 mm in diameter and 1 mm thick. In the experiment, the component of the magnetic induction perpendicular to the surface was measured by utilizing the magneto-optical Faraday effect in bismuth-doped iron garnet indicators with in-plane magnetization [30]. The experimental setup is shown in Fig. 10.1.

A flow-type liquid  $^4\text{He}$  cryostat with the sample in vacuum was used. The sample was positioned on top of a copper cold finger and an indicator was placed on top of the sample. The cryostat was positioned under a polarized-light reflection microscope and the colour images could be recorded on either video or high-resolution CCD cameras. When linearly polarized light passes through the indicator and reflects off the mirror sputtered on its bottom, it acquires a double Faraday rotation of the polarization direction proportional to the magnetic field intensity in the indicator film at a given location just above the sample surface. Observed through the (almost) crossed analyser, we recover a 2D image.<sup>3</sup> In all images, the contrast comes only from a magnetic field with the intensity proportional to the local induction values, so that bright areas correspond to the (almost) normal phase, whereas dark regions show superconducting regions from which the magnetic flux is expelled.

An example of a direct observation of the developing suprafroth pattern is shown in Fig. 10.2. In the experiment a disc-shaped single crystal of lead was cooled in zero applied

<sup>3</sup>Note that some images contain a tooth-shaped overlay of darker and brighter areas. This is a side effect of a birefringence in the magneto-optical indicator that has in-plane magnetic domains and at certain angles with respect to the polarization plane these domains also show up in the images. This, however, does not distort or alter the underlying image in any way.

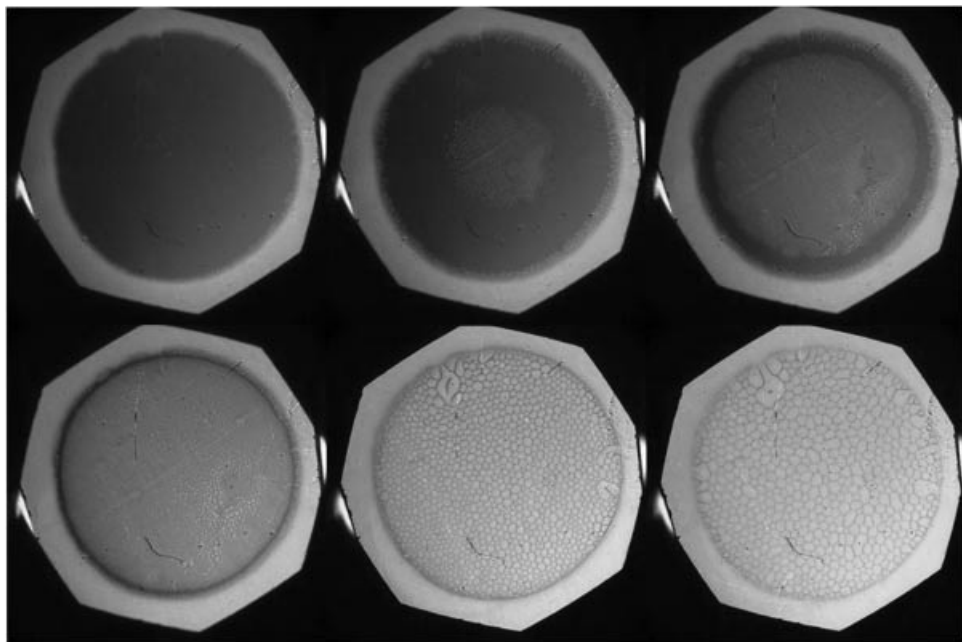


**Fig. 10.2** Development of the suprafroth in a 5 mm diameter single crystal of lead. The images were obtained at 6 K upon an increasing magnetic field. From top to bottom, left to right,  $H = 50, 120, 150, 190, 207, 220$  Oe.

magnetic field to  $T = 6$  K and then the field was applied. The top row shows images taken at  $H = 50, 120$  and  $150$  Oe (left to right) and the bottom row shows the formed suprafroth region imaged at  $190, 207$  and  $220$  Oe. The suprafroth pattern is formed at a higher magnetic field upon flux penetration. On flux exit, a laminar pattern is observed. This topological hysteresis [30] is related to a non-ellipsoidal shape of the superconducting sample [21]. In the case when a geometric barrier related to the sample shape is absent (ellipsoid or cone), a tubular pattern exists on both flux entry and flux exit [21]. Topological hysteresis is shown in Fig. 10.3. Both images were obtained at the same field ( $190$  Oe) and temperature ( $6$  K), but the left picture was taken after the magnetic field was applied after cooling in a zero field, whereas the right image was obtained after the external field was ramped above  $H_c$ .

Importantly, not only topology exhibits a clear difference between closed (left image) and open (right image), but macroscopic behavior such as magnetization is also hysteretic. The magnetization loop,  $M(H)$ , and the corresponding evolution of the intermediate state are shown in Fig. 10.4. Solid lines show the directly measured loop whereas symbols show results of the zero-field cooled and field-cooled measurements. The fact that the descending branch of  $M(H)$  coincides exactly with field-cooled magnetization as well as that hysteresis vanishes at  $H \rightarrow 0$  indicates the absence of pinning. This topological hysteresis cannot be removed by sample improvements, because it is related to the differences in topologies of the intermediate state patterns.

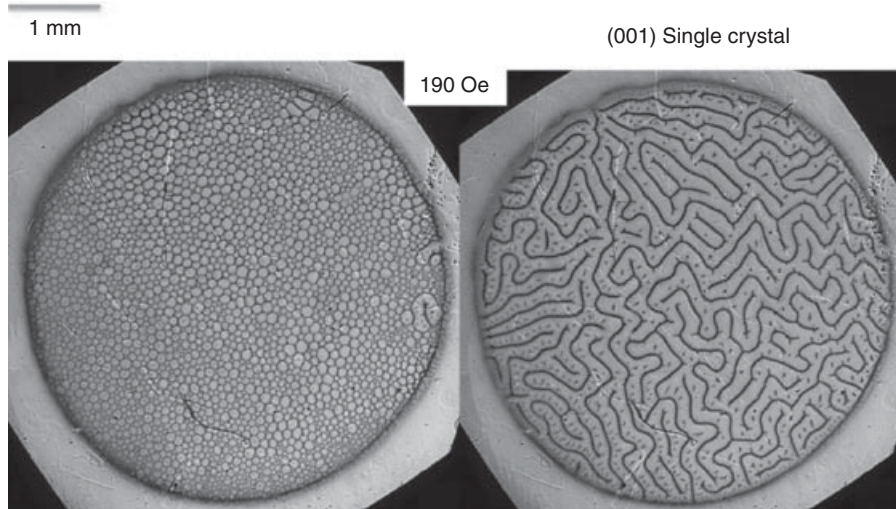


**Fig. 10.3** Topological hysteresis: comparison of patterns obtained on flux entry (left) and exit (right) imaged at the same magnetic field of 190 Oe and temperature of 6 K.

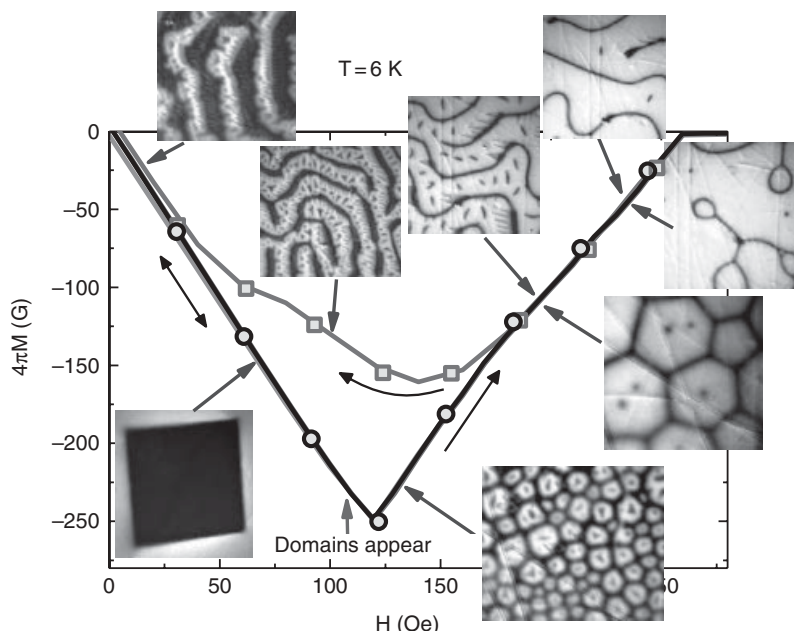


**Fig. 10.4** Magnetization loop of a stress-free sample accompanied by a visual guide of the developing suprafroth pattern upon flux penetration and of the laminar pattern upon flux exit. Squares show results of field-cooled measurements [30].

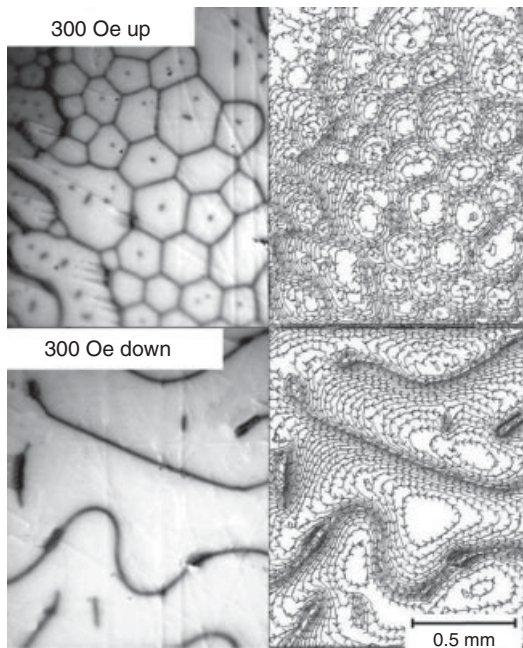


**Fig. 10.5**  $T = 5\text{ K}$ ,  $H = 300\text{ Oe}$ . Left: distribution of the magnetic induction upon flux penetration (top) and exit (bottom). Right: corresponding contour plots of shielding currents' density obtained by the numerical inversion. Arrows show the direction.

There is an important difference between this superconducting intermediate state pattern and other froths. In the latter all interactions are local (except for two-dimensional magnetic froths where dipolar interactions are important), whereas in the former the intricate unhomogeneous structure of the magnetic field is maintained by macroscopic loops of supercurrent. Using numerical inversion of the Biot–Savart law, we reconstruct these currents as shown in the right panel of Fig. 10.5. The left panels show the magnetic field upon penetration (top) and exit (bottom).

Finally, we show that the evolution of the disordered tubes at small fields finally leads to a formation of the suprafoam – a polygonal two-dimensional array of interconnected cells with the boundaries being superconducting phase and normal interior. According to Goren and Tinkham (GT), the average diameter,  $D$ , of the tubes should increase with a magnetic field as

$$D = [2\delta \cdot d / (1 - h)(1 - h^{1/2})]^{1/2} \quad (10.3)$$

where  $d$  is the sample thickness,  $h = H/H_c$  and  $\delta$  is the wall energy parameter [13, 15]. Figure 10.6 shows direct confirmation of the GT model from our measurements by analysing the mean tube diameter as a function of a magnetic field in Pb crystal. The solid line is a plot (not a fit) of the GT equation for the average tube diameter with experimentally determined  $\delta = 80\text{ nm}$  [13].

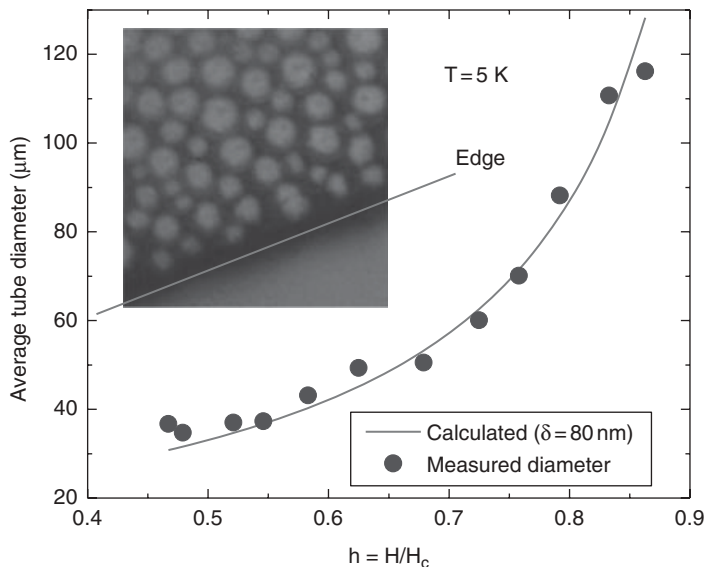


**Fig. 10.6** Average tube diameter as a function of the reduced applied field in Pb crystal measured at  $T = 5 \text{ K}$ . The continuous line is a GT plot (not a fit) as described in the text. Inset: example of the flux tubes (bright) penetrating the sample from the edge marked by a line.

As soon as the tubes start to interact at higher field densities and for a froth-like pattern, there is enough dynamic range (in terms of fields and temperatures) where the behavior of this suprafroth can be studied by the approaches developed for the conventional froths. This is summarized in Fig. 10.7 where the dark region shows part of the phase diagram where the suprafroth exists on flux entry after cooling in a zero field as shown by the schematic path.

The magneto-optical images show a clear pattern evolution upon increase of the applied magnetic field. Initially, separate flux tubes are injected into the sample (Fig. 10.7, lower inset). As their number increases, they coalesce and grow. As the field grows, the repulsive forces between the tubes ultimately lead to formation of the suprafroth with a well defined polygonal cellular structure (Fig. 10.7, large inset). For magnetic fields that approach the upper limit of superconductivity,  $H_c$ , this structure ultimately degrades and forms extended concave cells with rounded boundaries. The suprafroth structure is very different from that seen for the more common, type-II, superconductors where the interface energy is negative and the magnetic field inside the material exists in the form of Abrikosov vortices; each carries a single flux quanta and no suprafroth is possible.

#### 10.4 Structural Statistical Analysis of the Suprafroth

The coarsening of a suprafroth with applied magnetic field is shown in Fig. 10.8. The images were obtained at  $T = 6 \text{ K}$  when, after zero-field cooling, the indicated magnetic fields were applied. The observed patterns were traced and converted into black and white

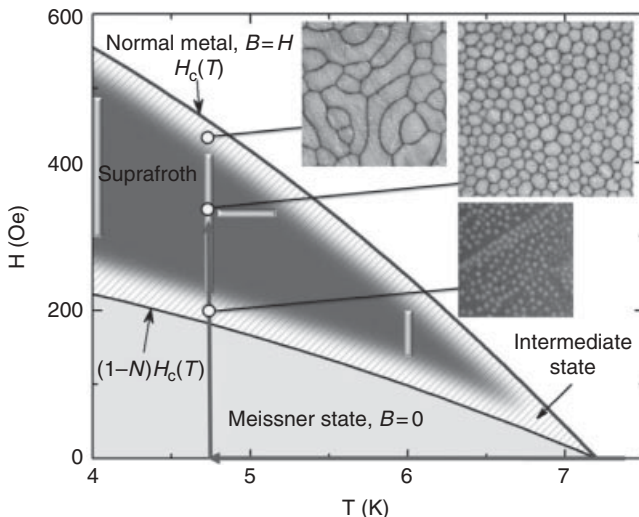


**Fig. 10.7** Phase diagram of a superconducting lead disk. Below the  $(1 - N)H_c(T)$  line, there is a genuine superconducting (Meissner) state in which no magnetic flux exists. Above the  $H_c(T)$  line, there is no superconductivity. The shaded region between these lines is the intermediate state. The solid colour inside this region shows where the suprafroth is stable. There is no well defined boundary for the suprafroth region. At small magnetic fields, separate tubes do not yet form a polygonal structure (lowest insert), whereas at higher fields, the structure evolves into more rounded and elongated objects that are difficult to call “froth” (upper left insert). Magneto-optical images illustrate this pattern evolution for magnetic field increasing after cooling in zero field (4.8 K path shown). Vertical lines at 4.0, 4.8, and 6.0 K as well as the horizontal line at 320 Oe show where images and data used in this work were acquired.

images as shown in Fig. 10.9. Traced images were analysed in terms of cell statistics. Our typical region of interest was  $2 \times 2$  mm and contained up to 160 cells.

Before we proceed to the discussion of the statistical laws, though, it is important to examine the question of reversibility. In conventional froths, the parameter that is varied to study coarsening is time, an irreversible quantity.

Therefore, conventional coarsening is inherently irreversible. However, the irreversibility can be twofold: changes in the froth matter (aging effects such as drying and drainage) and/or changes in the froth topology. While it is impossible to reverse time, in the case of the suprafroth the equivalent controlling parameter, magnetic field, can be increased and decreased so as to examine the topological elasticity of the structure, while the physical properties of cell walls remain perfectly reversible. Figure 10.10 examines the effect of a minor loop in the applied field on the suprafroth. In the experiment,  $H = 466$  Oe was applied after zero field cooling to  $T = 4.0$  K and an image taken (an underlying black trace in each of the three panels of Fig. 10.10). Then the magnetic field was increased by the amount shown and returned back to 466 Oe and a new image (shown in red) acquired. An immediate (and experimentally new compared to regular froth) conclusion is that the regions with the

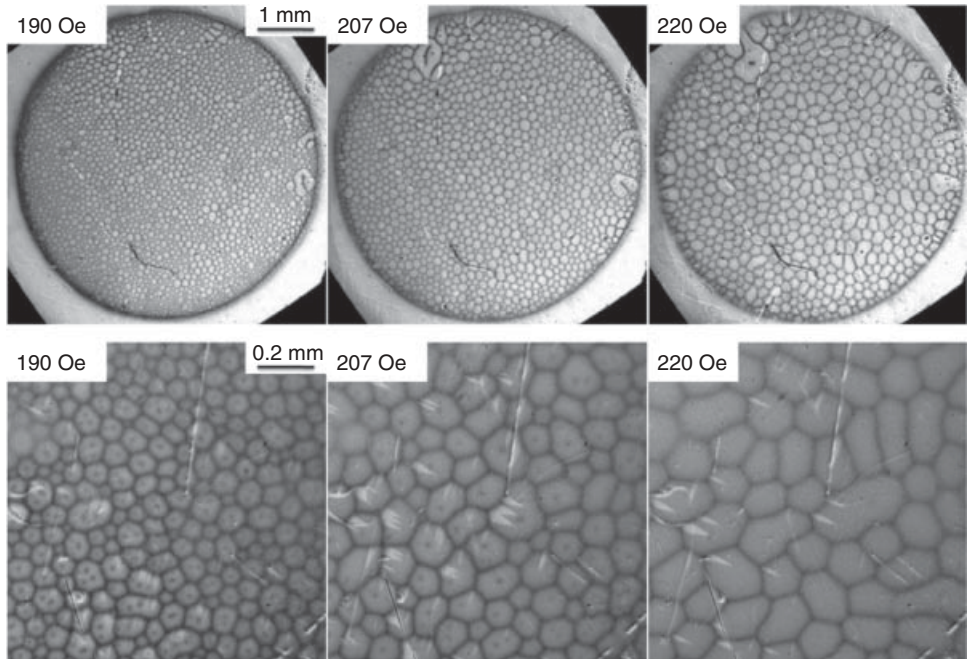


**Fig. 10.8** Coarsening of the suprafroth with increasing magnetic field at  $T = 6.0\text{ K}$ . The top row shows the entire sample ( $5\text{ mm}$  disc). The bottom row shows the same  $1 \times 1\text{ mm}^2$  region of the disc material, which was the most defect-free and chosen for the statistical analysis.

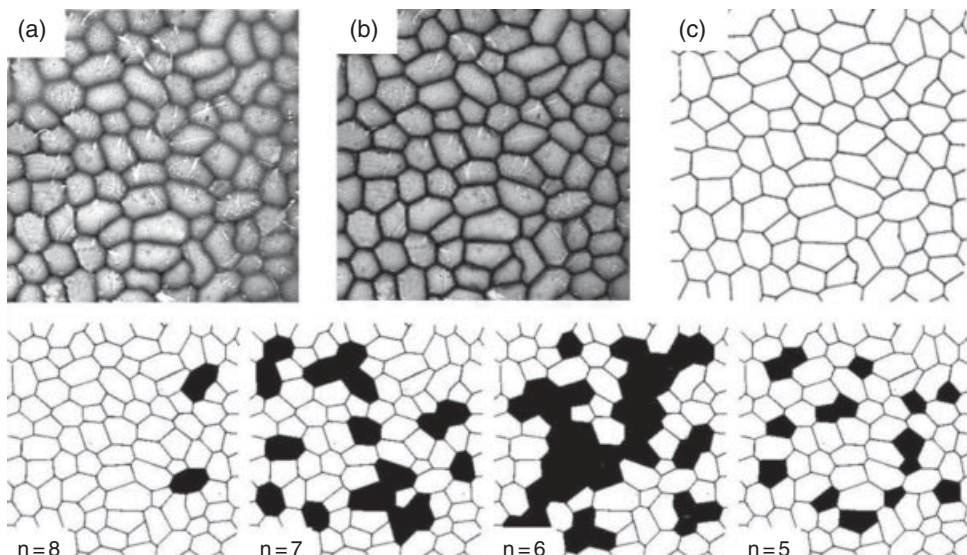


**Fig. 10.9** A  $2 \times 2\text{ mm}^2$  image measured at  $4.8\text{ K}$  and  $390\text{ Oe}$ . (a) Original image; (b) superimposed trace of the boundaries; (c) the B/W trace. Bottom row: identification of  $n$ -sided cells.

most uniform distribution of cell sizes (shown by the grey square in Fig. 10.10) are more robust compared to the regions with broader distributions. This result is directly related to the empirical Aboav–Weaire law [1] as applied to the dynamics of cells whose neighbours have certain number of sides. Moreover, after the initial cycle,  $H \rightarrow H + \Delta H \rightarrow H$ , the structure remains perfectly elastic and reproducible (for small  $\Delta H \sim 5$  Oe) upon several

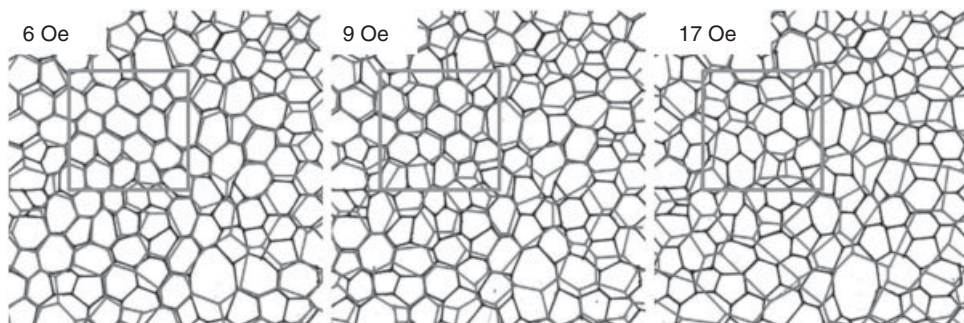


**Fig. 10.10** The structural evolution of the suprafoam at 4.0 K. Black lines correspond to the state obtained after cooling in zero field and applying 466 Oe. Grey lines show the structure obtained after the field was increased by  $\Delta H$  indicated in the figure and decreased back to 466 Oe. Grey square shows the region of most reversible behavior.

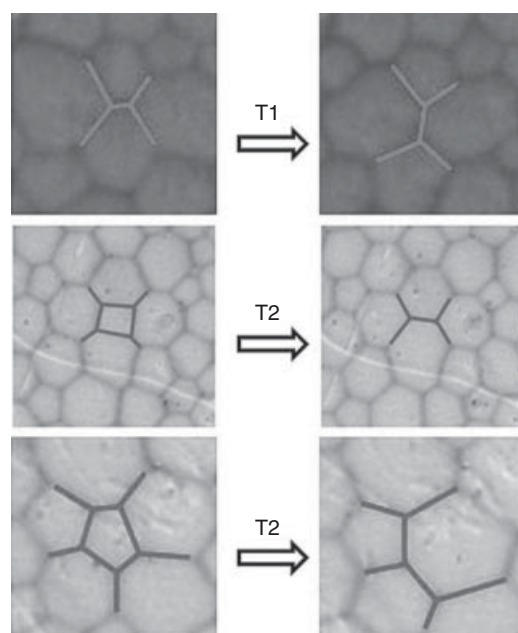


**Fig. 10.11** T1 process (top frame) and two T2 processes. Images obtained by examining suprafoam evolution at 4.8 K and in fields changing from 290 to 300 Oe.

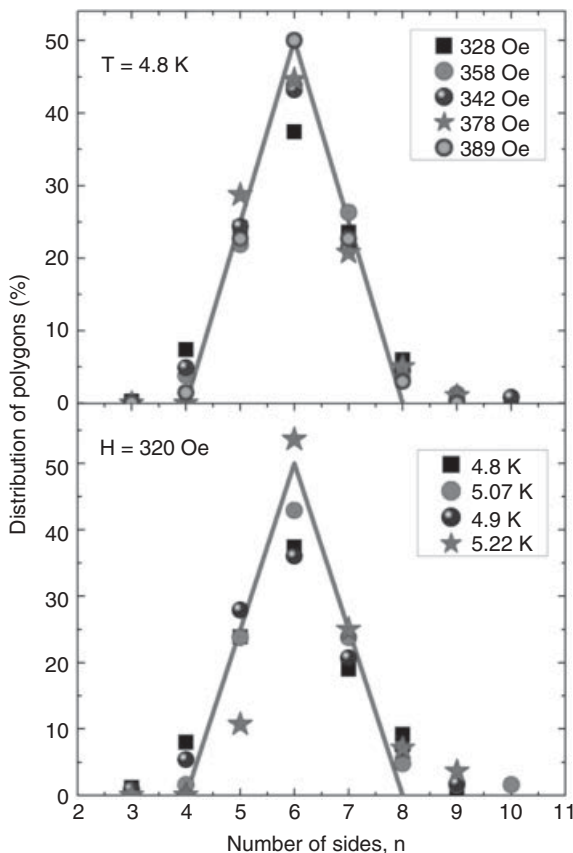


**Fig. 10.12** The distribution of the number of  $n$ -sided cells in froth coarsened by magnetic field (top) and temperature (bottom).

subsequent cycles. Similar elasticity is observed if the magnetic field was decreased by a small amount and returned back to the base field.

For further comparison with conventional froths, it is important to identify the elementary transformation processes in a suprafroth. Figure 10.11 shows what, in the physics of conventional froths, are known as T1 (sliding) and T2 (cell collapse) processes. These images are exactly like those observed in a coarsening soap froth. Therefore, the mesoscopic cellular dynamics in suprafroth appears to be quite similar to that of conventional froths.

Having examined the data in a qualitative manner, we now can proceed to a quantitative analysis of the cellular structure of the suprafroth using topological analysis similar to that depicted in Fig. 10.9. Figure 10.12 shows the distribution of the number of cells with  $n$  sides for suprafroth coarsened by an applied magnetic field at 4.8 K or coarsened by temperature at 320 Oe. In both cases, it is clear that  $n = 6$  is the most probable polygon, consistent with Euler's theorem that states that the average number of sides in a continuous

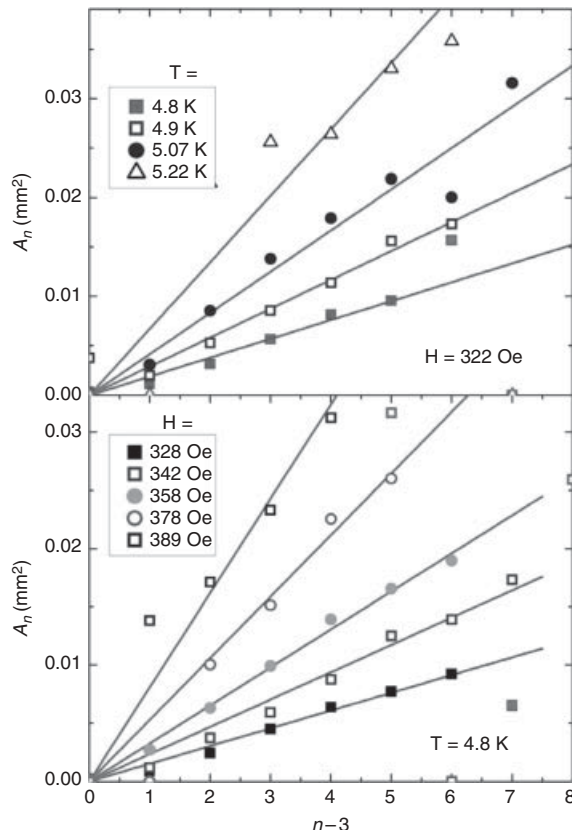


**Fig. 10.13** The  $n$ -dependence of an average cell area at different temperatures (top) and fields (bottom).

two-dimensional tiling with  $n$ -sided cells that have 3-fold vertices is  $N=6$  [1]. If  $C$  is the total number of cells in a studied area  $A$  and  $C_n$  is the number of  $n$ -sided cells, then the distribution function  $p_n = C_n/C$ . As shown by a solid line, a simple triangular distribution,  $p_n = 0.5(1 - 0.5|n - 6|)$  describes the observation quite well. Importantly,  $p_n$  does not depend significantly on either field or temperature.

We can also examine how the average area of an  $n$ -sided cell depends on  $n$  for different magnetic fields and temperatures (Fig. 10.13). This statistical correlation was first studied in biological, cellular structures by Lewis and is now known as Lewis's law [33, 34],

$$A_n = \frac{A}{C} \lambda \left( n - \left[ 6 - \frac{1}{\lambda} \right] \right) \quad (10.4)$$

where the empirical constant  $\lambda$  is typically between 1/3 and 1, but its microscopic meaning is not well understood. It is clear from Fig. 10.13 that in order to make our observation compatible with Lewis's law we need to set  $\lambda = 1/3$ , so that  $A_n = (A/3C)(n - 3)$ .

Having deduced a form for the coarsening of a suprafroth, we should recall that the physics of type-I superconductors in the intermediate state dictates a certain dependence of the total volume of the superconducting phase,  $V_s$ , on temperature and magnetic field. Specifically, in the intermediate state, the magnetic moment of a type-I superconductor of volume  $V$  is [35],

$$4\pi M = V \frac{H - H_c}{N} = -V_s H_c \quad (10.5)$$

Therefore, the total perimeter of all cell boundaries,

$$P = \frac{V_s}{\delta t} = \frac{A}{\delta} \frac{H_c - H}{NH_c} \quad (10.6)$$

where  $A$  is the total area,  $t$  is sample thickness, and  $\delta$  is the width of the superconducting walls in the suprafroth. It was found, by direct measurements, that  $\delta \approx 14 \mu\text{m}$  and is field independent in our range of fields and temperatures. On the other hand, the total perimeter is expressed via the distribution  $p_n$  and the average length of a side of an  $n$ -sided cell,  $s_n$ , as

$$P = \frac{C}{2} \sum np_n s_n = 1.85 \sqrt{AC} \quad (10.7)$$

Therefore, we expect for the total number of cells,  $C \sim (H_c - H)^2$ , which is, indeed, what we observe in Fig. 10.14(c). Similar behavior can be predicted for the temperature dependence of  $C$  (Fig. 10.14(d)). However, the most striking result is that the  $\lambda = 1/3$  coefficient of Lewis's law obtained from the linear fits shown in Fig. 10.12 is in excellent agreement with direct, parameter-free calculation of

$$\frac{dA_n}{dn} = \lambda \frac{A}{C} \quad (10.8)$$

with the experimental values of  $A$  and  $C$  as shown by the continuous (B-spline) line in Fig. 10.14(a, b). The deviations at higher temperatures are related to breaking the cellular structure apart.

One of the most studied and discussed statistical laws in the physics of froth coarsening is the von Neumann law [1, 36, 37], which predicts a linear dependence of the rate of change of the average area of an  $n$ -sided cell on its number of sides,  $n$ . In conventional froths, it has been shown both experimentally and theoretically that

$$\frac{dA_n}{dt} = \gamma(n - 6) \quad (10.9)$$

Historically, the fact that the offset to  $n$  was the number six was associated with the Euler tiling theorem: six being the most probable polygon. In the case of the suprafroth we can

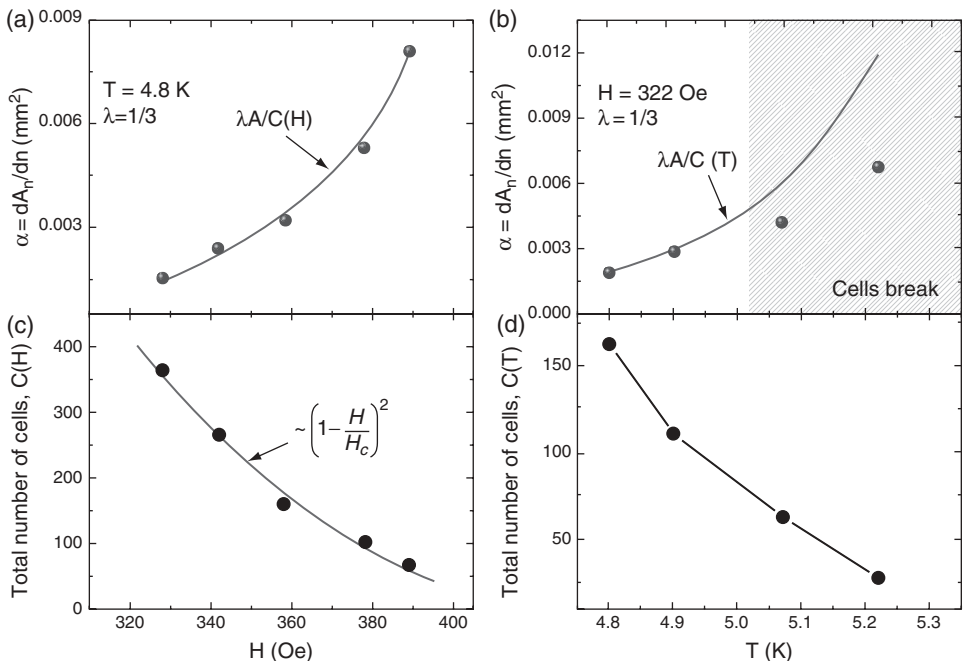


**Fig. 10.14** Top row: the coefficient in Lewis's law. Bottom row: field and temperature dependence of the total number of cells,  $C$ .

generalize von Neumann's law and consider the temperature and magnetic field derivatives. By direct differentiation of Lewis's law,  $A_n = (A/3C)(n-3)$ , with  $C = A(H_c - H)^2/(1.85\delta NH_c)^2$ , we expect

$$\frac{dA_n}{dH} = \frac{2.28}{H_c} \frac{(N\delta)^2}{(1 - H/H_c)^3} (n-3) = \beta(n-3) \quad (10.10)$$

If the derivative is calculated for the small variation of the magnetic field ( $\sim 5\%$  in our case), so that  $H/H_c \approx \text{const}$ , the pre-factor  $\beta$  does not vary by much. Therefore, despite the fact that we still have hexagons as most probable polygons, the rate of change is predicted to increase for any  $n > 3$ . This is, indeed, observed in the experiment as shown in Fig. 10.15 where the derivatives were evaluated in the small range of fields (or temperatures).

Clearly, a  $(n-3)$  dependence is seen in both graphs. We can even estimate the coefficient  $\beta$  by substituting the experimental values,  $H = 0.8H_c$ ,  $H_c = 0.044T$ ,  $\delta = 0.014 \text{ mm}$  and  $N = 0.63$ , so that we estimate  $\beta \approx 0.5$ , which is quite close to the observed value of 0.6 given the uncertainty in the demagnetization factor and superconducting wall width,  $\delta$  (upper frame of Fig. 10.15). It is more difficult to estimate the coefficient for  $dA_n/dT$  (lower frame of Fig. 10.15), because  $M(T)$  is a more complex function of temperature.

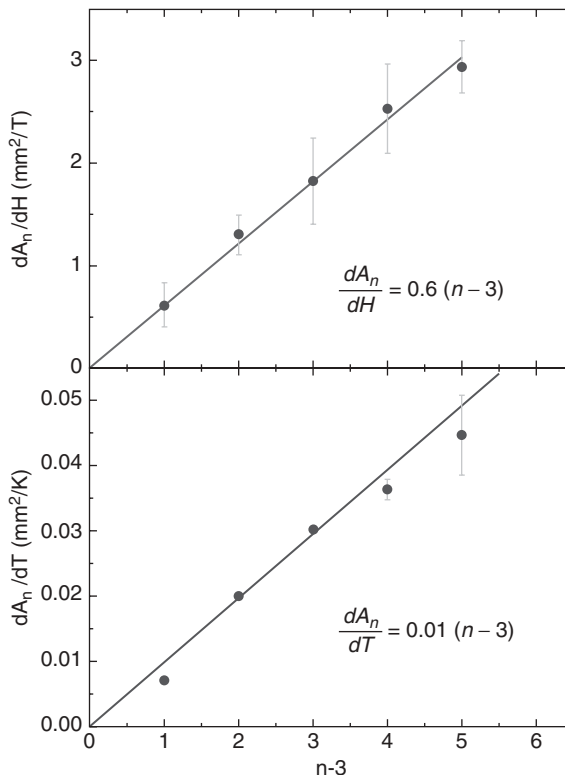


**Fig. 10.15** Generalized von Neumann's law for magnetic field and temperature derivatives.  $dA_n/dH$  was calculated at  $T = 4.8\text{ K}$  and  $dA_n/dT$  was calculated for  $H = 330\text{ Oe}$ .

The ultimate explanation for the observed  $(n - 3)$  rather than  $(n - 6)$  behavior has to be associated with the differences between the microscopic mechanisms of the coarsening. Whereas in conventional froths the amount of froth material remains constant or decreases via drainage and the process is controlled by the surface tension and diffusion of the boundaries, in suprafroth the coarsening is controlled by the magnetic field that exerts magnetic pressure inside the superconducting cells. Therefore, every polygon is inflated and the minimum planar object has  $n = 3$  sides, so all polygons grow. Moreover, the exact formula for the area of a regular polygon with side length  $s_n$ ,

$$A_n = \frac{n}{4} s_n^2 \cot \frac{\pi}{n},$$

can be roughly approximated by the  $(n - 3)$  behavior. On the other hand, the linearity of the growth rate with  $n$  is something that comes from the general physics of the coarsening froths. To this end this work on suprafroth formally divorces the most probable number of sides (6) and the offset in von Neumann's law (3 for the suprafroth).

## Acknowledgements

We thank Vladimir Kogan, Jörg Schmalian, Roman Mints, Rudolf Huebener, Nigel Goldengeld, Rinke Wijngaarden, Alan Dorsey, and Robert Kohn for helpful discussions. Work at Ames was supported by the US Department of Energy, Office of Basic Energy Science, Division of Materials Sciences and Engineering. Ames Laboratory is operated for the US Department of Energy by Iowa State University under Contract No. DE-AC02-07CH11358. R.P. Acknowledges support from the NSF Grant Number DMR-05-53285 and the Alfred P. Sloan Foundation.

## References

- [1] D. Weaire and S. Hutzler. *The Physics of Foams*. Oxford University Press, New York, 1999.
- [2] F. Elias, C. Flament, J.-C. Bacri, and F. Francer. Two-dimensional magnetic liquid froth. In *Foams and Emulsions*, J.F. Sadoc and N. Rivier (eds). Springer, New York, 1999.
- [3] D. Weaire, F. Bolton, P. Molho and J. A. Glazier. Investigation of an elementary model for magnetic froth. *J. Phys.: Condens. Matter*, **3**: 210114, 1990.
- [4] R. Prozorov, A. F. Fidler, J. R. Hoberg and P. C. Canfield. Suprafroth in type-I superconductors. *Nature Phys.*, **4**: 327–32, 2008.
- [5] M. Tinkham. *Introduction to Superconductivity*. McGraw-Hill, New York, 1975.
- [6] J. Bardeen, L. N. Cooper and J. R. Schrieffer. Theory of superconductivity. *Phys. Rev.*, **108**: 1175–204, 1957.
- [7] A. A. Abrikosov. *Fundamentals of the Theory of Metals, Part 2*. North Holland, Amsterdam, 1995.
- [8] A. A. Abrikosov and L. P. Gor'kov. Theory for the superconductivity of alloys. I. Electrodynamics of alloys at absolute zero. *Zhurnal Eksperimental'noi i Teoreticheskoi Fiziki*, **35**: 1558–71, 1958.
- [9] J. A. Osborn. Demagnetizing factors of the general ellipsoid. *Phys. Rev.*, **67**: 351, 1945.
- [10] L. Landau. The intermediate state of superconductors. *Nature*, **141**: 688, 1938.
- [11] L. D. Landau. *Sov. Phys. JETP*, **7**: 371, 1937.
- [12] L. D. Landau. *J. Phys. USSR*, **7**: 99, 1943.
- [13] R. P. Huebener. *Magnetic Flux Structures of Superconductors*. Springer-Verlag, New York, 2001.
- [14] J. D. Livingston and W. DeSorbo. The intermediate state in type I superconductors. In *Superconductivity, Vol. 2*, R. D. Parks (eds). Marcel Dekker, New York, 1969.
- [15] R. N. Goren and M. Tinkham. Patterns of magnetic flux penetration in superconducting films. *Journal of Low Temperature Physics*, **5**: 465–94, 1971.
- [16] D. Shoenberg. *Superconductivity*. Cambridge University Press, Cambridge, 1952.
- [17] A. Meshkovsky and I. A. Shalnikov. *Zh. Eksp. Teor. Fiz.*, **11**: 1, 1947.
- [18] P. R. Solomon, Flux motion in type-I superconductors, *Phys. Rev.*, **179**: 475, 1969.
- [19] P. R. Solomon and R. E. Harris. Current-induced flow of domains in the intermediate state of a superconductor. *Phys. Rev. B*, **3**: 2969, 1971.
- [20] P. R. Solomon and R. E. Harris. In 12th International Conference on Low Temperature Physics. Keigaku, Takaya, Japan, 1971.
- [21] R. Prozorov. Equilibrium topology of the intermediate state in type-I superconductors of different shapes. *Phys. Rev. Lett.*, **98**: 1–4, 2007.
- [22] A. T. Dorsey and R. E. Goldstein. Shapes of flux domains in the intermediate state of type-I superconductors. *Phys. Rev. B: Condensed Matter Mater. Phys.*, **57**: 3058–72, 1998.
- [23] R. E. Goldstein, D. P. Jackson and A. T. Dorsey. Current-loop model for the intermediate state of type-I superconductors, *Phys. Rev. Lett.*, **76**: 3818–21, 1996.

- [24] R. Choksi, R. V. Kohn and F. Otto. Energy minimization and flux domain structure in the intermediate state of a type-I superconductor. *J. Nonlinear Sci.*, **14**: 119–71, 2004.
- [25] F. Liu, M. Monledo and N. Goldenfeld. Kinetics of the superconducting transition. *Phys. Rev. Lett.*, **66**: 3071–4, 1991.
- [26] G. R. Berdiyorov, A. D. Hernandez and F. M. Peeters. Confinement effects on intermediate-state flux patterns in mesoscopic type-I superconductors, *Phys. Rev. Lett.*, **103**: 267002, 2009.
- [27] M. Menghini and R. J. Wijnngaarden. Patterns close to the critical field in type-I superconductors. *Phys. Rev. B*, **75**: 014529, 2007.
- [28] V. Jeudy and C. Gourdon. Stability of normal state bubbles in the intermediate state of type I superconductors. *Journal of Magnetism and Magnetic Materials*, **300**: 101–3, 2006.
- [29] V. Jeudy, C. Gourdon, A. Cebers and T. Okada. Pattern formation in type-I superconducting films. *Journal of Applied Physics*, **101**: 09G118, 2007; doi 10.1063/1.2712827 2007.
- [30] R. Prozorov, R. W. Giannetta, A. A. Polyanskii and G. K. Perkins. Topological hysteresis in the intermediate state of type-I superconductors. *Phys. Rev. B*, **72**: 1–4, 2005.
- [31] R. Prozorov and J. R. Hoberg. Dynamic formation of metastable intermediate state patterns in type-I superconductors. *J. Phys.: Conference Series*, **150**: 2009.
- [32] M. Barnsley. *Fractals Everywhere*. Academic Press, Oxford, 1988.
- [33] F. T. Lewis. The correlation between cell division and the shapes and sizes of prismatic cells in the epidermis of cucumis. *Anat. Rec.*, **38**: 341–62, 1928.
- [34] N. Rivier. Statistical thermodynamics of foam. *Foams and Emulsions*, **354**: 1999.
- [35] C. J. Poole, H. Farach, R. Creswick and R. Prozorov. *Superconductivity*. Elsevier, Amsterdam, 2007.
- [36] R. D. MacPherson and D. J. Srolovitz. The von Neumann relation generalized to coarsening of three-dimensional microstructures. *Nature*, **446**: 1053–5, 2007.
- [37] J. Von Neumann. *Metal Interfaces*. American Society of Metals, Cleveland, OH, 1952.

# **Part II**

## Applications

# 11

## Froth Phase Phenomena in Flotation

*Paul Stevenson and Noel W.A. Lambert*

### 11.1 Introduction

Flotation is a process that separates different species of particles on the basis of their hydrophobicity and serves as a workhorse of the mineral processing and coal preparation industries. There are numerous different types of devices for flotation, but the mechanism of flotation itself is common across them all. Hydrophobic particles attach to bubbles within the bubbly liquid (or pulp phase) and rise up the unit. The bubbles eventually form a froth, which continues to rise up the unit until it discharges at the top of the column in the ‘concentrate’ stream. Hydrophilic particles do not readily attach and these are not transported as bubble-particle aggregates but are rejected in the bottom ‘tailings’ stream. Of course, no process is ever perfect, and flotation performance is often characterised by its recovery (i.e. the proportion of target species entering in the feed that reports to the concentrate) because some valuable material may be discharged via the tailings or the grade (i.e. the quality of the concentrate product) because some unwanted gangue material might be entrained into the concentrate stream rather than rejected via the tailings.

Figure 11.1 shows a schematic representation of a flotation column [1]. In column flotation, the bubbly liquid (or pulp) is known as the collection zone since it is here where particles, which have been fed to typically the top of the zone, have the opportunity to attach to bubbles and commence their journey up the column. Air bubbles are sparged to the base of the column, and there is a sump through which the tailings stream passes on its way to disposal in a dam or further processing. Above the collection zone is the ‘cleaning zone’, which is a deep froth layer. This rises up the column, carrying with it the attached particles. However, liquid continuously drains from the froth, helping return entrained

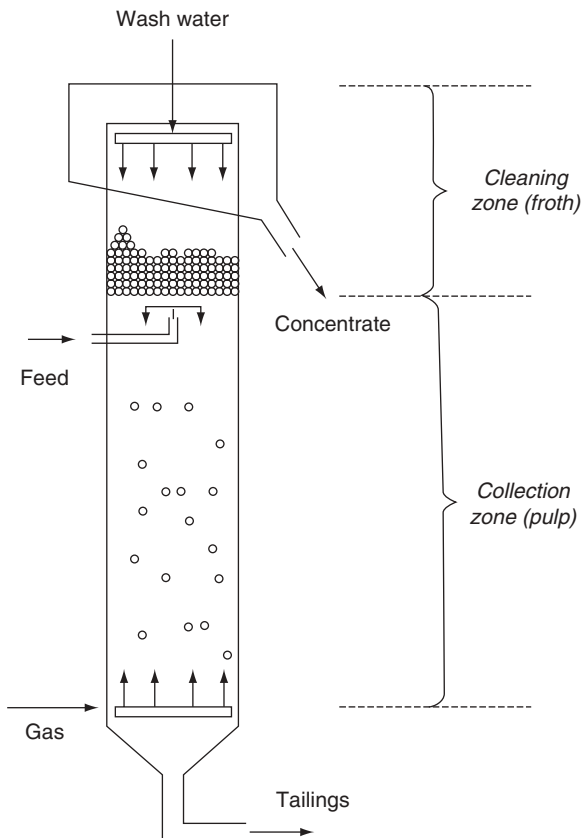


**Fig. 11.1** Schematic representation of column flotation, after [1].

unwanted gangue particles back the pulp. Washwater is typically added to the free surface of the froth via a spray in order to aid gangue rejection. If the rate at which washwater is added causes a net downward flow of liquid through the foam, then the column is said to be in ‘positive bias’. The performance of a flotation operation is dependent upon the suite of chemical reagents used, which can include:

1. frother: a surface-active compound used to stabilise the froth;
2. collector: used to adsorb to the valuable material to aid particle attachment to the gas–liquid interface; and
3. depressant: used to ameliorate recovery of unwanted particles in the concentrate.

Mechanical flotation cells use external agitation at the bottom the column to suspend particles. Typically the foam layer is less deep and the addition of washwater is less common. Mechanical cells have similarities with the Waldhof fermentor as described in Chapter 15. Proprietary devices that harness a froth layer in flotation include the Hydrofloat Separator that can float coarse particles from within a fluidised bed, and the Jameson Cell, the hydrodynamics of which are discussed in Chapter 15 in the context of gas–liquid

mass transfer, which is nominally good for floating fine particles but suffers from frother constraints as described in Section 11.7.

Flotation is related to the processes of foam fractionation and gas–liquid contacting in foam in that it relies on an overflowing pneumatic foam. However, it is a significantly more mature technology than these two other processes. Indeed the Australian Institute of Mining and Metallurgy held a Centenary of Flotation Symposium in 2005 nominally to mark 100 years since the introduction of the process to the minerals industry. During this time there has been enormous research and development investment in the process, and multifarious devices for yet greater recovery and grade of products have been marketed, although it is argued in Section 11.7 that development might be limited by operational constraints. It has been discussed in Chapters 14 and 15 that applications of concepts and technologies envisaged in the context of flotation can benefit the processes of foam fractionation and foam contacting, respectively.

Even though the design of various flotation machines may vary, the physical phenomena within the froth layer that influence flotation performance are common across all types of devices that exhibit a froth, and it is these phenomena that are considered herein. The particle-laden foam bubbles may exhibit changes in size as they rise through the foam caused by the rupture of films between them and inter-bubble gas diffusion (or Ostwald ripening). The wetness of the foam can diminish greatly with height because of capillary forces (which are mainly significant towards the bottom of the foam layer) and due to effects of bubble size distribution change. The bubbles at the bottom of the foam layer tend to be spherical, but take on a more polyhedral shape as the foam becomes progressively drier. At the top of the column, the foam must discharge across a weir into a launder vessel, and this exposes a free surface which can exacerbate film rupture. Bubble coalescence or other mechanical disturbances can cause hydrophobic particles to detach, which may or may not be recaptured, and unwanted hydrophilic particles can become entrained into the concentrate stream by convective-dispersive transport through the froth layer. Attached particles can modify the rheology of the gas–liquid surfaces, and entrained particles modify the bulk rheology of the interstitial liquid in the froth. Flotation froths are complicated physical systems indeed, and are much more involved than, say, foam fractionation froths, because the latter are ‘demineralised’ systems (i.e. it is a two-phase process with no solid phase present).

Pragmatic researchers looking for a mechanistic description of flotation froth sometimes perform studies upon two-phase gas–liquid systems to gain insights that would be impossible to obtain in a mineralised froth. However, as has been described in many other chapters, even two-phase stationary foam in not-well-understood and *a priori* predictions of its behaviour cannot be made with any great confidence. This is demonstrated in Fig. 11.2 by the diagram of Hilgenfeldt *et al.* [2], who show how drainage is interrelated to coarsening via both diffusion and rupture, and how these combine to influence foam rheology. Any error in predicting one mechanism can be greatly amplified through the interdependent nature of the pertinent phenomena. If one then adds in the processes of particle detachment and entrainment as well as rheology modification, then it is seen that a mechanistic model of phenomena in a flotation froth becomes singularly difficult.

The simulation of froth flotation is indeed a daunting task since the underlying physics behind the process is most complex. However, given the significance of froth flotation to the minerals processing industry, and the current high price of mineral and energy commodities, the motivation behind producing a resource that can simulate the behaviour

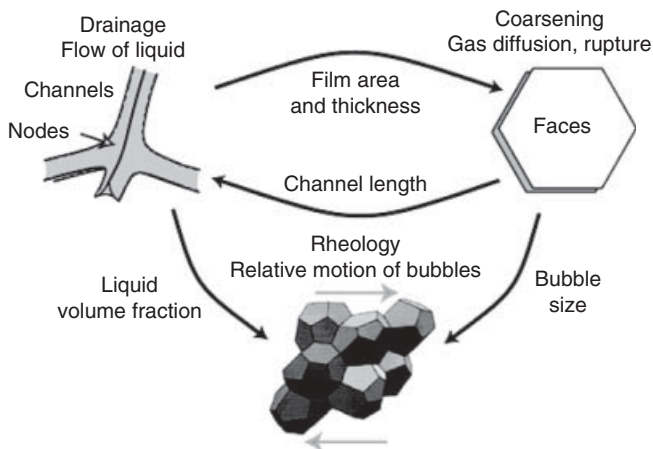


**Fig. 11.2** A representation of the interdependency of phenomena in a stationary demineralised foam [2].

of froth flotation cells, and banks and circuits thereof, is axiomatic. It is against this background that the research group of Jan Cilliers at Imperial College London have developed their ‘FrothSim’ flotation simulator, which is not currently commercially available. Neethling *et al.* [3] used FrothSim to investigate the effect of washwater on column performance, having previously used it to simulate the performance of flotation banks and circuits [4]. They claimed that ‘FrothSim is the first flotation simulator to predict the behaviour of not only the valuable mineral, but also the associated gangue and water’. This claim certainly raises high expectations, but may be considered by some to be premature since it is not apparent that the simulation correctly captures the underlying physics behind flotation froths. To give just one example, their simulation is critically dependent upon a parameter that is sometimes called ‘air recovery’, which is the fraction of air that leaves the column as unburst bubbles, and so is related to the degree of coalescence of the bubbles on the free surface of the froth [5]. An explicit relationship is given for this surface coalescence which assumed that the probability of film rupture is dependent upon external disturbances once the film has reached a specific thickness. This, however, is a gross oversimplification since bubble stability can be enhanced by attached particles (see Chapter 7) and stability is also dependent upon the evaporation rate from the free surface, none of which are taken into account in FrothSim. Even though some sub-elements of the model have been compared with plant data, there appears to be no proof that FrothSim can give *a priori* predictions of flotation performance.

Additionally, the Australian Minerals Industry Research Association (AMIRA) has provided major funding to a number of universities around the world to develop a steady-state flotation simulator, which is marketed by JKTech as JKSimFloat. Some of the modelling ideas that underpin this software are described by Harris *et al.* [6], with further details given in an AMIRA report [7], although the full details of the simulation do not appear to be in the public domain. Bouchard *et al.* [8] remark that the promise of JKTech has yet to be proved, and it will be excellent to see if this simulation can be fully validated against plant data in the future.

We prefer an alternative approach to understanding froth phase phenomena in flotation. Flotation is a microcosm of fluid mechanics and surface science. There is no doubt that a first principles approach to understanding the sub-process of, say, foam drainage or coalescence can help engender a fundamental understanding of the physics that underpin froth flotation. However, with the best will and the most intensive computing power, a complete *a priori* model of froth flotation process is not currently feasible. Thus, in flotation more than possibly any other unit operation, insight into plant practice is essential to gain an understanding of the process. There are multifarious correlations in the literature that nominally enable *a priori* predictions of various aspects of flotation froth, but the circumstances in which correlations are generally valid are often overlooked [9].

Thus, in the spirit of a pragmatic approach to understanding phenomena in the froth phase of flotation, this chapter is made up of elements that describe the physics of sub-processes that underpin the behaviour of a flotation froth, as well as a discussion of some practical considerations of implementing froth flotation on plant. The chapter is not intended to be a thorough description of the flotation process, but instead considers elements of flotation behaviour that occur in the froth phase only.

## 11.2 Froth Stability

One of the most important physical phenomena that governs flotation performance is that of the coalescence of bubbles (also known as bursting if failure is at the free surface). A thorough treatment of how particles can stabilise foam is given in Chapter 7. However, bubble coalescence can be exacerbated by the presence of hydrophobic particles (such as those attached in a flotation froth) if it bridges the film between adjacent bubbles. The particle will seek to minimise energy by moving to a central position in order to attain the contact angle, and it can then either stabilise the film or promote rupture. This mechanism was explained by Aveyard *et al.* [10], who showed that part of the film attached to a hydrophobic particle will attempt to dewet from the surface of a particle, thereby causing film rupture. It is because of this mechanism that although a degree of hydrophobicity is required to cause attachment to bubbles, very strongly hydrophobic particles are difficult to float because of their detrimental influence on froth stability. In a study that measured bubble size in columns in the presence of particles [11], it was found that froths with moderately hydrophobic particles were more stable than if very hydrophobic particles were introduced.

Triffett and Cilliers [12] have patented a device that can nominally give *in situ* information about the stability of a flotation froth that is based on the Bikerman [13] test of stability of a gas–liquid foam. Bikerman measured the equilibrium foam height  $H$ , created in a tube by sparging gas at a superficial velocity of  $j_g$  to the column, and defined the ‘foamability’,  $\Sigma$ , as the quotient of these parameters, i.e.  $\Sigma = H/j_g$ . Effectively, by placing a horizontal tube with the bottom end open and below the pulp–froth interface, the froth entering the tube has the opportunity to rise up the tube and eventually find an equilibrium height rather than reporting the concentrate.

However, Li *et al.* [14] have shown that results of the Bikerman foam stability for a test (for a demineralised foam) can be manipulated to give just about any required result by

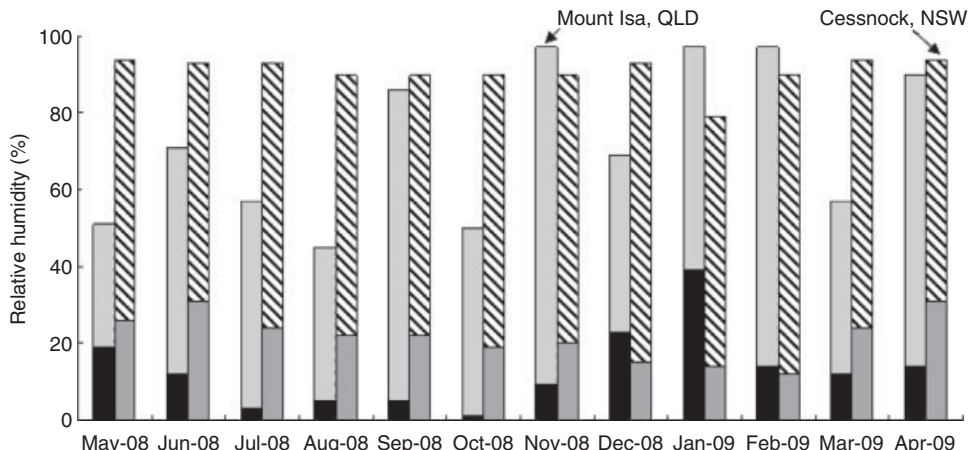


**Fig. 11.3** Monthly maximum and minimum values of relative humidity recorded at Mount Isa, Queensland, and Cessnock, New South Wales, Australia, over the period of one year, after [14]. The left-hand bar represents Mount Isa and the right Cessnock. The maximum recorded value for that month is the total height of the bar, and the minimum recorded value is the height of the sub-bar.

changing the humidity at the top of the column, as discussed further in Chapter 8. Further, Shaw *et al.* [15] have demonstrated that the liquid flux in a column of demineralised pneumatic foam is dependent upon the relative humidity above the free surface of the foam. It is our belief that the evaporation of liquid from the free surface can enhance film collapse rate (and therefore bursting of bubbles) and this influences the equilibrium foam height in the Bikerman test, and the overflow rate in a pneumatic foam. Although not yet proven, it seems likely that if surface coverage of particles is not sufficient to block all evaporation completely, then relative humidity, via the process of evaporation from the free surface, will influence the surface stability. Figure 11.3 shows meteorological measurements of monthly maximum and minimum relative humidity over the period of one year at Cessnock, New South Wales (in the Hunter Valley coal field) and Mount Isa, Queensland (a major mineral mining centre), both in Australia. This demonstrates that wide variation in environmental humidity is observed at both sites, and it is possible that this influences foam stability.

As mentioned in the introduction, the simulation of Neethling and Cilliers [5] is reliant upon a model of film rupture at the free surface of the froth, but this has no dependency upon how particles can stabilise films. Further, it has no dependency on humidity either.

Figure 11.4 shows the free surface of a flotation froth for the recovery of platinum. It can be seen that the surface is made up of a poly-dispersive bubble size distribution and is complex in nature. It is the stability of this froth surface that is of critical importance in determining the performance of the flotation operation. Froth stability can be manipulated by changing the concentration of frother, but this might be limited by frother constraints as described in Section 11.7.

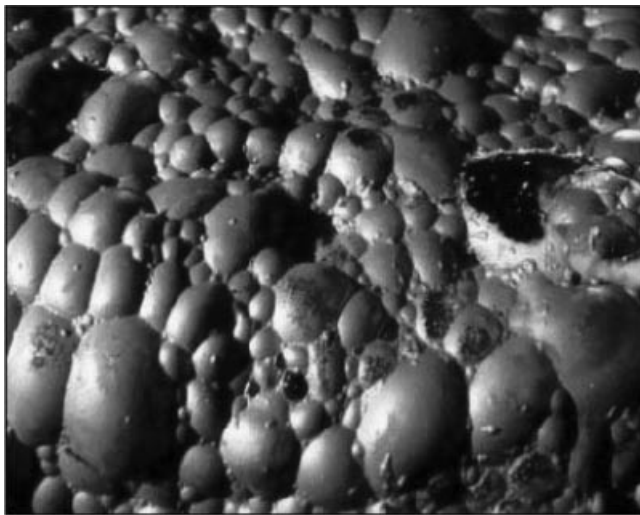


**Fig. 11.4** The free surface of a flotation froth in the beneficiation of platinum [16].

### 11.3 Hydrodynamic Condition of the Froth

A flotation froth is an overflowing pneumatic foam (described in Chapter 8) that is complicated by the fact of attached and entrained particles. The theory [17], for a demineralised foam, can describe the liquid flux and liquid fraction if, and only if, the bubble size distribution as a function of position in the foam is known. It does not enable *a priori* descriptions of the condition of a pneumatic foam, because reliable mechanistic models of bubble coalescence within the foam, as well as surface bursting do not exist.

Without repeating the full description given in Chapter 8, the liquid flux in a pneumatic foam,  $j_f$ , is related to the liquid fraction,  $\varepsilon$ , gas superficial velocity,  $j_g$ , and the liquid superficial drainage velocity measured in a Lagrangian reference frame moving with the bubbles  $j_d$  as follows:

$$j_f = \frac{\varepsilon j_g}{1 - \varepsilon} - j_d \quad (11.1)$$

The origin of eqn (11.1) is worthy of some description in this context. The absolute upwards velocity of the bubbles is  $j_g/(1 - \varepsilon)$ . Imagine, for one moment, that the interstitial liquid is frozen such that there is no slip between the liquid and gas phases. The liquid would then have the same absolute velocity (i.e.  $j_g/(1 - \varepsilon)$ ), but because the volume fraction is  $\varepsilon$ , the liquid superficial velocity is  $j_f = \varepsilon j_g / (1 - \varepsilon)$ . The assumption that the slip velocity is zero is relaxed by subtracting a liquid superficial drainage velocity,  $j_d$ . Because this drainage velocity is a function of the liquid fraction too, when the liquid superficial velocity is plotted against liquid fraction, it exhibits a maximum, and the maximum gives the equilibrium condition of the foam.

The Cilliers group has a large body of published work on the hydrodynamic condition of pneumatic foam. However, all of this work suffers from the same mistake, which is notable in [18, 19] but has been convected throughout their modelling work. They have incorrectly equated the absolute velocity of the gas bubbles with the gas superficial velocity. Thus, the liquid flux equation would, in the nomenclature of eqn (11.1), be:

$$j_f = \varepsilon j_g - j_d \quad (11.2)$$

It is noted that in the limit of infinitesimal liquid fraction, eqn (11.2) approaches equivalence with eqn (11.1), but even for very low but finite liquid fractions, the differences in the behaviour of eqns (11.1) and (11.2) *vis-à-vis* the calculation of the equilibrium liquid fraction are significant.

A key component of eqn (11.1) is the drainage superficial velocity, but the estimation of this parameter for a mineralised froth is far from trivial. In a demineralised froth the drainage rate is governed by the surface boundary condition, which is itself dependent upon surface properties such as surface shear and dilatational viscosities, as well as Marangoni stresses. However, when particles are attached to bubbles, the part of the liquid domain bounded by the particles exhibits a no-slip boundary condition. In their model of flotation froth, Neethling and Cilliers [5] assumed that the channel-dominated drainage equation [20, 21], which relies on a no-slip boundary condition, holds throughout the froth, although this assumption has been relaxed in subsequent work to allow for some surface slip. Of course, in practical mineralised froths, not all of the surfaces have particle coverage, but the parts of the foam network that do have attached particles will be topologically distorted.

However, froth drainage, and therefore the hydrodynamic condition of the froth, is further complicated by the presence of entrained particles in the interstitial liquid. Depending on the surface properties, size distribution, concentration and shape of particles [22] the rheology of the interstitial liquid will change, and could become shear-thinning. There are no known mechanistic descriptions of foam with non-Newtonian interstitial liquid, although an experimental study on shear-thinning egg white and meringue mixture froths has been conducted [23].

## 11.4 Detachment of Particles from Bubbles

Hydrophobic particles can enter the froth phase either by ‘true flotation’, by being attached to bubbles or by entrainment, which is the mechanism by which unwanted gangue particles also enter the froth. However, particles that had previously been attached to bubble surfaces can become detached and can return to the pulp, be recaptured, or report to the concentrate via entrainment rather than true flotation. The mechanisms for particle detachment within the foam itself are bubble coalescence and froth overloading by which there is no longer sufficient capacity to transport all of the previously attached particles. Of course, the latter mechanism is exacerbated by the former. The detachment process within the froth and subsequent recapture of particles can compromise the throughput of the process, but also can aid selectivity [24, 25].

There is, however, evidence to show that considerable particle detachment occurs at the pulp–froth interface. Falutsu and Dobby [26] observed the detachment at the interface of

up to about 60% of previously attached particles, and the phenomenon has been observed at the plant scale [27]. The detachment probability was observed to be a function of particle type and size. The velocity of the bubble particle aggregate in the pulp phase is much greater than in the foam, and so experiences rapid deceleration as the interface is encountered. Falutsu [28] attributed particle detachment to the ‘release of kinetic energy’, but kinetic energy does not in itself cause changes in the aggregate. Instead, the detachment is likely to be caused by the impulse due to the change in momentum, causing a d’Alembert force via Newton’s second law, which, if it can overcome the forces of attachment, will cause the release of the particle; see below for a consideration of such forces. However, the impulse caused on the particle by the rapid deceleration is unlikely to be the only mechanism that causes detachment, since significant bubble coalescence is observed at the interface [11, 29].

It is therefore apparent that to gain a better understanding of detachment in the froth phase, it is necessary to understand how particles behave when the bubble to which they are attached coalesces with another. To this end, Ata [30] studied the detachment of particles (glass spheres) from a pair of coalescing bubbles suspended from capillaries within a liquid. This arrangement is shown in Fig. 11.5, where images are taken just after the coalescence event has taken place. On coalescence the bubbles were seen to exhibit complex modes of oscillation, which attenuated over several tens of milliseconds. When two bubbles coalesce, surface area of the combined bubble is less than the sum of the parts, therefore the excess surface energy must be dissipated from the system. This energy is dissipated through shear heating of the surrounding liquid: the more the energy that needs to be dissipated, the more vigorous the oscillation, and therefore higher the probability of particle detachment. In fact, Ata’s bubbles were within a solution of the ionic surfactant CTAB, and the concentration of this was varied. It can be seen in Fig. 11.5 that when the surfactant concentration is high (i.e. the surface tension is low) fewer particles detach because the amount of energy needed to be dissipated is low, resulting in less vigorous oscillation.

Stevenson *et al.* [31] gave the forces that an attached particle is subjected to. In a quiescent system, the particle experiences:

1. a capillary force due to the surface force at the three-phase contact line;
2. buoyancy;
3. particle weight;
4. the hydrostatic force on the particle due to meniscus depression.

However, in an oscillating system, the particle also experiences:

5. drag, imparted by liquid on the particle;
6. a d’Alembert force arising from Newton’s second law (recognising the ‘added mass’);
7. the Bassett history force caused by acceleration of fluid around the particles.

A previous analysis of the forces [32] on an attached particle had neglected the added mass, and the drag and the Basset forces, although very crude approximate calculations showed these terms to be significant [31]. The force balance is complicated still further by the lag in response of the position of the three-phase contact line to excitation; thus, even for a particle oscillating on a semi-infinite gas–liquid surface, the prediction of the conditions at which it will detach is well beyond current capabilities.

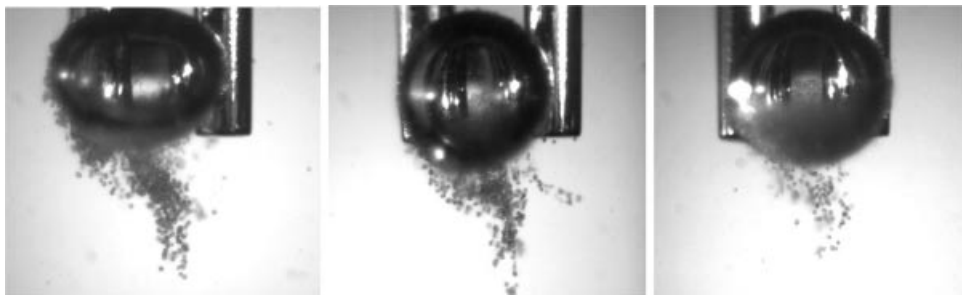


**Fig. 11.5** The detachment of glass spheres after a bubble coalescence event in various CTAB concentrations: left-to-right, 0.027, 0.55 and 1.7  $\mu\text{M}$  [30].

Of course in a flotation froth when bubbles coalesce amidst an assembly of others, or rupture on the free surface of the froth, the physics of detachment are greatly more complicated. The incorporation of a realistic particle detachment model into a nominally predictive model of the froth phase of flotation would appear to be a currently insurmountable problem.

Similarly, a predictive description of particle reattachment within the froth phase has not been proposed, although positron emission particle tracking studies of the froth phase [33, 34] have shown evidence of reattachment occurring subsequent to a detachment event. Ata *et al.* [35] showed that some hydrophobic particles added directly to the froth layer would rapidly attach to bubbles. Thus it is likely that, depending upon where in the froth the detachment occurs, recycling of hydrophobic particles back to the pulp is less likely than the particles being retained, but retarded, in the froth phase.

## 11.5 Gangue Recovery

The primary role of the foam layer in froth flotation is to aid the rejection of unwanted gangue particles from the concentrate. Attached hydrophobic particles are transported from the pulp into the froth along with their associated bubbles, but hydrophilic particles can transfer to the froth phase by (i) entrapment and (ii) entrainment [36]. The former mechanism occurs when particles become ‘wedged’ between adjacent bubbles so that the particles cannot move relative to the bubbles and are therefore forced into the froth, very much as if they were attached. However, the latter mechanism of entrainment is of more significance but can be mitigated in column flotation by the addition of washwater to create positive bias within the froth phase. Engelbrecht and Woodburn [37] and Zheng *et al.* [38] have shown that the particle entrainment rate approximately scales with the rate of water recovery. Kirjavainen [39] presented an empirical expression for this scaling factor as a function of water recovery rate, particle density, slurry viscosity and a particle shape factor. However, the expression is dimensionally inconsistent and is therefore only strictly effective for the system on which the data was taken. Thus we will consider the physical mechanism of entrainment before discussing predictive methods.

There are two stages necessary for a gangue particle to report to the concentrate: It must first reach the pulp froth interface, whence it must travel through the froth layer. In a mechanical cell, the agitation is such that particle suspension is assisted. Once in the froth phase, entrained particles move due to the gas bubbles moving up the column, upon which is superimposed liquid drainage relative to the bubbles, and particle settling relative to the liquid. Consider an isolated particle within the interstitial liquid in the froth. This is convected either up or down the column with the combined effects of absolute liquid velocity and particle settling velocity. However, the particle also experiences dispersion due to having to travel through the geometric network of Plateau borders having an essentially random orientation. Thus, just as tracers within flows through packed beds undergo a convective-dispersive transport process [40], so do entrained particles.

Because of this, it is important to understand the dispersion of particles within a draining foam to illuminate the phenomenon of gangue entrainment. The first tracer study within foam [41] observed the motion of a liquid dye in foam, but the results were compromised by convection associated with the drainage of excess dye liquid. However, the Cilliers group performed some excellent experiments [42] to measure the dispersion coefficients of both added pulses of dye and particles of diameter  $5\text{ }\mu\text{m}$  and density  $2350\text{ kg.m}^{-3}$  that overcame the limitations of the former experimental campaign. It was noticed that similar dispersion coefficients were obtained for both particles and dye. They fitted an expression to their data for the dispersion coefficient which was dimensionally inconsistent and therefore of limited value. However, by employing rigorous dimensional analysis [43] the following expression for the axial dispersion coefficient,  $D_A$ , of the particles in the froth was obtained:

$$D_A = 2.84r_b j_d Sk^{-1/3} \quad (11.3)$$

where  $r_b$  is a representative bubble radius,  $Sk$  is the Stokes drainage number:

$$Sk = \frac{\mu j_d}{\rho g r_b^2} \quad (11.4)$$

$\rho$  and  $\mu$  are the density and dynamic viscosity of the interstitial liquid, respectively, and  $g$  is the acceleration due to gravity. The dimensional analysis revealed that the dispersion was due to mechanical dispersion (due to flow through Plateau borders exhibiting random orientation) rather than Taylor dispersion [44] caused by the velocity profile within the flow of interstitial liquid. Figure 11.6 shows the efficacy of the correlation in describing the axial dispersion coefficient of both solid particles and liquid tracer. However, this is a case in point of how important it is to know when a correlation is valid, and when it is not, because all too often correlations are applied to circumstances where they have no validity. In the experiments upon which eqn (11.3) is based, the maximum particle Schmidt number (i.e. based on the particle self-diffusivity) can be calculated to be about 115, and the effective particle Schmidt number for the liquid tracer is zero. See [43] for more details. Thus it can be said that this correlation is valid for particle Schmidt numbers between zero and about 115. For systems with Schmidt numbers beyond this value, there is no reason why eqn (11.3) should have validity, but it might. Only further experiments can reveal this.

The expression for the axial dispersion coefficient can be combined with predictions of the hydrodynamic state of a pneumatic foam to derive a convective-dispersive transport of

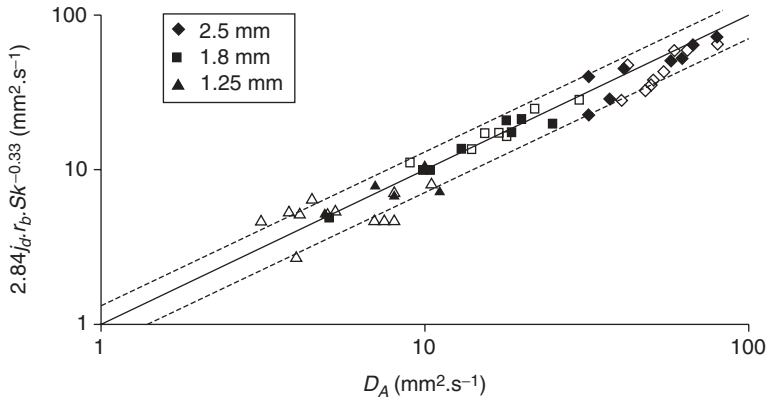


**Fig. 11.6** The efficacy of eqn (11.3) against data for axial dispersion [42]. The filled symbols are for the dispersion of particles and the open symbols are for the dispersion of liquid tracer. The continuous line indicates parity and the dashed lines indicate parity  $\pm 30\%$ . The shape of the symbols indicates the bubble diameter as shown in the legend.

entrained particles [45]. This is then used to obtain a description of the volumetric flux of gangue recovery from the top of the froth,  $R$ :

$$R = \min \left[ j_f^{\max} \phi \exp \left[ \frac{-1}{D_A} \left( \frac{j_B}{\varepsilon} + V_s \right) x_T \right], j_f^{\max} \phi \right] \quad (11.5)$$

where  $V_s$  is the particle settling velocity relative to the liquid,  $x_T$  is the froth depth,  $j_B$  is the bias rate,  $\phi$  is the volumetric solids fraction of the slurry in the pulp and  $j_f^{\max}$  is the maximum of the liquid flux versus liquid fraction curve of eqn (11.1).

It cannot be stressed strongly enough that this is merely a model, one that can illuminate the physics that govern gangue recovery from froth, but it cannot reliably be used for *a priori* predictions of the behaviour of practical plant. One of the reasons for this is that the inherent assumption of the dispersion coefficient is constant throughout the column, and this relies on an assumption that the bubble size distribution is constant throughout the foam. The latter assumption is invalid because of coalescence and Ostwald ripening. There are a total of nine major assumptions inherent in the development of eqn (11.5) and this is another example of how a balance must be struck between the desire to simulate and the practical utility of such models. Neethling and Cilliers [46] have explicitly, and correctly, pointed out that the assumption that liquid fraction and bubble size are constant throughout the foam is not practically valid. Once capillarity has relaxed, the liquid fraction changes through film rupture and Ostwald ripening, which are not explicitly explained in their work. In addition, their model relies on information about the rate of rupture of films on the free surface, which again does not include proven dependencies.

However, eqn (11.5) does in fact capture the features of much of the experimental and plant data. For instance Ata *et al.* [47] injected hydrophilic fluorescent particles of diameter 22, 34 and 57  $\mu\text{m}$  into a pneumatic foam and assessed how many were recovered in the concentrate. It was seen that a marginally higher fraction of the smaller class of

particles were recovered rather than the larger class, and this could be reflected in the weak dependency of eqn (11.5) upon settling velocity. This dependency of entrainment on size was observed on mechanical plant cells by Engelbrecht and Woodburn [37]. Clingan and McGregor [48] noted that the bias rate in column flotation was unimportant with respect to gangue entrainment so long as the bias is positive, and is mirrored by the dependency of bias rate of eqn (11.5).

Zhang *et al.* [38] took extensive entrainment data from a tank cell at the Mount Isa Copper Concentrator, and suggested dimensionally inconsistent fits to data as a function of particle size. The most recent empirical model to be proposed is due to Yianatos and Contreras [49] which has the advantage of being dimensionally consistent and, despite perhaps not capturing all of the pertinent physics, does appear to well describe the authors' own plant data as well as those of other workers [37, 38].

## 11.6 The Velocity Field of Froth Bubbles

The flow of froth discussed in Section 11.3 was implicitly assumed to be one-dimensional, whereas towards the top of the column the flow of foam will exhibit two- or three-dimensional characteristics as it flows into the froth launder. Moreover, in a mechanical cell, the assumption of one-dimensional foam flow may be a poor one at most positions in the froth phase. Thus, if one aspires to a totally mechanistic description of all elements of a flotation froth, it is necessary to solve for the velocity field of the foam flow.

The first worker to attempt this was Moys [50], who obtained a two-dimensional flowfield by solving the Laplace equation for the flow of the foam. The solution of Laplace's equation to obtain a flowfield is valid for irrotational potential flow (i.e. flows that are conservative and inviscid). Since foam rheology is certainly not inviscid because it exhibits a yield stress (indeed foam rheology is the subject of Chapter 6), Moy's potential flow solution for the velocity field in foam has no basis in fluid mechanics. In fact, Moys himself acknowledged that the procedure was flawed.

However, Moys had set a precedent that was emulated by others. Murphy *et al.* [51] numerically calculated potential flow solutions to the Laplace equation and presented them as simulations of flotation froth. They stated that 'If the viscosity and permeability of the froth is constant over the field, then the motion of bubbles is irrotational and Laplace's equation can be used to describe the streamlines of the bubble motion'. The relation of constant viscosity to irrotational flow is simply not valid in all cases other than if the viscosity is zero, which, in foam, it is not. However, potential flow solutions of froth flow were then presented by the Cilliers group in several studies [52–54], and presented as an accurate representation of the velocity field. The group subsequently acknowledged [5] that foam rheology was not, in fact, inviscid. They proposed that the foam may exhibit Bingham plastic-like rheology, but they continued with the potential flow solution of the velocity field nonetheless.

In practice, the computation of a realistic multidimensional flowfield of a foam is significantly difficult because the constitutive equation (i.e. the relationship between stress and strain in the foam) varies with liquid fraction and bubble size, but shear stress can classify bubbles on the basis of size and induced drainage.

## 11.7 Plant Experience of Froth Flotation

### 11.7.1 Introduction

Given the enormous physical complexity of the froth phase in flotation, and the limitations of current methods of modelling described above, it is clear that progress in flotation will be mainly achieved through innovation based on plant experience and the overcoming of operational constraints. In this section, some plant experiences gained by Clean Process Technologies Pty Ltd are shared and some thoughts about flotation practice are discussed. Opinions presented herein are likely to change over time due to the nature of experiential discovery.

Working froth flotation plants are very different to laboratory or pilot flotation systems and the difference between them is one reason for the relative slow advance in flotation in the past two decades. Many would argue that there have been great advances but this has generally not been borne out by improved flotation plant performance.

The bulk of the experience of Clean Process Technologies (CleanProTech) is in coal flotation and the bulk of that in Australia. From plant visits in the USA, conversations with process engineers in South Africa and Canada and from reading countless technical papers and books, it appears that the relative lack of recent progress in Australia has been mirrored internationally. It is also apparent that the minerals flotation industry suffers many of the same problems as coal flotation. In practical operation, there is, however, one major difference between minerals and coal flotation. In minerals flotation, the flotation product is generally the whole of the plant product. In coal flotation, the flotation product forms only a part of the total plant product and, in many cases, its contribution is small. This means that in coal preparation it is very easy for problems in the flotation circuit to be ignored.

Froth in a working coal or minerals plant is an extremely complex entity and it is doubtful that full understanding of it will ever be achieved, although a better physical understanding will bring great performance improvements. However, some methods of plant improvement are already known but not currently implemented.

### 11.7.2 Frother-constrained Plant

One of the most important parameters that has been indicated by analysis, visual appearance and wide discrepancy on the plant from lab and pilot date is the inability of plants to add frother at sufficiently high rates. Lab tests, pilot-scale investigations and data from plants show that frother addition is the most critical parameter for flotation performance. Simply put, frothers stabilise the bubbles in the froth (they also reduce the bubble size) and if there is insufficient frother, the bubbles burst. If bubbles burst within the froth cell, then the material attached to the bubbles falls back into the cell and possibly back into the tailings. The valuable particles are not carried out of the flotation cell. The situation is in reality more complex than this, but the crucial point is that without sufficient frother addition, flotation is not efficient.

Once a critical amount of frother has been achieved, any increases in frother make little difference. However, this required concentration is often higher than operating plants

can achieve. In fact, the manufacturers of Jameson and MicroCell flotation cells usually stipulate in the performance guarantees for their equipment that a minimum of 25 ppm of MIBC (a commonly employed frother) must be in the feed. We have found that many plants struggle to get to 10 ppm (v/v) because of problems of frother constraint as described below. Much has been written about scale-up factors for flotation cells, but curiously, little has been written about the scale-up of frother concentration. Laboratory and pilot scale rigs can use as much frother as they like, but on the full-plant scale, the amount of frother that can be used is determined by the rest of the plant. On a working plant, residual frother in the water stream causes bubbles to form in other areas of the plant and this often leads to large amounts of air building up in pumps that can result in loss of pump pressure. This often leads to the plant shutting down, and it is this constraint that determines the maximum concentration of frother that can be employed. When shutdown occurs due to this reason it is known as the plant 'frothing out', and many plants suffer from the problem. The usual remedy is to reduce the amount of frother injected into the flotation system until the plant is brought back under control. Whilst this is fine for the rest of the plant, reduction of frother addition compromises flotation performance causing large amounts of coal to be lost to flotation tailings. CleanProTech has found most plants to be frother-constrained, even if this is not recognised by plant management. When a plant is frother-constrained, it is very difficult for a plant operator to actually control the system as they would like. They are constrained in their use of the single most important control at their disposal. In addition, even before plant shutdown, the performance of the dense-medium cyclone (DMC) can be adversely affected by the changes in feed pressure caused by the presence of frothers.

Mechanically agitated cells in series (indeed any cells in series) suffer less from the effects of residual frother. The cells in series (one cell re-treating the tailings from the previous cell) tend to 'strip' the frother from the tailings of the previous cell. In this way, the residual frother in plant tailings is reduced. This has been successfully used in several coal preparation plants and CleanProTech terms this procedure 'frother stripping'. Of course, a similar thing occurs in mechanically agitated cells arranged in series, but perhaps without its significance being realised.

A common problem in plant design, which might be considered almost incredible, is for the product dewatering to have insufficient capacity. This leads to the plant operators having to reduce frother and collector addition to reduce flotation cell production and therefore match it to the dewatering capacity by deliberately destabilising the froth. However, a more sensible strategy would be to increase the dewatering capacity or use other means to achieve the same end. Unfortunately, again, plant managers, engineers and designers are often not willing to admit mistakes and so the problem is suppressed and any investigation into the froth in such a plant is artificially skewed by the deliberate 'detuning' of frother concentration. The advice of CleanProTech in the circumstances of insufficient dewatering capacity is to keep producing coal at the maximum rate, but to let the excess product that cannot be dewatered run to a collection dam. Once the wasted product is seen, it is generally easier to attract the investment for more dewatering equipment. The true proof that this problem is real is given by tailings reclamation companies that are finding huge amounts of coal in tailings dams.

The question arises, is there any point to industrial scale froth research whilst the plants are frother-constrained? If the frother constraint can be alleviated or removed (and this is

one of the areas that Clean Process Technologies is working on) then the entire behaviour of the froth, and of phenomena within the froth phase, changes.

### 11.7.3 Sampling, Data Manipulation and Data Presentation

One of the biggest problems in striving for process improvement in froth flotation is that plant performance is often not adequately measured. Sampling systems tend to be poor, so to even quantify flotation performance on a bulk scale has enormous error. Recently a plant process engineer sent CleanProTech some results for review. The analytical results showed that the flotation mass yield calculated from solids concentration and from ash values gave mass yields between -400 and 1200%. Obviously, the values are incorrect, but with such error in sampling, it is difficult to deduce anything meaningful. One of the major problems in industry is that even with such obviously erroneous systems, plant engineers and managers simply keep repeating the same tests until they get some that give a reasonable answer. Of course, with the same sampling systems in place, the errors are the same; it is just due to probability that some tests will give physically reasonable answers, although these results are highly likely to be inaccurate. Consequently, with such amounts of ‘uncertainty’ in measurement of plant performance, it is very difficult to realistically deduce the impact that changing one or another characteristic of the froth has had on the process as a whole.

Good process or metallurgical accounting standards should reveal the true situation. Such standards have been implemented in the minerals processing industry, but are a long way from implementation in the coal industry. Even when such a standard practice has been implemented, it is still imperative that the actual sampling and measuring points are checked. Too often, samplers and flowmeters are installed and the results from them are then used in mass accounting packages, but the errors from these can be huge. For the accounting or balancing system to work, the input data must be correct and its uncertainty known. No amount of data manipulation or ‘data molesting’ (least squares regression analysis and other techniques that make an inconsistent set of analysis and flow data ‘fit’ together) can help if the data is poorly collected in the first place. ‘Data molesting’ should never be used and instead the actual data should be used and any inconsistencies used to find the uncertainty. What might be an adequate sampling procedure in the laboratory may not have efficacy on the plant. However, most practitioners in laboratories do not understand the true impact of sampling and uncertainty, and this problem is only compounded on the plant.

Most plant managers do not know how well, or how badly, their plant is operating. If \$20–30 million dollars has been spent on a plant, ambitious managers may not want to report that they have installed a disaster. With flotation (and many other coal preparation processes, especially fines preparation), they can suppress information about the true performance of the plant simply because the sampling is so bad. However, there are other managers and process engineers who take a great interest in plant performance, but they are usually hampered by poor sampling systems.

There is a great reluctance to introduce correct slurry sampling systems around flotation in the coal industry. One of the reasons seems to be that managers and engineers think that if the new sampling system shows that all the system is running fine, then the money spent

on the sampling system will be a waste. In practice this would rarely be the case, but often this prevents investment in reliable sampling equipment and methods.

Many plant operators know that their sampling is not accurate and so use the results to track trends, rather than as absolute values. Plant engineers realise the limitations of the sampling systems that they have and so do not use these results in technical papers. Yet these same results or results gathered by similar sampling procedures will be used by academics or researchers to promote whatever equipment they have an interest in. In addition to this poor practice, the results will normally be given without uncertainties or errors and often made to seem better by using data molesting. A single result that may superficially indicate excellent flotation performance may be misleading because of large inherent uncertainties or because of small sample size. Given the uncertainties in sampling, data suppression can be very damaging to the conclusions of any study, and it is imperative that all plant data is fairly and equally presented. Of course, some plant engineers are guilty of the same practice and some academics and researchers do give uncertainties and errors. The point from this is that results of plant data cannot necessarily be given equal weight. If a sampling practice description (and this must be a definitive description) is not given and uncertainties are not calculated, then the results and conclusions should probably be discarded.

In addition to inadvertent difficulties with sampling, some systems can be deliberately poorly sampled in order to manipulate data to make a desired point. It is very simple to obtain samples with higher ash values in tailing than is representative by simply sampling from the base of the tailings pipe. Denser (higher ash) particles tend to accumulate on the base of pipes and if a sample is taken from a tapping point at the base, a higher ash sample will eventuate. Even spears may not alleviate this problem. Getting a system running properly, ensuring the maintenance is done correctly and in a timely manner and then operating the system correctly is not seen as exciting or a path to promotion. In such circumstances, questionable results can be produced to make the new installation look good. It is the perception that someone has done a great job by adopting a new technology that leads to the perception that they will get promoted, rather than by improving plant performance.

#### 11.7.4 Process Control

Usually, flotation cells are controlled ‘by eye’, i.e. the plant operators look at the performance of the flotation cell visually and make corrections based on this. Automating the control of froth flotation has been attempted by employing digital cameras to deduce information about the froth cameras, which is interpreted by specialist software. These have not proven a success in the froth flotation of coal, but that does not necessarily mean that advances will not be made in the future. Plants are operated ‘by eye’ (i.e. by relying on the experience of the plant operators) due to the time required for laboratory results to be produced. If samples are taken (e.g. for ash content), there is a time lag of hours, if not days or weeks, before the results are known. The flotation plant feed may have changed greatly since that time and the results are useless to those controlling the flotation. Shift composite results are very useful, however, as a means of monitoring the flotation to gauge the level of extra gains that can be made. Online measurement of properties is required to overcome the time lag between sampling and the implementation of process control. Elemental gauges have been introduced into minerals flotation, but for coal flotation, the situation is

more complex, and nucleonic devices for slurries have not proved successful. CleanProTech is currently producing monitoring devices based on particle density measurement.

Reagent dosing is also often poorly controlled. Where the reagent dosing is varying from what the plant operators think that it is, it becomes very difficult for the operators to adjust the system accurately. Another variable that typically suffers from control problems in plants is froth depth. Where this is controlled by pressure measurement devices, there generally exists a large discrepancy between the true froth depth and the measured one.

### **11.7.5 The Assessment of Newly Proposed Flotation Equipment**

There is seldom a revolutionary solution to any coal or minerals processing problem. If any such ‘magical’ piece of equipment is proposed, it should be initially viewed with scepticism. It is up to the producer of the equipment to prove that it works. It should be assumed, in the first case, that it does not. This involves good sampling and correct data analysis. Existing equipment should also be made to work at its best before making comparison with new equipment types. It is very easy to run a pilot unit that outperforms a poorly maintained mechanically agitated cell. Pilot units tend to have a qualified engineer running them at all times and they are compared to an operating piece of equipment that, in addition to be poorly maintained, may be left to run without intervention.

There is no ‘silver bullet’ and no new magical piece of equipment that will come along and solve all the existing problems in froth flotation, although there will certainly be incremental advances. However, significant improvements in working plants can be achieved by simply getting the existing systems to work better or, in many cases, as they should.

### **11.7.6 Conclusions about Froth Flotation Drawn from Plant Experience**

If we were to understand froth phenomena in the laboratory (as has been attempted in the studies described in Sections 11.2–11.6 in this chapter), would this better understanding transfer to improved flotation recovery on plants? The rationale for studying froth phase phenomena in flotation is to improve industrial performance, but if this performance is operationally limited (e.g. in frother-constrained plant) then improvements in the understanding of froth phase phenomena will have limited impact on industrial performance. Studies into such froth phase phenomena can only realise their true value when there are simultaneous improvements in plant practise, and this will only occur when plant data is properly sampled and then presented in an honest and transparent manner.

## **Nomenclature**

### **Roman**

$D_A$	Coefficient of axial dispersion	$[m^2.s^{-1}]$
$g$	Acceleration due to gravity	$[m.s^{-2}]$

$j_B$	Liquid superficial bias rate (positive downwards)	[m.s <sup>-1</sup> ]
$j_d$	Liquid superficial drainage velocity (positive downwards)	[m.s <sup>-1</sup> ]
$j_f$	Liquid superficial velocity up the column	[m.s <sup>-1</sup> ]
$j_f^{\max}$	Maximum liquid superficial velocity up the column	[m.s <sup>-1</sup> ]
$j_g$	Gas superficial velocity (positive upwards)	[m.s <sup>-1</sup> ]
$R$	Volumetric flux of recovered gangue	[m.s <sup>-1</sup> ]
$r_b$	Bubble radius	[m]
$Sk$	Stokes number ( $\equiv j_d \mu / (r_b^2 g \rho)$ )	[ $\text{--}$ ]
$V_s$	Particle settling velocity	[m.s <sup>-1</sup> ]
$x_T$	Height of the froth	[m]

## Greek

$\varepsilon$	Volumetric liquid fraction in the foam	[ $\text{--}$ ]
$\phi$	Solids fraction in the slurry	[ $\text{--}$ ]
$\rho$	Liquid density	[kg.m <sup>-3</sup> ]
$\mu$	Liquid dynamic viscosity	[Pa.s]

## References

- [1] J. A. Finch and G.D. Dobby. *Column Flotation*. Pergamon Press, Oxford, 1990.
- [2] S. Hilgenfeldt, S.A. Koehler and H.A. Stone. Dynamics of coarsening foams: Accelerated and self-limiting drainage. *Phys. Rev. Lett.*, **86**: 4704–7, 2001.
- [3] S.J. Neethling, K. Hadler, J.J. Cilliers and A.W. Stradling. The use of FrothSim to optimise the water addition to a column flotation cells. *Miner. Eng.*, **19**: 816–23, 2006.
- [4] S.J. Neethling and J.J. Cilliers. The simulation of flotation banks and circuits. In Proc. Centenary of Flotation Symp. Brisbane, 6–9 June, on CD-Rom.
- [5] S.J. Neethling and J.J. Cilliers. Modelling flotation froths. *Int. J. Miner. Process.*, **72**: 267–87, 2003.
- [6] M. Harris, K. Runge and R. Morrison. JKSimFloat as a practical tool for flotation process design and optimization. In *Mineral Processing Plant Design and Control*, A. Mular, D. Halbe and D. Barratt (eds), 2002.
- [7] AMIRA P9N 5th Technical Report. *The Optimisation of Mineral Processes by Modelling and Simulation*, 2006.
- [8] J. Bouchard, A. Desbiens, R. del Villar and E. Nunez. Column flotation simulation and control: an overview. *Miner. Eng.*, **22**: 519–29, 2009.
- [9] P. Stevenson and K.P. Galvin. On empiricism in minerals processing research. *Miner. Eng.*, **20**: 776–81, 2007.
- [10] R. Aveyard, B.P. Binks, P.D.I. Fletcher, T.G. Peck and C.E. Rutherford. Aspects of aqueous foam stability in the presence of hydrocarbon oils and solid particles. *Adv. Coll. Interface Sci.*, **48**: 93–120, 1994.
- [11] S. Ata, N. Ahmed and G.J. Jameson. A study of bubble coalescence in flotation froths. *Int. J. Miner. Process.*, **72**: 255–66, 2003.
- [12] B.B. Triffett and J.J. Cilliers. Measuring froth stability. International patent application number PCT/AU2004/000331, 2004.
- [13] J.J. Bikerman. The unit of foaminess. *Trans. Faraday Soc.*, **34**: 634–8, 1938.
- [14] X. Li, R. Shaw and P. Stevenson. Effect of humidity on dynamic foam stability. *Int. J. Miner. Process.*, **94**: 14–19, 2010.

- [15] R. Shaw, G.M. Evans and P. Stevenson. Dependency of liquid overflow rate upon humidity of a pneumatic foam. *Int. J. Miner. Process.*, **97**: 26–30, 2010.
- [16] M. Ryan. The story of platinum – review. *Platinum Metals Rev.*, **54**: 120–1, 2010.
- [17] P. Stevenson. The hydrodynamic theory of rising foam., *Miner. Eng.*, **20**: 282–89, 2007.
- [18] S.J. Neethling, H.T. Lee and J.J. Cilliers. The recovery of liquid from flowing foams. *J. Phys.: Condensed Matter*, **15**: 1563–76, 2003.
- [19] S.J. Neethling, H.T. Lee and J.J. Cilliers. Simple relationships for predicting the recovery of liquid from flowing foams and froths. *Miner. Eng.*, **16**: 1123–30, 2003.
- [20] R. Leonard and R. Lemlich. A study of interstitial liquid flow in foam. *AICHE J.*, **11**: 18–25, 1965.
- [21] G. Verbist, D. Weaire and A.M. Kraynik. The foam drainage equation. *J. Phys.: Condensed Matter*, **8**: 3715–31, 1996.
- [22] S.B. Johnson, G.V. Franks, P.J. Scales, D.V. Boger and T.W. Healy. Surface chemistry-rheology relationships in concentrated mineral suspensions. *Int. J. Miner. Process.*, **58**: 267–304, 2000.
- [23] P. Stevenson, M.D. Mantle and J.M. Hicks. NMRI studies of free drainage of egg white and meringue mixture froths. *Food Hydrocoll.*, **21**: 221–9, 2007.
- [24] R.Q. Honaker and A.V. Ozsever. Evaluation of the selective detachment process in flotation froth. *Miner. Eng.*, **16**: 975–82, 2003.
- [25] R.Q. Honaker, A.V. Ozsever and B.K. Parekh. Selective detachment process in column flotation froth. *Miner. Eng.*, **19**: 687–95, 2006.
- [26] M. Falutsu and G.S. Dobby. Froth performance in commercial sized flotation columns. *Miner. Eng.*, **5**: 1207–23, 1992.
- [27] D.R. Seaman, E.V. Manlapig and J.P. Franzidis. Selective transport of attached particles across the pulp-froth interface. *Miner. Eng.*, **19**: 841–51, 2006.
- [28] M. Falutsu. Column flotation froth characteristics – stability of the bubble-particle system *Int. J. Miner. Process.*, **40**: 225–43, 1994.
- [29] J.B. Yianatos, J.A. Finch and A.R. Laplante. Holdup profile and bubble size distribution of flotation column froths. *Canadian Metall. Q.*, **25**: 23–9, 1986.
- [30] S. Ata. The detachment of particles from coalescing bubble pairs. *J. Coll. Interface Sci.*, **338**: 558–65, 2009.
- [31] P. Stevenson, S. Ata and G.M. Evans. The behaviour of an oscillating particle attached to a gas-liquid surface. *Indus. Eng. Chem. Res.*, **48**: 8024–9, 2009.
- [32] A.V. Nguyen. New method and equations for determining attachment tenacity and particle size limit in flotation. *Int. J. Miner. Process.*, **68**: 167–82, 2003.
- [33] K.E. Waters, N.A. Rowson, X. Fan, D.J. Parker and J.J. Cilliers. Positron emission particle tracking as a method to map the movement of particles in the pulp and froth phases. *Miner. Eng.*, **21**: 877–82, 2008.
- [34] K.E. Waters, N.A. Rowson, X. Fan and J.J. Cilliers. Following the path of hydrophobic and hydrophilic particles in a Denver cell using positron emission particle tracking. *Asia-Pacific J. Chem. Eng.*, **4**: 218–25, 2009.
- [35] S. Ata, N. Ahmed and G.J. Jameson. Collection of hydrophobic particles in the froth phase. *Int. J. Miner. Process.*, **64**: 101–22, 2002.
- [36] V.M. Kirjavainen. Review and analysis of factors controlling the mechanical flotation of gangue minerals. *Int. J. Miner. Process.*, **46**: 21–34, 1996.
- [37] J.A. Engelbrecht and E.T. Woodburn. The effect of froth height, aeration rate and gas precipitation on flotation. *J. South African Inst. Mining Metall.*, **10**: 125–32, 1975.
- [38] X. Zheng, N.W. Johnson and J.-P. Franzidis. Modelling of entrainment in industrial flotation cells: Water recovery and degree of entrainment. *Miner. Eng.*, **19**: 1191–203, 2006.
- [39] V.M. Kirjavainen. Mathematical model for the entrainment of hydrophilic particles in froth flotation. *Int. J. Miner. Process.*, **35**: 1–11, 1992.
- [40] J.J. Fried and J.J. Combarous. Dispersion in porous media. *Adv. Hydrosci.*, **7**: 169–282, 1971.
- [41] P. Stevenson, S.P. Sullivan and G.J. Jameson. Short-time tracer dispersion in a two-dimensional rising froth. *Chem. Eng. Sci.*, **58**: 5025–43, 2003.
- [42] H.T. Lee, S.J. Neethling and J.J. Cilliers. Particle and liquid dispersion in foams. *Coll. Surf. A*, **263**: 320–9, 2005.

- [43] P. Stevenson. Dimensional analysis of particle and liquid dispersion in draining foam. *Canadian J. Chem. Eng.*, **84**: 614–17, 2006.
- [44] G.I. Taylor. Dispersion of soluble matter in solvent flowing slowly through a tube. *Proc. R. Soc. London A*, **219**: 186–203, 1953.
- [45] P. Stevenson, S. Ata and G.M. Evans. Convective-dispersive transport of gangue through flotation froth. *Chem. Eng. Sci.*, **62**: 5736–44, 2007.
- [46] S.J. Neethling and J.J. Cilliers. The entrainment factor in froth flotation: model for particle size and other operating parameter effects. *Int. J. Miner. Process.*, **93**: 141–8, 2009.
- [47] S. Ata, S. Pigram and G.J. Jameson. Tracking of particles in the froth phase: An experimental technique. *Miner. Eng.*, **19**: 824–30, 2006.
- [48] B.V. Clingan and D.R. McGregor. Column flotation experience at Magma Copper Co. *Miner. Metall. Process.*, **3**: 121–5.
- [49] J. Yianatos and F. Contreras. Particle entrainment model for industrial flotation cells. *Powder Technol.*, **197**: 260–7, 2010.
- [50] M.H. Moys. Residence time distributions and mass transport in the froth phase of the flotation process. *Int. J. Miner. Process.*, **13**: 117–42, 1984.
- [51] D.G. Murphy, W. Zimmerman and E.T. Woodburn. Kinematic model of bubble motion in a flotation froth. *Powder Technol.*, **87**: 3–12, 1996.
- [52] S.J. Neethling and J.J. Cilliers. A visual kinematic model of flowing foams incorporating coalescence. *Powder Technol.*, **101**: 249–56, 1999.
- [53] S.J. Neethling, J.J. Cilliers and E.T. Woodburn. Prediction of the water distribution in a flowing foam. *Chem. Eng. Sci.*, **55**: 4021–8, 2000.
- [54] S.J. Neethling and J.J. Cilliers. Simulation of the effect of froth washing on flotation performance. *Chem. Eng. Sci.*, **56**: 6303–11, 2001.

# 12

## Froth Flotation of Oil Sand Bitumen

*Laurier L. Schramm and Randy J. Mikula*

### 12.1 Introduction

Water-based flotation processing has long been applied to the separation of bitumen from surface mined oil sands in Alberta, Canada, and has been demonstrated for tar sand in Utah, in the United States. The flotation processes produce bituminous froths, which represent a special class of non-aqueous foams and are multi-phase, being composed of oil, water, gas, and solids. There are many interesting examples in the oil sands industry of how the physical structure of these froths impacts on aspects of the commercial operation from bitumen recovery to froth treatment. The complex physical and chemical make-up of these froths can be traced to the variability of the original oil sands ores, as well as to sometimes more subtle variations in the processes used to extract and concentrate the bitumen from the froth. This chapter presents an overview of the occurrence, nature, properties and treatment of bituminous froths.

### 12.2 Oil Sands

Oil sand deposits are present in many locations around the world, tending to occur along the rim of major sedimentary basins, in either fluvial or deltaic environments [1–7]. Collectively, these contain well over 2 trillion barrels [1, 2]. Canada alone has an estimated initial volume of crude bitumen of 1.7 trillion barrels, with about 173 billion barrels thought to be recoverable under current economic conditions [8]. Of the Canadian deposits the

**Table 12.1** Some hydrocarbon terminology [11–13].

Hydrocarbon	Viscosity range (mPa.s) at deposit temperature	Density range (kg/m <sup>3</sup> ) at 15.6°C
Crude oils	<10,000	<934
Heavy crude oil	<10,000	934–1000
Extra heavy crude	<10,000	>1000
Bitumen/tar	>10,000	>1000

Athabasca is estimated to contain over 600 billion barrels of bitumen; this is much larger than Ghawar, Saudi Arabia, the world's largest conventional oil field [2]. Smaller, but possibly commercial, tar sand resources exist in a variety of locations including Albania, Madagascar, and most notably Utah in the United States. Although there is some debate about the choice of the name as tar sands or oil sands, one convention is to use oil sands in cases where the final products are transportation fuels, and tar sands when the final product is an asphalt or bitumen. Significant pilot testing of the Asphalt Ridge tar sands in Vernal, Utah was aimed at producing a high grade asphalt [9, 10], as opposed to the transportation fuels that are the end product for the Canadian oil sands in the Athabasca region. Early use of the bitumen from the Canadian oil sands was in fact for road construction, although now the negative connotations associated with the words tar sands have prompted a move to the use of oil sands to describe this resource. Another argument for the terminology is the idea that tar is a by-product of a refining process and it is inappropriate to apply this name to a naturally occurring product. In any case, depending upon the context of the discussion or the history of the work being referenced, the terms oil sands or tar sands may appear to be used interchangeably.

The “oil” in oil sand (the “tar” in tar sand) is a very viscous hydrocarbon called bitumen. Bitumen is chemically similar to conventional oil but has comparatively high density (low API gravity) and high viscosity. Although a number of definitions for bitumen have been used by various authors, a reasonable set of definitions is given in Table 12.1, based on the United Nations institute UNITAR-sponsored attempts to establish definitions [11–13]. What Table 12.1 does not illustrate is how much greater the viscosity of bitumen really is. Athabasca bitumen viscosity is of the order of  $1 \times 10^6$  mPa.s (at reservoir temperature), while Utah bitumen viscosity is greater than  $1 \times 10^7$  mPa.s [14] (i.e. at least an order of magnitude greater at reservoir temperature). Such extremely high viscosities make the bitumen virtually immobile in the reservoirs. As a result, bitumen is produced either by mining the ore and separating the bitumen using a variety of methods at the surface, or *in situ* by mobilizing the bitumen with steam heating. Both methods are used commercially in the Canadian oil sands, whereas other pre-commercial deposits around the world are only being considered for mining. In the mining process, bitumen can be concentrated as a froth (to separate the bulk of the clays and other minerals) at a much lower temperature than is required to mobilize the reservoir bitumen in the *in situ* processes. The bitumen concentrate created from the froth is then treated by various solvent processes in order to change the nature of the froth and create a bitumen suitable for refining. In the commercial operations in Alberta, Canada, the bitumen is upgraded to a synthetic crude oil intermediate before being refined into other products such as transportation fuels.

The “sand” in oil sand is mostly unconsolidated quartz sediment surrounded by bitumen, water and a range of fine mineral solids. It is widely thought that the bitumen, in mobile form, originally migrated into the sediments and was then altered due to a combination of evaporation, oxidation and/or bacterial degradation [1, 7, 15, 16]. The oil-bearing sands have great variability in their compositions and properties, but some generalizations can be made. The mineral fraction is principally the quartz grains, with smaller amounts of heavy minerals, feldspar grains, mica flakes and clays [17–19]. The clays in this deposit are predominantly illite and kaolinite with some chlorite. In general, the oil-bearing sands are fine- to very fine-grained ( $62.5\text{--}250\,\mu\text{m}$ ) with only a small percentage of fines [20, 21]. The oil-bearing sands have fairly high porosities (25–35%) compared with the 5–20% porosity of most petroleum reservoirs [17]. The high porosity is achieved by having a low occurrence of mineral cements, which is why the deposits are classified as oil sands rather than sandstones [18]. The highest oil content Athabasca oil sands have oil saturations of about 18% w/w (36% v/v) and water saturations of about 2% w/w (4% v/v) [18]. The deposits in Utah also vary considerably, with several deposits having been characterized. With a successful pilot program completed for the Asphalt Ridge tar sands in 1998 to 2001, discussion later in this chapter focuses on that deposit. The Asphalt Ridge deposit has similar bulk composition, but at the lower end of bitumen and water saturation.

The arrangement of phases in oil sand is largely determined by the volume fractions of bitumen, water and quartz sand. The quartz sand forms the bulk of the material, with either the bitumen (in rich oil sand) or the water (in lean oil sand) forming the continuous phase. This results in a simple relationship between oil content (grade) and particle size distribution as reviewed elsewhere [18, 20, 22, 23]. The oil content of oil sand decreases as the median diameter of the particles decreases, and as the fraction of particles in the clay-size range increases. There is also a general consensus that for the most part, the mineral grains in Athabasca oil sand are water-wet and that water is present as pendular rings around sand grain contact points and also as roughly 10 nm thick films on sand grain surfaces, which in turn are surrounded by the oil [24–29].

The separation of oil from solids by a water film is widely held to be the characteristic difference between Athabasca oil sand and, for example, oil sand from other oil sand deposits in the world (e.g., California, New Mexico, or Utah). These other oil sand deposits are thought to consist of oil-wet solids. That is, the bitumen occurs in direct contact with the mineral grains. The significance of the distinction is that the “oil-wet” oil sands are considered to be more difficult to beneficiate using hot water flotation because of the difficulty in dislodging bitumen from an oil-wet surface. However, as the industry in Alberta has expanded to a wider area and therefore a more varied deposit geology, various locations in Alberta mining operations have yielded oil sands samples that might be defined as being oil-wet. For the Utah deposits, some authors differ, but in general the minerals are thought to be oil-wet [30].

## 12.3 Mining and Slurrying

Shallow oil sands deposits, underlying less than about 75 m of overburden, are amenable to processes in which the overburden is stripped away, the oil sand is mined, and then the oil sand is slurried and processed in surface facilities. Such processes typically have recovery

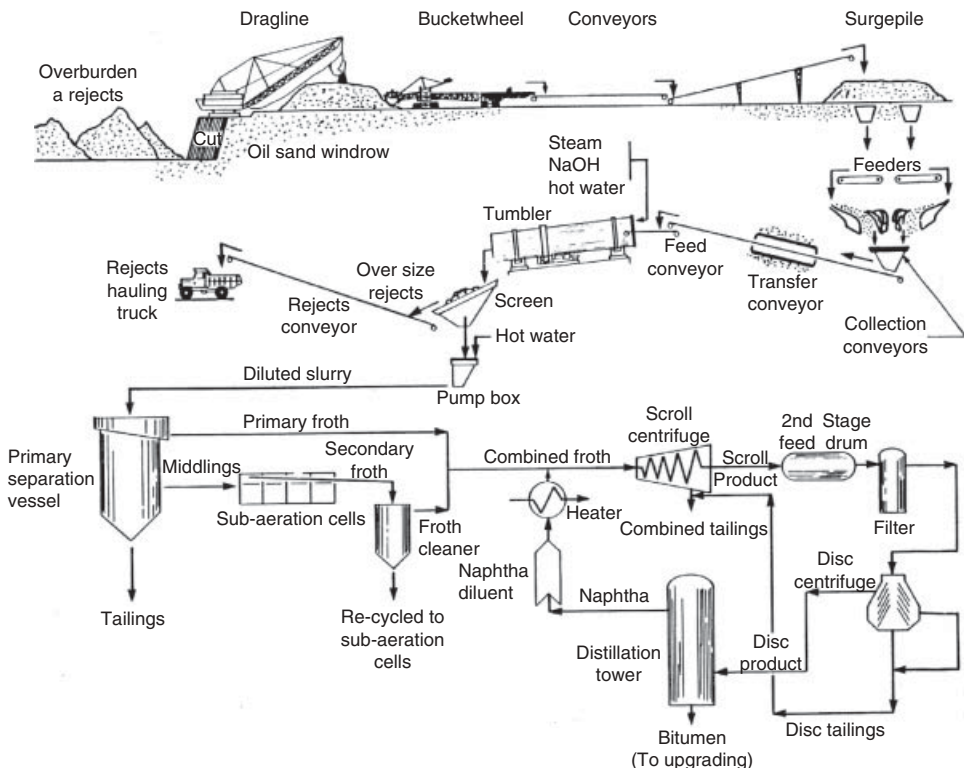


**Fig. 12.1** Illustration of a commercial oil sands dragline mining and hot water flotation process. From Schramm and Kwak [63]. Copyright 1988 Society of Petroleum Engineers.

factors greater than 95%. Surface mined oil sand is processed very differently than are the deeper oil sands deposits, underlying more than 75 m of overburden, which are developed using *in situ* reservoir drive processes that are somewhat similar to *in situ* heavy oil production except the bitumen is even more difficult to make flow. Much of the *in situ* production in Alberta is with SAGD processes (steam assisted gravity drainage) where a pair of horizontal wells are drilled, with the upper well supplying steam to heat the bitumen (reducing its viscosity) and allowing it to flow by gravity to the lower production well. With approximately 1 million barrels of bitumen per day being produced by this method, several improvements are being proposed that promise to reduce energy and/or the water (steam) requirements. These include addition of solvents, underground combustion processes, and processes that produce an upgraded bitumen product underground. Such processes are described elsewhere [31, 32].

Generally, the Athabasca oil sand is surface mined after removal of about 30–75 m of overburden material (see Fig. 12.1). The mining of the ore body, which might average about 60 m thick, is accomplished by large draglines, bucketwheel excavators, or mobile power shovels. The mining operation is often defined by TV to BIP or total volume

(including overburden) to bitumen in place. Efficiencies in the mining operations have meant that the method of choice for mining is now generally truck and shovel operations and this along with other improvements has meant that the TV/BIP has steadily increased from about 9–12 in 1990 to 14–16 in 2010. About 2 tonnes of oil sand of 10% (the average grade) bitumen content are needed to yield 1 barrel of oil (after extraction). As the grade of oil sand decreases, additional tonnes must be mined and processed to yield the same amount of oil, so each commercial operation will have a lower economic grade, or “cutoff” limit below which the ore is treated like overburden and either removed or avoided. Generally this ore cutoff is at 8%. In most surface mining operations the oil sand is mined directly by power shovels and moved by trucks to surge piles. From the surge piles an arrangement of feeding devices, crushers, and sizers deliver oil sand, at a uniform feed rate, to slurring and screening devices, which in turn feed hydrotransport pipelines. The hydrotransport slurry operates at relatively low temperatures (40–50°C) compared to the previously popular tumblers (80°C) and this substitution of mechanical energy (often several kilometers of pipelining) for heat energy has resulted in a significant energy reduction in the extraction process (about 40% since 1990). The conditioning that occurs during hydrotransport (previously in tumblers) serves to separate the bitumen from the mineral grains in the oil sands.

Figure 12.2 shows a section of core from the Athabasca deposit, illustrating the various layers. Each of the mining methods blends some of the different oil sand grades and also clay (lens) bands to various degrees. A certain degree of mixing also occurs during the subsequent handling and transferring operations. Modern truck and shovel operations permit more selective mining than was previously possible with draglines and bucketwheels, but more importantly, by choosing shovel locations, there is an opportunity to achieve some blending of the ore (an illustration of the value in selectively blending ores is given in reference [33]). In spite of this, the delivered oil sand is not homogeneous. Since oil sands having different natures and compositions are associated with different conditions for optimal separation and flotation, bitumen process control strategies are very important, as is the necessity of having an extraction process forgiving enough to tolerate feed variability.

Although many different separation methods have been tested, water-based conditioning, followed by bitumen flotation, has received the most attention and forms the basis for the existing large-scale commercial plants. Several descriptions of the commercial water-based flotation processes have been published [5, 6, 22, 34–40].

The water-based flotation process is used to separate the bitumen from the associated minerals by exploiting differences in both their bulk and surface properties. The commercial process layout is shown in Fig. 12.3, which highlights the differences between the tumbler and hydrotransport conditioning processes. First the oil sand is “conditioned” by slurring with water followed by transport in several kilometers of pipeline. Here heat (viscosity reduction) and shear are employed to overcome the forces holding oil sand lumps together. In this ablation successive layers of each lump are warmed and sheared off until everything is suspended. Besides shear in the pipeline to maintain a state of suspension a number of other things must happen in this “conditioning” step. The bitumen has to be separated from the solids (which make up about 70% of the slurry), and prepared for separation from the aqueous phase. In the previous tumbler conditioning process, several things are done to accomplish this. Steam is added to raise the (exit) temperature to 80°C. Air is not sparged in directly but becomes worked in to aerate the bitumen by inclusion of about

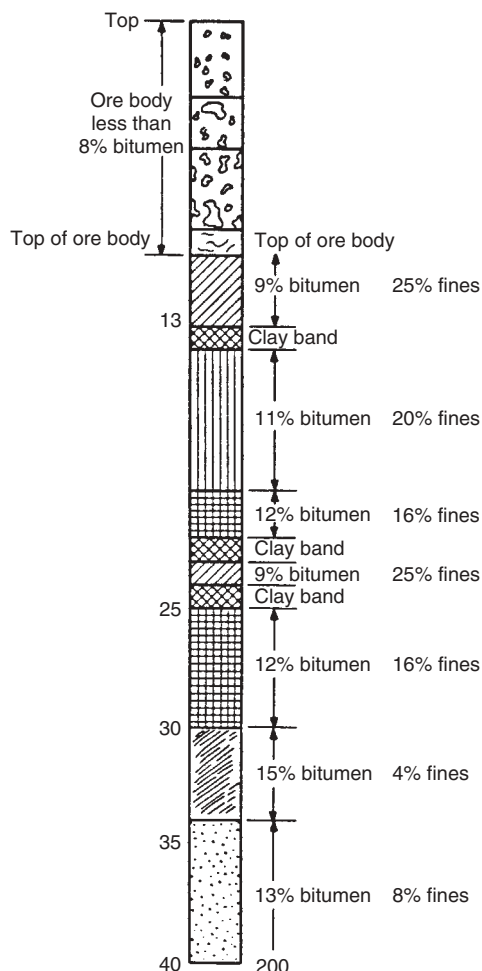


**Fig. 12.2** Cross-section of a core from the Athabasca oil sands. Reproduced with permission from Erskine [39]. Copyright 1984 McGraw-Hill.

30% v/v gas [22]. Sodium hydroxide is added to raise the solution pH. For tumbler slurrying and conditioning, the amounts of the reagents added are typically in the proportion: oil sand/water/NaOH(20%) = 1:0.19:0.0012 by mass. In general, about 200 p.p.m. sodium hydroxide is used on an ore basis. Some operations only added sodium hydroxide when the ore grade and clay content were at low and high levels respectively.

Pipeline conditioning or hydrotransport is almost exclusively used today and provides a much longer residence time. With more mechanical energy, lower extraction temperatures are possible (typically 40–50°C) and some operations have stopped the use of sodium hydroxide entirely. Bitumen to air attachment occurs in the ore breaking or crushing

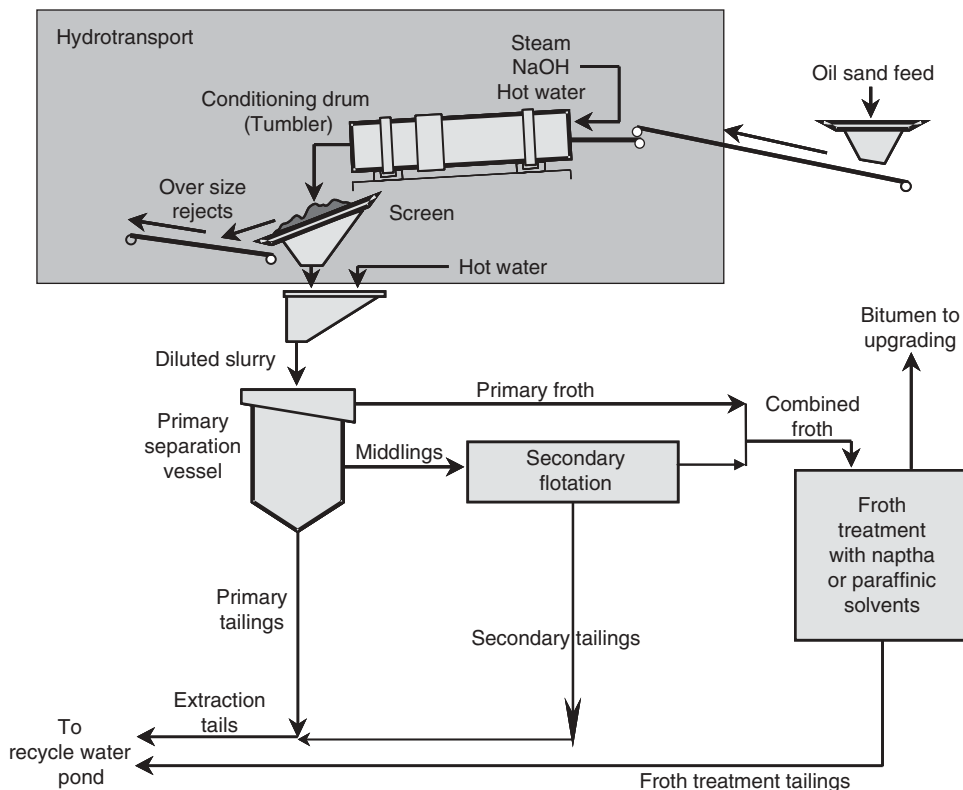


**Fig. 12.3** The major components of the commercial oil sands extraction process. The shaded area showing an ore conditioning process using tumblers for conditioning and a process that rejects large clay lumps from the extraction plant (an 80°C process often also involving 200 ppm NaOH as a process aid) has largely been superseded by hydrotransport conditioning. Hydrotransport involves crushing or breaking the ore and slurry transport to the separation vessel. Hydrotransport is typically done at 40–50°C, and generally does not include a clay lump rejection, so the resulting extraction process froths often contain more mineral.

operation and during hot water addition prior to formation of the oil sands slurry. The relationship between process temperature, mechanical energy, and process chemistry has been discussed elsewhere [41–46].

As mentioned earlier, whether in tumblers or pipelines, the mined and slurried oil sand being conditioned is neither homogeneous nor uniform. Although the mining and handling process (see Figs 12.1 to 12.3) causes the different layers of oil sands to be broken up and mixed, strong variations in feed quality persist. This necessitates constant adjustment to maintain optimal processing conditions. Sodium hydroxide (or other reagents) and slurry water addition are usually the main process control variables. An appreciable time is required to achieve good distribution of the bitumen, minerals and

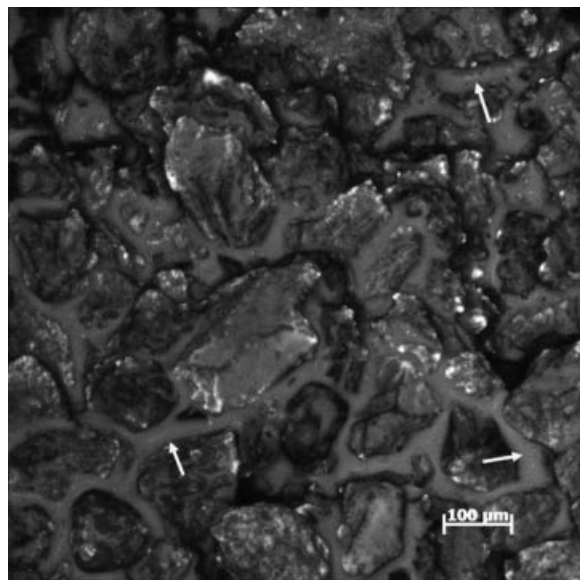


**Fig. 12.4** Optical micrograph of a high grade bitumen ore (14% by mass and over 30% by volume bitumen). The continuity of the bitumen structure leads to a rapidly rising and low mineral content froth. The arrows identify the largely continuous bitumen component between the sand grains. The bitumen is bright in these fluorescence images.

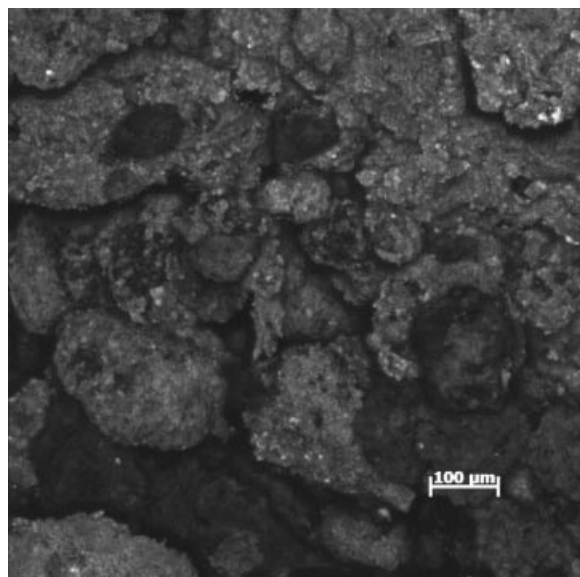


**Fig. 12.5** Optical micrograph (bitumen fluoresces and is bright in this image) of a low grade bitumen ore (7% by mass and less than 10% by volume bitumen). The lack of continuity of the bitumen structure leads to a bitumen froth that is composed of many smaller and non-continuous droplets with more difficulty in mechanically separating the bitumen from the mineral.

reagents and to allow chemical and surface reactions to occur. In 5–10 minutes a quasi-steady state is reached, probably not full thermodynamic equilibrium, and the slurry is discharged with a significant volume of flood water into separation cells or primary separation cells. Sometimes air can also be added to the hydrotransport pipeline, although the main air attachment occurs at the breakers/crushers and slurry preparation step. Many of the bitumen froth and foam differences are due to chemical differences in the bitumen and many are due to the physical differences between the bitumen distributions in the original ore. Figures 12.4 and 12.5 show high and low grade oil sands ore and the bitumen distribution. For the high grade ore, the higher concentration and continuity of the bitumen component makes for a higher quality froth product (lower mineral content).

During the conditioning process the bitumen becomes separated from the sand and mineral particles due to a combination of the effects of mechanical shear and disjoining pressure (Fig. 12.6a). The disjoining pressure in the aqueous films separating the bitumen and solids is increased by increasing electrostatic repulsion caused by a combination of ionizing surface functional groups and the adsorption of anionic surfactant molecules at the interfaces [47]. Next, bitumen–air attachment occurs (Fig. 12.6b). The process conditions

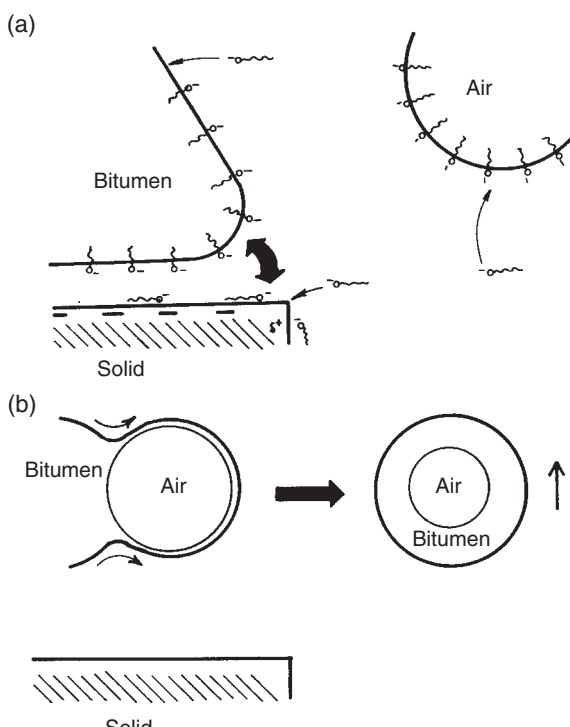


**Fig. 12.6** Illustration of two of the steps in the water-based flotation process, showing (a) adsorption of natural surfactants at the interfaces and the separation of bitumen from the solids, and (b) the attachment and filming of bitumen around gas bubbles. Reproduced with permission from Shaw et al. [41]. Copyright 1994 American Chemical Society.

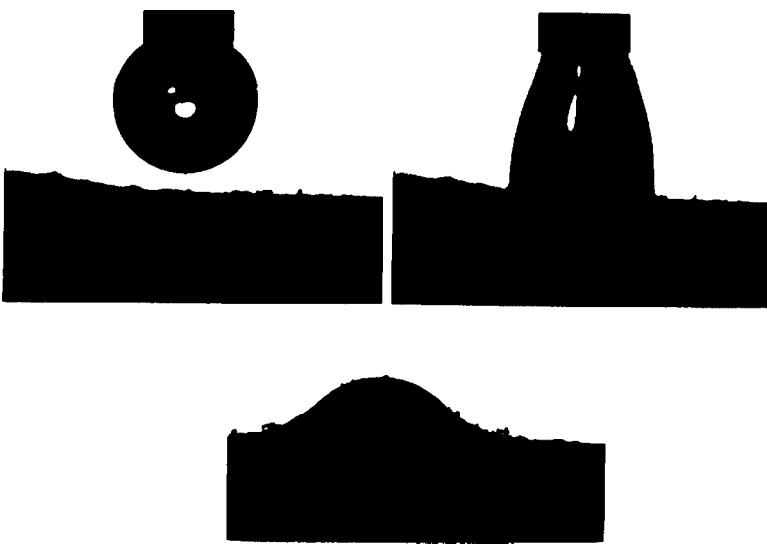


**Fig. 12.7** Photographic sequence in which an air bubble, on the tip of a capillary, is pushed down through an alkaline solution, at 80°C, until it just touches a layer of bitumen that had been coated onto a silica surface. The bitumen spontaneously spreads over the surface of the bubble, causing it to detach from the capillary and become engulfed. The presence of solid particles at the bitumen surface can be observed in the lower photo. Photomicrographs by L.L. Schramm. Reproduced from Shaw et al. [41]. Copyright 1994 American Chemical Society.

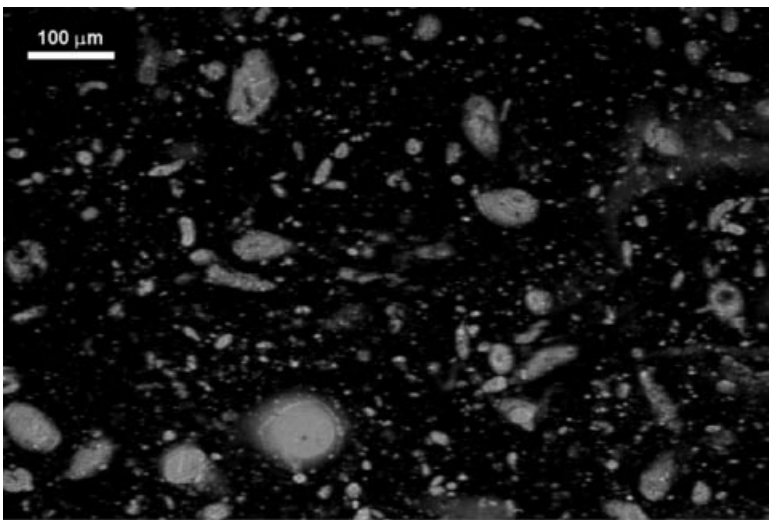


**Fig. 12.8** An optical microscope image of bitumen froth droplets at 25°C. At this temperature, most of the bitumen does not envelop an air bubble, but remains as independent droplets. Froths formed at these temperatures can have more mineral entrained because the flotation process is generally more aggressive, which also tends to float some mineral components. Photomicrograph by V. Muñoz.

that most favour bitumen–solids separation – that is, a high degree of electrostatic repulsion due to charged surfactant molecules at the interfaces – also will tend to act in opposition to gas–bitumen attachment since the gas bubbles also acquire a surface charge of the same sign [48]. On the other hand, in mineral flotation, where there is gas–solid attachment without filming, such electrostatic repulsion is not as important a factor as are inertial effects when the particles and droplets are larger than, say, 10–40 µm diameter. While it is possible for bitumen droplets to attach to gas bubbles and form bubble droplet pairs or aggregates, as in mineral flotation, it appears that for the most part a balance of interfacial tensions in the system favours filming of the bitumen around the gas bubbles. Figure 12.6(b) and the photographs in Fig. 12.7 show the spontaneous filming of bitumen around a gas bubble brought into contact with the solution/bitumen interface. These aerated bitumen globules are what float upwards in the flotation vessels to form froth. At temperatures above about 40°C, the bitumen to air interaction is very strong and the bitumen will envelop an air bubble forming a balloon of bitumen. At lower temperatures, the viscosity of the bitumen will not allow this to happen and interaction with air is not as strong. Figures 12.8 and 12.9 show two micrographs of a bitumen froth at 25 and 50°C. This temperature dependence on the bitumen to air attachment is then reflected in the structure of the resulting froth [44]. As the process temperature decreases, there is a greater proportion of bitumen that cannot (probably due to higher viscosity) envelop an air bubble. Viscosity of the bitumen in the ore can result in similar behavior and as a result the success of the Utah Asphalt ridge pilot program depended upon elevated extraction temperatures to move the more viscous Asphalt ridge bitumen into a region analogous to Athabasca

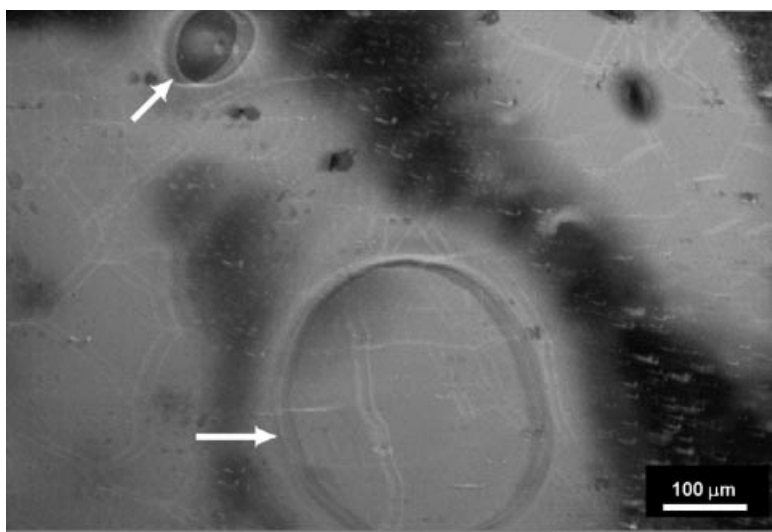


**Fig. 12.9** An optical microscope image of bitumen froth droplets at 50°C. At this temperature the bitumen–air interaction is very strong, resulting in the bitumen enveloping the air bubbles. The arrows point out the air bubbles in the coalescing bitumen foam or froth. Photomicrograph by V. Muñoz.

bitumen, thus allowing for the application of the hot water extraction process to this ore in spite of its high viscosity at room temperature.

The diluted (flooded) slurry contains about 7% aerated bitumen droplets, 43% water and 50% suspended solids. It is pumped to large primary separation (flotation) vessels. The vessels are maintained in a quiescent condition to facilitate the flotation of the aerated (lower density) bitumen droplets as well as the settling of the heavier (coarse) solids to the bottom. What is floated can be in some sense considered an aggregated colloid, rather than a dispersed one, and consequently high shear rates must be avoided to obviate destruction of the aggregates. The slurry is retained in these vessels for about 45 minutes to allow floating and settling, and to provide adequate time for aqueous film drainage from the froth and coalescence of the bitumen/air components into a bitumen continuous froth. To maximize the flotation and sedimentation processes viscosity and density in the central (middlings) vessel region are kept low by adjusting the flood water addition and middlings removal rates. Counter-current froth underwash water is also sometimes used to reduce the mineral content in the coalesced froth or bitumen concentrate. Since the process is continuous, the presence of fine minerals (e.g. clays) makes the vessel susceptible to build-ups in solids concentration which can increase the viscosity [22, 49, 50]. This can also be controlled by the regulation of flood/underwash water addition and middlings withdrawal rates.

At the surface, the rising droplet/bubbles gather to form a froth layer. A moderate depth of froth is necessary to allow some back-drainage to take place, with release of non-floated particles that have been, unavoidably, entrained to some extent between the bubbles. The froth layer is removed mechanically from the surface and flows away in a launder. A good quality froth might consist of 66% bitumen, 9% solids, and 25% water, but would be more typically 50–55%, bitumen 15% or more solids, and the remainder water. In general, the move to lower process temperatures with hydrotransport as opposed to tumbler conditioning has decreased the average bitumen froth quality. We return to this part of the process in the next section.

The smaller suspended solids that do not settle rapidly, and the smaller and poorly aerated bitumen droplets that do not float rapidly, are all drawn off in a slurry from the middle of the vessel (middlings). The bitumen droplets in middlings have either too little air content or too small diameters for rapid enough flotation. The middlings stream contains enough bitumen that it is pumped to a secondary (scavenging) flotation circuit for additional bitumen flotation. Here conventional flotation cells, employing vigorous agitation and air sparging, are used to cause further bitumen aeration and flotation. This results in a secondary froth which is much more contaminated with water and solids than is the primary froth, and typically contains 24% bitumen, 17% solids, and 59% water. Other variations of this process are also practiced. For example, in one commercial operation the middlings stream and primary tailings stream are combined and pumped to a special tailings oil recovery (TOR) flotation circuit [40]. The middlings from this TOR vessel are then pumped to scavenging circuits, as discussed in the text, while the TOR froth is recycled into the flooded slurry that is fed into the primary separation vessels. The TOR tailings are combined with the tailings from the scavenging circuits. Often the sign of a poorly processing ore (decreased bitumen recovery) is a higher than normal proportion of the total production coming from the secondary flotation cells. This is because the greater the proportion of oxidized bitumen, the greater is the affinity of the bitumen for minerals, and therefore the

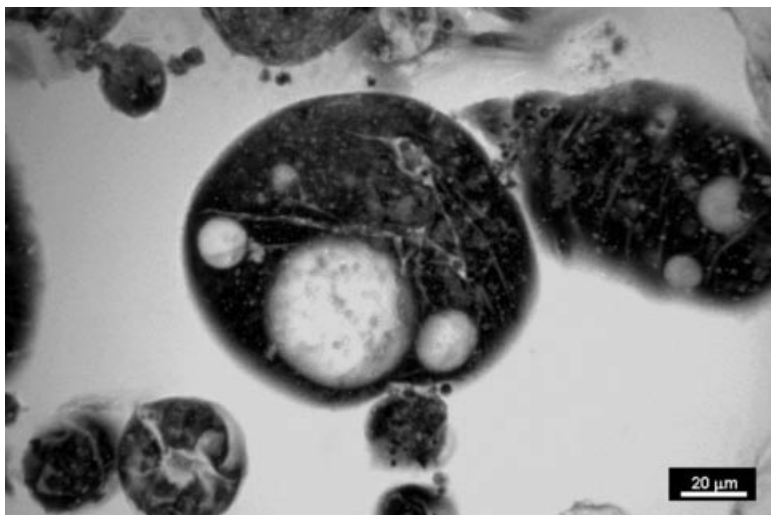


**Fig. 12.10** Confocal micrograph of a bitumen froth (deaerated) from an easily processed ore. The mineral is colored red and the bitumen is green. Most of the mineral is associated with the water phase that has been trapped as the bitumen bubbles collapse at the top of the separation cell. Photomicrograph by V. Muñoz. For a better understanding of the figure, please refer to the colour plate section.

less likely it is to associate with an air bubble and report in the primary froth. With the more aggressive air and bitumen collisions in the secondary flotation circuit, it is possible for this bitumen to now attach to an air bubble and report as a secondary froth product. The effect of this chemical difference at the bitumen surface (oxidation or degradation of the bitumen) has a similar effect on the froth or foam structure as lower temperatures. The bitumen tends to remain as independent droplets and does not coalesce as readily. This difference in froth structure sometimes has unexpected effects. For instance, the photomicrographs in Figs 12.10 and 12.11 show the bubble morphology and the mineral component in a high bitumen content froth. This unoxidized froth shows a significant amount of trapped mineral in the water that has been entrained in the collapsed froth. This is thought to be due to the rapid rise of bitumen in the separation cell and collapse of the froth to trap mineral. For an oxidized bitumen (Figs 12.12 and 12.13) there is a larger proportion of oil-wet mineral (the mineral particles associated with the hydrocarbon phase rather than simply being trapped in the water droplets). This stronger association of bitumen with the mineral phase is thought to be due to the surfactants associated with the oxidized bitumen. Figure 12.13 shows that this also tends to distort the bubbles associated with the froth. In spite of the strong mineral and bitumen interaction that often characterizes oxidized ore, because of the slow rate at which the bitumen will form a continuous phase, it is sometimes possible to have a better froth quality than for a high grade ore. This is because the application of a froth underwash can reduce mineral content in the more slowly collapsing oxidized bitumen droplets rising in the separation cell.

Gas bubble/mineral particle attachment also occurs for the fraction of mineral particles that are not hydrophilic, so that some bubble–particle aggregates also float upwards and

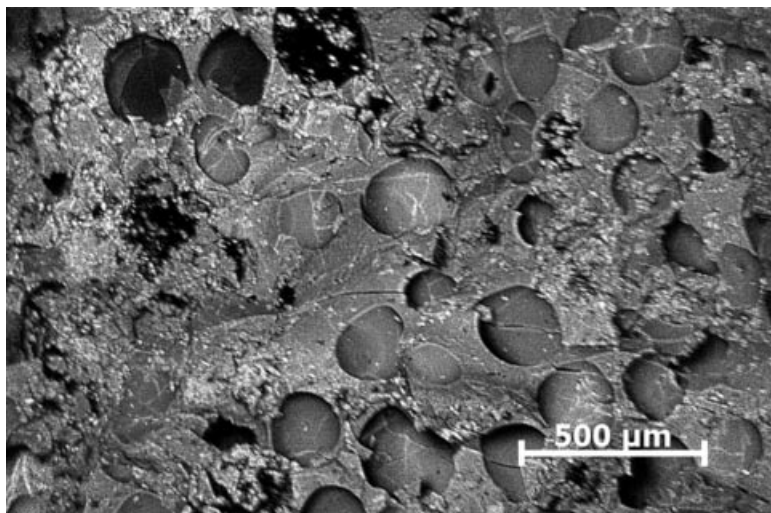


**Fig. 12.11** Air bubbles in an unoxidized bitumen froth from a commercial hydrotransport extraction process. The air bubble distribution is quite small and uniform prior to deaeration. Photomicrograph by V. Muñoz.

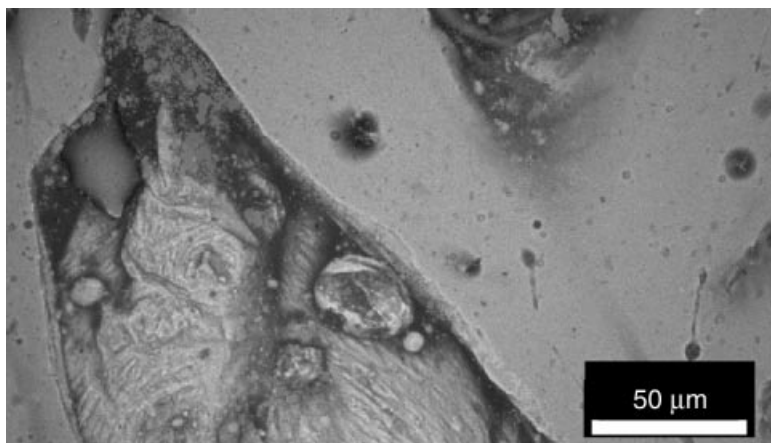


**Fig. 12.12** Confocal micrograph of a bitumen froth (deaerated) from a difficult to process ore. The mineral is colored red and the bitumen is green. Most of the mineral in this case is closely associated with the bitumen (oil wet solids) and a very complex emulsified froth structure is observed due to the high surfactant concentration in the bitumen. The bitumen component is imaged in a fluorescent mode and the decreased brightness in this image relative to Fig. 12.11 is indicative of a different bitumen chemistry in the bitumen component. Photomicrograph by V. Muñoz. For a better understanding of the figure, please refer to the colour plate section.

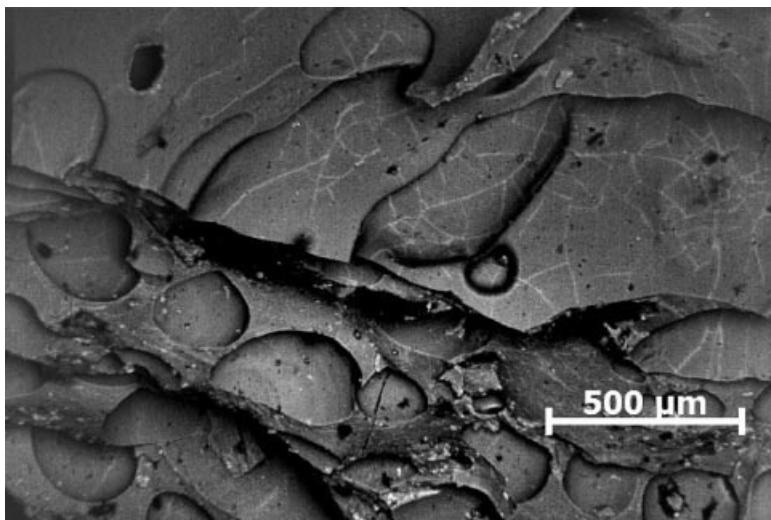


**Fig. 12.13** Air bubbles in an oxidized or high surfactant bitumen from a poorly processing ore. In this case, the froth bubbles are much larger and have a distortion or unusual structure. Photomicrograph by V. Muñoz.

become incorporated in the froth. An important goal of the flotation process is to produce bituminous froth without entraining large amounts of solids. Since the entrained water and froth are later removed only with considerable difficulty, the question of how to produce higher quality froth is of interest. Due to its higher quality, primary flotation froth does not need the difficult cleaning and is more highly valued than secondary froth. Thus much flotation process optimization is directed at optimizing the primary froth yield in the process. This is why so many oil sands patents are directed principally at the primary recovery aspect of the process (e.g. [36]). As a practical matter the solids floated do become part of the nature of the froths, and are discussed further in this work.

The coarse, rapidly settling, solids in the primary separation vessel are kept in motion by mechanical rakes at the bottom of the vessel and are drawn off from the bottom as a slurry (primary tailings). The tailings from the primary and secondary flotation processes are combined and transported to a tailings pond. Most of the supernatant water from the pond can be recycled into the process. The remaining fine solids and water undergo a slow consolidation into a silt and clay suspension known as fluid fine tailings. Further discussion of the tailings and the tailings ponds can be found in many references (e.g. [42, 51–53]).

## 12.4 Froth Structure

The froth recovered from the primary separation vessel is a complex mixture of bitumen, water, inorganic solids, and air. The quality of the product is determined by the relative amounts of water and solids present in the material and the ease by which these constituents

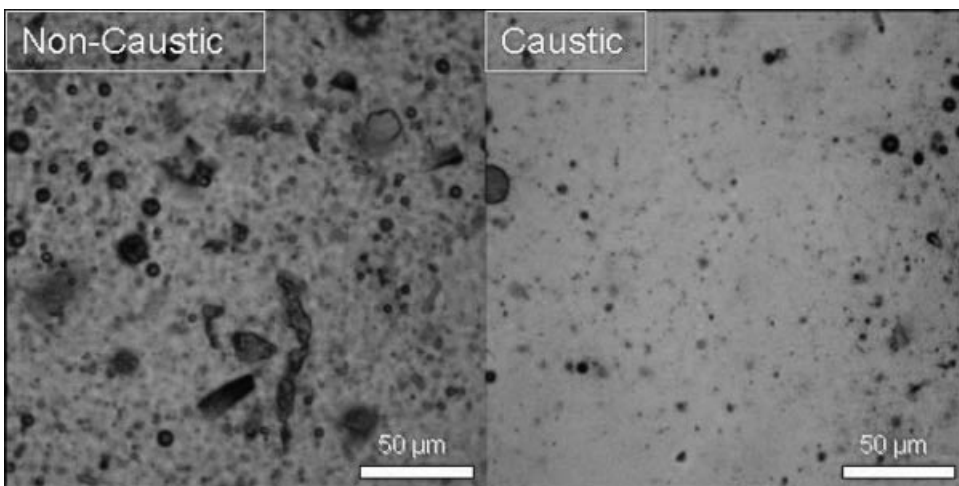


**Fig. 12.14** The loose froth (left) is from the same oil sand as the coalesced froth (right). The use of sodium hydroxide in the extraction process changes the nature of the bitumen, resulting in a froth that has significantly less mineral and water. In these confocal microscope images, the red colors are mineral components, the green are hydrocarbon, and the dark areas are water. Photomicrographs by V. Muñoz. For a better understanding of the figure, please refer to the colour plate section.

can be separated from the froth in downstream operations. These properties have their origin in the manner in which froth is formed, and in turn this is determined by the composition of the ore and the properties of the bitumen in that ore.

The aerated bitumen droplet diameters and size distribution are related to the slurry conditioning variables described above, such as the nature of the oil sand and the chemicals used to process the ore. Houlihan [54] has made extensive measurements of bitumen droplet diameters and rise velocities in the primary separation vessel of a continuous pilot-scale processing plant. He found that droplet size distributions for a given oil sand feed are relatively narrow, and that the bitumen droplets that float are mostly spherical, consisting of a thin film of oil enveloping an air bubble. At low alkali addition levels, the bitumen was attached to air bubbles as discrete particles. This mode of bitumen attachment is also seen at reduced temperatures and is akin to the type of mechanism encountered in mineral flotation. At moderate alkali addition levels (i.e. most processing conditions), however, the bitumen fully encapsulates the air bubbles. Houlihan also found that the size of the droplets tends to increase with increasing dosage of alkali, but that the bitumen droplet sizes did not vary with depth in the separation vessel (suggesting that bitumen droplets do not coalesce as they rise through the middlings phase).

The rising bitumen droplets, with their encapsulated air, pack together at the surface of the separation vessel in the initial stages of the froth formation process. Simple packing produces a “loose” froth. Better quality froths are bitumen-continuous and sometimes referred to as “stable” froth. The evolution of a dilute dispersion of bitumen/air aggregates from a “loose” to a “stable” froth is illustrated in Fig. 12.14.

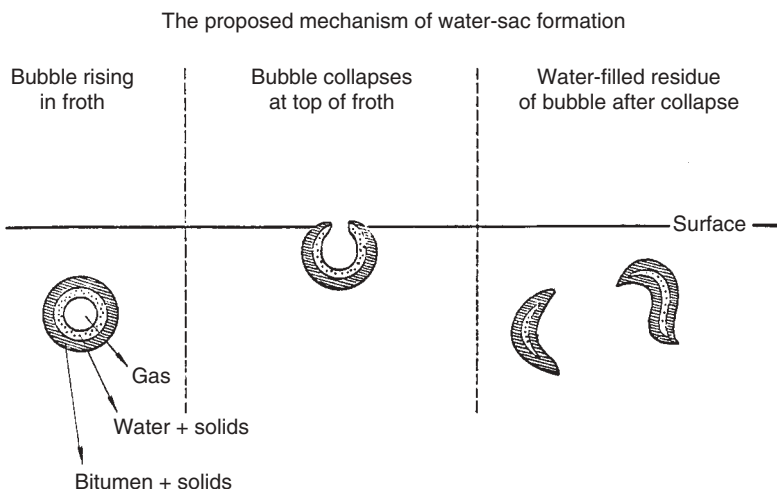


**Fig. 12.15** A proposed mechanism of membranous, emulsified water formation in froth, based on microscopic examination. From Swanson [56]. Copyright 1994 American Chemical Society.

It is generally thought that most of the water associated with froth is due to the entrainment of middlings as the froth layer is formed in the primary separation vessel. Experimental investigations conducted by Chung *et al.* [55] indicate that a smaller fraction, up to 16% of the water in the froth, actually originates from slurry water used during the original oil sand slurring. This water is believed to be carried downstream as W/O (water-in-oil) emulsion formed under the turbulent conditions experienced in the tumbler, pumps, and pipelines upstream of the primary separation vessel.

Over time, some of the bitumen-coated gas bubbles in the froth collapse yielding the emulsified water droplets dispersed in bitumen. The microscopic studies of Swanson [56] confirmed that high quality froth comprises a continuous phase of bitumen in which large water droplets are emulsified. The emulsified water is contained within “membranous sacs” and is rich in sub-micron sized mineral particles (Figs 12.15–12.17). The membranous interfacial film was concluded [56] to be formed from solids (mostly clays) having an organic coating, making them oil-wetting, or bi-wetted.

Given the description of froth formation one might expect that the collapse processes described would yield gas bubbles having diameters just smaller than those of the original bitumen globules, and also yield water droplets (from the original thin films in the oil sand), which should be much smaller. In addition, there should be quite a lot of larger-sized water droplets that were entrained into the froth layer from the middlings (termed free water). Swanson’s picture is, in fact, consistent with the available results for dispersed gas bubble and water droplet sizes. Figure 12.18 shows a photomicrograph of a bitumen froth captured from a commercial separation cell that confirms this view of the froth structure. The concept of emulsified water from the conditioning step being carried through the process can be carried a step further as illustrated by the micrograph in Fig. 12.19. Figure 12.19 shows that the smallest droplets of water in the froth have the highest

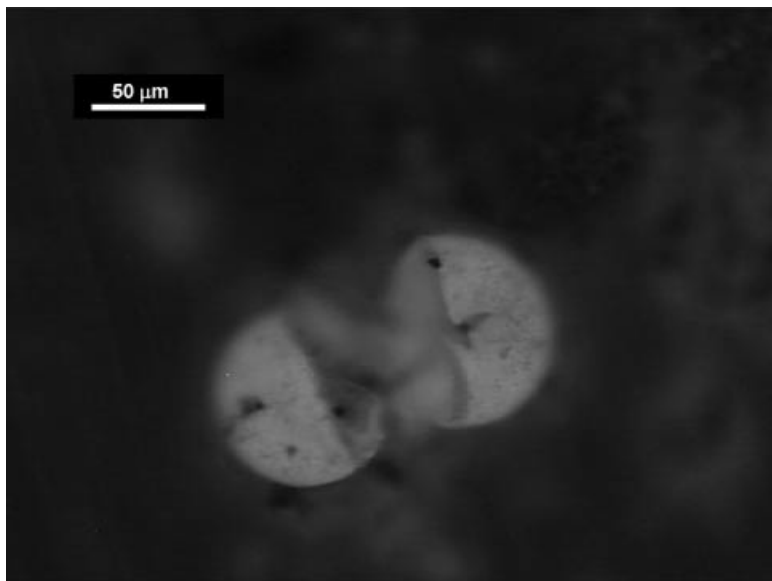


**Fig. 12.16** Optical image of a membranous sac from a froth treatment process. The stiff structure of this component is evident from the fact that it maintains its spherical shape even after being sheared open. Photomicrograph by V. Muñoz.

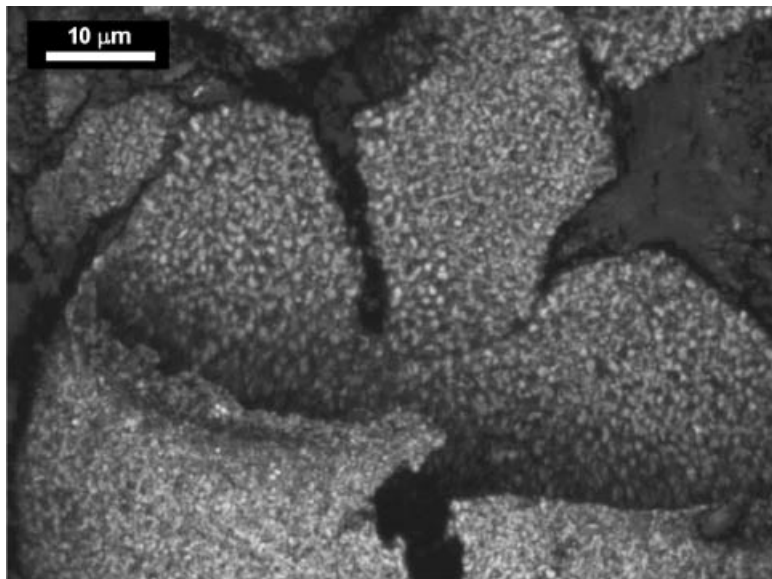


**Fig. 12.17** A detail of a similar membranous sac at higher magnification showing both mineral (red) and organic phases (green). The stronger the association between the mineral and organic components, the greater is the proportion of yellow in this image. Photomicrograph by V. Muñoz. For a better understanding of the figure, please refer to the colour plate section.

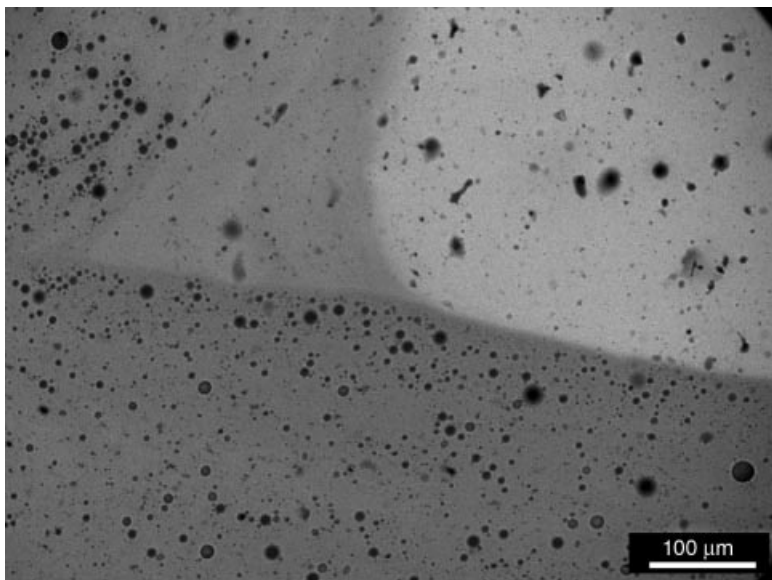


**Fig. 12.18** Fluorescent microscopic image of a commercial froth showing several distinct bitumen fluorescent areas. These differences in fluorescence intensity indicate different bitumen sources. These are due to the different shovel locations in the mine feeding the extraction process bitumen with different chemistries. Clearly the mixing of froth in the commercial operation is not complete and this heterogeneity of the feed is carried from the froth to downstream processes such as froth treatment. Photomicrograph by V. Muñoz.

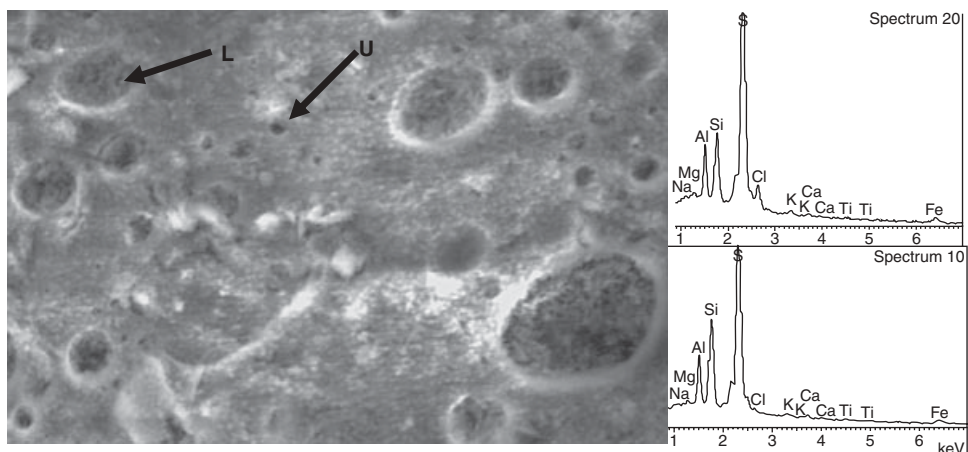


**Fig. 12.19** A cryo-scanning electron micrograph of a bitumen froth with accompanying X-ray spectra of the small emulsion droplet (U) and a larger emulsion droplet (L) corresponding to the upper and lower spectra to the right of the micrograph. The smaller droplet contains a high Cl proportion, related to the original connate water in the ore. The larger droplet is a result of the froth collapsing around a mixed water more representative of the process water. Photomicrograph by V. Muñoz.

chloride concentrations consistent with poor or no mixing of the original high-chloride connate water in the ore with the slurry conditioning water. Depending upon the source of the ore, the water associated with the ore can have salt concentrations consistent with the prehistoric sea water into which the bitumen was deposited. The water associated with the ore (or connate water) does clearly not blend completely with the recycled process water that has been diluted with Athabasca river water. The resulting froth or foam therefore has a subtle but very important substructure, with the smallest water droplets representing a larger proportion of the original water associated with the ore body. Since chloride can have some detrimental corrosive effects upon downstream processes after the froth or foam is collapsed and separated, it is important to appreciate this difference in structure.

Chung *et al.* [55] measured the emulsified water droplet sizes in froth. After removing the large-size free water droplets, a second, smaller-size fraction of water droplets was observed, which ranged up to about  $18\text{ }\mu\text{m}$ .

Houlihan [54] conducted a number of direct photomicrographic studies of rising bitumen droplets in a continuous pilot plant and found that under good processing conditions, the rising droplets were approximately spherical, with diameters of about  $280 \pm 140\text{ }\mu\text{m}$  (total range from 125 to 400). Various other similar studies have yielded droplet size ranges within the bounds  $100\text{--}600\text{ }\mu\text{m}$ . The thickness of the bitumen film has been estimated to be about  $30\text{ }\mu\text{m}$ , so that the above droplet diameters can also be taken as a first estimate of the gas bubble sizes to be expected in froth. The case of Houlihan's measured mean droplet size of  $280 \pm 140\text{ }\mu\text{m}$  would then translate into an expectation of bubble sizes of about  $216 \pm 140\text{ }\mu\text{m}$ . This would of course be a function of the relative bitumen volume in the ore and the temperature, mechanical energy, and chemistry in the conditioning.

Several studies have sought to further refine the model of froth structure (see the citations in [41]). As bitumen droplets deform and coalesce in the froth layer, some of the water is expelled. The remaining froth water content is determined by the packing density of the aerated bitumen droplets as they collect at the interface, which in turn is influenced by such factors as:

- bitumen droplet size distribution,
- thickness of the bitumen film enveloping individual air bubbles (which defines the bitumen droplet density),
- flux of material impinging on the froth/middlings interface,
- bitumen droplet deformability,
- bitumen droplet coalescence rate, and
- froth residence time (which governs the time available for water drainage and the extent to which droplets can orient themselves relative to one another).

Shaw *et al.* [41] have illustrated some of the model-system calculations that have been done to try to predict the relationships between froth quality, bitumen droplet aeration, and packing density. An example is calculations assuming an ideal system of uniform, spherical, deformation-resistant, aerated bitumen droplets congregating in a hexagonal-close-packed array with an occluded volume fraction of 0.74. Such calculations predict [41] that high bitumen content froth is favoured with increasing droplet density, which is consistent with experimental measurements by Danielson [57], although the experimentally obtained values suggest that small-sized droplets also fill the interstices between larger droplets, giving rise to increased bitumen concentration in the froth [41]. Primary froth assays from

**Table 12.2** Some bituminous froth viscosities.

Type of froth	Froth viscosity (mPa.s)	Shear rate (s <sup>-1</sup> )	Temperature (°C)	Reference
Lab-scale batch extraction	$1.8\text{--}3.0 \times 10^3$	58	80	[63]
Pilot-scale continuous process	$1.7\text{--}4.7 \times 10^3$	58	70	[41]
Commercial process (Suncor)	$7.5 \times 10^3$	Unknown	66	[72]
Commercial process (Syncrude)	$1.5 \times 10^3$	Unknown	71	[73]

All of the above froths were produced from the processing of Athabasca oil sand.

**Table 12.3** Phase saturations and mean droplet and bubble diameters for froth samples as determined by magnetic resonance imaging.

Location in froth layer	Froth composition (vol%)			Mean water droplet diameter (μm)	Mean gas bubble diameter (μm)
	Oil	Water	Gas		
Top	72.1	17.9	10.0	600–800	200–500
Middle	67.3	23.4	9.3	600–800	200–500
Bottom	68.2	23.6	8.2	600–800	200–500

All of the above froths were from pilot-scale continuous processing of Athabasca oil sand.

Source: Adapted from ref. [41].

commercial operations indicate a practical upper limit of 67.5% bitumen concentration [41]. Corti *et al.* [58] proposed a relationship between the bitumen content in the ore and the subsequent froth quality that used the volume fraction of the bitumen relative to the other ore and slurry components. For the series of samples he studied, the continuity of the original bitumen in the ore was thought to be related to the continuity of the bitumen in the subsequent froth and therefore to the relationship between ore grade and bitumen recovery. The predictive utility of these types of analyses is always difficult to assess in a commercial situation because several factors are often at odds. For instance, efficient conditioning demands a high enough slurry density to provide particle contact shearing the bitumen from the mineral, as well as a low enough bitumen viscosity in order for this shear to be effective. Unfortunately, in order to increase process temperature, more hot water has to be added and this will decrease the slurry density. Nevertheless, some of the temperature v. mechanical shear trade-offs are beginning to be understood [59]. Controlling these factors in a laboratory (often batch-processing) setting is of course straightforward, compared to understanding applicability in a commercial, continuous-processing context.

Shaw *et al.* [41] also used nuclear magnetic resonance imaging (MRI) to probe further into the arrangement of the phases in froth. In this work estimates for the relative phase saturations for each sample were determined from image intensity histograms and verified against reference samples that were collected and assayed by conventional means. Table 12.3 shows some typical froth compositions and mean water droplet and gas bubble

sizes. The total range of water droplet sizes observed in the froth samples was larger than suggested in Table 12.3. Whereas the mean droplet sizes were consistently in the range 600–800 µm, some droplets as large as 1400 µm and as small as <100 µm were observed. That the smaller size droplets were observed qualitatively corresponds with the measurements made by Chung *et al.* [55] for “emulsified” water droplets, which were up to about 18 µm. The larger droplets determined in the present work presumably correspond to the free water phase.

The range of gas bubble sizes observed in the froth samples also corresponds closely with the estimates made earlier based on Houlahan’s measured rising droplet sizes, where froth gas bubble sizes of about  $216 \pm 140$  µm were predicted. Table 12.3 shows that the mean bubble sizes fell in the range 200–500 µm. Here again, although the mean bubble sizes were consistently in that range, some bubbles as large as 1000 µm and as small as <100 µm were observed as well.

We conclude this section with some observations on the solids in froth. Fine solids dispersed within the interstitial middlings phase (water-wet clays and silica) can account for some of the mineral matter present in the froth. Oil sand minerals that are intrinsically hydrophobic and thus preferentially floated with the bitumen (heavy minerals, coal, and oil-wet clays) constitute another source of froth solids [60]. Particle size measurements on solids in froth tend to display a bimodal distribution that serves to differentiate hydrophobic and hydrophilic minerals. Oil-wet particles are typically coarser than the solids suspended in the middlings directly below the froth interface. The particle size distribution of solids in the aqueous phase of froth agrees well with that predicted from settling velocities given the bulk residence time in the primary separation vessel. Many minerals, such as pyrite, zircon, rutile, and ilmenite, concentrate in the froth due to their inherent oil wettability relative to the more numerous clay and silica minerals.

Experimental studies by Schutte [60] have shown that froth (compared with other process streams) is enriched in asphaltenes. It was postulated that asphaltenes play a key role in promoting air attachment to bitumen but that the same asphaltenes then inhibit coalescence of the droplets. In any case, under normal vessel loading conditions, the rate of bitumen coalescence is slow relative to the rate at which bitumen droplets collect at the interface, so much of the occluded water is unable to drain. Paths for drainage become exceedingly tortuous as the froth interface is continually replenished with aerated bitumen droplets.

## 12.5 Physical Properties of Froths

Density is of fundamental importance to any flotation process. The density of bitumen is much less variable and less dependent on temperature, for example, than is its viscosity. Thus, for example, the density data reported by Camp [22] and Ward and Clark [61] show only a slight temperature dependence for Athabasca bitumens. However, the density of froth is strongly influenced by the gas phase and also the entrained solid particles. Primary froth can have a wide variation in composition even if it “typically” has a composition of 66% bitumen, 25% water, and 9% solids, while secondary froth typically contains 24% bitumen, 59% water, and 17% solids. Having said that, freshly formed primary froth densities can vary from 0.7 to 0.9 g/cm<sup>3</sup> at about 70°C [41].

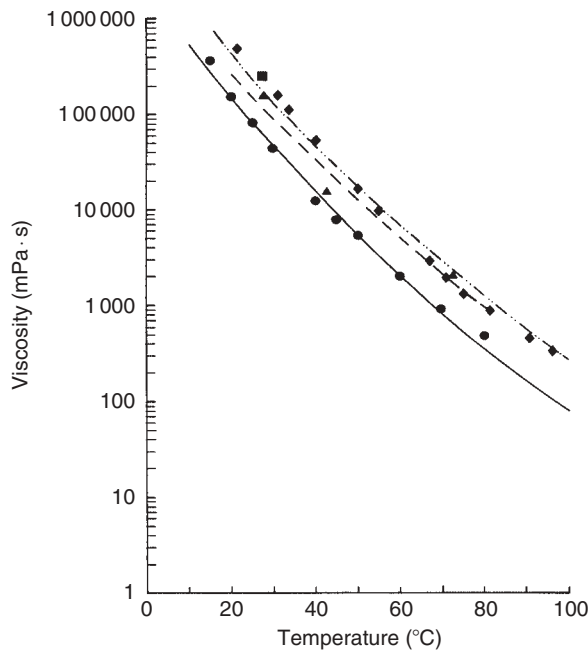


**Fig. 12.20** The viscosities of several Athabasca bitumens at different temperatures.  
From Schramm and Kwak [63]. Copyright 1988 Society of Petroleum Engineers.

As mentioned in the introduction, the viscosity of Athabasca bitumen in-place is so high that the bitumen in oil sand is practically immobile, making it difficult to displace in attempts at *in situ* recovery [18, 62]. Once mined and beneficiated bitumen viscosity becomes much reduced but still has some important influences, including a contribution to froth viscosity. Several studies of the rheological properties of Athabasca bitumen have been reported [61, 63, 64]. For practical purposes, Athabasca bitumen can be considered to be Newtonian in character except at quite low temperatures and very low shear rates [63, 64]. In an early study of bitumen viscosity Ward and Clark [61] found that the values vary with the type (location) of the host oil sand, the method by which the bitumen was extracted for study, and with temperature. Other studies [64–67] have concentrated on the influence of gas-saturation and pressure. For bitumen in the Athabasca deposit, the temperature dependence of the viscosity is shown in Fig. 12.20. It should be noted that the Athabasca bitumen rheology is not typical of that in other world locations. For example, the rheology of bitumen in the Utah deposits is more complex, exhibiting markedly non-Newtonian behavior [68] and having much higher effective viscosities [68–70]. It is important to note, however, that with increasing development of the Athabasca oil sands, wider variations in bitumen properties are being observed. Increasing the depth at which surface mining can access bitumen is also leading to differences in the observed bitumen properties, aside from the more commonly monitored clay and mineral compositional differences [44, 45]. In Utah, the seven major deposits can have widely

different properties. A very good summary of these differences for the Utah ores can be found in reference [71].

Only a limited amount of information on the rheological properties of froths has been published. This is partly due to the fact that the froths are not very stable and collapse with time. Also, great care is needed since froths, as a multiple dispersion of four phases, are very subject to phase rearrangements during the conduct of experimental measurements. Compared with bitumen, which is Newtonian in character, froths are much more viscous, non-Newtonian, shear-thinning, and thixotropic when produced [41, 63]. With time, however, these froths collapse upon standing, due to the escape of dispersed air, to eventually become Newtonian [41, 63]. Based on lab-scale batch extraction tests, little or no rheological difference could be discerned between primary and secondary froths [63]. Based on studies of continuously produced primary froth from pilot-scale (2270 kg/h) processing of Athabasca oil sand [41], the froth water and solids contents were found to be as high as 43%. Shaw *et al.* [41] found, in continuous pilot plant production, that froth viscosity is a strong inverse function of density, due to different degrees of dispersed air content, and also a strong inverse function of temperature (in the temperature range studied: 60–80°C).

The time-dependencies of froth rheology (and froth stability) have been observed to vary from no change in viscosity over 20–40 hours, to 50% reduction in viscosity in less than 20 hours [63]. Some reported bituminous froth viscosities from the literature are shown in Table 12.2. For comparison, the viscosity of Athabasca bitumen is 495 mPa.s at 80°C and 930 mPa.s at 70°C [63]. It can be seen from Table 12.2 that these bituminous froths exhibit viscosities that are 2–5 times higher than bitumen at the same temperature.

These physical differences might lead one to believe that transportation of bituminous froths would be difficult, but the previously mentioned distribution of water in the froth structure results in an interesting favourable condition. The larger water structures separate from the froth and in a pipeline these form a sleeve or annulus within which the viscous froth can be transported. In the Syncrude Aurora operation, with an extraction process located some distance from the refinery, bituminous froth is routinely transported approximately 37 km using this concept of core annular flow. The unique froth structure, which allows for movement of water structure to the pipe surface, is what allows this process to occur.

## 12.6 Froth Treatment

The two main properties of concern with regard to the processing behavior of froths are their high air content and high viscosity [63, 72, 73]. Primary froths, as shown above, are much more viscous than bitumen, and since they contain air they are highly compressible [72]. To make it easier to pump, primary froth is deaerated in towers by causing it to cascade over a series of cones, or shed decks, flowing against the upward flow of steam. The froth from secondary flotation is “cleaned” in stirred thickeners to remove some of the water and solids, and then deaerated. The primary and secondary froths, once deaerated, are combined into a single feed for further treatment. This interstage tank collects the primary and secondary froths after deaeration and, in spite of the mechanical

energy (mixing) imparted in the various steps, the froth is still very heterogeneous on a microscopic scale. This has already been shown in Fig. 12.18, illustrating fluorescence micrographs of commercial interstage tank froth where the presence of several distinctly different regions of fluorescence indicates poor mixing of the bitumen from several shovel locations. Single ore samples do not exhibit these differences in fluorescence so the conclusion is that bitumen from different shovel locations in the mine were not well mixed even after slurry hydrotransport, flotation, and deaeration. As noted above, the complicated and heterogeneous nature of the bitumen froth makes systematic measurements of froth properties incredibly challenging.

This deaerated froth contains about 65% oil, 25% water, and 10% solids. It also contains emulsions: the microscopic studies of Swanson [56] showed that emulsified water droplets in froth persist through the deaeration process, and were also found in naphtha-diluted deaerated froth. This persistence of small droplets can be attributed to the original connate water as noted in Fig. 12.19. Emulsions of water-in-bitumen and of bitumen-in-water, both thought to be stabilized by asphaltenes and fine bi-wetted solids, have also been found in interface layer emulsions in enhanced gravity separators [74]. Despite the presence of appreciable amounts of water and solids, the deaeration process returns the viscosity of the froths to very nearly that of bitumen itself [63]. It has already been noted that the unique froth structure allows for efficient pipeline transportation in spite of these high viscosities.

Froth treatment processes are used to remove water and fine solids from the froth [5, 6, 34, 36, 39]. There are two kinds of froth treatment processes commercially being used in Canada [59, 75], which we will refer to as the napthenic froth treatment process and the paraffinic froth treatment process. Each of these has some permutations and subsets of operational details; stationary versus centrifuge for the napthenic process and low and high temperature for the paraffinic process.

In the napthenic froth treatment process, the froth is diluted with heated naphtha in about 1:1 volume ratio (this varies from operation to operation) to create a density difference between the bitumen and water and to reduce the viscosity of the bitumen. The diluted froth is then either separated in inclined plate separators, centrifuged (or both). The scroll centrifuges, operating at about 350 G, remove coarse solids (greater than 44 µm). Surfactants are added to promote the flocculation and settling of emulsified water and the froth is next filtered and pumped to high speed disc-stack nozzle centrifuges. Here higher G forces (about 2500 G) are used to remove most of the remaining solids and most of the water. The diluted bitumen product from this froth treatment step can then be sent to the upgrader (the first step of which is a coker) after the solvent is recovered by distillation. Prior to distillation, the diluted bitumen product typically contains approximately 2% water and 0.5% fine solids. The “coker feed” bitumen product obtained after distillation typically contains approximately 1% fine solids. Syncrude, Suncor, and Canadian Natural Resources Ltd (CNRL) all use a modification of this process to create a coker feed.

In the paraffinic froth treatment process, a C5 to C7 solvent blend is added to the froth to reduce the bitumen density, decrease viscosity, and promote flocculation of the emulsified water and suspended solids. Flocculation and removal of the water and solids is achieved as a fraction of the asphaltenes are precipitated to achieve a product that is more suitable to feed some kinds of bitumen upgraders. By controlling the solvent to bitumen ratio, the minimum amount of asphaltenes can be precipitated (lost) with all of the water and solids. The resulting high quality diluted bitumen can be fed directly to a catalyst upgrading

process, negating the need for a coker. The water and solids are separated from the solution in a multistage gravity settling process. A diluted bitumen product is obtained free of water and solids. Some of the solvent is distilled off and a less dilute bitumen is transported to a refinery. Shell Albion uses this process to prepare diluted bitumen for pipeline transport 450 km to their refinery, where cokers are not required.

While centrifugation is quite efficient in separating hydrocarbon from water and solids, it is an energy and maintenance intensive process. The application of lamella settlers has been advocated as a means of improving process performance [76]. A lamella settler comprises a stack of parallel plates, spaced apart from each other, and inclined from the horizontal. The space between each set of plates forms a separate settling zone. The deaerated and diluted froth is pumped into these spaces, at a point near the longitudinal middle of the plates. The relatively less dense diluted bitumen phase rises to the underside of the upper plates and flows to the tops of those plates. Meanwhile, the relatively more dense water and solid phases settle down to the upperside of the lower plates and flow to the bottoms of those plates. Thus, the diluted bitumen is collected at the tops of the plate stack while the water and solids are collected at the bottom of the plate stack. Such an inclined lamella settling process is much more efficient than vertical gravity separation. Suncor uses inclined plate settlers for the bulk of its froth treatment process, with scroll and disk-stacks for the remainder.

The froth model described above, and shown in Figs 15–17, produces collapsed globules comprising a water (and solids) droplet surrounded by a membranous layer (thought to be) made up of asphaltenes and bi-wetted solids. When such froth is contacted with naphtha the time required to penetrate the bitumen-membrane coating is on the order of 30 min, whereas in a commercial process the elapsed time between naphtha addition and introduction into a settling vessel is less than 1 min. Thus, the diluted froth process stream can contain these globules, probably in flocs, which would have a bulk density intermediate between diluted bitumen and water. Such flocs would then tend to accumulate in the separation vessel and form an interface layer (sometimes called rag layer) emulsion, and could potentially form an effective barrier to gravity separation [74].

In commercial practice, a staged series of lamella settlers is used in which the tailings stream from one vessel is treated and used to form the feed to the next vessel and so on [76]. Without proper management and in the absence of process aid chemicals, highly emulsified samples can be observed. Such emulsions are apparently composed of the water-in-oil globules, dispersed in water; that is, an emulsion of water-in-oil-in-water (W/O/W) [41, 74]. These emulsions appear gel-like and exhibit extremely high viscosities at very low shear rates (as high as 200,000 mPa.s at 80°C). Under moderate shear, however, the emulsions apparently invert so that their viscosities are dramatically reduced (to about 10–20 mPa.s at 80°C). Figure 12.21 illustrates the effects of shear, including the shear-induced inversion from water-continuous (W/O/W) to oil-continuous (W/O). Depending upon how a separation vessel is operated, such emulsions could accumulate into an emulsified layer in the vessel, forming an effective barrier to gravity separation. Shaw *et al.* [41] concluded that the emulsion structure-related problems encountered in the treatment of diluted froths have their origin in elements of the original froth structure.

Figure 12.22 shows on a small scale how these rag layers can form and in this case the rag layer is due to the presence of oxidized bitumen in the laboratory-simulated diluted bitumen. In the case with little or no observable rag layer, sodium hydroxide (NaOH) was

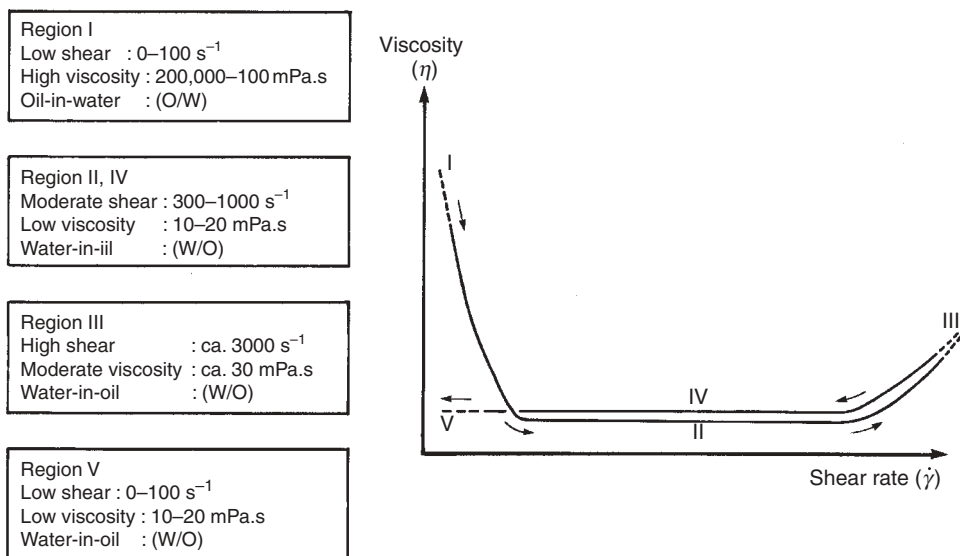


**Fig. 12.21** Illustration of changes taking place upon subjecting a diluted froth sample to progressively higher and then lower shear rates. The initial emulsion (Region I) is actually a water-in-oil-in-water (W/O/W) multiple emulsion. From Schramm and Hackman [74]. Copyright 1994 American Chemical Society.

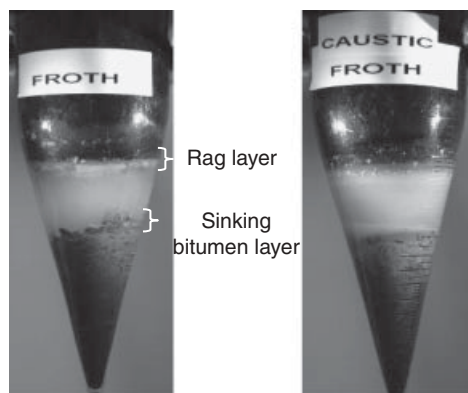


**Fig. 12.22** Rag layer emulsions at the oil–water interface and at the solids–water interface in a laboratory simulation of the naphtha-based froth treatment process. The surfactant loading in the bitumen that is responsible for this incomplete separation of the phases in bitumen processing is responsible for a variety of difficulties in commercial operations. Photographs by V. Muñoz.

used to control the bitumen chemistry, change the surfactants associated with the oxidized ore and almost completely eliminate the rag layer. Clearly both physical and chemical properties of the original froth structure determine the optimum performance of many downstream bitumen recovery and processing steps, and in the case of bitumen froths and foams, significantly different properties can be developed depending upon water chemistry and process temperature. Since bitumen is a complex mixture of a variety of hydrocarbon compounds, the froth structure can change significantly as other factors are varied.

## 12.7 Conclusion

Bituminous froths from the surface processing of mined oil sands or tar sands provide an example of extremely complex and dynamic non-aqueous foams. Such froths are multiphase (containing oil, water, gas, and solids) and contain multiple substructures. The properties of the froths are influenced by both the nature of the original oil or tar sands and the manner in which the oil sand conditioning and separation processes are conducted. The properties of these froths also influence the subsequent downstream processing steps as the bitumen from the froths is ultimately converted into fuels or other products.

## Acknowledgements

The authors thank Vicente Muñoz of Natural Resources Canada for providing most of the photomicrographs presented in this work.

## References

- [1] E.J. Walters. Review of the world's major oil sands deposits. In *Oil Sands: Fuel of the Future*, L.V. Hills (ed.). Memoir 3, Can. Soc. Petrol. Geologists, Calgary, 1974.
- [2] G.J. Demaison. Tar sand and supergiant oil fields. In *The Oil Sands of Canada-Venezuela 1977*, D.A. Redford and A.G. Winestock (eds). CIM Special Volume 17, Canadian Inst. Mining and Metallurgy, Calgary, 1977.
- [3] IOCC. *Major Tar Sand and Heavy Oil Deposits of the United States*. Interstate Oil Compact Commission, Oklahoma City, OK, 1984.
- [4] B.F. Meyer and C.T. Steele (eds). *The Future of Heavy Crude Oils and Tar Sands*. McGraw-Hill, New York, 1981.
- [5] D. Towson. Tar sands. In *Kirk-Othmer Encyclopedia of Chemical Technology*, 3rd edn. Wiley, New York, 1983.
- [6] W. Ruhl. *Tar (Extra Heavy) Sands and Oil Shales*. Ferdinand Enke, Stuttgart, 1982.
- [7] G.V. Chilingarian and T.F. Yen (eds). *Bitumens, Asphalts and Tar Sands*. Elsevier, Amsterdam, 1978.
- [8] AEUB. *Alberta's Energy Reserves 2006 and Supply/Demand Outlook 2007–2016*. Report ST98–2007, Alberta Energy and Utilities Board, Calgary, 2007.
- [9] P.W. Coleman and R.B. Adams. Study and demonstration of a process to extract bitumen from a Utah tar sand. In *Proc. SPE International Thermal Operations and Heavy Oil Symposium*. SPE paper 86945, Society of Petroleum Engineers, Richardson, TX, 2004.

- [10] R.J. Mikula, V.A. Munoz and O. Omotoso. Laboratory and pilot experience in the development of a conventional water based extraction process for the Utah Asphalt Ridge tar sands. In *Proc. Cdn. Int. Petrol. Conf.*, paper 06-131. Petroleum Society of CIM, Calgary, 2006.
- [11] A.R. Martinez. Report of working group on definitions. In *The Future of Heavy Crude and Tar Sands*, R.F. Meyer, J.C. Wynn and J.C. Olson (eds). UNITAR, New York, 1982.
- [12] M. Danyluk, B. Galbraith, and R. Omana. Toward definitions for heavy crude oil and tar sands. In *The Future of Heavy Crude and Tar Sands*, R.F. Meyer, J.C. Wynn and J.C. Olson (eds). UNITAR, New York, 1982.
- [13] M. Khayan. Proposed classification and definitions of heavy crude oils and tar sands. In *The Future of Heavy Crude and Tar Sands*, R.F. Meyer, J.C. Wynn, and J.C. Olson (eds). UNITAR, New York, 1982.
- [14] J. Hupka, J.D. Miller and A. Cortez. Importance of bitumen viscosity in the hot water processing of domestic tar sands. *Mining Eng.*, **35**(12): 1635–41, 1983.
- [15] G.A. Stewart and G.T. MacCallum. *Athabasca Oil Sands Guide Book*. Can. Soc. Petrol. Geol., Calgary, 1978.
- [16] G.H. Kendall. *Geology of the Heavy Oil Sands – Alberta*. GAC/MAC Symposium, 1976.
- [17] N.D. O'Donnell and J.M. Jodrey. Geology of the Syncrude mine site and its application to sampling and grade control. In *Proc. SME-AIME Meeting*, preprint 84-421. SME-AIME, Denver, 1984.
- [18] G.D. Mossop. Geology of the Athabasca oil sands. *Science*, **207**: 145–52, 1980.
- [19] L.W. Vigrass. Geology of Canadian heavy oil sands. *Am. Assoc. Petrol. Geol. Bull.*, **52**: 1984, 1968.
- [20] M.A. Carrigy. The physical and chemical nature of a typical tar sand: bulk properties and behaviour. *Proc. 7th. World Petrol. Congr.*, **3**: 573–81, 1967.
- [21] M.A. Carrigy. The significance of a grain size classification of the sands of the McMurray formation, Alberta. *Proc. 5th. World Petrol. Congr.*, **1**: 575, 1959.
- [22] F.W. Camp. *Tar Sands of Alberta, Canada*, 3rd edn. Cameron Engineers Inc., Denver, 1976.
- [23] M.A. Carrigy. Effect of texture on the distribution of oil in the Athabasca oil sands. *J. Sedimentary Petrol.*, **32**: 312, 1962.
- [24] K.A. Clark. Hot-water separation of Alberta bituminous sand. *Trans. Can. Inst. Mining Metall.*, **47**: 257, 1944.
- [25] M.W. Ball. Development of the Athabasca oil sands. *Trans. Can. Inst. Mining Metall.*, **44**: 58–91, 1941.
- [26] M.W. Ball. Athabasca oil sands: apparent example of local origin of oil. *Bull. Am. Assoc. Petrol. Geol.*, **19**: 153, 1935.
- [27] W.T. Sobol, L.J. Schreiner, L. Miljkovic, M.E. Marcondes- Helene, L.W. Reeves and M.M. Pintar. NMR line shape-relaxation correlation analysis of bitumen and oil sands. *Fuel*, **64**(5): 583–90, 1985.
- [28] K. Takamura. Microscopic structure of Athabasca oil sand. *Can. J. Chem. Eng.*, **60**: 538–45, 1982.
- [29] J. Czarnecki, B. Radoev, L.L. Schramm and R. Slavchev. On the nature of Athabasca oil sands. *Adv. Colloid Interface Sci.*, **114/115**: 53–60, 2005.
- [30] A.G. Oblad, J.W. Bunger, F.V. Hanson, J.D. Miller, H.R. Ritzma and J.D. Seader. Tar sand research and development at the University of Utah. *Ann. Rev. Energy*, **12**: 283–356, 1987.
- [31] L.L. Schramm and E.E. Isaacs. Development of “Technology Oil”: *in situ* oil sands and heavy oil reservoirs in Canada. In *Handbook on Bitumen Recovery from Oil Sands: Theory and Practice*, forthcoming.
- [32] L.L. Schramm, J.W. Kramers and E.E. Isaacs. Saskatchewan's place in the Canadian oil sands. In *Proc. Cdn. International Petrol. Conf.*, paper 2009-116. Petroleum Society of CIM, Calgary, 2009.
- [33] R.G. Smith and L.L. Schramm. Blending tar sands to provide feedstocks for hot water process. United States patent 4,474,616, October 2, 1984; Canadian patent 1,214,421, November 25, 1986.
- [34] R. Schutte and R.W. Ashworth. Oil sands. In *Ullmanns Encyklopädie der technischen Chemie*, vol. **17**, 423–36, 1979.

- [35] E.D. Innes and J.V.D. Fear. Canada's first commercial tar sand development. *Proc. 7th World Petrol. Congr.*, **3**: 633–50, 1967.
- [36] L.L. Schramm and R.G. Smith. Control of process aid used in hot water process for extraction of bitumen from tar sand. Canadian patent 1,188,644, June 11, 1985; United States patent 4,462,892, July 31, 1984.
- [37] E.M. Perrini. *Oil from Shale and Tar Sands*. Noyes Data Corp., Park Ridge, 1975.
- [38] M.W. Ranney. *Oil Shale and Tar Sands Technology*. Noyes Data Corp., Park Ridge, 1979.
- [39] H.L. Erskine. Suncor hot water process. In *Handbook of Synfuels Technology*, R.A. Meyers (ed.), McGraw-Hill: New York, 1984.
- [40] D.G. Adam. Syncrude's technology evolution since start-up. In *Proc. Advances in Petroleum Recovery and Upgrading Technology*, paper 1. AOSTRA, Edmonton, 1985.
- [41] R.C. Shaw, J. Czarnecki, L.L. Schramm and D. Axelson. Bituminous froths in the hot water flotation process. In *Foams: Fundamentals and Applications in the Petroleum Industry*, L.L. Schramm (ed.). American Chemical Society, Washington, DC, 1994.
- [42] R. Shaw, L.L. Schramm and J. Czarnecki. Suspensions in the hot water flotation process. In *Suspensions: Fundamentals and Applications in the Petroleum Industry*, L.L. Schramm (ed.), American Chemical Society, Washington, DC, 1996.
- [43] L.L. Schramm, E.N. Stasiuk and M. MacKinnon. Surfactants in Athabasca oil sands extraction and tailings processes. In *Surfactants: Fundamentals and Applications in the Petroleum Industry*, L.L. Schramm (ed.). Cambridge University Press, Cambridge, 2000.
- [44] V.A. Munoz, K.L. Kasperski, O. Omotoso and R.J. Mikula. The use of microscopic bitumen froth morphology for the identification of problem oil sand ores. *Petrol. Sci. Technol.*, **21**(9/10): 1509–29, 2003.
- [45] R.J. Mikula, V.A. Munoz, N. Wang, B. Bjornson, D. Cox, B. Moisan and K. Wiwchar. Characterization of bitumen properties using microscopy and near infrared spectroscopy: the processability of oxidized or degraded ores. *J. Can. Petrol. Technol.*, **42**(8): 50–4, 2002.
- [46] N. Wang and R.J. Mikula. Small scale simulation of pipeline or stirred tank conditioning of oil sands: Temperature and mechanical energy. *J. Can. Petrol. Technol.*, **41**(1): 8–11, 2002.
- [47] L.L. Schramm and R.G. Smith. The influence of natural surfactants on interfacial charges in the hot water process for recovering bitumen from the Athabasca oil sands. *Coll. Surf.*, **14**: 67–85, 1985.
- [48] L.L. Schramm and R.G. Smith. Unpublished results. Syncrude Canada Ltd, Edmonton, 1985.
- [49] L.L. Schramm. The influence of suspension viscosity on bitumen rise velocity and potential recovery in the hot water flotation process for oil sands. *J. Can. Petrol. Technol.*, **28**: 73–80, 1989.
- [50] L.L. Schramm. Use of a submersible viscometer in the primary separation step of the hot water process for recovery of bitumen from tar sand. Canadian patent 1,232,854, February 16, 1988; United States patent 4,637,417, January 20, 1987.
- [51] J.D. Scott and M.B. Dusseault. Behavior of oil sand tailings sludge. In *Proc. 33rd Ann Tech. Meeting*. Petrol. Soc. CIM, Calgary, June 6–9, 1982.
- [52] M.D. MacKinnon. Development of the tailings pond at Syncrude's oil sands plant: 1978–1987, *AOSTRA J. Res.*, **5**: 109–33, 1989.
- [53] Fine Tailings Fundamentals Consortium. *Advances in Oil Sands Tailings Research*. Alberta Dept of Energy, Edmonton, 1995.
- [54] R.N. Houlihan. Unpublished results. Syncrude Canada Ltd, Edmonton, 1976.
- [55] K.H. Chung, S. Ng and E.C. Sanford. Formation of W/O emulsions in the hot water extraction process. *AOSTRA J. Res.*, **7**: 183–93, 1991.
- [56] W.D. Swanson. Unpublished results. Syncrude Canada Ltd, Edmonton, 1965–6.
- [57] L. Danielson. Unpublished results. Syncrude Canada Ltd, Edmonton, 1989.
- [58] A. Corti and F. Roett. Hot water extraction processes: two different philosophies. In *Proc. 3rd District Meeting*, Can. Inst. Mining, Fort McMurray, 1987.
- [59] U.G. Romanova, M. Valinasab, E.N. Stasiuk, H.W. Yarranton, L.L. Schramm and W.E. Shelfantook. The effect of oil sands bitumen extraction conditions on froth treatment performance. *J. Can. Petrol. Technol.*, **45**(9): 36–45, 2006.
- [60] R. Schutte. Unpublished results. Syncrude Canada Ltd, Edmonton, 1974.

- [61] S.H. Ward and K.A. Clark. Determination of the viscosities and specific gravities of the oils in samples of Athabasca bituminous sand. Report No. 57, Research Council of Alberta, Edmonton, 1950.
- [62] S.M. Farouq Ali. Application of *in situ* methods of oil recovery to tar sands. In *Oil Sands Fuel of the Future*, L.V. Hills (ed.). Can. Soc. Petrol Geologists, Calgary, 1974.
- [63] L.L. Schramm and J.C.T. Kwak. The rheological properties of an Athabasca bitumen and some bituminous mixtures and dispersions. *J. Can. Petrol. Technol.*, **27**: 26–35, 1988.
- [64] J.M. Dealy. Rheological properties of oil sand bitumens. *Can. J. Chem. Eng.*, **57**: 677–83, 1979.
- [65] F.A. Jacobs, J.K. Donnelly, J. Stanislav and W.Y. Svrcik. Viscosity of gas-saturated bitumen. *J. Can. Petrol. Technol.*, **19**: 46–50, 1980.
- [66] W.Y. Svrcik and A.K. Mehrotra. Gas solubility, viscosity and density measurements for Athabasca bitumen. *J. Can. Petrol. Technol.*, **21**: 31–8, 1982.
- [67] F.A. Jacobs. Viscosity of carbon dioxide saturated Athabasca bitumen. MSc thesis, University of Calgary, Calgary, 1978.
- [68] R.J. Christensen, W.R. Lindberg and S.M. Dorrence. Viscous characteristics of a Utah tar sand bitumen. *Fuel*, **63**: 1312–17, 1984.
- [69] M. Misra and J.D. Miller. The effect of feed source in the hot water processing of Utah tar sand. *Mining Engineering*, **32**: 302–11, 1980.
- [70] J. Hupka, J.D. Miller and A. Cortez. Importance of bitumen viscosity in the hot water processing of domestic tar sands. *Mining Engineering*, **35**: 1635–41, 1983.
- [71] J.W. Gwynn and F.W. Hanson. *Annotated Bibliography of Utah Tar Sands Deposits*, Utah Geological Survey Open File Report 503. Utah Dept Natural Resources, Salt Lake City, 2007.
- [72] R. Wood. Bitumen-deaeration process carried out in the separation cell. Canadian patent 1,137,906, December 21, 1982.
- [73] T.E. Kizior. Deraerator circuit for bitumen froth. Canadian patent 1,072,474, February 26, 1980.
- [74] L.L. Schramm and L.P. Hackman Unpublished results. Syncrude Canada Ltd, Edmonton, 1986.
- [75] U.G. Romanova, M. Valinasab, E.N. Stasiuk, H.W. Yarranton, L.L. Schramm and W.E. Shelfantook. The effect of oil sands bitumen extraction conditions on froth treatment performance. In *Proc. 6th Cdn. Int. Petrol. Conf.*, paper 2005-037. Petroleum Society of CIM, Calgary, 2005.
- [76] W.E. Shelfantook, A.W. Hyndman and L.P. Hackman. Purification process for bitumen froth. United States patent 4,859,317, August 22, 1989.

# 13

## Foams in Enhancing Petroleum Recovery

*Laurier L. Schramm and E. Eddy Isaacs*

### 13.1 Introduction

There exists a huge body of research and knowledge of the basic principles of foam formation, stabilization, destabilization, and break-down, much of which is summarized in the many books on foams (e.g., [1–5]). Given the extremely small sizes of the foam lamellae, this is the realm of nanotechnology, colloid, and interface science [6].

The fundamentals provide an important base for developing foam applications in industrial processes, but such a base is just a starting point since every industrial application area has its own unique circumstances, not the least of which being that industrial processes inevitably involve complex multiphase systems that are seldom at equilibrium and frequently not even in steady state. Applications of foams in enhancing petroleum (oil and gas) production require an understanding of the basic principles involved in foam generation, stability, and propagation, but also involve many aspects that go beyond these. Several books provide useful introductions to the properties, importance, and treatment of petroleum industry foams [1, 2, 4, 7, 8], while others provide introductions to the applications of other aspects of colloid and interface science and nanotechnology in the petroleum industry [9–24].

We survey the most important applications of foams in enhancing petroleum production, illustrate some of the practical considerations involved, and discuss some of the areas in which the basic principles connect well into practice, and others that do not. It is these latter

areas of empirical practice that remain something of an “art” and for which there remains a need for research at the interface between principles and applications.

Foams occur or are created throughout the full range of processes in the petroleum-producing industry (see [1, 7, 8, 16]), including:

- foams in well applications such as drilling and completion,
- foams in near-well applications such as fracturing and stimulation (acidizing),
- reservoir applications such as blocking and diverting, and gas-mobility control foams
- producing well applications such as foamy heavy oil production, and
- “surface” foams such as in refining (distillation and fractionation towers) and/or upgrading, tank (truck) foams, and fire fighting foams.

In this chapter we discuss the application of foams to enhancing petroleum production from underground reservoirs. Discussions of the applications of foams to surface and downstream operations can be found in references [7, 8, 25].

## 13.2 Foam Applications for the Upstream Petroleum Industry

Foams applied in wells and to the near-wellbore regions around wells are usually intended to ensure that injection and production wells are able to operate effectively to enable good penetration of fluids into a reservoir, and/or good production of fluids out of a reservoir. Foams intended for deep reservoir penetration are usually intended to accomplish one or more of the following:

- ensure that a gas or liquid phase is placed in a geographically specific region (zone) of a reservoir, such as at the top of (overlying) a reservoir,
- ensure that a gas or liquid phase is placed in a zone of a reservoir that has a specific range of (usually relatively large) permeabilities, and/or
- ensure that injected fluids move through a reservoir with a fairly uniform flow pattern (this is explained more fully below).

### 13.2.1 Selection of Foam-Forming Surfactants

A major challenge in any potential foam application, whether for bulk foams (such as in wells) or for foams in porous media (such as in reservoir applications), is the proper selection of foam-forming surfactants. Some of the characteristics that are needed for a foam-forming surfactant to be effective in stabilizing bulk foams that may be used at the surface, in a drilling fluid, in a near-wellbore treatment are:

- **Stable lamellae.** A strong ability to promote and stabilize foam lamellae. This is the bulk foam criterion that most people immediately think of, and is usually determined using a bulk foam stability test.
- **Thermal stability.** Thermal stability of the foaming surfactants at surface and/or reservoir conditions is critical; otherwise the surfactant may decompose and not be able to stabilize foam. Some reservoirs have initial temperatures levels that exceed 127 °C [26]. More

stringent are the requirements of steam flooding conditions, for which the steam temperatures are in the range of 200–300 °C.

- **Good solubility.** Precipitation can occur when the surfactant is incompatible with the brine at surface and/or reservoir conditions. Some reservoirs can have salinity levels that approach the saturation limits. For example, Canada's Beaverhill Lake carbonate and Gilwood sandstone reservoir pools have salinities that range as high as 24.5–29.6% (245,000–296,000 µg/g) and hardness levels as high as 2.5% (25,000 µg/g) [26]. Under these conditions many surfactants precipitate out and will not stabilize the foam, and may actually act as a defoamer.
- **Low partitioning.** Surfactants can be lost by partitioning or migrating into the crude oil phase. This is called phase-trapping, and causes the amount of surfactant available to promote foaming to be significantly reduced such that no foaming occurs. For the very hydrophilic surfactants selected for many foam flooding applications, the partitioning into crude oil can be low [27], but this still needs to be evaluated in advance. Precipitation and partitioning of anionic surfactants have a tendency to increase with increasing temperatures.

The characteristics that are needed for a foaming agent to be effective in porous media under petroleum reservoir conditions include all of the above plus the following [25, 26, 28, 29]:

- **Flow behavior.** Foams are significantly more stable in porous media than in the bulk. Coalescence occurs as the films between bubbles drain and rupture. The reservoir is an excellent medium for re-forming the foam by the mechanics of bubble break-up as the foam flows through the pore constrictions. In addition, there are a number of additives that can be used to stabilize the foam, including non-condensable gas [30–32].
- **Mobility reduction.** There should be a strong ability of the foam to reduce gas mobility in porous media. This is the reservoir foam criterion most people think of and is usually measured by causing foam to flow through samples of porous rock, using either model rock or actual reservoir core samples. The mobility reduction factor (MRF) is the ratio of pressure drops caused by the simultaneous flow of gas and liquid through the rock in the presence and absence of surfactant in the aqueous phase (see, for example, reference [26]).

$$\text{MRF} = \frac{\Delta P_{G/L(\text{surfactant})}}{\Delta P_{G/L(\text{nosurfactant})}}$$

The fluid saturations are not generally the same when these two different pressure gradients are measured so, strictly speaking, the MRF is due not only to the rheological properties of the foam but also to three-phase relative permeability effects. The latter are usually ignored, enabling MRF to be used as a dimensionless indication of *in situ* foam rheology, as shown by the foam viscosity ratio below (where  $\eta_{\text{app G/L (surfactant)}}$  is the apparent viscosity of the foam). Another parameter, the foam flow resistance (FFR) factor, which is a non-dimensional pressure gradient normalized to permeability, gas viscosity, and gas (Darcy) velocity, is quite similar to the MRF and the foam viscosity ratio except for the additional influence of the gas velocity term.

$$\text{MRF} = \frac{\Delta P_{G/L(\text{surfactant})}}{\Delta P_{G/L(\text{nosurfactant})}} \approx \frac{\eta_{\text{app G/L (surfactant)}}}{\eta_{\text{app G/L (nosurfactant)}}} \propto \text{FFR}$$

- **Low adsorption.** Surfactants can be lost in porous media due to adsorption on the reservoir rock. The economics of foam flooding are determined to a large degree by the amount of surfactant required to generate and propagate the foam. Surfactant loss through partitioning into the crude oil phase and through adsorption on the rock surfaces cannot be completely eliminated, and these are therefore important (but undesirable) mechanisms of surfactant loss. Usually the most serious are the adsorption losses for foam flooding surfactants. Even a nominal adsorption level of 1 mg/g can cause adsorption losses of more than 1000 tonnes in a typical mature, waterflooded reservoir, and can lead to increased costs of as much as \$100 per m<sup>3</sup> of potentially recoverable oil [33]. The actual adsorption levels can be as high as 2.5 mg/g [28, 33–35]. This can lead to vastly reduced distances of foam propagation in a reservoir, so the selection of a surfactant formulation with acceptable adsorption levels under the reservoir conditions specific to a particular application is crucial. The adsorption of surfactant tends to be less important at elevated temperatures, including steam flooding conditions. Surfactant adsorption in reservoirs is reviewed in more detail elsewhere [35–37].
- **Rock wettability.** The generation of aqueous foams *in situ* depends in part on having a water-wet porous medium acting as the foam generator. Also aqueous lamellae can usually only span the pore walls in the rock if they can be supported by Plateau borders at the solid surfaces [38]. The injected surfactant can also alter the native wettability of reservoir rock, which can be beneficial for foam generation and propagation. Some foam-forming surfactants have been found to alter wettability from intermediate-wet to water-wet, improving foam performance [27, 38, 39].
- **Oil tolerance.** Foaming surfactants are sensitive to oil and the tendency of the foam is usually to break down almost instantaneously when it comes into contact with the oil. This, in fact, is a desirable feature when oil is flowing into the producing well. However, during the foam formation stage, the presence of residual oil in the porous medium delays foam formation. This is consistent with results from field testing that suggest that foams achieve lower gas mobility reductions than would otherwise be anticipated due to the defoaming action of residual crude oil [40]. This in turn has led to an interest in the formulation of oil-tolerant foams. Although crude oils tend to act as defoamers, it turns out that foams actually exhibit a wide range of sensitivities to the presence of crude oils, as discussed below.

A range of tools has been developed for the evaluation and selection of foam-forming surfactants for reservoir applications. These tools range from assessing physical properties of the solution (such as solubilities, surface tensions, and critical micelle concentrations), to assessing bulk foam properties (such as static and dynamic foam stability tests), to assessing porous media foam properties (such as coreflood pressure drop tests). Some of these are described in references [7, 26, 28, 33, 41].

Polymer-enhanced (thickened) and gelling foams are also increasingly being used in the petroleum industry. Incorporating polymers into foaming solutions increases foam viscosity and also stability [42–51]. This suggests that polymer-thickened foams, with their enhanced viscosities and increased stability, could be effective mobility control agents [43, 52, 53]. A range of polymer additives has been tested, including polyacrylamide, polyvinyl alcohol, polyvinylpyrrolidone, and xanthan biopolymers. In addition to changing foam quality and texture, the effective viscosities of polymer-thickened foams

can also be adjusted by varying the polymer concentration and molar mass. In general, polymer-thickened foams are shear thinning. Gelling foams, i.e. polymer-thickened foams to which time-delayed cross-linking agents have been added, can be used to block swept zones and to divert fluids into underswept zones in reservoirs containing large permeability variations and/or fractures [54–57]. Once gelled, these foams can function in a similar fashion to conventional gels, but with only a small fraction of the pore space being occupied by gelled liquid (see references [58, 59] for photomicrographs of gelled-foam lamellae spanning pores in sandstone rock). As is the case for *in situ* processes involving surfactants, those involving polymers are adversely affected by the adsorption of polymer onto rock and mineral surfaces, which can lead to vastly reduced distances of polymer propagation in a reservoir. Polymer adsorption in reservoirs is reviewed in more detail elsewhere [60].

Finally, there is another class of foams, namely micro-foam, or colloidal gas aaphrons. These terms refer to a dispersion of aggregates of very small foam bubbles in aqueous solution. They can be formed by dispersing gas into surfactant solution under conditions of very high shear [61–63], creating very small gas bubbles (of the order of 50 µm), each surrounded by a bimolecular film of stabilizing surfactant molecules. There is some evidence that such micro-foams tend to be more stable than comparable foams that do not contain the bimolecular film structure [61–63]. Micro-foam injection for reservoir oil recovery has been reported in the literature [64, 65], as has micro-foam flushing for soil remediation [66–68]. The literature to date is somewhat conflicting regarding the physical properties of these foams, but micro-foams may find useful application in reservoir oil recovery processes.

### 13.3 Foam Applications in Wells and Near Wells

#### 13.3.1 Drilling and Completion Foams

New high-performance drilling fluids are constantly being developed and improved in order to assist safe and efficient drilling of oil and gas wells. Drilling fluids are used to achieve several goals [24, 25]:

- maintain hydrostatic pressure in the borehole;
- avoid reducing reservoir permeability in the near-wellbore region;
- minimize fluid losses into the reservoir;
- clean the wellbore by carrying drilled rock cuttings to the surface;
- cool and lubricate the drill bit, maintain wellbore stability; and
- be amenable to disposal with minimal environmental impact.

The classical drilling fluids are suspensions (i.e., drilling muds) of clays in aqueous solutions for which the DLVO theory of colloid stability and various rheological models (see reference [8]) have been successfully applied [69]. Modern drilling fluids, however, can be much more complex multiphase dispersions, of which there are two broad classes: water-based (water-continuous) and oil-based (oil-continuous). Some of the water-based drilling fluids are now in the form of foams.

The reason for developing foam drilling fluids (variously termed air, mist, or foam drilling fluids) is that they can yield superior drilling penetration rates compared with conventional mud systems [70–76]. There are several possible flow regimes [70, 77]. In mist drilling the fluids are injected as a mist, which changes to foam before returning up the annulus of the well, removing with it formation brine that has entered the well. Since foams can exhibit a high carrying capacity (viscosity), they can also be used for sand or scale clean-outs. Foam drilling fluids are used for underbalanced drilling of horizontal wells [70, 78–80], a method in which the drilling fluid is kept at lower pressure than the reservoir so that the drilling fluid and cuttings will neither erode nor penetrate and potentially damage the reservoir. Polymer-thickened foams have also been used for enhanced cuttings carrying capacity [25, 81]. Foam qualities in the range 95–98% (v/v) tend to provide the best carrying capacities. By carefully selecting the type of surfactant one can adjust the brine salinity and oil tolerances of the foam.

Foams intended for use in wells and in most near-well reservoir processes are pre-formed at the surface before injection. The foam generators used can be quite simple, involving mixing surfactant-containing and gas streams at a high flow velocity and then causing them to experience a sudden pressure drop across a choke, a valve, or a canister containing packed, porous media. Such methods produce very high shear rates, which can cause a problem if high molar mass, long-chain molecules such as polymers are incorporated into the foam. More sophisticated foam generators, which permit some control over the shear forces imparted, are also available [82]. In some cases the foam is continuously reconditioned and recirculated [70].

### 13.3.2 Well Stimulation Foams: Fracturing, Acidizing, and Unloading

Although suspensions have traditionally been used in hydraulic fracturing, foam fracturing fluids can also be used to increase the injectivity or productivity of oil and gas wells. There are three basic types of fracturing fluid foams: water-, oil-, and alcohol-based [72, 73, 83–86]. These are designed to:

- increase flow capacity in the near-well region of a reservoir by injecting fluid at higher than the parting pressure of the formation in order to create and extend fractures;
- provide good fluid loss control and good transport properties; and
- cause less damage to the reservoir than water-based suspension or emulsion fluids.

A related application is the use of foams to carry acid into a reservoir in order to improve reservoir injectivity or productivity by dissolving fine particles from within flow channels, particularly in the near-well region. Foaming an acidizing fluid increases its effective viscosity, providing mobility control when it is injected [87]. Acidizing foams are aqueous, and the acids themselves are usually hydrochloric, formic, or acetic acid (carbonate reservoirs) or hydrochloric or hydrofluoric acid (sandstone reservoirs), or a blend, together with suitable surfactants and other stabilizers [25, 29, 87, 88]. As with almost any other desirable petroleum industry foam, careful formulation is needed. The foam-stabilizing surfactants may also be needed to reduce the capillary forces that would otherwise trap spent acid in pores of the rock, to cause wettability alteration towards water-wet conditions, to break *in situ* emulsions, or to help displace fine particles [8, 23, 87]. Sometimes a separate

foam, distinct from the stimulation fluid, is first injected into a reservoir, in order to have the foam fill high permeability zones or channels and therefore prevent the entry into these areas of subsequently injected stimulation fluid [87]. This can help to ensure that the stimulation fluid is directed only to the lower permeability regions for which its action is desired.

Another well-bore foam application is in gas wells. Gas well production is impaired when water builds up into a column at the bottom of the well, which increases hydrostatic back-pressure on the formation. Eventually this can lead to a reduction, or even a halting, of gas production from the well. This effect can be alleviated by adding a suitable surfactant down-hole and using the gas flowing from the reservoir to create foam at the bottom of the well [89, 90]. The foam's much lower density compared with that of water causes less hydrostatic back-pressure on the formation, making it easier to produce water from the well. Meanwhile, having bottom-hole foam present can also act to reduce pressure fluctuations and stabilize gas flow from the well. Some of the kinds of surfactants that have been used for this purpose (mostly anionic or anionic/non-ionic blends) are described in references [91, 92].

## 13.4 Foam Applications in Reservoir Processes

### 13.4.1 Reservoir Recovery Background

Oil is first produced from an underground reservoir (primary production) when naturally available pressure, caused by dissolved gas in the oil and/or from an adjacent pressurized fluid layer such as overlying gas or underlying water, makes it flow through permeable porous rock formations and into production wells from which it is pumped to the surface. Not all, or even most, of the oil flows to the production wells, however, because either the natural pressure in the reservoir becomes consumed or capillary forces have essentially trapped most of the oil in pores of the rock. By the culmination of primary production, virtually anywhere in the world, only about 15% of the oil from the reservoir (less if it is a heavy oil reservoir) will have been recovered.

Most often, the next stage of oil production (secondary production) involves drilling additional wells and using them to pump water underground and into the oil-bearing formation. Pumping the water acts to build up pressure again and the water, as it flows, pushes (drives) more oil to the producing wells. This works for quite a while (perhaps 15 years) but ultimately it only produces another 15% or so of the oil from the reservoir. Eventually the production wells start producing mostly water rather than oil, causing revenues to drop (less oil) and costs to rise (water treating, handling and disposal is expensive). By the time these wells have to be shut in about 65% (world average) of the original oil-in-place remains left behind in a typical reservoir. There are two principal reasons for this: (i) capillary trapping, and (ii) sweep efficiency. It is these two phenomena that enhanced (tertiary) oil recovery processes are intended to address [93, 94]. In attempting to deal with these issues, by injecting various fluids deep into a reservoir, there are four key practical issues with which to contend:

1. Fluid placement: ensuring that injected EOR fluids get into the desired zones in a reservoir.
2. Sweep efficiency: ensuring that the injected fluids, once in the desired zones, are effective in contacting as much as possible of the desired flow pathways.

3. Displacement: displacing oil from pores in the rock in which it is trapped, and causing that oil to flow.
4. Flow rate: ensuring that the displaced oil, which may be emulsified, flows towards a production well at an acceptable rate.

These features manifest themselves differently in different reservoir situations and for different processes, and are discussed further in the section on primary and secondary recovery applications below, in terms of specific foam applications. Before discussing these specific applications, however, we provide a simplified introduction to the concepts of sweep efficiency and capillary trapping.

#### *13.4.1.1 Sweep Efficiency*

When one fluid is being used to push (drive) another fluid through a porous medium, an important consideration is the degree to which the fluid displacement is uniform. In a reservoir, a drive fluid is commonly injected through a vertical well that is perforated at a depth corresponding to the oil-containing zone (layer) of interest in the reservoir. Flow outwards from such a well will be radial flow. Uniform flow in this case will be the radial equivalent of plug-flow, and would ensure that the entire desired reservoir zone is contacted by the drive fluid.

However, non-uniform flow occurs when a drive fluid of low viscosity is used to push a target fluid that has a significantly higher viscosity. Examples of this occur when water is used to drive a heavy crude oil, or when a gas is used to drive an oil. The mobility of fluid  $i$  in a porous medium is given by  $M_i$ :

$$M_i = k/\eta_i \quad (13.1)$$

where  $k$  is the permeability of the porous medium and  $\eta_i$  is the viscosity of the fluid. The mobility ratio,  $M$ , between water ( $w$ ) and oil ( $o$ ) is given by:

$$M = M_w/M_o \quad (13.2)$$

The mobility ratio is unfavorable when  $M > 1$ , and the result is a very non-uniform fluid displacement pattern referred to as “fingering.” The “fingers” will reach producing wells first (breakthrough), leaving swept pathways of low resistance, through which almost all subsequently injected fluids will follow, leaving substantial portions of the reservoir uncontacted (unswept) and still retaining residual oil (see Fig. 13.1). The mobility ratio is favourable when  $M < 1$ , in which case a much more uniform and effective displacement pattern results.

A related flow concern is when the drive fluid has a very different density compared to the target fluid, as the drive fluid will then tend to move upwards and over (override) or downwards and under (underride) the target zone. Examples of this occur when water is used to drive a heavy crude oil (underride), or when a gas is used to drive oil (override). Thus, for reasons of viscosity difference and/or density difference, or both, a drive fluid may not enter a target zone in a reservoir, and it may not effectively drive fluids out from such a zone. As shown below, foams can be used to improve these situations.

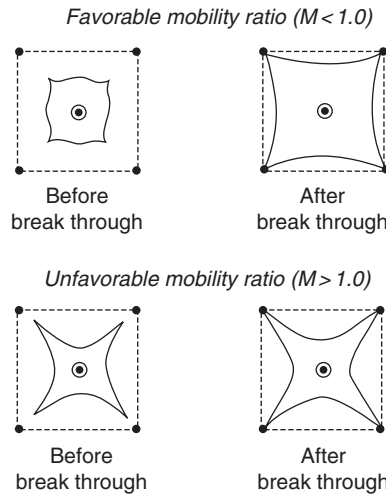


**Fig. 13.1** Illustration, in two-dimensions, of a central injection well and four corner producing wells showing favorable and unfavorable mobility ratio displacement processes. In the unfavorable case early breakthrough occurs and oil is left behind.

#### 13.4.1.2 Capillary Trapping

The capillary forces described by the Young and Young–Laplace equations are what cause most of the oil to be retained (residual oil) in parts of the pore structure in the rock. At any location in a reservoir, the relative oil and water saturations depend on the distribution of pore sizes in the rock. The capillary pressure in a pore is given by:

$$P_c = 2\gamma \cos \theta / R \quad (13.3)$$

where  $R$  is the pore radius, and at some height  $h$  above the free water table  $P_c$  is fixed at  $\Delta\rho h$ . The interfacial tension ( $\gamma$ ) and contact angle ( $\theta$ ) are initially fixed, and if the rock is essentially water-wetting (low  $\theta$ ), then the smaller pores will tend to have more water in them (less oil) than larger pores, and if the rock is essentially oil-wetting (high  $\theta$ ), then the smaller pores will tend to have more oil in them (less water) than larger pores [95].

The ratio of viscous forces to capillary forces correlates well with residual oil saturation and is termed the capillary number. One formulation of the capillary number is

$$N_c = \eta v / (\gamma \varphi) \quad (13.4)$$

where  $\eta$  and  $v$  are the viscosity and velocity of the displacing fluid,  $\gamma$  is the interfacial tension and  $\varphi$  is the porosity. The functional form of the correlation is illustrated in references [96, 97]. The larger the value of  $N_c$ , the greater is the ability of a drive fluid to displace oil from the pores. This is termed the microscopic displacement efficiency. Following the primary oil production phase in a new reservoir, water is the most common drive fluid to be employed (secondary production). For typical waterflooding,  $N_c$  is about  $10^{-6}$  and the residual oil saturation becomes about 40% [96, 97]. The waterflood residual

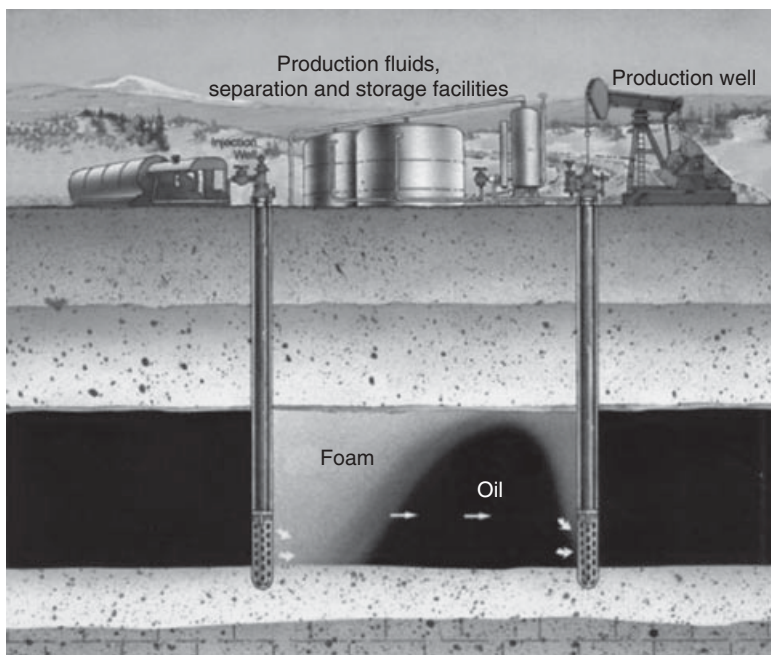


**Fig. 13.2** Illustration of a reservoir enhanced oil recovery process involving foam-flooding. Courtesy Alberta Innovates – Energy and Environment Solutions, Calgary, Canada.

oil is left in the form of oil ganglia trapped in the larger pores (in water-wet reservoirs) where the viscous forces of the driving waterflood could not completely overcome the capillary forces holding the oil in place. To recover additional oil requires increasing the capillary number significantly.

One solution is to reduce the capillary forces restraining the oil and/or alter the viscosity of the displacing fluid, in order to modify the viscous forces being applied to drive oil out of the pores and in so doing improve the oil displacement efficiency. The addition of polymer to the water can increase the viscosity by a sufficient amount to match or slightly exceed that of the oil in the reservoir. The addition of a suitable surfactant to the water can decrease the interfacial tension. One or both of these additives are involved in most chemical-based tertiary oil recovery processes.

### 13.4.2 Foam Applications in Primary and Secondary Oil Recovery

Foams can be produced during primary production because pressure is greater in the reservoir at the locations from which oil is being drained and lower near the wellbore. The pressure decreases further between the bottom of producing wells and near the surface. As oil moves toward a producing well and then into the bottom of the well, the reduced pressure it experiences can cause dissolved gas to come out of solution and be released. When this happens to a light crude oil, the gas normally separates from the oil. In the case

of some heavy oils, however, the gas remains dispersed in the oil as an *in situ* oil foam [98]. The expanding gas bubbles provide a mechanism for driving the foamy oil towards producing wells [99]. The flow through a reservoir to, and up through, a producing well of a dispersion of these gas bubbles in heavy oil is called foamy-oil production. The foam created is oil-continuous, is thought to be stabilized by high molar mass porphyrins, and has a similar appearance to a chocolate mousse emulsion [98].

Not all reservoirs respond favourably to this approach [100], but where it does work foamy (heavy) oil production can cause increases in both production rates and recovery factors over what would be achieved from non-foamy-oil production. In fact, the combination of solution gas drive and sand production can lead to oil production of four to ten times what Darcy's equation would predict [101, 102].

It is thought that the formation of foamy oil delays the formation of a continuous gas phase (increases the trapped gas saturation), contributes a natural pressure-maintenance function, and increases effective permeability by expanding the unconsolidated sands (sand dilation) [98]. These effects are not thought to be available to heavy oil reservoirs undergoing thermal (steam) EOR production because the gas would be released into a separate continuous phase at quite low gas saturations due to the high temperatures involved. As a result foamy heavy oil production is a "cold" production mechanism.

### 13.4.3 Foam Applications in Enhanced (Tertiary) Oil Recovery

Enhanced (tertiary) oil recovery worldwide is dominated by gas and/or vapor flooding using one of steam, carbon dioxide ( $\text{CO}_2$ ), or hydrocarbon. The low density and low viscosity associated with any injected gas causes inefficiencies due to poor sweep efficiency. To alleviate this, surfactants that form foams are sometimes injected for mobility control and/or for blocking and diverting. For example, in a gas flooding process, injecting the gas as a foam lowers the gas mobility and diverts at least some of the gas into parts of the reservoir formation that would otherwise remain unswept (or underswept) due to channeling or gravity override. Such diverting action produces increased oil recovery. Since foam mobility tends to be reduced disproportionately more in higher permeability zones, improvement in both vertical and horizontal sweep efficiency can be achieved.

Suitable foams for deep reservoir applications are always aqueous foams. They can be formulated for injection with air/nitrogen [103–106], as is the case for steam foams, but there are some special advantages to be gained by changing the gas phase to carbon dioxide or a hydrocarbon such as natural gas.

Deep reservoir foam applications may involve slug injection, in which foaming surfactant solution is added into the injected gas stream at the wellhead over a period of time (followed by resuming gas-only injection), semi-continuous injection, in which surfactant solution is injected at intervals, and continuous injection, in which surfactant solution is injected continuously for months or even years.

The requirements for foam performance in different gas flooding processes are sufficiently different that there is no magic foam-forming surfactant molecule or class that can be used in all cases. For example, as shown below, alkyl aryl sulfonates, which tend to have excellent chemical stability at the high temperatures encountered in steam flooding, are among the least soluble in the high salinity/hardness brines that can be encountered in hydrocarbon gas flooding.

### *13.4.3.1 Foams in Carbon Dioxide Flooding*

Suitable foams for improving reservoir sweep efficiency can be formulated for injection with carbon dioxide ( $\text{CO}_2$ ) gas [107–109].  $\text{CO}_2$  is of interest to operators in locations where it is available at low cost, such as in the Central and Western United States. It is also increasingly being considered where it can be relatively inexpensively pipelined from large industrial point-source emitters. In this case the interest in the  $\text{CO}_2$  is not just for enhanced oil recovery, but also for the potential to be part of a carbon capture and storage process. In this case an operator would complete the secondary or tertiary production cycle by leaving the reservoir full of  $\text{CO}_2$  [110, 111], thus storing<sup>1</sup> or “sequestering” potentially large amounts of captured  $\text{CO}_2$ , away from the earth’s atmosphere. Major field demonstrations of such “sequestration” have been conducted in Canada (Weyburn-Midale), Norway (Sleipner), and Algeria (In Salah) [110, 111]. Additional such demonstration projects are being considered for other countries as well (e.g., [112]).

$\text{CO}_2$  can be an attractive choice because it becomes supercritical under many of the temperatures and pressures found in oil reservoirs. Supercritical (dense)  $\text{CO}_2$  is miscible with light hydrocarbons and is therefore at least partially miscible with most crude oils while being sparingly soluble in the aqueous phase. Although supercritical  $\text{CO}_2$  exhibits densities that approach that of crude oil (typically 0.5–0.9 g/cm<sup>3</sup> [109]), its viscosities are similar to those of the gas phase and are therefore as much as 100 times lower than that of crude oil. The result is that supercritical  $\text{CO}_2$  fluid has the potential to be an effective displacing agent in an EOR process except for its high mobility in a reservoir, which leads to flow instabilities, fingering, and potentially poor sweep efficiency. A solution to both the partial miscibility of the  $\text{CO}_2$  with the crude oil and the high mobility is to inject the fluid as a foam.

Bernard and Le Roy describe injecting the  $\text{CO}_2$  with either water-soluble surfactants and aqueous drive fluid, or oil-soluble surfactants and mineral oil [107]. Fisher *et al.* [108] specify the use of surfactants selected for their stability at elevated temperature and pressure, such as sodium lauryl sulfoacetate. A number of other sources discuss the selection of suitable surfactants for foams that can be injected with carbon dioxide [103, 109, 113]. Although continuous injection of  $\text{CO}_2$  foam has been practiced in the United States, a more common approach is to employ water-alternating-gas (WAG) injections (sometimes referred to as surfactant-alternating-gas, or SAG) with cycle times on the order of a year and WAG ratios in the range 1:1 to 2:1 [109]. A review of the special qualities of  $\text{CO}_2$  floods that can make foam particularly attractive as a mobility control agent has been provided by Heller [109].

Finally, another issue with  $\text{CO}_2$  flooding is that oilfield brines containing dissolved  $\text{CO}_2$  are very corrosive. This situation can be exacerbated by the introduction of foam-forming surfactants since some surfactants are capable of removing corrosion-inhibiting coatings [109]. For this reason other choices for the displacing gas phase may be made even in fields for which  $\text{CO}_2$  is readily available.

### *13.4.3.2 Foams in Hydrocarbon Flooding*

Hydrocarbon gas flooding dominates Canada’s EOR production and is used in many other parts of the world, particularly in offshore production areas such as the North Sea.

---

<sup>1</sup>It has been estimated that the  $\text{CO}_2$  captured and stored as a result of the  $\text{CO}_2$  EOR process being used in the Weyburn reservoir in Western Canada will remain substantially trapped underground for at least 5000 years [110].

Considerable work has been invested in the development of suitable foaming systems for improving reservoir sweep efficiency when injecting hydrocarbon gas [103, 114–118]. Such foams can greatly increase the effective viscosity of a hydrocarbon gas, thus decreasing gas mobility and in some cases blocking high relative permeability preferential flow channels. Foaming hydrocarbon gases effectively involves some differences from CO<sub>2</sub> or steam foaming in that the hydrocarbon “gas” can be gas, liquid, or supercritical fluid at different locations in the reservoir, the hydrocarbon gas composition can vary widely depending on the application, and the properties of the hydrocarbon fluid can approach those of a very light oil phase and take on a strong defoaming ability [38, 119, 120].

In terms of foaming surfactant selection, technology developers have not been particularly concerned with thermal stability since the reservoirs considered for hydrocarbon gas flooding don’t usually have reservoir temperatures greater than 80–127 °C [26]. However, as noted above, Western Canada’s Beaverhill Lake carbonate and Gilwood sandstone reservoir pools, which have been of interest for hydrocarbon gas flooding, have salinities that range as high as 24.5–29.6% (245,000–296,000 µg/g) and hardness levels as high as 2.5% (25,000 µg/g) [26]. The higher limits of these salinity and hardness levels are close to the solubility limits of the salts, and are more than high enough to cause most common foaming surfactants to precipitate. It is not just the high salinity and hardness levels that have to be taken into account. Some surfactants actually exhibit improved foaming performance as salinity and hardness increase. Given that most reservoirs that would be considered for hydrocarbon gas flooding have already been extensively waterflooded, any injected surfactants will encounter a range of salinities and hardness levels as they propagate. This means that the ideal foaming surfactants have to be effective over a wide range of salinities and hardness levels, and not just the extremes. Novosad *et al.* [26] tested the brine sensitivity of 152 surfactants recommended by commercial suppliers. Of the 152 they found only nine to be suitable for potential use under conditions of extreme salinity and hardness. The nine surfactants came from four classes: amine oxides, betaines, sulfobetaines, and diphenyl ether disulfonates.

Having established brine solubility, surfactant adsorption on the reservoir rock is an important economic consideration since it can cause substantial amounts of surfactant to be effectively “lost” and unavailable for foam stabilization. In general, surfactant adsorption on the rock increases with decreasing temperature, increasing salinity and hardness, and increasing molar mass within a given surfactant class [27, 121].

Surfactant foaming effectiveness for hydrocarbon gas flooding foams has been evaluated via a combination of static and dynamic bulk foam stabilities at varying temperatures and pressures for initial screening of prospective surfactant candidates, followed by core-flood evaluations prior to final selections [26]. The mobility reduction factors (MRFs) determined for otherwise suitable surfactant-stabilized foams flowing in linear cores under varying conditions of foam quality, brine salinity and hardness, temperature, and pressure have ranged from less than 10 to greater than 300 [26]. However, most such foams exhibit significant reductions in MRF (i.e., achieve lower gas mobilities) when a residual oil saturation is present [26, 122].

Although crude oils generally tend to act as defoamers, it turns out that foams actually exhibit a wide range of sensitivities to the presence of crude oils, as discussed elsewhere [119, 120, 123]. In most cases crude oil can be expected to exert a significant adverse effect on foam stability at saturations above about 5–20% [123]. Overall, it is clearly possible to make foams that are reasonably stable in the presence of light and heavy crude oils [124],

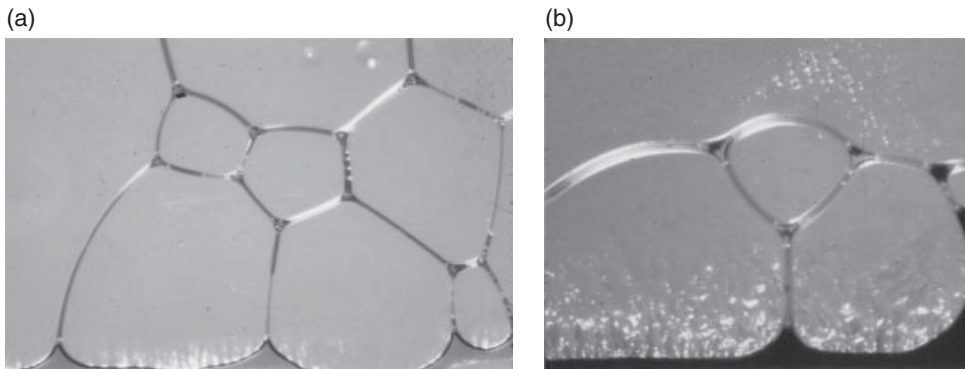


**Fig. 13.3** Photomicrographs of foams flowing in the presence of crude oil, in a glass micro-visual cell. The two images show a foam contacting a conventional light crude oil (a) and a different foam contacting a conventional heavy crude oil (b). The emulsification of the oil and imbibition into and through Plateau borders is also evident. Descriptions of the actual experiments and the micro-visual apparatus are provided in references [41, 119]. © Laurier Schramm.

using either relatively pure foaming agents (usually quite expensive) or specially formulated mixtures, which can be cost-competitive with traditional foaming agents (e.g., [125, 126]). Some of these foams, intended for mobility control, can even improve microscopic displacement, by emulsifying oil into droplets that are small enough to permit their passage inside the foam's lamellar structure, and thus contribute an incremental oil recovery [124, 126]. Figure 13.3 shows two examples.

An example of the successful application of foam in immiscible hydrocarbon gas flooding is in Western Canada's Pembina Ostracod (sandstone) pool. In this case the operator decided to inject solution gas as an alternative to waterflooding and wanted to use foam for mobility control [127]. In this hydrocarbon foam process foam-forming surfactant in aqueous solution was co-injected continuously with the gas, using the reservoir as the foam generator. Surfactant selection was based mostly on solubility, foaming ability, adsorption, and cost [40]. The surfactant chosen was a formulation based on diphenyl ether disulfonate. A field pilot test demonstrated that the foam did reduce the average gas mobility and caused a significant increase in oil production rates [40].

Generally, the most effective foams are formed by co-injection, and foams suitable for mobility control in hydrocarbon flooding have been successfully applied to WAG processes. An example is in the Snorre field in the North Sea, where the main recovery mechanism of waterflooding has been adapted to WAG using produced hydrocarbon gas (mostly methane with some ethane and propane and minor amounts of higher hydrocarbons) [128]. In a surfactant-WAG process foam-forming surfactant is added to the aqueous solution ("water") that is injected alternately with gas. The reservoir itself acts as the foam generator and naturally tends to generate more foam where permeability is relatively higher and oil saturations are relatively lower. In this case the foam is intended to improve mobility control in three ways: by reducing gravity segregation, by blocking gas flow into completely swept zones, and by reducing or eliminating early breakthrough caused by preferential

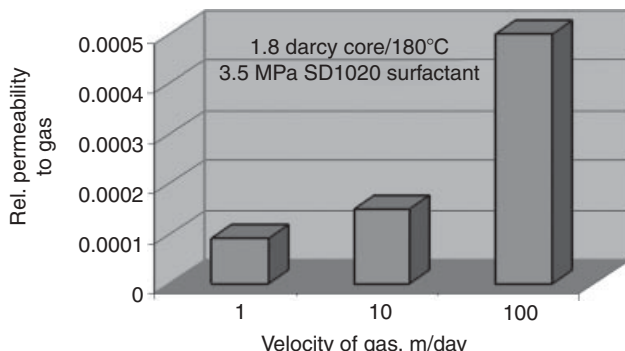


**Fig. 13.4** Illustration of the effect of the steam flow velocity (in porous media) on the flow resistance of the foam at elevated temperatures (see also reference [140]). Courtesy of Alberta Innovates – Energy and Environment Solutions, Calgary, Canada.

flow through the more highly permeable layers and thief zones in a heterogeneous (layered) reservoir [129]. Surfactant selection was based on solubility, foaming ability, oil sensitivity, adsorption, availability, cost, and environmental health and safety [130, 131]. In this case the operator chose to deploy a  $C_{14/16}$  alpha olefin sulfonate surfactant as the foaming agent. A field pilot test demonstrated that an average gas mobility reduction factor of 260 and a produced gas-to-oil ratio (GOR) reduction of 50% were achieved through the introduction of foam to the WAG flooding [132].

#### 13.4.3.3 Foams in Steam Flooding

Suitable foams can also be formulated for injection with steam, but employing different foam-forming surfactants [103, 133–137]. Steam is of interest for heavy oil reservoirs where the function of the steam is to heat the crude oil and increase its mobility. As is the case with other gas injection technologies, two of the problems with steam injection are that areal and vertical sweep efficiencies can be low due to fingering and gravity override. The application of steam foam can be used to counteract both of these difficulties.

Developers of steam foams have been particularly concerned with the need for chemical stability of the surfactants at the high temperatures that will be encountered [134, 138]. The sulfate surfactants that can be used in lower temperature applications decompose rapidly above 100 °C but anionic surfactants with sulfonate groups can be quite stable to 300 °C for periods of weeks under favorable pH conditions [137]. Sulfonate surfactants decompose at low pH as the reaction is acid catalyzed but are stable in neutral and high pH conditions. Some of the more stable foam-forming surfactant classes for use in steam flooding, in descending order of stability, are: alkyl aryl sulfonates > olefin sulfonates > petroleum sulfonates > ethoxylated alcohols  $\approx$  ethoxylated sulfates [138].

To perform successfully, steam-foams must withstand a vast range of conditions and still maintain their integrity and flow resistance properties. For example, near-well fluid velocities are generally very high and decline with distance. The steam-foam has a self-correcting property that can withstand drastic changes in velocity (see Fig. 13.4) with

relatively low resistance near the injection well (at high velocities) and high resistance further into the reservoir (low velocities) [137].

Steam-foams are also sensitive to oil and the tendency of the foam is to break up almost instantaneously in the presence of the oil. This, in fact, is a desirable feature when oil is flowing into the producing well. However, during the foam formation stage the presence of residual oil in the porous media delays foam formation. The foam formation process can be considerably accelerated by injecting a pre-foam slug that effectively reduces the oil saturation in the steam zone [139].

Much of the steam-foam EOR technology has been developed and demonstrated in the heavy oil fields of the Southwest United States and Western Canada [133, 134, 137]. Steam-foam injection has been accomplished in a number of different ways, including continuous injection, surfactant slug placement followed by continuous injection, and cyclic steam injection. Cyclic steam-foam injection is unusual in that for this situation it is actually desirable that the foam breaks down in the presence of crude oil. This is so as not to impede the flow of the oil during the production parts of the cycle [137]. A recent publication has examined the potential of cyclic steam-foam injection using horizontal wells [140].

### 13.5 Occurrences of Foams at the Surface and Downstream

Foams are generally undesirable when produced at a wellhead. This could include foams that have propagated from injection right through to production, newly generated foams stabilized by foam-forming surfactants that have propagated through a reservoir zone, and also foams resulting from surfactants from other kinds of enhanced oil recovery processes or even from components in the crude oil itself, that may be capable of foam stabilization. Whatever their origin, these foams can present some immediate handling, process control, and storage problems.

When a foam drilling fluid is brought to the surface, defoaming is needed to prevent overfoaming of the pit or tank. This can be accomplished by adding a defoamer, such as a polydimethylsiloxane [25, 141]. In primary oil production, oil flows under its own pressure, through permeable porous rock formations, to a production well. When oil nears and enters the annulus of a production well, it experiences a decreased system pressure, dissolved gas may come out of solution, and the oil may foam. In the non-thermal production of heavy oil, such foaming of the oil is thought to improve production (as described earlier), but the beneficial impacts relate to reservoir flow and recovery and not to well-head production. In surface emulsion treaters (e.g. oil-water separators) the occurrence of foams is generally undesirable and any such foams will have to be broken, either down-hole or at the surface [3,46]. Oilfield produced water may also foam, which can cause problems in handling and in gas separation. This is usually dealt with by adding antifoaming or defoaming chemicals such as silicones or polyglycol esters.

Further downstream, in both upgraders and refineries, the occurrence of foams in process streams and vessels is undesirable since it causes operating instabilities and foam-over. These are beyond the scope of the present chapter. A review of refinery foam occurrences and treatment is given by Lewis and Minyard [142], and numerous examples of commonly used foam inhibitors and foam breakers (antifoamers) are provided by Kerner [141].

### 13.6 Conclusion

As we have illustrated, there exists a wide range of potential foam applications in enhancing oil recovery. Although some of the practice remains empirical, enough principles have been established that there have been numerous successful field demonstrations and commercial applications. As always, there is much scope for continuing research and development, particularly where it comes to the search for quantitative linkages among surfactant structures, solution physical properties, bulk foam formation and stability, and porous media foam formation, propagation, and stability. The recent volatility in crude oil prices adds uncertainty to the medium-term economics of oil production so there are not always as many field foam applications under way as has been the case in the past, but this is a cyclical trend, and with increasing crude oil prices industry attention to the benefits of foam field applications should return as it has in previous cycles. Meanwhile, a wealth of established foam technology remains available to operators.

### References

- [1] J.J. Bikerman, J.M. Perri, R.B. Booth, and C.C. Currie,. *Foams: Theory and Industrial Applications*. Reinhold, New York, 1953.
- [2] R.J. Akers (ed.). *Foams*. Academic Press, New York, 1976.
- [3] C. Isenberg. *The Science of Soap Films and Soap Bubbles*. Tieto, Clevedon, 1978.
- [4] J.J. Bikerman. *Foams*. Springer-Verlag, New York, 1973.
- [5] A.J. Wilson (ed.). *Foams: Physics, Chemistry, and Structure*. Springer-Verlag, London, 1989.
- [6] L.L. Schramm. *Dictionary of Nanotechnology, Colloid and Interface Science*. Wiley-VCH, Weinheim, 2008.
- [7] L.L. Schramm (ed.). *Foams: Fundamentals and Applications in the Petroleum Industry*. American Chemical Society, Washington, DC, 1994.
- [8] L.L. Schramm. *Emulsions, Foams, and Suspensions: Fundamentals and Applications*. Wiley-VCH, Weinheim, 2005.
- [9] H.B. Bradley (ed.). *Petroleum Engineering Handbook*. Society of Petroleum Engineers, Richardson, TX, 1992.
- [10] J.G. Speight. *The Chemistry and Technology of Petroleum*, 3rd edn. Marcel Dekker, New York, 1999.
- [11] P.H. Ogden (ed.). *Chemicals in the Oil Industry: Developments and Applications*. Royal Society of Chemistry, Cambridge, 1991.
- [12] N.R. Morrow (ed.). *Interfacial Phenomena in Petroleum Recovery*. Marcel Dekker, New York, 1991.
- [13] M.K. Sharma and G.D. Sharma (eds). *Particle Technology and Surface Phenomena in Minerals and Petroleum Production*. Plenum Press, New York, 1991.
- [14] D.O. Shah and R.S. Schechter (eds). *Improved Oil Recovery by Surfactant and Polymer Flooding*. Academic Press, New York, 1977.
- [15] D.O. Shah (ed.). *Surface Phenomena in Enhanced Oil Recovery*. Plenum Press, New York, 1981.
- [16] D.H. Smith (ed.). *Surfactant-Based Mobility Control*. American Chemical Society, Washington, DC, 1988.
- [17] A.L. Smith (ed.). *Theory and Practice of Emulsion Technology*. Academic Press, New York, 1976.
- [18] P. Becher. *Emulsions: Theory and Practice*, 3rd edn. American Chemical Society, Washington, DC, 2001.
- [19] K.J. Lissant. *Demulsification, Industrial Applications*. Marcel Dekker, New York, 1983.

- [20] S.E. Friberg and P. Bothorel (eds). *Microemulsions: Structure and Dynamics*. CRC Press, Boca Raton, FL, 1987.
- [21] L.L. Schramm (ed.). *Emulsions: Fundamentals and Applications in the Petroleum Industry*. American Chemical Society, Washington, DC, 1992.
- [22] L.L. Schramm (ed.). *Suspensions: Fundamentals and Applications in the Petroleum Industry*. American Chemical Society, Washington, DC, 1996.
- [23] L.L. Schramm (ed.). *Surfactants: Fundamentals and Applications in the Petroleum Industry*. Cambridge University Press, Cambridge, 2000.
- [24] G.V. Chilingarian and P. Vorabutr (eds). *Drilling and Drilling Fluids*. Elsevier, Amsterdam, 1981.
- [25] J.K. Borchardt. Chemicals used in oil-field applications. In *Oil-Field Chemistry*, J.K. Borchardt and T.F. Yen (eds). American Chemical Society, Washington, DC, 1989.
- [26] J.J. Novosad and E.F. Ionescu. Foam forming surfactants for Beaverhill Lake Carbonates and Gilwood Sands reservoirs. In *Proc. CIM Annual Technical Meeting*, paper CIM 87-38-80. Canadian Inst. Mining, Metallurgical and Petroleum Engineers, Calgary, AB, 1987.
- [27] K. Mannhardt and J.J. Novosad. The effects of wettability and residual oil saturation on adsorption of foam-forming surfactants. *In Situ*, **18**(2): 145–83, 1994.
- [28] L.L. Schramm, K. Mannhardt, and J.J. Novosad. Selection of oil-tolerant foams for hydrocarbon miscible gas flooding. In *Proc. 14th International Workshop and Symposium*, paper 18. International Energy Agency Collaborative Project on Enhanced Oil Recovery, E. Rieder (ed.), OMV Energie, Vienna, Austria, 1993.
- [29] D.K. Olsen and P.S. Sarathi (eds). *Proc. Field Application of Foams for Oil Production Symposium*. US Department of Energy, Bartlesville, OK, 1993.
- [30] A.H. Falls, J.B. Lawson and G.J. Hirasaki. The role of noncondensable gas in steam foams. *J. Petrol. Technol.*, **1**: 95–104, 1988.
- [31] E.E. Isaacs, J. Ivory and D.H.-S. Law. Strategies for field applications of foams in heavy oil reservoirs. In *Proc. 6th UNITAR Internat. Conf. Heavy Crude and Tar Sands*. UNITAR/UNDP Inf. Centre, NY, 1995.
- [32] W.C. Shen. Steam foam floods with a caustic agent. United States patent 4,702,317, October 27, 1987.
- [33] J.J. Novosad. On minimizing adsorption of foam-forming surfactants in porous media. In *Chemicals in the Oil Industry: Developments and Applications*, P.H. Ogden (ed.). Royal Society of Chemistry, Cambridge, 1991.
- [34] K. Mannhardt, L.L. Schramm and J.J. Novosad. Adsorption of anionic and amphoteric foam-forming surfactants on different rock types. *Coll. Surf.*, **68**: 37–53, 1992.
- [35] K. Mannhardt and J.J. Novosad. Adsorption of foam-forming surfactants for hydrocarbon-miscible flooding at high salinities. In *Foams, Fundamentals and Applications in the Petroleum Industry*, L.L. Schramm (ed.). American Chemical Society, Washington, 1994.
- [36] L.L. Wesson and G.H. Harwell. Surfactant adsorption in porous media. In *Surfactants, Fundamentals and Applications in the Petroleum Industry*. L.L. Schramm (ed.). Cambridge University Press, Cambridge, 2000.
- [37] E.W. Malmberg and L. Smith. The adsorption losses of surfactants in tertiary recovery systems in porous media. In *Improved Oil Recovery by Surfactant and Polymer Flooding*, D.O. Shah and R.S. Schechter (eds). Academic Press, New York, 1977.
- [38] K. Mannhardt. Core flood evaluation of solvent compositional and wettability effects on hydrocarbon solvent foam performance. *J. Can. Petrol. Technol.*, **38**(13): 1–12, 1999.
- [39] E.A. Spinler and B.A. Baldwin. Surfactant induced wettability alteration in porous media. In *Surfactants: Fundamentals and Applications in the Petroleum Industry*, L.L. Schramm (ed.). Cambridge University Press, Cambridge, 2000.
- [40] J. Chad, P. Matsalla and J.J. Novosad. Foam forming surfactants in Pembina/Ostracod “G” Pool. In *Proc. CIM Annual Technical Meeting*, paper CIM 88-39-40. Canadian Inst. Mining, Metallurgical and Petroleum Engineers: Calgary, AB, 1988.
- [41] L.L. Schramm and J.J. Novosad. Micro-visualization of foam interactions with a crude oil. *Coll. Surf.*, **46**: 21–43, 1990.
- [42] P.B. Rand. Stabilized aqueous foam systems and concentrate and method for making them. United States patent 4,442,018, April 10, 1984.

- [43] J.T. Patton, M.S. Kuntamukkula and S.T. Holbrook. *Polymer Preprints*, **22**: 46–8, 1981.
- [44] D.L. Dauben and S. Raza. Polymer-stabilized foams for improved oil recovery. United States patent 3,530,940, September 29, 1970.
- [45] D.S.H.S. Ram Sarma, J. Pandit and K.C. Khilar. Enhancement of stability of aqueous foams by addition of water-soluble polymers – measurement and analysis. *J. Coll. Interface Sci.*, **124**: 339–48, 1988.
- [46] R.D. Sydansk. Polymer-enhanced foam: laboratory development and evaluation. In *Proc. Internat. Symp. Oilfield Chemistry*, SPE paper 25168. Society of Petroleum Engineers, Richardson, TX, 1993.
- [47] S. Lioniatti-Addad and J.-M. di Meglio. Stabilization of aqueous foam by hydrosoluble polymers. I. Sodium dodecyl sulfate–poly(ethylene oxide) system. *Langmuir*, **8**: 324–7, 1992.
- [48] M.S. Pradhan, D.S.H.R. Sarma and K.C. Khilar. Stability of aqueous foams with polymer additives. II. Effects of temperature. *J. Coll. Interface Sci.*, **139**: 519–26, 1990.
- [49] M.S. Pradhan and K.C. Khilar. Stability of aqueous foams with polymer additives. *J. Coll. Interface Sci.*, **168**, 333–8, 1994.
- [50] S.E. Friberg and J.-H. Fang. Foams from aqueous systems of polymerizable surfactants. *J. Coll. Interface Sci.*, **118**: 543–52, 1987.
- [51] R.D. Sydansk. Polymer-enhanced foam propagation through high-permeability sandpacks. In *Proc. Internat. Symp. Oilfield Chem.*, SPE paper 25175. Society of Petroleum Engineers, Richardson, TX, 1993.
- [52] G.G. Bernard and L.W. Holm. Method for storing gas in subterranean formations. United States patent 3,393,738, July 23, 1968.
- [53] I.N. Zhukov, T.I. Polozova and O.S. Shatava. *Kolloidn. Zh.*, **49**: 758–62, 1987.
- [54] R.D. Hazlett and E.T. Strom. In-situ foaming of polymer profile control gels. United States patent 4,844,163, July 4, 1989.
- [55] M.J. Miller and H.S. Fogler. A mechanistic investigation of waterflood diversion using foamed gels. In *Proc. Annual Technical Conf.*, SPE paper 24662. Society of Petroleum Engineers, Richardson, TX, 1992.
- [56] R.D. Sydansk. Foam for improving sweep efficiency in subterranean oil-bearing formations. United States patent 5,105,884, April 21, 1992.
- [57] Y. Qing, W. Yefei, Z. Wei, Q. Ziyuan and Z. Fulin. Study and application of gelled foam for in-depth water shut off in a fractured oil reservoir. *J. Can. Petrol. Technol.*, **48**(12): 51–5, 2009.
- [58] L.L. Schramm, S.M. Kutay, R.J. Mikula and V.A. Munoz. The morphology of non-equilibrium foam and gelled foam lamellae in porous media. *J. Petrol. Sci. Eng.*, **23**: 117–32, 1999.
- [59] L.L. Schramm and S. Kutay. Petroleum industry emulsions and foams. In *Surfactants: Fundamentals and Applications in the Petroleum Industry*, L.L. Schramm (ed.). Cambridge University Press, Cambridge, 2000.
- [60] G.P. Willhite and J.G. Dominguez. Mechanisms of polymer retention in porous media. In *Improved Oil Recovery by Surfactant and Polymer Flooding*, D.O. Shah and R.S. Schechter (eds). Academic Press, New York, 1977.
- [61] F. Sebba. Microfoams: an unexploited colloid system. *J. Colloid Interface Sci.*, **35**(4): 643–6, 1971.
- [62] F. Sebba. *Foams and Biliquid Foams: Aphrons*. Wiley, New York, 1987.
- [63] F. Sebba. An improved generator for micron-sized bubbles. *Chem. Ind.*, **4**: 91–3, 1985.
- [64] A.K. Mirzadjanzade, I.M. Ametov, A.O. Bogopolsky, R. Kristensen, U.N. Anziryaev, S.V. Klyshnikov, A.M. Mamedzade and T.S. Salatov. Micronucleus water-gas solutions: a new efficient agents for water-flooded oil reservoirs. In *Proc. 7th European IOR Symp.*, Moscow, 1993.
- [65] A.K. Mirzadjanzade, I.M. Ametov, A.A. Bokserman and V.P. Filippov. In *Proceedings, 7th European IOR Symp.*, Moscow, 1993.
- [66] D. Roy, R.R. Kommalapati, K.T. Valsaraj and W.D. Constant. Soil flushing of residual transmission fluid: Application of colloidal gas aphron suspensions and conventional surfactant solutions. *Water Res.*, **29**: 589–95, 1995.
- [67] D. Roy, S. Kongara and K.T. Valsaraj. Application of surfactant solutions and colloidal gas aphron suspensions in flushing naphthalene from a contaminated soil matrix. *J. Hazardous Mat.*, **42**: 247–63, 1995.

- [68] M.V. Enzien, D.L. Michelsen, R.W. Peters, J.X. Bouillard and J.R. Frank. Enhanced in situ bioremediation using foams and oil aphrons. In *Proc. 3rd Int. Symp. In-Situ and On-Site Reclamation*. San Diego, CA, 1995.
- [69] G.C. Maitland. Oil and gas production. *Curr. Opinion Coll. Int. Sci.*, **5**: 301–11, 2000.
- [70] T.R. Thomas and T.M. Wilkes. The use of surfactants in lightweight drilling fluids. In *Surfactants, Fundamentals and Applications in the Petroleum Industry*, L.L. Schramm (ed.). Cambridge University Press, Cambridge, 2000.
- [71] G.W. Anderson. In *Proc. Rotary Drilling Conference of IADC*. Int. Assoc. Drilling Contractors, Houston, TX, March 9–12, 1976.
- [72] N.W. Bentsen and J.N. Veny. Preformed stable foam performance in drilling and evaluating shallow gas wells in Alberta. *J. Petrol. Technol.*, **28**(10): 1237–40, 1976.
- [73] S.O. Hutchison and G.W. Anderson. Preformed stable foam aids work over drilling. *Oil and Gas J.*, **May**: 74–9, 1972.
- [74] A.H. Beyer, R.S. Milhone and R.W. Foote. Flow behavior of foam as a well circulating fluid. In *Proc. 47th Annual Fall Meeting*, paper SPE 3986. Society of Petroleum Engineers, Richardson, TX, 1972.
- [75] G.W. Anderson. Stable foam circulation cuts surface hole costs. *World Oil*, **Sept.**: 39–42, 1971.
- [76] G.W. Anderson, T.F. Harrison and S.O. Hutchison. The use of stable foam circulating fluids, *The Drilling Contractor*, **May/June**: 44–7, 1966.
- [77] H. Lorenz. Air, mist and foam drilling has worldwide application. *World Oil*, **June**: 187–93, 1980.
- [78] J. Rovig. The evolution of stable foam as a drilling medium. *APPEA J.*, **36**: 557–61, 1996.
- [79] T. Biesman and V. Emeh. An introduction to underbalanced drilling. In *Proc. 1st Underbalanced Drilling International Conference*, The Hague, 1995.
- [80] Y. Li and E. Kuru. Numerical modelling of cuttings transport with foam in horizontal wells. *J. Can. Petrol. Technol.*, **42**(10): 54–61, 2003.
- [81] B.A. Russell. How surface hole drilling was improved 65%. In *Proc. SPE/IADC Drilling Conference*, SPE/DOE paper 25766. Society of Petroleum Engineers, Richardson, TX, 1993.
- [82] G.P. Southwell. In-line foam generator for hydrocarbon recovery applications and its use. United States patent 5,356,565, October 18, 1994.
- [83] W.M. Harms. Application of chemistry in oil and gas well fracturing. In *Oil-Field Chemistry: Enhanced Recovery and Production Stimulation*, J.K. Borchardt and T.F. Yen (eds). American Chemical Society, Washington, DC, 1989.
- [84] P. Valko, M.J. Economides, S.A. Baumgartner and P.M. McElfresh. The rheological properties of carbon dioxide and nitrogen foams. In *Proc. Symposium on Formation Damage Control*, paper SPE 23778. Society of Petroleum Engineers, Richardson, TX, 1992.
- [85] P.C. Harris. Application of foam fluids to minimize damage during fracturing. In *Proc. International Meeting on Petroleum Engineering*, paper SPE 22394. Society of Petroleum Engineers, Richardson, TX, 1992.
- [86] D.J. Chambers. Foams for well stimulation. In *Foams, Fundamentals and Applications in the Petroleum Industry*, Schramm, L.L. (ed.). American Chemical Society, Washington, DC, 1994.
- [87] H.A. Nasr-El-Din. Surfactant use in acid stimulation. In *Surfactants, Fundamentals and Applications in the Petroleum Industry*, Schramm, L.L. (ed.). Cambridge University Press, Cambridge, 2000.
- [88] H.A. Nasr-El-Din, A.M. Al-Othman, K.C. Taylor and A.H. Al-Ghamdi. Surface tension of HCl-based stimulation fluids at high temperatures. *J. Petrol. Sci. Eng.*, **43**: 57–73, 2004.
- [89] J. Lea, H.V. Nickens and M. Wells. *Gas Well Deliquification*. Gulf Professional Publishing, Burlington, MA, 2003.
- [90] W. Jelinek and L.L. Schramm. Improved production from mature gas wells by introducing surfactants into wells. In *Proc. International Petroleum Technology Conference, Doha, Qatar*, paper IPTC 11028. Society of Petroleum Engineers, Richardson, TX, 2005.
- [91] R.G. Turner, M.G. Hubbard and A.E. Dukler. Analysis and prediction of minimum flow rate for the continuous removal of liquids from gas wells. *J. Petrol. Technol.*, **21**(11): 1475–82, 1969.
- [92] J. Yang, V. Jovancicevic and S. Ramachandran. Foam for gas well deliquification. *Coll. Surf. A*, **309**: 177–81, 2007.

- [93] N.R. Morrow (ed.). *Interfacial Phenomena in Petroleum Recovery*. Marcel Dekker, New York, 1991.
- [94] D.O. Shah and R.S. Schechter (eds). *Improved Oil Recovery by Surfactant and Polymer Flooding*. Academic Press, New York, 1977.
- [95] N.J. Clark. *Elements of Petroleum Reservoirs*. Society of Petroleum Engineers, Richardson, TX, 1969.
- [96] K. Taylor and B. Hawkins. Emulsions in enhanced oil recovery. In *Emulsions, Fundamentals and Applications in the Petroleum Industry*, L.L. Schramm (ed.). American Chemical Society, Washington, DC, 1992.
- [97] T. Austad and J. Milter. Surfactant flooding in enhanced oil recovery. In *Surfactants, Fundamentals and Applications in the Petroleum Industry*, L.L. Schramm (ed.). Cambridge University Press, Cambridge, 2000.
- [98] B. Maini and H. Sarma. Role of nonpolar foams in production of heavy oils. In *Foams, Fundamentals and Applications in the Petroleum Industry*, L.L. Schramm (ed.). American Chemical Society, Washington, DC, 1994.
- [99] B.B. Maini, H.K. Sarma and A.E., George. Significance of foamy oil flow during primary production of heavy oil. *J. Can. Petrol. Technol.*, **32**(9): 50–4, 1993.
- [100] L.L. Schramm and E.E. Isaacs. Development of “Technology Oil”: *in situ* oil sands and heavy oil reservoirs in Canada. In *Handbook on Bitumen Recovery from Oil Sands: Theory and Practice*, J. Masliyah and J. Czarnecki (eds). University of Alberta Press, Edmonton, submitted.
- [101] L.L. Schramm, P.R. Jamieson, R. Moberg and D.B. Stewart. Improved oil recovery science and technology priorities for Western Canada. In *Proc. 12th European Symposium on Improved Oil Recovery*. European Association of Geoscientists and Engineers, Houten, The Netherlands, 2003.
- [102] Y. Liu, R.G. Wan and Z. Jian. Effects of foamy oil and geomechanics on cold production. *J. Can. Petrol. Technol.*, **47**(4): 55–61, 2008.
- [103] D.K. Olsen and P.S. Sarathi (eds). *Proceedings, Field Application of Foams for Oil Production Symposium*. US Department of Energy, Bartlesville, OK, 1993.
- [104] L.W. Holm. Foam injection test in the Siggins field, Illinois. *J. Petrol. Technol.*, **22**: 1499–506, 1970.
- [105] D.L. Kuehne, D.I. Ehman and A.S. Emanuel. Design and engineering of a nitrogen-foam field trial. In *Proc. SPE/DOE Symposium on EOR*, SPE/DOE paper 17381. Society of Petroleum Engineers, Richardson, TX, 1988.
- [106] S. Thach, K.C. Miller, Q.J. Lai, G.S. Sanders, J.W. Styler and R.H. Lane. High-stability foams for long-term suppression of hydrocarbon vapors. In *Proc. SPE Annual Technical Conference*, SPE paper 36616. Society of Petroleum Engineers, Richardson, TX, 1996.
- [107] G.G. Bernard and W.H. Le Roy. Method for recovering oil from subterranean formations. United States patent 3,342,256, September 19, 1957.
- [108] P.W. Fischer, L.W. Holm and D.S. Pye, inventor. Carbon dioxide foam flooding. United States patent 4,088,190, May 9, 1978.
- [109] J.P. Heller. CO<sub>2</sub> foams in enhanced oil recovery. In *Foams, Fundamentals and Applications in the Petroleum Industry*, L.L. Schramm (ed.). American Chemical Society, Washington, DC, 1994.
- [110] B. Metz, O. Davidson, H. de Coninck, M. Loos and L. Meyer (eds). *IPCC Special Report on Carbon Dioxide Capture and Storage*. Cambridge University Press: Cambridge, 2005.
- [111] M. Wilson and M. Monea (eds). *IEA GHG Weyburn CO<sub>2</sub> Monitoring and Storage Project. Summary Report 2000–2004*. Petroleum Technology Research Centre, Regina, SK, 2004.
- [112] L. Zhang, B. Niu, S. Ren, Y. Zhang, P. Yi, H. Mi and Y. Ma. Assessment of CO<sub>2</sub> storage in DF1-1 South China Sea gas field for CCS demonstration. *J. Can. Petrol. Technol.*, **49**(8): 9–14, 2010.
- [113] L.W. Holm and W.H. Garrison. CO<sub>2</sub> diversion with foam in an immiscible CO<sub>2</sub> field project. *SPE Res. Eng.*, **3**: 112–18, 1988.
- [114] T. Holt and T.S. Kristiansen. Improved sweep efficiency during gas injection: mobility control. In *Proc. SPOR Seminar*. Norwegian Petroleum Directorate: Stavanger, Norway, 1990.
- [115] P.C. Liu and G.J. Besserer. Application of foam injection in Triassic Pool, Canada: Laboratory and field test results. In *Proc. SPE 63rd Annual Technical Conf.*, SPE paper 18080. Society of Petroleum Engineers, Richardson, TX, 1988.

- [116] M.G. Aarra and A. Skauge. A foam pilot in a North Sea oil reservoir: preparation for a production well treatment. In *Proc. SPE 69th Annual Technical Conf.*, SPE paper 28599. Society of Petroleum Engineers, Richardson, TX, 1994.
- [117] M.G. Aarra, A. Skauge, S. Sognesand and M. Stenhaug. A foam pilot test aimed at reducing gas inflow in a production well at the Oseberg field. *Petrol. Geoscience*, **2**: 125–32, 1996.
- [118] I. Svorstøl, T. Blaker, M.J. Tham and A. Hjellen. A production well foam pilot in the North Sea Snorre Field: application of foam to control premature gas breakthrough. In *Proc. 9th European Symposium on Improved Oil Recovery*, paper 001. The Hague, The Netherlands, 1997.
- [119] L.L. Schramm, A. Turta and J.J. Novosad. Micro-visual and coreflood studies of foam interactions with a light crude oil. In *Proc. SPE/DOE 7th Symp. on EOR*, SPE/DOE paper 20197. Society of Petroleum Engineers, Richardson, TX, 1990.
- [120] L.L. Schramm and J.J. Novosad. The effects of different oils on the stability of EOR foams. In *Proc. 12th. Internat. Workshop and Symp. IEA Collaborative Project on Enhanced Oil Recovery*. Bath, UK, October 28–30, 1991.
- [121] K. Mannhardt, J.J. Novosad and K.N. Jha. Adsorption of foam-forming surfactants in Berea sandstone. *J. Can. Petrol. Technol.*, **33**(2): 34–43, 1994.
- [122] J. Chad, P. Matsalla and J.J. Novosad. Foam forming surfactants in Pembina/Ostracod “G” Pool. In *Proc. CIM Annual Technical Meeting*, paper CIM 88-39-40. Canadian Inst. Mining, Metallurgical and Petroleum Engineers, Calgary, AB, 1988.
- [123] L.L. Schramm. Foam sensitivity to crude oil in porous media. In *Foams: Fundamentals and Applications in the Petroleum Industry*, L.L. Schramm (ed.). American Chemical Society, Washington, DC, 1994.
- [124] L.L. Schramm and J.J. Novosad. The destabilization of foams for improved oil recovery by crude oils: Effect of the nature of the oil. *J. Petrol. Sci. Eng.*, **7**: 77–90, 1992.
- [125] W.A. Rendall, C. Ayasse and J.J. Novosad. Surfactant-stabilized foams for enhanced oil recovery. United States patent 5,074,358, December 24, 1991.
- [126] L.L. Schramm, C. Ayasse, K. Mannhardt and J.J. Novosad. Method for improving enhanced recovery of oil using surfactant-stabilized foams. United States patent 5,060,727, October 29, 1991.
- [127] Enhanced Recovery Week. Signalta tests surfactant at Pembina gas flood. *Enhanced Recovery Week*, October 27: 1–2, 1986.
- [128] G. Nybraten, I. Svorstol and P.O. Andfossen. WAG pilot evaluations for the Snorre Field. In *Proc. 7th European IOR Symposium*. Moscow, 1993.
- [129] J.E. Hanssen, L. Surguchev, I. Svorstol and T. Blaker. SAGA injection: a new combination IOR process for stratified reservoirs. In *Proc. 7th European IOR Symposium*. Moscow, 1993.
- [130] I. Svorstol, T. Blaker, T. Holt and F. Vassenden. Foam pilot evaluations for the Snorre Field. Part 1. Project planning and laboratory results. In *Proc. 8th European IOR Symposium*, Vol. 1. Vienna, 1995.
- [131] I. Svorstol, F. Vassenden and K. Mannhardt. Laboratory studies for design of a foam pilot in the Snorre Field. In *Proc. 10th SPE/DOE Symposium on IOR*, paper SPE/DOE 35400. Society of Petroleum Engineers, Richardson, TX, 1996.
- [132] I. Svorstol, T. Blaker, M.J. Tham and A. Hjellen. A production well foam pilot in the North Sea Snorre Field: application of foam to control premature gas breakthrough. In *Proc. 9th European IOR Symposium*, paper 001. The Hague, 1997.
- [133] L.M. Castanier. Steam with additives: field projects of the eighties. *J. Petrol. Sci. Eng.*, **2**: 193–206, 1989.
- [134] R.L. Eson and R.W. Cooke. A comprehensive analysis of steam foam diverters and application methods. In *Proc. SPE California Regional Meeting*, SPE paper 18785. Society of Petroleum Engineers, Richardson, TX, 1989.
- [135] R.W. Cooke and R.L. Eson. Field results of optimizing the steam foam diversion process in cyclic steam applications. In *Proc. SPE International Thermal Operations Symposium*, SPE paper 21531. Society of Petroleum Engineers, Richardson, TX, 1991.
- [136] T.W. Patzek and M.T. Koinis. Kern River steam foam pilots. In *Proc. SPE/DOE Symposium on EOR*, SPE/DOE paper 17380. Society of Petroleum Engineers, Richardson, TX, 1988.

- [137] E.E. Isaacs, J. Ivory and M.K. Green. Steam-foams for heavy oil and bitumen recovery. In *Foams, Fundamentals and Applications in the Petroleum Industry*, L.L. Schramm (ed.). American Chemical Society, Washington, DC, 1994.
- [138] D.H. Scharer, D.B. Bright, C.L. Merrill, P.K. Shankar and T.A.B.M. Bolsman. Olefin sulphonates in crude oil production. In *Proc. American Oil Chemists Soc. Ann. Mtg*, Philadelphia, 1985.
- [139] E.E. Isaacs, M.K. Green, W.E. Jossy and J.D. Maunder. Conformance improvements by using high temperature foams and gels. In *Proc. 2nd SPE Latin American Conference*, SPE paper 23754. Society of Petroleum Engineers, Richardson, TX, 1992.
- [140] E.E. Isaacs and J.-Y. Yuan. Enhancing heavy oil recovery using foam injection in applications to cyclic steam stimulation. Presented at *World Heavy Oil Congress*, Edmonton, March 2008.
- [141] H.T. Kerner. *Foam Control Agents*. Noyes Data Corp., Park Ridge, NJ, 1976.
- [142] V.E. Lewis and W.F. Minyard. Antifoaming and defoaming in refineries. In *Foams, Fundamentals and Applications in the Petroleum Industry*, L.L. Schramm (ed.). American Chemical Society: Washington, DC, 1994.

# 14

## Foam Fractionation

*Xueliang Li and Paul Stevenson*

### 14.1 Introduction

An aqueous foam is a dispersion of gas in an aqueous liquid containing a foam-stabilising agent, such as detergents (e.g. soap foam) and proteins (e.g. beer head). If the volume fraction of the aqueous phase and bubble size distribution is given, we can calculate the specific surface area,  $S$ , of a static foam by

$$S = \frac{3(1-\varepsilon)}{r_{32}\varepsilon} \quad (14.1)$$

where  $S$  ( $\text{m}^2/(\text{m}^3 \text{ foamate})$ ) is the specific surface area of a static foam per unit volume of liquid,  $\varepsilon(-)$  is the liquid fraction and  $r_{32}$  ( $\text{m}$ ) is the Sauter mean bubble radius defined statistically by

$$r_{32} = \frac{\int_0^\infty r_b^3 f(r_b) dr}{\int_0^\infty r_b^2 f(r_b) dr} \quad (14.2)$$

where  $f(r_b)$  is the probability density function of the given bubble size distribution. So for a foam with a liquid fraction of 1% and a Sauter mean radius of 1 mm, the specific surface area is as high as  $2.9 \times 10^5 \text{ m}^2 \text{ per m}^3$  of liquid.

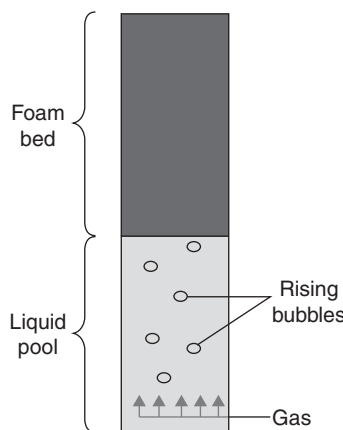


**Fig. 14.1** Schematic diagram of a simple foam fractionator.

Foam fractionation is an adsorptive bubble separation technique [1] that employs the high specific surface area of foam, coupled with the fact that surface-active materials tend to accumulate to the gas–liquid interface. Figure 14.1 shows a schematic representation of the simplest foam fractionation unit. It consists of a column of foam at the top of a vessel containing the solution to be foamed. A foam fractionation column can be operated in different modes such as batch, semi-batch or continuous. In the simplest batch operation, foam is initially generated up to a desired height by passing gas into the liquid pool through a sparger which gives the desired bubble size. Then the gas supply is stopped, the foam is allowed to drain and the liquid fraction of the foam decreases as the drainage proceeds. The average bubble size will also change due to inter-bubble gas diffusion [2, 3] (see Chapter 4) and rupture of foam lamellae (see Chapter 5), although the rate at which these processes occur may be very low [4–7]. After a desired time of drainage, gas is turned on again and the newly generated foam drives the dry foam out of the column and a new cycle of foam generation and drainage takes place. The foam is collapsed mechanically or chemically by using a defoamer, and the resulting liquid, enriched in surface-active species, is called the foamate.

The concentration of surface-active material in the foamate is a function of the specific surface area of the original foam and the surface excess (i.e. the surface concentration). The enrichment ratio is

$$E = \frac{C_f}{C_b} = 1 + \frac{\Gamma S}{C_b} \quad (14.3)$$

where  $C_f$  (mol.m<sup>-3</sup>) is the foamate concentration and  $C_b$  (mol.m<sup>-3</sup>) is the bulk concentration (i.e. the concentration in the liquid);  $\Gamma$  (mol.m<sup>-2</sup>) is the surface excess. For instance, the equilibrium surface excess for a  $5 \times 10^{-3}$  mol.m<sup>-3</sup> solution of the non-ionic surfactant C<sub>10</sub>E<sub>8</sub> is about  $1.7 \times 10^{-6}$  mol.m<sup>-2</sup> [8], if a foam with the above-mentioned specific surface area is used to enrich this solution, assuming that the surface excess is in

equilibrium with the bulk concentration. The resultant enrichment ratio will be about 100. A practical example is a beer head, where the protein concentration was found to be around 73% (w/w) with about less than 10% (w/w) of water [9], while the actual beer beneath has a protein concentration of 0.3% (w/w) only, which means that protein is enriched in the foam by a factor of around 240.

In the above discussion, batch mode operation has been employed as an example. This is because, in a batch mode operation, the foam is essentially static so that the enrichment can be simply calculated from eqn (14.3). However, in a rising column of foam, such as those employed in semi-batch (continuous with respect to the gas phase, batch with respect to the liquid) or continuous (continuous with respect to both phases) operations, the liquid fraction of the foam in the column is not directly related to the final enrichment of the process due to the slip velocity between the liquid phase and gas phase (see Chapter 8 for more details).

Batch mode operation does not require a continuous gas supply; therefore a syringe pump can be used for highly accurate gas volume and gas flow rate control, if necessary. It also enables the assumption that the bulk concentration is constant (in each cycle), since only a fractional amount of surface-active material is removed from the bulk in each cycle of foaming. Batch operation greatly simplifies the liquid fraction measurement as well because it can be directly determined from the change in liquid level and the height of the foam layer. These features of batch operation make it a common choice for studying the adsorption in a laboratory-scale foam fractionation column [10, 11]. Despite its great simplicity, batch operation has little practical utility because of its low time efficiency (the system is in idle during the drainage phase) in comparison with semi-batch and continuous operations. Batch operation is not suitable for studying the hydrodynamics of foam either, because of its temporal and spatial variation. A true steady state can only be achieved in a continuous operation.

Although there has recently been a surge of application-related research in foam fractionation and a large number of publications have emerged where foam fractionation is used to separate or concentrate proteins [10–21], enzymes [22–25], various metal ions [26–29] etc., the technique has largely failed to achieve its commercial potential. Most of the above-mentioned work has been on a laboratory scale. The most commonly encountered foam fractionators are the so-called ‘protein skimmers’ [30, 31] used for the removal of dissolved organic compounds including proteins and fatty acids, and possibly particles, from aquaria. The only reported industrial-scale foam fractionation is the extraction of Nisin from its fermentation broth, directly or with the help of some other surfactant [32–34], depending on the actual composition of the fermentation broth and the stability of the foam generated from it. Nisin is an antimicrobial peptide produced by some strains of *Lactococcus lactis*, which is effective against a wide range of G+ bacteria. It is accepted as a natural preservative in more than 50 countries around the world [35]. A flow chart of the unit operations involved in the production of Nisin is given in Fig. 14.2, where foam fractionation is employed as an early step in the downstream processing. Nisin is produced in a liquid medium by batch-wise fermentation. Once the fermentation process is finished, the broth is acidified to pH 2~3 by the addition of HCl solution and then it is heated up to 90 °C to kill the Nisin-producing microbe. Debris of the producer microbe and undigested fermentation media are then removed from the broth by ultrafiltration. The filtrate normally has a Nisin titre of about 5000 IU.ml<sup>-1</sup>. The foam fractionation unit operation can concentrate

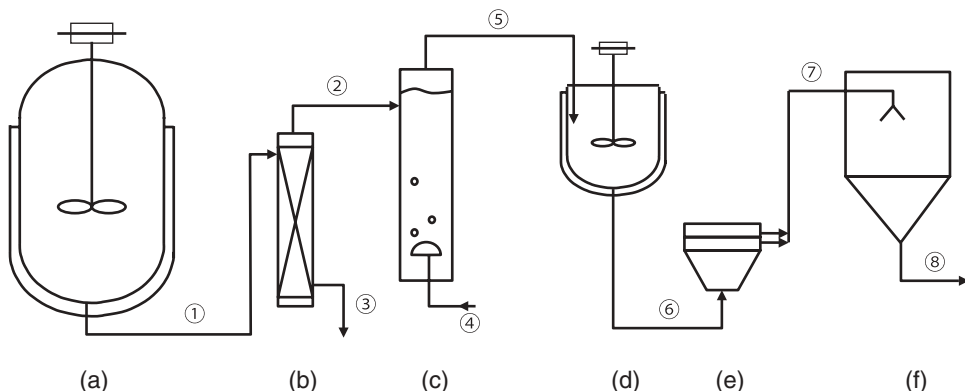


**Fig. 14.2** Process flow sheet of the manufacture of Nisin. Unit operations: (a) fermentation, acidification and sterilisation; (b) ultra filtration; (c) foam fractionation; (d) precipitation; (e) centrifugation; (f) spray drying. Material flows: (1) sterilised fermentation broth; (2) filtrate; (3) cell debris; (4) compressed clean air; (5) foamate; (6) precipitate soliquid; (7) concentrated precipitate soliquid; (8) final product.

the filtrate thus to reduce its volume by a factor of 10. This significantly reduces the amount of ammonium sulphate that is used in the subsequent precipitation process. For instance, when a 50% (w/w) ammonium sulphate concentration is used, by reducing the volume of the filtrate from 20 tons to 2 tons, the amount of ammonium sulphate saved by employing foam fractionation is 9 tons. This can also significantly reduce the duty of the subsequent unit operations and waste-water treatment.

Regardless of the mode of operation, the enrichment of the objective species is determined by both the surface excess and specific surface area of the foam. The former is mainly a function of the physicochemical properties of the substance in question and the adsorption time, while the latter is more strongly affected by operating conditions, which have a direct effect on bubble size and foam drainage.

In the following section, interfacial adsorption is briefly discussed. We do not give an exhaustive description. Only those aspects that are directly relevant to foam fractionation process design and application are considered.

## 14.2 Adsorption in Foam Fractionation

In the foam fractionation of proteins, the protein itself is amphipathic. In the case of surface-inactive substances such as metal ions, a carrier surfactant has to be added to the solution. In either case, the interfacial adsorption is critical, not only because this is the mechanism by which the objective species is extracted from the liquid solution by adhering to the bubble surface, but also because the adsorption, which lowers the surface tension, plays an important role in stabilising the foam.

### 14.2.1 Adsorption Kinetics at Quiescent Interface

It is recognised that in a foam fractionation column, a quiescent gas–liquid interface does not exist since bubbles are rising in the liquid pool and the interstitial liquid is draining in the foam layer. However, an understanding of the adsorption at quiescent interfaces helps the understanding of the actual adsorption behaviour in a foam column.

The adsorption kinetics of non-ionic surface-active molecules at a planar quiescent gas–liquid interface can be described quantitatively by the Ward–Tordai equation [36], which gives the time dependence of the surface tension, which is related to the surface excess of the adsorbing molecules via the Gibbs isotherm. The concept of a ‘sub-surface’ is adopted in the model of Ward–Tordai and it is assumed that the sub-surface is in equilibrium instantaneously with the interface; thus the rate of adsorption is controlled by the mass transfer from the bulk solution to the sub-surface. In a quiescent solution, the mass transfer from the bulk solution to the sub-surface can be described by Fick’s law of diffusion. The Ward–Tordai equation has the following form:

$$\Gamma(t) = 2\sqrt{\frac{D}{\pi}} \left\{ C_b \sqrt{t} - \int_0^{\sqrt{t}} C(\tau) d(\sqrt{t-\tau}) \right\} \quad (14.4)$$

where  $t$  (s) is the time since the formation of the fresh surface,  $D$  ( $\text{m}^2.\text{s}^{-1}$ ) is the coefficient of molecular diffusion and  $\tau$  is a dummy variable with the units of time, respectively.  $C$  ( $\text{mol}.\text{m}^{-3}$ ) is the sub-surface concentration. Note that the Ward–Tordai equation has direct utility for a planar interface, which can be treated as though the surfactant molecules are diffusing from an infinite external solution. In case of adsorption onto bubbles, the interface is convex. An adapted version of the Ward–Tordai equation was proposed by Mysels [37] to account for the effect of interface curvature. For a bubble of the radius  $r_b$  (m), the time-dependent surface excess is the following equation:

$$\Gamma(t) = 2\sqrt{\frac{D}{\pi}} \left\{ C_b \sqrt{t} - \int_0^t C(\tau) d\sqrt{t-\tau} \right\} + \frac{D}{r_b} \left\{ C_b t - \int_0^t C(\tau) d(t-\tau) \right\} \quad (14.5)$$

of which the first part is mathematically identical to the planar version of the Ward–Tordai equation and the second part accounts for the surface curvature. Figure 14.3 shows the simulated time-dependant surface excess of the adsorption onto bubbles of different radii [8]. It can be seen that the bubble radius does not significantly affect the adsorption rate when it increases from 1 to 10 mm.

The Ward–Tordai model assumes that the diffusional transport of the surface-active molecules from the bulk to the interface is the rate-controlling process and the sub-surface is in immediate equilibrium with the interface. If the rate of diffusion is fast or comparable with the rate of the transfer of molecules between the sub-surface and the interface, i.e. there is an energy barrier between the sub-surface and the interface, the so-called kinetic-controlled models or mixed models apply [38]. Different mechanisms for kinetic-controlled

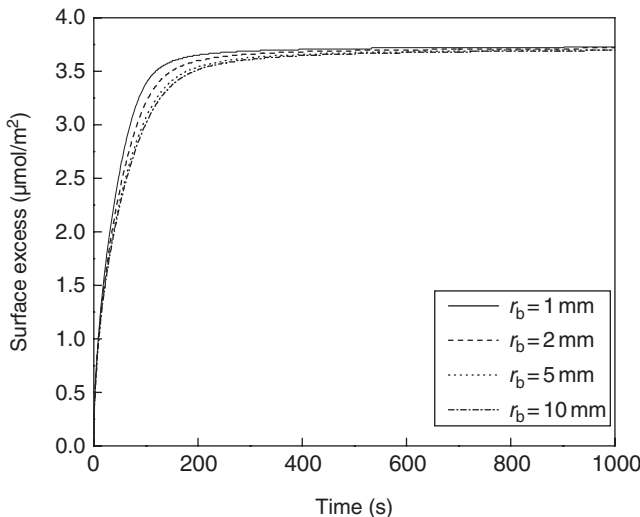


**Fig. 14.3** Simulation of diffusion-controlled adsorption onto the surface of bubbles.  
 $D = 5 \times 10^{-10} \text{ m}^2 \cdot \text{s}^{-1}$ ,  $C_b = 5.44 \times 10^{-3} \text{ mol} \cdot \text{m}^{-3}$ ; the legend indicates the different bubble radii.

adsorption have been proposed [39], most of which consider both the rates of the transfer from the sub-surface to the interface (adsorption) and that in the opposite direction (desorption). Below is the frequently used rate equation of the Langmuir mechanism

$$\frac{d\Gamma}{dt} = k_{ad} C_b \left( 1 - \frac{\Gamma}{\Gamma_\infty} \right) - k_{des} \frac{\Gamma}{\Gamma_\infty} \quad (14.6)$$

where  $k_{ad}$  ( $\text{m} \cdot \text{s}^{-1}$ ) and  $k_{des}$  ( $\text{mol} \cdot \text{m}^{-2} \cdot \text{s}^{-1}$ ) are the adsorption and desorption rate constants, respectively.  $\Gamma_\infty$  ( $\text{mol} \cdot \text{m}^{-2}$ ) is the saturation surface excess. The term  $1 - (\Gamma/\Gamma_\infty)$  is the driving force of adsorption, while  $\Gamma/\Gamma_\infty$  is the driving force of desorption. The equilibrium state of adsorption corresponds to  $d\Gamma/dt = 0$ , i.e. the rate of adsorption is equal and opposite to the rate of desorption. The solution to the Langmuir mechanism model is simple and can be obtained analytically. There are also more complicated models where numerical solution methods are necessary.

Although non-ionic surfactants are frequently considered for modelling adsorption process, foam fractionation of proteins and ionic surfactant (as a carrier of metal ions) is more actively investigated due to its potential application in the food and pharmaceutical industries, and in waste-water treatment. The adsorption of proteins and ionic surfactants, however, is far more complicated than that of non-ionic surfactants. Protein molecules, in their native conformation, are interconnected polypeptides arranged in specific structures. Generally speaking, both hydrophobic and hydrophilic groups exist at the surface of a protein molecule. At the air–water interface, those hydrophobic groups tend to escape from the water side to spread at the interface, while the hydrophilic groups prefer to stay in the water side.

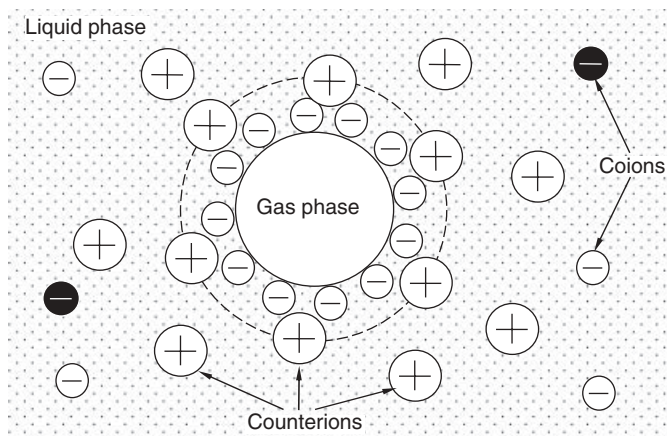


**Fig. 14.4** Illustrative diagram of the electric double layer around a gas bubble in an aqueous solution of ionic surfactant. The dashed circles denote the Stern layer where counterions are adsorbed.

Given enough time, the structure of the protein molecule (tertiary conformation) will be changed, sometimes combined with the loss of its bioactivity (denaturation) if the unfolding is irreversible [40–44]. In the production of Nisin, a 10% denaturation is considered normal (see Section 14.6).

The surface tension of a non-ionic surfactant solution is directly related to the surface excess of the surfactant molecules and becomes constant when adsorption equilibrium is established. In contrast, the surface tension of protein solution can continue to change as a result of the relaxation of its tertiary structure. In addition, multilayer adsorption of protein molecules is also possible. Although experimental studies have been conducted [40, 43, 45], quantitative modelling of the dynamic adsorption of proteins remains in its infancy.

The complexity that arises in ionic surfactant adsorption compared with non-ionics is the effect of electrostatic interactions on both the equilibrium state and the rate of transport to the interface, due to the existence of the electric double layer (EDL) near the interface.

Figure 14.4 illustrates the EDL around a gas bubble. The diagram is adapted from the EDL at a planar interface from [46]. Generally speaking, the electrostatic repulsion between adsorbed ions decreases the equilibrium surface excess and therefore the adsorbed ions are not closely packed at the interface. Under non-equilibrium conditions, the electrostatic repulsion between the ions inside and outside the adsorption layer retards the adsorption kinetics. Oppositely charged ions (counterions) can be immobilised at the adsorption layer, which forms the Stern layer [47]. Conditions such as pH and ionic strength, which can affect the electrostatic repulsion, will also affect the adsorption kinetics. Quantitative modelling of the adsorption of ionic surfactants emerged in the 1980s [48, 49] and is still of interest to current researchers [47]. A recent review [50] of the equilibrium adsorption of both ionic and non-ionic surfactants at the gas–liquid interface compared and validated various models.

### 14.2.2 Adsorption at Dynamic Interfaces

The mass transfer and the surface excess distribution on the bubble surface are dependent upon the fluid flow around the bubble, and *vice versa*, because the adsorption of the surface-active materials modifies the properties of the bubble surface, which in turn affect the stress state of the surface and the drag force exerted on the surface. Experimental [51–53] and computational fluid dynamics (CFD) [52, 53] studies have shown that the adsorption isotherms of quiescent and moving interfaces (i.e. where a slip velocity exists between liquid and gas phases, as it does in foam fractionation) are different, because of an interdependency between hydrodynamic conditions and adsorption. This effect is more significant in the liquid pool, where the gas–liquid interface exists in the form of buoyant bubbles, than in the foam bed, especially when the foam is dry. Simple material balance analysis showed that the equilibrium surface excess on a rising bubble in the liquid pool is roughly 51% of the equilibrium value on a quiescent interface, while that in the foam layer is about 71% [54].

The dynamic adsorption layer theory and the stagnant cap model were developed to describe the interaction between the adsorption/desorption of surfactant and flow field around a buoyant bubble [39, 55]. According to this theory, a steady state is reached a certain time after the formation of the bubble. After the attainment of steady state, the total amount of adsorbed substance does not change, because the adsorption rate on one part of the bubble surface is equal to the amount desorbed from another part. The movement of the bubble induces a surface excess gradient: at the leading pole of the bubble the surface concentration is lowest, while at the rear stagnation point it is at maximum. The angular surface concentration gradient generates the Marangoni effect, which retards the motion of the surface, as well as the rising velocity of the bubble, which is one of the reasons why a bubble in a surfactant solution has a lower terminal velocity than that in chemically pure water.

The dynamic adsorption layer theory is only valid for small Reynolds numbers, while in foam fractionators the mixing caused by the motion of the different sized bubbles, which induces Reynolds stresses, invalidates the simplifying assumptions demanded by the theory. Therefore few in the foam fractionation community have considered the phenomenon. Another reason why this has been overlooked is that even though it is clear that there is an effect of the dynamic nature of the interface, it is more difficult to control it as compared to other design parameters, such as the depth of the liquid pool and the foam bed.

When considering the foam fractionation of proteins, Bhattacharjee *et al.* [10, 11] assumed that the liquid in a gas–liquid foam is mostly contained in the Plateau borders and, as the surface area of the films is far more than that of the Plateau borders, once a bubble leaves the liquid pool, the protein contained in the film liquid is not enough to cause any further significant adsorption onto the gas–liquid interface. Thus, they assumed that the adsorption occurs only while the bubbles rise in the liquid pool, and the extent of adsorption onto the surface of a bubble is dependent on its residence time in the liquid pool, which in turn is determined by the depth of the liquid pool and bubble rise velocity. Maruyama *et al.* [13, 14] also adopted the assumption that adsorption occurs only in the liquid pool, but the effect of residence time on the adsorption density was not considered and instantaneous

equilibrium between the bulk solution and the bubble surface was assumed. The assumption that adsorption occurs only in the liquid pool greatly simplifies the modelling process because the only enrichment mechanism in the foam layer is drainage. Examples of such models can be found in the literature [10, 11, 18].

Researchers who have flotation backgrounds usually take into consideration the possibility of adsorption within the foam bed. This is partly due to the fact that flotation columns are often operated with wash-water, which has an analogy to external reflux (see Section 14.5.2) in foam fractionation, and thus the liquid fraction of the froth is much higher than that normally seen in protein foam, so that a considerable amount of bubble surface is in contact with the liquid. This can be seen from the differences between the designs of a foam fractionation column and a flotation cell. At the top of a foam fractionation column, there is normally a conduit directing the foam to a collector, while in a flotation cell the froth is allowed to overflow freely, as it contains more liquid and is less viscous (Fig. 3 in [56]). In foam fractionation, adsorption in the foam bed has to be taken into account when any kind of reflux is used or the column is run as an enricher or stripper or a combination of the two [57]. In these cases, the feed solution or part of the product stream is introduced into the foam bed at some distance above the liquid–foam interface, and thus the liquid fraction of the foam is enhanced. Unlike the models based on the assumption that adsorption happens only in the liquid pool, stage-wise counter-current approaches, by analogy to distillation models, are used to model the adsorption in foam bed [57–59], where material balances and equilibrium relationships are applied. However, as there was no simplifying assumption, such as constant molar overflow used to model distillation, to describe the foam drainage, previous models were all highly empirical and lacked genuine predictive capability. A remedy for this situation is the recent development of the hydrodynamic theory of pneumatic foam [60]. An example of the application of this theory to modelling a continuous enricher with reflux has been demonstrated [61].

The question as to where in the foam column (i.e. the liquid pool or the foam layer) the adsorption takes place is of great importance to foam fractionation device design. This is discussed in detail in Section 14.5.2.

### 14.3 Foam Drainage

Once interfacial adsorption has reached equilibrium (or saturation), foam drainage becomes the only means of improving the performance of a foam fractionation process, especially in the case of proteins where the bioactivity of the target molecule has to be maximally preserved, therefore enhancing the adsorption by altering the chemical conditions such as the pH [25] is not feasible. Foam drainage is discussed in depth in Chapter 3. Only pertinent details are considered here.

The prediction and measurement of the drainage in gas–liquid foams is even more actively discussed in the literature than the adsorption-related problems in the field of foam fractionation. Most theoretical models have attempted to account for the geometric structure of the Plateau border network and the interfacial and bulk rheology. The models have become increasingly complex, but foam drainage is still not completely mechanistically understood. In addition, as the measurements of some of the interfacial properties are still

unreliable [62], the actual practical efficacy of these models is open to question. We argue that a different approach by Stevenson [63], which contains a dimensional analysis for calculating the slip velocity between the gas phase and liquid phase in foam, represents a good balance between simplicity and physical relevance to the drainage process.

It is emphasised that the lack of understanding of foam drainage and the hydrodynamics of pneumatic foam has created confusion in foam fractionation-related studies. The most frequently encountered mistake is the application of the temporal liquid fraction profile of free-draining foam [64–66] to the spatial liquid fraction profile of a rising foam. Stevenson [60] showed that if the bubble size distribution remains constant with height, then the liquid fraction within the foam, remote from the very bottom where capillarity is significant, is spatially constant. However, several authors [18–20] explained the observation in practical systems that the liquid fraction decreases with height upon residence time arguments. The argument goes that as the foam gets higher in the column, it has had longer to drain and therefore becomes drier. This has consequences for foamate rate and enrichment. Lockwood *et al.* [67] and Webb *et al.* [68] measured the axial liquid hold-up profile of a rising foam by gamma scintigraphic methods and concluded that the height of a column necessary to produce *well-drained* foam is an important characteristic to define in the design of a foam fractionation procedure because a column that is too short could result in the collection of wet foam. Clearly, these studies have, like those mentioned above, failed to recognise the fundamental hydrodynamic basis of the foam fractionation process. The liquid fraction in a pneumatic foam *does* change with height, but it is because of the change of bubble size distribution and not because a longer residence time gives greater opportunity for the foam to drain. The cause of changes in bubble size distribution is discussed below. An in-depth description may be found in Chapters 4 and 5.

#### 14.4 Coarsening and Foam Stability

A stable foam is essential for successful foam fractionation. However, there is a paradox: For a ‘good’ surfactant, such as the widely used sodium dodecyl sulphate (SDS), a small surface excess is sufficient to support a stable foam and there is hardly any coalescence within the bulk of the foam [69]; therefore it cannot be significantly enriched just because the surface concentration cannot be very high [54]. In other systems [23, 70] where the foam stability is lower, enrichment can be much higher because a higher surface excess is required to stabilise the foam. In ideal cases, the target molecule should be able to produce a foam that is stable enough to allow continuous operation. In a batch or semi-batch process, the liquid pool becomes depleted of surfactant as the foaming proceeds, so the foam stability also decreases. *Foaming out*, which occurs when no stable foam can be produced from the liquid, indicates the end of the operation.

Coarsening of foam is of two types: rupture of films between two cells and Ostwald ripening [2, 57] (see Chapter 4). The former is related to the drainage and stability of foam films, while the latter is caused by inter-bubble gas diffusion. As the rate of inter-bubble gas diffusion is typically very slow [3–7], it is usually not important to the continuously overflowing foams employed in foam fractionation, due to their relatively short residence time [69]. Ostwald ripening may be significant in long-term foam stability tests, and the poor reproducibility of such tests is partly attributed to the sensitivity of the rate of inter-bubble gas diffusion to the initial bubble size distribution [7].

The result of coarsening is the decrease in surface area and increase of average bubble size, as observed in many studies, e.g. [67, 68]. Because the coarsening causes competing effects with regard to recovery and enrichment, whether it is desirable depends upon the application. Lemlich [57] briefly remarked that coalescence within a rising foam destroys the surface and releases adsorbed material, which flows back down through the rising foam, and this rich drainage acts as *internal reflux*. Thus it is normally considered that internal reflux tends to enhance enrichment [19, 71] and creates a further opportunity for proteins to enrich. No systematic experimental investigation of the internal reflux can be found in the literature. However, a mechanism for internal reflux [72] has been proposed based on the hydrodynamic theory of rising foam of Stevenson [60].

Although a high foam stability is required during the foam fractionation process, it immediately becomes undesirable as soon as the foam leaves the unit operation. When the foam stability is relatively low, mechanical methods can be used to break the foam. However, if the stability is high, a mechanical paddle may make the foam more stable because it merely breaks big bubbles into small bubbles, as we had experienced when handling foam stabilised by an SDS solution. In fermentation processes, unwanted foam is normally destroyed by using a suitable antifoaming agent. However, antifoaming agent cannot be used in foam fractionation when external reflux is adopted.

We have recently found an effective way for manipulating the apparent stability of foam: by altering the humidity of the air that is in contact with the foam [69]. This ‘thermodynamic method’ may be of use when the mechanical and chemical methods are inappropriate. In addition, the humidity dependency may also account for the low reproducibility of the foam stability test.

## 14.5 Foam Fractionation Devices and Process Intensification

As briefly mentioned in the introduction, conventional foam fractionation columns can be operated in different modes, such as batch, semi-batch (batch charging of feed liquid, continuous bubbling) and continuous. Batch and semi-batch columns are simple to design and operate, but their utilisation for investigating the physics of the process is problematical due to their temporal variation. In batch operation, the bulk concentration can be considered constant for each cycle, because only a fractional amount of surface-active material is removed each time. However, the foam is freely draining and therefore changing with time. In a semi-batch operation, the liquid pool becomes depleted of surfactant as the process proceeds, which affects both the adsorption and the drainage. In this section, we first use a time-independent continuous operation as an example to explain the limitations of the conventional foam fractionation devices. Second, several different approaches to process intensification are introduced.

### 14.5.1 Limitations of Conventional Columns

Making the common assumption that the surfactant concentration in the interstitial liquid of the foam is equal to that in the bubbly liquid [1, 10, 11, 14, 18], a steady-state material balance gives the recovery rate of a conventional column,

$$R = j_f C_f = \phi_s + j_f C_b \quad (14.7)$$

where  $R$  (mol.m<sup>-2</sup>.s<sup>-1</sup>) is the recovery rate and  $\phi_s$  (mol.m<sup>-2</sup>.s<sup>-1</sup>) is the molar flux of the surfactant that is adsorbed at the surface of the bubbles in the foam. If the superficial gas velocity,  $j_g$  (m.s<sup>-1</sup>), and bubble size distribution in the foam is known, the flux of surface area,  $j_s$  (s<sup>-1</sup>), can be calculated by

$$j_s = \frac{3j_g}{r_{32}} \quad (14.8)$$

$\phi_s$  can then be expressed as the product of the surface flux and the surface excess,  $\Gamma$ , i.e.

$$\phi_s = j_s \Gamma \quad (14.9)$$

The enrichment ratio in a continuous system can then be derived similarly to eqn (14.3):

$$E = \frac{C_f}{C_b} = 1 + \frac{j_s}{j_f} \frac{\Gamma}{C_b} \quad (14.10)$$

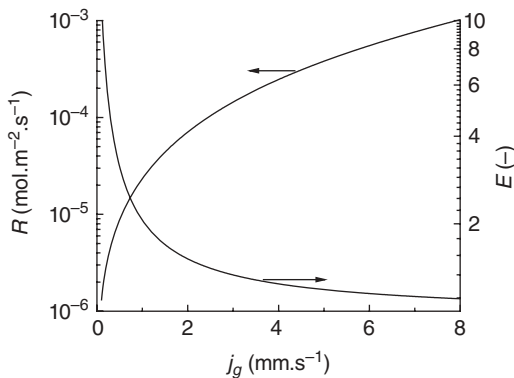
Eqn (14.10) clearly shows the two groups of factors that determine the enrichment of a foam fractionation process, i.e. the hydrodynamic quotient,  $j_s/j_f$ , and the physico-chemical quotient,  $\Gamma/C_b$ . The value of  $j_s/j_f$  is mostly determined by parameters such as bubble size and superficial gas velocity, while the value of  $\Gamma/C_b$  is affected by interfacial adsorption rate and the adsorption isotherm. For a given system,  $j_s/j_f$  can be evaluated by numerically solving the equation

$$\frac{\mu j_g}{nmpgr_b^2} = \varepsilon^{n-1} (1 - \varepsilon)^2 \quad (14.11)$$

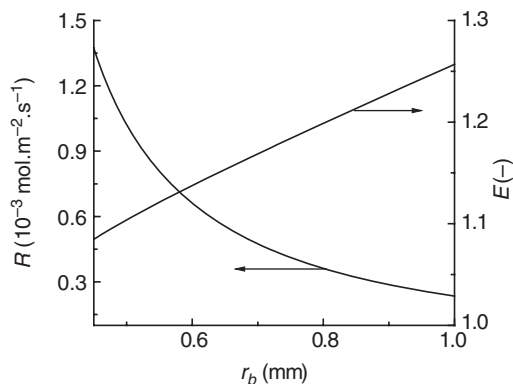
which is derived from the hydrodynamic theory of rising foam of Stevenson [60]. Using a 0.5 g/L SDS solution as an example and assuming that when the foam leaves the column the interfacial adsorption has reached equilibrium (the corresponding equilibrium surface excess =  $2 \times 10^{-6}$  mol.m<sup>-2</sup> [73]), the effect of superficial gas velocity and bubble size on the enrichment and recovery of the process can be simulated, as shown in Figs 14.5 and 14.6. Other parameters used here include  $\mu = 0.001$  Pa.s,  $\rho = 1000$  kg.m<sup>-3</sup>,  $m = 0.016$  and  $n = 2$ . It can be seen from Fig. 14.5 that because  $j_f$  increases faster than  $j_s$  does when  $j_g$  is increased, the value of the hydrodynamic quotient decreases while the physico-chemical group keeps constant, so the enrichment ratio decreases as a consequence. Both  $\phi_s$  and  $j_f$  increase as  $j_g$  is increased, and hence the recovery rate also increases, according to eqn (14.10).

Figure 14.6 demonstrates similar competing effects of the bubble size on the recovery rate and enrichment ratio. Reducing bubble size increases the specific surface area, which favours the adsorption. But it also reduces the drainage rate, resulting in a lower enrichment factor. Increasing the bubble size makes the drainage faster so enrichment is higher, but it reduces the specific surface area, which lowers the recovery rate.

In addition to the competing effects of bubble size and gas rate, foam fractionation operation is also subjected to other constraints. For example, the hydrodynamic theory of rising foam of Stevenson [60] demonstrated that there exists a gas rate threshold above



**Fig. 14.5** Enrichment and recovery rate as a function of the superficial gas velocity.



**Fig. 14.6** Enrichment and recovery as a function of bubble size.

which no stable foam can be produced. When handling bioactive materials such as proteins in a practical application, even more restrictions will be placed on process design and operation. See Section 14.6 for some details.

### 14.5.2 Process Intensification Devices

Due to the limitations and restrictions, different approaches have been proposed to modify a conventional column to intensify the process, and these can be classified into two main categories that depend upon either (i) adsorption enhancement or (ii) drainage enhancement.

#### 14.5.2.1 Adsorption Enhancement Methods

In general, there is a relationship between the bulk concentration,  $C_b$ , and the equilibrium surface excess,  $\Gamma^*$ . An example of such a relationship is the Langmuir adsorption isotherm

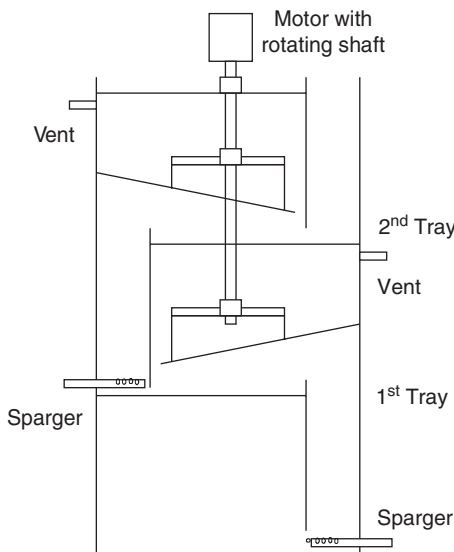


**Fig. 14.7** A compact multistage foam fractionator [77].

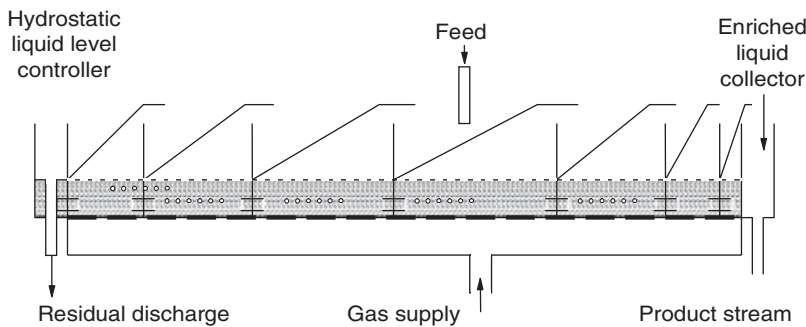
$$\Gamma^* = \Gamma_\infty \left( \frac{K_L C_b}{1 + K_L C_b} \right) \quad (14.12)$$

where  $K_L$  ( $\text{m}^{-3} \cdot \text{mol}^{-1}$ ) is a constant. By increasing  $C_b$ , the equilibrium surface excess can be increased until  $\Gamma^* = \Gamma_\infty$ , if there is enough time for equilibrium to be established. Depending upon where in the column the adsorption of surface active molecules occurs, there are two methods to enhance the extent of gas–liquid surface adsorption.

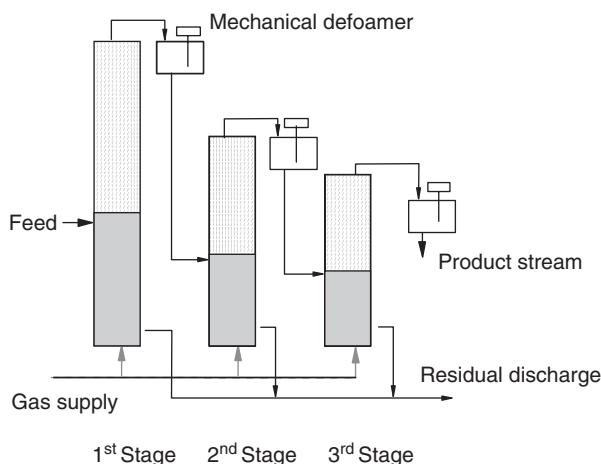
(a) Multistage approaches. Foam fractionation devices with physically distinct stages, either in the compact form of a single column with internal components that resembles those found in distillation columns [74–79] or in a series of conventional columns connected with pipes and fittings [80], have been proposed. These designs are based on the assumption that adsorption occurs mainly in the liquid pool and that only one equilibrium stage of adsorption can be achieved in a conventional column. Therefore, a higher surface excess can be achieved by repeated foaming cycles.

Figure 14.7 shows the compact multistage foam fractionation device developed by Darton *et al.* [77]. The foam is destroyed by mechanical paddles between each stage and the resulting foamate is mixed with the feed; therefore the bulk concentration is increased.

The multistage bubble fractionator shown in Fig. 14.8 shares the same basic concept with the vertical column, except that in this design, the different stages are arranged in a horizontal array. Feed is introduced in a middle stage. The liquid pools of adjacent stages are connected by a horizontal tube located near the bottom, allowing the liquid to flow between stages, driven by the hydrostatic pressure. Foam flows horizontally, in the opposite direction to the liquid. No foam-breaking mechanism is employed and therefore the device only has utility for foam with a low stability. Because of this, the foam layer is shallower compared to conventional foam fractionation columns.



**Fig. 14.8** A horizontal-multistage foam fractionation device [79].



**Fig. 14.9** Multistage foam fractionators aiming at high enrichment [80].

In Fig. 14.9, multistage operation is achieved by operating single conventional columns in series. The foamate from an earlier stage is used as the feed to the adjacent later stage. Note that if the foamate is added to the foam layer of the adjacent stage, the system will be a multistage-external-reflux device. See below.

(b) Reflux approaches [61, 81–83]. Figure 14.10 shows a schematic of a foam column with external reflux. Unlike multistage approaches, reflux methods can be effective if the adsorption that occurs in the foam layer contributes significantly to the overall surface excess, and this surface excess is in equilibrium with the interstitial liquid. Therefore, multiple equilibrium stages can be engendered within a continuous foam layer by returning some of the foamate to the foam layer as an external reflux stream, or it can be autogenously created by bubble coalescence causing internal reflux [1, 72].

It is clear that both multistage and reflux approaches enhance interfacial adsorption by increasing the surfactant concentration in the liquid, be it the bulk liquid or the interstitial liquid in the foam. Although the equilibrium surface excess may be different due to the

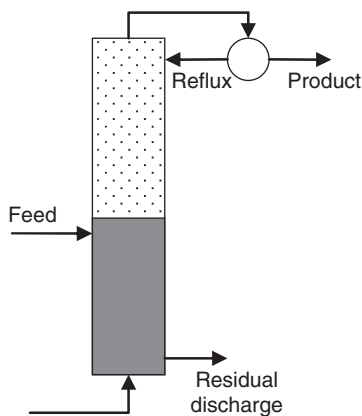


**Fig. 14.10** Continuous foam fractionation with external reflux.

different hydrodynamic conditions in the foam layer and in the bulk liquid (see Section 14.2.2 for an explanation). Note that in most previous work on foam fractionation, the adsorption isotherms of quiescent interfaces have been used to describe the equilibrium adsorption onto the surface of a rising bubble in the liquid pool or foam.

Both the multistage and the reflux methods of process intensification could be effective to some extent, depending on the relative importance of the adsorption in the liquid and foam layers. Of course, the saturation surface excess gives an upper limit to the extent of adsorption. In addition, both multistage and reflux approaches require effective collapse of the foam. This could be difficult if the foam exhibits high stability. In cases of biomaterials such as proteins and peptides, multiple foam generation/bursting cycles may also cause serious denaturation of the target molecule [41, 42, 44].

#### 14.5.2.2 Drainage Enhancement Methods

Several different methods have been proposed for reducing the liquid flux of the foam. Bando *et al.* [84] inserted a draft tube into the bubbly liquid of a conventional column and constructed a device resembling an air-lift reactor (Fig. 14.11), where small bubbles were recirculated into the downcomer due to convection, resulting in a foam layer consisting mainly of large bubbles. Increasing the bubble size can indeed reduce liquid flux, but this is at the expense of losing interfacial area and therefore reducing recovery rate. In addition, bigger bubbles can be generated more easily by using a bigger pore size of the sparger, thus achieving precisely the same result as using the draft tube. The use of perforated plates to reduce liquid flux has also been investigated [85, 86] but results have been mixed. A schematic diagram of the foam fractionators used by Tsubomizu *et al.* [85] is shown in Fig. 14.12. The authors postulated that part of the ‘bubble film’ could be removed from the bubbles when the foam is squeezed through the small pores, thus reducing the liquid content of the foam and increasing the enrichment. The authors stated that volumetric liquid flux on a lower state,  $Q_n$ , is greater than that on a higher stage,  $Q_{n+1}$ , but no accumulation of liquid between stages was observed, which does not satisfy mass balances.

A foam fractionation column with parallel inclined channels (PIC) was investigated and found to be effective in intensifying the foam fractionation of the surfactant

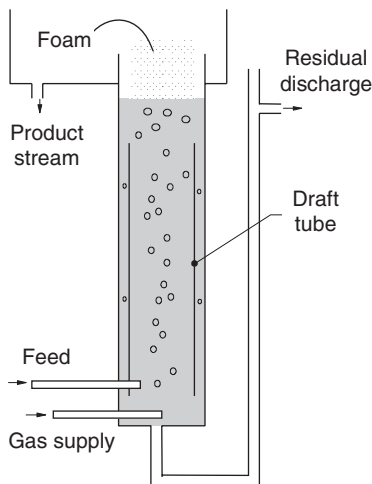


**Fig. 14.11** Foam fractionator with a draft tube in the liquid pool [84]. Small bubbles are circulated back to the bottom of the column.

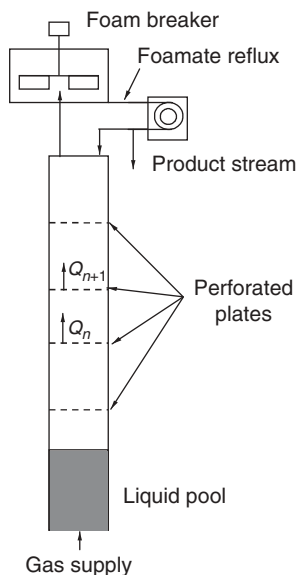


**Fig. 14.12** Foam fractionator with perforated plates in the foam layer [85].

cetyltrimethylammonium bromide (CTAB) by changing the flow direction and thus increasing the liquid drainage rate [87]. In the case of the recovery of surface-active proteins, the increased column wall surface-to-foam volume ratio in a PIC column could cause greater loss of the product, as a significant amount of the protein molecules can adsorb onto the surface of the plates that is in contact with the foam [88]. Therefore special treatment of the plate surface may be required if this method is applied to foam fractionation of proteins.

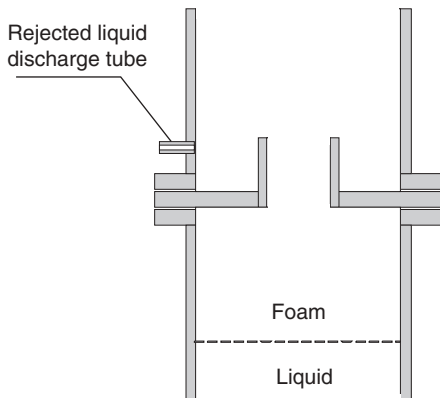


**Fig. 14.13** Drainage enhancement by successive contraction and expansion of foam flow area [54].

A simple drainage enhancement device consisting of a foam riser mounted in the centre of a plate (Fig. 14.13) was designed and systematically investigated by our group [54]. The device creates a contraction of flow area of the foam, followed by an expansion. During the expansion, part of the interstitial liquid was rejected from the foam and was drained back to the feed through a tube in the wall of the column, allowing for steady-state continuous operation. A 35% reduction in liquid flux was observed by using a single plate-foam riser assembly in a foam stabilised by an SDS solution, and the liquid rejected from the foam had the same concentration as the feed solution. The mechanism of this device has previously been described [89] although attempts to quantitatively model the process encountered difficulties in dealing with foam rheology and foam drainage in accelerating foam.

Generally speaking, studies on the process intensification of foam fractionation are still highly empirical. Although some adsorption-enhancing approaches have been modelled, these have been based on sets of simplifying assumptions. For example, in the compact multistage designs, immediate adsorption equilibrium was assumed and therefore the dimensions of the column including the internal structure are essentially arbitrary numbers. Drainage enhancement appears to be more promising because it can improve the enrichment without sacrificing the surface area. The development of drainage-enhancing devices relies on better understanding of the hydrodynamics of rising foam.

## 14.6 Concluding Remarks about Industrial Practice

Foam fractionation, with its low equipment and operation cost, can serve as a very promising alternative method for the extraction of surface-active materials from solutions, and there are indeed successful industrial-scale applications. When one of the authors (X. Li) was completing his master's degree in the Hebei University of Technology, China, he provided on-site technical support to Tianjin Kangyi

Biotechnology Co. Ltd, which was then the second largest Nisin manufacturer in China and was collaborating with his department. Batch fermentation was adopted by the manufacturer at that time, due to its relatively lower hygiene requirement and simplicity of operation in comparison with continuous fermentation. Nisin has to be salted out from the broth and then collected by centrifugation. However, as the concentration of Nisin in the broth was very low, a huge amount of salt was required if the fermentation broth was put directly to the salting-out step. Thus, foam fractionation was used as a pre-concentration step at the beginning of the series of recovery and purification unit operations. High enrichment within the foam fractionators is of primary importance to the company in order to reduce the amount of salt required in the downstream processing. During the 2 years (2005 to 2007) that Li spent with the company he was tasked to improve the foam fractionation process.

The foam fractionation was run in semi-batch mode for the reason that hygiene regulations are less strict than for continuous operation. In addition, semi-batch operation is selected over a continuous system to match the schedule of the batch fermentation. Thirty tons per day of fermentation broth was processed by 18 foam columns (with throughputs of 1.25 or 5 tons per day). We believe this to be the largest foam fractionation operation in the world. The average concentrating ratio, defined by the original volume of the broth (i.e. 30 m<sup>3</sup>, approximately) and the volume of the foamate collected from the 18 columns, was about 10–15, with a recovery of bio-activity around 75–85%, while about 10% of the bioactivity was lost due to denaturation during the foaming process. How and at which section the denaturation occurs failed to be identified, however.

Optimisation of a real industrial process is much more difficult than performing experiments in laboratories. For instance, in the production of Nisin, the pH of the broth has to be adjusted to below 3 to retain the bioactivity of the product, as otherwise it will be quickly deactivated irreversibly. The ionic strength could not be altered either because the following ‘salting-out’ unit operation required strict ionic strength control. Implementation of external reflux was considered for enhancing the enrichment, but as the foam produced from the fermentation broth was very stable, defoaming agent had been used to help destroy the foam, which precluded the return of the foamate as a reflux stream. There was also evidence that multiple bubbling and collapsing, such as those involved in multistage foam fractionation, could aggravate denaturation. These restrictions in a practical application make it even more important to understand the fundamentals of the process, only after which can real practical progress be made.

## Nomenclature

### Roman

$C_f$	foamate concentration	[mol.m <sup>-3</sup> ]
$C_b$	bulk concentration	[mol.m <sup>-3</sup> ]
$C$	sub-surface concentration	[mol.m <sup>-3</sup> ]
$D$	coefficient of molecular diffusion	[m <sup>2</sup> .s <sup>-1</sup> ]
$E$	enrichment factor	[–]

$j_f$	superficial liquid velocity	[m.s <sup>-1</sup> ]
$j_g$	superficial gas velocity	[m.s <sup>-1</sup> ]
$k_{ad}$	adsorption rate constant	[m.s <sup>-1</sup> ]
$k_{des}$	desorption rate constant	[mol.m <sup>-2</sup> .s <sup>-1</sup> ]
$K_L$	a constant in the Langmuir isotherm	[m <sup>3</sup> .mol <sup>-1</sup> ]
$m, n$	adjustable parameters used in eqn (14.11)	[–]
$Q$	volumetric liquid flow rate used in Fig. 14.12	[m <sup>3</sup> .s <sup>-1</sup> ]
$R$	recovery rate	[mol.m <sup>-2</sup> .s <sup>-1</sup> ]
$S$	specific surface area per unit volume of liquid	[m <sup>-1</sup> ]
$r_{32}$	Sauter mean bubble radius	[m]
$r_b$	bubble radius	[m]
$t$	time	[s]

## Greek

$\varepsilon$	volumetric liquid fraction of the foam	[–]
$\phi_s$	molar flux of the adsorbed species	[mol.m <sup>-2</sup> .s <sup>-1</sup> ]
$\Gamma$	surface excess	[mol.m <sup>-2</sup> ]
$\Gamma_\infty$	saturation surface excess	[mol.m <sup>-2</sup> ]
$\Gamma^*$	equilibrium surface excess	[mol.m <sup>-2</sup> ]
$\mu$	bulk dynamic viscosity	[Pa.s]
$\rho$	density	[kg.m <sup>-3</sup> ]
$\tau$	a dummy variable used in eqn (14.4)	[s]

## References

- [1] R. Lemlich. Adsorptive bubble separation methods: foam fractionation and allied techniques. *Ind. Eng. Chem.*, **60**: 16–29, 1968.
- [2] R. Lemlich. Prediction of changes in bubble size distribution due to interbubble gas diffusion in foam. *Ind. Eng. Chem. Fundam.*, **17**: 89–93, 1978.
- [3] P. Stevenson. Inter-bubble gas diffusion in liquid foam. *Curr. Opinion Coll. Interface Sci.*, **15**: 374–81, 2010.
- [4] S.A. Magrabi, B.Z. Dlugogorski and G.J. Jameson. Bubble size distribution and coarsening of aqueous foams. *Chem. Eng. Sci.*, **54**: 4007–22, 1999.
- [5] F.G. Gandolfo and H.L. Rosano. Interbubble gas diffusion and the stability of foams. *J. Coll. Interface Sci.*, **194**: 31–6, 1997.
- [6] A.J. Markworth. Comments on foam stability, Ostwald ripening, and grain growth. *J. Coll. Interface Sci.*, **107**: 569–71, 1985.
- [7] A. Monsalve and R.S. Schechter. The stability of foams: Dependence of observation on the bubble size distribution. *J. Coll. Interface Sci.*, **97**: 327–35, 1984.
- [8] X. Li, R. Shaw, G.M. Evans and P. Stevenson. A simple numerical solution to the ward-tordai equation for the adsorption of non-ionic surfactants. *Comput. Chem. Eng.*, **34**: 146–53, 2010.
- [9] J.R. Couper, W.R. Penney, J.R. Fair and S.M. Walas. *Chemical Process Equipment*. Gulf Professional Publishing, Boston, 2010.
- [10] S. Bhattacharjee, R. Kumar and K.S. Gandhi. Prediction of separation factor in foam separation of proteins. *Chem. Eng. Sci.*, **52**: 4625–36, 1997.

- [11] S. Bhattacharjee, R. Kumar and K.S. Gandhi. Modelling of protein mixture separation in a batch foam column. *Chem. Eng. Sci.*, **56**: 5499–510, 2001.
- [12] L. Du, V. Loha and R.D. Tanner. Modeling a protein foam fractionation process. *Appl. Biochem. Biotechnol.*, **84–6**: 1087–99, 2000.
- [13] H. Maruyama, H. Seki, A. Suzuki and I. Norio. Batch foam separation of a soluble protein. *Water Res.*, **41**: 710–18, 2007.
- [14] H. Maruyama, A. Suzuki and H. Seki. Adsorption of water-soluble proteins onto bubbles in continuous foam separation. *J. Coll. Interface Sci.*, **224**: 76–83, 2000.
- [15] N.Y. Chan, M.M. Hossain and M.S. Brooks. A preliminary study of protein recovery from mussel blanching water by a foaming process. *Chem. Eng. Process.*, **46**: 501–4, 2007.
- [16] C.E. Lockwood, P.M. Bummer and M. Jay. Purification of proteins using foam fractionation. *Pharm. Res.*, **14**: 1511–15, 1997.
- [17] F. Uraizee and G. Narsimhan. Foam fractionation of proteins and enzymes. II. Performance and modelling. *Enzyme Microb. Technol.*, **12**: 315–16, 1990.
- [18] H. Maruyama, A. Suzuki, H. Seki and N. Inoue. Enrichment in axial direction of aqueous foam in continuous foam separation. *Biochem. Eng. J.*, **30**: 253–9, 2006.
- [19] A.K. Brown, A. Kaul and J. Varley. Continuous foaming for protein recovery: Part i. Recovery of beta-casein. *Biotechnol. Bioeng.*, **62**: 278–90, 1999.
- [20] C. Crofcheck and K. Gillette. Evaluation of foam fractionation column scale-up for recovering bovine serum albumin. *Trans. ASAE*, **46**: 1759–64.
- [21] S. Aksay and G. Mazza. Optimization of protein recovery by foam separation using response surface methodology. *J. Food Eng.*, **79**: 598–606.
- [22] D. Linke, H. Zorn, B. Gerken, H. Parlar and R.G. Berger. Laccase isolation by foam fractionation—new prospects of an old process. *Enzyme Microb. Technol.*, **40**: 273–7, 2007.
- [23] B.M. Gerken, A. Nicolai, D. Linke, H. Zorn, R.G. Berger and H. Parlar. Effective enrichment and recovery of laccase c using continuous foam fractionation. *Sep. Purif. Technol.*, **49**: 291–4, 2006.
- [24] D. Linke, M. Nimtz, R.G. Berger and H. Zorn. Separation of extracellular esterases from pellet cultures of the basidiomycete *Pleurotus sapidus* by foam fractionation. *J. Am. Oil Chem. Soc.*, **86**: 437–44, 2009.
- [25] W.D. Lambert, L. Du, Y. Ma, V. Loha, V. Burapatana, A. Prokop, R.D. Tanner and N.B. Pamment. The effect of pH on the foam fractionation of  $\beta$ -glucosidase and cellulase. *Bioresour. Technol.*, **87**: 247–53, 2003.
- [26] V. Rujirawanich, S. Chavadej, J.H. O'Haver and R. Rujiravanit. Removal of trace Cd<sup>2+</sup> using continuous multistage ion foam fractionation. Part I: The effect of feed SDS/Cd molar ratio. *J. Hazard. Mater.*, **182**: 812–19, 2010.
- [27] J. Zhang, Y. Jing, Z. Wu and Q. Li. Removal of trace Cu<sup>2+</sup> from aqueous solution by foam fractionation. *Desalination*, **249**: 503–6, 2009.
- [28] Y.H. Qu, G.M. Zeng, J.H. Huang, K. Xu, Y.Y. Fang, X. Li and H.L. Liu. Recovery of surfactant SDS and Cd<sup>2+</sup> from permeate in MEUF using a continuous foam fractionator. *J. Hazard. Mater.*, **155**: 32–8, 2008.
- [29] R.D. Siy and F.D. Talbot. Foam fractionation of Zinc. *Can. J. Chem. Eng.*, **55**: 67–9, 1977.
- [30] G.C. Blasiola. *The Saltwater Aquarium Handbook*, 3rd edn. Barron's Educational Series, 2009.
- [31] P.R. Escobal. *Aquatic Systems Engineering: Devices and How They Function*, 2nd edn. Dimension Engineering Press, 2000.
- [32] E. Dotchi and M.K. Pyotr. *Foam and Foam Films: Theory, Experiment, Application*. Elsevier, Amsterdam, 1998.
- [33] X. Li, Z. Wu, Y. Zhao and Y. Wu. Effects of Span-20 and Tween-80 on foam fractionation behavior of Nisin in fermentation broth. *Chinese J. Process Eng.*, **9**: 279–83, 2009.
- [34] R.H. Hall. United States patent 3,093,551, 1963.
- [35] EFSA Panel on Food Additives, F., Processing Aids and Materials in Contact with Foods (AFC). Opinion of the scientific panel on food additives, flavourings, processing aids and materials in contact with food on a request from the commission related to the use of Nisin (e 234) as a food additive. *EFSA J.*, **4**(1): 2006.

- [36] A.F.H. Ward and L. Tordai. Time-dependence of boundary tension of solutions I. The role of diffusion in time-effects. *J. Chem. Phys.*, **14**: 453–61, 1946.
- [37] K.J. Mysels, Diffusion-controlled adsorption kinetics. General solution and some applications. *J. Phys. Chem. B*, **86**: 4648–51, 1982.
- [38] J.F. Baret, Theoretical model for an interface allowing a kinetic study of adsorption. *J. Coll. Interface Sci.*, **30**: 1–12, 1969.
- [39] S.S. Dukhin, G. Kretzschmar and R. Miller. *Dynamics of Adsorption at Liquid Interfaces: Theory, Experiment, Application*. Elsevier, Amsterdam, 1995.
- [40] C. Ybert and J.M. di Meglio. Study of protein adsorption by dynamic surface tension measurements: diffusive regime. *Langmuir*, **14**: 471–5, 1998.
- [41] J.R. Clarkson, Z.F. Cui and R.C. Darton. Protein denaturation in foam. II: Surface activity and conformational change. *J. Coll. Interface Sci.*, **215**: 333–8, 1999.
- [42] J.R. Clarkson, Z.F. Cui and R.C. Darton. Protein denaturation in foam. I: Mechanism study. *J. Coll. Interface Sci.*, **215**: 323–32, 1999.
- [43] R. Miller, V.B. Fainerman, R. Wustneck, J. Kragel and D.V. Trukhin. Characterisation of the initial period of protein adsorption by dynamic surface tension measurements using different drop techniques. *Coll. Surf. A*, **131**: 225–30, 1998.
- [44] Z. Liu, D. Wang, F. Ding and N. Yuan. On the denaturation of enzymes in the process of foam fractionation. *Bioseparation*, **7**: 167–74, 1998.
- [45] A.V. Makievski, G. Loglio, J. Krägel, R. Miller, V.B. Fainerman and A.W. Neumann. Adsorption of protein layers at the water/air interface as studied by axisymmetric drop and bubble shape analysis. *J. Phys. Chem. B*, **103**: 9557–61, 1999.
- [46] P.A. Kralchevsky, K.D. Danov, G. Broze and A. Mehreteab. Thermodynamics of ionic surfactant adsorption with account for the counterion binding: effect of salts of various valency. *Langmuir*, **15**: 2351–65, 1999.
- [47] O. Stern. The theory of the electrolytic double-layer. *Zeitschrift fuer Elektrochemie und Angewandte Physikalische Chemie*, **30**: 508–16, 1924.
- [48] R. Miller, S.S. Dukhin and G. Kretzschmar. On the theory of adsorption-kinetics of ionic surfactants at fluid interfaces. 2. Numerical-calculations of the influence of a quasiequilibrium electric double-layer. *Coll. Polym. Sci.*, **263**: 420–3, 1985.
- [49] S.S. Dukhin, R. Miller and G. Kretzschmar. On the theory of adsorption-kinetics of ionic surfactants at fluid interfaces. 1. The effect of the electric double-layer under quasi-equilibrium conditions on adsorption-kinetics. *Coll. Polym. Sci.*, **261**: 335–9, 1983.
- [50] S. Karakashev, A. Nguyen and J. Miller, Equilibrium adsorption of surfactants at the gas–liquid interface. In *Interfacial Processes and Molecular Aggregation of Surfactants*. Springer, Berlin/Heidelberg, 2008.
- [51] V.N. Sharifullin and A. Luebbert. Adsorption processes and the velocity of a bubble rising in the presence of surfactants. *Theor. Found Chem. Eng.*, **35**: 357–60, 2001.
- [52] Y. Zhang, J.B. McLaughlin and J.A. Finch. Bubble velocity profile and model of surfactant mass transfer to bubble surface. *Chem. Eng. Sci.*, **56**: 6605–16, 2001.
- [53] Y. Matsumoto, T. Uda and S. Takagi. The effect of surfactant on rising bubbles. In *Proc. IUTAM Symposium on Computational Multiphase Flow*. Springer, Dordrecht, 2006.
- [54] X. Li, G.M. Evans and P. Stevenson. Process intensification of foam fractionation by successive contraction and expansion. *Chem. Eng. Res. Des.*, **89**: 2298–308, 2011.
- [55] S.S. Dukhin, R. Miller and G. Loglio. Physico-chemical hydrodynamics of rising bubble. In *Studies in Interface Science*. Elsevier, Amsterdam, 1998.
- [56] P. Stevenson, C. Stevanov and G.J. Jameson. Liquid overflow from a column of rising aqueous froth. *Miner. Eng.*, **16**: 1045–53, 2003.
- [57] R. Lemlich. Adsorptive bubble separation methods: foam fractionation and allied techniques. *Ind. Eng. Chem.*, **60**: 16–29, 1968.
- [58] C.B. Neely, J. Eiamwat, L. Du, V. Loha, A. Prokop and R.D. Tanner. Modeling a batch foam fractionation process. *Biologia*, Bratislava, **56**: 583–9, 2001.
- [59] L. Du, V. Loha and R.D. Tanner. Modeling a protein foam fractionation process. *Appl. Biochem. Biotechnol.*, **84–6**: 1087–99, 2000.
- [60] P. Stevenson. Hydrodynamic theory of rising foam. *Miner. Eng.*, **20**: 282–9, 2007.

- [61] P. Stevenson and G.J. Jameson. Modelling continuous foam fractionation with reflux. *Chem. Eng. Process.*, **46**: 1286–91, 2007.
- [62] P. Stevenson. Remarks on the shear viscosity of surfaces stabilised with soluble surfactants. *J. Coll. Interface Sci.*, **290**: 603–6, 2005.
- [63] P. Stevenson. Dimensional analysis of foam drainage. *Chem. Eng. Sci.*, **61**: 4503–10, 2006.
- [64] G. Narsimhan. A model for unsteady state drainage of a static foam. *J. Food Eng.*, **14**: 139–65, 1991.
- [65] A. Bhakta. and E. Ruckenstein. Drainage of standing foam. *Langmuir*, **11**: 1486–92, 1995.
- [66] A. Bhakta and E. Ruckenstein. Drainage and coalescence in standing foams. *J. Coll. Interface Sci.*, **191**: 184–201, 1997.
- [67] C.E. Lockwood, S.H. Kim, P.M. Bummer and M. Jay. Scintigraphic measurement of liquid holdup in foam fractionation columns. *J. Coll. Interface Sci.*, **227**: 24–31, 2000.
- [68] S.D. Webb, R.C. Page, M. Jay and P.M. Bummer. Characterization and validation of the gamma-scintigraphic method for determining liquid holdup in foam. *Appl. Radiat. Isot.*, **57**: 243–55, 2002.
- [69] X. Li, R. Shaw and P. Stevenson. Effect of humidity on dynamic foam stability. *Int. J. Miner. Process.*, **94**: 14–19, 2010.
- [70] Z.D. Chang, H.Z. Liu and J.Y. Chen. Foam separation of tributyl phosphate from aqueous solutions. Part I: Experiment. *Sep. Purif. Technol.*, **19**: 131–6, 2000.
- [71] R.K. Singh and S.S.H. Rizvi. *Bioseparation Processes in Foods*. Marcel Dekker, New York, 1995.
- [72] P. Stevenson, X. Li and G.M. Evans. A mechanism for internal reflux in foam fractionation. *Biochem. Eng. J.*, **39**: 590–3, 2008.
- [73] A.M. Poskanzer and F.C. Goodrich. Surface viscosity of sodium dodecyl sulfate solutions with and without added dodecanol. *J. Phys. Chem.*, **79**: 2122–6, 1975.
- [74] S. Boonyasuwat, S. Chavadej, P. Malakul and J.F. Scamehorn. Anionic and cationic surfactant recovery from water using a multistage foam fractionator. *Chem. Eng. J.*, **93**: 241–52, 2003.
- [75] S. Boonyasuwat, S. Chavadej, P. Malakul and J.F. Scamehorn. Surfactant recovery from water using a multistage foam fractionator. Part I: Effects of air flow rate, foam height, feed flow rate and number of stages. *Sep. Sci. Technol.*, **40**: 1835–53, 2005.
- [76] S. Boonyasuwat, S. Chavadej, P. Malakul and J.F. Scamehorn. Surfactant recovery from water using a multistage foam fractionator: effect of surfactant type. *Sep. Sci. Technol.*, **44**: 1544–61, 2009.
- [77] R.C. Darton, S. Supino and K.J. Sweeting. Development of a multistaged foam fractionation column. *Chem. Eng. Process.*, **43**: 477–82, 2004.
- [78] K. Schügerl. Recovery of proteins and microorganisms from cultivation media by foam flotation. In *Advances in Biochemical Engineering/Biotechnology*. Springer-Verlag, Berlin/Heidelberg, 2000.
- [79] R.A. Leonard and J.D. Blacyki. Multistage bubble fractionator. *Ind. Eng. Chem. Process. Des. Dev.*, **17**: 358–61, 1978.
- [80] G. Morgan and U. Wiesmann. Single and multistage foam fractionation of rinse water with alkyl ethoxylate surfactants. *Sep. Sci. Technol.*, **36**: 2247–63, 2001.
- [81] K. Yamagiwa, M. Iwabuchi, H. Tsubomizu, M. Yoshida and A. Ohkawa. Effect of external reflux on foam fractionation of poly(vinyl alcohol). *J. Chem. Eng. Jpn*, **34**: 126–31, 2001.
- [82] S.L. de Lucena, E.A. Miranda and C.C. Santana. The effect of external reflux on the foam fractionation of proteins. *Appl. Biochem. Biotechnol.*, **57/58**: 57–65, 1996.
- [83] P.J. Martin, H.M. Dutton, J.B. Winterburn, S. Baker and A.B. Russell. Foam fractionation with reflux. *Chem. Eng. Sci.*, **65**: 3825–35, 2010.
- [84] Y. Bando, T. Kuze and T. Sugimoto. Development of a bubble column for foam separation. *Korean J. Chem. Eng.*, **17**: 597–9, 2000.
- [85] H. Tsubomizu, R. Horikoshi, K. Yamagiwa, K. Takahashi, M. Yoshida and A. Ohkawa. Effect of perforated plate on concentration of poly(vinyl alcohol) by foam fractionation with external reflux. *J. Chem. Eng. Jpn*, **36**: 1107–10, 2003.
- [86] G.A. Aguayo and R. Lemlich. Countercurrent foam fractionation at high rates of throughput by means of perforated plate columns. *Ind. Eng. Chem. Process. Des. Dev.*, **13**: 153–9, 1974.

- [87] J.E. Dickinson, D. Laskovski, P. Stevenson and K.P. Galvin. Enhanced foam drainage using parallel inclined channels in a single-stage foam fractionation column. *Chem. Eng. Sci.*, **65**: 2481–90, 2010.
- [88] H.M.L.J. Joosten and M. Nuñez. Adsorption of Nisin and enterocin 4 to polypropylene and glass surfaces and its prevention by tween 80. *Lett. Appl. Microbiol.*, **21**: 389–92, 1995.
- [89] X. Li, X. Wang, G.M. Evans and P. Stevenson. Foam flowing vertically upwards in pipes through expansions and contractions. *Int. J. Multiphase Flow*, **37**: 802–11, 2011.

# 15

## Gas–Liquid Mass Transfer in Foam

*Paul Stevenson*

### 15.1 Introduction

The absorption of gases into liquids is an important industrial process, not least for the oxygenation of liquid in aerobic reactors and the stripping of contaminants from gaseous streams. In order to maximise the rate of gas absorption, one process challenge is often to try to increase the interfacial area between liquid and gas phases without excessive consumption of energy. In addition, for some biological processes, the cells have a propensity to become disrupted by high shear stresses, thereby placing an upper limit upon the shear stress that can be experienced in the column.

Charpentier [1] surveyed the literature for values of interfacial area per unit column volume (specific surface area),  $a$ , for a variety of gas–liquid contacting devices (see Table 15.1). Shah and Mahalingham [2] reported values of  $a$  as high as  $2645\text{ m}^{-1}$  for their own experiments on gas–liquid foam, which corresponded to a column with a Sauter mean bubble diameter of 2.2 mm. It is demonstrated that much greater values of  $a$  can be achieved in foam devices compared to other processes, making the foam contactor potentially a candidate for a variety of process applications. The only device that can come close to the values that are possible with foam is the packed bed, but higher values of  $a$  in packed beds are achievable only with specialist packing such as Pall Rings or Intalox Saddles. Because the parameter  $a$  is of fundamental importance in gas–liquid mass transfer operations, foam contactors are immediately seen to be promising candidates for gas–liquid mass transfer unit operations because of their superior specific gas–liquid surface area, and the absence of the cost of packing materials.

**Table 15.1** Values of specific interfacial area,  $a$ , liquid side mass transfer coefficient  $k_L$ , and volumetric mass transfer coefficient,  $k_L a$ , for a variety of gas–liquid contacting devices, after [1].

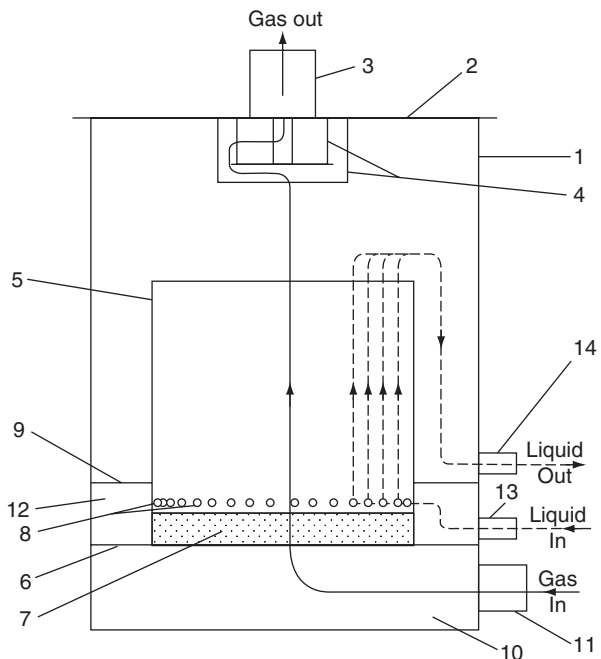
Reactor type	$a$ ( $\text{m}^2/\text{m}^3$ )	$k_L$ ( $\text{m.s}^{-1}$ ) $\times 10^3$	$k_L a$ ( $\text{s}^{-1}$ ) $\times 10^3$
Spray column	10–100	0.07–0.15	0.7–15
Bubble column	50–600	0.1–0.4	5–240
Packed bubble column	50–300	0.1–0.4	5–120
Mechanically agitated bubble reactor	100–2000	0.03–0.4	3–800
Sieve plate column	100–200	0.1–2	10–400
Bubble cap plate column	100–400	0.1–0.4	10–200
Counter-current packed column	10–350	0.04–0.2	4–70
Cocurrent packed column	10–1700	0.04–0.6	5–1,020
Foam column investigated in [20]	2100–3200	—	Up to 180

Source: After [1].

One application is to use foam columns for the supply of oxygen to aerobic bioreactors. Cell growth, product formation and substrate removal are all dependent upon oxygen availability, so oxygenation is of primary importance in bioreactor design. The oxygen demand of most bioreactors does not exceed that which can be provided by conventional gas–liquid contactors (Table 15.1). However, broths in bioreactors can exhibit high viscosity, so the energy requirements to achieve oxygenation can be great if conventional contacting devices are employed. Achieving sufficient oxygenation into viscous broths within conventional gas–liquid contactors means that the liquid may have to experience high shear stress, and this can cause cell damage. Thus, the use of foam in aerobic bioreactors not only can reduce energy consumption, but may offer benefits with respect to cell integrity.

Other reported benefits of foam contactors are a moderate pressure gradient in the column and a long contact time between gas and liquid phases [3], and therefore there are non-biological applications for the use of foam columns as gas absorbers and reactors, especially for stripping operations (i.e. the removal of contaminants from gaseous streams), the oxygenation of sodium sulphide and the adsorption of carbon dioxide into a slurry containing calcium hydroxide. All of these processes are discussed in this chapter. However, the efficacy of foam contactors was questioned by Valentin [4], who asserted that, because of the relatively low volume of interstitial liquid within a foam and the relatively static liquid films, the liquid would soon become saturated with absorbing gas, so mass transfer and equilibrium considerations are of importance when assessing the potential efficacy of a foam gas–liquid contactor.

Gas absorption into the interstitial liquid is related to the process of foam fractionation that is the subject of Chapter 14. In the latter process, mass (i.e. amphipathic molecules) is transferred from the bulk of the interstitial liquid to adsorb onto the gas–liquid interface, whereas in gas absorption there is a transfer of mass from the gas phase to absorb across the interface into the bulk of the liquid phase. Foam fractionation has been the subject of significant research but has failed to gain an important role in the process industries that is commensurate with its potential. In Chapter 8, it is argued that this disappointment has been caused, at least in part, by a lack of a mechanistic understanding of the behaviour of columns of foam upon which the foam fractionation process relies. Precisely the same comments can be made in the context of gas absorption into foam. Previous studies have



- |  |                               |
|--|-------------------------------|
| 1. Body.                               | 8. Liquid distributing holes. |
| 2. Lid.                                | 9. Barrier supporting ring.   |
| 3. Gas outlet.                         | 10. Gas chamber.              |
| 4. Droplet separator.                  | 11. Gas inlet.                |
| 5. Barrier.                            | 12. Liquid chamber.           |
| 6. Supporting ring for diffuser plate. | 13. Liquid inlet.             |
| 7. Ceramic diffuser plate.             | 14. Liquid outlet.            |

**Fig. 15.1** The gas-absorption device of Helsby and Birt [5].

measured the efficacy of a foam absorber for one particular application or another, without providing a general mechanistic application that describes the nature of the foam itself. That said, the development of another related process, froth flotation in which the mass transfer is due to the attachment of hydrophobic particles to gas–liquid interfaces, might have been retarded by a lack of a mechanistic understanding of the behaviour of foam columns, but it has not prevented it from becoming an important unit operation in the mineral processing industry over the past century.

The earliest experimental investigation of the absorption of gas into the liquid in a foam was due to Helsby and Birt [5], who absorbed lean mixtures of CO<sub>2</sub> in air into foam made of aqueous solutions of monoethanolamine (MEA) and sodium hydroxide. Absorption of CO<sub>2</sub> into MEA is of particular current interest because it is a regenerative process used widely in carbon capture operations; see [6] for a review of CO<sub>2</sub> capture technologies. Helsby and Birt's drawing of their device is shown in Fig. 15.1. The gas was continuously sparged to the liquid via a ceramic diffuser plate, which caused a foam to rise inside a

barrier (i.e. the central portion of the device) in which the gas effectively contacted the liquid, enabling transfer of CO<sub>2</sub>. At the top of the barrier, the foam collapsed, enabling the disengaged gas to exit the column at the top, and the liquid to drop down the outer annulus to discharge. This type of arrangement will be known hereafter as an overflowing pneumatic foam. (A pneumatic foam is one that is caused to rise up a column due to continuous sparging of gas bubbles into a pool at the bottom of the column.) They found that mass transfer in a foam column was more efficient than in a comparable tower packed with 1 inch Raschig Rings, an observation that has given great encouragement to subsequent researchers.

From the observations of Helsby and Birt, it is clear that mass transfer in gas–liquid foam is reliant upon an interplay between the hydrodynamic state of the foam and mass transfer rate. Thus, this chapter begins with a description of various types of devices that have been used for mass transfer, i.e.

1. Non-overflowing pneumatic foam
2. Overflowing pneumatic foam
3. Waldhof Fermentor
4. Induced air devices
5. Horizontal foam contacting

This is followed by a calculation of specific surface area in foam, a brief explanation of how an understanding of pneumatic foam, more fully described in Chapter 8, can illuminate the use of foams for mass transfer operations and an exposition of relevant mass transfer issues. Finally, a model of mass transfer in an overflowing pneumatic foam that incorporates recent advances in understanding of the hydrodynamics of such systems is given.

## **15.2 Non-overflowing Pneumatic Foam Devices**

One of the earliest studies of gas–liquid mass transfer in foam, published in 1956 by Metzner and Brown [7], investigated the desorption of CO<sub>2</sub> from out of aqueous solution into a gas stream. Although this specific system is of limited practical interest, their general observations of mass transfer in foam are of considerable interest for the stripping of contaminants into an aqueous phase. Metzner and Brown employed a spray-controlled non-overflowing pneumatic foam operating in semi-batch mode, and a similar generic device operating as a gas stripper is shown schematically in Fig. 15.2a.

A non-overflowing pneumatic foam is one that is created by constant sparging of bubbles to a liquid pool at the bottom of the column such that a foam is formed above. However, the stability of the foam is such that it does not reach the top of the column, thereby enabling it to overflow, but instead reaches a particular height in the column. At this height, all of the bubbles on the free surface burst, enabling the gas to continuously disengage from the foam. Metzner and Brown exploited such a non-overflowing pneumatic foam, to which liquid was sprayed from the freeboard of the column to the top of the foam, as demonstrated schematically in Fig. 15.2a. This spray served two purposes: (i) the transfer of momentum from the spray to the free surface of the foam encouraged film rupture on the surface, and therefore maintain the height of the foam layer, and (ii) served as a source of fresh liquid so that mass transfer could progress. Metzner and Brown conducted experiments on two different types of spray devices, but did not find a significant difference. Pertinent findings of their experimental campaign included:

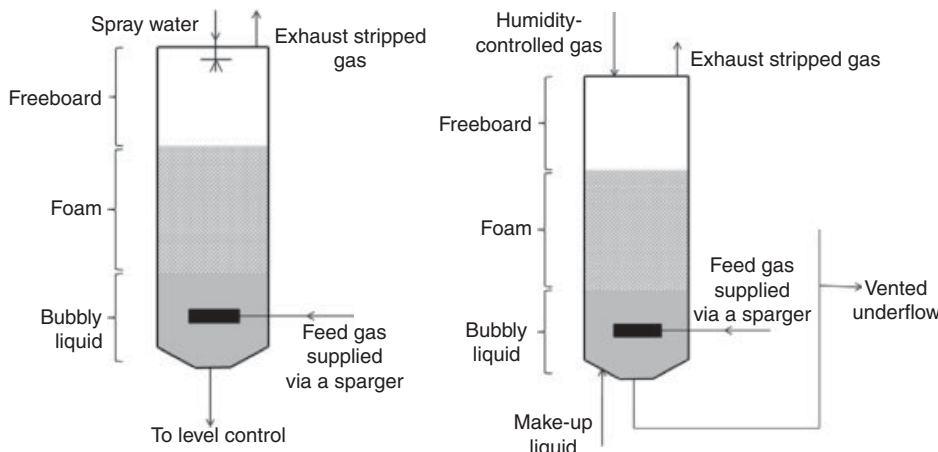


**Fig. 15.2** Schematic representations of non-overflowing pneumatic foam contacting devices. (a) A batch system with spray to the free surface and (b) a continuous system featuring humidity control and vented underflow level control.

1. A strong decrease in mass transfer rates because of interfacial resistance caused by the adsorbed detergent ('Glim') used to stabilise the foam. Such interfacial resistance is discussed in Section 15.9.2.
2. The foam density (i.e. liquid fraction) decreased with increasing gas rate during the 'quiet' (i.e. plug flow) regime, whence it then increased with further gas rate as plug flow was lost. This decreased density with increasing gas rate must have been due to bubble size effects.
3. The achievable mass transfer rate (expressed as height of a transfer unit, HTU, see Section 15.9.2) was comparable in the foam column to a column packed with 2 inch Raschig Rings, but not as good as a bubble column. The latter was thought to be due to resistance to mass transfer caused by the detergent used to stabilise the foam.
4. The HTU first decreased, and then increased, with increasing gas rate, and this was thought to be due to the parallel changes in liquid fraction with increasing gas rate.

Metzner and Brown concluded that foam-contacting devices such as their own had utility when viscous liquids, highly foaming liquids or slurries were being processed, whereas in all other cases conventional absorption columns should be preferred.

Whereas Metzner and Brown investigated desorption of species, Brander *et al.* [8] used a similar spray foam column as a stripper to remove contaminants (hydrogen sulphide, formaldehyde and acetaldehyde) from air into reactive foams, and significant success was reported. They concluded that a reactant within the interstitial liquid was a particularly useful method of increasing mass transfer because the consumption of absorbed species increases the driving force for mass transfer. Similarly, renewal of interstitial liquid was also important, and this could be enhanced by rupture of surface lamellae by the foam spray. It was concluded that the type of surfactant used did not influence performance, but that 'channelling' in foam could compromise the utility of the device.

Another study to employ a similar spray column was due to Workman and Calvert [9], who designed column internals made up of a series of vertical tubes that enhanced the

liquid fraction and stability of the foam. This caused an increase in the foam height, and therefore enhanced the residence time of the gas within the foam, which improved mass transfer efficiency. However, the use of column internals has not since been replicated, and enhanced foam stability can be achieved via humidity control, as described below.

An extended programme of research into non-overflowing pneumatic foam that had no liquid spray to the free surface was conducted at the Indian Institute of Science, Bangalore, in the 1980s. A column was constructed that continuously fed liquid to the bubbly pool at the bottom of the column, and liquid was simultaneously removed from the pool to maintain inventory within the column. This device was used to strip lean CO<sub>2</sub> from air [10], to oxidise sodium sulphate both without catalysis [11] and in the presence of activated carbon particles [12], and for the carbonation of lime slurries to precipitate calcium carbonate [13]. The latter two studies are notable for their use of a solid phase that is entrained within the interstitial liquid of the foam, with the last study finding that almost all of the reaction occurred in the foam phase rather than the ‘storage section’ (i.e. the bubbly liquid pool). All of these studies gave models employing careful mass balances on the absorbing and reacting species (with further modelling given in [14]) but, crucially, did not benefit from a hydrodynamic description of the foam. The latest incarnation of the model [15] still does not employ a hydrodynamic model of the system and considers dry polyhedral foams.

The control of the bubbly liquid–foam interface, and therefore liquid inventory, in both types of non-overflowing pneumatic foam devices (i.e. both with and without spray) could be more effective by employing the ‘vented underflow’ arrangement that is commonly used in flotation columns and laboratory studies thereon. The vented underflow is shown schematically in Fig. 15.2b. It consists of a tube leading from the bubbly liquid section to some elevated position where a T-piece is placed in the tube. The vertical leg of the ‘T’ forms the vent to atmosphere, whereas the horizontal leg provides a path for efflux of liquid. By changing the elevation of the T-piece, the hydrostatic pressure at the bottom of the column is manipulated and this governs the liquid inventory in the column, with sufficient outflow of liquid autogenously ensured to maintain this inventory.

In addition, much of the study on non-overflowing pneumatic foam for gas absorption operations has been made of foam stability and how it governs foam height. Indeed, special column internals have been designed to enhance foam stability [9]. However, it has recently been demonstrated that the stability, and therefore height, of a non-overflowing foam is highly dependent upon the humidity gradient within the freeboard, and this can be manipulated by supplying moist or dry air to the top of the column [16], as shown schematically in Fig. 15.2b. This recent observation should be amenable to exploitation for control of stripping operations in columns of non-overflowing pneumatic foam.

### 15.3 Overflowing Pneumatic Foam Devices

In the section above, devices that employ *non-overflowing* pneumatic foam were described. A further class of devices are those that employ an *overflowing* pneumatic foam. The foam continuously rises up the column and discharges from the column by either an inverted U-tube or via a weir into a froth ‘launder’. Overflowing pneumatic foams are found in column flotation [17] in which the particles that are attached to the gas–liquid interfaces in

a foam are recovered at the top of a column into a launder, or in foam fractionation in which the foam is typically removed in an inverted U-tube [18]. See [19] for an overview of foam recovery devices.

Brander *et al.* [8] used non-overflowing pneumatic foam with great success to strip contaminants from air. However, in applications in which the process fluid is the liquid phase (i.e. the unit is being used as an absorber), for instance, in the oxygenation of biological broths, it is more convenient to have a continuous flow of the liquid phase, and this can be engendered by continuously removing liquid overflow from a column. My own background is in froth flotation and foam fractionation, and it was surprising to me that any gas–liquid mass transfer operations employed anything but an overflowing pneumatic foam. However, the earliest studies on overflowing foams appear to be from the 1980s, which was three decades after non-overflowing pneumatic foams were first studied.

Wolinski and Postings [20] investigated the digestion of sewage sludge at a UK wastewater works. When oxygen was sparged to the sludge via a venturi, limited foam formed at the surface of the sludge. However, oxygen absorption efficiency (i.e. the proportion of the supplied oxygen utilised in thermophilic oxidative digestion) was only 50–85%, which was still much higher than in other studies. However, when air was sparged to the digester in place of the oxygen there was greatly increased production of foam onto the top of the sludge, which meant that liquid inventory had to be reduced to prevent periodic spillage. Crucially, once this had been done, it was found that oxygen absorption efficiency was 100%. This was attributed to the foam layer improving mass transfer from the liquid to the gas phase. Clearly the use of air meant that the gas rate became sufficient to support a foam, whereas, when oxygen was used, the amount of gas available to create the foam was limited; no frother was added to aid foam production. Samples were taken as a function of foam height, and it was shown that significant mass transfer was indeed occurring in the foam layer, providing startling evidence for the utility of foam for enhanced oxygenation of sludge. The foam was continuously removed from the digester as a side-draw as indicated in the schematic diagram given in Fig. 15.3. Downstream of the side-draw was an auxiliary column for the disengagement of gas from the sludge, and therefore collapse of the foam. The evident success of this work to aerate sewage sludge prompted Perry [21] to investigate the use of other foaming methods to digest the waste from a chicken processing plant (see Section 5).

Shah and Mahalingham [2] measured gas absorption rates with subsequent reaction in an overflowing pneumatic for two systems: in one, the absorption of CO<sub>2</sub> and reaction with sodium hydroxide, the reaction rate was almost instantaneous, and the other reaction rate, the reaction of CO<sub>2</sub> with sodium carbonate–bicarbonate solution, was slower. They proposed an extensive model from the perspective of mass transfer, but, again, they did not benefit from a hydrodynamic description of the foam. They asserted that interfacial resistance to mass transfer was significant when the reaction rate was rapid, but was insignificant when it was slow. Subsequent work by Stangle and Mahalingham [3] extended their device to operate as a three-phase slurry reactor.

One of the most extensive research programmes on gas–liquid mass transfer in pneumatic foam is the doctoral thesis from the University of Newcastle, Australia, of David Perry [21]. Unfortunately nothing of Perry's work has been published in primary archival journals. Perry investigated overflowing pneumatic foams in a device that was reminiscent of a column flotation unit in that (i) the interface between bubbly liquid and foam was controlled by use of a vented underflow (described above), (ii) the foam overflowed into a

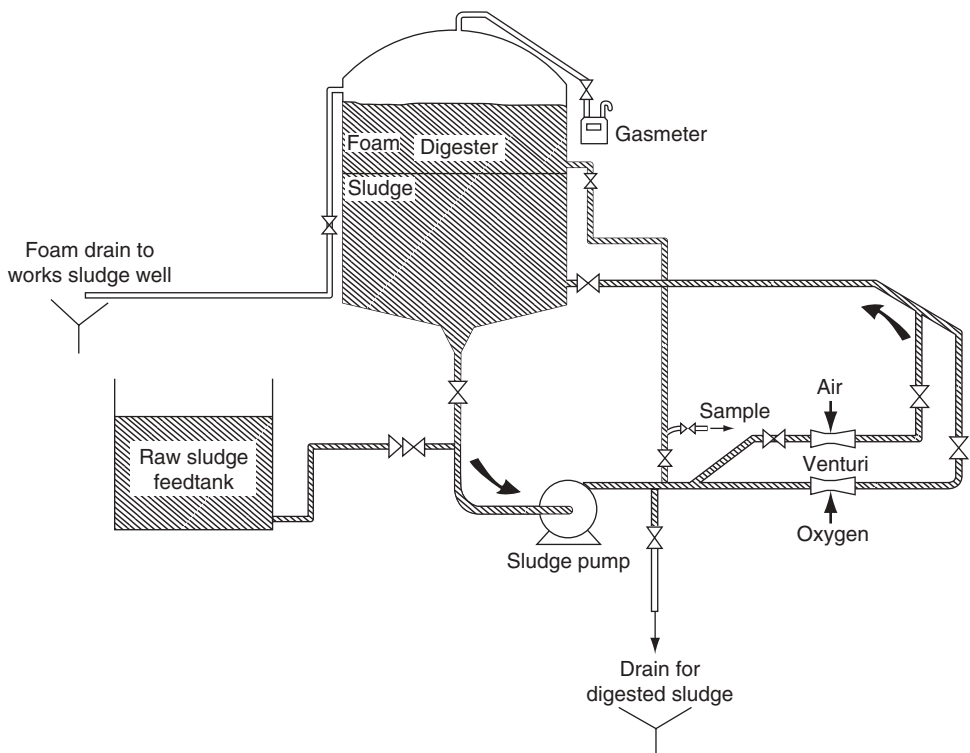


**Fig. 15.3** Schematic diagram of the sludge aeration unit of Wolinski and Postings [19].

froth launder vessel, and (iii) a device to spray liquid onto the top of the foam was included, as is common to supply washwater to the top of flotation columns. That Perry's design included features commonly found in flotation devices was unsurprising since he carried out his work in a lab notable for its flotation research. Perry measured the rate of absorption of carbon dioxide gas into a pneumatic foam formed from a sodium carbonate-bicarbonate buffer solution stabilised by a polyglycol frother. By adding washwater to the free surface of the foam, a wetter and more stable foam was created that exhibited a high liquid fraction and therefore avoided film saturation and created greater liquid convection past the gas–liquid surfaces, thereby enhancing the mass transfer coefficient. A specific surface area of up to  $3,200 \text{ m}^{-1}$  was obtained. The method of calculating the mass transfer coefficient that was suggested by Perry is discussed in Section 15.5.

## 15.4 The Waldhof Fermentor

The Waldhof Fermentor for producing fodder yeast was first reported by Saeman [22] after industrial surveys of Germany at the end of the Second World War uncovered the device at Zellstofffabrik Waldhof. The fermentor employed a rotary air dispersal device at the bottom

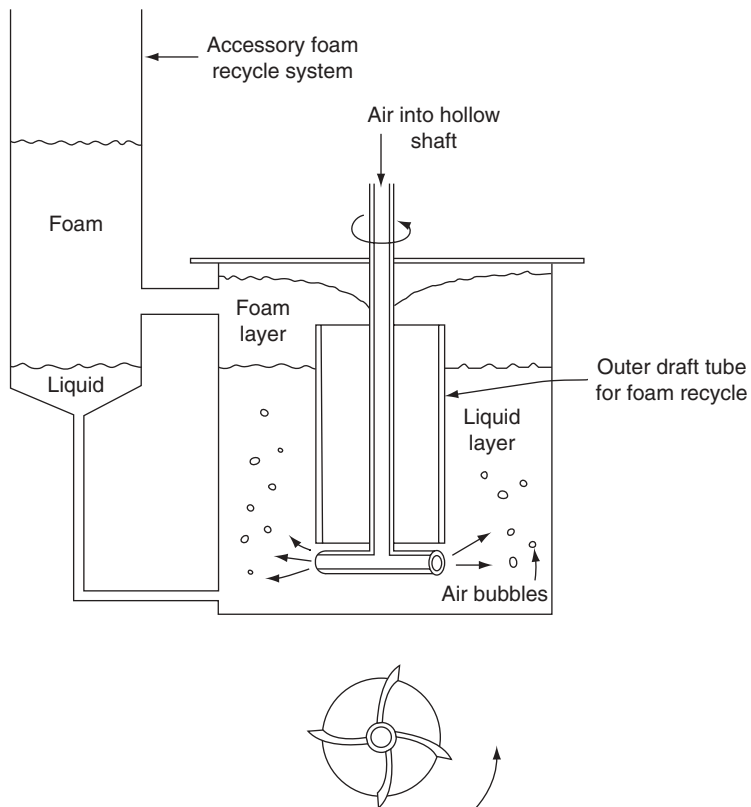


**Fig. 15.4** Schematic representation of the Waldhof-type fermentor of Tsao and Cramer [24].

of the unit that was mounted on a hollow shaft through which air was induced by the rotation. The device was reported to reach a steady state whence the foam product stream was removed in an overflow tube; the product was then subjected to mild agitation or low dosage of antifoam to break the foam. Subsequently the Waldhof Fermentor was used to produce penicillin [23], where significant foaming was reported to be detrimental to performance, which could be improved by employing antifoams.

Tsao and Cramer [24] designed a Waldhof-type fermentor, shown schematically in Fig. 15.4, in which the foam left via a side-draw into a secondary column in which the gas disengaged from the liquid by foam collapse, whence the liquid could be recycled back to the fermentor. They utilised their device to aerate aqueous food wastes with a view to disposal. They found that the foam layer actively enhanced the rate of oxygen absorption in the fermentor. This, presumably, was because of enhanced gas-liquid surface area. However, since the work of Tsao and Cramer, there appears to have been no further investigation. The work of Perry [21], described in Section 15.5, is related in that it utilises a different type of induced-air device in the aerobic fermentation of waste from a chicken processing factory.

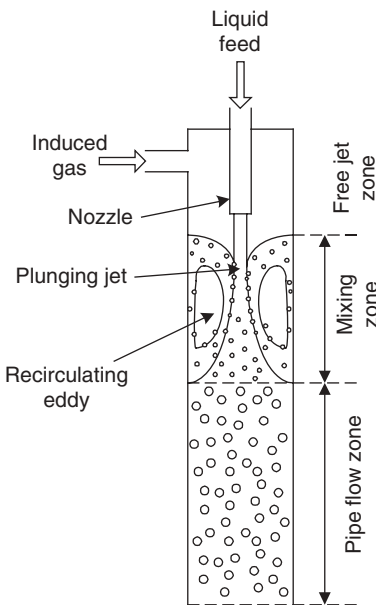


**Fig. 15.5** Perry's [21] schematic representation of the plunging jet.

It is noted that the Waldhof Fermentor is reminiscent of the Denver Flotation Cell, currently marketed by Metso Minerals, which is a bench-scale flotation device that introduces gas down a hollow shaft too, as well as some common designs of plant-scale mechanical flotation cells.

## 15.5 Induced Air Methods

The Waldhof Fermentor of Tsao and Cramer induced air into the liquid phase through a hollow rotating shaft rather than requiring external air compression followed by sparging to the column. Another method of inducing air into the liquid phase is through the use of a confined plunging jet [25]. This mechanism (shown schematically in Fig. 15.5), which forms the basis of the Jameson flotation cell [26], operates by entraining gas into a free jet, whence this plunges into a gas–liquid mixture (the mixing zone), which causes the break-up of bubbles. Such devices are characterised by having high mixing and mass transfer. The bubbles then pass down a ‘pipe flow zone’ to a ‘disengagement zone’, which is made up of a bubbly liquid below an overflowing pneumatic foam. The plunging jet column produces very small bubbles in an environment of high mixing, both of which are conducive to gas–liquid mass transfer.

These characteristics were harnessed by Perry, who designed a plunging jet unit, shown in Fig. 15.6, for the aerobic autothermal thermophilic aerobic digestion (ATAD) of the waste sludge from a chicken processing factory. The unit exploited a foam layer to enhance oxygenation rates into the sludge.

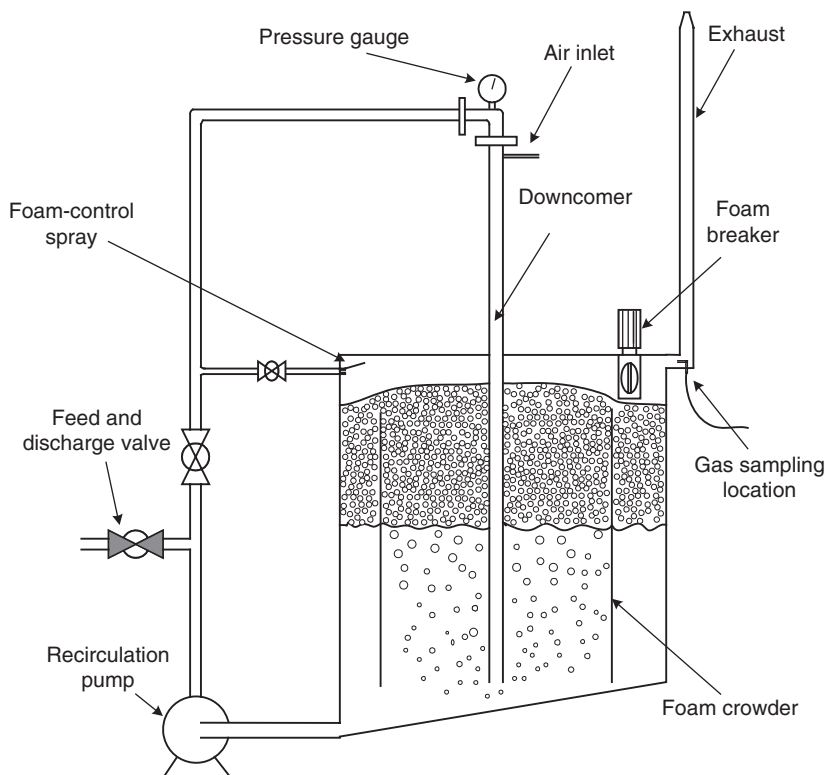


**Fig. 15.6** Perry's [21] schematic representation of his design of a foam autothermal thermophilic aerobic digester.

High oxygen demand occurred during the thermophilic aerobic digestion of the high strength waste due to the rapid rates of biological oxidation that manifest at elevated temperatures. The combination of rapid mixing and small bubble size due to the plunging jet and enhanced interfacial area due to the foam layer helped satisfy the oxygen demand. The presence of foam was found to be beneficial to reactor operation. The foam was produced in a 'crowder' draft tube that enabled internal recirculation within the digester, and the foam was prevented from overflowing the unit by application of a control spray. Proper foam management increased the oxygen transfer efficiency of the ATAD reactors without increasing the energy consumption. Conditions of high solids concentration and high temperature stimulated foam formation in the reactor and resulted in higher rates of biological activity. Unfortunately, Perry's study has not been published beyond his doctoral thesis.

## 15.6 Horizontal Foam Contacting

All of the devices described above have employed vertical pneumatic foams. However, Weissman and Calvert [27] employed a horizontal tube for gas–liquid contacting and investigated rates of desorption of carbon dioxide and ammonia from surfactant-containing

water into air. As the foam progressed, liquid drained towards the invert of the horizontal tube, which drained from the device at discrete intervals so that the foam became progressively drier. A cross-flow model was used to estimate the desorption behaviour of the system. The *raison d'être* of the horizontal contacting design is curious, because it actively promotes segregation of liquid from the gas phase as it drains, which seems to be counterproductive in terms of interphase mass transfer. This horizontal device has failed to gain any traction, and no similar studies appear to have been conducted.

## 15.7 Calculation of Specific Interfacial Area in Foam

Now that various designs of foam gas–liquid contactor have been presented, it is appropriate to discuss some theoretical aspects of the process. Consider a gas–liquid foam of volumetric liquid fraction  $\varepsilon$ . Foams rarely exhibit a uniform bubble size distribution, but, because we are interested in surface area per unit volume, the appropriate one-parameter descriptor of the bubble size distribution is the Sauter mean bubble radius,  $r_{32}$ , which in discrete form is given by:

$$r_{32} = \frac{\sum_{i=1}^N r_{b,i}^3}{\sum_{i=1}^N r_{b,i}^2} \quad (15.1)$$

where  $r_b$  is the radius of bubble  $i$  in a total population of  $N$  bubbles, and, in continuous form:

$$r_{32} = \frac{\int_0^\infty r_b^3 f(r_b) dr_b}{\int_0^\infty r_b^2 f(r_b) dr_b} \quad (15.2)$$

Since the volume of gas in unit volume of the foam is  $(1 - \varepsilon)$ , then:

$$a = \frac{4\pi r_{32}^2 (1 - \varepsilon)}{\frac{4}{3}\pi r_{32}^3} = \frac{3(1 - \varepsilon)}{r_{32}} \quad (15.3)$$

This result was given elsewhere [3]. Shah and Mahalingham [2] reported a maximum specific surface area of  $2645 \text{ m}^{-1}$  whereas in an unpublished doctoral study, Perry [21] has reported values of up to  $3220 \text{ m}^{-1}$  and the early work of Metzner and Brown reported  $1260 \text{ ft}^{-1}$  ( $= 4134 \text{ m}^{-1}$ ). However, significantly higher specific surface area is possible if the bubbles are smaller. For instance, in continuous production by cavitation, bubbles of mean diameter of around  $40 \mu\text{m}$  are possible [28]. In a foam of wetness fraction of 10%, say, these would give a large specific surface area of  $135,000 \text{ m}^{-1}$ .

## 15.8 Hydrodynamics of Pneumatic Foam

Despite the extensive modelling work on foam gas–liquid contactors, very briefly described in the above section, no study had the advantage of being based upon a realistic hydrodynamic model of the gas–liquid foam itself. A pneumatic foam, more fully described in Chapter 8, is one that is established by the continuous sparging of gas bubbles to a pool of solution such that a gas–liquid foam is formed in a column above the pool of bubbly liquid. In an *overflowing pneumatic foam*, such as those found in froth flotation columns and in the gas–liquid contacting devices described in Section 15.3, foam rises through the column and is discharged from the top of column via an inverted ‘U’ or into a ‘froth launder’. A recent theory [29] gives the liquid fraction and liquid flux in such foams, and these are parameters upon which gas–liquid mass transfer is dependent. Very briefly the foam changes its liquid fraction to maximise the liquid flux in the column, and this is crucially dependent upon the size distribution of bubbles at the top.

A *non-overflowing pneumatic foam*, upon which the device described in Section 15.2 is designed, is one in which the foam collapses in the column before it can reach the top. Therefore the foam attains an equilibrium foam height despite continuous sparging with gas bubbles. The gas disengages from the foam at its free surface as all of the bubbles collapse. A mechanistic description of non-overflowing pneumatic foam exists elsewhere [30].

However, non-overflowing pneumatic foam with liquid sprayed to the free surface has been proposed for stripping contaminants from gaseous streams [7–9], so it is pertinent in this context to briefly describe the hydrodynamics of such columns, as such a treatment has not before been given. The nomenclature and concepts used in Chapter 8 will be adopted, and the interested reader is encouraged to first consult there.

Consider a foam made up of bubbles of radius  $r_b$  with an interstitial liquid of density  $\rho$  and dynamic viscosity of  $\mu$ . Gas is sparged at a superficial velocity of  $j_g$  to the bottom of the column, and liquid is sprayed to the top at a superficial velocity of  $j_s$ . The acceleration due to gravity is  $g$ . In any pneumatic foam in the absence of significant global capillary effects, the liquid superficial velocity up the column,  $j_f$ , can be written as:

$$j_f = \frac{\varepsilon j_g}{1 - \varepsilon} - \frac{\rho g r_b^2}{\mu} m \varepsilon^n \quad (15.4)$$

In a non-overflowing pneumatic foam with no liquid spray to the surface, the net flux is zero, and thus the relationship between bubble radius and liquid fraction is determined through the solution of:

$$0 = \frac{\varepsilon j_g}{1 - \varepsilon} - \frac{\rho g r_b^2}{\mu} m \varepsilon^n \quad (15.5)$$

However, if liquid is sprayed to the column, and the foam remains in a non-overflowing state, the net liquid flux (upwards) in the column is  $-j_s$  since all of the applied liquid must

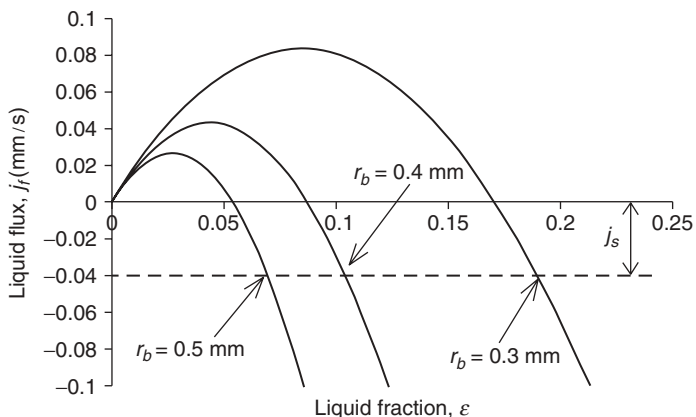


**Fig. 15.7** Calculation of the hydrodynamic condition of a non-overflowing pneumatic flow with surface spray.

travel downwards. Thus, the relationship between bubble radius and liquid fraction can be determined through the solution of:

$$-j_s = \frac{\varepsilon j_g}{1-\varepsilon} - \frac{\rho g r_b^2}{\mu} m \varepsilon^n \quad (15.6)$$

It is recognised that, in the special case of  $n = 2$ , this is cubic and can be solved analytically by employing Cardano's method. The relationship between liquid flux and liquid fraction can be demonstrated graphically as well; see Fig. 15.7. The curves represent eqn (15.4) for three bubble radii of 0.3, 0.4 and 0.5 mm. Foam drainage parameters of  $m = 0.016$  and  $n = 2$  are adopted, and the interstitial liquid is assumed to have viscosity and density of 1 mPa.s and 1000 kg.m<sup>-3</sup> respectively, with the foam being sparged at a gas superficial velocity of 2 mm.s<sup>-1</sup>. The hydrodynamic condition relevant to each bubble size is given by the intersection of the curve with the dotted line representing the liquid flux caused by spray to the column (i.e.  $-0.04 \text{ mm.s}^{-1}$ ).

It is necessary to state that drainage parameters are a function of the type and concentration of surfactant/detergent used to stabilise the foam. If water with no surfactant is sprayed to the top of the column, as was done by the early work of Metzner and Brown [7], the drainage parameters will change with height and time. Note also that design of the spraying mechanism must ensure that sufficient momentum is transferred to the free surface of the foam to cause bursting of the bubbles on the surface.

It is worth mentioning at this juncture that Helsby and Birt [5] cautioned to avoid 'channelling', whereby gas could bypass substantive contact with the liquid phase as it travelled through the foam. One mechanism of gas-bypassing is the gross bubble flow that occurs after the foam has attained its maximum liquid fraction, as explained in Chapter 8.

## 15.9 Mass Transfer and Equilibrium Considerations

It is beyond the scope of this chapter to present a full treatment of gas–liquid mass transfer. The interested reader is directed to the authoritative monograph of Danckwerts [31] for such a treatment. This section instead serves as an introduction to particular aspects of gas–liquid mass transfer that are relevant to foam contactors. In particular, considerations of simultaneous mass transfer and liquid-side reaction are not tackled herein.

### 15.9.1 Gas–Liquid Equilibrium

The driving force for mass transfer from gas to liquid (or *vice versa*) is a concentration gradient in the vicinity of the interface. However, this driving force for mass transfer of a species disappears when the partial pressure of the species in the gas phase is in equilibrium with the concentration of the liquid phase. The equilibrium is conveniently expressed as a Henry’s law relationship, i.e.

$$C^* = HP \quad (15.7)$$

where  $C^*$  is the equilibrium concentration ( $\text{mol} \cdot \text{m}^{-3}$ ) in the liquid phase of the transferring species,  $P$  is the partial pressure of the species in the gas phase, and  $H$  is Henry’s law coefficient which, in this form, is given in units of  $\text{mol} \cdot \text{m}^{-3} \cdot \text{Pa}^{-1}$ . For carbon dioxide in water at pH 7, for example, the value of  $H$  is approximately  $3.5 \times 10^{-4} \text{ mol} \cdot \text{m}^{-3} \cdot \text{Pa}^{-1}$  [32] and increases, for  $\text{CO}_2$ , with increasing pH. Of course, if a chemical reaction consumes the absorbing species, the driving force for mass transfer will be enhanced [2, 21].

### 15.9.2 Rate of Mass Transfer

There are three approaches to gas–liquid mass transfer worth considering in the context of gas–liquid mass transfer in foam. The first is Whitman’s two-film theory [33], which takes into account a gas-side and a liquid-side resistance to mass transfer. For very soluble gases, the mass transfer is gas-side controlled (i.e. it is the rate of transport from the bulk of the gas to the interface that governs the overall rate). For such highly soluble gases, a foam gas–liquid contactor is hardly needed to perform a specific absorption duty. However, if the gas is moderately insoluble, such as is typical in a gas–liquid absorption operation, the assumption that the mass transfer is liquid-side controlled is justified. Thus, the molar flux through the interface,  $J$ , is given by

$$J = k_L(C^* - C) \quad (15.8)$$

where  $k_L$  is the gas-side mass transfer coefficient,  $C^*$  is the liquid concentration at equilibrium with the gas phase and  $C$  is the concentration within the bulk of the liquid.

Because Whitman’s approach is strictly valid only if the gas- and liquid-side films are stagnant, it underpredicts mass transfer rate when the process is enhanced by turbulence.

Higbie [34] modelled this turbulent enhancement in his ‘penetration’ model by considering that finite ‘packets’ of liquid were convected to the surface from the bulk by eddies, whence transfer occurred to them. Danckwerts [35] refined this model by proposing that these packets had a distributed residence time at the surface during which transfer could take place. Danckwerts’ model has utility for mass transfer to and from bubbles in swarms and, for all but the very smallest of bubbles, the use of Whitman would be inappropriate for estimating the behaviour of such swarms. However, in typical gas–liquid foams, the Reynolds number of the flow in the Plateau border through which most liquid flows is so small [36] that very little turbulent mixing would be anticipated. Thus the use of Whitman’s two-film theory for estimating mass transfer rate in the foam is appropriate, although in the bubbly pool beneath the foam, it is probably better to adopt the theory of Danckwerts.

The question arises as to whether surface-active species adsorbed to the gas–liquid interfaces, such as are necessary to stabilise the foam, resist mass transfer. The evidence on this question is conflicting. Cullen and Davidson [37] showed that a pure adsorbed layer of the soluble ionic surfactant sodium dodecyl sulphate provided no resistance to mass transfer but when impure surfactants were used, the mass transfer rate fell by up to 25%. However, Metzner and Brown [7] found that increasing the concentration of an undefined type of detergent increased the interfacial resistance to mass transfer. The detergent used was, presumably, chemically impure, although there is not sufficient evidence to conclude that it was the mixed nature of the adsorption layer that caused the interfacial resistance. Further, Shah and Mahalingham [2] showed that interfacial resistance was significant when the rate of consumption of absorbent due to reaction in the liquid phase was high, but insignificant when the reaction rate was low. This observation is consistent with the interfacial resistance being significant when the absorption is gas-side controlled, but no causal link can be deduced from the data. It is clear that a definitive experimental campaign is needed to assess the contribution of adsorbed surfactants to surface resistance to mass transfer.

Metzner and Brown [7] invoked the HTU (height of a theoretical unit) to describe the performance of their foam gas–liquid contactor, which is a concept historically adopted to describe the performance of packed beds [38]. It gives the notional height of a slice of the column out of which the liquid travelling downwards is at equilibrium with the gas moving upwards, and has utility for estimations of the performance of counter-current gas–liquid contacting operations. The more rapid the mass transfer, the lower the HTU.

### 15.9.3 Estimation of Mass Transfer Coefficient

Liquid flow past a surface generally enhances mass transfer rate if the process is diffusion-controlled. It can be shown via dimensional analysis that the mass transfer coefficient from an isolated solid sphere, non-dimensionalised as a Sherwood number,  $Sh$ ,

$$Sh = \frac{k_L d}{D} \quad (15.9)$$

where  $k_L$  is the fluid film mass transfer coefficient,  $d$  is the diameter of the sphere (or, in this context, the diameter of the bubbles) and  $D$  is the coefficient of molecular diffusion of the transferring species in the liquid phase, can be expressed as a function of the Reynolds number,  $Re$ :

$$Re = \frac{\rho Vd}{\mu} \quad (15.10)$$

where  $V$  is the absolute slip velocity between the solid and fluid phases and  $\rho$  and  $\mu$  are the density and dynamic viscosity of the fluid phase, respectively, and the Schmidt number,  $Sc$ :

$$Sc = \frac{\mu}{\rho D} \quad (15.11)$$

For  $Re < 1$ , Levich [39] analytically derived:

$$Sh = 0.66Re^{1/3}Sc^{1/3}, \quad (15.12)$$

For  $Re > 1$ , Frössling, cited in Tosun [40], gave the empirical expression:

$$Sh = 2 + 0.56Re^{1/2}Sc^{1/3} \quad (15.13)$$

The above two correlations are for the mass transfer from single spheres. The correlation of Wakao and Kaguei [41] for the mass transfer coefficient for a closely packed bed of solid spheres is given by:

$$Sh = 2 + 1.1Re^{0.6}Sc^{1/3} \quad (15.14)$$

where it is valid for  $Re < 3000$ , which is a condition met in all practical foams.

Perry [21] has shown that Wakao and Kaguei's correlation is, in fact, very effective at estimating the mass transfer coefficient in a foam bed, and is much better than Frössling's correlation. Thus, it is preliminarily recommended that Wakao and Kaguei's correlation is adopted for estimation of the mass transfer coefficient, although it is recognised that Perry's work has not appeared in an a primary archival journal. Of course, *a priori* estimations of the mass transfer coefficient can only be made with knowledge of the slip velocity  $V$ , and the hydrodynamic theory of rising foam [28] provides a facility for just this. By using the drainage expression incorporated in eqn (15.4), the slip velocity within the foam is given by:

$$V = \frac{\rho gd^2}{4\mu} m \varepsilon^{n-1} \quad (15.15)$$

which is used to compute the Reynolds number and hence the liquid-side mass transfer coefficient via the Sherwood number. It is worth noting that the plunging jet device described in Section 15.5 experiences such high degrees of turbulent mixing in the 'mixing zone' that eqn (15.14) could well greatly underestimate the value of the mass transfer coefficient.

## 15.10 Towards an Integrated Model of Foam Gas–Liquid Contactors

Perry's [21] work was significant in that it established an effective method of calculating the liquid side mass transfer coefficient in a pneumatic foam and, in conjunction with hydrodynamic descriptions of the foam has the potential to provide a design method for

foam gas–liquid contactors. However, it should be stressed that there is no integrated study that has measured both the hydrodynamic characteristics of the foam and the mass transfer behaviour of a foam contactor, and the following methodological approaches should be considered as no more than conjecture.

An example of how the hydrodynamic theory of rising foam can be used in conjunction with mass-transfer considerations is in estimating the maximum rate at which a gas can be stripped by a pneumatic foam. The maximum fraction of absorbed gas is achieved when the liquid leaving the top of the column is in equilibrium with the gas, and the rate of liquid efflux from the top of the column is maximised. The hydrodynamic theory of rising foam holds that the maximum liquid fraction such a foam can attain,  $\varepsilon^*$ , is:

$$\varepsilon^* = \frac{n-1}{n+1} \quad (15.16)$$

and this occurs when the gas superficial velocity is:

$$j_g^* = \frac{\rho g r_b^2}{\mu} m n \left( \frac{2}{n+1} \right)^2 \left( \frac{n-1}{n+1} \right)^{n-1} \quad (15.17)$$

Substituting eqns (15.16) and (15.17) into the expression for liquid flux eqn (15.4), the maximum liquid flux in an overflowing pneumatic foam, assuming that  $r_b$  is constant up the column, is:

$$j_f^* = \frac{\rho g r_b^2}{\mu} m \left( \frac{n-1}{n+1} \right)^{n+1} \quad (15.18)$$

The maximum concentration of absorbate is that which is at equilibrium (eqn 15.7) with the gas phase. Thus the molar flow rate per column cross-sectional area of absorbate transferred to the liquid phase from the gas,  $J_A$ , is:

$$J_A = C^* j_f^* = P H \frac{\rho g r_b^2}{\mu} m \left( \frac{n-1}{n+1} \right)^{n+1} \quad (15.19)$$

Thus eqn (15.19) gives the theoretical maximum stripping capacity of an overflowing pneumatic foam, but it cannot be stressed strongly enough that this has not been experimentally verified.

The theory of rising foam can also be utilised in an illustrative example of how the concentration of an absorbate species in the interstitial liquid might be calculated in an overflowing pneumatic foam operating as a stripper. Consider an elemental slice of foam of depth  $\delta x$  with a vertical normal direction, shown schematically in Fig. 15.8. At steady state, the liquid flux in a pneumatic foam,  $j_f$ , does not vary with height, but the concentration of the absorbate in the interstitial liquid is allowed to vary with height. Writing a mass balance on the absorbate species gives:

$$j_f C + k_L a (C^* - C) \delta x = j_f \left( C + \frac{\partial C}{\partial x} \delta x \right) \quad (15.20)$$

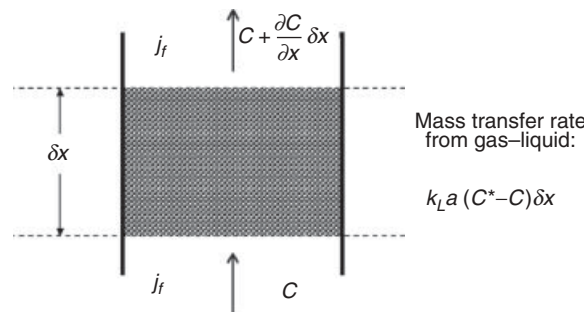


**Fig. 15.8** Mass balance on an elemental slice of foam.

which simplifies to:

$$\frac{dC}{dx} = \frac{k_L a (C^* - C)}{j_f} \quad (15.21)$$

If the concentration at the bottom of the column is denoted by  $C_0$ , eqn (15.21) may be integrated to give the concentration,  $C$ , at any position in the column,  $x$ :

$$C = C^* \left( 1 - \exp \left[ \frac{-k_L a x}{j_f} \right] \right) + C_0 \exp \left[ \frac{-k_L a x}{j_f} \right] \quad (15.22)$$

According to eqn (15.22), at large  $x$  (i.e. at the top of a very deep foam)  $C$  approaches the equilibrium concentration  $C^*$ , as expected. Estimates of both the mass transfer coefficient and liquid flux can be made via the hydrodynamic theory of rising foam [28]. Note that if the absorbate is consumed by reaction in the liquid phase, this can be readily accounted for by including a reaction term in eqn (15.20).

The modelling explained in this section is not intended to be a comprehensive description of mass transfer in practical pneumatic foam. Practically, the bubble size distribution in a foam can change with height due to Ostwald ripening and coalescence, and this has an impact on the liquid fraction and liquid flux in the column. Thus, the modelling given here is merely intended to be indicative of how the theory of rising foam [29] might be used in conjunction with mass transfer considerations to build a mechanistic description of the performance of foam gas-liquid contactors.

## 15.11 Discussion and Future Directions

Previous research [20] has shown that values of volumetric liquid-side mass transfer coefficient,  $k_L a$ , of up to  $0.18 \text{ s}^{-1}$  are possible in an overflowing pneumatic foam gas-liquid contactor. By reference to Table 15.1, it is seen that this does not surpass values for other types of gas-liquid contactor. Indeed, Charpentier [1] claims a value of up to  $1.02 \text{ s}^{-1}$  for a concurrent packed column. However, by making foams with smaller bubbles than those

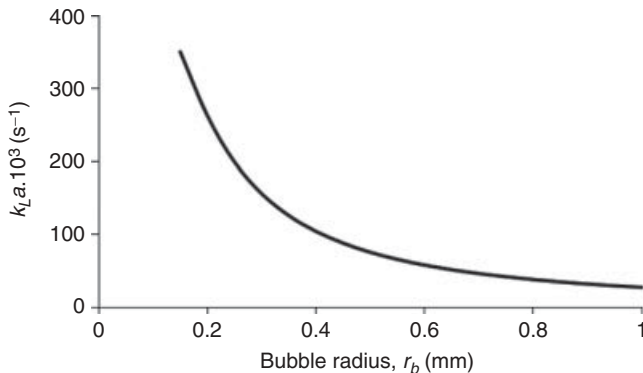


**Fig. 15.9** Predicted volumetric liquid-side mass transfer coefficient versus bubble radius assuming  $m = 0.016$ ,  $n = 2$ ,  $\rho = 1,000 \text{ kg.m}^{-3}$ ,  $\mu = 1 \text{ mPa.s}$ ,  $D = 10^{-9} \text{ m}^2.\text{s}^{-1}$ ,  $j_g = 2 \text{ mm.s}^{-1}$ ,  $g = 9.81 \text{ m.s}^{-2}$ .

used in previous studies, a significantly higher value of specific surface area,  $a$ , can be achieved by creating a foam made up of very small bubbles. It is therefore appropriate to explore how the value of  $k_L$  might change for very small bubbles.

For a single bubble rising in isolation, the slip velocity between gas and liquid phases diminishes as the size reduces. Thus by eqn (15.12) it is seen that, because the Reynolds number becomes smaller by the combined reduction of both velocity and length scale, so does the mass transfer coefficient via the Sherwood number. However, for a pneumatic foam bubble, there isn't a corresponding result. Reduction in bubble size has a detrimental impact on the value of the Reynolds number. But, since liquid fraction increases and bubble size decreases, the foam becomes wetter, and this acts to increase the slip velocity and therefore enhance the Reynolds number. As a case study, the values of  $k_L a$  were calculated as a function of bubble radius using the methods suggested in Section 15.9 assuming typical parameters given in the caption to Fig. 15.9. It can be seen that the effect of liquid fraction increasing with decreasing bubble size is dominant, and the predicted volumetric liquid-side mass transfer coefficients increase to levels that are beginning to approach the maximum claimed for any type of device by Charpentier [1].

Despite some 60 years of research, there is no systematic design method for foam gas–liquid contactors. However, recent advances in the understanding of pneumatic foam [29] combined with a promising method of estimating the mass transfer coefficient in foam [41] can direct future experimental researches and process development. Reducing the bubble size is likely to increase values of  $k_L a$ . Thus, foam contactors have the potential for still more excellent mass transfer rates as the bubble size decreases. The air-induced apparatus of Perry [21], described in Section 15.5, appears to be able to form small bubbles for relatively low energy expenditure, and the efficacy of this device has been demonstrated at pilot scale on an industrial waste sludge. Moreover, the plunging jet feature of this device has the potential for very high values of  $k_L a$  in the mixing zone.

Just like foam fractionation, foam gas–liquid contacting is a relatively immature technology that has failed to achieve its potential in the process industries. However, with the combination of increased mechanistic understanding of the process, and exploitation of process design that is commonplace in the mature technology of froth flotation, it is hoped

that foam columns for gas–liquid mass transfer will become an established alternative to other competing devices.

## Nomenclature

### Roman

$a$	Interfacial area per unit volume	[m <sup>-1</sup> ]
$C$	Concentration of absorbate in the bulk liquid	[mol.m <sup>-3</sup> ]
$C^*$	Equilibrium concentration of absorbate at the interface	[mol.m <sup>-3</sup> ]
$d$	Bubble diameter	[m]
$D$	Coefficient of molecular dispersion	[m <sup>2</sup> .s <sup>-1</sup> ]
$g$	Acceleration due to gravity	[m.s <sup>-2</sup> ]
$H$	Henry's law constant	[mol.m <sup>-3</sup> .Pa <sup>-1</sup> ]
$j_f$	Superficial liquid velocity up the column	[m.s <sup>-1</sup> ]
$j_f^*$	Maximum superficial liquid velocity up the column	[m.s <sup>-1</sup> ]
$j_g$	Superficial gas velocity	[m.s <sup>-1</sup> ]
$j_g^*$	Maximum superficial gas velocity	[m.s <sup>-1</sup> ]
$j_s$	Superficial liquid velocity of spray to the free surface	[m.s <sup>-1</sup> ]
$J$	Molar flux	[mol.m <sup>-2</sup> .s <sup>-1</sup> ]
$J_A$	Molar absorbance rate per unit column cross-sectional area	[mol.m <sup>-2</sup> .s <sup>-1</sup> ]
$k_L$	Liquid-side film mass transfer coefficient	[m.s <sup>-1</sup> ]
$m$	Dimensionless pre-factor in the foam drainage term	[–]
$n$	Dimensionless index in the foam drainage term	[–]
$P$	Partial gas pressure	[Pa]
$r_b$	Bubble radius	[m]
$r_{32}$	Sauter mean bubble radius	[m]
$Re$	Reynolds number defined in eqn (15.10)	[–]
$Sc$	Schmidt number defined in eqn (15.11)	[–]
$Sh$	Sherwood number defined in eqn (15.9)	[–]
$V$	Absolute slip velocity between gas and liquid phases	[m.s <sup>-1</sup> ]
$x$	Vertical dimension in the froth measured positive upwards	[m]

### Greek

$\varepsilon$	Volumetric liquid fraction in the foam	[–]
$\varepsilon^*$	Maximum volumetric liquid fraction in the foam	[–]
$\mu$	Interstitial liquid dynamic viscosity	[Pa.s]
$\rho$	Interstitial liquid density	[kg.m <sup>-3</sup> ]

## Acknowledgements

Thanks are due to Dr David Perry for discussions and the provision of his doctoral thesis. Mr Xueliang (Bruce) Li is thanked for reviewing a draft of this chapter and making valuable suggestions.

## References

- [1] J.C. Charpentier. Mass transfer in gas liquid absorbers and reactors. *Adv. Chem. Eng.*, **11**: 3–133, 1981.
- [2] P.S. Shah and R. Mahalingham. Mass transfer with chemical reaction in liquid foam reactors. *AICHE J.*, **30**: 924–4, 1984.
- [3] G.C. Stangle and R. Mahalingham. Mass transfer with chemical reaction in a three-phase foam slurry reactor. *AICHE J.*, **36**: 117–25, 1990.
- [4] F.H.H. Valentin. *Absorption in Gas-Liquid Dispersions: Some Aspects of Bubble Technology*. E. and F.N. Spon, London, 1967.
- [5] F.W. Helsby and D.C.P. Birt. Foam as a medium for gas absorption. *J. Appl. Chem.*, **5**: 347–52, 1955.
- [6] N. MacDowell, N. Florin, A. Buchard, J. Hallett, A. Galindo, G. Jackson, C.S. Adjiman, C.K. Williams, N. Shah and P. Fennell. An overview of CO<sub>2</sub> capture technologies. *Energy Environ. Sci.*, in press, 2011.
- [7] A.B. Metzner and L.F. Brown. Mass transfer in foams. *Ind. Eng. Chem.*, **48**: 2040–5, 1956.
- [8] S.M. Brander, G.I. Johansson, B.G. Kronberg and P.J. Stenius. Reactive foams for air purification. *Environ. Sci. Technol.*, **18**: 224–30, 1984.
- [9] W.L. Workman and S. Calvert. Mass transfer in supported froths. *AICHE J.*, **12**: 867–76, 1966.
- [10] J. Biswas and R. Kumar. Mass transfer with chemical reaction in a foam bed contactor. *Chem. Eng. Sci.*, **36**: 1547–56, 1981.
- [11] A.N. Bhaskarwar and R. Kumar. Oxidation of sodium sulphide in a foam bed contactor. *Chem. Eng. Sci.*, **39**: 1393–9, 1984.
- [12] A.N. Bhaskarwar and R. Kumar. Oxidation of sodium sulphide in the presence of fine activated carbon particles in a foam bed contactor. *Chem. Eng. Sci.*, **41**: 399–404, 1986.
- [13] R.K. Asolekar, P.K. Deshpande and R. Kumar. A model for a foam-bed slurry reactor. *AICHE J.*, **34**: 150–5, 1988.
- [14] A.N. Bhaskarwar, D. Desai and R. Kumar. General model of a foam bed reactor. *Chem. Eng. Sci.*, **45**: 1151–9, 1990.
- [15] S.K. Jana and A.N. Bhaskarwar. Modeling gas absorption accompanied by chemical reaction in bubble column and foam-bed slurry reactors. *Chem. Eng. Sci.*, **65**: 3649–59, 2010.
- [16] X. Li, R. Shaw and P. Stevenson. Effect of humidity on dynamic foam stability. *Int. J. Miner. Process.*, **94**: 14–19, 2010.
- [17] J.A. Finch and G.S. Dobby. *Column Flotation*. Pergamon Press, London, 1990.
- [18] R. Lemlich. Adsorptive bubble separation methods: foam fractionation and allied techniques. *Ind. Eng. Chem.*, **60**: 16–29, 1968.
- [19] X. Li, X. Wang, G.M. Evans and P. Stevenson. Foam flowing vertically upwards in pipes through expansions and contractions. *Int. J. Multiphase Flow*, **37**: 802–11, 2011.
- [20] W.K. Wolinski and I. Postings. The effect of foam on sewage sludge aeration. *Effluent Water Treatment J.*, **24**: 49–51, 1984.
- [21] D.C. Perry. Gas absorption in foam reactors. PhD thesis, University of Newcastle, Australia, 2003.
- [22] J.F. Saeman. Aerobic fermentor with good foam-control properties. *Anal. Chem.*, **19**: 913–15, 1947.
- [23] W.E. Brown and W.H. Peterson. Penicillin fermentations in a Waldhof-type fermentor. *Ind. Eng. Chem.*, **42**: 1823–6, 1950.
- [24] G.T. Tsao and W.D. Cramer. Waldhof type fermenters in disposal of food wastes. *Chem. Eng. Prog. Symp. Series*, **67**: 158–63, 1971.
- [25] G.M. Evans and G.J. Jameson. Hydrodynamics of a plunging liquid jet bubble column. *Trans. Inst. Chem. Eng. A*, **73**: 679–84, 1995.
- [26] R. Clayton, G.J. Jameson and E.V. Manlapig. The development and application of the Jameson Cell. *Miner. Eng.*, **4**: 925–33, 1991.
- [27] E.Y. Weissman and S. Calvert. Mass transfer in horizontally moving stable aqueous foams. *AICHE J.*, **11**: 356–63, 1965.

- [28] H.J.B. Couto, D.G. Nunes, R. Neumann and S.C.A. Franca. Micro-bubble size distribution measurements by laser diffraction technique. *Miner. Eng.*, **22**: 330–5, 2009.
- [29] P. Stevenson. Hydrodynamic theory of rising foam. *Miner. Eng.*, **20**: 282–9, 2007.
- [30] P. Stevenson, A.J. Sederman, M.D. Mantle, X. Li and L.F. Gladden. Measurement of bubble size distribution in a gas-liquid foam using pulsed-field gradient nuclear magnetic resonance. *J. Coll. Interface Sci.*, **352**: 114–20, 2010.
- [31] P.V. Danckwerts. *Gas–Liquid Reactions*. McGraw-Hill, New York, 1970.
- [32] R. Sander. *Compilation of Henry's Law Constants for Inorganic and Organic Species of Potential Importance in Environmental Chemistry* (Version 3), 1999. <http://www.henrys-law.org>
- [33] W.K. Lewis and W.G. Whitman. Principles of gas absorption. *Ind. Eng. Chem.*, **16**: 1215–20, 1924.
- [34] R. Higbie. The rate of absorption of a pure gas into a still liquid during short periods of exposure. *Trans. AIChE*, **35**: 36–60, 1935.
- [35] P.V. Danckwerts. Significance of liquid-film coefficients in gas absorption. *Ind. Eng. Chem.*, **43**: 1460–7, 1951.
- [36] P. Stevenson and X. Li. A viscous-inertial model of foam drainage. *Chem. Eng. Res. Des.*, **88**: 928–35, 2010.
- [37] E.J. Cullen and J.F. Davidson. The effect of surface active agents on the rate of absorption of carbon dioxide by water. *Chem. Eng. Sci.*, **6**: 49–56, 1951.
- [38] J.F. Richardson, J.H. Harker, J.R. Backhurst and J.M. Coulson. *Coulson and Richardson's Chemical Engineering. Vol. 2, Particle Technology and Separation Processes*. Butterworth, Oxford, 2002.
- [39] V.G. Levich. *Physiochemical Hydrodynamics*. Prentice-Hall, Englewood Cliffs, NJ, 1962.
- [40] I. Tosun. *Modelling in Transport Phenomena: A Conceptual Approach*. Elsevier Science, Amsterdam, 2002.
- [41] N. Wakao and S. Kaguei. *Heat and Mass Transfer in Packed Beds*. Gordon and Breach Science, London, 1982.

# 16

## Foams in Glass Manufacturing

*Laurent Pilon*

### 16.1 Introduction

The glass manufacturing industry provides products critical to a wide range of applications, including (i) container glass for consumer products, (ii) flat glass for automotive and buildings, (iii) fiberglass for thermal insulation, roofing, and reinforced composite materials, and (iv) specialty glass such as liquid crystal displays, optical communication, and lighting, to name a few [1]. Container glass represents more than 65% of the mass of glass produced worldwide [2]. In 2009, the US glass industry produced about 20 millions tons of glass or 20% of the global production and employed about 91,000 people for industry revenues of \$21.6 billion [3]. During the past two decades, business competition and economic challenges have forced glass manufacturers worldwide to increase productivity and product quality. They have also faced ever more stringent regulations for combustion-generated pollutant emissions.

Soda-lime-silica glass, also known as soda-lime glass, is the most common type of glass used for containers, lighting devices, and windows for buildings and automotive applications [4, 5]. It typically contains 60–75 wt%  $\text{SiO}_2$ , 12–18 wt%  $\text{Na}_2\text{O}$ , and 5–12 wt%  $\text{CaO}$ . Borosilicate glass is another common type of glass used for its chemical durability and its low thermal expansion coefficient as glassware in the chemical industry and laboratories, as flat panel display, and as cookware [4]. Their typical composition contains 70–80 wt%  $\text{SiO}_2$ , 7–13 wt%  $\text{B}_2\text{O}_3$ , 4–8 wt%  $\text{Na}_2\text{O}$  and  $\text{K}_2\text{O}$ , and 2–7 wt%  $\text{Al}_2\text{O}_3$  [4]. In addition, E-glasses are used in fiberglass for thermal and acoustic insulation for buildings as well as for textile and reinforced plastics. They are aluminosilicate glass with typical composition of 52–6 wt%

$\text{SiO}_2$ , 16–25 wt%  $\text{CaO}$ , 12–16 wt%  $\text{Al}_2\text{O}_3$ , 5–13 wt%  $\text{B}_2\text{O}_3$  and 1 wt%  $\text{Na}_2\text{O}$  and  $\text{K}_2\text{O}$  [6,7]. Finally, vitreous silica is made only of  $\text{SiO}_2$  and used for optical fiber, optical components, and in high temperature applications due to its large melting temperature [8].

The cost and quality of nearly all commercial glass products, as well as pollutant emissions associated with their production, are determined by the performance of the glass melting and delivery systems. Their performance depends, for a large part, on efficient heat transfer from the hot combustion space to the raw materials and to the glassmelt [9]. Heat transfer by thermal radiation accounts for the major fraction of the energy required for the fusion and melting of the raw materials [10].

Unfortunately, for numerous reasons discussed in this chapter, glass foam typically covers at least one-third of the molten glass surface [11]. Bubbles contained in the foam act as a collection of scatterers that reflect and backscatter part of the incident radiation coming from the combustion space [12–17]. Therefore, glass foam constitutes a major resistance to radiative heat transfer from the combustion space to the raw material and to the glassmelt [12, 13]. This, in turn, negatively affects the glass quality, energy efficiency, pollutant emission, and furnace lifetime [18].

### 16.1.1 The Glass Melting Process

Figure 16.1 shows a flow diagram of the glass manufacturing process from the mixing and conditioning of the raw material to the final glass product. The so-called batch is the raw material consisting of silica sand, sodium carbonate (soda ash), calcium carbonate (lime), cullets (broken glass), and various compounds including potassium carbonate (potash), boron compounds, nitrates, alumina, stabilizer, and coloring agents depending on the desired final glass composition [4, 19]. Refining agents are also added to the batch to help remove small gas bubbles. The batch is melted and the resulting molten glass is refined to remove potential bubbles and ensure homogenization, i.e., the dissolution and uniform distribution of all components [4, 20]. The refined glass then flows to the forehearth where it is conditioned before being formed and annealed into the final glass products. The forehearth consists of a cooling and a conditioning zone. The cooling zone ensures controlled cooling and uniform temperature of the molten glass, while the conditioning zone reheats and sometimes stirs the glassmelt.

Glass melting tanks commonly used in the glass industry include combustion-type furnaces and cold-top electric melters [2, 21, 22]. They represent a major capital investment. Combustion-type furnaces feature a waist or a submerged throat connecting the melting to the conditioning regions [23]. For example, float glass furnaces are often waist-type and cross-fired regenerative furnaces [1, 24]. The bottom of the tank is often stepped [24]. This type of furnace is fairly large and used to produce large quantity of glass products (100–1000 tons/day) such as flat glass sheets [4]. Submerged throat furnaces are used, for example, to produce glassware, TV panels, and container glass [1]. They consist of a melting tank and a refiner (or working end) connected by a channel also called a throat. Figure 16.2 shows a schematic of a typical submerged throat glass melting tank consisting of the combustion space, the glassmelt, and the refractory walls including the ceiling of the furnace called the crown.

The combustion space features large turbulent flames providing thermal energy necessary to melt the glass batch and to refine the molten glass. Combustion-type furnaces may differ in terms of (i) fuel (e.g., natural gas or pulverized coal), (ii) oxidizer (air or commercial

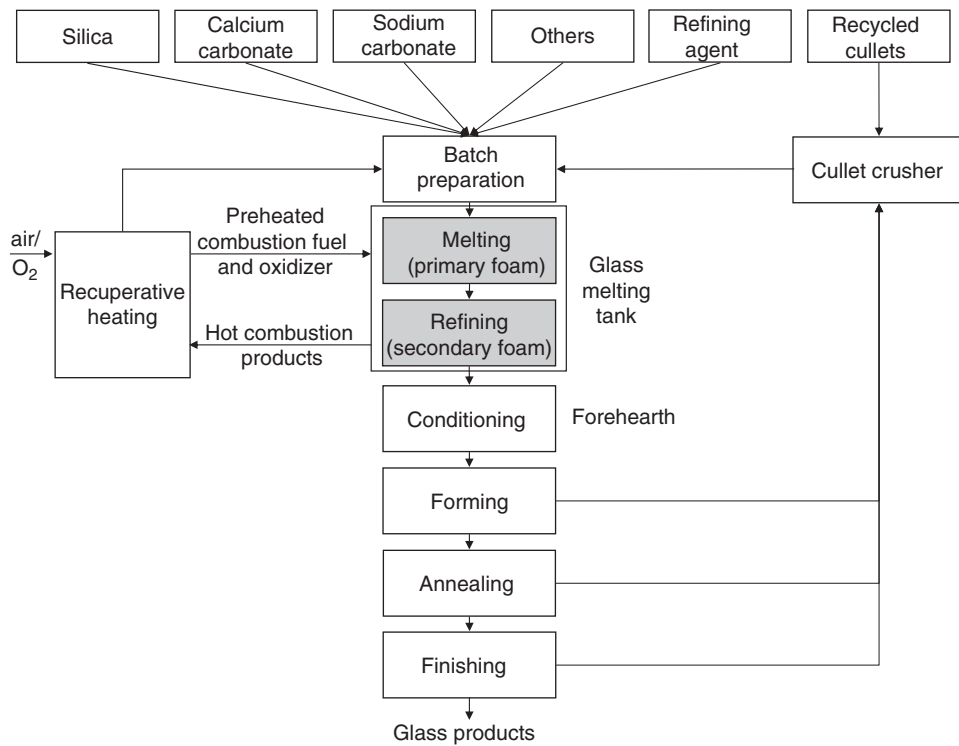


**Fig. 16.1** Diagram of the glass manufacturing process. Grey boxes indicate where glass foams are observed.

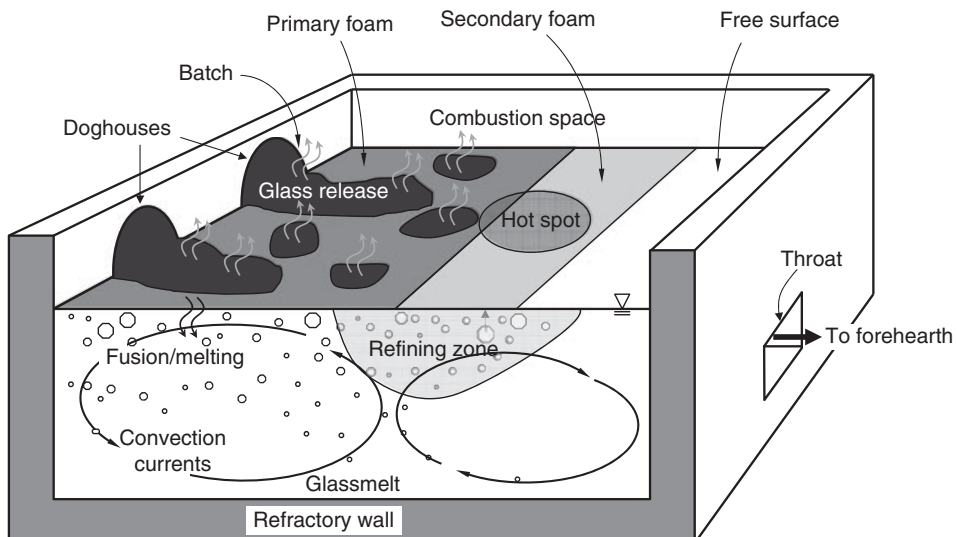


**Fig. 16.2** Schematic of a submerged throat glass melting tank showing primary and secondary foams [9, 25].



**Fig. 16.3** Photographs of the combustion space and the surface of the glassmelt in glass melting furnaces, transverse flames with batch logs, secondary foams, and free melt surface. Reproduced by permission of Research Association of the German Glass Industry (HVG) © 2010.

grade oxygen), (iii) flame direction (e.g., downward or sideways), and (iv) shape (e.g., cylindrical or flat). Heat transfer from the combustion space to the batch and to the glassmelt drives convection currents within the glassmelt to increase the retention time of the glass in order to achieve complete melting of raw materials, homogenization of the melt, and removal of gas bubbles from the melt prior to pulling it out for final processing.

The refractory walls thermally insulate the glassmelt. The furnace crown reradiates the thermal radiation from the flames to the floating batch and to the glassmelt surface. The batch can be introduced into the furnace either through inlet ports called doghouses from the back wall in the longitudinal direction (as shown in Fig. 16.2) or from the sides by using different types of chargers [4]. Due to density differences, the batch floats at the surface of the glassmelt where it spreads carried by the convection currents. The resulting batch coverage can assume many different shapes, from a uniform blanket to dispersed batch logs floating at the surface of the glassmelt. Figure 16.3 shows photographs taken in an actual industrial furnace featuring batch logs floating over the molten glass and so-called primary foam between the batch logs along with the so-called secondary foam and the glass free surface.

Glass melting tanks can be equipped with electric boosters or bubblers to enhance temperature uniformity and refining of the glassmelt. On the one hand, electric boosters provide additional energy for melting batch by passing an electrical current between electrodes inserted in the glassmelt and resulting in Joule heating [27]. On the other hand, bubblers inject large gas bubbles in the glassmelt in order to modify the convection

currents and further increase the residence time of the molten glass [28]. It also enhances heat transfer and glassmelt homogenization [23, 29]. Both electric boosting and air bubbling result in higher melt temperature, which accelerates the refining process as bubbles grow and rise more quickly to the glass surface [30]. Moreover, heat regeneration from the hot gases exiting the combustion space can be used as an energy saving measure to preheat the air or oxygen prior to combustion [4] and the batch before introducing it into the furnace [1].

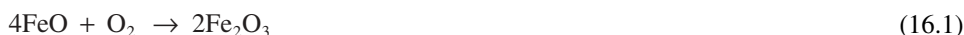
Pilon *et al.* [31] showed that, for a specified heat input profile, the presence of glass foam in the submerged throat glass melting tank can significantly reduce the glassmelt temperature, which negatively affects the glass quality. More recently, Wang *et al.* [18] performed comprehensive three-dimensional numerical simulations of a 150 ton/day oxygen-fuel fired furnace consisting of coupled models for (i) the combustion chamber predicting the turbulent flow field along with temperature, combustion chemistry, and pollutant emission, (ii) the batch melting, (iii) velocity and temperature fields in the glassmelt, and (iv) foam treated as a static insulating layer with uniform thickness and known thermal conductivity. The authors established that the presence of foam over the glassmelt resulted in (i) increased temperatures of the crown, of the bottom furnace, and of the exhaust gas, (ii) lower glassmelt surface temperature, as well as (iii) larger net heat flux to the batch.

Finally, cold-top electric glass melters are commonly used for fiberglass and specialty glasses [2, 5, 21, 22]. Such melters are also used in nuclear waste vitrification [27, 32–36] where high level nuclear wastes are immobilized in borosilicate glasses [32, 33, 35]. Thermal energy required to melt the batch is entirely provided by electrodes submerged in the glassmelt [27, 37, 38]. This type of melter is typically smaller and more energy efficient than conventional fossil-fuel fired furnaces. They are also intrinsically cleaner since they do not emit  $\text{NO}_x$ ,  $\text{SO}_x$ , or dust [2]. Glass foam also forms in electric glass melters as a result of gas released and bubbles rising at the glassmelt surface. On the one hand, the glass foam reduces heat losses from the melt to the surroundings and thus increases the melt temperature [32, 34]. On the other hand, it acts as a thermal insulator between the hot glassmelt and the cold incoming batch loaded from the top [32, 34, 39, 40], thus reducing the batch melting rate [32, 34, 41]. In addition, higher melt temperatures result in more intense foaming due to the release of gases caused by (i) gas solubility typically decreasing with temperature [42], and (ii) thermally activated chemical reactions. Even in electric melters, the presence of foams has, overall, a detrimental impact on melter operation as excessive foaming slows down and may even halt the production process, resulting in losses in productivity and energy efficiency [32, 35].

### 16.1.2 Melting Chemistry and Refining

#### 16.1.2.1 Redox State of Glass

The redox state of the glassmelt controls the refining reactions and the amount and gas species evolved [43–45]. The oxidation state of the glassmelt can be determined by considering the equilibrium between ferrous ( $\text{FeO}$ ) and ferric ( $\text{Fe}_2\text{O}_3$ ) oxides present in the glass, which may react according to



Thus, the oxidation state of the glass is directly related to the concentration or partial pressure of oxygen dissolved in the glassmelt [6], which can be measured using an oxygen sensor [46, 47]. The ratio of ferrous to ferric ions  $\text{Fe}^{2+}/\text{Fe}^{3+}$  in soda-lime-silica glass can be estimated from absorption measurements at 380 and 1060 nm wavelengths [48]. The redox state of the glassmelt can also be monitored by wet chemistry or Mössbauer spectroscopy [33]. Glass can be oxidized by adding oxidizing material to the batch, including sodium sulphate ( $\text{Na}_2\text{SO}_4$ ), cerium oxide ( $\text{CeO}_2$ ), iron oxides (e.g.,  $\text{Fe}_2\text{O}_3$ ), sodium and potassium nitrate ( $\text{NaNO}_3$  or  $\text{KNO}_3$ ), or oxidized glass cullets. Reducing conditions can be achieved by adding carbon, anthracite, chromite ( $\text{FeCr}_2\text{O}_4$ ), nitrates, and iron pyrite ( $\text{FeS}_2$ ) or reduced glass cullets [34, 43].

Green glasses owe their color to absorption by  $\text{Fe}^{3+}$  ions around 380 nm and to a lesser extent to absorption of  $\text{Fe}^{2+}$  at 1060 nm. Green glasses are typically oxidized glass, whereas blue glasses are mildly reduced due to an increasing amount of  $\text{Fe}^{2+}$  ions. Similarly, amber and dark amber glasses owe their color to the overwhelming presence of  $\text{Fe}^{2+}$  ions compared to  $\text{Fe}^{3+}$  and are referred to as reduced and strongly reduced glasses, respectively [43].

### 16.1.2.2 Melting Chemistry

Melting of the batch is a complex physicochemical process that involves a large number of chemical reactions and phase transformations occurring over a wide range of temperatures [28]. The basic and most important reactions in the batch involve silica ( $\text{SiO}_2$ ), sodium carbonate ( $\text{NaCO}_3$ ), and calcium carbonate ( $\text{CaCO}_3$ ) as follows [43],



Large amounts of carbon dioxide ( $\text{CO}_2$ ) gas are produced as a result of the last three reactions. In fact, about 0.6 kg of  $\text{CO}_2$  are produced per kilogram of soda-lime silica glass [49] or 1440 liters of gas (at standard temperature and pressure) are produced per liter of soda-lime-silica glass [4]. The majority passes through the batch and escapes to the combustion space. Some of the produced  $\text{CO}_2$  diffuses into the melt [49]. A small fraction of the gas contributes to heterogeneous nucleation of bubbles within or just below the batch [50]. A fraction of these bubbles is entrapped in the batch and in the primary melt between the batch logs to produce the *primary foam* [43]. Bubbles generated at the bottom of the batch and too small to rise to the surface become trapped in the glassmelt and are carried with the convection currents.

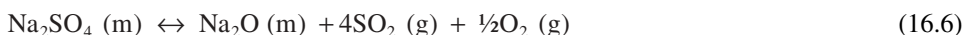
### 16.1.2.3 Refining Chemistry

Refining agents are added to the batch to remove any bubbles from the glassmelt [49–52]. They mediate thermally activated redox reactions that produce or consume gases depending on the local conditions in the glass. In high temperature regions, the equilibrium of the refining reaction shifts to gas production [49]. Then, the fining gas produced diffuses from the molten glass into already existing gas bubbles. In addition, gases already contained in

bubbles are diluted by the incoming fining gas [30, 49]. This, in turn, enhances the diffusion of gases from the melt into the growing bubbles. Diffusion of fining gases makes bubbles grow in size until the buoyancy force is large enough to enable them to rise to the glassmelt free surface where they may aggregate and form foam. On the other hand, at low temperatures, the equilibrium of the fining reaction shifts to gas consumption, resulting in gas diffusion from the bubbles to the melt. Small bubbles, which did not yet grow to a sufficiently large size, then dissolve in the glassmelt [49, 53]. Note also that the solubility of refining gases in the glassmelt, most notably  $\text{SO}_2$ , decreases as temperature increases, thus enhancing gas transfer from the melt to the bubbles at high temperatures and from bubbles to glassmelt at low temperatures [19, 42].

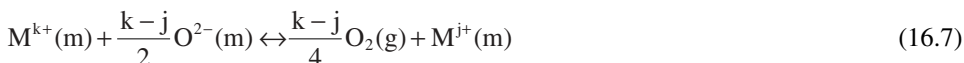
In practice, as the refining agents are carried by the glassmelt convection currents, they encounter high temperature regions (above 1400°C) where refining reactions take place and refining gases are generated. These gases either form new bubbles through nucleation at the surface of unmelted batch particles [54] or dissolve in the glassmelt and eventually diffuse into existing gas bubbles. Such high temperature regions are typically encountered in the refining zone in the center of tank near the hot spot (see Fig. 16.2). Buoyancy enables sufficiently large bubbles to rise to the free surface of the glassmelt, where they accumulate and lead to the formation of *secondary foam* [43]. Refining reactions also take place in high temperature regions close to the tip of the batch.

Three types of refining agents are commonly used [43], namely (i) sulfates in the form of  $\text{Na}_2\text{SO}_4$ , (ii) variable-valence metal oxides, and (iii) halide compounds. Sodium sulfate ( $\text{Na}_2\text{SO}_4$ ) is the most commonly used refining agent and decomposes at high temperatures, around 1400°C in soda-lime-silica glass [4, 55], for example. It also accelerates the primary melt formation if introduced into the batch in suitable proportions [56]. Sodium sulfate is used in 90% of the glass produced worldwide for its relatively low cost [2, 4, 45]. Chemical reactions involving sulfates during glass melting have been the subject of intense studies [45, 49, 57]. In brief, sulfur is present in molten glass as sulfate ( $\text{SO}_4^{2-}$ ) or sulfite ( $\text{SO}_3^{2-}$ ) under oxidizing conditions or as sulfide ( $\text{S}^{2-}$ ) under reducing conditions [55]. In oxidized melt at elevated temperatures, sodium sulfate undergoes the following reaction [55, 58],



where  $\text{SO}_2$  and  $\text{O}_2$  are released in the form of gases which dissolve in the glassmelt and diffuse into existing gas bubbles.

Variable-valence metal oxides refining agents include antimony oxide ( $\text{Sb}_2\text{O}_5/\text{Sb}_2\text{O}_3$ ), arsenic oxide ( $\text{As}_2\text{O}_5/\text{As}_2\text{O}_3$ ), and cerium oxide ( $\text{CeO}_3/\text{CeO}_2$ ) [51, 59]. As these refining agents encounter high temperature regions, they decompose according to the following equilibrium chemical reaction, written in a generalized form as [60]



In the case of antimony oxide, Kawachi and Kawase [50, 52] and Kawachi and Kato [61] showed that the rate of the forward reaction can be neglected in the production of TV panel glass. Therefore, the refining reaction is an irreversible decomposition of the refining agent generating  $\text{O}_2$  gas.

Finally, halide ions such as fluoride, chloride, bromide, and iodine ions evaporate at elevated temperatures rather than participate in refining reactions [62]. For example, sodium chloride is often used as a fining agent in borosilicate glasses by releasing HCl vapors [49].

#### *16.1.2.4 Reduced-pressure Refining*

Another method for refining glasses consists of flowing the unrefined molten glass through a reduced pressure chamber using a siphon principle [63–68]. The low pressure causes bubbles to nucleate and grow rapidly to form foam. This process accelerates fining and can be implemented over small surface areas without requiring high temperatures [64], unlike the chemical refining previously discussed. In fact, it may not require additional heating of the melt, thus reducing the energy consumption. The refining process is favored by the melt expansion and foaming. However, the process throughput is limited by the amount of foam generated [69]. Indeed, glass foam can rapidly fill up the headspace of the vacuum chamber and hinder the process and limit the pressure reduction that can be achieved. Note that imposing near vacuum pressures over a large surface area and volume is very challenging and requires gas-tight container [69]. Thus, this method is limited to relatively small throughput furnaces.

#### **16.1.3 Motivations**

There are numerous fundamental and practical reasons for studying the formation and stability of glass foams appearing at different stages of the glass manufacturing process. They can be listed as follows [9]:

- Energy efficiency. According to indirect measurements and estimates by Trier [11], the resistance to radiative heating due to the presence of glass foam is significant. In fact, it could lead to a decrease by as much as 60% in radiative fluxes to the batch and glassmelt [11]. This results in significant reduction of the energy efficiency of the furnace and an increased fuel consumption [49, 70] in order to reach the glassmelt temperature required for refining and homogenization.
- Glass quality. Reduction in heat transfer from the combustion space to the glassmelt reduces the glass bath temperature and, hence, limits the rate of refining reactions, thereby increasing the number of bubbles and unmelted sand grains contained in the final product [70, 71].
- Productivity. The presence of primary and secondary foams at the surface of the glassmelt negatively impacts the productivity in many ways. It leads to an increase in the residence time of the glassmelt to reach the desired glass quality. In addition, primary foaming is also responsible for decreasing the batch melting rate [72]. Moreover, an increase in the pull rate favors foaming, thereby limiting the maximum pull rate allowed [43, 71]. Finally, extreme glass foaming can cause overflow of the melting tank and stop the production process altogether [32, 71].
- Pollutant emissions. Reflection and back-scattering of thermal radiation by glass foams result in a considerable increase in combustion-generated  $\text{NO}_x$  pollution, owing to an increase in the refractory's temperature by several hundreds of degrees Celsius [18, 49]. In addition, the presence of glass foam influences mass transfer of gas species (e.g.,  $\text{SO}_2$ ) from the molten glass to the combustion space. This affects furnace atmosphere composition and pollutant emission.

- Furnace integrity. The presence of foam enhances the refractory's attack at the metal-line [55] and also the wear of the crown due to increased temperatures [18, 70]. In addition, gas such as oxygen, water vapor, and sulfur oxide contained in foam bubbles tend to react with molybdenum and tungsten used as refractory metals for electrodes in all-electric or electric-boosted glass melting furnaces [73].
- New melting technologies. Led by economic and environmental concerns, new industrial practices use oxygen-fuel burners and significant amounts of recycled cullets in the batch. However, both of these measures have been shown to favor glass foaming [43, 55].

These issues underscore the critical importance of a detailed understanding of the formation and stability of primary and secondary glass foams not only for improving the process efficiency, reducing cost, and addressing environmental concerns associated with glass manufacturing but also for improving the quality of the final glass products. This chapter reviews the physical phenomena responsible for foam formation in glass melting furnaces. It also discusses experimental techniques used to investigate glass foams along with the resulting experimental observations. The associated physical models are presented and discussed in detail. Finally, strategies to mitigate the negative impacts of glass foams on operating cost, product quality, energy consumption, and pollutant emission are discussed.

## 16.2 Glass Foams in Glass Melting Furnaces

### 16.2.1 Primary Foam

Prior to melting, the batch goes through the heating and fusion stages, involving exo- and endothermic solid-state reactions between various batch components (eqn 16.2) [74]. As the temperature increases beyond 800°C, a liquid phase called primary melt begins to appear. As previously discussed, formation of the primary melt is accompanied by generation of significant amounts of carbon dioxide (eqns 16.3–16.5). A part of the released CO<sub>2</sub> is trapped in the viscous liquid phase, whereas the remaining gas percolates through the open channels present in the batch [34, 74]. As melting proceeds, the melt fraction and its connectivity increase, and the open pores get filled with molten glass whose viscosity is large at these relatively low temperatures [34]. Consequently, gas bubbles get trapped within the batch, resulting in batch expansion [74]. This phenomenon can be exacerbated when using cullets [43, 55]. Then, the batch may be covered by a layer of viscous melt preventing gases from escaping to the combustion space. In addition, the presence of trapped gases within the batch lowers its effective thermal conductivity and, in turn, reduces its melting rate [72]. Gas bubbles in primary foams contain CO<sub>2</sub> and CO and possibly other gases in lesser amounts depending on temperature, glass oxidation state, and batch composition and in particular its sulfate, nitrate, and carbon content [43, 44, 55].

### 16.2.2 Secondary Foam

Secondary foams are formed in glass melting furnaces due to gases generated by refining reactions responsible for bubble nucleation at the surface of unmelted grains that rise and

accumulate at the glass free surface [43, 55, 71]. In addition, bubbles trapped under the batch and carried by the convection currents eventually grow in the refining zone and rise to the glass free surface to contribute to secondary foaming [43]. It has been established experimentally that the secondary foam made of sulfate-refined glasses contains mostly  $\text{SO}_2$  and  $\text{O}_2$  in oxidized glass [49]. In reduced or mildly reduced glasses refined with sulfates,  $\text{S}_2$  is also present in the gas bubbles. In addition, secondary foams from glass refined with variable-valence metal oxides contain mainly  $\text{O}_2$ .

If the batch is heated at temperatures higher than 1400°C it undergoes two consecutive expansions: the first one is due to  $\text{CO}_2$  release, and the second is due to the generation of refining gases [55, 74]. Then, the “foaming temperature” refers to the temperature at which bubble generation becomes significant and foaming occurs [75]. A lower foaming temperature correlates with stronger glass foaming. Finally, note that in actual glass melting furnaces it is impossible to distinguish between primary and secondary foams as a continuous foam blanket covers part of the glassmelt.

### 16.2.3 Reboil

The term “reboil” is used to describe the reappearance of bubbles caused by supersaturation of gases physically or chemically dissolved within a previously refined and bubble free glass [8, 75]. In other words, bubbles form when the gas concentration dissolved in the molten glass exceeds its solubility at the local temperature and pressure. Reboil may occur upon heating after the glassmelt has been refined and cooled down. It can also be induced by lowering the pressure above the melt or by stirring the glassmelt [76]. Reboil is caused by gases whose solubility in the melt (i) decreases with temperature and/or pressure [8] and (ii) is relatively large so that large volume of gases can be released during reheating and/or pressure reduction [77]. This is the case of water and  $\text{SO}_3$ , which rapidly decomposes in  $\text{SO}_2$  when released from the melt into gas bubbles [45]. Reboil can also occur when oxidized and reduced glasses are brought into contact due to the mismatch in their gas solubility [8].

In glass melting furnaces, reboil may occur in the forehearth due to reheating or stirring [76]. Indeed, after the glassmelt has been refined at relatively high temperature, it cools down as it flows out of the furnace through the throat. It is then reheated in the forehearth before being formed.

Quantitatively, reboil is assessed through the so-called “reboil temperature” corresponding to the temperature above which bubbles start forming typically under atmospheric pressure. Similarly, the so-called “reboil pressure” is the reduced gas pressure below which bubbles appear under isothermal conditions [32, 76]. In reboil, bubbles form due to heterogeneous nucleation often taking place at the melt/refractory interface [77, 78]. Reboil and foaming differ in the intensity of the gas release rate, in the volume fraction occupied by gas bubbles, and in the bubble size and the distance separating them [77]. Thus, reboil and glass foaming should not be confused and reboil is not discussed further in this chapter.

In summary, Table 16.1 presents the different type of glass foams encountered in glass melting furnaces, the source of gases, the bubble size, and the furnace location where each type may be found.

**Table 16.1** Summary of the different types of glass foams encountered in glass melting furnaces.

Foam type	Gas source	Gas species	Bubble size	Location
Primary	Batch melting and refining reactions	CO <sub>2</sub> , N <sub>2</sub> , CO, SO <sub>2</sub>	Small	Around batch logs
Secondary	Refining reactions	CO <sub>2</sub> , SO <sub>2</sub> , O <sub>2</sub> , S <sub>2</sub> , HCl	Large	Refining zone

### 16.2.4 Parameters Affecting Glass Foaming

The formation and stability of glass foams are affected by obvious parameters such as temperature and glassmelt composition which determine its properties, including viscosity, surface tension, and gas solubility. They also depend on bubble size distribution, bubble generation rate or gas flow rate to the glassmelt surface. If it were only for these parameters, glass foams would behave similarly to any other foams, including aqueous foams, which have been investigated extensively. Understanding glass foams is complicated by the facts that they are also affected by complex and intimately coupled phenomena such as (i) the oxidation state of the glass as its components are involved in numerous reversible redox reactions, (ii) the amount of dissolved gases in the glassmelt, (iii) the refining agent and the associated thermally activated reactions, (iv) the batch composition (cullets, sulfates) and its conditioning (grain size, heat treatment, or compaction), (v) the composition and pressure of the atmosphere above the foams, and (vi) the temperature history of the batch.

These elements are related in complex ways to operating parameters of the glass melting tank such as (i) the use of recycled and contaminated cullet of mixed colors, (ii) the type and amount of refining agents added to the batch, (iii) the furnace pull rate, (iv) the combustion fuel and oxidizer and the atmosphere composition, (v) the heat flux incident on the foam from the combustion space and the crown, (vi) the potential temperature gradient across the foam, and even (vii) the luminosity of the flame [79, 80].

Figure 16.4 summarizes the different parameters affecting glass foams forming in glass melting furnaces. It aims to illustrate the diversity and complexity of the physical phenomena responsible for glass foaming. This may also explain why predicting the behavior of glass foams and controlling foaming in industrial furnaces has remained elusive, as discussed in the following sections.

## 16.3 Physical Phenomena

### 16.3.1 Glass Foam Physics

#### 16.3.1.1 Mechanisms of Foam Formation

A number of intimately interacting physical phenomena govern the dynamics of glass foam formation and decay as well as its steady-state behavior. They include (i) bubble built-up in the foam due to the bubble influx from the bottom of the foam layer, (ii) drainage of the

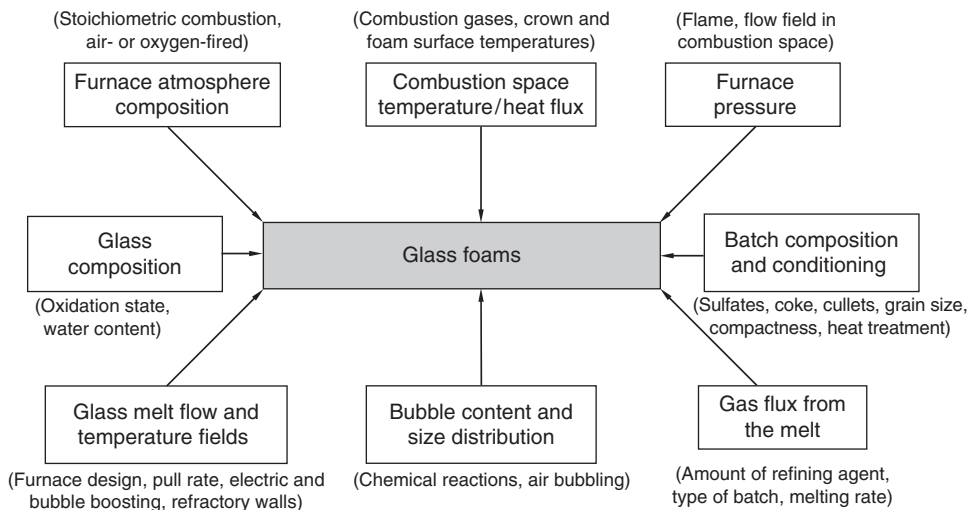


**Fig. 16.4** Schematic of the various parameters affecting primary and secondary glass foams.

molten glass from the Plateau borders, (iii) gravity-induced drainage of the liquid from the foam through the Plateau border channels, (iv) abrupt liquid discharge within the foam due to the rupture of the lamellae and coalescence of adjacent bubbles, and (v) so-called bubble disproportionation or Ostwald ripening caused by interbubble gas diffusion from smaller bubbles (higher pressure) to larger bubbles (lower pressure) [39, 81, 82]. Different mechanisms dominate the life of a bubble as it moves from the bottom to the top of the foam. Initially, foam growth is primarily defined by the balance between the bubble build-up and the liquid drainage from Plateau borders and Plateau border channels. However, near the top of the foam where liquid lamellae separating the bubbles are sufficiently drained, bubble coalescence and interbubble gas diffusion tend to dominate. The above phenomena also take place in aqueous foams. However, glass foams differ from aqueous foams in the following ways:

1. The formation and stability of aqueous foams is associated with the formation of an electrical double layer at the gas–liquid interface due to the presence of surfactant molecules. However, it is unclear whether such a phenomenon takes place in glass foams [78].
2. On the other hand, the viscosity of the glassmelt is large and depends strongly on temperature and glassmelt water content [71, 83–85].
3. Volatilization of some components of the glassmelt due to large temperatures is a critical phenomenon [49, 71].
4. Glass foams are very good thermal insulators and are, in practice, subject to very large temperature gradients.
5. Glass foaming also strongly depends on the redox state of the melt and on chemical reactions taking place between the different components of the melts and the gases released by chemical reactions and/or present in the atmosphere above the foam.
6. The formation of primary foams is affected by the presence of unmelted sand grains, which may stabilize or destabilize the bubble interface [35, 86].

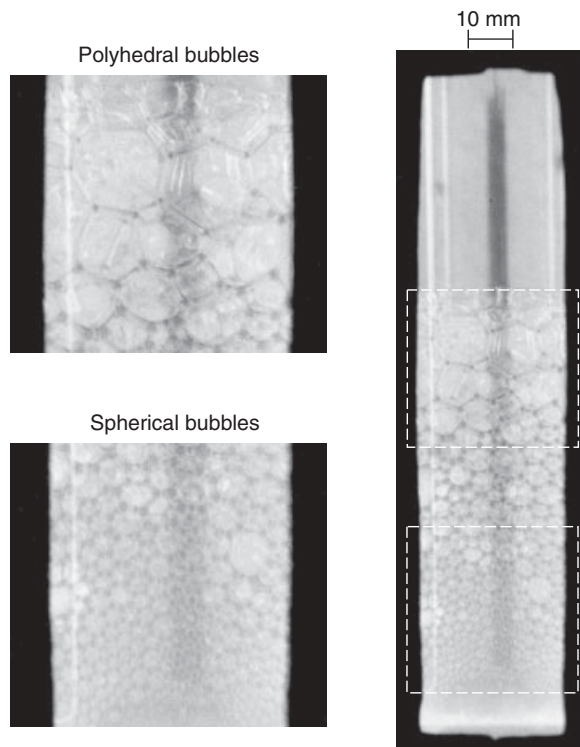


**Fig. 16.5** Photographs of spherical and polyhedral bubbles in glass foams generated from soda-lime-silica glass by sulfate thermal decomposition at 1480°C. Reproduced by permission of Paul Laimböck © 1998.

### 16.3.1.2 Glass Foam Morphology

Glass foams consist of an ensemble of bubbles whose size distribution function varies across the foam layer. The bubbles at the bottom of the foam layer are usually spherical in shape, and their size distribution is primarily determined by how they were generated and the history of their transport through the melt. The bubbles at the top of the foam layer are usually polyhedral, and their geometry typically obeys Plateau's laws [82]: (i) three and only three films or lamellae, called Plateau borders, meet at an edge of a polyhedral bubble at an angle of 120°, and (ii) four and only four edges, called Plateau border channels, meet at a point at an angle of 109°. The dodecahedron nearly satisfies Plateau's laws and, thus, is commonly used as an idealized model for polyhedral bubbles in the foam. Laimböck [43] observed both spherical and polyhedral bubbles in glass foam generated by sulfate thermal decomposition in soda-lime-silica glass in laboratory experiments as illustrated in Fig. 16.5. Similar observations were made in foams scooped from industrial glass furnaces [44] and laboratory experiments [71]. Bubbles generated by chemical reactions are typically much smaller than those generated by gas injection in the laboratory system. Glass foams

generated in the laboratory by bubbling gas through the melt at 1400°C have a typical diameter between 15 and 20 mm [43]. Finally, the thickness of the lamellae separating two adjacent bubbles in glass foams was observed to be about 100 nm [43, 71, 79].

### 16.3.2 Surface Active Agents and Surface Tension of Gas/Melt Interface

Surface active agents are elements whose addition to the glassmelt in small amounts reduces surface tension. They, in turn, increase the stability of the bubbles and tend to inhibit bubble coalescence. Elements in the composition of the glass have been identified as surface active agents. For example, Cooper and Kitchener [79] suggested that  $P_2O_5$  and  $SiO_2$  in the  $CaO-SiO_2-P_2O_5$  system could be treated as surface active agents since they were found to adsorb at the melt surface and lower its surface tension for various  $CaO/SiO_2$  ratios. In fact, these glasses were shown not to foam significantly unless they contained more than 67 wt%  $SiO_2$  and 1–2 wt%  $P_2O_5$ . Cooper and Kitchener [79] also mentioned that  $B_2O_3$  and less significantly  $Al_2O_3$  acted as surface active agents while  $TiO_2$  did not. In addition, Kucuk *et al.* [87] showed that  $MoO_3$ ,  $Rb_2O$ ,  $B_2O_3$ ,  $K_2O$ , and  $PbO$  reduce the surface tension of silicate melts. Finally, silanol groups  $Si-OH$  formed by reaction with water vapor contained in the bubbles have also been identified as surface active agents in molten glass [88].

Laimböck [43] also measured the composition across a quenched vertical film of soda-lime-silica glass. He showed that the film surface was enriched in  $Na_2O$  and became depleted in  $CaO$  and  $SiO_2$ . The surface tension decreases with increasing  $Na_2O$  and decreasing  $CaO$  and  $SiO_2$ . Thus,  $Na_2O$  behaves as a surface active agent. These results confirmed earlier measurements by Kappel and Roggendorf [89].

Moreover, Bindal *et al.* [35] investigated three-phase foaming by heating a mixture of precipitate hydrolysis aqueous (PHA) and sludge-simulating plutonium/uranium extraction (PUREX) nuclear waste. Upon heating, the sludge boiled at around 102°C and gases were generated, resulting in foaming. The authors established that foams made of liquid containing fine solid particles can be stabilized by the particles based on the following two mechanisms:

- 1. Adsorption of biphilic particles** at the gas–liquid interface. As the liquid drains, the particle concentration increases and steric repulsion between particles on each face of the liquid film stabilizes the bubble lamellae and in turn the glass foams [35].
- 2. Layering of solid particles** inside the liquid film separating the gas bubbles caused by the confinement of the particles in the films. This results in long-range forces that stabilize the bubble lamellae [35].

Finally, the composition of the gas phase in contact with the melt also affects the surface tension of the glassmelt/gas system. According to Parikh [90], polar gases such as sulfur dioxide ( $SO_2$ ), ammonia ( $NH_3$ ), hydrogen chloride ( $HCl$ ), and water vapor ( $H_2O$ ) lower the surface tension of soda-lime-silica glass, whereas non-polar gases such as dry air, dry nitrogen, helium, and hydrogen have no effect. Among the polar gases cited, water has the largest dipole moment and therefore has the strongest effect on surface tension [90]. In fact, Parikh [90] showed that the surface tension of soda-lime-silica glass decreases with the square root of the partial pressure of water vapor.

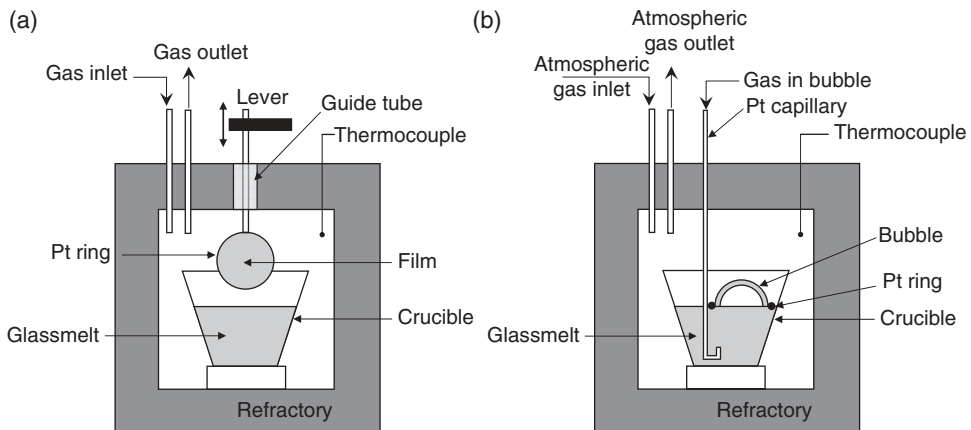


**Fig. 16.6** Schematic of the experimental apparatus used to study (a) liquid drainage and stability of a vertical molten glass film and (b) the lifetime of a single bubble formed from molten glass [43, 71].

### 16.3.3 Drainage and Stability of a Single Molten Glass Film

Figure 16.6a shows a schematic of a typical experimental apparatus designed to investigate the drainage and stability of a vertical single liquid film [43, 71]. Kappel *et al.* [71] used such an apparatus to investigate a single vertical molten glass film made of soda-lime-silica glass between 990 and 1100°C and under various atmosphere compositions. The single film was created by dipping a Pt ring into molten glass. First, the authors established that the film thickness  $\delta(t)$  decreased exponentially with time according to  $\delta(t) = \delta(0)\exp(-k_L t)$  where  $k_L$  varied with temperature, glass and atmosphere compositions. As expected, the film drainage was faster as the temperature increased. However, this could not be solely attributed to the exponential decrease of melt viscosity with temperature. More importantly, the film drainage halted for thickness around 100 nm and could be stable for nearly one hour. Lamellae of similar thickness were also observed in glass foams made of soda-lime-silica glass [71] and silicate glass [79]. In addition, the presence of water vapor in the atmosphere did not affect the film drainage. This is in contradiction with what was observed for foam made of the same glass [71].

Moreover, Kappel *et al.* [71] investigated film stability by blowing hot nitrogen gas, under different pressure or flow rates, directly at the film for different furnace temperatures. The authors showed that the average lifetime of a drained film decreased exponentially with gas pressure and almost linearly with temperature [71]. The authors concluded that tearing of the film was independent of the drainage even though the film had to be thin enough to break. Thus, the lifetime of a molten glass film depends on two independent time scales: the drainage time and the lifetime of the critically thin film [39].

Finally, Laimböck [43] performed similar experiments to those reported by Kappel *et al.* [71] for vertical lamellae drawn from (i) oxidized soda-lime-silica melts without and with sulfate in the form of  $\text{SO}_3$  and (ii) reduced soda-lime-silica melts with sulfate in the form of  $\text{S}^{2-}$ . He also observed that the lifetime of the lamellae from all melts decreased as

the temperature increased. In addition, the lifetime of the film was found to decrease significantly as dissolved  $\text{SO}_3$  content in oxidized soda-lime glass increased. In fact, a sulfate gall was observed at the film surface below 1300–1350°C, which either destabilized the film or prevented its stabilization. In general, gall formation occurred in oxidized glass below 1300°C and varied with sulfate concentration, temperature, and glass oxidation state. Gall formation was observed neither in sulfate-free oxidized glass nor in reduced glass. Above 1300°C, the gall disappeared due to the dissolution and volatilization of sulfate, which created fluid flow in the glassmelt similar to Marangoni flows [43].

### **16.3.4 Gas Bubbles in Molten Glass**

#### *16.3.4.1 Bubble Nucleation*

Heterogeneous bubble nucleation can occur on the surface of undissolved sand grains or on refractory walls due to local supersaturation of the glassmelt with gases [49]. Němec [54] experimentally observed, under uniform temperature conditions, that heterogeneous bubble nucleation occurs at the surface of undissolved sand grains only if a refining agent is present, while homogeneous bubble nucleation could never be observed. It indicates that bubble nucleation takes place if the glassmelt is supersaturated with refining gases. Cable and Rasul [78] reported that heterogeneous bubble nucleation occurred at the surface of the refractory even at small supersaturation. Finally, Roi *et al.* [91] discussed bubble generation and the formation of a bubble curtain consisting of very small bubbles close to the refractory walls.

#### *16.3.4.2 Stability of a Single Bubble at the Glassmelt Surface*

Figure 16.6b shows a schematic of an experimental setup for studying the stability of a single bubble at rest at the surface of molten glass as described by Kappel *et al.* [71]. The single bubble can be formed by injecting an arbitrary gas inside the molten glass through a Pt capillary. A Pt ring, placed on the glassmelt free surface, prevents the bubble from drifting. Finally, the composition of the furnace atmosphere can be controlled by injecting any arbitrary gases and can be different from the gases contained inside the bubble.

Kappel *et al.* [71] investigated single bubbles formed at the surface of molten soda-lime-silica without and with addition of  $\text{Na}_2\text{SO}_4$  and of reduced brown glass. The furnace temperature was 1100°C and its atmosphere consisted of humid air while the bubbles contained air,  $\text{N}_2$ ,  $\text{CO}_2$ , or  $\text{SO}_2$ . For reduced brown glass and soda-lime-silica with or without sulfates, air bubbles were found to be more stable than those filled with  $\text{N}_2$  and  $\text{CO}_2$ . In all cases,  $\text{SO}_2$ -containing bubbles were the most unstable regardless of the sulfur content and redox state of the glass. In addition, the lifetime of a single air bubble on soda-lime-silica glass decreased from about 300 to 30 seconds when the glass was refined with sulfate. Laimböck [43] attributed these observations to the formation of a destabilizing sulfate gall at the surface of bubbles below 1300°C as previously discussed for vertical films. In addition, the authors established that replacing the air furnace atmosphere by  $\text{N}_2$  and  $\text{CO}_2$  had no effect on the bubble stability [71].

Note that Debrégeas *et al.* [92] performed similar experiments with single air bubbles made from pure and uncontaminated polydimethylsiloxane (PDMS) at room temperature.

The authors observed that the metastable film thickness at the top of the bubble was about 70 nm when the bubble burst. The characteristic drainage time was found to be  $\tau = \mu/\rho gr$  where  $\mu$  and  $\rho$  are the dynamic viscosity and density of the fluid while  $g$  and  $r$  are the gravitational acceleration and the cap bubble radius, respectively. The authors demonstrated that a single bubble can be stable for several minutes thanks to PDMS's high viscosity ( $\approx 10^3$  Pa.s) and despite the absence of surface active agents.

Finally, some experimental observations made on single molten glass films or bubbles contradict well known observations made with glass foams in the laboratory and in industrial furnaces. This led Cooper and Kitchener [79] and Kappel *et al.* [71] to question the approach of extending experimental observations on a single film or bubble to predicting the behavior of glass foams.

#### 16.3.4.3 Bubble Rise through Molten Glass

Studies of the bubble motion have been concerned mainly with a single bubble rising in an infinitely large quiescent pool of molten glass under uniform temperature. In brief, if the bubble is small and/or its surface is contaminated, no gas circulation takes place inside [93]. Then, the bubble behaves like a solid sphere (immobile interface) and rises in the molten glass with the relative vertical terminal velocity given by Stokes's law [93],

$$w_r = \frac{2}{9} \frac{\rho gr}{\mu}, \quad (16.8)$$

where  $\rho$  and  $\mu$  denote the density and viscosity of the glassmelt while  $r$  is the bubble radius and  $g$  is the gravitational acceleration.

On the other hand, if the spherical bubble is large and/or its surface is contamination-free, the vertical terminal velocity, relative to the molten glass, follows the Hadamar–Rybczynski formula [93–95],

$$w_r = \frac{1}{3} \frac{\rho_\infty gr^2}{\mu_\infty}. \quad (16.9)$$

Experimental results suggested that the velocity of bubbles with diameter larger than 1 mm satisfies eqn (16.9) while smaller bubbles rise with velocity given by eqn (16.8) [95]. Similarly, Jucha *et al.* [93] established that the Hadamar–Rybczynski formula was valid for bubbles larger than 10  $\mu\text{m}$  rising in borate glass at temperatures between 800 and 1000°C.

The bubble rise in the glassmelt is complicated by gas diffusion in and out of the bubble, which changes its size and therefore the buoyancy force. Numerous studies have investigated the shrinkage or growth of a stationary bubble containing a single gas [96, 97], sometimes accounting for refining reactions [59, 98]. Other studies were concerned with the growth of a stationary bubble containing several gases with or without refining reactions [98–100]. More realistic situations were investigated by accounting for the bubble rise due to buoyancy for a single gas bubble [101, 102] or a bubble containing several gases [103, 104], including the presence of refining reactions [51, 62, 105].

Even though modeling the behavior of individual bubbles provides insight into the mechanism of bubble generation, motion, growth, and shrinkage, it does not predict the

**Table 16.2** Summary of experimental studies of glass foams reported in the literature.

Glass	Batch or gas in bubble	Gas source/method	Heating	Temperature (°C)	Atmosphere	Ref.
Soda-lime, brown, E-glass, crystal, borosilicate (decay)	Cullet compressed at 2.5 MPa	CaCO <sub>3</sub> or Na <sub>2</sub> CO <sub>3</sub>	Isothermal	1000–1200	Dry/wet air N <sub>2</sub> ' + SO <sub>2</sub> Air + NH <sub>3</sub>	[71]
Sodium, lithium, potassium silica	Melted glass	Na <sub>2</sub> SO <sub>4</sub>	Heat ramp (3–4°C/min)	1100–1500	N <sub>2</sub> ' + H <sub>2</sub> ' CO <sub>2</sub> ' SO <sub>2</sub> ' dry/wet O <sub>2</sub> '	[77]
Sodium, lithium, potassium silica	Premelted glass cullet	Na <sub>2</sub> SO <sub>4</sub>	Heat ramp (3–4°C/min)	1150	N <sub>2</sub> ' N <sub>2</sub> -H <sub>2</sub> ' CO <sub>2</sub> ' dry/wet O <sub>2</sub> ' CO <sub>2</sub> '	[78]
Soda-lime silica	Loose	Na <sub>2</sub> SO <sub>4</sub>	Heat ramp (3–4°C/min)	Up to 1515	N <sub>2</sub> ' N <sub>2</sub> -H <sub>2</sub> ' CO <sub>2</sub> , dry/wet O <sub>2</sub> '	[75]
Sheet glass	Loose	0–13 wt% Na <sub>2</sub> SO <sub>4</sub>	Isothermal Time gradient method	1450, 1480 1500	Air Air	[20] [70]
Fiberglass	Loose with fine or coarse grains	Fluorine				
Simulated nuclear waste with borosilicate	Loose/compacted Cold/pre-heating	Variable-valence metal oxides Na <sub>2</sub> SO <sub>4</sub>	Heat ramp (5–10°C/min) Isothermal or heat ramp (14°C/min)	500–1150	Air	[72]
Soda-lime silica (with Al <sub>2</sub> O <sub>3</sub> , Sr(CO <sub>3</sub> ))	Loose (coarse or fine)	Na <sub>2</sub> SO <sub>4</sub>	Isothermal	1400 or up to 1450	Air	[74]
Soda-lime silica (with Al <sub>2</sub> O <sub>3</sub> )	Loose (coarse or fine)	Na <sub>2</sub> SO <sub>4</sub>	Heat ramp (14°C/min)	Up to 1450	Air	[113]
Soda-lime silica (with Al <sub>2</sub> O <sub>3</sub> )	Loose (with or without cullets)	Na <sub>2</sub> SO <sub>4</sub>	Heat ramp	Up to 1500	Dry/wet air	[43]
Soda-lime silica (oxidized or reduced) E-glass	Loose	Na <sub>2</sub> SO <sub>4</sub>	Heat ramp (5–10°C/min)	Up to 1500	CO <sub>2</sub> , O <sub>2</sub> ', air, H <sub>2</sub> O mixtures Wet air (11–100 vol.%)	[115]
Soda-lime silica	Loose	Na <sub>2</sub> SO <sub>4</sub> with carbon	Heat ramp (10°C/min)	1300, 1400, 1500	2% O <sub>2</sub> + 55% H <sub>2</sub> O	[57, 116]
E-glass	Loose	Na <sub>2</sub> SO <sub>4</sub>	Heat ramp (10°C/min)	Up to 1250 and 1500		[46]
Soda-lime silica (various SO <sub>3</sub> wt%)	Molten glass	Gas injection (air)	Isothermal	1425–1500	Air	[43]
Float glass	Molten glass	Gas injection (N <sub>2</sub> ', CO <sub>2</sub> )	Isothermal	1300 or 1400	Air	[117]
Silicate slag (decay)	Molten slag (CaO-SiO <sub>2</sub> + P <sub>2</sub> O <sub>5</sub> )	Gas injection (10% H <sub>2</sub> -90% N <sub>2</sub> )	Isothermal	1500–1750	10% H <sub>2</sub> -90% N <sub>2</sub>	[79]
Flat, optical, wool glass (decay)	Melted glass	Reduced pressure method	Isothermal	1200–1500	Air (50–750 mmHg)	[70]
Iron alkali borosilicate	Cullet	Reduced pressure method	Isothermal	1150	Air (0–1 bar)	[32]

volumetric gas flow rate and size distribution of bubbles rising to the surface of the glassmelt to form glass foams. However, it can be used to trace individual bubbles introduced at the batch/glassmelt interface and predict their growth and shrinkage as they are transported through regions with different temperatures, gas concentrations, and pressures [30, 49, 50, 52]. Alternatively, Ungan *et al.* [106] solved the conservation equation for the total number of bubbles and took into account the effect of bubbles on the flow and temperature fields of the molten glass through the reduction of the effective density of the two-phase mixture. By contrast, population balance theory [107] enables one to predict in detail the radius and gas content of polydispersed bubbles and their density function throughout the glass melting tank. A limited number of studies have applied population balance theory to the bubble dynamics in glass melting tanks in 2D or 3D with various assumptions and different levels of refinement [108–112]. The latter studies enable the prediction of the local superficial gas velocity reaching the glassmelt surface, which can then be used in dynamic or steady-state models described in Section 16.5.

## 16.4 Experimental Studies

### 16.4.1 Introduction

As previously discussed, it is of fundamental and practical interest to understand each type of glass foaming process and to predict (i) the conditions under which glass foam forms, (ii) how fast it grows and decays, and (iii) how stable it is under various conditions in order to operate the process in an optimum manner.

Table 16.2 summarizes laboratory experiments performed to investigate the effect of the numerous parameters affecting glass foam formation and stability summarized in Fig. 16.4. Most of the studies focused on soda-lime-silica glass, E-glass, and borosilicate glasses as well as binary glasses. The majority of the studies investigated glass foams created by ramp-heating of a batch under different heating rates. Both fine and coarse batch grains were investigated. In addition, steady-state and transient decay of glass foams were typically studied under isothermal conditions. Most experiments were performed under atmospheric pressure and various atmosphere compositions.

Figure 16.7 shows a typical experimental setup used to study both primary and secondary glass foams [115, 118]. Typically, glass foaming is performed in a furnace with a fused quartz window on the front door enabling visual access inside the furnace. The sample height is recorded over time with a visual or infrared video camera and filters. The furnace can be equipped with a rear recess kept at a temperature lower than that of the crucible to provide a darker background for a better contrast [115]. The furnace atmosphere can be controlled by injecting different gases or gas mixtures at predetermined temperatures. In particular, furnace humidity can be controlled by bubbling compressed gas through water in a flask kept at a constant temperature [43, 71, 75, 77, 78, 115], as illustrated in Fig. 16.7. The temperature of the incoming atmospheric gas can also be controlled by heating the gas line with an insulated resistive heating coil wrapped around the gas tube. This also helps prevent water condensation in the gas inlet system when wet atmospheres are tested [115].

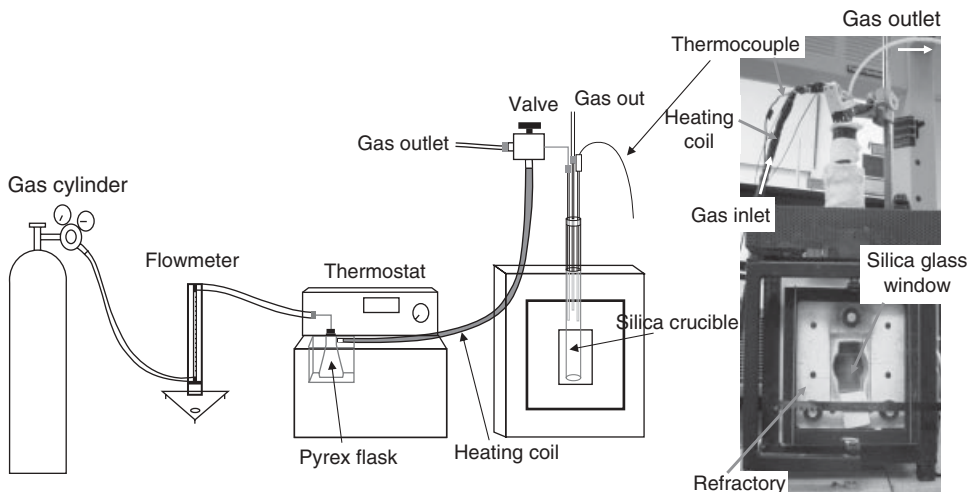


**Fig. 16.7** Schematic of typical experimental apparatus used to investigate glass foaming along with photographs of the furnace used by Kim et al. [115, 118].

## 16.4.2 Transient Primary and Secondary Glass Foams

### 16.4.2.1 Experimental Apparatus and Procedure

Figure 16.8a shows the inside of the furnace used to study the dynamic behavior of glass foaming. In this method, the batch is placed as a loose or compacted blanket in a transparent crucible (e.g.,  $\text{SiO}_2$ ) tall enough to contain the glass foam. Foaming is achieved by increasing the batch temperature either by ramp-heating the furnace or by placing the crucible inside a pre-heated isothermal furnace. Glass foams are produced as a result of gas generation due to batch conversion and refining. This method results in glass foam that grows and eventually collapses when all the gas generating reactions end [71, 74, 75, 77, 78, 113–115]. In other words, the glass foam height continuously changes over time and never reaches a steady state. This method can simulate growth and decay of primary and secondary foams depending on the maximum temperature reached [43, 115].

Alternatively, Cable and co-workers [75, 77, 78] used an apparatus similar to that depicted in Fig. 16.8a to investigate secondary foaming with the capability to vary the atmosphere composition and control the heating rate. First, the authors melted glass in air in a separate electric furnace at different temperatures (1200–1400°C) and for various durations (5–28 h) until the glass melt was free of bubbles. The produced melts were cooled and stored in desiccators. The produced glass was then crushed into 5–10 mm pieces and then used for secondary glass foaming experiments to measure the foaming temperature for various conditions.

Moreover, Gerrard and Smith [70] described a reduced pressure apparatus where the batch was introduced into a crucible placed in a furnace with prescribed temperature and pressure. The pressure of the atmosphere above the sample was controlled by evacuating the furnace with a vacuum pump. Visual access was possible through a quartz window to

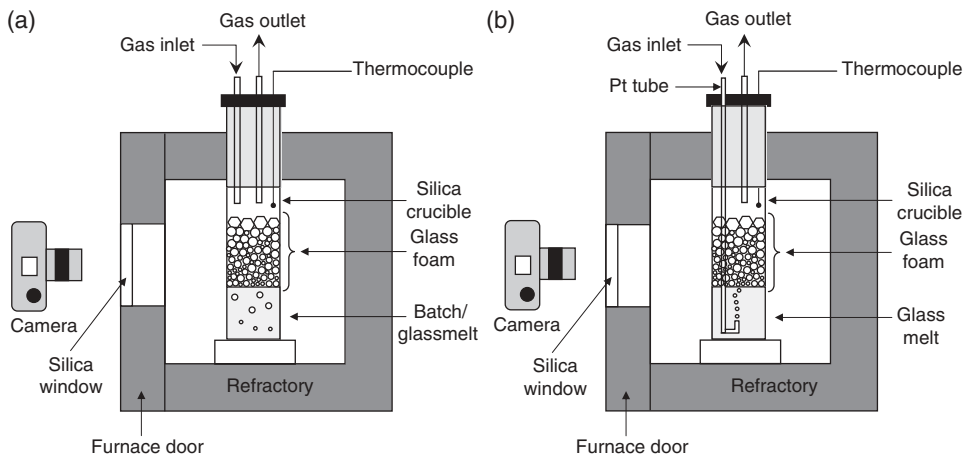


**Fig. 16.8** Schematic of experimental setup used to study (a) batch melting with primary and secondary foaming and (b) foaming by gas injection. Visual access and video recording are made possible through a glass window on the furnace door.

monitor foaming. The batch was first melted between 1200 and 1500°C at atmospheric pressure. After an arbitrary melting time, the pressure was reduced until foaming was observed corresponding to the reboil pressure. The authors also used this apparatus to monitor the decay of the glass foam. Similar experimental setup and procedure were used by Goldman *et al.* [32].

Finally, Gerrard and Smith [70] proposed an alternative setup to investigate primary foaming. Their experimental procedure consisted of continuously introducing, with an arbitrary speed, loose batch placed in a rhodium or platinum “boat” into a pre-heated furnace at constant temperature in an atmosphere with arbitrary composition. After a few minutes, the boat was withdrawn from the furnace and cooled. This procedure was meant to reproduce the temperature history of the batch from the time it is introduced in the furnace until it melts. It is commonly used in industry to assess the effect of different batch compositions and process parameters. Unfortunately, this method can only provide qualitative results, as acknowledged by Gerrard and Smith [70].

#### 16.4.2.2 Experimental Observations

Figure 16.9 shows typical experimental results of transient foaming experiments (Fig. 16.8a). It plots the batch/foam height and furnace temperature as a function of time for 4 g of loose batch of E-glass batch containing sulfate ramp-heated at 5°C/min up to 1500°C [115]. As the temperature increased, the volume of the sample decreased slightly as sintering and gas release took place. Around 1100°C the batch started melting, resulting in a dramatic reduction in sample thickness. Shortly thereafter, the melt thickness increases as CO<sub>2</sub> bubbles are generated and get trapped in the molten glass and expand due to CO<sub>2</sub> generated by fusion reactions (period I). This is followed by a rapid growth around 1400°C (period II) caused by the release of fining gases, SO<sub>2</sub> in this case. Similar plots have been reported throughout the literature for different glass compositions and heating rates [43, 49, 72, 74, 117].

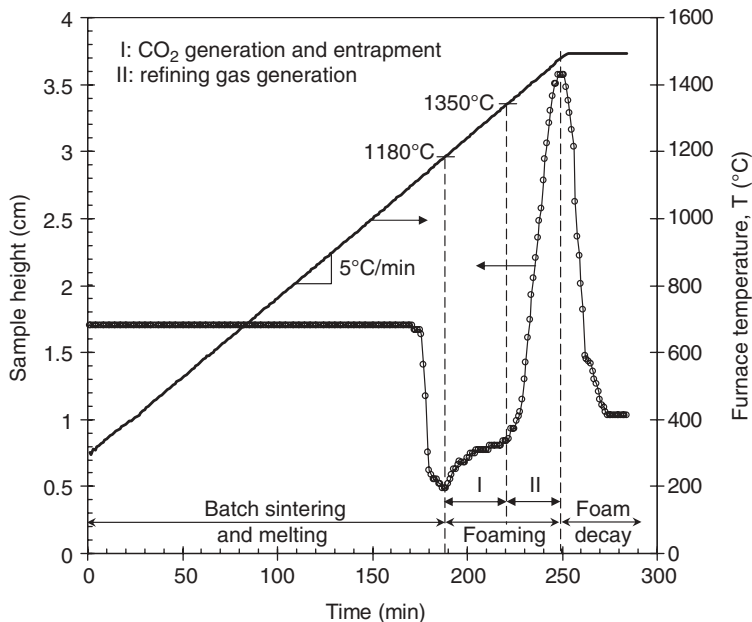


**Fig. 16.9** Temporal evolution of sample height and furnace temperature during primary foaming of E-glass batch ramp-heated at 5°C/min [115].

The following subsections review studies investigating the effects, on glass foaming, of (i) temperature and heating rate, (ii) redox state, (iii) batch preparation, (iv) batch and glass compositions, (v) sulfate addition, as well as (vi) atmosphere composition and pressure.

**Effect of Temperature and Heating Rate.** Laimböck [43] performed a thorough study of the effect of redox state on glass foaming. The author melted oxidized soda-lime-silica batch containing 1.0 wt% of  $\text{Na}_2\text{SO}_4$  at a constant heating rate of 4°C/min up to 1465, 1480, and 1500°C. He observed that secondary foaming and sulfate losses were larger as the final temperature increased. This can be explained by the fact that beyond the refining temperature (~1400°C in this case), more and more refining gases ( $\text{SO}_2$  and  $\text{O}_2$ ) are generated by thermal decomposition of refining agents ( $\text{Na}_2\text{SO}_4$ ). In addition, under a constant heating rate, it takes longer to reach a higher final temperature, thus giving more time for the refining reactions to proceed.

Moreover, Fig. 16.10a shows the ratio of volume of gas in the foam  $V_{\text{gas}}$  to the volume of soda-lime-silica melt  $V_{\text{melt}}$ , denoted by  $\Psi = V_{\text{gas}} / V_{\text{melt}}$  as a function of temperature between 1250 and 1500°C for three different heating rates namely 5, 10, and 15°C/min as reported by Kim *et al.* [58, 115]. It establishes that glass foaming increases as the heating rate increases [115].

Hrma [58] distinguished between (a) surface foams observed at low heating rates and (b) bulk foams observed under high heating rates and in a deep enough container. Surface foams consist of three stratified layers: (i) a bubble-free melt, (ii) a bubbly layer, and (iii) the glass foam layer. On the contrary, bulk foams consist of bubbles expanding

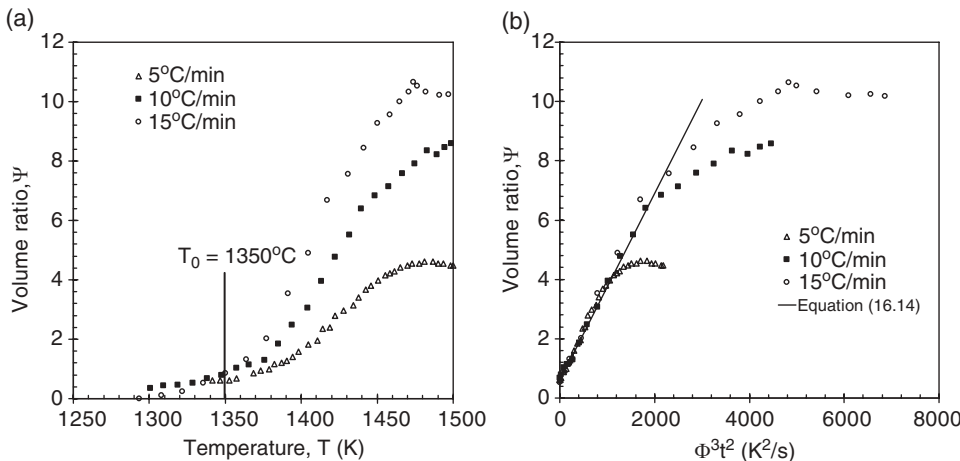


**Fig. 16.10** Gas volume to melt volume ratio  $\Psi$  for primary foaming of E-glass during ramp-heated at 5, 10, and 15°C/min as a function of (a) temperature and (b)  $\Phi^3 t^2$  where  $\Phi = dT/dt$  (eqn 16.14) with  $t = 0$  for  $T_0 = 1350^\circ\text{C}$  [58].

throughout the batch and melt in a manner similar to volcanic foam and solid glass foam produced for thermal insulation applications [119–131]. Hrma [58] also explained that “the decay of bulk foam tends to be more erratic than the decay of surface foam” by virtue of the fact that surface foam decays as bubbles burst at the top of the foams while bulk foam decays by bubble coalescence within the melt and eventually releases to the atmosphere.

**Effect of Redox State.** Laimböck [43] added carbon as a reducing agent, in the form of active carbon or graphite, to a soda-lime-silica batch refined with sulfate. First, the author observed that during the primary foaming process, more CO gas was generated at temperatures above 750°C than in oxidized melts. This was attributed to the oxidation of carbon by  $\text{CO}_2$  according to [43],



In addition, more CO was generated with active carbon than with graphite thanks to its extremely porous structure offering a large surface area for the above reaction. In practice,  $\text{CO}_2$  may react with carbon-containing components such as coke added to the batch or organic substances present in contaminated cullets [49].

Figure 16.11(a) shows the furnace temperature and the volume of foam per unit mass of batch as a function of time for oxidized and reduced soda-lime-silica glasses. The reduced batch contained 0.1 wt%  $\text{Fe}_2\text{O}_3$  and 0.2 wt% of either active carbon or graphite carbon. In all cases, 1 wt%  $\text{Na}_2\text{SO}_4$  was added to the batch and the atmosphere was dry nitrogen [43]. Note that the temperature rise was different from that imposed by Kim *et al.* [115]. Figure 16.11(a) shows that adding carbon to the batch, as a reducing agent, increases primary foaming but significantly decreases the maximum foam height and

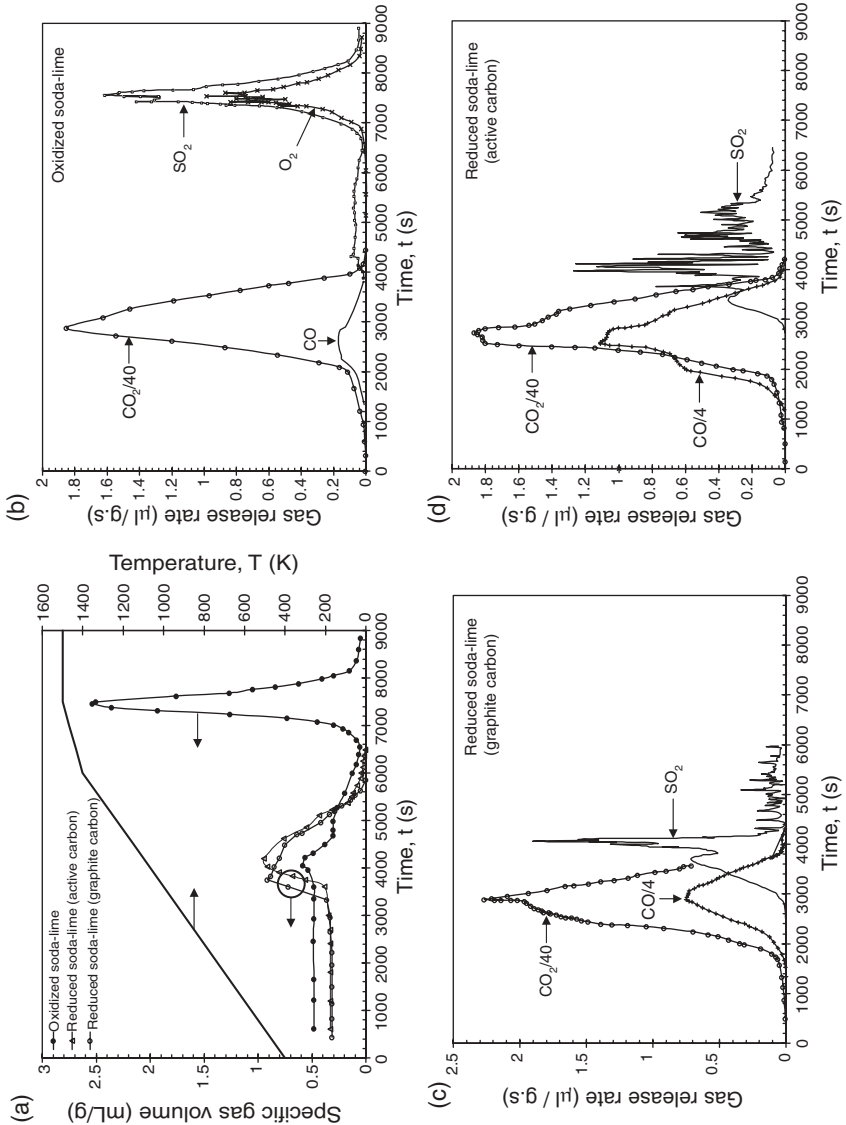
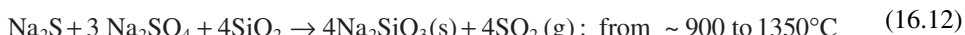
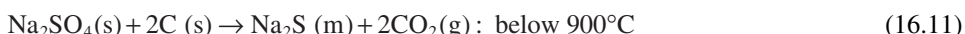


**Fig. 16.11** (a) Temperature ramp and specific gas volume and (b-d) gas release rate as a function of time for (b) oxidized soda-lime-silica, and reduced soda-lime-silica with 0.1wt%  $\text{Fe}_2\text{O}_3$ , and (c) 0.2wt% of active carbon, (d) 0.2wt% of graphite carbon. In all cases, 1 wt%  $\text{Na}_2\text{SO}_4$  was added to the batch, the atmosphere was dry nitrogen, and the temperature was a function of time [43].

secondary foaming. In fact, adding a sufficient amount of carbon can entirely eliminate secondary foaming. Similar results were obtained by Faber *et al.* [46] for E-glass. This can be explained by considering the gas release rates during melting and fining.

Figure 16.11(b-d) shows the release rates of CO<sub>2</sub>, CO, SO<sub>2</sub> and O<sub>2</sub> for each batch as functions of time. It establishes that adding carbon lowered the temperature at which SO<sub>2</sub> production occurred and decreased sulfate retention in the glassmelt. This was also observed by Faber *et al.* [46] for E-glass. These observations were attributed to chemical reactions taking place at relatively low temperatures between carbon and sulfate SO<sub>4</sub><sup>2-</sup> to form sulfide (S<sup>2-</sup>), which at higher temperature reacts with sulfates to form SO<sub>2</sub> gas according to [55, 132]



Moreover, in sulfide rich soda-lime-silica melts depleted of sulfates consumed by the above chemical reactions caused by large addition of carbon to the batch, sulfur gas (S<sub>2</sub>) also evolves according to [43]



Overall, reducing the glass resulted in early consumption of sulfates, thus depleting the melt of refining agents. This, in turn, reduced the volume of refining gases (SO<sub>2</sub> and S<sub>2</sub>) produced during secondary foaming taking place at higher temperatures. Consequently, the smaller amounts of refining gases SO<sub>2</sub> and S<sub>2</sub> dissolved in the glassmelt may not be sufficient to cause supersaturation and bubble nucleation.

Moreover, primary foaming is affected by redox state and organic contamination of glass cullets. Using mixed (green, amber, and flint) cullets results in stronger primary foaming compared with clean cullets with a small variation in redox state [43]. In fact, the mismatch in redox state of mixed cullets causes sulfate (SO<sub>4</sub><sup>2-</sup>)/sulfide (S<sup>2-</sup>) reactions producing additional SO<sub>2</sub> [55] according to reaction (16.12). Finally, in sulfate-refined batches, organic contaminants present in the cullets react with CO<sub>2</sub> and SO<sub>4</sub><sup>2-</sup> to produce additional SO<sub>2</sub>, CO<sub>2</sub>, and CO according to reactions (16.10–16.12). These gases released at low temperature enhance primary foaming [43, 55].

Finally, foaming during nuclear waste vitrification in electric glass melters is not caused by the release of SO<sub>2</sub> gas. In fact, foaming in such systems is caused by the release of water vapor and O<sub>2</sub> from the oxidized melt [32, 34]. First, glasses used for vitrification are typically iron-alkali borosilicate glass rich in iron [32, 41]. Thus, oxygen gas is released at high temperatures during the reduction of polyvalent metal ions, mainly Fe<sub>2</sub>O<sub>3</sub>/FeO (reaction 16.1), but also manganese, cerium, or chromium [8, 32, 41]. Here also, reduced glasses were found to be less susceptible to foaming [32]. Carbon can be added as a reducing agent that reacts with Fe<sub>2</sub>O<sub>3</sub> at relatively low temperatures before oxygen gas can be trapped in the melt [41]. This was attributed to the lower content of dissolved O<sub>2</sub> in reduced glasses combined with the larger release of water vapor [32]. The latter decreases the melt viscosity [71, 83–85] and affects surface tension, resulting in less stable foams. These results were confirmed by Bickford *et al.* [34].

**Effect of Batch Grain Size, Compaction, and Cullets.** The size of the batch particles plays an important role in primary foam formation [70]. Using fine grains was found to reduce the foaming temperature and increase primary foaming during both ramp-heating and isothermal heating of soda-lime-silica glass with sulfate refining agent [74, 113, 114]. This was also observed with fiberglass [70]. The use of finer grains accelerates melting at the top of the batch, thereby sealing the batch and preventing gases generated at the bottom from escaping to the atmosphere [74]. By contrast, an increase in the particle size of the batch powder results in reduction of primary foaming [43]. Heating of coarse silica grains shifts the equilibrium of batch reactions towards higher temperatures compared with fine grains. At larger temperatures, the viscosity of the melt is significantly reduced, thereby easing the escape of gas bubbles to the atmosphere [74].

Similarly, using fine glass cullets (<1–2 mm) results in stronger primary foaming compared with coarse cullets [43]. Sintering of fine cullets occurs at much lower temperatures than for coarser grains, resulting in a viscous liquid layer covering the batch logs and preventing gas bubbles from escaping freely to the combustion space [43, 55]. By contrast, in coarse cullets, the gases generated at low temperatures escape through the pores between the cullets. Upon further heating, the gas released at higher temperatures can escape in bubbles rising to the surface thanks to the lower melt viscosity.

Finally, conditioning the batch material can significantly reduce foaming [72]. In fact, compacting the batch before melting leads to reduced primary foaming and increased foaming temperature. For example, Ahn and Hrma [72] showed that compacting and heat treating simulated nuclear waste batch above 1150°C prior to its introduction into the glass melting furnace limited significantly the extent of the primary foam. On the contrary, loose batch foams immediately upon contact with hot borosilicate melt [72]. In addition, the authors established that sintering of loose batch before introducing it on the glassmelt can delay foam formation. What is more, heat treatment of loose batch at high temperatures for several hours followed by sintering for less than one hour can completely prevent foaming [72].

**Effect of Batch and Glass Compositions.** The batch composition and that of the resulting melt have a strong effect on glass foaming mainly through their effects on the melt viscosity, redox state, and sulfate solubility [43]. For example, Cable *et al.* [75] as well as Kim and Hrma [114] found that the presence of  $\text{Al}_2\text{O}_3$  increased foaming of soda-lime-silica glass by decreasing the foaming temperature and stabilizing the glass foams. Retention of gases generated by batch melting was reduced by adding melting agents such as  $\text{Na}_2\text{NO}_3$  and by decreasing the amount of  $\text{SrCO}_3$  and  $\text{Al}_2\text{O}_3$  in the batch [74]. Finally, Laimböck [43] also showed that increasing the  $\text{Na}_2\text{O}$  content of soda-lime-silica glass or adding  $\text{Al}_2\text{O}_3$  while reducing  $\text{CaO}$  resulted in (i) an increase in foaming, (ii) a decrease in foaming temperature, and (iii) larger sulfate loss. This can be attributed to the following phenomena. First, adding small amounts of  $\text{SiO}_2$  and  $\text{Al}_2\text{O}_3$  or reducing the  $\text{Na}_2\text{O}$  and  $\text{CaO}$  content of soda-lime-silica glass significantly increases melt viscosity, which leads to more stable primary and secondary glass foams. Similarly, fluorine addition to fiberglass batch was found to reduce primary foaming due to the reduction in melt viscosity [70]. Second, increasing  $\text{SiO}_2$  or  $\text{Al}_2\text{O}_3$  content and/or decreasing  $\text{Na}_2\text{O}$  content reduces sulfate solubility in soda-lime-silica glass [133]. This in turn results in (i) lower foaming temperature, (ii) increased foam stability and height, and (iii) larger sulfate loss [43].

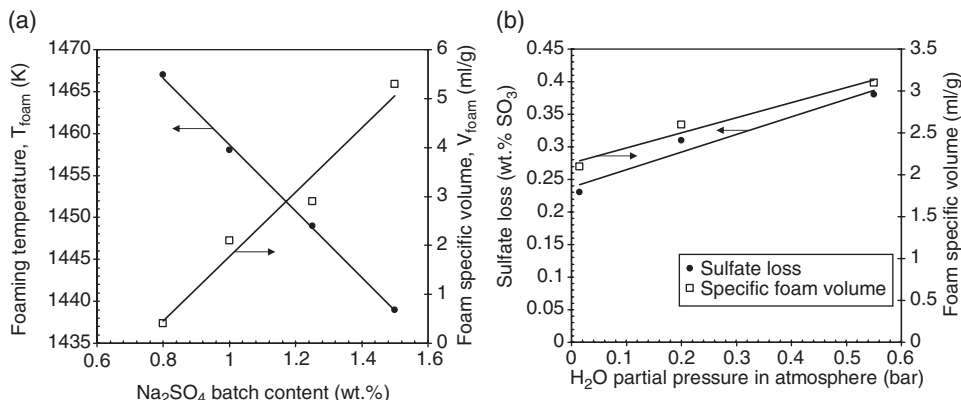


**Fig. 16.12** (a) Foaming temperature and foam specific volume as a function of mass fraction of  $\text{SO}_3$  added to soda-lime-silica glass melted in air at 1 atm. (b) Sulfate ( $\text{SO}_3$ ) loss and foam specific volume as a function of water vapor partial pressure in the atmosphere over the glassmelt. In all cases, the melt was made of soda-lime-silica glass with 1 wt%  $\text{Na}_2\text{SO}_4$  [43].

**Effect of Sulfate Addition.** Adding  $\text{Na}_2\text{SO}_4$  to the batch was found to (i) decrease significantly primary foaming (below  $1400^\circ\text{C}$ ) and (ii) increase secondary foaming (above  $1400^\circ\text{C}$ ) [20, 43]. Its decomposition caused mechanical stirring of the batch and accelerated the dissolution of sand grains [20, 43].

First, the reduction in primary foaming was attributed to the phase separation of sulfate from the glass, resulting in a sulfate gall also observed on single melt films of oxidized glass below  $1300^\circ\text{C}$ , as previously discussed [43]. Thus,  $\text{CO}_2$  bubbles tended to coalescence and the foam was less stable. Moreover, secondary foaming of mixed alkali and soda-lime silica was found to be stronger when water vapor and sulfate were present in the glassmelt [75, 77, 78]. In the absence of sulfate, secondary foaming of soda-lime-silica glass took place only in atmospheres containing oxygen [75]. The foaming temperature was also found to decrease with increasing sulfate addition to the batch as illustrated in Fig. 16.12(a). Adding sulfate to the batch resulted in stronger secondary foaming due to larger amounts of refining gases ( $\text{SO}_2$  and  $\text{O}_2$ ) generated during the sulfate thermal decomposition [43]. In addition, sulfur-containing oxidized glass melts are prone to secondary foaming due to decreasing  $\text{SO}_3$  solubility with increasing temperature [42] and dissolved oxygen concentration [134]. However, the amount of sulfate remaining in the glassmelt after refining was the same regardless of the initial sulfate concentration in the batch [43].

Finally, Faber *et al.* [46] proposed dissociating the oxidizing function of  $\text{Na}_2\text{SO}_4$  at low temperatures from its refining function at high temperature. To do so, they replaced 75% of the  $\text{Na}_2\text{SO}_4$  added to the batch of E-glass (0.05 wt% instead of 0.2 wt%) with oxidizing agents such as  $\text{NaNO}_3$ ,  $\text{MnO}_2$ ,  $\text{CaO}_2$ , and  $\text{NaBO}_3 \cdot \text{H}_2\text{O}$ . This ensured stable redox state while reducing the production of refining gases and therefore secondary foaming at high temperatures. They observed that adding these oxidizing agents (i) increased the foaming temperature, (ii) decreased the volume of  $\text{SO}_2$  released and the foam thickness, and

(iii) increased the residual  $\text{SO}_3$  content in the glass at 1500°C. They identified sodium perborate ( $\text{NaBO}_3 \cdot \text{H}_2\text{O}$ ) as having the strongest effect, followed by  $\text{CaO}_2$  and  $\text{NaNO}_3$ .

**Effect of Atmosphere Composition and Pressure.** The atmosphere composition is known to affect the stability of glass foams by virtue of the fact that gas species can influence (i) important physicochemical properties such as glassmelt viscosity and/or surface tension as well as (ii) sulfate chemistry, and (iii) melt redox state [49, 55]. It is generally believed that severe foaming in oxygen-fuel fired furnaces is caused by a higher partial pressure of water in the furnace atmosphere [49]. In fact, the atmosphere in oxygen-fired furnaces contains 40–60 vol.% of water vapor compared with 12–18 vol.% for air-fired furnaces.

First, water vapor has arguably the strongest effect on the physicochemical properties of glassmelts. For example, water dissolved in the glass reduces viscosity [83, 135] and therefore foam stability by enhancing foam drainage. Water also reduces surface tension, which tends to stabilize the foams [90]. Water can be introduced to the glassmelt entrapped in the batch minerals or due to batch moistening. It can also be introduced from the atmosphere by diffusion and/or convective mass transfer [136]. Laimböck [43] established that water vapor infiltrates the glassmelt preferably during melting of the batch and/or during foaming. In addition, water initially contained in the batch does not evaporate as easily when the water vapor partial pressure in the atmosphere is large, as encountered in the oxygen-fuel fired furnaces.

Laimböck [43] reported that wet atmosphere (i) increased foaming of soda-lime-silica glass refined with  $\text{Na}_2\text{SO}_4$ , (ii) reduced foaming temperature, and (iii) increased sulfate losses. This is illustrated in Fig. 16.12(b). He also observed that foaming in wet atmospheres lasted longer than in dry ones. This can be explained by the fact that as the amount of water dissolved in the glassmelt increases, the partial pressure of  $\text{H}_2\text{O}$  in bubbles also increases, thus diluting the fining gases in the bubbles and promoting further mass transfer of fining gases from the melt to the bubbles. This also shifts the equilibrium reaction (6) towards a more extensive decomposition of the sulfate refining agents. As a result, sulfate begins to decompose at a lower temperature resulting in lower sulfate retention. This mechanism was formulated as the “dilution model” [43]. This interpretation was confirmed by Kim *et al.* [115] for E-glass. However, Arkosiová *et al.* [57, 116] offered an alternative explanation by suggesting that water reacted with sulfate ( $\text{SO}_4^{2-}$ ), sulfite ( $\text{SO}_3^{2-}$ ), and sulfide ( $\text{S}^{2-}$ ) to produce  $\text{O}_2$ ,  $\text{SO}_2$ , and even  $\text{H}_2\text{S}$  in reduced soda-lime-silica glass refined with sulfate and containing carbon in the form of coke. Overall, water in the furnace atmosphere helps the refining action of the sulfate, making it possible to lower the addition of sulfate to obtain an equally efficient refining process compared to dry atmosphere.

Moreover, Fig. 16.13 shows the gas volume  $V_{\text{gas}}$  to melt volume  $V_{\text{melt}}$  ratio  $\Psi (= V_{\text{gas}} / V_{\text{melt}})$  as a function of temperature for primary foaming of E-glass containing sulfates during ramp-heating at 5°C/min under dry or wet air and dry or wet carbon dioxide atmospheres [115]. It is evident that the presence of water vapor in the atmosphere reduced the foaming temperature and the amount of gas entrapped in the glass foam. Similar results were obtained by Cable and co-workers [77, 78] for binary silicate melts. The authors also found that soda-lime-silica and alkali-silica glass foaming was stronger in pure oxygen atmosphere. Kappel *et al.* [71] also showed that humidity in the atmosphere destabilized the foams made of various glasses. This apparent contradiction with results reported by Laimböck [43] (Fig. 16.12b) can be explained by the dilution effect of water vapor during the batch melting process, which

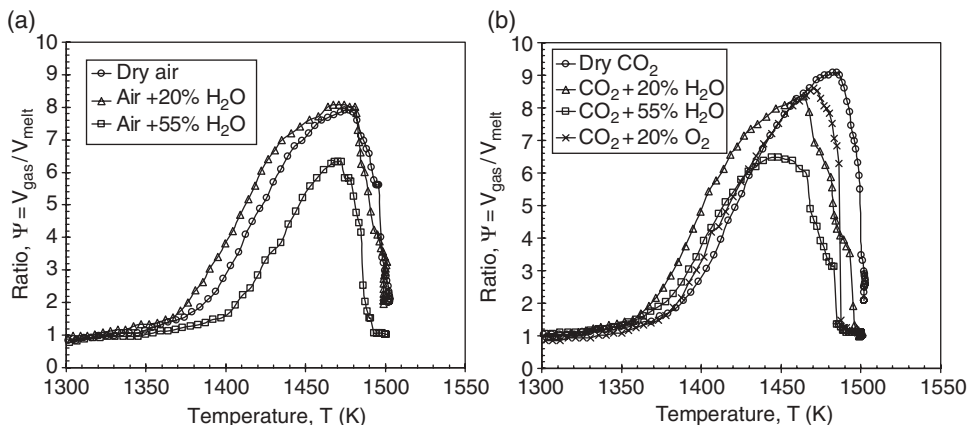


**Fig. 16.13** Gas volume to melt volume ratio for primary foaming of E-glass containing sulfates during ramp-heating at 5°C/min under (a) dry and wet air and (b) dry and wet carbon dioxide atmosphere [115].

enhanced sulfate losses at temperature below 1250°C. This effect was enhanced by the facts that (i) significantly less sulfate was added to the E-glass batch (0.17 wt%) [115] compared with the soda-lime batch (0.55 wt%) [43], and (ii) the amount of batch used by Laimböck [43] (~150 g) was much larger than that used by Kim *et al.* [115] (4–5 g).

Furthermore, reducing atmosphere in contact with glass foam tends to destabilize it, if not destroy it [43, 75, 79]. In industrial furnaces, reducing atmosphere is achieved by firing with an excess of fuel (reducing firing) as opposed to an excess of air or oxygen (oxidizing firing) [43]. For example, Cooper and Kitchener [79] reviewed the fact that foam made of molten silicate slags was more prevalent in oil-fired furnaces, which usually burn with excess air (i.e., oxidizing). However, it was rarely observed in reducing atmospheres such as so-called “coke-oven gas” consisting of H<sub>2</sub>, CH<sub>4</sub>, N<sub>2</sub>, and CO, and so-called “producer gas” consisting of H<sub>2</sub>, N<sub>2</sub>, and CO. Reducing atmospheres used experimentally have included (i) N<sub>2</sub> [78], and mixtures of (ii) N<sub>2</sub> and CO [43] or (iii) N<sub>2</sub> and H<sub>2</sub> [75], for example. Laimböck [43] showed that primary foam made of oxidized soda-lime-silica glass decayed dramatically as soon as a mixture of CO in N<sub>2</sub> was introduced in the furnace. The effect was stronger as the concentration of CO increased from 0.1 to 1.0 wt%. The author suggested that a minimum content of CO in the atmosphere should be reached in order to reproduce this effect in industrial furnaces [43]. In addition, the polyhedral bubbles at the top of the foam were found to be extremely sensitive and collapsed in contact with reducing atmosphere [43]. Similarly, Cable and co-workers [75, 77, 78] showed that binary glasses did not foam in a pure N<sub>2</sub> or a N<sub>2</sub>-H<sub>2</sub> mixed atmosphere. In addition, increasing the partial pressure of SO<sub>2</sub> in the atmosphere destabilized foams made from various glass batches [71, 78] due to the fact that SO<sub>2</sub> causes the glassmelt viscosity to decrease significantly.

Finally, a decrease in pressure of the surrounding atmosphere reduces the mass of gas retained in the batch and in the glassmelt. It lowers the temperature at which carbon dioxide is generated in the batch and thus promotes primary foaming [74]. It also decreases the solubility of SO<sub>2</sub>, H<sub>2</sub>O, and O<sub>2</sub> and favors secondary foaming as observed in reduced-pressure refining [69].

### 16.4.3 Steady-state Glass Foaming by Gas Injection

#### 16.4.3.1 Experimental Apparatus and Procedure

Figure 16.8b schematically shows the interior of a furnace used to study steady-state glass foams. In this method, an arbitrary gas mixture is continuously injected within the molten glass contained in a transparent crucible placed in a furnace at constant temperature. Here, bubbles are not generated by chemical reactions but instead injected in the glassmelt through a Pt capillary. The gas inside the bubble can be different from that in the furnace atmosphere. For example, van der Schaaf and Beerkens [117] injected N<sub>2</sub> and CO<sub>2</sub> bubbles in molten soda-lime-silica glass at temperatures between 1300 and 1400°C in air atmosphere. This method produces a steady foam layer with constant height after a rapid growth phase [43]. It can also be used to analyze foam decay by simply stopping the gas supply [117].

#### 16.4.3.2 Experimental Observations and Foaming Regimes

Experimental observations indicate that glass foams produced by gas injection do not form for any arbitrarily small gas flow rate. To scale for the container cross-section, the superficial gas velocity  $j$  is defined as the volumetric gas flow rate  $Q_g$  (in m<sup>3</sup>/s) divided by the cross-sectional area of the container denoted by  $A$  (in m<sup>2</sup>) so that  $j = Q_g / A$  (in m/s) [137]. A minimum superficial gas velocity  $j_m$  should be reached to initiate foaming when injecting air bubbles in molten glass [39, 43]. The same observations have been made for various aqueous solutions [138–143] as well as for slag foaming [144–150]. The onset of foaming corresponds to the situation when bubbly flow coexists with only a single layer of closely packed bubbles accumulating at the free surface. Three different foaming regimes have been identified [39]:

- If  $j < j_m$ , the gas flux  $j$  reaching the liquid surface is not sufficient to create a stable foam layer (Fig. 16.14a). If  $j = j_m$ , the foam layer consists of a monolayer of bubbles whose thickness is  $2r_0$  where  $r_0$  is the average radius of the bubbles (Fig. 14b).
- If  $j_m < j \leq j_{cr}$ , the foam reaches a steady state and its thickness increases as the gas influx increases (Fig. 16.14c) [39].
- If  $j \geq j_{cr}$ , the excess of mass flux over the critical superficial gas velocity  $j_{cr}$  cannot be released at the top of the foam and has to be stored within the foam. Thus, the foam volume grows continuously until all available liquid is dispersed in the foam, so a steady state is never reached [39]. Beyond a certain mass flux, vent holes may start developing within the foam, which stops growing or may even start decaying [138, 151].

Note that the last regime is not shown in Fig. 16.14 as the foam looks very similar to that shown in Fig. 16.14(c) except that bubbles may be bigger and the foam thicker with large pockets of air and possible vents. Note also that in glass melting furnaces this regime is less likely to be observed since the foam is not confined. Instead, foam is more likely to flow and spread horizontally over the glassmelt surface [152, 153].

#### 16.4.3.3 Onset of Glass Foaming

Figure 16.15 shows the steady-state foam thickness  $H_1$  as a function of superficial gas velocity  $j$  measured by bubbling air in sulfate-free molten soda-lime-silica glass at different temperatures [43]. It illustrates the existence of a minimum superficial gas velocity for onset of foaming  $j_m$  which can be determined by extrapolating the linear curve fit to the limiting case when  $H_\infty = 0.0$ .

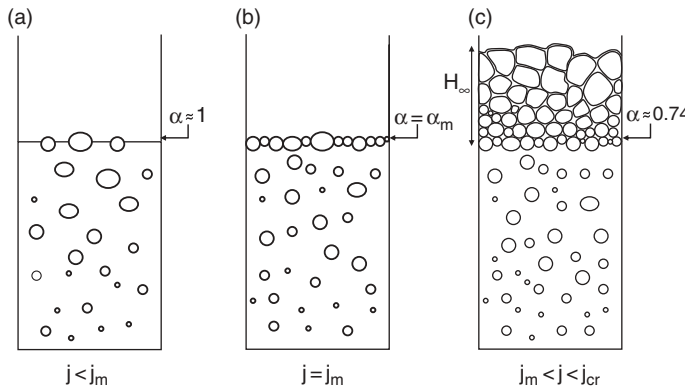


**Fig. 16.14** Schematic of the behavior of a foaming solution as the superficial gas velocity increases (a) bubbly flow without foam, (b) onset of foaming, (c) developed foam layer.

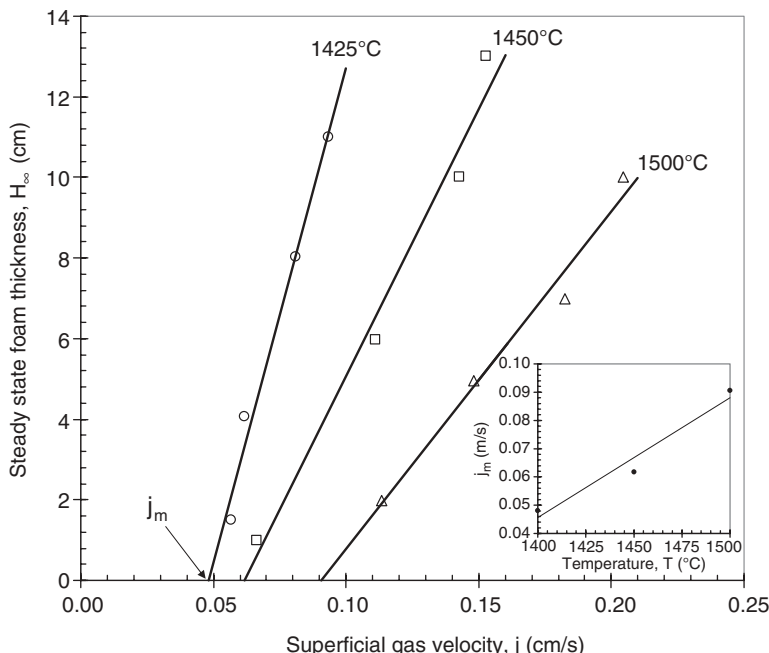


**Fig. 16.15** Steady state foam thickness v. superficial air velocity for sulfate-free soda-lime-silica glass (75 SiO<sub>2</sub>-15 NaO<sub>2</sub>-10 CaO, wt%) at different temperatures [43].

#### 16.4.3.4 Steady-state Foam Thickness

**Effect of Temperature.** The stability and steady-state thickness of glass foams decrease with increasing temperature [43, 79]. This is illustrated in Fig. 16.15 where, for a given superficial gas velocity  $j$  larger than  $j_m$ , the foam thickness decreases with increasing

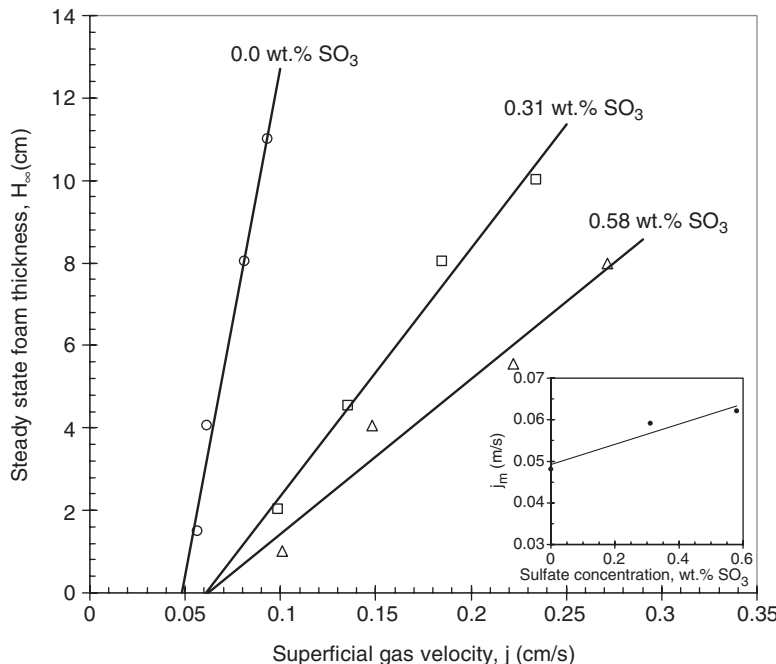


**Fig. 16.16** Steady state foam thickness v. superficial argon velocity for soda-lime-silica glass with different initial sulfate content at 1425°C [43].

temperature. This can be attributed to the fact that the melt viscosity decreases as the temperature increases, resulting in shorter drainage time. For the same reasons, the inset in Fig. 16.15 shows that  $j_m$  increases as the temperature increases, which makes the bubbles less stable, requiring larger flow rates for onset of foaming.

**Effect of Sulfate Addition.** Figure 16.16 shows the steady-state foam thickness as a function of superficial gas velocity reported by Laimböck [43] for soda-lime-silica glass with different initial  $\text{SO}_3$  content. The foam was generated by injecting argon into the glassmelt at 1425°C [43]. First, the inset of Fig. 16.16 indicates that  $j_m$  increases as sulfate concentration increases. In addition, the foam tended to be less stable for larger sulfate content. This can be attributed to the decrease of viscosity caused by the presence of sulfate [43]. Note that here only the effect of sulfates on the thermophysical properties of the glassmelt and their impact on foaming were assessed.

## 16.5 Modeling

### 16.5.1 Introduction

In order to design, optimize, and operate industrial glass melting furnaces and to mitigate the negative effects of glass foaming, it is necessary to develop physical models informed by experimental observations and accounting for the most important physical phenomena.

Models reported in the literature can be divided into two categories: (i) time-dependent models predicting foam growth and decay; and (ii) steady-state models predicting the onset of foaming and the steady-state foam thickness. Note that most models presented and developed for glass foams can typically be used for foams made of other viscous fluids.

### 16.5.2 Dynamic Foam Growth and Decay

#### 16.5.2.1 Foaming by Thermal Decomposition

Kappel *et al.* [71] showed experimentally that the thickness of glass foams generated from soda-lime-silica, E-glass, borosilicate, and brown glasses systematically decayed exponentially during foam collapse and could be expressed as  $H(t) = H_0 \exp(-k_s t)$  where  $H_0$  is the initial foam thickness. The empirical constant  $k_s$  was a function of (i) temperature, (ii) glassmelt properties (e.g., density, surface tension, viscosity), and (iii) partial pressures of  $\text{H}_2\text{O}$  and  $\text{SO}_2$  in the furnace atmosphere. However, the authors did not provide a relationship between  $k_s$  and all these parameters. Moreover, they reported that  $k_s$  was approximately equal to  $20k_L$  reported for the vertical film thickness as previously discussed.

Recently, Hrma [58] proposed a model for foaming caused by  $\text{SO}_2$  and  $\text{O}_2$  release during sulfate thermal decomposition in E-glass between 1335 and 1440°C. The author expressed the gas to melt volume ratio  $\Psi(t)$  as a function of time as

$$\Psi(t) = \frac{V_{\text{gas}}}{V_{\text{melt}}} = \Psi_0(1 + b \Phi^3 t^2) \quad (16.14)$$

where  $\Phi = dT/dt$  is the heating rate while  $b$  and  $\Psi_0$  are empirical parameters determined from experimental data. The time  $t = 0$ s was set for temperature  $T_0 = 1335^\circ\text{C}$  so that  $T = T_0 + \Phi t$ . This model successfully predicted the behavior of glass foam made of E-glass batch subjected to heating rates of 5, 10, and 15°C/min beyond  $T_0$  as reported by Kim *et al.* [115]. Figure 16.10(b) plots  $\Psi(t)$  versus  $\Phi^3 t^2$  and illustrates how the experimental data shown in Fig. 10(a) for different heating rates collapse on a single line during the exponential growth phase as predicted by eqn (16.14) with  $b = 5.39 \times 10^{-3} \text{ s/K}^3$  and  $\Psi_0 = 0.587$ .

#### 16.5.2.2 Foaming by Gas Injection

Pilon *et al.* [154] presented an experimentally validated model to analyze the transient formation of a foam layer produced by injecting gas bubbles in a foaming solution. Their model was based on the mass conservation equation for the gas phase in the foam combined with models for the average foam porosity. The authors assumed that, during the growth phase ( $t \leq \tau_{bf}$ ), no gas escapes at the top of the foam via bubble bursting. Then, the foam thickness can be expressed as [154]

$$H(t) = \frac{jt}{\bar{\phi}} \text{ for } t \leq \tau_{bf} \quad (16.15)$$

where  $j$  is the incoming superficial gas velocity at the bottom of the foam while  $\bar{\phi}$  is the average foam porosity. The latter can be taken as constant and equal to  $\bar{\phi} = 0.82$  for practical calculations [154]. The time constant  $\tau_{bf}$  corresponds to the characteristic lifetime

of a lamella at the top of the foam. The model predictions showed very good agreement with experimental data for aqueous solutions with 10% glycerine + 80 mg/l of Marlophen-89 [138] for low superficial gas velocity. It can also provide an upper limit of the foam thickness for intermediate and large superficial gas velocities.

More recently, Van der Schaaf and Beerken [117] developed a dynamic model for the growth and decay of glass foams. The authors assumed that foam was made of superimposed layers of monodisperse hemispherical shells. The mass conservation equation for the gas phase in the foam was given by [117]

$$\frac{dH}{dt} = j(t) - j(t - \tau_{bf}) \quad (16.16)$$

where  $j(t)$  is the superficial gas velocity for bubble entering the foam layer at the bottom and  $j(t - \tau_{bf})$  is the superficial gas velocity leaving the foam due to the bursting of bubbles at the top of the foam after spending an average lifetime  $\tau_{bf}$ . The average lifetime  $\tau_{bf}$  of a bubble at the top of the foam was estimated by solving mass and momentum conservation equations for the molten glass draining in the lamella of an hemispherical shell. The fluid was treated as non-compressible and Newtonian and the interfaces were assumed to be (i) fully mobile, (ii) partially mobile, or (iii) fully immobile. An expression for the average bubble lifetime was derived for each boundary conditions as a function of density  $\rho$ , viscosity  $\mu$ , and average bubble radius  $r_0$  and given by [117]

$$\tau_{bf} = \frac{\mu}{3\rho g r_0} \left[ \ln\left(\frac{\delta_0}{\delta_c}\right) + 2 \frac{\psi r_0^2}{\mu / \delta_c} \right] \quad (16.17)$$

where  $\delta_0$  is the initial lamella thickness,  $\psi$  is a parameter ranging from 0 to infinity corresponding to the limit cases of fully mobile and fully immobile bubble interface, respectively. The critical lamella thickness  $\delta_c$  was taken to be 100 nm based on empirical observations [43, 71]. The advantage of this model is that it can predict both the growth and the decay of foam. The expression for  $\tau_{bf}$  was in good agreement with those derived by Pilon *et al.* [154] by considering the intersection of their transient foam model [154] given by eqn (16.15) and the semi-empirical steady-state model [155] discussed in the following section (eqn 16.28).

The model was solved in a discontinuous manner in terms of time. Its predictions were compared with experimental data for foam made by injecting either N<sub>2</sub> or CO<sub>2</sub> in soda-lime-silica glass at 1300 and 1400°C [117]. The resulting foam porosity was 91% and the average bubble radius varied from 5 to 8.3 mm as the gas flow rate increased. Good agreement was observed between model predictions and experimental data for  $\psi$  equal to 2.5/m. However, it remains unclear how this value of  $\psi$  was obtained and what value of  $\delta_0$  was used to achieve these results.

For constant superficial gas velocity  $j$ , the model developed by Van der Schaaf and Beerken [117] predicts the foam height as

$$H(t) = jt \text{ for } t \leq \tau_{bf} \quad (16.18)$$

$$H_{\infty} = j\tau_{bf} \text{ for } t > \tau_{bf} \quad (16.19)$$

where  $H_{\infty}$  denotes the steady-state foam thickness. Note that eqn (16.18) ignores the contribution of the liquid to the overall foam thickness, unlike the transient model given by eqn (16.15) [154], i.e., it assumes  $\bar{\phi} = 1.0$ . In addition, eqn (16.19) corresponds to the concept of unit of foaminess introduced by Bikerman [137]. However, the validity of this concept has been questioned extensively in the literature, as discussed in detail in the next section [39, 155–158]. Finally, eqn (16.19) predicts that foam forms for any superficial gas velocity, which contradicts the concept of the onset of foaming introduced by Hrma [39] and illustrated in Figs 16.15 and 16.16.

### 16.5.3 Steady-state Glass Foams

Based on experimental observations previously reviewed, steady-state foams are characterized by the minimum superficial gas velocity for onset of foaming  $j_m$  and by their thickness  $H_{\infty}$ . The following sections discuss models associated with both of these parameters.

#### 16.5.3.1 Onset of Foaming

Pilon and Viskanta [159] argued that coalescence of rising bubbles with bubbles at rest at the liquid free surface was the main physical phenomenon controlling the onset of foaming. The authors used the drift flux model [160] to derive the following expression for  $j_m$  as a function of the maximum void fraction for onset of foaming  $\alpha_m$ , operating conditions, and physico-chemical properties of the two phases,

$$j_m = v_{\infty} f(r^*) \alpha_m (1 - \alpha_m)^{n-1} \quad (16.20)$$

where  $f(r^*)$  is a function of the dimensionless bubble radius  $r^*$ . Both depend on the thermophysical properties of the melt and on whether the two-phase flow regime in the liquid below the foam was viscous, distorted bubble, and churn-turbulent as summarized in Table 16.1 of ref. [159]. Figure 16.17 compares the experimental data for the minimum superficial gas velocity for onset of foaming  $j_m$  with the model predictions given by eqn (16.20), using a maximum void fraction  $\alpha_m = 0.85$  corresponding to the case of small probability of coalescence ( $P < 66\%$ ) between a rising bubble and a bubble at rest at the liquid free surface. Relatively good agreement was found between model predictions and experimental data for a wide range of  $j_m$  values and various viscous fluids (e.g., slags, glass, glycerol) [159].

#### 16.5.3.2 Steady-state Foam Thickness

**Foaming Index and Related Models.** The first model predicting the steady-state foam height as a function of superficial gas velocity  $j$  was proposed by Bikerman [137]. He suggested that below the critical superficial gas velocity  $j_{cr}$ , the steady-state foam thickness  $H_{\infty}$  increases linearly with superficial gas velocity [137],

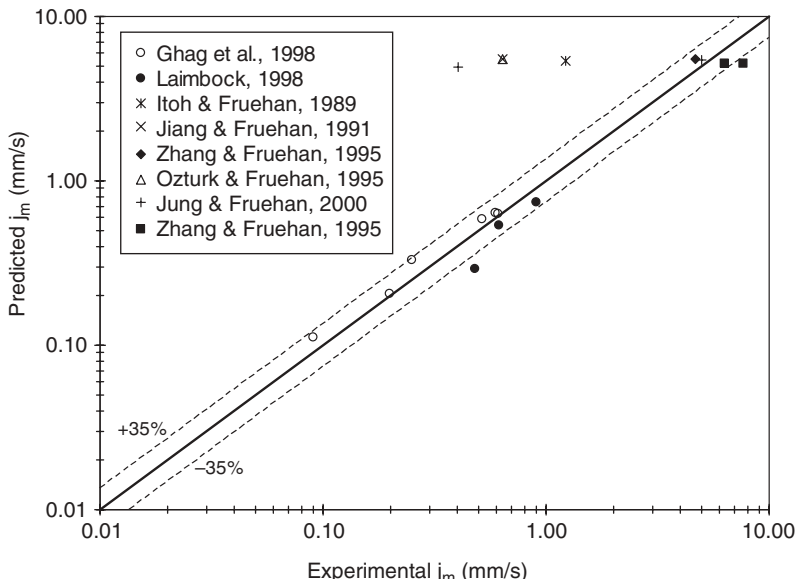


**Fig. 16.17** Comparison between experimental and predicted minimum superficial gas velocity for onset of foaming for viscosity dominated drainage associated with a probability of bubble coalescence less than 66% [159].

$$H_{\infty} = \Omega j \quad \text{if } j \leq j_{cr} \quad (16.21)$$

where  $\Omega$  is a constant called the “unit of foaminess” or “foaming index.” It was considered to be a physical characteristic of the liquid corresponding to the average residence time of a bubble in the foam [44, 117], i.e.,  $\Omega = \tau_{bf}$ . Beyond the critical mass flux  $j_{cr}$ , the entrainment of the liquid into the foam by rising bubbles cannot be balanced by drainage and the foam thickness increases without limit. However, experimental data for viscous oils [39, 157] indicate that the transition from a steady-state foam to a constantly growing foam is not abrupt at  $j = j_{cr}$  but continuous, thereby indicating that  $\Omega$  is not a fluid property but increases as the mass flux  $j$  increases. Lin and Guthrie [158] confirmed the validity of eqn (18.21) for small superficial gas velocity. However, the foam tended to become unstable with decreasing steady-state thickness as the superficial gas velocity increased.

Jeelani *et al.* [138] proposed a model for the steady-state foam thickness accounting for binary bubble coalescence taking place within the foam. The steady-state foam thickness was expressed as a function of the thermophysical properties of the liquid phase, the binary coalescence time, and the average foam porosity. The binary coalescence time as well as the average foam porosity were determined experimentally from the measurements of the average bubble diameter as a function of depth of foam made of nitrogen bubbles in water with 10% glycerinate Marlophen 89 and 812 [138]. Good agreement was found between the model predictions and the experimental data. Unfortunately, most of the other experimental

studies of steady-state foam thickness did not provide the variation of the average bubble diameter along the foam height. Also, neither the binary coalescence time nor the average foam porosity could be determined, making the model validation impossible for other solutions [155].

A series of studies on slag foams in iron and steelmaking processes was carried out by Fruehan and co-workers to correlate the foaming index with slag properties and bubble size [144–148, 150, 161]. All the experiments consisted of bubbling argon in a cylindrical tank containing liquid slag with various amounts of CaO, SiO<sub>2</sub>, FeO, MgO, and Al<sub>2</sub>O<sub>3</sub> at high temperatures. Zhang and Fruehan [147] performed a dimensionless analysis using the Buckingham–Pi theorem to relate the unit of foaminess  $\Omega$ , liquid viscosity  $\mu$ , density  $\rho$ , surface tension  $\sigma$ , and average bubble diameter  $D_0$ . Three dimensionless groups were identified and related by a power-type of law. Experimental data for CaO-SiO<sub>2</sub>-FeO-MgO-Al<sub>2</sub>O<sub>3</sub> suggested the following semi-empirical expression for the unit of foaminess  $\Omega$  [147]:

$$\Omega = 115 \frac{\mu^{1.2}}{\sigma^{0.2} \rho D_0^{0.9}} \quad (16.22)$$

This semi-empirical model was based on experimental data obtained for similar slag compositions, thermophysical properties, and average bubble diameter, making this model valid for a very narrow range of fluids and operating conditions. In fact, Ghag *et al.* [140] studied pneumatic foams formed by bubbling nitrogen in different viscous solutions containing water, glycerinate (78 to 95 vol.%), and SDBS surfactant. The authors showed that “there was a poor correlation” between their experimental data and eqn (16.22). Experimental results indicated that the foaming index predicted by eqn (16.22) should be more sensitive to changes in surface tension and that the exponent associated with the average bubble diameter  $D_0$  was a major cause of discrepancies. From these observations, Ghag *et al.* [162, 163] also developed a model for the unit of foaminess  $\Omega$  using the Buckingham–Pi theorem. They performed the same analysis as that by Zhang and Fruehan [147] but replaced the equilibrium surface tension by the effective elasticity of liquid films  $E_{eff}$  for solutions following Langmuir behavior to yield [140]

$$\Omega = 1.0 \times 10^6 \frac{(\rho g)^2 D_0^3}{\mu E_{eff}} \quad (16.23)$$

Unfortunately,  $E_{eff}$  is not always available and its measurements may be tedious [140]. Thus, validation of the model for a wide range of experimental conditions and fluid has not been performed.

Finally, Beerkens and Van der Schaaf [44] combined the above described model given by eqns (16.17) and (16.19) with a model predicting the gas generation rate during refining to predict the steady-state foam thickness. The authors developed a thermochemical model to estimate the volume of gases released during refining of glassmelt and accounting for the temperature, composition, and redox state of the glassmelt along with sulfate decomposition and other redox reactions involving various gas species (e.g., SO<sub>2</sub>, O<sub>2</sub>, N<sub>2</sub>, CO<sub>2</sub>). Their model assumed thermodynamic equilibrium between the melt and the gas phases. It

enabled the prediction of  $j$  as a function of temperature necessary to predict the foam thickness and foaming temperature.

**Hrma's Model.** Hrma [39] developed a model for a steady-state foam blanket that did not use the concept of foaming index or the Buckingham–Pi theorem. Instead, the steady-state foam thickness was described in terms of the two previously discussed limiting gas fluxes  $j_m$  and  $j_{cr}$  according to [39]

$$H_\infty = 2r_0 + 2r_0 b_h \left[ \frac{1/j_m - 1/j_{cr}}{1/j - 1/j_{cr}} - 1 \right] \quad (16.24)$$

where  $r_0$  is the average radius of bubbles in the foam, and  $b_h$  is a constant depending on the gravitational drainage and on the survival time of a critically thin film separating the foam from the atmosphere.

Hrma [39] suggested that eqn (16.21) proposed by Bikerman [137] is only valid (i) for evanescent foams for which the liquid lamellae separating the bubbles in the foam rupture as soon as the critical thickness of the foam is reached, and (ii) for very small superficial gas velocity (i.e.,  $j \ll j_{cr}$ ). In that case, eqns (16.21) and (16.24) are equivalent as long as  $b_h = 1$  and  $\Omega \approx 2r_0/j_m$ . In addition, for foams characterized by similar superficial gas velocities  $j_m$  and  $j_{cr}$ , only a narrow range of superficial gas velocity  $j$  can generate a steady-state foam. This might have been the case observed by Watkins [151].

Finally, Hrma's model [39] provides insights into the mechanism of foam formation and stability by qualitatively explaining reported experimental data. Unfortunately, it lacks expressions for  $j_{cr}$  and  $b_h$ . However, the expression for  $j_m$  given by eqn (16.20) could be used in eqn (16.24).

**Dimensional Analysis of Foam Thickness Governing Equation.** More recently, Pilon and co-workers [155, 164] developed a general correlation capable of predicting the steady-state foam thickness for a variety of systems having widely different thermophysical properties and average bubble diameters. Instead of using the Buckingham–Pi theorem, the mass and momentum conservation equations for the liquid phase derived by Bhakta and Ruckenstein [82] were adapted to derive the governing equation for the steady-state foam thickness  $H_\infty$ . The authors assumed that (i) the foam consisted of dodecahedron bubbles of the same size, (ii) the Plateau borders were randomly oriented, (iii) the drainage through the Plateau borders due to film thinning was negligible compared to that due to gravity (see [82, 165] for additional discussion), (iv) coalescence of bubbles and Ostwald ripening within the foam were absent, (v) surface tension was constant, (vi) the container wall effects were negligible, and (vii) the temperature was constant and uniform throughout the foam. This governing equation was then scaled by dimensional analysis based on physical arguments to obtain the following two dimensionless numbers  $\Pi_1$  and  $\Pi_2$  [155]:

$$\Pi_1 = \frac{\rho g r_0^2}{\mu(j - j_m)} \text{ and } \Pi_2 = \frac{\mu(j - j_m)}{\sigma} \times \frac{H_\infty}{r_0} \quad (16.25)$$

The number  $\Pi_1$  can be interpreted as the ratio of the gravitational force to the viscous force on an average bubble of radius  $r_0$  having a velocity  $(j - j_m)$ . Similarly,  $\Pi_2$  corresponds to the ratio of the viscous force to the surface tension force times the ratio of the steady-state

foam thickness to the average bubble radius. Both  $\Pi_1$  and  $\Pi_2$  can be expressed as functions of well known dimensionless numbers [155]:

$$\Pi_1 = \frac{Re}{Fr} \text{ and } \Pi_2 = Ca \left( \frac{H_\infty}{r_0} \right) \quad (16.26)$$

where  $Re$ ,  $Fr$ , and  $Ca$  are the Reynolds, Froude, and Capillary numbers, respectively, defined as,

$$Re = \frac{\rho_c(j - j_m)r_0}{\mu}, \quad Fr = \frac{(j - j_m)^2}{gr_0}, \quad Ca = \frac{\mu(j - j_m)}{\sigma} \quad (16.27)$$

The relationship between  $\Pi_1$  and  $\Pi_2$  was assumed to follow a power-law, i.e.,  $\Pi_2 = K\Pi_1^n$  where  $K$  and  $n$  were constant parameters determined from experimental data. More than 120 experimental data points for foams formed from high viscosity liquids and various gases and injection methods were considered [43, 140, 144–150, 161]. The superficial gas velocity for onset of foaming  $j_m$  can be determined either by eqn (16.20) or from experimental data assuming a linear relationship between  $H_\infty$  and  $j$  as illustrated in Figs 16.15 and 16.16. The ranges of thermophysical properties and experimental conditions were the following: (i)  $46 \text{ mPa.s} < \mu < 12,100 \text{ mPa.s}$ , (ii)  $1,200 \text{ kg/m}^3 \leq \rho \leq 3,000 \text{ kg/m}^3$ , (iii)  $69.5 \text{ mN/m} \leq \sigma \leq 478 \text{ mN/m}$ , (iv)  $0 \leq j \leq 40 \text{ mm/s}$ , and (v)  $0.7 \text{ mm} \leq r_0 \leq 20 \text{ mm}$  [155]. The corresponding dimensionless parameters  $\Pi_1$  and  $\Pi_2$  cover the range from 80 to 5030 and from  $5 \times 10^{-4}$  to 0.76, respectively. Figure 16.18 shows the relationship between the

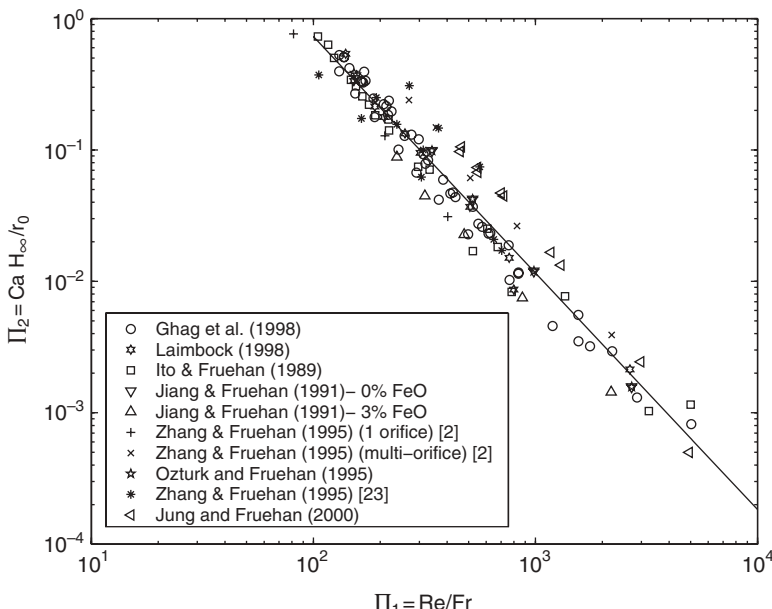


**Fig. 16.18** Correlation of dimensionless numbers  $\Pi_2$  v.  $\Pi_1$  for foams made from a wide range of viscous liquids.

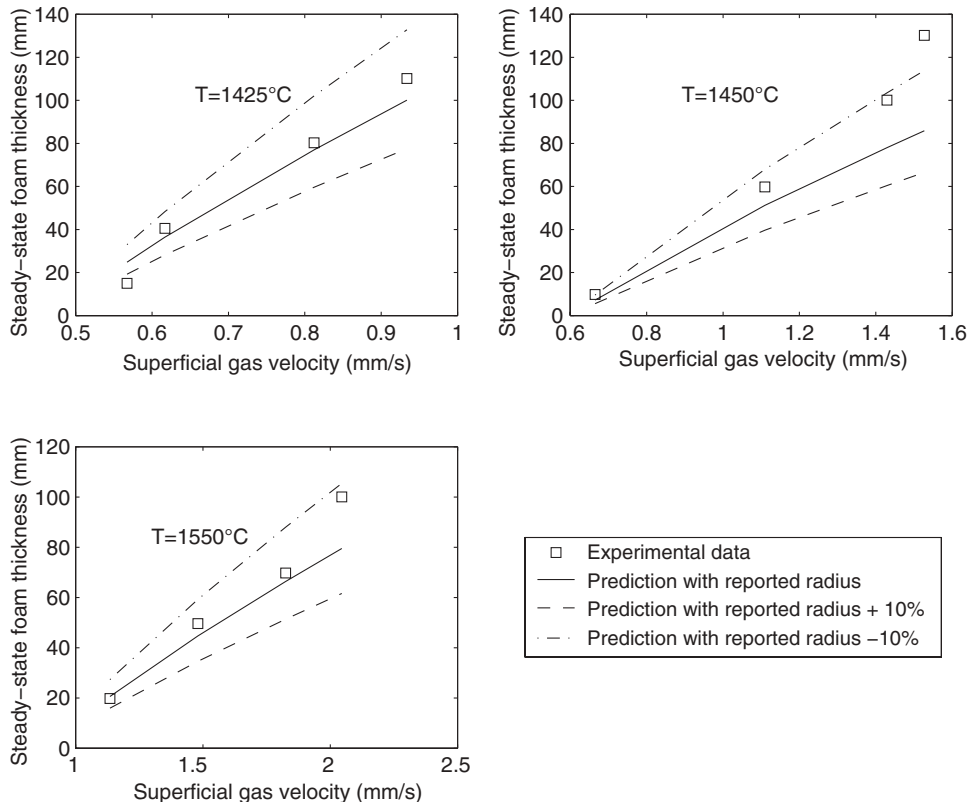


**Fig. 16.19** Influence of the bubble radius on the model predictions and comparison with experimental data for glass foams made by injecting air into sulfate free soda-lime-silica melt at 1425, 1450, and 1550°C [43].

dimensionless parameters  $\Pi_1$  and  $\Pi_2$  with  $K = 2905$  and  $n = -1.80$ . The following relationship between the physically relevant dimensionless numbers can be written as

$$\frac{H_\infty}{r_0} = \frac{2905}{Ca} \left( \frac{Fr}{Re} \right)^{1.80} \quad (16.28)$$

Figure 16.19 compares the steady-state foam thickness measured experimentally with predictions by eqn (16.28) using the reported radius  $r_0$  and the reported radius with  $\pm 10\%$  deviation. The foam was made by injecting air in sulfate-free soda-lime-silica glass at different temperatures (see Fig. 16.15) [43]. The predictions vary significantly depending on the average bubble radius  $r_0$  used and, in this particular case, the experimental data lie within the prediction range. In general, predictions of  $H_\infty$  by eqn (16.28) fell within 35% of experimental data. This is quite acceptable given the wide bubble size distribution and the uncertainty in the experimental data and the thermophysical properties.

Moreover, Lotun and Pilon [164] applied the Buckingham–Pi theorem based on six independent variables ( $\mu, \rho, \sigma, j - j_m, H_\infty, r_0$ ) but did not use the concept of foaming index. Their analysis resulted in four dimensionless numbers, namely  $Fr$ ,  $Re$ ,  $Ca$ , and  $H_\infty/r_0$ , given by eqn (16.27). Their final power-law correlation was in excellent agreement with that derived by Pilon *et al.* [155] and given by eqn (16.28).

#### 16.5.4 Experiments and Model Limitations

It should be noted that all previously discussed experimental results and associated models were obtained in laboratory crucibles; thus, one should be careful in extending these results to glass foams in industrial glass melting furnaces [74]. Some of the more important effects that are difficult to observe or reproduce in small-scale laboratory systems are as follows:

1. The refining reactions observed in crucibles at high temperature would most probably occur only at the top of the batch in the actual furnace that is directly exposed to radiant heating, whereas the center of the batch is too cold for initiation of fusion reactions due to the “insulation effect” of the expanded batch.
2. Partition of the gas generated in the batch between what is released (escaped) to the combustion space and what is entrapped in the form of gas bubbles in the glassmelt and then carried away by the convection currents is difficult if not impossible to study in laboratory systems since convection currents encountered in glass melting tanks cannot be reproduced in small crucibles.
3. Volatilization of glass volatile compounds takes place at high temperatures [49]. Such compounds are present at the surface of the liquid film located at the top of the foam layer and exposed to the furnace atmosphere and to intense heating from the combustion space. They include alkali oxides, lead oxides, and boric oxides as well as sodium hydroxide (NaOH) or HCl in borosilicate glass [49, 71]. Their volatilization may significantly disturb concentration profiles in the liquid film and increase the liquid viscosity [49]. Then, the film surface becomes more rigid and even solid [49, 71]. However, the effect of volatilization on glass foam stability has received very little attention and is not accounted for in existing glass foam models.
4. In glass melting furnaces, the glass foam may be subjected to large temperature gradients but its effect on the foam dynamic behavior and stability remains to be explored and modeled. Bickford *et al.* [34] proposed an expression for the temperature gradient across the foam layer. The model accounted for heat generation due to chemical reactions and heat conduction. However, it did not account for radiative heat transfer within the foam where incident radiation from the furnace is scattered and absorbed [12, 13].
5. All the previously reviewed models used an average bubble radius. However, bubble size distribution can strongly affect the foam behavior. Thus, the model that explicitly accounts for the bubble size distribution rather than using the average bubble radius should be developed.

## 16.6 Measures for Reducing Glass Foaming in Glass Melting Furnaces

Destroying glass foam forming at the surface of glassmelt in industrial glass melting furnaces has been identified as one of the major issues in glass-melting technology [1]. The following sections make recommendations for reducing primary and secondary glass foaming based on the experimental observations and models previously described, as well as methods used in industry and described in patents. They consist of (i) facilitating the release of gases early in the melting process before a viscous liquid phase seals the batch, (ii) reducing the amount of gas generated, and/or (iii) destabilizing the liquid films separating the foam bubbles through various means.

### 16.6.1 Batch Composition

It has been established that secondary foaming can be reduced by facilitating the release of gases to the combustion space before the first liquid phase appears and becomes interconnected [74]. This can be achieved by adding carbonaceous compounds (e.g., coke, active carbon, graphite) to the batch. In particular, it can completely eliminate secondary foaming in high temperature regions of the furnace. However, it also tends to promote primary foaming due to early release of refining gases [55] and may change the oxidation state of the glass and its color. In addition, reducing conditions may attack metals, resulting in electric shorting between the electrode through the molten metal in electric melters [27].

Moreover, addition of  $\text{Na}_2\text{SO}_4$  to the batch reduces primary foaming in oxidized glasses [43, 74]. One should note that although  $\text{Na}_2\text{SO}_4$  reduces primary foaming, it also increases secondary foaming by enhancing refining reactions and gas production in the refining section. Therefore, the amount of  $\text{Na}_2\text{SO}_4$  to be added to the batch needs to be optimized by considering both primary and secondary foaming. Excessive reduction in the amount of refining agent may reduce glass fining and therefore result in reboil in the forehearth and reduced product quality. In furnaces equipped with oxygen-fuel burners the amount of refining agents added to the batch can be reduced compared with air-fuel burners. Here too, the batch content of refining agents needs to be optimized. Laimböck [43] proposed a semi-empirical expression for the optimal mass of sodium sulfate that should be added to the batch for producing soda-lime-silica glass with a given composition. It accounts for the maximum melting temperature, the water vapor partial pressure in the combustion space, the batch weight, the sulfate losses during initial fusion/melting reactions, and the small variations in the batch composition [43]. In particular,  $\text{SiO}_2$  and  $\text{Na}_2\text{O}$  contents should be carefully controlled as small variations (~0.2 wt%) may result in significant increase in the amount of refining gases released [43].

Alternatively, Pedebosq *et al.* [166] proposed adding sulfide to the batch as a way of reducing or eliminating secondary foaming in E-glass, alkali-resistant (AR) glass, C-glass, and S-glass featuring silica content less than 70 wt%. The sulfide can be added in the form of pure or mixed metal sulfide including  $\text{Na}_2\text{S}$ ,  $\text{CaS}$ ,  $\text{ZnS}$ ,  $\text{MOS}_2$ , and  $\text{CdS}$  as well as in the form of slag. It is also preferable to use sulfide particles smaller than 200  $\mu\text{m}$  with concentration between 5 and 50 mol.% of refining agents  $\text{Na}_2\text{SO}_4$  or  $\text{CaSO}_4$ .

Furthermore, dissociating the oxidizing function of  $\text{Na}_2\text{SO}_4$  at low temperatures from its refining function at high temperature was proven to be successful at reducing glass foaming.

In fact, large amounts of  $\text{Na}_2\text{SO}_4$  could be replaced by oxidizing agents such as  $\text{NaBO}_3 \cdot \text{H}_2\text{O}$ ,  $\text{CaO}_2$ , and  $\text{NaNO}_3$  while maintaining the glass redox state. This proved to significantly reduce foaming in oxidized E-glass [46]. Similarly, Huang [7] proposed to add a high-temperature oxidizing agent to the batch such as cerium oxide and potassium permanganate. Such compounds are inactive at temperatures less than 1315°C, while they decompose and release oxygen gas above this temperature.

Finally, precise control of the glass redox state is important in controlling foaming. This is particularly challenging when recycled cullets, possibly contaminated, are mixed with the batch. Then, it is desirable to separate cullets by color and adjust the batch composition according to the type and amount of cullets used both to limit foaming and to achieve the desired glass redox state and color [43].

### 16.6.2 Batch Conditioning and Heating

Fine silica grains melt more quickly and create a viscous silica rich melt that traps the  $\text{CO}_2$  generated during primary foaming. Thus, using coarse silica grains and cullets favors the release of gases before the liquid phase is formed, thereby reducing primary foaming [113, 114]. However, more unmelted silica grains could remain in the final product. Alternatively, batch and cullets could be charged in the furnace in stratified layers with a moist batch layer consisting of coarse grains loaded on top of a layer of fine cullets [43]. This would not only enable the release of  $\text{CO}_2$  gas without being entrapped by a viscous melt but also accelerate the dissolution of silica sand [43].

Furthermore, compacting and preheating the batch and the cullets with the hot combustion products before introducing them into the furnace can significantly reduce foaming [72]. In particular, preheating the cullets enables the decomposition of organic contaminants in the form of  $\text{CO}_2$  and  $\text{CO}$ .

### 16.6.3 Furnace Temperature

On the one hand, increasing the furnace temperature tends to destabilize primary foaming [55, 70, 71] since the foam decay rate increases exponentially with temperature [71]. Note that directing the flames towards the batch logs to increase their temperature was not recommended as this may melt the top layer of the batch, thus preventing further gas release [43]. On the other hand, increasing temperature also shifts refining reactions towards gas production, which results in stronger secondary foaming. Thus, temperature increase should be accompanied by reduction in the content of refining agent. In addition, higher operating temperatures increase the fuel consumption, operating cost, and pollutant emissions, while reducing furnace lifetime. Moreover, slowly heating the batch was shown to reduce primary foaming [72, 74, 113–115], but it would also limit the plant productivity.

### 16.6.4 External and Temporary Actions

Numerous patents have been filed to control glass foams in industrial furnaces by using external means or temporary actions. The simplest way to destroy glass foams is to mechanically break the liquid films separating the bubbles. This can be achieved by using

mechanical rotators in the shape of a cone or a bar mounted on a rotating rod [67]. Alternatively, continuous or pulsating high pressure gas jets impinging onto the foams can be used [67, 167]. The gas jets may also carry large solid particles whose impact can mechanically break the liquid films [67]. During these processes, care should be taken not to affect the foam temperature and to choose gases that can be dissolved in the glassmelt as well as solid particles that do not contaminate the glass or generate gases.

Alternatively, Ito [168] proposed a method to eliminate foaming in molten slag by throwing a solid block containing (i) 17–72 wt% of organic material such as wood chips or powder as well as rice hulls, coal, tar, and pitch, (ii) 20–80 wt% of refractory materials such as silica, clay, olivine, limestone, dolomite, magnesite, and alumina, and (iii) 3–15 wt% of binder such as starch, sugars, and resins to hold the block together. The refractory ensured that the density of the block was heavier than the slag. Then, throwing the block caused significant mechanical disturbances, thus destroying the foam. In addition, the organic matter burns and decomposes at high temperatures, which destabilizes the foam. We speculate that the latter effect may be due to the fact that combustion of the organic matter consumes oxygen, producing a reducing atmosphere, known to destabilize liquid films, within the foam itself.

Moreover, Laimböck [43] proposed spraying  $\text{Na}_2\text{SO}_4$ ,  $\text{NaOH}$ , and  $\text{KOH}$  solutions on the glass foam blanket as an efficient way to destroy it. Indeed, these elements significantly reduce surface tension of the glassmelt and induce a large surface tension gradient in the liquid films at the top of the foam, resulting in their destabilization.

More recently, Takei and Oda [169] patented a procedure to destroy glass foams by directly spraying inside the furnace metal oxide powders (e.g.,  $\text{TiO}_2$ ,  $\text{Al}_2\text{O}_3$ ,  $\text{ZnO}$ ) or solutions of organic metal compounds (e.g., tetramethyl silicate, metal tetrachloride, aluminum sulfate or nitrate) in water or organic solvents such as alcohols (e.g., ethanol) or hydrocarbons (hexane, toluene, kerosine). Metals of interest include Al, Ca, Ce, Co, Cr, Fe, Mg, Si, Ti, and Zn, which easily form metal oxide under oxidizing conditions and high temperatures. The metal compounds can be introduced by spraying particles or solutions in the air or oxygen flow used for combustion or through a separate carrier gas (e.g.,  $\text{N}_2$ ). They can also be mixed with heavy oil or natural gas before injection into the burner. They can also be mixed with water or organic solvents to form a slurry that can then be sprayed. As the metal compounds enter the furnace they oxidize and land on the glass foam preferably in the form of very fine metal oxide particles. The authors reported strong reduction in both foam coverage and energy consumption. The physical mechanism responsible is not clearly understood but it was suspected that these particles upon landing at the top of the glass foam disturb the liquid films by locally affecting the surface tension [169]. It could also be explained by the bridging–dewetting mechanism discussed in detail by Denkov and co-workers [86, 170].

Kappel *et al.* [71] observed that an increase in the pressure and pressure fluctuations of the furnace atmosphere favors decay of the foam. Harris [171] patented a method and apparatus to destroy foam in glass melting furnaces by directing pulses of compressed air or other gases towards the foam surface through pipes with or without nozzles. Alternatively, ultrasonic waves could be used to destroy glass foams [172]. These techniques have the advantage of not altering the glass composition. However, their practical implementation remains extremely challenging due to the large area of the glassmelt free surface and the high temperature and chemical conditions encountered in the combustion space.

Finally, Hammond *et al.* [173] proposed using a pulsed laser with emission wavelength corresponding to the absorption peak of the liquid phase. The laser produces local heating

of the foam, which destabilizes the liquid films. The laser beam can be shaped and scanned to cover a large surface area. The authors have successfully implemented this technique for aqueous foams but it could, in principle, be applied to glass foams.

### 16.6.5 Atmosphere Composition and Flame Luminosity

Sudden changes from oxidizing to reducing firing in the combustion space was found to be an effective way of destroying secondary foam in laboratory experiments [43, 55]. Direct implementation of this approach in industrial furnaces would require changing from an oxidizing to a reducing atmosphere in the entire combustion space. Indeed, partially implementing this method for some burners was not always successful as the changes at the foam surface need to be large enough to destabilize it [43]. Moreover, reducing atmosphere results in larger CO emission. Post-combustion of excess fuel may also cause excessive heating of the refractory walls, which reduces the furnace lifetime [43, 174]. Alternatively, Huang [7] proposed blowing an oxidizing gas such as oxygen, air, or steam onto the secondary foam to destroy it.

Rough [174] patented a method to prevent glass from foaming or to destabilize existing foams present at the surface of glassmelt by rapidly changing the oxygen concentration immediately above the glass foam. To do this, the author proposed repeatedly spraying oil, fuel gas, or finely divided carbonaceous materials such as carbon powder and cellulosic materials (e.g., wood, paper) directly on the glass foam. “Throwing wood” onto the foam was also described as a “conventional method” to destroy foams in molten slags [168]. These substances undergo rapid ignition and combustion, thus consuming the oxygen in the immediate vicinity of the glass foam. This action locally creates a reducing atmosphere, causing the glass foam to collapse as previously discussed [174]. The author also noticed that it was not necessary to change the composition of the entire combustion space to achieve the desired effects.

Finally, Barrow and Bird [80] proposed a method to destroy glass foam in industrial furnaces by directing a diffuse and luminescent flame towards the foam in the refining section or downstream region of the glass melting tank. Such a flame can be produced by injecting fuel (oil or natural gas) and oxidizer (air or oxygen) through two different ports or nozzles separated by a distance such that their mixing and combustion takes place far away from the injection ports. The fuel and oxygen ports should preferably be parallel and directed towards the glass melt surface. The authors reported partial or complete destruction of foams in flat glass furnaces using oxy-fuel firing. Note that the effect of the flame luminosity was also noticed in slag foaming [79]. The physical mechanism responsible for foam destruction was not completely understood but the authors speculated that soot particles made of carbon forming in diffuse luminescent flames might mechanically burst bubbles at the top of the foam [80]. Based on the phenomena reviewed in this chapter, other more likely mechanisms can be proposed, such as (i) temperature gradient along the foam surface, which destabilizes the liquid films, (ii) bridging and dewetting of the liquid thin films by the carbon particles [86,170], and (iii) local consumption of oxygen above the glass foam, which reacts with carbon, resulting in  $\text{CO}_2$  production and a reducing atmosphere in a manner similar to that proposed by Rough [174].

### 16.6.6 Control Foaming in Reduced-pressure Refining

Several strategies have been proposed to control foaming in reduced-pressure refining. Note that many of them can be used in conventional furnaces under atmospheric pressure. First, Schwenninger *et al.* [175] proposed heating, by combustion, the headspace of the vacuum chamber in order to control foaming. Indeed, increasing the chamber temperature lowers the glassmelt viscosity and destabilizes the foam. In addition, the authors noted that the gases (e.g., CO<sub>2</sub> and N<sub>2</sub>) to be removed from the glassmelt should not be the products of the combustion reactions. Thus, they suggested burning carbon-free fuel, in particular H<sub>2</sub>, with mainly O<sub>2</sub>. The resulting water vapor dissolves in the melt and further lowers its viscosity and destabilizes the foam. Alternatively, they proposed the use of a plasma torch using carrier gases such as steam, hydrogen, oxygen, and inert gases. Note that combustion was sustained under reduced pressure and that no refining agents were needed for this refining process to be successful.

Moreover, Schwenninger *et al.* [176] suggested periodically applying short pulses of higher and/or lower pressure to control foaming during reduced-pressure refining. Alternatively, Pecoraro *et al.* [177] proposed adding large amounts of water (>0.05 wt%) to the glassmelt prior to entering the vacuum chamber. Then, water acts as a foaming agent and can serve as a substitute for a sulfate-refining agent with the advantage of being inexpensive and reducing equipment corrosion. In addition, water reduces both viscosity and surface tension. This results in larger bubbles that can easily escape the melt and accelerate foam decay. Water can be introduced to the melt by (i) melting the glassmelt in humid atmosphere, (ii) directly injecting steam within the glassmelt, or (iii) adding hydroxil-rich batch components such as NaOH or Na<sub>2</sub>SiO<sub>3</sub>. Water also dilutes other gases present in the bubble and enhances refining as described in the so-called dilution model.

In addition, Welton *et al.* [178] suggested controlling foaming by spraying droplets of water and/or alkali metal (e.g., NaOH, Na<sub>2</sub>CO<sub>3</sub>) solutions over the glass foam. In all cases, foam decay was attributed to several possible mechanisms responsible for destabilizing the liquid films separating the bubbles, including (i) mechanical breaking due to the impact of the droplet, (ii) thermal shock of the bubble lamellae, (iii) natural convection within the bubbles, and (iv) viscosity reduction caused by the increased water vapor or alkali contents of the melt. The authors also suggested the use of liquid fuel such as alcohol or fuel oil, whose combustion would increase the melt temperature, reduce its viscosity, and destabilize the foam. They also proposed injecting these liquids within the foam itself.

Finally, several methods have been developed to enhance foaming in reduced-pressure refining as a way to accelerate refining. In addition, rapid bubble expansion also accelerates the foam collapse by stretching the film separating bubbles [69]. The simplest method is to divide the stream of molten glass entering the vacuum chamber in smaller streams with possibly non-cylindrical shape in order to increase the surface area of glassmelt in contact with the low-pressure chamber [179]. Indeed, foaming is initiated near the surface of the glass stream and expands inside. Thus, reducing the thickness of the stream accelerates foaming and refining. A similar effect can be achieved by increasing the time during which the glass stream is in contact with the low pressure chamber [179]. In addition, Gerutti *et al.* [69] proposed adding very volatile selenium and/or tellurium to molten glass prior to entering the reduced-pressure chamber. Their premature volatilization can be minimized by adding oxidizing agents (e.g., NaNO<sub>3</sub>) to the batch. The majority of the selenium can be

removed from the melt during the foaming process and thus does not affect significantly the glass composition and color. Finally, the use of other highly volatile substances featuring high vapor pressure has been proposed, including sulfates and halogens, also used as refining agents in conventional refining [180]. These enhanced foaming methods can be combined with the destruction methods previously reviewed to control excessive foaming.

## 16.7 Perspective and Future Research Directions

Despite advances in our understanding of glass foaming, numerous questions remain unanswered and further research is needed to be able to understand, predict, and control processes responsible for the formation of primary and secondary foams in industrial glass melting furnaces.

First, numerous defects and gas bubbles are produced during batch melting. Thus, it is essential to understand and model the retention of gas bubbles generated within the batch and their partitioning between the release to the combustion space and entrapment within the glassmelt. Such a model should account for the effects of (i) the batch grain and/or cullet size, (ii) the fusion/melting reactions, (iii) the heating rate, (iv) the refining reactions and gas generation, (v) the entrapment and escape of gases generated within the batch, (vi) the liquid flow and the liquid connectivity within the batch, (vii) changes in the effective thermal conductivity of the batch due to the appearance of entrapped gases, and (viii) the temperature gradients across the batch.

Moreover, several physical phenomena and foam characteristics are currently ignored in models predicting the transient and steady-state foam thickness of the foam layer. They include (i) the effects of bubble size distribution on glass foam stability, (ii) the temperature gradient across the foam layer, (iii) the fluctuations in the chemical composition, pressure, and temperature of the atmosphere surrounding the foam, (iv) the volatilization of volatile compounds and the resulting gradient in the local glass composition of the film, as well as (v) the possible chemical reactions and (vi) gas (e.g., H<sub>2</sub>O) transport that may take place within the foams.

Furthermore, foam in glass melting furnaces may be generated in a specific area of the tank and spread over the glassmelt surface as it gets carried by surface convection currents or under its own weight and momentum. This increases the foam coverage of the glassmelt surface, which reduces its temperature. Therefore, experimental measurements and mathematical models for rheological properties of glass foams and their dependence on the foam morphology, chemical composition, and thermophysical properties are needed for predicting the spreading of the foam over the glassmelt free surface [152, 153].

In order to validate the physical models it would be highly desirable to develop a complete set of experimental data to verify the predictions of the theoretical models for glass foaming under controlled conditions representative of experimental and actual glass melting furnaces. Such a data set should contain complete characterization of (i) the batch (e.g., composition, grain size, compactness, porosity), (ii) the glassmelt composition, and (iii) glass foams (e.g., bubble size distribution and gas composition as well as porosity). The associated thermophysical properties of the glassmelt should also be available or measured. This is particularly true for the gas solubility, glassmelt viscosity,

and surface tension as a function of composition, temperature, and dissolved gas content. In addition, thermodynamics data are necessary to properly account for equilibrium redox reactions taking place at different stages and temperatures of the batch melting and foaming processes.

Finally, measurements of glass foams are made difficult by the fact that foams are metastable and by the thermal and chemical conditions present in glass melting furnaces. Experimentalists often have to rely on quenching the glass foams to “freeze” their state at a specific time during their formation [43, 46]. This is very difficult to perform without significantly affecting the sample and therefore can only provide partial information. Therefore, continuous and non-invasive diagnostic techniques able to monitor glass foams inside laboratory and industrial glass melting furnaces are highly desirable. Such techniques should be able to measure the thickness, porosity, gas composition, bubble size distribution, and temperature profile across the glass foam at high temperatures in both oxidizing and reducing atmospheres. These techniques, if available, would enable the investigation of highly temperature-dependent physical phenomena taking place in glass foams. They would also enable better real-time control of industrial furnaces and help us to understand phenomena that cannot be reproduced in laboratory experiments. For example, Solovjov *et al.* [181] proposed the use of diffusive-wave spectroscopy using steady-state and time-modulated laser beams to non-invasively determine thickness and optical properties of non-absorbing foams. Alternatively, Mengüç and co-workers [182–184] proposed the use of elliptically polarized light scattering to non-invasively determine the foam porosity and bubble size distribution.

## Acknowledgements

The author is indebted to Prof. Raymond Viskanta of Purdue University (West Lafayette, Indiana, USA) and Mr Rei Kitamura, Dr Shingo Urata and Mr Nagai of Asahi Glass Corporation (Yokohama, Japan) for kindly and thoroughly reviewing an earlier draft of this chapter.

## References

- [1] C.P. Ross and G.L. Tincher. *Glass Melting Technology: A Technical and Economic Assessment*. Glass Manufacturing Industry Council, Westerville, OH, 2004.
- [2] J.L. Barton. Present trends in industrial glass making. In *Proceedings of the XXI International Congress on Glass*, Beijing, China, vol. 1, October 9–14, 1995.
- [3] Barnes Reports. *2010 US Glass & Glass Product Manufacturing Industry Report*. NAICS 37721, C.Barnes & Co., March 2010.
- [4] H. G. Pfaender. *Schott Guide to Glass*. Chapman and Hall, London, 1996.
- [5] E. Worrell, C. Galitsky, E. Masanet and W. Graus. *Energy Efficiency Improvement and Cost Saving Opportunities for the Glass Industry*. Tech. Rep. LBNL-57335-Revision, Lawrence Berkeley National Laboratory, Berkeley, CA, 2008.
- [6] R. H. Doremus. *Glass Science*. John Wiley & Sons, New York, 1994.

- [7] J. Huang. Method for controlling secondary foam during glass melting. US patent no. 5,665,137, September 9, 1997.
- [8] J.E. Shelby. *Introduction to Glass Science and Technology*, 2nd edn. The Royal Society of Chemistry, Cambridge, 2005.
- [9] A.G. Fedorov and L. Pilon. Glass foam: formation, transport properties, and heat, mass, and radiation transfer. *J. Non-Crystalline Solids*, **311**(2): 154–73, 2002.
- [10] A. Ungan. Three dimensional numerical modeling of glass melting process. PhD thesis, Purdue University, West Lafayette, IN, 1985.
- [11] W. Trier. Wärmeübergang zwischen Flamme und Glasbad Glasschmelzwannenofen. *Glastechnische Berichte*, **36**(3): 73–86, 1963.
- [12] A.G. Fedorov and R. Viskanta. Radiative transfer in a semitransparent glass foam blanket. *Phys. Chem. Glasses*, **41**(3): 127–35, 2000.
- [13] A.G. Fedorov and R. Viskanta. Radiative characteristics of glass foams. *J. Am. Ceramic Soc.*, **83**(11): 2769–76, 2000.
- [14] L. Pilon and R. Viskanta. Radiation characteristics of glass containing gas bubbles. *J. Am. Ceramic Soc.*, **86**(8): 1313–20, 2003.
- [15] D. Baillis, L. Pilon, H. Randrianalisoa, R. Gomez and R. Viskanta. Measurements of radiation characteristics of fused-quartz containing bubbles. *J. Optical Soc. Am. A*, **21**(1): 149–59, 2004.
- [16] H. Randrianalisoa, D. Baillis and L. Pilon. Improved inverse method for determining radiation characteristics of fused quartz containing bubbles. *J. Thermophys. Heat Transfer*, **20**(4): 871–83, 2006.
- [17] L. Dombrovsky and D. Baillis. *Thermal Radiation in Disperse Systems: an Engineering Approach*. Begell House, New York, 1996.
- [18] J. Wang, B.S. Brewster, B.W. Webb and M.Q. McQuay. A numerical investigation on the thermal impact of foam on an oxy-fuel-fired glass furnace. *J. Energy Inst.*, **78**(3): 117–25, 2005.
- [19] F.W. Krämer. Properties of glass-forming melts. In *Properties of Glass-Forming Melts*, L.D. Pye, A. Montenero and I. Joseph (eds). Taylor & Francis, Boca Raton, FL, 2005.
- [20] Y. Kokubu, J. Chiba and T. Okamura. The behavior of sodium sulfate during glass melting process. In *Proceedings of the XI International Congress on Glass*, vol. 4, J. Götz (ed.). Prague, July 4–8, 1977.
- [21] D.W. Freitag and D.W. Richerson. Glass industry. In *Opportunities for Advanced Ceramics to Meet the Needs of the Industries of the Future*. Tech. Rep., US Department of Energy, 1998.
- [22] J. Stanek and J. Matej. Electric melting of glass. *J. Non-Crystalline Solids*, **84**(1–3): 353–62, 1986.
- [23] Y. Zhiqiang and Z. Zhihao. Basic flow pattern and its variation in different types of glass tank furnaces. *Glastechnische Berichte*, **70**: 165–72, 1997.
- [24] R. Viskanta, Review of three-dimensional mathematical modeling of glass melting. *J. Non-Crystalline Solids*, **177**: 347–62, 1994.
- [25] L. Pilon, *Interfacial and Transport Phenomena in Closed-Cell Foams*, PhD thesis, Purdue University, West Lafayette, IN, USA, 2002.
- [26] German Glass Societies HVG-DGG, View into a modern glass-melting tank, May 2010.
- [27] C.C. Chapman, J.M. Pope, and S.M. Barnes, Electric melting of nuclear waste glasses state of the art, *J. Non-Crystalline Solids*, **84**(1–3): 226–240, 1986.
- [28] A. Ungan and R. Viskanta. Effect of air bubbling on circulation and heat transfer in a glass-melting tank. *Journal of the American Ceramic Society*, **69**(5): 382–91, 1986.
- [29] B. Balkanli and A. Ungan. Numerical simulation of bubble behaviour in glass melting tanks. Part 2. gas concentration. *Glass Technol.*, **37**(3): 101–5, 1996.
- [30] B. Balkanli and A. Ungan. Numerical simulation of bubble behaviour in glass melting tanks. Part 3. bubble trajectories. *Glass Technol.*, **37**(4): 137–42, 1996.
- [31] L. Pilon, G. Zhao and R. Viskanta. Three-dimensional flow and thermal structures in glass melting furnaces. Part I. Effects of the heat flux distribution. *Glass Sci. Technol.*, **75**(2): 55–68, 2002.
- [32] D.S. Goldman, D.W. Brite and W.C. Richey. Investigation of foaming in liquid-fed melting of simulated nuclear waste glass. *J. Am. Ceramic Soc.*, **69**(5): 413–17, 1986.

- [33] D.S. Goldman. Melt foaming, foam stability and redox in nuclear waste vitrification. *J. Non-Crystalline Solids*, **84**(1–3): 292–8, 1986.
- [34] D.F. Bickford, P. Hrma, and B.W. Bowen. Control of radioactive waste glass melters: II, residence time and melt rate limitations. *J. Am. Ceramic Soc.*, **73**(10): 2903–15, 1990.
- [35] S.K. Bindal, A.D. Nikolov, D.T. Wasan, D.P. Lambert and D.C. Koopman. Foaming in simulated radioactive waste. *Environ. Sci. Technol.*, **35**(19): 3941–7, 2001.
- [36] M.I. Ojovan and W.E. Lee. Immobilisation of radioactive wastes in glass. In *An Introduction to Nuclear Waste Immobilisation*. Elsevier, Oxford, 2005.
- [37] C.F. De Voe. Electric glass melting furnace. US patent no. 2,490,339, December 6, 1949.
- [38] M. Williamson. Electric glass melting furnace. US patent no. 4,324,942, April 13, 1982.
- [39] P. Hrma. Model for a steady state foam blanket. *J. Coll. Interface Sci.*, **134**(1): 161–8, 1990.
- [40] D.K. Peeler, T.H. Lorier and J.D. Vienna. Melt rate improvement for DWPF MB3: Foaming theory and mitigation techniques. Tech. Rep. SR-1-6-WT-31, Pacific Northwest National Laboratory, Richland, WA, 2001.
- [41] P. Hrma. Melting of foaming batches: nuclear waste glass. In *Proceedings of the 2nd International Conference on Advances in the Fusion and Processing of Glass*, Düsseldorf, Germany, October 22–25, 1990.
- [42] F.W. Krämer. Solubility of gases in glass melts. *Berichte der Bunsengesellschaft für physikalische Chemie*, **100**(9): 1512–14, 1996.
- [43] P. R. Laimböck. Foaming of glass melts. PhD thesis, Technical University of Eindhoven, The Netherlands, 1998.
- [44] R.G.C. Beerkens and J. van der Schaaf. Gas release and foam formation during melting and fining of glass. *J. Am. Ceramic Soc.*, **89**(1): 24–35, 2006.
- [45] R.G.C. Beerkens. Sulphur chemistry and sulphate refining and foaming of glass melts, *Glass Technol.: Eur. J. Glass Sci. Technol. A*, **48**: 41–52, 2007.
- [46] A.J. Faber, O.S. Verheijen and J.M. Simon. Redox and foaming behavior of E-glass melts. In *Proceedings of the 7th International Conference on Advances in Fusion and Processing of Glass III*, Rochester, NY vol. 141, J.R. Varner, T.P. Seward III and H.A. Schaeffer (eds). The American Ceramic Society, July 27–31, 2003.
- [47] P.R. Laimböck and R.G.C. Beerkens. Oxygen sensor for float production lines. *Am. Ceramic Soc. Bull.*, **85**(5): 33–6, 2006.
- [48] C.R. Bamford. *Colour Generation and Control in Glass*. Elsevier Scientific Publishing Co., New York, 1977.
- [49] R.G.C. Beerkens. The role of gases in glass melting processes. *Glastechnische Berichte*, **71**(12): 369–80, 1995.
- [50] S. Kawachi and Y. Kawase. Evaluation of bubble removing performance in a TV glass furnace. Part 2. Verification using real furnace data. *Glastechnische Berichte*, **71**(5): 111–19, 1998.
- [51] E. Itoh, H. Yoshikawa, H. Miura and Y. Kawase. A quasi-stationary model for bubble behaviour in glass melts with refining reactions. *Glass Technol.*, **38**(4): 134–40, 1997.
- [52] S. Kawachi and Y. Kawase. Evaluation of bubble removing performance in a TV glass furnace. Part 1. Mathematical formulation. *Glastechnische Berichte*, **71**(4): 83–91, 1998.
- [53] M. Cable and A. A. Naqvi. The refining of a soda-lime-silica glass with antimony. *Glass Technol.*, **16**(1): 2–11, 1975.
- [54] L. Němec. Refining in the glassmelting process. *J. Am. Ceramic Soc.*, **60**(9/10): 436–40, 1977.
- [55] R.G.C. Beerkens and P. Laimböck. Foaming of glass melts. In *60th Conference on Glass Problems – Urbana, IL*, J. Kieffer (ed.). American Ceramic Society, October 19–20, 1999.
- [56] M. Cable and D. Martlew. The dissolution of silica in melts containing sodium carbonate, sodium sulphate, and silica. *Glass Technol.*, **37**(4): 137–42, 1996.
- [57] M. Arkosiová, J. Kloužek and L. Němec. The role of sulfur in glass melting processes. *Ceramics–Silikáty*, **52**(3): 155–9, 2008.
- [58] P. Hrma, Effect of heating rate on glass foaming: transition to bulk foam. *J. Non-Crystalline Solids*, **355**(4/5): 257–63, 2009.
- [59] R.G.C. Beerkens and H. De Wall. Mechanism of oxygen diffusion in glassmelts containing variable-valence ions. *J. Am. Ceramic Soc.*, **73**(7): 1857–61, 1990.

- [60] R. Pyare, S. P. Singh, A. Singh and P. Nath. The As<sup>3+</sup>-As<sup>5+</sup> equilibrium in borate and silicate glasses. *Phys. Chem. Glasses*, **23**(5): 158–68, 1982.
- [61] S. Kawachi and M. Kato. Evaluation of reaction rate of refining agents. *Glastechnische Berichte*, **72**(6): 182–7, 1999.
- [62] L. Němec. The behaviour of bubbles in glass melts. Part 1. Bubble size controlled by diffusion. *Glass Technol.*, **21**(3): 134–8, 1980.
- [63] J.-T. Olink. Apparatus for melting and refining glass. US patent no. 3,519,412, July 7, 1970.
- [64] G.E. Kunkle, W.M. Welton and R.L. Schwenninger. Melting and vacuum refining of glass or the like and composition of sheet. US patent no. 4,738,938, April 19, 1988.
- [65] S. Takeshita, C. Tanaka and K. Ishimura. Refining method for molten glass and an apparatus for refining molten glass. US patent no. 5,849,058, December 15, 1998.
- [66] T. Kawaguchi, K. Obayashi, M. Okada. and Y. Takei. Vacuum degassing method for molten glass flow. US patent no. 6,332,339, December 25, 2001.
- [67] J.C. Hayes, R.A. Murnane, R.W. Palmquist and F. Woolley. Method for controlling foam production in reduced pressure fining. US patent no. 6,854,290 B2, February 15, 2005.
- [68] J.C. Hayes. Method for controlling foam production in reduced pressure fining. US patent no. 7,134,300 B2, November 14, 2006.
- [69] R.L. Gerutti, D.R. Haskins, R.B. Heithoff, R.L. Schwenninger and W.M. Welton. Method of vacuum refining of glassy materials with selenium foaming agent. US patent no. 4,886,539, December 12, 1989.
- [70] A. Gerrard and I.H. Smith. Laboratory techniques for studying foam formation and stability in glass melting. In *Glastechnische Berichte XIII. Internationaler Glaskongreß*, vol. 56K, July 4–9 1983.
- [71] J. Kappel, R. Conradt and H. Scholze. Foaming behavior on glass melts. *Glastechnische Berichte*, **60**(6): 189–201, 1987.
- [72] J.S. Ahn and P. Hrma. Effect of heat pretreatment on foaming of simulated nuclear waste in a borosilicate glass melt. *Adv. Ceramics*, **20**: 181–90, 1986.
- [73] G.A. Pecoraro. How the properties of glass melts influence the dissolution of refractory materials. In *Properties of Glass-Forming Melts*, L.D. Pye, A. Montenero and I. Joseph (eds). Taylor & Francis, Boca Raton, FL, pp. 337–389, 2005.
- [74] D.-S. Kim and P.R. Hrma. Volume changes during batch to glass conversion. *Am. Ceramic Soc. Bull.*, **69**(6): 1039–43, 1990.
- [75] M. Cable, C.G. Rasul and J. Savage. Laboratory investigation of foaming and reboil in soda-lime-silicate melts. *Glass Technol.*, **9**(2): 25–31, 1968.
- [76] S.M. Budd, V.H. Exelby and J.J. Kirwan. The formation of gas bubbles in glass at high temperature. *Glass Technol.*, **3**(4): 124–9, 1962.
- [77] C.G. Rasul and M. Cable. Spontaneous bubble formation in silicate melts at high temperatures. *J. Am. Ceramic Soc.*, **49**(10): 568–71, 1966.
- [78] M. Cable and C.G. Rasul. Spontaneous bubble formation in silicate melts at high temperatures. II: Effect of we atmospheres and behavior of mixed alkali glasses, *J. Am. Ceramic Soc.*, **50**(10): 528–31, 1967.
- [79] C. F. Cooper and J.A. Kitchener. The foaming of molten silicates. *J. Iron and Steel Inst.*, **48**–55, 1959.
- [80] T. Barrow and D.A. Bird. Melting of glass. US patent no. 6,715,319, April 6, 2004.
- [81] G. Narsimhan and E. Ruckenstein. Effect of bubble size distribution on the enrichment and collapse in foams. *Langmuir*, **2**: 494–508, 1986.
- [82] A. Bhakta and E. Ruckenstein. Decay of standing foams: drainage, coalescence and collapse. *Adv. Coll. Interface Sci.*, **70**: 1–124, 1997.
- [83] F. Geotti-Bianchini, J.T. Brown, A.J. Faber, H. Hessenkemper, S. Kobayashi and I.H. Smith. Influence of water dissolved in the structure of soda-lime-silicate glass on melting, forming and properties: state-of-the-art and controversial issues. *Glastechnische Berichte*, **72**(5): 145–52, 1999.
- [84] K.-H. Hess and D.D. Dingwell. Viscosities of hydrous leucogranitic melts: a non-Arrhenian model. *Am. Mineralogist*, **81**: 1297–300, 1996.

- [85] K. Zähringer, J.-P. Martin, and J.P. Petit. Numerical simulation of bubble growth in expanding perlite. *J. Mater. Sci.*, **36**: 2691–705, 2001.
- [86] J.T. Petkov and N.D. Denkov. Dynamics of particles on interfaces and in thin liquid films. In *Encyclopedia of Surface and Colloid Science*, 2nd edn, P. Somasundaran and A. Hubbard (eds). Taylor and Francis, New York, 2006.
- [87] A. Kucuk, A.G. Clare, and L. Jones. An estimation of the surface tension of silicate glass melts at 1400°C using statistical analysis. *Glass Technol.*, **40**(5): 149–53, 1999.
- [88] N. P. Bansal and R.H. Doremus. *Handbook of Glass Properties*. Academic Press, San Diego, CA, 1986.
- [89] J. Kappel and H. Roggendorf. Origin, stability, and decay of foam on glass melts. In *Proceedings of the 2nd International Conference on Advances in the Fusion and Processing of Glass*, Düsseldorf, October 22–5, 1990.
- [90] N. M. Parikh. Effect of atmosphere on surface tension of glass. *J. Am. Ceramic Soc.*, **41**: 18–22, 1958.
- [91] O. T. Roi, G. Nölle Seidel and D. Höhne. Formation and behavior of bubble curtains in glass melts. *Glastechnische Berichte*, **68**(7): 222–7, 1995.
- [92] G. Debrégeas, P.-G. de Gennes and F. Brochard-Wyart. The life and death of bare viscous bubbles. *Science*, **279**: 1704–7, 1998.
- [93] R.B. Jucha, D. Powers, T. McNeil, R.S. Subramanian and R. Cole. Bubble rise in glassmelts *J. Am. Ceramic Soc.*, **65**(6): 289–92, 1982.
- [94] J.E. Shelby. *Handbook of Gas Diffusion in Solids and Melts*. ASM International, Materials Park, OH, 1996.
- [95] E.M. Hornyak and M.C. Weinberg. Velocity of a freely rising gas bubble in a soda-lime silicate glass melt. *Comm. Am. Ceramic Soc.*, **67**(11): C244–6, 1984.
- [96] L. Němec. Diffusion-controlled dissolving of water vapor bubbles in molten glass. *Glass Technol.*, **10**: 176–81, 1969.
- [97] M.C. Weinberg, P.I.K. Onorato and D.R. Uhlmann. Behavior of bubbles in glass-melts: I, dissolution of a stationary bubble containing a single gas. *J. Am. Ceramic Soc.*, **63**: 175–80, 1980.
- [98] H. Yoshikawa and Y. Kawase. Significance of redox reactions in glass refining processes. *Glastechnische Berichte*, **70**(2): 31–40, 1997.
- [99] M. Cable and J.R. Frade. Theoretical analysis of the dissolution of multi-component gas bubbles. *Glastechnische Berichte*, **60**(11): 355–62, 1987.
- [100] M.C. Weinberg, P.I.K. Onorato and D.R. Uhlmann. Behavior of bubbles in glassmelts: II, dissolution of a stationary bubble containing a diffusing and a non-diffusing gas. *J. Am. Ceramic Soc.*, **63**: 435–8, 1980.
- [101] P.I.K. Onorato, M.C. Weinberg and D.R. Uhlmann. Behavior of bubbles in glassmelts: III, dissolution and growth of a rising bubble containing a diffusing a single gas. *J. Am. Ceramic Soc.*, **64**: 676–82, 1981.
- [102] B. Balkanli and A. Uungan. Numerical simulation of bubble behaviour in glass melting tanks. Part 1. under ideal conditions. *Glass Technol.*, **37**(1): 29–34, 1996.
- [103] E. Itoh, H. Yoshikawa. and Y. Kawase. Modeling of bubble removal from glassmelts at refining temperatures. *Glastechnische Berichte*, **70**(1): 8–16, 1997.
- [104] J.I. Ramos. Behavior of multicomponent gas bubbles in glass melts. *J. Am. Ceramic Soc.*, **69**(2): 149–54, 1986.
- [105] H. Yoshikawa, H. Miura and Y. Kawase. Dissolution of bubbles in glassmelts with equilibrium redox reactions: approximations for a moving bubble boundary. *J. Mater. Sci.*, **33**(10): 2701–7, 1998.
- [106] A. Uungan, W.H. Turner and R. Viskanta. Effect of gas bubbles on three-dimensional circulation in a glass melting tank. *Glastechnische Berichte*, **56K**: 125–9, 1983.
- [107] D. Ramkrishna. *Population Balances: Theory and Applications to Particulate Systems in Engineering*. Academic Press, San Diego, CA, 2000.
- [108] O. T. Roi, G. Nölle Seidel and D. Höhne. Modeling of bubble population in glass melts. *Glastechnische Berichte*, **67**(10): 263–71, 1994.
- [109] B. Balkanli and A. Uungan. Numerical simulation of bubble behaviour in glass melting tanks. Part 4: Bubble number density distribution. *Glass Technol.*, **3**(5): 164–8, 1996.

- [110] L. Pilon, A.G. Fedorov, D. Ramkrishna and R. Viskanta. Bubble transport and generation in glass melting furnaces. part I. mathematical formulation. *J. Non-Crystalline Solids*, **336**(2): 71–83, 2004.
- [111] L. Pilon and R. Viskanta. Bubble transport and generation in glass melting furnaces. Part II: Numerical results. *J. Non-Crystalline Solids*, **336**(2): 84–95, 2004.
- [112] S.L. Chang, C.Q. Zhou and B. Golchert. Eulerian approach for multiphase flow simulation in a glass melter. *Appl. Thermal Eng.*, **25**(17/18): 3083–103, 2005.
- [113] D.-S. Kim and P.R. Hrma. Foaming in glass melts produced by sodium sulfate decomposition under isothermal conditions. *J. Am. Ceramic Soc.*, **74**(3): 551–5, 1991.
- [114] D.-S. Kim and P.R. Hrma. Foaming in glass melts produced by sodium sulfate decomposition under ramp heating conditions. *J. Am. Ceramic Soc.*, **75**(11): 2959–63, 1992.
- [115] D.-S. Kim, B.C. Dutton, P.R. Hrma and L. Pilon. Effect of furnace atmosphere on E-glass foaming, *J. Non-Crystalline Solids*, **352**(50/51): 5287–95, 2006.
- [116] M. Arkosiová, J. Kloužek and L. Němec. Sulfur functioning during glass melting. *Advanced Materials Research*, **39/40**: 413–18, 2008.
- [117] J. van der Schaaf and R.G.C. Beerkens. A model for foam formation, stability, and breakdown in glass-melting furnaces. *J. Coll. Interface Sci.*, **295**(1): 218–29, 2006.
- [118] D.-S. Kim, M. Portch, J. Matyas, P.R. Hrma and L. Pilon. *Foaming of E-Glass II*. Tech. Rep. PNLL-15394, Pacific Northwest National Laboratory, Richland, WA, 2005.
- [119] G. Bayer. Foaming of borosilicate glasses by chemical reactions in the temperature range 950–1150°C. *J. Non-Crystalline Solids*, **38/39**(2): 855–60, 1980.
- [120] E. Bernardo and F. Albertini. Glass foams from dismantled cathode ray tubes. *Ceramics Int.*, **32**: 603–8, 2006.
- [121] E. Bernardo, R. Cedro, M. Florean and S. Hreglich. Reutilization and stabilization of wastes by the production of glass foams. *Ceramics Int.*, **33**(6): 963–8, 2007.
- [122] E. Bernardo. Micro- and macro-cellular sintered glass-ceramics from wastes. *J. Eur. Ceramic Soc.*, **27**(6): 2415–22, 2007.
- [123] E. Bernardo, G. Scarinci, P. Bertuzzi, P. Ercole and L. Ramon. Recycling of waste glasses into partially crystallized glass foams. *J. Porous Mater.*, **17**(3): 359–65, 2010.
- [124] F. Méar, P. Yot, M. Cambon and M. Ribes. Elaboration and characterisation of foam glass from cathode ray tubes. *Adv. Appl. Ceramics*, **104**: 123–30, 2005.
- [125] F. Méar, P. Yot, M. Cambon and M. Ribes. The changes in lead silicate glasses induced by the addition of a reducing agent (tin or sic). *J. Non-Crystalline Solids*, **351**(40–2): 3314–19, 2005.
- [126] F. Méar, P. Yot and M. Ribes. Effects of temperature, reaction time and reducing agent content on the synthesis of macroporous foam glasses from waste funnel glasses. *Mater. Lett.*, **60**(7): 929–34, 2006.
- [127] F. Méar, P. Yot, M. Cambon and M. Ribes. The characterization of waste cathode-ray tube glass. *Waste Management*, **26**(12): 1468–76, 2006.
- [128] F. Méar, P. Yot, M. Cambon, R. Caplain and M. Ribes. Characterisation of porous glasses prepared from cathode ray tube (CRT). *Powder Technol.*, **162**(1): 59–63, 2006.
- [129] F. Méar, P. Yot, R. Viennois and M. Ribes. Mechanical behaviour and thermal and electrical properties of foam glass. *Ceramics Int.*, **33**(4): 543–50, 2007.
- [130] S. Herat. Recycling of cathode ray tubes (CRTs) in electronic waste. *CLEAN: Soil, Air, Water*, **36**(1): 19–24, 2008.
- [131] D. Lv, X. Li, L. Wang, J. Du and J. Zhang. Effect of carbon as foaming agent on pore structure of foam glass. *Adv. Mater. Res.*, **105/106**: 765–8, 2010.
- [132] R.G.C. Beerkens, L. Zaman, P. Laimböck and S. Kobayashi. Impact of furnace atmosphere and organic contamination of recycled cullet on redox state and fining of glass melts. *Glastechnische Berichte*, **72**(5): 127–44, 1999.
- [133] K. Papadopoulos. The solubility of SO<sub>3</sub><sup>2-</sup> in soda-lime-silica melts. *Phys. Chem. Glasses*, **14**(3): 60–5, 1973.
- [134] C.J.B. Fincham and F.D. Richardson. The behaviour of sulphur in silicate and aluminate melts. *Proc. R. Soc. Lond. A*, **223**(1152): 40–62, 1954.
- [135] F. Geotti-Bianchini and L. De Riu. Water content of sulfate-fined industrial soda-lime glass and its influence on workability. *Glastechnische Berichte*, **71**(8): 230–42, 1998.

- [136] P.B. McGinnis and J.E. Shelby. Diffusion of water in float glass melts. *J. Non-Crystalline Solids*, **177**: 381–8, 1994.
- [137] J.J. Bikerman. The unit of foaminess. *Trans. Faraday Soc.*, **38**: 634–8, 1938.
- [138] S.A.K. Jeelani, S. Ramaswami and S. Hartland. Effect of binary coalescence on steady-state height of semi-batch foams. *Chem. Eng. Res. Des.*, **68**(3): 271–7, 1990.
- [139] S. Hartland, J.R. Bourne and S. Ramaswami. A study of disproportionation effects in semi-batch foams. II: Comparison between experiment and theory. *Chem. Eng. Sci.*, **48**: 1723–33, 1993.
- [140] S.S. Ghag, P.C. Hayes and H.-G. Lee. Physical model studies on slag foaming. *ISIJ Int.*, **38**: 1201–7, 1998.
- [141] D.B. Buruk, D. Petrovic and J.G. Daly. Flow regime transitions in a bubble column with a paraffin wax as the liquid medium. *Ind. Eng. Chem. Res.*, **26**: 1087–92, 1987.
- [142] L.Z. Pino, M.M. Yepez, A.E. Saez and G. De Drago. An experimental study of gas holdup in two-phase bubble columns with foaming liquids. *Chem. Eng. Comm.*, **89**: 155–75, 1990.
- [143] Y.T. Shah, S. Joseph, D.N. Smith and J.A. Ruether. On the behavior of the gas phase in a bubble column with ethanol–water mixtures. *Ind. Eng. Chem. Process Des. Dev.*, **24**: 1140–8, 1985.
- [144] K. Ito and R.J. Fruehan. Study of the foaming of CaO-SiO<sub>2</sub>-FeO slags. Part I: Foaming parameters and experimental results. *Metall. Mater. Trans. B*, **20B**: 509–14, 1989.
- [145] K. Ito and R.J. Fruehan. Study of the foaming of CaO-SiO<sub>2</sub>-FeO slags. Part II: Dimensional analysis and foaming in iron and steelmaking processes. *Metall. Mater. Trans. B*, **20B**: 515–21, 1989.
- [146] R. Jiang and R.J. Fruehan. Slag foaming in bath smelting. *Metall. Mater. Trans. B*, **22B**: 481–9, 1991.
- [147] Y. Zhang and R.J. Fruehan. Effect of bubble size and chemical reactions on slag foaming. *Metall. Mater. Trans. B*, **26B**: 803–12, 1995.
- [148] Y. Zhang and R.J. Fruehan. Effect of gas type and pressure on slag foaming. *Metall. Mater. Trans. B*, **26B**: 1089–91, 1995.
- [149] B. Ozturk and R.J. Fruehan. Effect of temperature on slag foaming. *Metall. Mater. Trans. B*, **26B**: 1086–8, 1995.
- [150] S.-M. Jung and R.J. Fruehan. Foaming characteristics of BOF slags. *ISIJ Int.*, **40**: 348–54, 2000.
- [151] R.C. Watkins. An improved foam test for lubricating oils. *J. Inst. Petrol.*, 106–13, 1973.
- [152] B.Y. Lattimer and J. Trelles. Foam spread over a liquid pool. *Fire Safety J.*, **42**(4): 249–64, 2007.
- [153] B. Persson, A. Lönnemark and H. Persson. Foamspec: large scale foam application-modelling of foam spread and extinguishment. *Fire Technol.*, **39**: 347–62, 2003.
- [154] L. Pilon, A.G. Fedorov and R. Viskanta. Analysis of transient thickness of pneumatic foams. *Chem. Eng. Sci.*, **57**: 977–90, 2002.
- [155] L. Pilon, A.G. Fedorov and R. Viskanta. Steady-state foam thickness of liquid–gas foams. *J. Coll. Interface Sci.*, **242**: 425–36, 2001.
- [156] L.L. Schramm. *Dictionary of Colloid and Interface Science*. Wiley and Sons, New York, 2001.
- [157] R. McElroy. Air release from mineral oils. PhD thesis, Department of Pure and Applied Chemistry, Strathclyde University, 1978.
- [158] Z. Lin and R.I.L. Guthrie. A model for slag foaming for the in-bath smelting process. *Iron and Steelmaker*, **22**(5): 67–73, 1995.
- [159] L. Pilon and R. Viskanta. Superficial gas velocity for onset of foaming. *Chem. Eng. Process.*, **43**(2): 149–60, 2004.
- [160] G.B. Wallis. *One-Dimensional Two-Phase Flow*. McGraw-Hill, New York, 1969.
- [161] Y. Zhang and R.J. Fruehan. Effect of carbonaceous particles on slag foaming. *Metall. Mater. Trans. B*, **26B**: 813–19, 1995.
- [162] S.S. Ghag, P.C. Hayes and H.-G. Lee. Model development of slag foaming. *ISIJ Int.*, **38**: 1208–15, 1998.
- [163] S.S. Ghag, P.C. Hayes and H.-G. Lee. The prediction of gas residence times in foaming CaO-SiO<sub>2</sub>-FeO. *ISIJ Int.*, **38**: 1216–24, 1998.

- [164] D. Lotun and L. Pilon. Physical modeling of slag foaming for various operating conditions and slag compositions. *ISIJ Int.*, **45**(6): 835–40, 2005.
- [165] G. Narsimhan. A model for unsteady state drainage of a static foam. *J. Food Eng.*, **14**: 139–65, 1991.
- [166] P. Pedebosq, R. Jacques and A. Berthereau. Glass melting in the presence of sulfur. US patent application publication no. US 2009/0277227 A1, November 12, 2009.
- [167] W.H. Echols. Apparatus for breaking up a foam. US patent no. 3,298,615, January 17, 1964.
- [168] H. Ito. Method for defoaming molten slag. US patent no. 4,042,410, August 16, 1977.
- [169] Y. Takei and K. Oda. Method for melting glass. US patent no. 6,470,710 B1, October 29, 2002.
- [170] N.D. Denkov and K.G. Marinova. Antifoam effects of solid particles, oil drops and oil-solid compounds in aqueous foams. In *Colloidal Particles at Liquid Interfaces*, B.P. Binks and T.S. Horozov (eds). Cambridge University Press, Cambridge, 2006.
- [171] J.L. Harris. Apparatus for dissipating foam on molten glass. US patent no. 3,649,235, March 14, 1972.
- [172] S.V. Komarov, M. Kuwabara and M. Sano. Control of foam height by using sound waves. *ISIJ Int.*, **39**(12): 1207–16, 1999.
- [173] P. Hammond. Foam control. US patent no. 6,599,948 B1, July 29, 2003.
- [174] R.R. Rough. Method of eliminating a foam blanket on the surface of molten glass. US patent no. 3,350,185, October 31, 1967.
- [175] R.L. Schwenninger and J.M. Matesa. Vacuum refining of glassy materials with controlled foaming. US patent no. 4,704,153, November 3, 1987.
- [176] R.L. Schwenninger, D.A. Hanekamp, and H.R. Foster. Pulsed pressure method for vacuum refining of glassy materials. US patent no. 4,849,004, July 18, 1989.
- [177] G.A. Pecoraro, L.J. Shelestak and J.E. Cooper. Vacuum refining of glassy materials with selected water content. US patent no. 4,919,700, April 24, 1990.
- [178] W.M. Welton. Foam control method for vacuum refining of glassy materials. US patent no. 4,794,860, January 3, 1989.
- [179] R.L. Schwenninger, W.M. Welton, B.S. Dawson, J.M. Matesa and L.J. Shelestak. Vacuum refining of glass or the like with enhanced foaming. US patent no. 4,780,122, October 25, 1988.
- [180] G.A. Pecoraro, L.J. Shelestak and J.E. Cooper. Vacuum refining of glassy materials with selected foaming rate. US patent no. 4,919,697, April 24, 1990.
- [181] V.P. Solovjov, M.R. Jones, K.E. Fackrell and B.W. Webb. Characterization of industrial foams. In *Proceedings of the ASME International Mechanical Engineering Congress*, New Orleans, November 17–22, 2002, IMECE 2002–33905.
- [182] B.T. Wong and M.P. Mengüç. Depolarization of radiation by non-absorbing foams. *J. Quant. Spectroscopy Radiative Transfer*, **73**(2–5): 273–84, 2002.
- [183] J.N. Swamy, C. Crofcheck and M.P. Mengüç. A Monte Carlo ray tracing study of polarized light propagation in liquid foams. *J. Quant. Spectroscopy Radiative Transfer*, **104**(2): 277–87, 2007.
- [184] J.N. Swamy, C. Crofcheck and M.P. Mengüç. Time dependent scattering properties of slow decaying liquid foams. *Coll. Surf. A: Physicochem. Eng. Aspects*, **338**(1–3): 80–6, 2009.

# 17

## Fire-fighting Foam Technology

*Thomas J. Martin*

### 17.1 Introduction

Fire-fighting foams are applied to the surfaces of combustible solid or liquid materials to extinguish an ongoing fire and to suppress reignition. Foams are also used in a defensive manner to suppress vapors and prevent ignition initially. Fire-fighting foams are comprised primarily of a mixture of surfactants in a dilute, aqueous solution. Since it is impractical in most cases to transport and store the entire foam solution, the active ingredients for a fire-fighting foam are supplied as a concentrate. The water and air required to create the finished foam are typically supplied on-site just prior to use. Mechanical agitation, or turbulent shear, is a critical component for foam generation in two respects: The foam concentrate must be mixed with water to form a homogeneous foam solution, and the foam solution must be combined with air with an adequate degree of shear to create the finished foam (Fig. 17.1).

The first step, diluting the foam concentrate with water, is referred to as “proportioning” and is characterized by the use of a specific proportioning rate, expressed as a percentage. The term “rate” is preferred since proportioning is often done in a continuous manner with the foam concentrate being drawn (or fed) into a flow of dilution water. The proportioning rate is a characteristic dilution ratio for a given foam product when used in a specific application and is traditionally stated as 6, 3, or 1%. In other words, an  $x\%$  proportioning rate requires  $x$  parts of foam concentrate by volume to be mixed with  $100 - x$  parts of water to make the foam solution. (Some foam products are meant to be used at alternate proportioning rates, including non-integer values.) Foam concentrates labeled with *lower proportioning rates* have *higher concentrations* of active ingredients (a designation that can cause confusion). Likewise, foam concentrate products with *higher*

Foam concentrate + Water + Agitation = Foam solution

Foam solution + Air + Agitation = Finished foam

**Fig. 17.1** *The role of mechanical agitation in foam generation.*

**Table 17.1** NFPA fire classifications.

Class	Fuel type
A	Ordinary combustibles
B	Flammable liquids
C	Electrical equipment
D	Combustible metals

*proportioning rates* have *lower concentrations* of active ingredients (i.e., the foam concentrates are more diluted). Foam concentrate products with higher proportioning rates require more concentrate to achieve the same overall volume of foam solution and finished foam than foam concentrates with lower proportioning rates. The trend is to develop products with lower proportioning rates because of the obvious benefit of not having to transport and store diluted products.

The second step in Fig. 17.1, shearing the foam solution with excess air, creates the air/water dispersion observed as foam. The amount of air incorporated into the finished foam is expressed in terms of an expansion ratio, which is essentially the volume of finished foam divided by the volume of foam solution used to make it. The expansion ratio is not prescribed, but instead is a consequence of the combination of the chosen foam solution, the applied shear rate and pressure, temperature, and the mechanical device utilized to generate the finished foam (more on this below, see Hardware).

The combustible material is often referred to as “fuel,” despite its intended use otherwise, and can be either a combustible solid (e.g., wood, dry brush or grass, paper, tires) or a typical flammable liquid hydrocarbon (e.g., solvents, gasoline, crude oil). The selection of the correct fire-fighting foam depends primarily on the type of fuel hazard encountered. In the United States, the National Fire Protection Association (NFPA) and other organizations classify fire-fighting agents by the fuel type on which they are applicable (Table 17.1). Fire-fighting foams are applied to Class A and Class B fires only. Although various other national standards differ from the NFPA designations, the definitions of Class A and Class B fire types agree such that confusion with regard to fire-fighting foam application is minimal.

In addition to the fuel type, fire-fighting foams are subclassified by their ingredient base (see History) and whether or not the applicable fuel is water-soluble (the term “miscible” – solubility in all proportions – is often misapplied within this industry in reference to some “water-soluble” fuels of limited intermixing ability). Solubility is particularly relevant given that fire-fighting foams are aqueous formulations, and some foam types will quickly degrade if applied to a fuel that has any degree of water-solubility. Most fuels are hydrocarbons, with no significant water solubility, and are simply referred

to as hydrocarbon, or non-polar, fuels. Fuels with such a degree of water solubility that foam properties are adversely affected when in contact are referred to as polar fuels (see Table 17.2). A proper foam intended for use on polar fuels will not be degraded. The degradation process and formulation technology used to overcome it are discussed below.

A wide assortment of hardware is needed to store, proportion, and mix a foam concentrate with the available water source, to incorporate an adequate amount of air into the foam, and to project or apply the finished foam onto the fuel surface. To add to the complexity of foam generation, in most cases, all the above steps happen almost instantaneously. Accordingly, foam concentrates and their associated hardware require a great deal of prior testing and development work to insure reliability during an emergency. These concentrated surfactant solutions are complex mixtures and have demanding performance expectations, more so when employed in dynamic applications, such as fire fighting, where life and property are at stake. A thorough, fundamental understanding of the physical and chemical properties of fire-fighting foams is essential to provide reliable and effective products at reasonable costs.

## 17.2 History

A variety of foaming materials have been employed throughout the past century, some eventually falling out of favor, others proving their dependability and cost effectiveness.

Many of the earliest foams were made by mixing inorganic powders in water containing natural soaps to produce CO<sub>2</sub> [1]. Other early foams made use of protein hydrolysate, a keratin-based by-product from slaughterhouses and tanneries made water-soluble by various treatments to degrade the disulfide bonds [2]. For these foams, a concentrate is made by blending the protein hydrolysate with stabilizers, preservatives, and metal salts as complexing agents [3, 4]. These so-called protein (P) foams, along with various derivatives, are still used extensively today. The characteristically strong, but slow acting, protein foam blanket is enhanced by the addition of certain fluorosurfactants, creating a fluoroprotein (FP) foam [22]. (The name might imply that the protein molecule itself has been modified to contain fluorinated substituents, but this is not the case.)

To distinguish foams derived from natural resources such as protein foams, the term “synthetic foam” (S) is used to denote fire-fighting foams based on synthetic detergents and other petrochemicals. This category includes all Class A foams and non-protein-based Class B foams (although some hybrid products exist).

A key feature of most modern Class B fire-fighting foams is their ability to spread spontaneously across a hydrocarbon fuel surface and form a vapor-suppressing film. This feature is enabled by fluorosurfactants of various types. Such foams are referred to as aqueous film-forming foams (AFFFs) and are intended for use on non-polar hydrocarbon fuels. An AFFF foam can be made “alcohol resistant” (AR) by formulating it with certain high-molecular-weight polymers (more on this below). These so called AR-AFFFs resist degradation when applied to polar fuels, fuels that have a significant degree of water solubility (e.g., isopropyl alcohol, methanol, ethanol, methyl ethyl ketone, ethyl acetate, acetone, methyl *t*-butyl ether, etc.), as mentioned above. AR-AFFFs are the most robust Class B foam types and can be used on both polar and non-polar fuels.

**Table 17.2** Properties of selected fuels and solvents.

Fuel or solvent	CAS	MW	mp	bp	visc	ST	SG	FP	auto-ign.	LEL	UEL	heat vap.	heat comb.	polar	
Acetic acid	64-19-7	60.1	16.6	117.9	1.23 (0°C)	27.4 (0°C)	1.05	39	465	5.4	16.0	23.7	875 (25°C)	y	
Acetone	67-64-1	58.1	-94.6	56.5	0.39	24.0 (10°C)	0.79	-18	465	2.6	12.8	29.1	1792 (25°C)	y	
Acetonitrile	75-05-8	41.1	-45.0	81.6	0.40	27.2 (10°C)	0.79	5	524	4.4	16.0	29.8	1266 (25°C)	y	
Benzene	71-43-2	78.1	5.5	80.1	0.65	28.9 (15°C)	0.88	-11	562	1.4	8.0	30.7	3270 (25°C)	n	
Butyl acetate	123-86-4	116.2	-73.5	126.1	0.73	25.4 (25°C)	0.88	37	425	1.4	7.5	36.3	— (25°C)	y	
Cyclohexane	110-82-7	84.2	6.5	80.7	0.65	25.2 (25°C)	0.78	-18	245	1.3	8.4	30.0	3922 (25°C)	n	
Diethyl ether	60-29-7	74.1	-116.3	34.6	0.25	17.1 (25°C)	0.71	-40	443	1.4	7.9	29.1	— (25°C)	y	
Diisopropyl ether	108-20-3	102.2	-86.9	68.4	0.38	17.8 (25°C)	0.73	-12	443	1.4	7.9	29.1	— (25°C)	y	
Ethanol	64-17-5	46.1	-114.5	78.3	1.21 (15°C)	22.4 (15°C)	0.79	8	423	3.3	19.0	38.6	1368 (25°C)	y	
Ethyl acetate	141-78-6	88.1	-84.0	77.1	0.47	24.0 (25°C)	0.90	-3	427	2.2	11.0	31.9	2248 (25°C)	y	
Ethylene diamine	107-15-3	60.1	9.0	116.0	1.54	42.0 (25°C)	0.90	38	385	2.7	16.0	— (25°C)	1895 (25°C)	y	
Ethyleneglycol	107-21-1	62.1	-12.6	197.3	26.1 (15°C)	48.4 (15°C)	1.11	110	400	3.2	15.3	49.6	1180 (25°C)	y	
Gasoline	8006-61-9	—	—	—	~0.5	—	0.71 —	—	280 —	1.4	7.6	— (25°C)	20400 (25°C)	n	
Heptane	142-82-5	100.2	-90.6	98.4	0.42	20.1 (15°C)	0.68	-4	223	1.1	6.7	31.8	4814 (25°C)	n	
Hexane	110-54-3	86.2	-95.4	68.7	0.31	18.4 (15°C)	0.65	-23	225	1.2	7.5	28.9	4166 (25°C)	n	
Isopropyl alcohol (IPA)	67-63-0	60.1	-89.5	82.4	2.86	21.3 (15°C)	0.79	12	402	2.3	10.4	39.9	20655 14220 (25°C)	y	
Kerosene	8008-20-6	—	-20.0	150-	~2	—	0.80	37-65	210	0.7	5.0	— (25°C)	— (25°C)	n	
Methanol	67-56-1	32.0	-97.7	64.7	0.68	22.5 (10°C)	0.79	12	470	6.0	36.5	35.2	727 14582 (25°C)	y	
2-Butanone (MEK)	78-93-3	72.1	-86.0	79.6	0.43	24.5 (25°C)	0.81	-9	505	1.8	10.1	31.3	2446 (25°C)	n	
Solvent naphtha (pet. ether)	8032-32-4	—	—	60-80	~20	—	0.66	30	288	1.1	5.9	— (25°C)	— (25°C)	n	
Propanal	123-38-6	58.1	-81.0	46-50	0.36	15°C (25°C)	—	0.81	—	207	2.9	17.0	— (25°C)	y	
Propylene glycol	57-55-6	76.1	-60.0	188.0	56.0	75 (25°C)	1.04	107	371	2.6	12.6	57.9	1805 10194 (25°C)	y	
Toluene	108-88-3	92.1	-95.0	110.6	0.62	15°C (25°C)	28.5	0.87	4	480	1.3	7.0	33.2	3911 18250 (25°C)	n
Units	g/mol	°C	°C	cP	dyne/cm	°C	°C	vol. % at 25°C	kJ/mol	kJ/mol	BTU/lb				

All values at 20°C, unless otherwise noted. CAS, Chemical Abstract Service number; MW, molecular weight; mp, melting point or range; bp, boiling point or range; visc, viscosity; ST, surface tension; SG, specific gravity; FP, flash point; auto-ign., auto ignition temperature; LEI, lower explosion limit; UEL, upper explosion limit; heat vap., heat of vaporization; heat comb., heat of combustion; polar, polar fuel classification.

Source: Refs [5-7, 23, 26].

In various publications (as in this chapter in some instances), the term AFFF may refer to film-forming Class B foams as a general class, including AR-AFFFs. Elsewhere AFFF and AR-AFFF foams are differentiated. The context of the discussion has to be considered to interpret the meaning of the term.

## 17.3 Applications

Foams are used in a variety of fire-fighting applications, including fixed fire-fighting systems (fuel loading docks, aircraft hangers, warehouses, fuel storage tanks, etc.) and hand-line applications (municipal fire-fighting trucks, airport emergency response vehicles, portable extinguishers, etc.). Foams are applied both to extinguish an ongoing fire and to suppress reignition of the remaining fuel. On many occasions, foam is applied as a safety precaution to prevent a flash fire from unignited fuel while rescue workers perform their duties in and near the hazard. This preventative application may be useful, for example, when a local fire department responds to a fuel spill resulting from a truck or automobile accident or when an internal roof of an oil storage tank has sunk due to heavy rain.

Fire-fighting foam concentrates and related equipment must be developed, engineered, constructed, installed, and applied by qualified professionals; they are not retail or consumer products (aside from portable premix units, for example). The staging and use of fire fighting foams is ubiquitous, although typically hidden from view from the average person. Most municipal fire trucks carry foam, for example, and building codes require fire protection and, under certain circumstances, specify certified foam products and application systems (e.g., sprinkler systems). Approval and enforcement of the necessary certifications is the responsibility of the “authority having jurisdiction,” as defined in NFPA 11 [85]. The process for approving foams for use in specific application areas (hand-line, sprinklers, etc.) is costly and requires their passing rigorous, detailed testing specifications.

### 17.3.1 Foam Market

According to Underwriters Laboratory (UL), currently 47 manufacturers produce fire-fighting foams (or ‘Foam Liquid Concentrates’) [8], 13 in North America and 14 in the European Union (EU). A 2004 report [9] estimates the US inventory of AFFF to be about 10 million gallons. Another report [10] references a 2006 figure of 13,000 tons of foam used per year in the EU. A rough estimate of the annual production by foam type, as a proportion of the total Western Hemisphere production, appears in Table 17.3. Class A and synthetic (non-protein-based) Class B fire-fighting foams are chosen as the primary focus of this chapter, given their market proportion and the relative sophistication of their formulation technology.

### 17.3.2 Hardware

As mentioned above, the application of fire-fighting foams is equipment-intensive. Although the focus of this chapter is on the technology of foam, some mention of the equipment used

**Table 17.3** Estimated annual foam concentrate production for the Western Hemisphere in 2008 by type [11].

Foam type	Percentage
Class A*	12
High expansion (Hi-Ex)	13
Protein (P)	6
Fluoroprotein (FP)**	10
Film-forming fluoroprotein (FFF)	8
Alcohol-resistant film-forming fluoroprotein (AR-FFF)	<1
Aqueous film-forming foam (AFFF)	30
Alcohol-resistant aqueous film-forming foam (AR-AFFF)	21
	100

\*Including wetting agents and training foams. \*\*Including AR-FP.

for foam generation is needed to better understand the performance demands placed on foam. For more details, see other references [12], including supplier literature.

A fire-fighting foam is expected to have a “shelf life” of 20-plus years. A typical foam concentrate is stored in its original shipping container, a tank, or a bladder tank until it is needed. Certain foam products such as AFFFs may be stored as “premixes,” with the foam concentrate mixed with the dilution water ahead of time and stored as foam solution (see Fig. 17.1). Premixes are observed on occasion to degrade faster than AFFF concentrates upon long-term storage. AR-AFFFs are not generally stored as premixes due to the potential for component separation.

Typically, a foam concentrate is mixed with water at the proportioning ratio instantaneously prior to foam generation. The foam concentrate is either suctioned or pressured into a water stream by a proportioning device. The proportioning device may be a self-educting nozzle, an in-line eductor, a balanced-pressure proportioner, or a direct-injection pump separate from the water supply pump. The finished foam is then produced by a foam-generating device, which may be a handline nozzle, a fixed or portable monitor, an array of sprinkler heads, foam pourers or foam chambers mounted on a fuel storage tank, grate-nozzles installed in a trench, high expansion generators, or a foam maker for subsurface injection (among others). A given foam-generating device may be classified as either aspirating or non-aspirating; the former denotes the ability of the device to mix air with the foam solution to generate the finished foam prior to discharge from the device, the latter relies on the projection or impact of the foam solution to adequately expand it.

Examples of fire-fighting foam hardware appear in Figs 17.2–17.8.

## 17.4 Physical Properties

This section outlines the requirements of fire-fighting foams in terms of their underlying physical properties, the individual principles doubtlessly covered more thoroughly in other chapters. Section 17.5 of this chapter contains formulation options available to meet the various physical property requirements.



**Fig. 17.2** Example foam generating device: a non-aspirating handline nozzle. Reproduced with permission from ChemGuard © 2011.



**Fig. 17.3** Example foam generating device: a high expansion, aspirating handline nozzle shown with eductor and siphon hose. Reproduced with permission from ChemGuard © 2011.

#### 17.4.1 Mechanism of Action

Water, unsurprisingly, is by far the most commonly used medium for fire extinguishment. The use of water alone, however, is limited to Class A fires; that is, fires involving combustible solids. Water used without additives extinguishes fires primarily by cooling the combustible solids as the water heats and vaporizes. The steam produced displaces oxygen within a confined space, furthering the extinguishment action in such instances. Pure water has a high surface tension, which prevents penetration into some porous solids and retards wetting of certain combustible materials, especially materials containing a hydrophobic surface. Also, after application water flows from non-horizontal surfaces and provides no lasting protection against reignition. A foam structure counters these wetting and run-off problems, as detailed below.

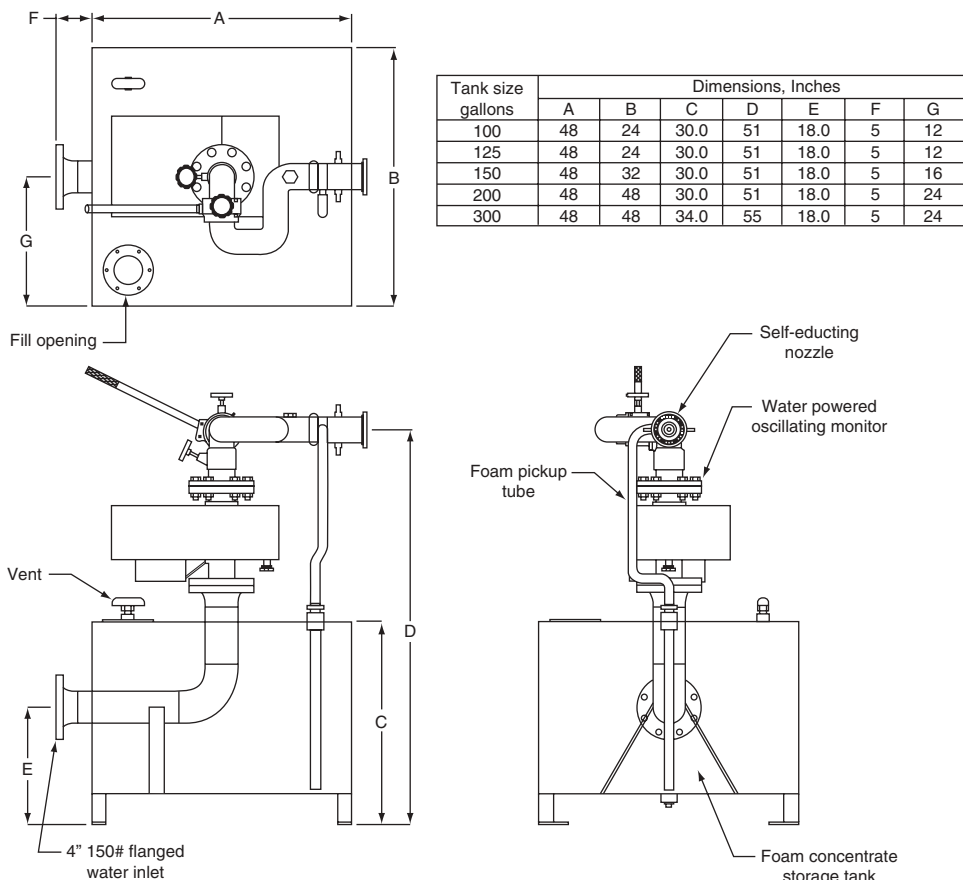


**Fig. 17.4** Example foam generating device: a self-contained, water-powered, oscillating monitor station. Foam concentrate is stored below the monitor and is drawn by the self-educting, non-aspirating nozzle. Water pressure alone supplies the motive force for operation. Reproduced with permission from ChemGuard © 2011.

To extinguish a Class B fire (flammable liquids), a medium is needed that floats on the fuel surface. Most liquid hydrocarbon fuels have a specific gravity of less than 1.0. When water is applied to such a fuel surface, it has almost no effect mitigating the flame intensity, but instead sinks ineffectually below the fuel surface or, worse, spreads the fuel, intensifying the fire. Dry powders such as Purple K ( $\text{KHCO}_3$ ) and urea are often used for Class B fires, but these products provide no protection against reignition after the initial fire has been extinguished (i.e., burnback protection). Also, powders do not flow across a fuel surface and have to be applied manually to all areas, which limits their use to small fires and requires close approach by the firefighter. In contrast, aqueous foams, which spread spontaneously across the fuel surface from the point of application, are ideal for long-range, high-volume applications and provide fast extinguishment and excellent burnback

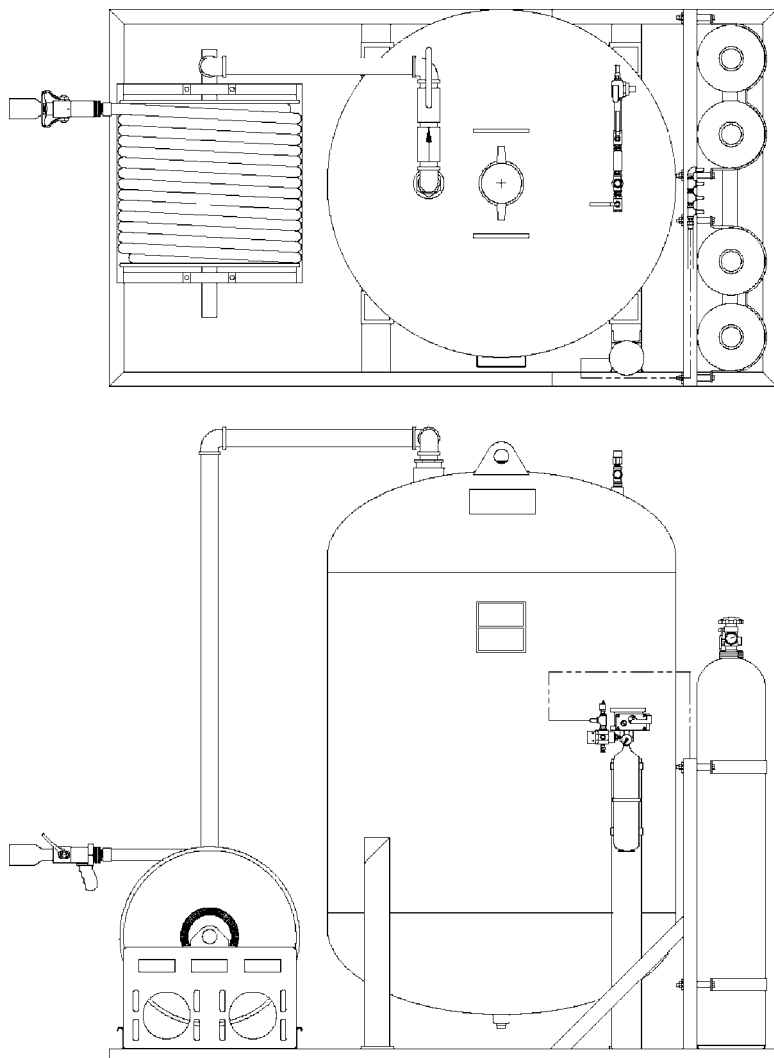


**Fig. 17.5** Example foam storage unit: a self-contained premixed foam solution tank, hose reel, and a non-aspirating handline nozzle. Nitrogen pressure is used to discharge the unit. Reproduced with permission from ChemGuard © 2011.

protection. Common low-expansion foams (an expansion ratio of less than 20) have an effective specific gravity of 0.05–0.20, meeting the floatation requirement with some degree of excess. Furthermore, high-expansion (Hi-Ex) foams, used for quickly flooding an area with foam, have expansion ratios greater than 200. Medium-expansion foams, used in handheld premix units, fall in between [12].

Consider the traditional fire triangle in Fig. 17.9 to help understand the mechanism of fire-fighting foams, for both Class A and Class B fires. The vertices are labeled fuel,



**Fig. 17.6** Example foam generating device: a high-flow, mobile, non-aspirating foam monitor with a 2000–4000 gallons per minute foam solution flow rate. The foam concentrate is supplied by jet pumps that draw from drums or totes (not shown). Reproduced with permission from ChemGuard © 2011.

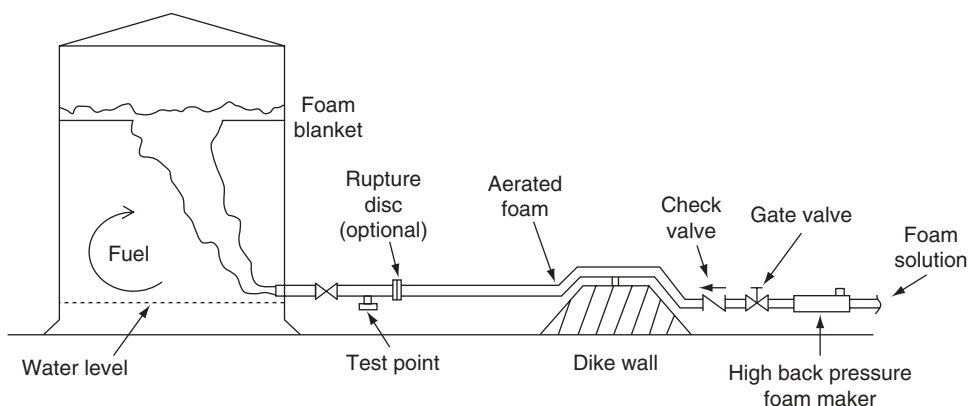


**Fig. 17.7** Sub-surface foam injection. Foam solution is fed under pressure through the in-line foam maker. The foam is injected into the fuel storage tank below the surface and rises through the fuel to form a blanket on top. Used for fixed-roof tanks. Such foams must be very resistant to fuel pick-up. Reproduced with permission from ChemGuard © 2011.

oxidizer, and ignition. When all three elements are present, a physical-chemical chain reaction occurs, observed variably as a modest flame or a rolling fireball. Removal of any one of these essential elements destroys the triangle, thus the fire, including any potential for reignition.

Application of a fire-fighting foam to a fuel surface, whether the fuel is aflame or not, has no effect on the overall quantity of air (oxidizer) or fuel available, nor are their respective bulk properties significantly altered. A typical fire-fighting foam is not intended to emulsify

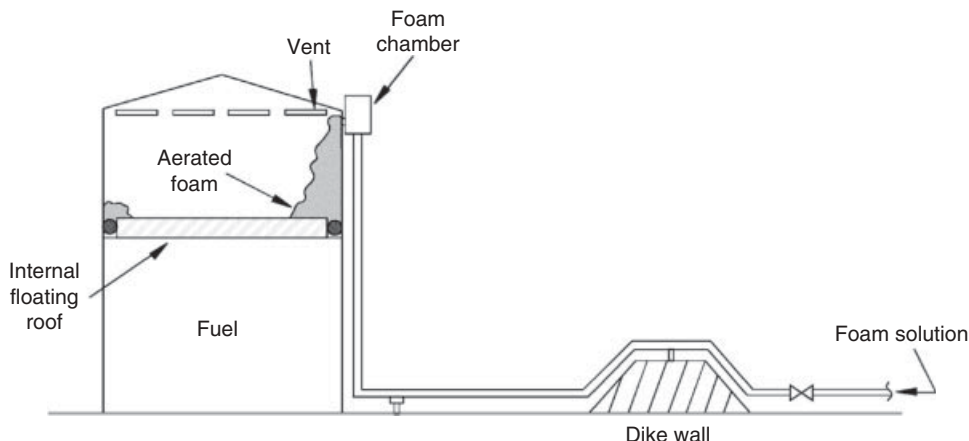


**Fig. 17.8** Topside foam application, used with floating-roof tanks. Foam solution is supplied to the foam chamber mounted along the top of a fuel storage tank. When pressurized, a seal breaks within the chamber and the foam solution is aerated to produce foam, which cascades down the side of the walls to seal the fuel surface. Reproduced with permission from ChemGuard © 2011.

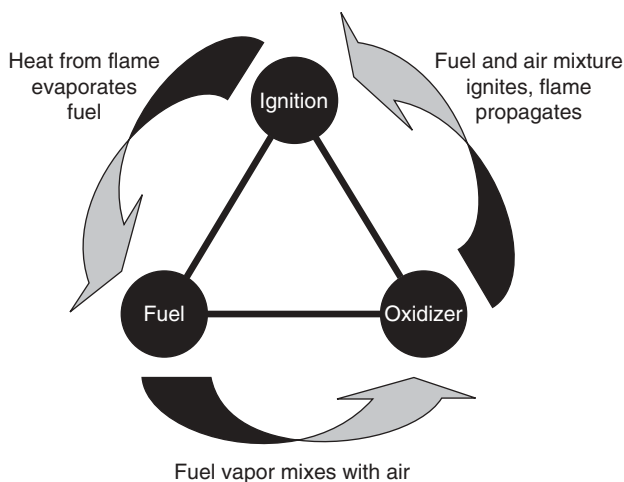


**Fig. 17.9** The fire triangle.

the fuel, for example (although there are other products that rely on this mechanism). Instead, the foam blanket breaks the chain reaction by insulating the liquid fuel from the heat of the fire (and other ignition sources), suppresses fuel evaporation, and separates the air from the liquid fuel surface. Contrary to intuition, a flammable *liquid* does not burn; only the *vapor* above the fuel, when mixed with oxygen at a sufficient ratio, is inflammable.

Thus, the foam removes the fuel element from the fire triangle by acting as a thermal insulating blanket and a barrier to transfer of both oxygen and fuel vapor, all of which is enabled by the expansion (low specific gravity) of the foam.

### 17.4.2 Class A Foams

Class A fire-fighting foams are used to improve the wetting of a fuel substrate and are thus often included under the broader classification of “wetting agents.” The use of such additives is preferred over water alone when the fuel substrate has a charred, resinous, or otherwise hydrophobic character, or for a porous structure that may harbor embers. Examples include wood, dry brush or grass, tire rubber and plastics, and coal. (Consideration must be given to flexible plastics and rubber, which may emit a liquid hydrocarbon component when burned, in which case a Class B foam is more applicable.) The most common use of Class A foams is for suppression of fires in grassland or forested areas by aerial application. The white foam, which clings to objects, provides a visual indication to pilots of treated areas.

When discussing the primary physical requirements of a Class A foam, it is often sufficient to consider the foam solution alone. This is justified because contact between the foam blanket and a fully wetted substrate is a thin aqueous layer. The interaction at this liquid–solid interface is critical for foam performance. Thus, the dispersed air phase within the foam, needed for its insulating and barrier properties, is neglected in the following discussion on wetting behavior.

For a Class A foam to be most effective, it must completely wet the solid fuel surface and penetrate all pores. To assure this, the surface tension has to be less than the critical surface tension  $\gamma_c$  of the combustible substrate. The method of Zisman [13, 14] is used to determine  $\gamma_c$  by plotting the cosine of the contact angles ( $\theta$ ) for a homologous series of solutions versus the surface tension  $\gamma$  of each solution and extrapolating to  $\cos \theta = 1$  (i.e.,  $\theta = 0$ , indicating complete wetting) as shown in Fig. 17.10. Wood of various types have critical surface tensions in the range of 45–48 dyn/cm [15, 16], in agreement with values reported for cotton and cellulose. This implies that a good Class A foam *solution* (the diluted product as used) should have, as a minimum requirement, a surface tension of less than about 45 dyn/cm.

Spontaneous spreading predicted from surface tension properties above is a thermodynamic phenomenon representing equilibrium conditions, not a kinetic process. A Class A foam is further required to wet a fuel surface at an appreciable rate. Several methods are available to quantify the wetting rate of a given Class A foam [17–19]. (See also Section 17.6.)

### 17.4.3 Class B Foams

Non-polar hydrocarbon fires cannot be extinguished with water alone. With its high specific gravity and high interfacial tension, water beads up and drops through the fuel. If applied with force, water displaces the fuel, creating even more surface area and more flammable vapor. Polar hydrocarbon fuels may be extinguished with water, but only if excessively diluted, which is impractical except for very small fires.

Foam transitions across the fuel surface from the point of application as a viscose, cohesive structure [20] without apparent vertical rolling or tumbling, since the underlying liquid

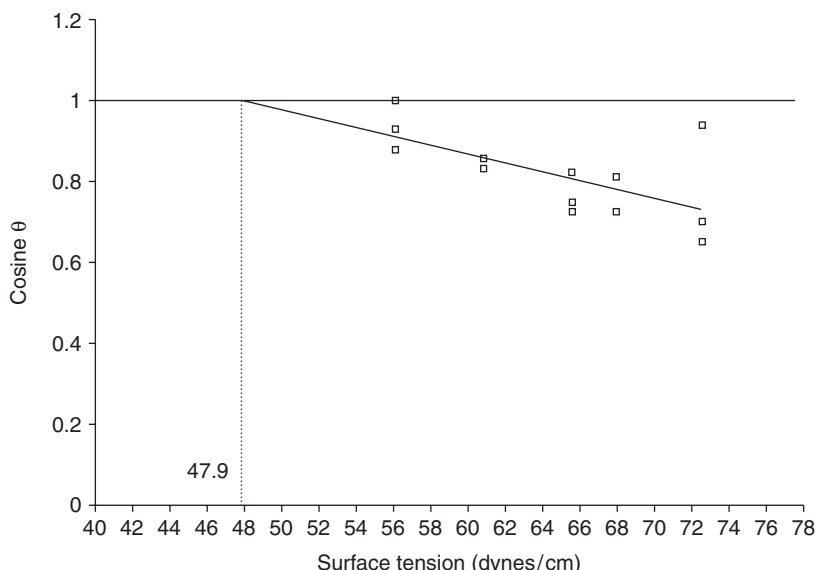


**Fig. 17.10** An example Zisman plot showing the critical surface tension for a wood sample. Data were gathered using aqueous acetic acid at various strengths as the liquid phase.

Reprinted with permission from [15] © 1991 American Chemical Society.

fuel offers little resistance to flow. The foam blanket will form horizontal eddy currents as it is applied at a point on the surface, however. The hydrostatic pressure caused by the differences in foam height tends to level the foam over time.

The mechanical energy used to generate the foam is stored in the foam structure. This structure in a highly expanded foam has a solid-like behavior exhibiting a yield stress [20] that resists deformation, so much so that some foams are designed for use in blast mitigation (so called “bomb foams” [21]). These most resemble Hi-Ex or Class A foam types in terms of composition.

Hi-Ex foams are used to displace large volumes of air and blanket extensive areas very quickly. This foam type is applicable to both Class A and Class B fire dangers, although they do not typically contain fluorosurfactants. A Hi-Ex foam has a very low density and is typically used in interior structures, such as in aircraft hangers or in underground mines.

Some fire safety professionals imprudently choose Class A, Hi-Ex, or other fluorine-free foams for use as low-expansion foams on Class B fire hazards. While Class B foams can be used on Class A fires, the opposite is inadvisable. Although they may extinguish a Class B fire if applied in sufficient quantities and at sufficient rates, Class A foams are not recommended for Class B fires due to their poor burnback characteristics. Also, Class A and Hi-Ex foams are not recommended in alternative applications since they are very rich and would represent an excessive use of active ingredients. Current synthetic fluorine-free foams, intended to replace AFFFs, rely on a very strong foam cell structure to compensate for the lack of film formation. These foams are not robust and have been proven in only limited applications.

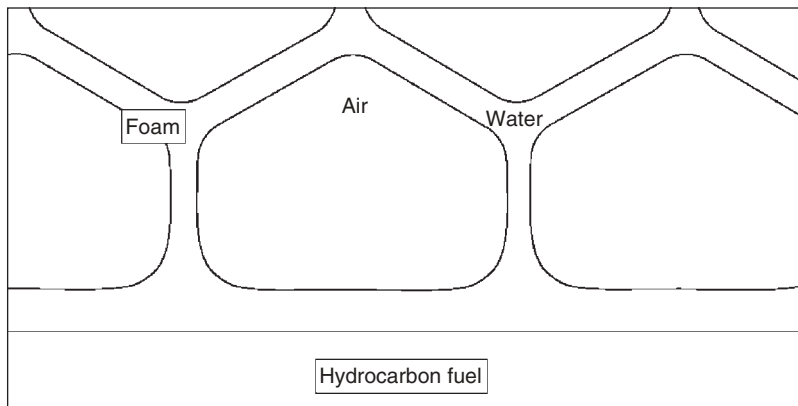


**Fig. 17.11** Film-forming foam on a hydrocarbon fuel.

There are a few implications in the literature that fire-fighting foams extinguish fires by cooling the fuel through water evaporation from the foam. This may be misleading. As an example, a UL 162 test fire [23] consumes up to 10 gallons of heptane when extinguished within the specified 3 minutes, releasing a total of about 1.1 to 1.2 million BTUs. The quantity of water in the fire-fighting foam applied within the same 3 minutes is about 50 pounds, the heating and evaporation of which would require only about 52,000 BTUs, or less than 5% of the total energy released from the burning fuel (admittedly, only a portion of which is radiated toward the foam blanket). For the foam to remain substantially intact, as it does when applied across the flame onto the burning fuel, certainly only a small fraction of the total water is evaporated. Thus, it would appear that evaporation is an insignificant contribution to the overall fire extinguishing effect of foams, and that insulation and mass transfer barrier effects predominate.

Foam is not without a cooling function, however. Firstly, consider that the temperature of a burning liquid fuel never exceeds its boiling point. The heat absorbed at the liquid fuel surface results primarily in more emitted vapor, more so than conductive heating of the liquid. This explains the relatively slow rate of temperature rise downward through a burning crude oil tank, measured in feet per hour. (Incidentally, the same UL fire test mentioned above can be conducted with an ice layer below the fuel without melting it.) A foam blanket, once applied, acts as a heat sink to cool the liquid fuel beneath it. Therefore, as the foam and fuel reach thermal equilibrium following extinguishment, the vaporization potential decreases, complementing the foam barrier effect.

Additionally, foam is often sprayed onto structural elements, such as piping and container walls, to prevent hot spots that might evaporate fuel and cause reignition. Because the foam clings to structures, it provides a visual indication to the fire fighter that the surface is sufficiently cool.

As with Class A foams above, focus is placed on the interface between the Class B foam and the fuel surface. Ideally, cells within a foam blanket in contact with a hydrocarbon substrate will be separated by a continuous, aqueous film (Fig. 17.11). This thin, but vital, underlying film is responsible for vapor suppression and for protecting the foam from fuel vapor

contamination. The film thickness is limited by surface tension and the hydrostatic head pressure [25]. When the film exceeds a characteristic thickness, the solution will form a bead (or pendant drop) below the water–fuel interface, disconnect, and then sink into the fuel layer. Foam applied excessively to a non-polar fuel will create a substantial water layer below the fuel. In the case of a crude oil fire, it is necessary to remove water from the bottom of the tank to avoid a catastrophic boil-over (cf. Fig. 17.7) [12].

For a fire-fighting foam to form a continuous film between the foam blanket and the fuel surface, its spreading coefficient  $SC$  must be positive. As defined by Harkins, the  $SC$  [24] is given by

$$SC = \gamma_{a/f} - (\gamma_{a/w} + \gamma_{w/f}) \quad (17.1)$$

where  $\gamma_{a/f}$  is air/fuel surface tension,  $\gamma_{a/w}$  is air/water surface tension,  $\gamma_{w/f}$  is water/fuel interfacial tension.

The  $SC$  expresses the difference in energy between the bare and the fully wetted fuel substrate. For clarity, the term *water* is used to mean foam solution, and *fuel* used in place of the more commonly used term *oil*. Measurements are typically made on standardized test fuels, such as cyclohexane or heptane, since the composition of common fuels, such as gasoline, varies considerably with geographic location and season.

By definition, the solution of a film-forming foam (e.g., AFFF or AR-AFFF) has a positive  $SC$  on cyclohexane [23]. Some researchers have suggested that the  $SC$  be several units above zero (dyn/cm) to show effective film formation, while others [12] suggest there is no link between fire-fighting performance and  $SC$ . These differences may be explained by the use of cyclohexane as the *laboratory test fuel* (since it has a significantly higher surface tension than heptane and other *fire test fuels*), by temperature effects, or by overly economized foams, as noted in the references. Ultimately, the *solution draining from the foam* should have a positive  $SC$  on the *fire test fuel*, which is accomplished by judicious selection of fluorosurfactant types and usage levels, as described below.

Without fluorosurfactants, a fire-fighting foam solution will not fully wet a hydrocarbon fuel surface; that is,  $SC < 0$ . In this scenario, Young's equation applies,

$$\gamma_{a/f} = \gamma_{a/w} \cos \theta + \gamma_{w/f} \quad (17.2)$$

where  $\theta$  is contact angle of the aqueous liquid phase adjacent to the fuel substrate.

Young's equation is illustrated in Fig. 17.12 for a droplet of protein or fluorine-free foam solution. This is an idealized view in which gravity is negligible: the droplet is a spherical section and the substrate is unperturbed by the weight of the droplet. In reality, a spherical lens would form that would distort the liquid substrate surface from planarity, and gravity would flatten the droplet such that it would not exceed a certain thickness [25, 26].

The application of a non-film-forming foam to a fuel surface is illustrated in Fig. 17.13, which shows that a contact angle is likewise formed at the interface. The hydrostatic pressure from the foam column, augmented by viscosity and the various capillary forces

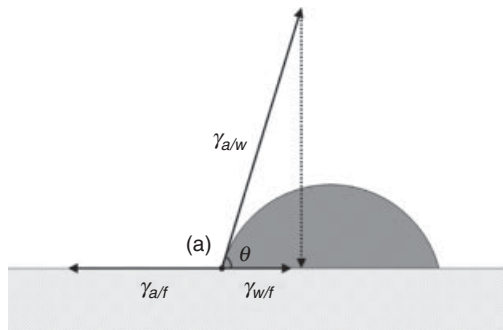


**Fig. 17.12** Idealized contact angle, surface tension, and interfacial tensions for a small, non-wetting droplet of protein or fluorine-free foam solution on cyclohexane ( $\gamma_{a/w} = 45$ ,  $\gamma_{w/f} = 12$ ,  $\gamma_{a/f} = 25$  dyn/cm). The cyclohexane fuel and water are mutually saturated, but immiscible. The SC is -32 dyn/cm, and  $\theta = 73.2^\circ$ . The projection of  $\gamma_{a/w}$  onto the horizontal axis is shown (i.e.,  $\gamma_{a/w} \cos \theta$ ). These forces act horizontally along the contact line (a) around the perimeter of the droplet.

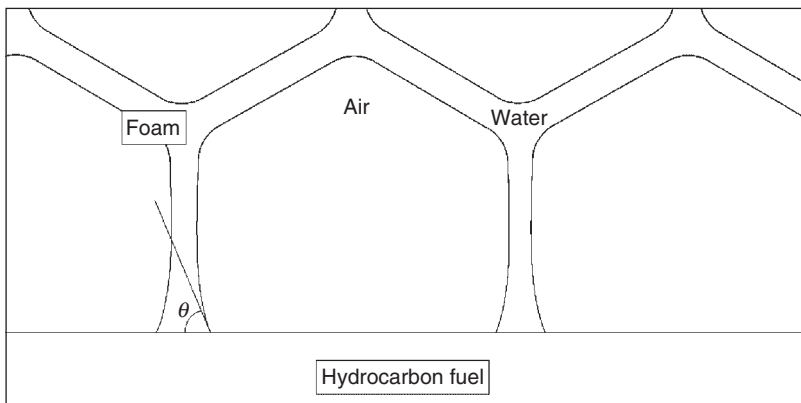


**Fig. 17.13** Non-film-forming foam on a hydrocarbon fuel.

(Plateau border suction, disjoining pressure, etc. [27]), may alter the shape of the foam columns extending upward from the fuel surface, but the contact angle  $\theta$  should resemble the angle observed for a droplet.

Non-film-forming foams allow fuel vapors to mix with the air within the foam cells, creating a localized flammable environment. Such foam types may extinguish a fire by providing thermal insulation and containing the fuel within (not beneath) the foam blanket; however, the fuel vapor-contaminated foam will flash easily when the foam coarsens over a period of time, allowing the vapor-containing cells to intermix with other cells throughout the blanket. This characteristic of non-film-forming foams is the cause of the poor burnback resistance.

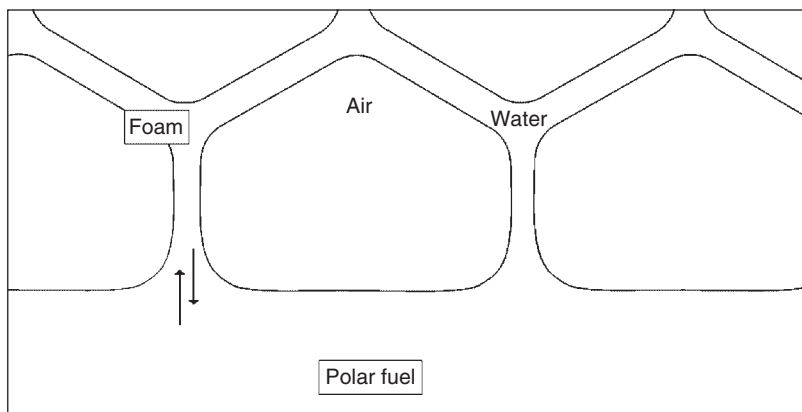


**Fig. 17.14** Non-membrane-forming foam on a polar fuel. With no barrier to intermixing of the aqueous phase and the polar fuel, the foam rapidly collapses.

Foams that contain fluorosurfactants and spread a thin film over the fuel surface (i.e.,  $SC > 0$ ), are depicted in Fig. 17.11. Here,  $\theta = 0$ , and the equivalence in eqn (17.2) is exceeded, making it inapplicable. The forces (or energies) contributing to the spreading outweigh those opposing it, leading to eqn (17.1). There is always a degree of diffusion of the fuel molecules through thin films, but the continuous film between the foam blanket and fuel surface significantly protects the foam from vapor contamination, enabling the foam, as it drains water and coarsens, to resist flashing and to provide the required burnback protection.

As mentioned above, polar hydrocarbon fuels (i.e., those with some degree of water solubility, or solubility in water), tend to degrade an AFFF foam (Fig. 17.14). As the water drains from the foam, it intermixes along the plane of contact with the fuel. Simultaneously, polar fuels (or the more-polar components in the fuel, e.g., ethanol in today's gasoline) diffuse into the foam structure. This combined effect markedly destabilizes the air/water interface by dissolving the surfactants (raising the effective critical micelle concentration, CMC, and the surface tension). As the foam degrades, gravity continuously pulls the foam blanket down against the fuel surface, and the foam collapse continues until only the bare fuel surface remains. This process may occur faster than the foam can be applied.

This degradation effect is countered by the addition of high-molecular-weight polymers (formulation details are given below). As the initial water drains, the dissolved polymer is carried to the polar fuel interface, where it precipitates to form a continuous membrane (Fig. 17.15), which acts as a mass transfer barrier to the intermixing fuel and water. The membrane resembles a thin plastic film or a soft, opaque mat, depending on its thickness and fuel type. This membrane allows for film formation on top of it, similar to the situation above for non-polar hydrocarbon fuels, which prevents fuel vapor contamination of the foam.

Class B foams are applied directly to the surface of non-polar hydrocarbon fuels, but indirectly to polar fuels. In other words, it is helpful in practice to apply AR-AFFF foams against a container wall or other vertical surface so the foam will slide down and land gently on the polar fuel surface. This practice minimizes foam intermixing with the fuel

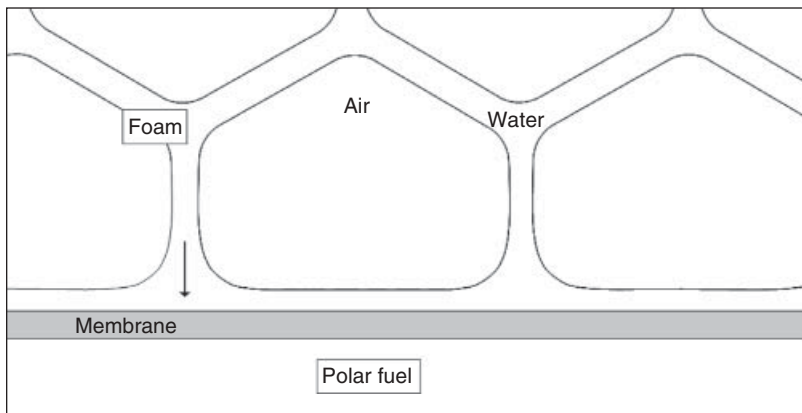


**Fig. 17.15** Membrane-forming foam on a polar fuel. A composition gradient is formed initially between the aqueous phase of the foam and the polar fuel, as in Fig. 17.14, to precipitate the polymer, which then forms a membrane to protect the foam. The lower amount of polar fuel in water needed to cause precipitation, the better the polymer performs for membrane formation.

and allows the membrane to form and remain intact without excessive turbulence. Alternatively, with non-polar hydrocarbon fuels, an AFFF (or AR-AFFF) foam is projected from the generation device, often through very intense flames, onto the burning fuel surface directly. If this is a so-called fuel-in-depth fire – for instance, where a large volume of fuel is contained in a storage tank – the foam likely impinges the surface of the fuel at a point surrounded by an atmosphere of fuel vapor. For example, in the center of a large fire, where heat evaporates fuel and air is effectively displaced, a significant layer of unignited fuel vapor exists. In this vapor-rich environment, the foam impacting the fuel surface may undergo further shear and expansion, incorporating fuel vapor into the foam cells. This is particularly problematic for overly rich foam solutions or those that have not been “fully” expanded by the generating device.

Fuel emulsification by the foam is another issue to contend with. This occurs when foam is plunged into the fuel surface or applied sub-surface. Any foam solution that spreads spontaneously across a planar fuel surface will likewise fully wet a spherical droplet of fuel [26]. This is to say, AFFF foams are able to emulsify fuel to an extent that is dependent on the amount of applied shear. Emulsified fuel (see Fig. 17.16) is not by itself flammable, but if there is significant time for diffusion of the fuel molecules through the aqueous phase into the foam cells, a flammable microenvironment is created. Foams formulated with certain fluorosurfactants are referred to as “fuel-shedding.” These foams may prevent small, emulsified fuel droplets from being stabilized and suspended. Thus, larger droplets will percolate down through the liquid structure of the foam and rejoin the bulk layer of fuel below it before significant diffusion and contamination of the foam can occur.

A desirable foam will display a certain adhesiveness when in contact with a container wall or other solid object, which prevents vapors from bypassing the foam blanket at the

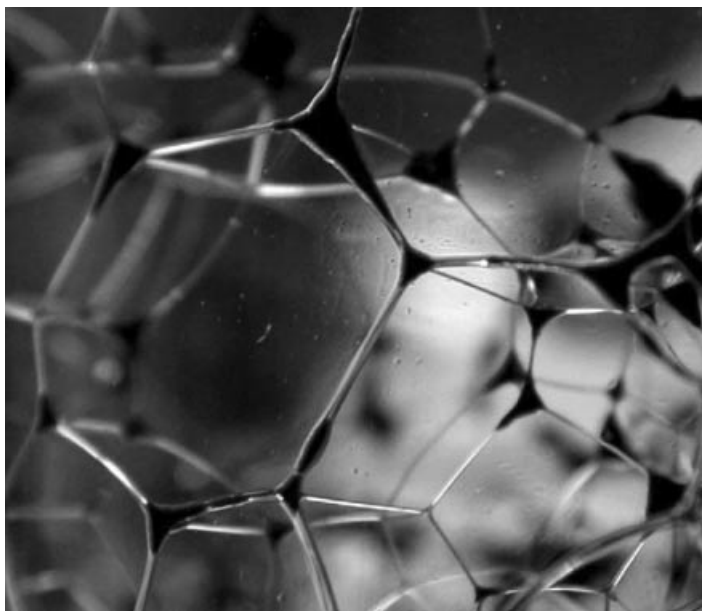


**Fig. 17.16** Crude oil emulsified within Plateau borders of a foam. Note the lack of oil in the lamella. The polyhedral foam structure, formed with the expansion ratio greater than about 3.9, is apparent. Emulsified oil does not necessarily compromise the structure of the foam. Larger oil droplets are not suspended and percolate down through the foam structure.  
Reprinted with permission from [29] © 2005 Elsevier.

edge. These objects are often very hot and tend to degrade the foam to a degree when contact is made. The so-called “edge-seal” property is imparted to the foam by fluorosurfactants, which demonstrably stabilize the foam structure and prevent collapse. This is another wetting phenomenon; however, the mechanism for it is not completely clear.

Foams used in sprinkler applications must withstand a deluge of pure water (should the sprinkler system run out of foam concentrate at some time after being triggered, for instance). The AFFF foam structure is remarkably resistant to a spray of water. As water passes through a foam blanket, however, all surfactants are gradually washed out. The more water-soluble the surfactant, the higher its CMC is and the more easily it is carried away. Conversely, surfactants with lower CMCs attach more strongly to the air–water interface and are resistant to the deluge. A continuous, impervious foam blanket is maintained as long as the spreading coefficient is positive, which is imparted by fluorosurfactants. When the fluorosurfactant components that are responsible for surface tension reduction and spreading are gradually depleted, the spreading coefficient drops below zero and holes will open in the foam blanket to expose the fuel. To forestall this, specific fluorosurfactants selected from the foam stabilizer group (outlined below) are also used in foam formulation for sprinkler applications. These fluorosurfactants have low water solubility and are more securely anchored to the air–water interface, thus resisting washing out. This keeps the spreading coefficient positive for a longer time across the entire foam blanket.

The effectiveness of a fire-fighting foam is dependent to a large degree on the drainage rate of water from the foam. Foams that stay “wet” longer are preferred. A typical low-expansion AFFF has an expansion ratio of about 6–7, giving a liquid fraction of about 0.14–0.17. The more subdivided the liquid fraction (i.e., the smaller the cell size), the slower the drainage rate [29]. Water trickling down through the foam can be thought of as following a tortuous path. The smaller the cell size, the longer the effective path length, thus the longer the drain time. Foam generation devices that are aspirated or operated with high pressure give foams with longer drain times. In general, any increase in the degree of agitation of the combined air and foam solution will increase the drain time. Geometry, however, is merely one of many factors affecting drainage rates. The effects of gravity, viscosity, Marangoni forces, and other factors on drainage and coarsening are discussed in other chapters.

## 17.5 Chemical Properties

This section explains how choices are made from among the available raw materials to meet the physical property requirements outlined above, again focusing on Class A and synthetic Class B fire-fighting foam types.

The approximate composition of a premium AR-AFFF foam is shown in Table 17.4. The percentage ranges apply equally to foams meant for 1%, 3%, 6%, and other proportioning rates, since the water component has been excluded. Fluorosurfactants, it should be noted, although an essential ingredient, are relatively minor by percentage. A general description for each ingredient category appears below, and example foam concentrate recipes are provided toward the end of this section.

### 17.5.1 Ingredients and Purpose

#### 17.5.1.1 Water

Water is the largest component of any fire-fighting foam concentrate. A foam concentrate is further diluted prior to use, not unlike household products (e.g., detergents, shampoos, soaps, and cleaners). Ultimately, the active ingredients used to create a finished foam are essentially minor additives to water.

**Table 17.4** AFFF foam ingredients as a percentage of active (non-water) components.

Ingredient	Percentage
Organic solvents	10–40
Hydrocarbon surfactants	20–40
Fluorosurfactants	2–15
Polymers	0–10
Salts, buffers, preservatives and other additives	5–10

Water used for manufacturing a foam concentrate is usually taken from a municipal source. Deionization and distillation are not typically necessary, since salts in various forms are added to the formulation anyway. Care should be taken to exclude excessive chloride from the water source due to corrosion issues. Water is a cheap and abundant solvent, so it is obviously preferable to maximize its use. However, because of the practical need to maintain the storage stability of the foam concentrate in a ready state for many years prior to use, certain water-soluble organic solvents may be required.

#### 17.5.1.2 Organic Solvents

The storage conditions for a given foam concentrate may range from subzero temperatures to extreme heat. Concentrated surfactants and polymers in solution form complex molecular aggregates [30]. Water alone as a solvent may be insufficient to prevent separation of the components, especially the higher-performing (more-active) foam concentrates subject to various environmental conditions. Instability is manifested variably by such conditions as freeze-thaw separation, sedimentation, and syneresis, for example. As described below, organic solvents are needed to aid in storage stability of the concentrate, as well as to improve the performance of the foam itself.

Typical solvents used for fire-fighting foams are (Chemical Abstract Service numbers noted):

*t*-butyl alcohol (75-65-0)  
diethylene glycol (111-46-6)  
diethylene glycol monobutyl ether (112-34-5)  
dipropylene glycol monomethyl ether (34590-94-8)  
ethanol (64-17-5)  
ethylene glycol (107-21-1)  
ethylene glycol *n*-butyl ether (111-76-2)  
glycerol (56-81-5)  
hexylene glycol (107-41-5)  
isopropanol (67-63-0)  
*n*-propanol (71-23-8)  
propylene glycol (57-55-6)  
propylene glycol *n*-butyl ether (5131-66-8)  
propylene glycol *t*-butyl ether (57018-52-7)  
tetraethylene glycol dimethyl ether (143-24-8)

For foam products requiring substantial freeze protection (down to  $-30^{\circ}\text{C}$ , for instance), common antifreeze solvents, such as ethylene glycol, propylene glycol, and glycerol, are used in place of an equivalent portion of water, depending on cost and performance requirements. Glycerol (glycerin or glycerine) is attractive due to its relatively low cost and abundance as a by-product from biodiesel production. However, handling glycerol as a raw material can be difficult, especially when it is cold, due to its syrup-like viscosity. Ethylene glycol is likewise economical, but its toxicity raises concerns. Propylene glycol, used in aircraft deicing, is the most environmentally friendly antifreeze.

Alcohols and glycol ethers offer some degree of freeze protection, but they are not as efficient by weight as glycols. However, both may be present in small amounts in a foam

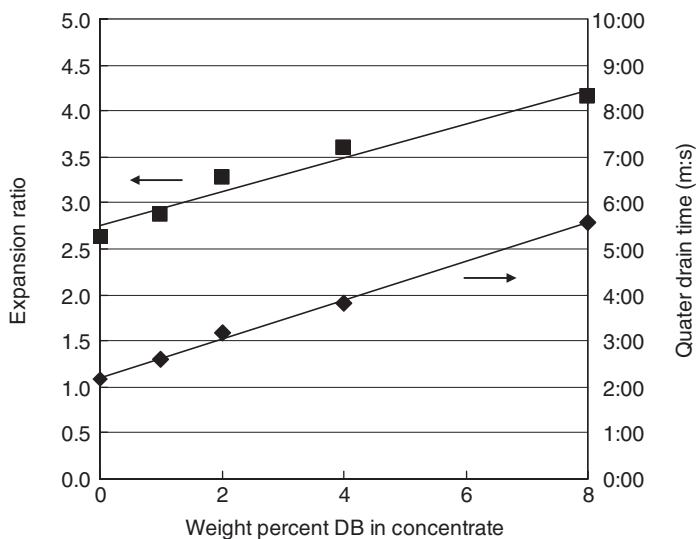


**Fig. 17.17** Diethylene glycol monobutyl ether (DB) as a foam booster in an AFFF foam. DB was substituted for water, while all other components were held constant.

concentrate due to incorporation as a solvent from other raw materials. Heavy use of lower alcohols is avoided due to product flammability issues.

Concentrated surfactants form irregular, elongated micelle structures that increase bulk viscosity of the solution [31, 32]. Depending on the other solvent components, phase separation may occur. Often, this is not immediately apparent, but may take place as the foam concentrate sits for a long period of time. Freeze-thaw cycling, high temperatures, or temperature variations may accentuate this effect. Glycols and glycol ethers are used to solvate and compatibilize the various surfactants and other ingredients to prevent phase separation, as well as to lower the viscosity of the product.

Solvents have little if any surface activity and contribute only slightly to surface tension reduction. However, some solvents display a kinetic effect that aids the initial foam generation and improves the ultimate degree of foam expansion, the underlying principle of which is similar to the mechanism for freeze protection. Water is a very cohesive liquid due to its extensive three-dimensional hydrogen-bonded network. A solvent (or solute) that disrupts the hydrogen bonds allows the bulk foam solution to deform more easily into thin sheets and ultimately sub-micron-thick films that comprise the foam structure. In this way, protic solvents, such as glycols and glycol ethers, act as “foam boosters” [33]. This is especially useful in low-shear foam generation, such as sprinkler heads and non-aspirated nozzles. Figure 17.17 illustrates this effect as measured by both the expansion and drain time.

Although freeze protection to any significant degree requires 10–30% of a glycol or glycol ether in the concentrate, much less is needed for foam boosting (e.g., 2–10%). The industrial trend appears to be toward lower solvent use in foam concentrates where freeze protection is not needed, mainly for cost reduction and other forms of recipe optimization. Some glycol or glycol ether is present in most AR-AFFF foams, since it is used as a dispersant when adding the polysaccharide (see Polymers below).

### 17.5.1.3 Hydrocarbon Surfactants

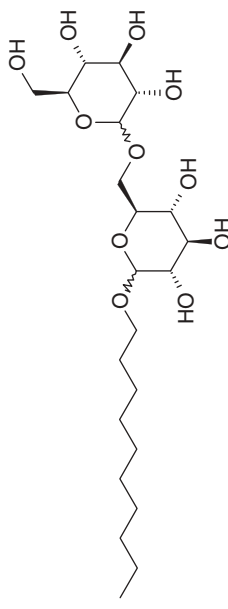
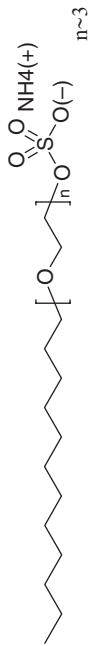
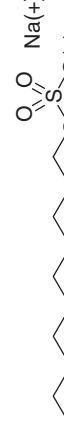
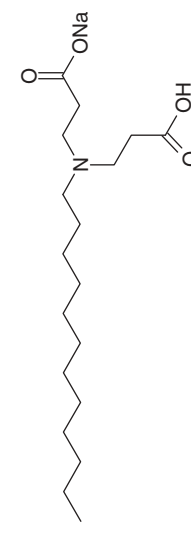
In general, a surfactant molecule has a hydrophilic segment inextricably linked to a hydrophobic segment. For a typical, low-molecular-weight surfactant, the former is referred to as the “head” group and the latter is referred to as the “tail” group. Surfactants are generally characterized as anionic, cationic, non-ionic, and amphoteric, referring to the head group. All types can be used in fire-fighting foams, depending on the foam’s functional requirements. Naturally, preference is given to surfactants that provide the greatest foam volume and stability. Of these surfactants, selected non-ionics, anionics, and amphoteric are preferred (see Table 17.5). Certain non-ionics (e.g., ethoxylates) and anionics (e.g., phosphate esters) are generally known to be poor foamers and are not typically used in fire-fighting foams. These low-foaming surfactants reduce surface tension comparably [34], but they do not stabilize the foam structure, probably because they pack inefficiently at the air–water interface. Alkyl phenol ethoxylates (as an example non-ionic surfactant) are historically very effective foamers, but are avoided now due to environmental concerns. Hydrocarbon surfactants with shorter chain tail groups are generally lower in aquatic toxicity [35, 36] than longer chain homologs. Typically, C<sub>8</sub>–C<sub>12</sub> alkyl chain types are employed.

A common practice across many product applications, not just fire-fighting foams, is to use synergistic mixtures of surfactants of different types; for example, anionics and non-ionics. Figure 17.18 shows an example of this for an AFFF recipe using an alkyl polyglycoside (APG) and sodium decyl sulfate (NADS) (further defined in Table 17.5), where foam expansion is used to optimize the surfactant ratio. APG is a naturally derived non-ionic surfactant, while NADS is an alkyl sulfate. The maximum foam expansion at about 55% by weight of APG corresponds to an equimolar ratio. It is believed that the bulky APG molecules occupy sites at the air–water interface, ideally arranged in a hexagonal packing pattern, with the smaller NADS located in alternating interstitial spaces (Fig. 17.19). This assembly would allow the APG molecules to separate and shield the negatively charged NADS molecules from each other. Fluorosurfactants and other surfactants included in a full foam formulation are imagined to substitute for one surfactant or the other within the idealized 2D matrix.

Cationic and anionic surfactants are incompatible, and thus customarily not combined (which is why shampoo and conditioner are in separate bottles [37]). Exceptions are noted for fluorocarbon surfactants, where ultra-low solubility (high surface activity) is desired, as explained in References 47 and 57.

The CMC (critical micelle concentration) is a fundamental characteristic of a surfactant in a given solution at a set temperature (although not all surfactants exhibit a CMC). It represents the saturation point in solution at which no more individual surfactant molecules, or unimers [38], can be solvated [31, 36]. Additional surfactant molecules added to solution, increasing the bulk concentration, undergo a phase separation of sorts, whereby the hydrophobic chains aggregate as micelles to avoid contact with water. Likewise, the CMC is the saturation point of the surfactant at the air–water interface. Below the CMC, the interface can accommodate a certain proportion of the overall surfactant added to the bulk solution, thus it is further stabilized and the surface tension decreases. Above the CMC, the air–water interface is saturated and the surface tension remains constant as more surfactant is added to the bulk solution. Additional surfactant has no recourse but to form more micelles, while both the interfacial and unimer concentrations remain constant.

**Table 17.5** Hydrocarbon surfactants for fire-fighting foam.

Common name	Structure	Conc.*	CMC†	References
Alkyl polyglycoside (APG)		50%	0.026 <sup>a</sup> 0.019 <sup>b</sup> 0.031 <sup>c</sup>	30, 46, 60, 65
Ammonium alkyl ether sulfate (AES)		60%	0.013 <sup>a</sup> 0.012 <sup>b</sup> 0.31 <sup>c</sup>	
Ammonium lauryl sulfate (ALS)		30%	0.006 <sup>b</sup>	
Sodium octyl sulfate (NOS)		40%	0.15 <sup>a</sup>	30, 52, 58
Sodium decyl sulfate (NADS)		33%	0.042 <sup>a</sup>	30, 52
N-lauryl imino-dipropionate (LIDP)		30%	0.027 <sup>a</sup> 0.023 <sup>b</sup> 0.025 <sup>c</sup>	30, 47, 58, 59

Sulfobetaine (CAS)		33%	0.004 <sup>a</sup> 0.006 <sup>b</sup>	52
Sodium alpha olefin sulfonate (AOS)		40%	0.005 <sup>a</sup> 0.007 <sup>b</sup>	
Lauryl betaine (LB)		30%	—	30
Linear alkyl benzene sulfonate (LAS)		100%	—	
Alkyl phenol ethoxylate (APE) deprecated		100%	0.015 <sup>a</sup> 0.019 <sup>c</sup>	n~9-10

\*Active concentration as supplied. <sup>a</sup>Percentage actives by weight (for illustration purposes only; it is advised to measure CMC under applicable conditions and water type).  
<sup>b</sup>Artificial seawater. <sup>c</sup>0.05% MgSO<sub>4</sub> in deionized water. <sup>c</sup>Literature value or supplier data.

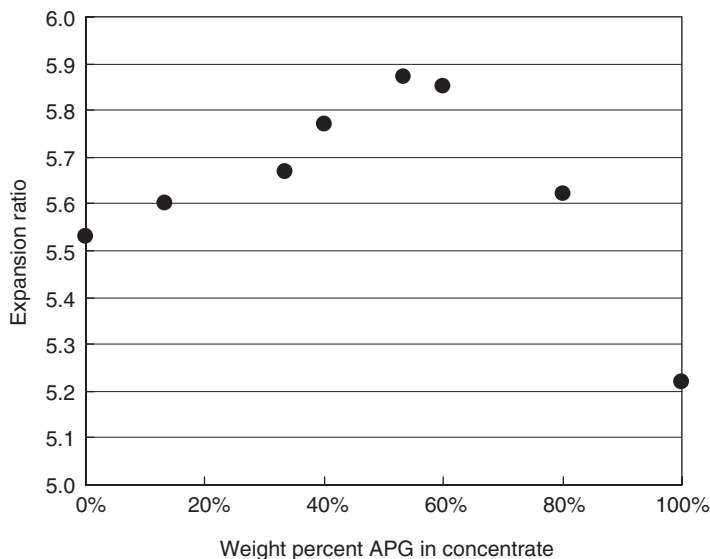


**Fig. 17.18** Optimal APG to NADS ratio in an AFFF foam. The weight percentage of the sum of APG and NADS surfactants and all other components were held constant.

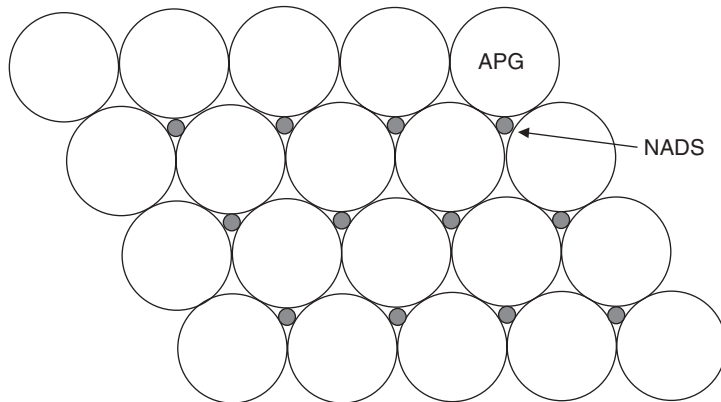


**Fig. 17.19** Theoretical packing of anionic (NADS) and nonionic (APG) hydrocarbon surfactants at the air–water interface (not to scale).

Hydrocarbon surfactants make up the majority of the active ingredients in a fire-fighting foam and are often of the same type used in detergents, shampoos, soaps, and other household products. These are less expensive than fluorocarbon surfactants and are therefore maximized as the foaming agents within a formulation. In other words, it makes little sense to improve foam quality using a fluorocarbon surfactant (detailed below) when a hydrocarbon surfactant will do. Since the primary purpose of hydrocarbon surfactants is to

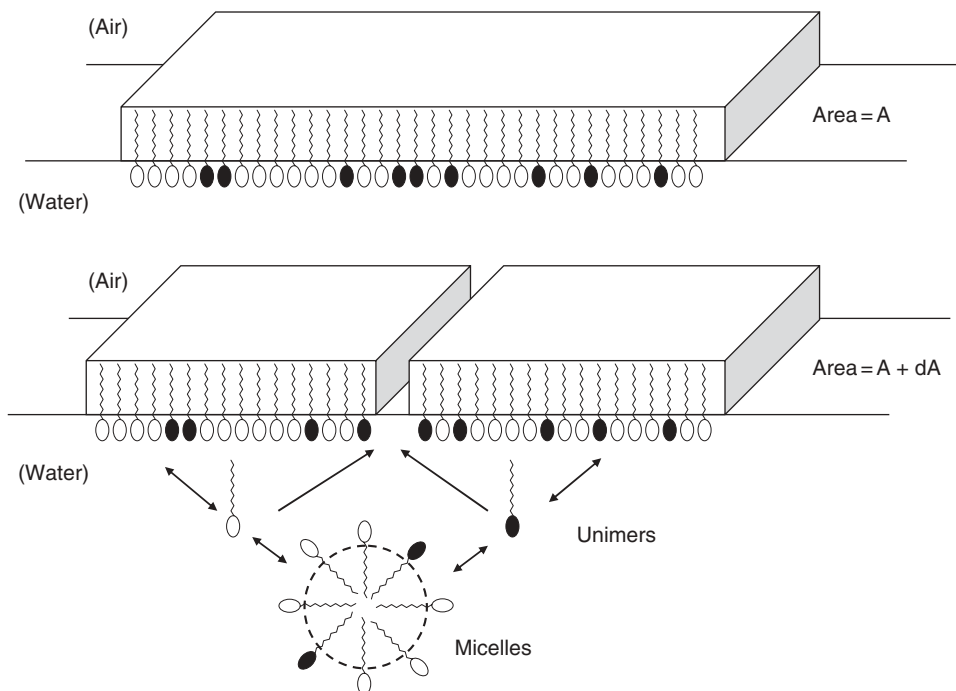


**Fig. 17.20** Schematic of the air–water interface stabilized with both hydrocarbon surfactants (open symbol) and fluorosurfactants (filled symbol). (Apologies for the use of the head group to differentiate between surfactant types.) The overall molar ratio of hydrocarbon surfactants to fluorosurfactants can be as high as 16:1. Newly created surface area  $dA$  is stabilized by the available unimers. Above the effective CMC, micelles provide unimers to stabilize the new surface area,  $dA$ . How fluorosurfactants are grouped in the mixed micelles and at the air–water interface is unclear [48].

maintain the foam structure by stabilizing the air–water interface, the ultimate surface tension reduction attainable while minimizing the surfactant concentration is of utmost importance. The use of a given surfactant below its CMC in the foam solution is inefficient since the solution is subsaturated and the maximum surface tension reduction will not yet have been achieved. Any increase in interfacial area caused by fluctuations or further expansion cannot be optimally stabilized, and the foam integrity is diminished. Use of a surfactant far above its CMC is wasteful, since no further surface tension reduction is possible. Therefore, candidate hydrocarbon surfactants are used slightly above their CMC concentration in the foam solution, which requires the formulation of the foam concentrate to be adjusted accordingly.

Surfactant molecules exchange in and out of micelles (Fig. 17.20), and attach to and detach from the air–water interface. When an air–water interface is created, either initially when the foam is formed or if the foam blanket is disturbed, micelles act as reservoirs to supply surfactant to the new interface. If micelles are too stable, the foam stability suffers [39, 40]. With the many solvents and surfactants included in a typical foam formulation, it is reasonable to view the resulting micelles as multi-surfactant,

solvent-swollen structures, depending on the ingredient types [41–44]. This dynamic, liquefied structure is advantageous. For the surfactants to stabilize the large, newly created surface area of a newly created foam, they must be easily extracted from the micelle structure and homogeneously distributed throughout the bulk of the water phase of the foam solution. In limited cases, the foam concentrate is premixed with water to form the foam solution, which gives ample time for dissolution. However, more often the dilution occurs instantaneously prior to foam generation. The speed and uniformity with which a concentrate is diluted is critical for maximum foam generation and stability.

Often highly water-soluble surfactants are used in foam at sub-CMC levels. Their usefulness is more as foam boosters, similar in effect to the solvents, but not through hydrogen-bonding disruption. Highly water-soluble surfactants of low molecular weight are not contained in micelles and diffuse very quickly through solution. These surfactants are thought to act to temporarily stabilize the initial air–water interface within a nascent foam, allowing time for other surfactants to diffuse and replace them, providing the ultimate foam stability and maximizing the foam expansion.

Reported surface tension values using the Wilhelmy plate method, for example (see Testing), are measured using a small cup with a relatively minor specific surface area (approximately  $0.4\text{ cm}^2/\text{g}$ ). Considering instead a nominal low-expansion fire-fighting foam with an expansion ratio of around 6 and a cell size of about  $100\text{ }\mu\text{m}$  (a dodecahedral foam cell is presumed), the specific surface area  $A$  would be about  $4200\text{ cm}^2/\text{g}$ . Let  $C$  be the surfactant concentration in the bulk solution. The total moles of surfactant molecules  $n$  in the initial foam solution of volume  $V$  partition between the bulk liquid of the fully expanded foam and the air–water interface; that is,

$$n = CV + \Gamma A \quad (17.3)$$

where  $\Gamma$  is the Gibbs surface excess concentration. In other words, the large surface area of the foam, stabilized by a surfactant, depletes the surfactant from the bulk liquid of the foam (i.e., the lamella and Plateau borders) such that  $C$  may drop below the CMC, and reservoirs of micelles would not exist. This has to be accounted for in the foam recipe and is the basis for using a surfactant at a concentration in the initial foam solution above its CMC.

For example, APG has a CMC of 0.019% by weight in seawater (measured by the Wilhelmy plate method). The Gibbs surface excess calculation using

$$\Gamma = \frac{-d\gamma}{RTd(\ln C)} \quad (17.4)$$

shows that about 74% of the APG is at the air–water interface within the above foam at saturation, with the remainder dissolved in solution as either unimers or micelles. To maintain saturation, 0.071% APG is needed in the initial foam solution, as opposed to the CMC value.

The above discussion, which contemplates a single surfactant type in solution, is to be used merely as a starting point for foam formulation work. Real foams contain mixtures of surfactants that are expected to form mixed micelles with an amalgamated CMC. Pair-wise surfactant CMC measurements can be conducted to understand the surfactant interaction and further refine the starting point formulation. However, it is often better to construct the initial recipe based on the above theoretical basis and then adjust components individually,

based on empirical test results and the formulator's practical knowledge of which ingredient contributes to (or detracts from) each desired property of the foam.

In addition to the reservoir effect, studies have shown that micelle structures within a foam physically enhance foam stability by propping apart the opposing film surfaces in the foam lamella [39, 40, 45]. Interestingly, the film thickness is observed to be quantized as the water drains and the number of intervening layers of micelles is reduced stepwise.

#### 17.5.1.4 Fluorosurfactants

Fluorocarbon surfactants, or simply fluorosurfactants, are an important subclass of surface-active agents. Fluorosurfactants have been referred to as "super surfactants" [48] due to their unique ability to lower the surface tension of water far below that obtainable from hydrocarbon surfactants, leading to the desired positive *SC* described above. Like hydrocarbon surfactants, fluorosurfactants are classified as anionic, cationic, non-ionic, or amphoteric, referring to the hydrophilic head group. Fluorosurfactants also contain, as part of the hydrophobic tail group, an alkyl segment on which all available hydrogens are replaced by fluorine, referred to as a perfluoroalkyl chain. The perfluoroalkyl chain has the added property of being oleophobic, in addition to hydrophobic. Thus, the perfluoroalkyl group does not like either water or fuel but would rather protrude from the liquid surface into the air. In this way, the perfluoroalkyl chain acts as an anchor at the air–water interface. This characteristic, as we shall see, is very useful in a number of respects.

Alternatively, fluorosurfactants may self-associate as a micelle in solution. Fluorosurfactants exhibit surface tension versus concentration curves and CMC values, just as hydrocarbon surfactants do. However, the ultimate surface tension reduction (i.e., above the CMC) and the CMC values are both lower than those attainable from any other surfactant type, hydrocarbon or otherwise. Fluorosurfactants may reduce the surface tension of water from 72 dyn/cm down to about 15 dyn/cm (Fig. 17.21), whereas hydrocarbon surfactants give about 26 dyn/cm at best. The surface tensions attainable for both surfactant types may seem substantially low, but considering the requirements for, and implications of, foam spreading on a fuel surface (or not), the difference is significant. No other surfactants offer the performance of fluorosurfactants.

The extreme surface tension reduction by fluorosurfactants is a result of, not only the strong partitioning from the bulk solution to the air–water interface, but also of the close packing of the molecules and the alignment of the perfluoroalkyl chains. It is known that branching reduces the efficiency of the surface tension reduction. Small, neutral head groups are advantageous. For charged head groups (e.g., anionics), multivalent salts are helpful for screening the otherwise mutual repulsion (see below). Because of the very strong, inert C–F bonds, perfluoroalkyl chains do not interact strongly with anything, including themselves. With these chains occupying the air–water interface, the energy (*dE*) required to expand or create more surface area (*dA*) is greatly reduced, giving rise to the low-surface-tension values

$$\gamma = \frac{dE}{dA}, \quad (17.5)$$

which is illustrated in Fig. 17.20.

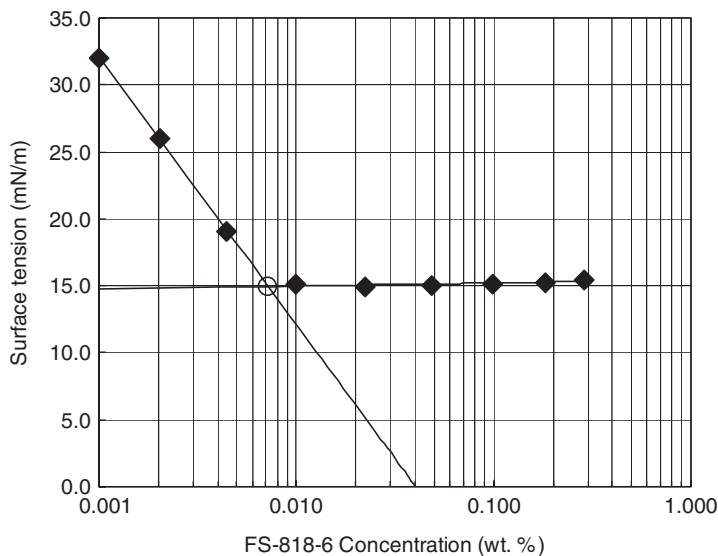


**Fig. 17.21** Semi-logarithmic plot of surface tension v. concentration for Chemguard FS-818-6 in 0.05%  $MgSO_4$ . The CMC is derived from the intersection between the lines fitted to the data points on opposite sides of the apparent inflection point (note:  $mN/m \equiv dyn/cm$ ).

Representative fluorosurfactants are given in Table 17.6 and can be classified into two general groups, depending on their respective uses. The first such class contains the film formers, while the second class can be thought of as foam stabilizers (Fig. 17.22). Certainly, there are numerous properties imparted by any single surfactant, and some surfactants serve more than one purpose, but this demonstrable classification is helpful to frame the benefits of each surfactant ingredient.

Fluorosurfactants classified as film formers are meant to drain out of the foam quickly and lower the surface tension of the underlying aqueous film. Such properties provide for the positive SC beneath the foam described above. These fluorosurfactants are more water-soluble than the opposite class (which is not to say that they preferentially partition into the bulk aqueous phase), so they exchange between the interface and the bulk solution sufficiently easily such that they are carried out of the foam with the draining liquid to form a continuous aqueous film between the foam blanket and the fuel surface.

The role of the second class of fluorosurfactants, the foam stabilizers, is easily demonstrated but less well understood. These are usually fluoropolymer surfactants [49–54] that may serve to increase the surface viscosity [55, 56] or participate in membrane formation along with the high-molecular-weight polymer. As the foam ages (i.e., coarsens and drains), it is likely that the fluorosurfactants remaining attached at the air–water interface prevent more extensive draining by increasing the disjoining pressure [45] within the film regions, possibly by straightforward steric effects or by osmotic pressure required to keep the hydrophilic portions of the anchored fluorosurfactant solvated. Particular properties of a fire-fighting foam, such as edge-seal, low fuel pick-up, and water-deluge resistance (Fig. 17.23), are significantly improved by the presence of these types of fluorosurfactants.

**Table 17.6** Fluorosurfactants for fire-fighting foam.

Chemguard trade name	Common Name	Structure <sup>†</sup>	Conc.*	CMC <sup>†</sup>	References
FS-220B	Fluorotelomer surfactant		40%	na	57, 58, 59
FS-818-6	Fluorotelomer surfactant		35%	0.0053 <sup>a</sup> 0.0072 <sup>b</sup> 0.0060 <sup>d</sup>	57, 58, 59
FS-9090	Fluorotelomer surfactant		35%	0.031 <sup>b</sup> 0.038 <sup>d</sup>	3
FS-183	N-oxide fluorosurfactant		40%	0.013 <sup>a</sup> 0.0076 <sup>d</sup> 0.014 <sup>e</sup>	60, 61

(continued overleaf)

Table 17.6 (continued)

Chemguard trade name	Common Name	Structure <sup>#</sup>	Conc.*	CMC <sup>†</sup>	References
FS-157	Amphoteric (betaine) fluorosurfactant		27%	0.0068 <sup>b</sup> 0.0051 <sup>d</sup>	60, 62
S-103A	Anionic fluorosurfactant		45%	0.038 <sup>a</sup> 0.081 <sup>d</sup>	58
S-106A	Cationic fluorosurfactant		30%	0.021 <sup>a</sup> 0.023 <sup>b</sup> 0.55 <sup>d</sup>	58

\*Active concentration as supplied.<sup>#</sup>Percentage actives by weight (for illustration purposes only; it is advised to measure CMC under applicable conditions and water type). <sup>a</sup>Rf = CF<sub>3</sub>CF<sub>2</sub>(CF<sub>2</sub>CF<sub>2</sub>)<sub>n</sub>.  
 typically n = 2–5, linear chains only. <sup>b</sup>Artificial seawater. <sup>c</sup>Deionized water. <sup>d</sup>Tap water.

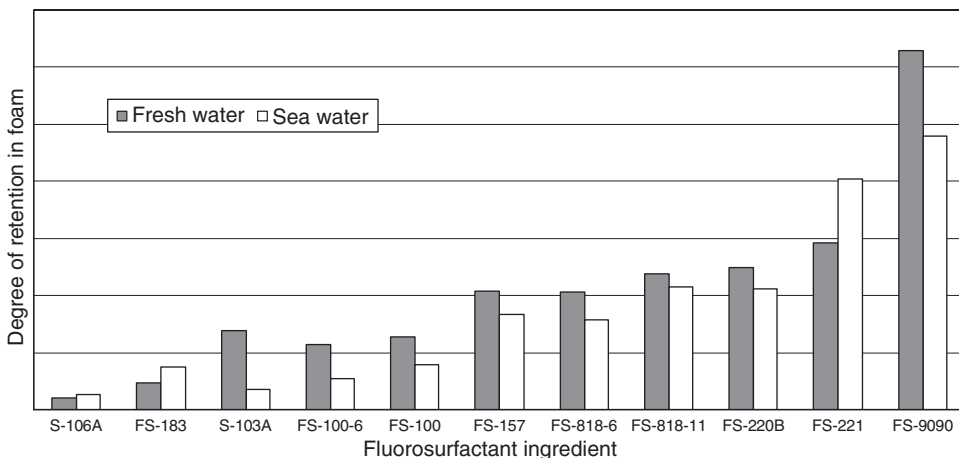


**Fig. 17.22** Retention of select Chemguard fluorosurfactants in AFFF foams (larger values indicate a greater relative amount of retention in the foam). The products to the left are film formers; to the right are foam stabilizers. Chemguard FS-818-6 and FS-818-11 combine both properties and represent the approximate division between the two classes.

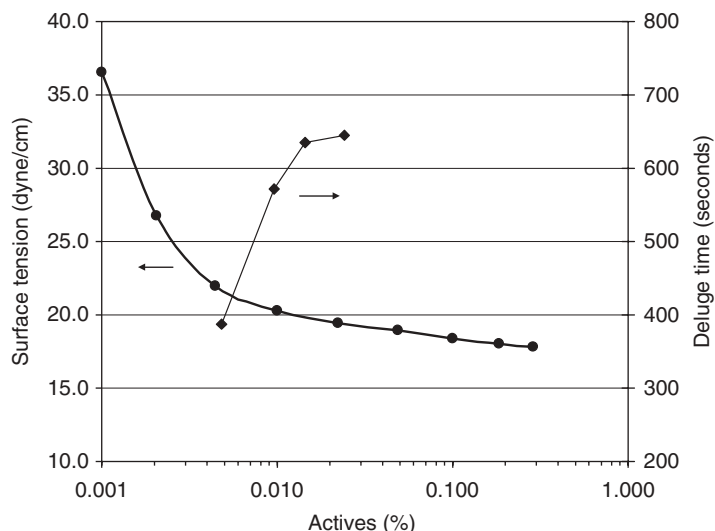


**Fig. 17.23** Surface tension and deluge-resistance time v. active concentration for Chemguard FS-220B. The effectiveness of a surfactant at preserving foam life (i.e., resisting wash out) is shown to level off at around the solution saturation point (no clear CMC is observed since this particular product is a mixture of homologs).

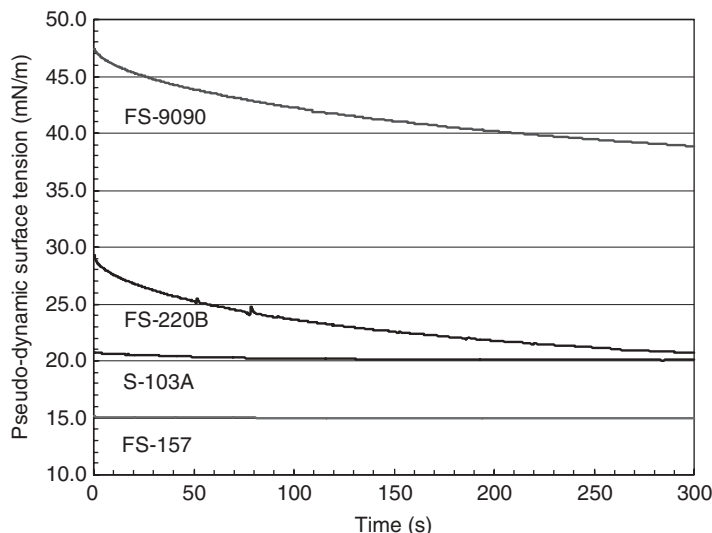


**Fig. 17.24** Pseudo-dynamic surface tension data for select Chemguard fluorosurfactants. Smaller, lower molecular weight species equilibrate faster (see Table 17.6).

As with hydrocarbon surfactants, fluorosurfactants diffuse at various rates to stabilize the air–water interface. Pseudo-dynamic surface tension data are given in Fig. 17.24, which shows that the smaller, more-mobile fluorosurfactants reach maximum surface tension reduction more quickly than the larger molecules.

As mentioned, a foam concentrate is expected to remain viable for 20 years or more. Therefore, all ingredients, including the hydrocarbon surfactants and fluorosurfactants, must be resistant to hydrolysis and other forms of degradation. As can be seen from the representative structures in Tables 17.5 and 17.6, there are no esters (aside from the sulfates), but only functional groups that are more resistant to hydrolysis under neutral pH conditions and ambient temperatures.

#### 17.5.1.5 Polymers

Polymers are included in fire-fighting foams to prevent the foam from collapsing on polar fuels and to significantly lengthen the drain time by viscosifying the aqueous phase. Useful polymers include:

- cellulose ethers
- hydrolyzed proteins
- modified starches
- polyacrylamides
- polyacrylates
- polyethylene glycol
- polysaccharides
- polyvinyl alcohol
- polyvinylpyrrolidone

**Table 17.7** Synergism between polysaccharides and foam-stabilizing fluorosurfactants in AR-AFFF foams (samples A–F).

Ingredient included in sample?	A	B	C	D	E	F
Polysaccharide	No	No	No	Yes	Yes	Yes
Fluorosurfactant 1 (foam stabilizer type)	No	Yes	No	No	Yes	No
Fluorosurfactant 2 (foam stabilizer type)	No	No	Yes	No	No	Yes
Resulting quarter drain time (min:s)	3:04	3:11	3:15	7:40	8:23	9:32

Typically, polysaccharides such as xanthan gum and variants are preferred. These are very-high-molecular-weight “gums” that are water-soluble and tolerant of surfactants, salts, and (to a degree) solvents. However, the dissolved polysaccharide polymer precipitates from the foam solution when the local concentration of non-solvent (polar fuel) exceeds a finite limit. This precipitated polysaccharide forms a soft mat, or membrane, between the foam blanket and fuel to block further intermixing. In practice, the precipitation occurs instantaneously as the foam is applied to a polar fuel and little foam degradation is observed. Analytically, however, a minor degree of water drainage and foam collapse are required to provide a sufficient precipitated polymer mass to form the membrane. The lower the concentration of polar solvent needed to precipitate the polymer, the more efficient the polymer is at protecting the foam. The chains of *low-molecular-weight* polymers do not overlap sufficiently when precipitated to form a durable membrane. The high molecular weight is essential to allow for contact between polymer chains in the very early stages of precipitation, which form a nascent two-dimensional network on which further precipitated polymer builds. As mentioned above for AR-AFFF applied to polar fuels, gentle (indirect) foam application is best to facilitate the membrane formation.

The polysaccharide polymers, used for increasing viscosity and drain time, are not surface active [63], so their effectiveness is primarily within the bulk aqueous phase. This leaves the interfacial region within the foam somewhat unaffected. By combining the foam stabilizing fluorosurfactants with the polysaccharide, the entire lamella and Plateau border regions are viscosified from one air–water interface to the other [3, 55, 64]. The fluorosurfactant is efficiently anchored to the interface and immobilized, increasing the surface viscosity. This synergistic effect is demonstrated in Table 17.7.

Polysaccharides such as xanthan gum are supplied as dry powders. Once almost all the other foam concentrate ingredients are dissolved and homogenized, the polysaccharide is added to the concentrate formulation as a slurry using the glycol or glycol ether solvent. A slurry is used to disperse the polysaccharide prior to hydration, as otherwise clumps would form and the required mixing time would become excessive. (Sifting the dry powder into the foam solution, the alternative to the slurry technique, is not recommended due to handling difficulties.) The rate of hydration is dependent on the particle size of the polysaccharide [65]. Smaller particles hydrate more quickly and produce a more viscous AR-AFFF concentrate. The extent of hydration is limited in rate and duration by the

surfactants and solvents present in the formulation. A foam batch is observed to increase in viscosity over time (e.g., years). This can be offset somewhat by heat-cycling – raising the temperature above ambient for a set amount of time – the final AR-AFFF concentrate prior to use [66]. Heat-cycling has the added benefit of homogenizing the viscous foam concentrate.

Hydrolyzed proteins technically fall under the polymer additive category, but the use of protein base is considered to be a separate class of fire-fighting foam, as indicated above. Proteins are high molecular weight and surface active [55], will foam well, and therefore function as a foam base without added surfactants (given the drawbacks noted above). The protein base is typically additized with fluorosurfactants to make FP, FFFP, and AR-AFFF variants. Numerous labs have modified various other naturally derived polymers for use in fire-fighting foams and other purposes. Some of them contain fluorocarbon groups [67, 68] while others have only hydrocarbon chain additions [44, 69–75].

#### *17.5.1.6 Salts, Buffers, Preservatives and Other Additives*

Several other additives may be included in a fire-fighting foam concentrate, primarily as stabilizers and performance enhancers:

- The pH of a foam concentrate may be adjusted to be near neutral or slightly alkaline to prevent corrosion and degradation (hydrolysis) of the various active ingredients. Caustic soda (50% NaOH) and acetic acid are typically used for this.
- Salts may be added to screen anionic surfactant charges at the air–water interface and to weakly couple various acid groups, such as those on polysaccharides and surfactants. They may also be used to alter the polysaccharide rheology [63].
- When multivalent charges are undesirable, EDTA or citric acid, for example, may be included in the recipe.
- Corrosion inhibitors may be added to prevent degradation to both storage containers and equipment that the foam may come in contact with (aircraft aluminum, for instance).
- Urea may be added as a viscosity reducer in polysaccharide-containing AR-AFFF and as an antifreeze agent [76].
- Old or improperly stored samples may smell of hydrogen sulfide [77], a sign of alkyl sulphate decomposition. Biocides may be used to prevent microbial attack of the polysaccharide chains and other components. These are typically meant to be broad spectrum, “in-can” preservatives for the stored foam concentrate, but provide no protection once diluted, so biodegradation processes would occur uninhibited.

We digress for a moment to consider the proportioning water sources and the rationale for the use of some particular salts in the formulation. In an emergency, water to dilute the foam concentrate and create the foam solution is drawn from any convenient, available source – a municipal water supply, a fresh water river or lake, brackish water, or even seawater. Therefore, the water type to be used is unpredictable and foam products have to be formulated with this in mind. A robust and reliable foam must perform comparably well when composed of water from any reasonable source.

Seawater – which often degrades the performance of AR-AFFF foams but enhances the performance of AFFFs – has the following approximate salt composition [78]:

Representative salt	%
NaCl	58.5
MgCl <sub>2</sub> ·6H <sub>2</sub> O	26.4
Na <sub>2</sub> SO <sub>4</sub>	9.8
CaCl <sub>2</sub>	2.8
KCl	1.6
NaHCO <sub>3</sub>	0.5
KBr	0.2
H <sub>3</sub> BO <sub>3</sub>	0.1
SrCl <sub>2</sub> ·6H <sub>2</sub> O	0.1
NaF	0.01

It is thought that multivalent cations interact with and bind to the carboxylate groups of the polysaccharide gum in AR-AFFFs [76]. As the salt concentration increases, the multivalent cations may ionically cross-link the gum, detrimentally reducing its solubility and bulk viscoelastic property. The drain time is shortened in such cases. Alternatively, in an AFFF, where no gum is used, the beneficial effect of Mg<sup>2+</sup> and Ca<sup>2+</sup> may be to shield the alkyl sulfate groups at the air–water interface, allowing better packing and possibly greater foam stability via an enhanced surface viscosity or viscoelasticity.

Salts are used in a foam formulation to level performance between the various possible proportioning water types and to impart some of the preferential benefits of seawater. MgSO<sub>4</sub> is added to most AFFFs and AR-AFFFs to improve performance in fresh water. In pure water MgSO<sub>4</sub> lowers the surface tension significantly more than NaCl (for example) on an equimolar basis, indicating lattice disruption as the mechanism, as opposed to surface activity. (Chloride salts are generally avoided in foams due to corrosion issues.) Whether originally chosen by experimentation or design, MgSO<sub>4</sub> has curious hydration properties. Water forms a tetrahedral lattice, even as a liquid [79]. To solvate an ion, the lattice must conform to the ionic species by forming a solvation shell around it. Small, multivalent ions, such as Mg<sup>2+</sup> and SO<sub>4</sub><sup>2-</sup>, are strongly hydrated. It has been shown that this cation/anion pair, in particular, forms a semirigid hydration sphere with high hydration numbers (i.e., the number of water molecules tightly bonded to the ion) [80]. Mg<sup>2+</sup> and SO<sub>4</sub><sup>2-</sup> act cooperatively and are solvated by a greater number of water molecules than predicted from analogous Mg<sup>2+</sup> or SO<sub>4</sub><sup>2-</sup> salts used separately. (Surfactants, solvents, and other salts in a foam formulation certainly complicate this simple situation.) Although MgSO<sub>4</sub> levels in a typical foam solution are not sufficiently high to immobilize a very large proportion of water molecules, it is likely that the effect of this hydration mechanism around the sulfate-containing surfactants in the very thin bubble films of the foam increases the surface viscosity enough to stabilize the foam structure to a significant degree [39, 81, 82].

### 17.5.2 Example Recipes

Understandably, foam manufacturers keep most of their formulation details as trade secrets, so the patent literature is one of the few sources for detailed recipe information. A few example formulations are given, with some redundancy, to illustrate the range of formulation variability.

**Table 17.8** Example Class A foam concentrate.

Ingredient	Purpose	Percentage
AOS	Foamer	32.3 (100% actives basis)
C12-14 alcohol	Stabilizer	5.0
Hexylene glycol	Solvent	26.0
Water	Solvent	35.6
Inert	—	1.1

Source: adapted from ref. [83].

**Table 17.9** Example 3% AFFF foam concentrate for Class B non-polar fuels.

Ingredient	Purpose	Percentage
Water	Solvent	60.0
Corrosion inhibitor	Corrosion inhibitor	0.1
Chemguard FS-157	Film former	5.8
APG	Foamer	17.5
Buffer	Buffer	0.1
Diethylene glycol monobutyl ether	Solvent	8.7
Ethylene glycol	Solvent	5.8
Urea	Stabilizer	2.0

Source: adapted from Ref. [60].

**Table 17.10** Alternate example 3% AFFF foam concentrate for Class B non-polar fuels.

Ingredient	Purpose	Percentage
Water	Solvent	74.9
Chemguard	Film former, foam stabilizer	6.0
F-102R*	stabilizer	
NOS	Foamer	2.0
LIDP	Foamer	5.0
Diethylene glycol	Solvent	12.1

Source: adapted from ref. [84].

## 17.6 Testing

Testing is an essential component of foam formulation and quality control efforts. A fire-fighting foam must perform as specified and maintain its performance characteristics throughout its shelf life—failure is not a matter of inconvenience. NFPA guidelines [85] state that a stored foam concentrate should be tested annually to insure performance. This

**Table 17.11** Example 3% AR-AFFF foam concentrate for Class B polar and non-polar fuels.

Ingredient	Purpose	Percentage
Water	Solvent	78.8
Chemguard FS-157	Film former	4.7
APG	Foamer	4.3
NADS	Foamer	8.2
EDTA	Stabilizer	0.1
Preservative	Preservative	0.1
Diethylene glycol monobutyl ether	Solvent	3.3
Xanthan gum	Thickener, membrane former	0.5

Source: adapted from ref. [60].

**Table 17.12** Example 6% AR-AFFF foam concentrate for Class B polar and non-polar fuels.

Ingredient	Purpose	Percentage
Water	Solvent	71.8
Chemguard F-102R*	Film former, foam stabilizer	6.0
Chemguard FS-157	Film former	2.0
NOS	Foamer	2.0
LIDP	Foamer	5.0
Xanthan gum	Thickener, membrane former	1.1
Diethylene glycol	Solvent	12.1

\*A proprietary blend of fluorosurfactants.

Source: adapted from Ref. 84.

section summarizes some of the more common laboratory and standardized fire tests conducted during various stages of product development and production.

### 17.6.1 Lab Test Methods

#### 17.6.1.1 Expansion and Quarter Drain Time

These two tests, the results of which are often referred to collectively as “foam quality,” are the most critical for a fire-fighting foam. Expansion and drain time values are correlated to an extent, with low-expansion foams giving low drain times, and vice versa. The selection of the foam generating device and the operating conditions determine the ultimate foam quality.

In the lab, foam is made by surrogate or representative foam-generating devices [52]. A waring blender is often used. These are very-high-shear devices that limit the amount of air entrained into the vortex once the initial foam is formed. Therefore, the foam has a limited expansion but long drain times. The advantage is that small foam concentrate sample sizes are used, on the order of 4–5 g. When used with AR-AFFFs, the resulting foam is usually unhomogeneous, however. Preferably a positive displacement pump is used to feed a standard fire test nozzle at the optimum pressure. This produces foam most representative of the foam used in fire testing; however, larger concentrate samples are required, approximately 30–60 g.

Low shear conditions, such as with sprinklers, can be mimicked by the use of a bottle shake test. The same small volume of foam solution used in the blender test is added to a 1 liter bottle, which is then shaken by hand a set number of times. The shaking intensity and duration have an effect on the foam quality, however. Foaming hand soap dispensers are particularly convenient as an alternate lab foam generating device.

In all cases, a foam solution of volume  $V_s$  is prepared with the proper proportioning ratio, and then the finished foam is produced. The finished foam is immediately placed in a tarred, 1 liter graduated cylinder. The foam volume  $V_f$  is noted and a timer is started. The expansion ratio is  $V_f/V_s$ . Liquid is observed to drain from the bottom of the foam. When the drained liquid volume equals  $V_s/4$ , the time is recorded as the quarter drain time (min:sec). Half drain time,  $V_s/2$ , is sometimes reported. AR-AFFFs generally expand less than AFFFs under equivalent conditions and have significantly longer drain times.

#### 17.6.1.2 pH

The correct pH is needed for product stability and performance. Generally, the pH of a foam concentrate is near neutral or slightly basic. If it is significantly different from this range, corrosion or product degradation problems due to hydrolysis or phase separation may occur.

#### 17.6.1.3 Specific Gravity (SG)

SG (unitless), or density (g/ml), is used to judge the concentration of the active ingredients in a foam concentrate. Components with heteroatoms (those other than carbon and hydrogen, e.g., oxygen, sulfur, nitrogen, etc.) increase the specific gravity substantially. Fluorosurfactants are high-density substances and contribute significantly to the specific gravity, more so than hydrocarbon surfactants, all things being equal.

#### 17.6.1.4 Refractive Index (RI)

RI (unitless) is a measure of the polarizability of a medium and is likewise an indication of the strength of the actives of a foam concentrate or solution. Aqueous solvents and surfactants raise the RI of the solution with increasing concentration.

#### 17.6.1.5 Brookfield Viscosity

Viscosity (cP) measurements are most informative for AR-AFFF concentrates, which contain significant amounts of polysaccharide. The amount of polysaccharide, coupled with

the degree of hydration, is measured by viscometry, usually using a Brookfield instrument (giving not a true viscosity but an apparent value). Measurement parameters, such as temperature, spindle type, and rotation speed, affect the measurement result, so it is advisable to know these variables when comparing viscosity values. Viscosities for typical AR-AFFF foam concentrates are observed to be in the 1000–5000 cP range.

#### 17.6.1.6 Film Formation

This is a simple, direct measure of an AFFF foam solution's ability to spread on a non-polar hydrocarbon and form a vapor-resistant film. Drops of a foam solution are gently placed on top of a hydrocarbon, such as cyclohexane or toluene, and allowed to spread into a thin film, despite its higher density. A small flame is carefully passed above the liquid. If there is no ignition, then a suitable barrier film has formed (pass/fail).

#### 17.6.1.7 Surface Tension (ST), Interfacial Tension (IFT), Spreading Coefficient (SC), and Critical Micelle Concentration (CMC)

These values may be measured by a number of techniques, the most common of which is by use of a Wilhelmy plate [31, 36, 48]. Other methods include pendant drop and maximum bubble pressure. The Wilhelmy plate method uses a platinum probe with specific dimensions placed at the surface of the test liquid or at the interface of the two liquid phases. Test specifics:

- Under the proper conditions, ST or IFT (both in dyn/cm) is simply  $F/P$ , where  $F$  is the net force exerted on the probe in contact with the meniscus and  $P$  is the wetted perimeter of the probe.
- $SC$  is readily obtained from eqn (17.1).
- The CMC can be determined from the inflection point in the plot of surface tension against the logarithm of the surfactant concentration (Fig. 17.21).

#### 17.6.1.8 Proportioning Rate

The proportioning rate, or dilution ratio of a concentrate used to make a foam solution, can be determined by use of RI or conductivity measurements. Lab standards are made, using the same foam concentrate and water source as the sample, that bracket the desired or suspected proportioning rate. A linear calibration plot is made with the measurement values versus the concentration of the standards. The unknown foam solution is measured and the linear regression curve from the calibration plot is used to determine the unknown concentration. Proportioning using seawater is problematic for conductivity measurements, since adding the foam solution may actually lower the reading, producing a plot with a negative slope.

#### 17.6.1.9 Deluge-resistance Time

This lab test mimics the water deluge on a foam blanket during a sprinkler system test (see Section 17.6.2). Foam is placed on a thin layer of heptane in a tarred container and allowed to sit for 5 min. A light spray of water at constant pressure is applied to the foam blanket. The point at which holes open in the foam blanket is noted as the deluge time (min:sec) (see Fig. 17.23). The amount of water captured is determined by weight to insure consistency of the application rate.

#### *17.6.1.10 Degree of Surfactant Retention in Foam*

This is an approximate measure of the amount of a fluorosurfactant retained in a foam as it drains, a rather indirect measure and only useful for relative comparisons. The surface tension of a foam solution with and without the subject fluorosurfactant is measured. The difference is the range of the measurement. A foam quality test is run on the foam solution containing the fluorosurfactant. The surface tension of the drained foam solution at the quarter drain time is compared to the range set previously. If the surface tension of the drained solution equals that of the base case without fluorosurfactant, no fluorosurfactant is presumed to have drained out and the retention of fluorosurfactant within the foam structure is approximately 100%. If the drained solution surface tension is equal to the fluorosurfactant-containing foam solution, then almost all the fluorosurfactant has drained out and the retention is approximately 0%. Individual sample results then fall in between. This test requires the fluorosurfactant be studied near or just below its CMC.

#### *17.6.1.11 Drave's Wetting Rate*

According to the US Department of Agriculture Forest Service [17], a qualified Class A foam tested at 1% proportioning must have a wetting time of 20 seconds or less, among other requirements. This property is most readily measured using a skein test, in which an elongated bundle of cotton yarn, weighted on one end, is placed vertically into a cylinder of the foam solution. The skein is initially buoyant due to entrapped air bubbles within the fibers. As the solution penetrates the yarn, the bubbles are displaced; when the effective density of the bundle exceeds the solution density, the skein sinks. The time it takes to reach this saturation point, akin to the Class A foam wetting a porous substrate, is referred to as the wetting time.

### **17.6.2 Fire Test Standards**

Buyers of fire-fighting foams do not simply rely on manufacturers' claims of performance. Foams are subjected to a multitude of fire test standards, which attempt to model real world fire situations. Foams that pass the various tests, performed or witnessed by a third party, are referred to as being "listed" or "approved" by the respective standard-publishing agencies.

The UL test standard for Class B foams is summarized below. Other fire test standards include US Military Specification [86], Coast Guard [85], EN1568 [87, 88], ICAO [89], and LASTFIRE [90]. For complete details, refer to specific test standard specifications.

#### *17.6.2.1 UL 162 Fire Tests*

The UL 162 fire test standard encompasses three general application types [23, 52]:

- Sprinkler systems, used for both polar and non-polar fuels.
- Indirect application ("Type II"), for polar fuels, with the stream of foam directed at a wall and allowed to fall onto the fuel.
- Direct application ("Type III"), for non-polar fuels, with the stream of foam directed at the fuel surface.

All UL 162 fire tests use a 50 square foot test pan containing about 50–60 gallons of fuel, depending on the application type. The fuel temperature has to be above 50 °F. Heptane is used as a representative non-polar fuel, and isopropyl alcohol as a representative polar fuel. Other fuel types can be substituted and tested. The foam solution application rate ranges from 0.04 to 0.10 gallons/minute/square foot, depending on the application type. For designing equipment and actual foam use, a scale up factor (1.6–2.7 times) is included in the application rate to insure reliability by addressing any shortcomings of the particular test method and any non-idealities of the actual application.

Once the pan is set up and filled with fuel, it is ignited and allowed to “preburn” – 15 s for sprinkler tests and 1 min for indirect and direct tests – to heat the metal pan and fuel. The foam is applied for 3 or 5 min, depending on the application type. The fire must be extinguished within this application period to pass. Afterward, a torch is passed over the foam blanket one or more times during a waiting period to check for vapor release. To perform the burnback part of the test, a sleeve (or “stovepipe”) is inserted vertically into the foam blanket and the foam is removed from the inside, exposing the fuel. The fuel is ignited at a set time and allowed to burn for 1 min. The sleeve is then removed and the ability of the foam to contain the fire is observed. If the flame is contained within 10 square feet, the burnback test is passed. A quality AFFF product will reseal the exposed fuel and self-extinguish during the burnback test.

## 17.7 The Future

As with household cleaning and personal care products, developers of fire-fighting foams are constantly looking for alternatives that further reduce the products’ environmental footprint while continuing to meet the various performance demands. By any reasonable measure, the availability and use of fire-fighting foams certainly passes all cost–benefit analyses.

AFFFs, in particular, cannot be made without fluorosurfactants. Fluorosurfactants are unique members of the surfactant family that cannot be replaced without substantial performance loss [9]. Historically, fluorosurfactants with C8 chain lengths have been preferred due to their favorable cost–performance properties. Chief among them, perfluorooctanyl sulfonate (PFOS) and perfluorooctanoic acid (PFOA) salts were made by the electrochemical fluorination process. These have been scrutinized because the very stable C–F bond prevents biodegradation. However, today’s AFFFs are not made with PFOS or PFOA ingredients as in the past.

Modern fluorosurfactants used in today’s AFFFs are made by the much cleaner telomerization process and cannot degrade to PFOS [91, 92]. Furthermore, C6 fluorosurfactants obviously cannot degrade to either PFOS or PFOA, which is the basis for the current trend to convert all AFFFs to include only “short chain” fluorosurfactants [93]. Perfluorohexanoic acid (PFHA), the *presumed* ultimate degradation product of C6 fluorosurfactants, has a favorable toxicity profile, and perfluorohexylethylsulfonate, the *likely* degradation product of many fluorosurfactants, has a low bioaccumulation rate [92]. Making use of C6 perfluoroalkyl-based chemistry for all AFFF fluorosurfactants is a challenge, but not an insurmountable one. Experience, creativity, and a thorough understanding of the principles of chemistry and physics will lead to sustainable and responsible solutions to further improve fire-fighting foams.

## Acknowledgements

The author wishes to thank Mr Randy Hendrickson and Dr Kirtland Clark for their thoughtful conversations and advice on this subject; Mr Dan Edson and Dr Ming Li for their thorough reviews of the manuscript; and Ms Norma Vargas and Mr Bryan Mortenson for their data contributions. Support from Chemguard, Inc., is gratefully acknowledged.

## References

- [1] J.L. Bryan. *Fire Suppression and Detection Systems*, 2nd edn. Macmillan, New York, 1982.
- [2] R. Karthikeyan, S. Balaji and P.K. Sehgal. Industrial applications of keratins: a review. *J. Sci. Ind. Res.*, **66**: 710–15, 2007.
- [3] K.P. Clark, M. Jacobson and C.H. Jho. Compositions for polar solvent fire fighting containing perfluoroalkyl terminated co-oligomer concentrates and polysaccharides. US patent 5,218,021, June 8, 1993.
- [4] L.R. DiMaio and P.J. Chiesa. Foam concentrate. US patent 5,225,095, July 6, 1993.
- [5] J.A. Dean (ed.), *Lange's Handbook of Chemistry*, 14th edn. McGraw-Hill, New York, 1992.
- [6] R.C. Weast, *CRC Handbook of Chemistry and Physics*, 70th edn. CRC Press, Boca Raton, FL, 1989.
- [7] Sigma-Aldrich Co., <http://www.sigmaaldrich.com> (accessed June 11, 2010).
- [8] UL Online Certifications Directory, <http://database.ul.com> (accessed July 6, 2010).
- [9] R.L. Darwin. *Estimated Quantities of Aqueous Film Forming Foam (AFFF) in the United States*. Hughes Associates, Inc., August 2004.
- [10] *Perfluorinated Substances and Their Uses in Sweden*. Swedish Chemicals Agency, Stockholm, November 2006.
- [11] Chemguard internal data compiled by Twana Connors, Elena Lamperti, Tammy Koberlein.
- [12] T. Briggs. Foams for firefighting. in *Foams: Theory, Measurements, and Applications*, R.K. Prud'homme and S.A. Khan (eds). Surfactant Science Series 57, Marcel Dekker, New York, 1996.
- [13] H.W. Fox and W.A. Zisman. The spreading of liquids on low energy surfaces. I. polytetrafluoroethylene. *J. Coll. Sci.*, **5**: 514, 1950.
- [14] ASTM Method Standard Test Method for Wetting Tension of Polyethylene and Polypropylene Films, D2578-09.
- [15] D.J. Gardner, N.C. Generalla, D.W. Gunnells and M.P. Wolcott. Dynamic wettability of wood. *Langmuir*, **7**: 2498, 1991.
- [16] D.J. Gardner. Application of the Lifshitz-van Der Waals acid-base approach to determine wood surface tension components. *Wood and Fiber Science*, **28**: 422–8, 1996.
- [17] US Department of Agriculture Forest Service. Specification 5100-307a, Specification for Fire Suppressant Foam for Wildland Firefighting (Class A Foam). June 1, 2007.
- [18] NFPA 18: Standard on Wetting Agents, 2006.
- [19] ASTM Method Standard Test Method for Evaluation of Wetting Agents by the Skein Test, D2281-68, 2005.
- [20] R.K. Prud'homme and S.A. Khan. Experimental results on foam rheology. In *Foams: Theory, Measurements, and Applications*, R.K. Prud'homme and S.A. Khan (eds). Surfactant Science Series 57, Marcel Dekker, New York, 1996.
- [21] J.G. Bureaux, G. Cowan, E.N. Cundasamy and J.G. Purdon. Foam formulations. US patent 6,553,887, April 29, 2003.
- [22] G. Garcia and P. Durual. Alcohol resistant film-forming fluoroprotein foam concentrates. US patent 5,824,238, October 20, 1998.
- [23] *UL 162: Standard for Foam Equipment and Liquid Concentrates*, 7th edn. Underwriters Laboratories Inc., 1999.

- [24] W.D. Harkins and A. Feldman. Films: the spreading of liquids and the spreading coefficient. *J. Am. Chem.*, **44**: 2665, 1992.
- [25] P. deGennes, F. Brochard-Wyart and D. Quéré. *Capillarity and Wetting Phenomena: Drops, Bubbles, Pearls, Waves*. Springer, New York, 2004.
- [26] S. Ross and I.D. Morrison. *Colloidal Systems and Interfaces*. Wiley Interscience, New York, 1988.
- [27] H. Mollet and A. Grubenmann. *Formulation Technology: Emulsions, Suspensions, Solid Forms*. Wiley-VCH, Weinheim, 2001.
- [28] A. Britan, M. Liverts, G. Ben-Dor, S.A. Koehler and N. Bennani. The effect of fine particles on the drainage and coarsening of foam. *Coll. Surfaces A: Physicochem. Eng. Aspects*, **344**: 15–23, 2009.
- [29] A.K. Vikingstad, A. Skauge, H. Høiland and M. Aarra. *Coll. Surfaces A: Physicochem. Eng. Aspects*, **260**: 189–98, 2005.
- [30] M. Pabon and J.M. Corpant. Fluorinated surfactants: synthesis, properties, effluent treatment. *J. Fluor. Chem.*, **114**: 149, 2002.
- [31] L.L. Schramm. *Emulsions, Foams and Suspensions*. Wiley-VCH, Weinheim, 2005.
- [32] R.J. Farn. *Chemistry and Technology of Surfactants*. Blackwell Publishing, Oxford, 2006.
- [33] R.A. Falk. Aqueous wetting and film forming compositions. US patent 4,042,522, August 16, 1977.
- [34] M.J. Rosen, A.W. Cohen, M. Dahanayake and X. Hua. Relationship of structure to properties in surfactants. 10. Surface and thermodynamic properties of 2-dodecyloxypoly(ethenoxyethanol)s,  $C_{12}H_{25}(OC_2H_4)_xOH$ , in aqueous solution. *J. Phys. Chem.*, **86**: 541, 1982.
- [35] J.S. Leal, J.J. González, F. Comelles, E. Campos and T. Ciganda. Biodegradability and toxicity of anionic surfactants. *Acta Hydrochim. Hydrobiol.*, **19**: 703, 1991.
- [36] T.F. Tadros. *Applied Surfactants*. Wiley-VCH, Weinheim, 2005.
- [37] T. Hargreaves. *Chemical Formulation: An Overview of Surfactant-based Preparations Used in Everyday Life*. RSC, London, 2003.
- [38] S.E. Webber, P. Munk and Z. Tuzar. Solvents and self-organization of polymers. *Ser. E: Appl. Sci.*, **327**: 1996, 4, 20, 31, 96, 314, 332, 376.
- [39] S. Pandey, R.P. Bagwe and D.O. Shah. Effect of counterions on surface and foaming properties of dodecyl sulfate. *J. Coll. Interface Sci.*, **267**: 160, 2003.
- [40] D.L. Schmidt. Nonaqueous foams. In *Foams: Theory, Measurements, and Applications*, R.K. Prud'homme and S.A. Khan (eds). Surfactant Science Series 57, Marcel Dekker, New York, 1996.
- [41] M. Abu-Hamdiyah and I.A. Rahman. Distribution coefficients of nonpolar additives and factors determining the solubilization tendency as a function of surfactant chain length in aqueous solutions of sodium alkyl sulfates. *J. Phys. Chem.*, **91**: 1530, 1987.
- [42] D. Myers. *Surfactant Science and Technology*, 3rd edn. John Wiley & Sons, New York, 2006.
- [43] K.R. Lange. *Surfactants: A Practical Handbook*. Carl Hanser Verlag, Munich, 1999.
- [44] K. Holmberg, B. Jönsson, B. Kronberg and B. Lindman. *Surfactants and Polymers in Aqueous Solution*, 2nd edn. John Wiley & Sons, Chichester, 2003.
- [45] Kratchevsky et al. Thin liquid film physics. In *Foams: Theory, Measurements, and Applications*, R.K. Prud'homme and S.A. Khan (eds). Surfactant Science Series 57, Marcel Dekker, New York, 1996.
- [46] S. Thach, K.C. Miller and K.S. Schultz. High-stability foams for long-term suppression of hydrocarbon vapors. US patent 5,434,192, July 18, 1995.
- [47] R.A. Falk. Perfluoralkyl anion/perfluoroalkyl cation ion pair complexes. US patent 4,420,434, December 13, 1983.
- [48] E. Kiss. *Fluorinated Surfactants and Repellents*, 2nd edn. Surfactant Science Series 97, Marcel Dekker, New York, 2001.
- [49] J. Jennings, T. Deisenroth and M. Haniff. Poly-perfluoroalkyl substituted polyamines as grease proofing agents for paper and foam stabilizers in aqueous fire-fighting foams. US patent 6,156,222, December 5, 2000.
- [50] J. Jennings, T. Deisenroth and M. Haniff. Poly-perfluoroalkyl substituted polyamines as grease proofing agents for paper and foam stabilizers in aqueous fire-fighting foams. US patent 6,365,676, April 2, 2002.

- [51] J. Jennings. Perfluoroalkyl-substituted amino acid oligomers or polymers and their use as foam stabilizers in aqueous fire-fighting-foam agents and as oil repellent paper and textile finishes. US patent 6,436,306, August 20, 2002.
- [52] K.P. Clark. Fire extinguishing or retarding material. US patent 7,011,763, March 14, 2006.
- [53] K.P. Clark. Fluorochemical foam stabilizers and film formers. US patent 5,750,043, May 12, 1998.
- [54] K.P. Clark and E.K. Kleiner. Synergistic surfactant compositions and fire fighting concentrates thereof. US patent 5,616,273, April 1, 1997.
- [55] S.A. Koehler, S. Hilgenfeldt, E.R. Weeks and H.A. Stone. Drainage of single Plateau borders: direct observation of rigid and mobile interfaces. *Phys. Rev. E*, **66**: 040604, 2002.
- [56] G. Narsimhan and E. Ruckenstein. Structure, drainage, and coalescence of foams and concentrated emulsions. In *Foams: Theory, Measurements, and Applications*, R.K. Prud'Homme and S.A. Khan (eds). Surfactant Science Series 57, Marcel Dekker, New York, 1996.
- [57] E.K. Kleiner, T.W. Cooke and R.A. Falk. Protein hydrolyzate compositions for fire fighting containing perfluoroalkyl sulfide terminated oligomers. US patent 4,460,480, July 17, 1984.
- [58] C.H. Jho, Y. Loh and K.F. Mueller. Low viscosity polar-solvent fire-fighting foam compositions. US patent 5,496,475, March 5, 1996.
- [59] S.W. Hansen. Aqueous foaming fire extinguishing composition. US patent 6,231,778, May 15, 2001.
- [60] E.C. Norman and A.C. Regina. Alcohol resistant aqueous film forming firefighting foam. US patent 5,207,932, May 4, 1993.
- [61] R. Bertocchio, L. Foulletier and A. Lantz. Perfluoroalkylamine oxides and use of these products in fire extinguishing compositions. US patent 4,983,769, January 8, 1991.
- [62] D.J. Mulligan. Fire-fighting compositions. US patent 4,424,133, January 3, 1984.
- [63] L.B. Smolka and A. Belmonte. Charge screening effects on filament dynamics in xanthan gum solutions. *J. Non-Newtonian Fluid Mech.*, **137**: 103, 2006.
- [64] K.P. Clark and R.A. Falk. Polysaccharide/perfluoroalkyl complexes. US patent 4,859,349, August 22, 1989.
- [65] H. Achtmann. Biodegradable foam compositions for extinguishing fires. US patent 5,882,541, March 16, 1999.
- [66] S. Szönyi and A. Cambon. Influence of water-soluble polymers/new fluorochemical surfactants interaction according to extinguishing efficiency of multipurpose foam compounds. *Fire Safety J.*, **16**: 363, 1990.
- [67] S. Szönyi, F. Szönyi, I. Szönyi and A. Cambon. Modification of water-soluble polymers constituting multipurpose fire-fighting foams by new reactive fluorinated surfactants. *Progr. Colloid Polym. Sci.*, **81**: 136, 1990.
- [68] A. Polidori, M. Presset, F. Lebaupain, B. Ameduri, J. Popot, C. Breyton and B. Pucci. Fluorinated and hemifluorinated surfactants derived from maltose: synthesis and application to handling membrane proteins in aqueous solution. *Bioorganic Medicinal Chem. Lett.*, **16**: 5827, 2006.
- [69] G. Bai, C. Gonçalves, F.M. Gama and M. Bastos. Self-aggregation of hydrophobically modified dextrin and their interaction with surfactant. *Thermochim. Acta*, **467**: 54, 2008.
- [70] C. Gonçalves, J.A. Martins and F.M. Gama. Self-assembled nanoparticles of dextrin substituted with hexadecanethiol. *Biomacromolecules*, **8**: 392, 2007.
- [71] W.H. Daly and A.A. Bahamdan. Hydrophobic polysaccharide derivatives. US patent application 20080281000, November 13, 2008.
- [72] D.J. Boonstra and F. Berkhout. Preparation of redispersible hydrophobic starch derivatives. US patent 3,891,624, June 24, 1975.
- [73] P.L. Buwalda, R.P.W. Kesselmans, A.A.M. Maas and H.H. Simonides. Hydrophobic starch derivatives. US patent 7,157,573, January 2, 2007.
- [74] W. Maliczsyzn, J.G. Atkinson and M. Tolchinsky. Method for preparing hydrophobic starch derivatives. US patent 6,037,466, March 14, 2000.
- [75] I. Piirma. *Polymeric Surfactants*. Surfactant Science Series 42, Marcel Dekker, New York, 1992.
- [76] P.J. Chiesa and E.C. Norman. Preparing fire-fighting concentrates. US patent 4,464,267, August 7, 1984.

- [77] R.S. Sheinson and B.A. Williams. Preserving shipboard AFFF fire protection system performance while preventing hydrogen sulfide formation. *Fire Technol.*, **44**: 283–95, 2008.
- [78] ASTM Method Standard Practice for the Preparation of Substitute Ocean Water, D1141-98, 2008.
- [79] K.A. Dill and S. Bromberg. *Molecular Driving Forces: Statistical Thermodynamics in Chemistry and Biology*. Garland Science, New York, 2003.
- [80] K.J. Tielrooij, N. Garcia-Araez and H.J. Bakker. Cooperativity in ion hydration. *Science*, **328**: 1006, 2010.
- [81] T. Hargreaves. *Chemical Formulation: An Overview of Surfactant-Based Preparations Used in Everyday Life*. RSC, London, 2003.
- [82] A.K. Chattopadhyay, L. Ghaïcha, S.G. Oh and D.O. Shah. Salt effects on monolayers and their contribution to surface viscosity. *J. Phys. Chem.*, **96**: 6509, 1992.
- [83] J.A. Bronner and R.K. Ostroff. Concentrated composition for forming an aqueous foam. US patent 4,849,117, July 18, 1989.
- [84] M.J. Hubert, S.A. Barker and D.N. Valley. Dye colored fire fighting foam concentrate. US patent application 20030001129, January 2, 2003.
- [85] NFPA 11: Standard for Low-, Medium-, and High-Expansion Foam. National Fire Protection Association, 2005.
- [86] Military Specification Fire Extinguishing Agent, Aqueous Film-Forming Foam (AFFF) Liquid Concentrate, for Fresh and Seawater, MIL-F-24385F, 1989.
- [87] BS EN 1568-3:2008. Fire extinguishing media. Foam concentrates. Specification for low expansion foam concentrates for surface application to water-immiscible liquids, 2008.
- [88] BS EN 1568-4:2008. Fire extinguishing media. Foam concentrates. Specification for low expansion foam concentrates for surface application to water-miscible liquids, 2008.
- [89] International Civil Aviation Organization Airport Services Manual: Part 7: Airport Emergency Planning, 2nd edn. ICAO 9137-AN/898, 1991.
- [90] LASTFIRE, <http://www.lastfire.co.uk> (accessed 8/05/2010).
- [91] J.L. Scheffey and C.P. Hanauska. *Status Report on Environmental Concerns Related to Aqueous Film Forming Foam (AFFF)*. Hughes Associates, Inc., 2002.
- [92] T. Cortina and S. Korzeniowski. AFFF industry in position to exceed environmental goals. *Asia Pacific Fire*, July, 2008.
- [93] EPA 2010/2015 PFOA Stewardship Program, <http://www.epa.gov/oppt/pfoa/pubs/stewardship/index.html> (accessed 7/07/2010).

# 18

## Foams in Consumer Products

*Peter J. Martin*

### 18.1 Introduction

Consumer products are defined as manufactured goods sold in large quantities, at low cost and which are typically used by the consumer soon after purchase. The rapid speed of use and repurchase also leads to their alternative name, fast moving consumer goods. They make up a very wide category of products, but their purchase and use characteristics give them important characteristics in common. This chapter details the significance of aerated structures and foams in consumer products and explores the interaction of formulation, processing and foam structure from creation to use.

#### 18.1.1 Foams and Consumer Appeal

First and foremost, foams contribute to consumer appeal across the broad range of the consumer products market. Foam's contribution to the technical performance of a product is important, but secondary to the need to please the user. The market is often divided up into household care, personal care, food and drink products. The product photographs reproduced in Fig. 18.1 illustrate the immediate sensory role foams can play in each of these categories. Competition is fierce in the consumer produce marketplace so consumers are likely to quickly switch product if they are unsatisfied with its performance. Manufacturers try to counter this by building brand awareness and loyalty in customers, but ultimately a product must meet or exceed expectations every time it is used at the right price [1].

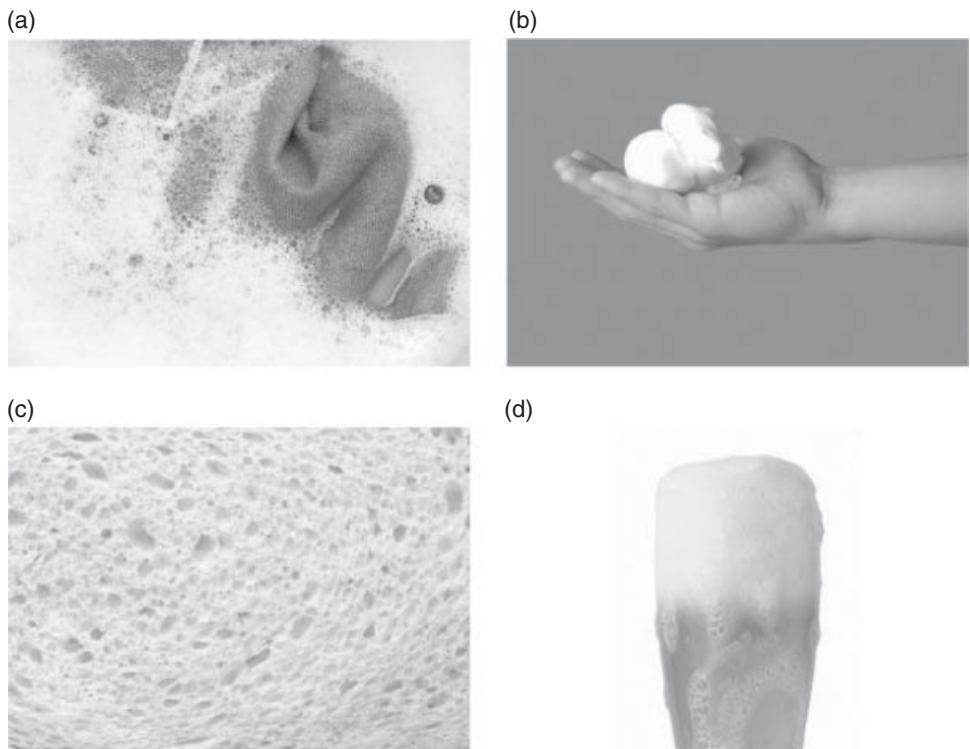


**Fig. 18.1** Examples of consumer product with significant foam contributions. (a) Laundry detergent, (b) shaving foam, (c) bread crumb, (d) lager. Reproduced with permission from © iStockPhoto.com.

Foams stimulate and intrigue the senses; the scientist's curiosity of foams is only one branch of humans' fascination with them. The hero of Tennyson's *Maud* [2] captures this from a poet's perspective.

What are the physical laws according to which water becomes foam, and foam falls along the back of a wave – that is one question; and what impression does this condition of things produce upon a mind that observes closely, and feels with exquisite delicacy of sense the beauty of the movement of the foam, and its subtle relation to other material things, as well as to certain analogues in the sphere of spirit, to function and states of the human spirit – this is a totally different question. I submit that the office of the poet in this connection is to answer the latter question, and that of the scientific man to answer the former.

However, it might be said that commerce's perpetual appetite for year-on-year growth has pushed the scientist into the depths of the question, 'what is the beauty of movement of foam?' Of course, this is then followed with, 'how can it be quantified?' and then, 'how can it be recreated, but more cheaply?'

Food and drink foams have enjoyed a renaissance of interest in the past decade. A new generation of chefs, often associated with the molecular gastronomy technique, have used foams to help create new signature dishes worldwide, from shellfish foams in Montreal [3] to clouds of goat's milk foam in Barcelona [4]. Moreover, the application of novel widget technology has helped canned beers and stouts to begin to match the reputation of their bar-pulled counterparts [5].

The reverse has been true in other areas. Laundry detergent foaming is an important product feature in regions of the world where hand-washing is common. On the one hand, the foam serves to illustrate the efficacy of the product to the user, and then the collapse of foam with increase in oil droplets in the mixture is taken as an indication that the solution is no longer suitable for washing. However, laundry and dish washing are becoming more automated across the world, and with this the user is distanced from the actual process. The visual impact of any foams created in the process has been diminished and excessive foaming can be a hindrance to smooth operation of the process [6].

### 18.1.2 Market Descriptions and Directions

In most industrialized countries the various consumer product markets are relatively mature and are dominated by a small number of very large companies. Unilever has twin headquarters in the United Kingdom and the Netherlands and tends to dominate the European food, personal care and fabric care markets. Proctor and Gamble is headquartered in the USA where it tends to be dominant in similar markets. Other leading companies include Nestlé, Kraft, Sara Lee, Coca-Cola, Kleenex and Pepsi. This leads to two general strategies for growth. A major opportunity is afforded by focusing on emerging Asia-Pacific-Africa markets where increased affluence is rapidly increasing the number of potential customers [7]. Second, growth is targeted through existing markets by increasing either market share or product margins, which may be achieved through novel functionality or, increasingly, perceived health benefits for the consumer.

Table 18.1 summarises some of the main foam product types found within each market sector. A brief description of the main market influences is given in each case. Foams offer manufacturers and marketers new ways of increasing margin or market share in large, but mature, markets. However, product and brand loyalty can be a barrier to rapid market change. Loyalty may lead consumers to be cautious of changes in products they have been familiar with for a long time, but also manufacturers may be cautious and not want to risk losing loyalty by making unwelcome changes to the formulation or properties of longstanding products. The large manufacturers that dominate this market typically aim to focus their efforts on only the top few brands within each market, so there can be limited room for flexibility or experimentation. In this context understanding the role of foams in the product and the way in which they are created is increasingly important since mistakes cannot be afforded when taking a new product to market.

Sustainability is a market driver affecting all of these products. In terms of food and drink, many people are concerned to have more sustainable lifestyles, which they associate with healthier living, less waste and greater use of 'natural' products. In home and personal care products people want to use products that are effective with less water, at lower temperatures, and that are formulated from more environmentally friendly ingredients.

**Table 18.1** The scope of foams within consumer product market sectors.

Sector	Products types	Market notes
Home care	Laundry detergent Dish washing detergent Cleaning fluid	The traditional association is that effective products will foam. Careful formulation has to be followed to create sufficient foam in application while not becoming unmanageable. Products must be suited to local market expectations and laundry practices.
Personal care	Shampoo Shaving gel/foam Hand wash Soap Bubble bath	Foams are traditionally associated with these projects because early functional ingredients, principally soap, had a foaming effect. The foam and efficacy of product have come to be associated with each other, although this is often not the case with today's formulations. Foam plays an important role in bulking out products. For example, the amount of surfactant required to wash hands or hair is typically significantly smaller than that used by the consumer. Dispensing the product in a foam can match the required amount with that used, while also putting it into a popular physical form. Foam yield stress also contributes to the attractiveness of this approach.
Food	Bread Cake Mouse Milk shake Ice cream Soufflé	Markets in industrialized countries tend to be mature. Margin can be gained by using foams to replace substitute gas for more expensive or less healthy ingredients and to create novel textures.
Drink	Beer and lager Cider Sparkling wine Carbonated soft drinks	Foams have long been an essential part of drinks. A key development has been to create the traditional foams associated with products in more mobile forms that can be consumed on the move or at home.

This may mean that the ingredients are derived from natural sources or involve less pollution during production. Alternatively, it may mean that the ingredients have a lower environmental impact when disposed of; for instance, they biodegrade readily by the time they exit municipal sewage treatment systems.

The regulatory framework is generally following these same trends, in both health and sustainability. There is an increasing requirement to publicize the health credentials on food and drinks and there are increasing restrictions on which chemical ingredients can be used in personal and homecare products. For example, the immediate context of the laundry market is the increasingly restrictive legislation on synthetically derived surfactants due to environmental concerns. The United States' Environmental Protection Agency announced plans in 2010 to introduce new regulations on alkoxylates, most widely used in the USA in detergents, on the basis of their identification as persistent, bioaccumulative

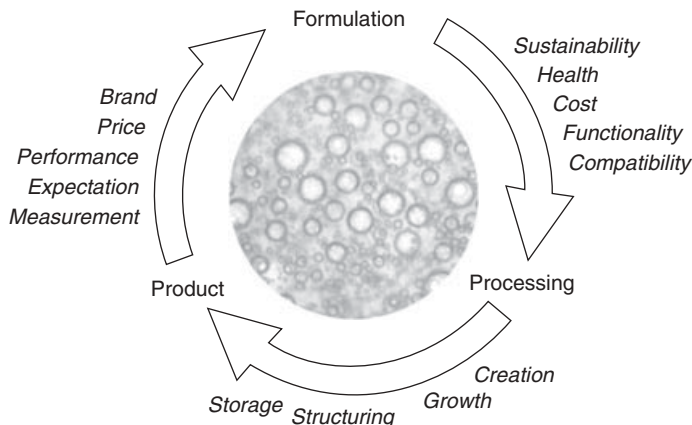


**Fig. 18.2** Locating consumer foam product form requirements in the total product design process.

and toxic chemicals [8]. In 2007 the annual surfactant demand for household detergents in the United States was 1.6 million tonnes and \$3.2 billion, which face a requirement for alternative surfactants with improved biodegradability and reduced toxicity [9].

### 18.1.3 The Scope of This Chapter

This chapter presents an overview of the creation, control and utilization of foams across the breadth of consumer products. Figure 18.2 illustrates the coupled factors that interconnect formulation, processing and product. Space is too limited to provide a detailed examination of each aspect of this broad topic. Instead, three sections follow the process engineering of the foam within typical products and all of these seek to link the inherent interaction between formulation and processing. First the creation processes are examined, then the resultant product structure is considered and finally both of these are appraised under the light of consumer sensory appeal. This structure affords the opportunity to draw out the similarities and differences between the product sectors and build on the fundamentals of foams detailed in previous chapters of this book.

## 18.2 Creation and Structure

A wide variety of foam production techniques are required across the range of consumer products. Requirements range from stable, monodisperse foams of micron-sized bubbles in beer heads to transitory bubbles of up to a centimetre in bubble baths or laundry detergents. The point of creation also varies, from on the production line to at the point of use. The range of foam creation requirements is illustrated in Table 18.2.

Despite this breadth, all methods of foam creation can be conceptualized as the creation and evolution of bubble structure. This section first explores the types of additives,

**Table 18.2** Bubble size and density in different products.

Products	Bubble diameter ( $\mu\text{m}$ )	Estimated number density ( $\text{cm}^{-3}$ )	Notes
Shaving foam	10–20	$10^8$	Aerosol generated with initial $\phi = 0.926$ [10].
Ice cream	15–40	$10^7$	For a 100% overrun ice cream $\phi = 0.5$ [11].
Microcellular starch foam	50–200	$10^6$	Continuous supercritical $\text{CO}_2$ fluid extrusion [12].
Bread	2500 area av. 600 number av.	$10^3$	Many small cells contribute to the foam, but visual appearance is dominated by the larger cohort of the population [13].
Hand dish washing-up detergent	3000	$10^2$	Shaking/tumbling/impinged jets, initial $\phi = 0.995$ [14].
Bubble bath	5000	$10^1$	Bubble size depends on generation method.

ingredients or constituents that are required to enable foam to be created from a liquid. Consideration is given to strategies that can be used to select the right sort of additives for a desired product performance. Following this, the phenomena and technologies exploited for bubble creation are presented. Bubble growth is then considered separately as a means of converting a bubbly liquid into foam. Application of the structures achieved once recognizable foam has been formed are considered and then, finally, the issue of how these desired structures can be maintained for sufficient lengths of time is addressed.

### 18.2.1 Surfactants and Their Application

Liquids that are absolutely pure generally do not foam, as any gas bubbles will immediately coalesce on contact or rupture at a surface. Rosen [15] provides a detailed overview of how surface active chemicals or particles must be added, which in various ways promote the stability of the interface, which forms when two bubbles ‘touch’ for long enough for the foam to be of practical use. As foams last longer they move from a *transient* (unstable) nature, which may be useful in certain applications, to a *persistent* (metastable) nature that is more commonly desired in consumer products.

In practice there are some exceptions to this rule for very viscous liquids. An example comes from nature where the bubbles nucleate and grow in magma due to gas release as pressure rapidly decreases, which can ultimately set as rocks such as pumice [16]. A similar process occurs during the steam or supercritical  $\text{CO}_2$ -based extrusion foaming production of starch snack foods where starch is melted and pressurized in an extruder, and experiences rapid pressure drop and water vaporization in the die exit [17]. While additives can enable foam creation, they may be insufficient to achieve the desired foam persistence. The extension of foam lifetime afforded by increased liquid phase viscosity offers significant opportunities

**Table 18.3** Foam stabilization strategies for different product sectors.

Products	Surfactant type	Bulk liquid	Drivers
Home care	Controllable	Generally dilute concentrations in use	Source is important: clean, white. More sustainable.
Personal care	Soft, gentle	Thick and smooth	Source is important: clean, white. More sustainable. Compatible with formulation. Product chemical and physical stability.
Food	Egg protein; milk protein (casein); fat droplets; hydrophobin	Xanthan gum; protein matrix	Regulated material. Consumer acceptance. More stability. Longevity of small bubbles. Oil foams.
Drink	Cereal proteins; milk proteins; fermentation products	Little scope for independent control	Foam control. Oil resistance for beer heads. Low stability for fizzy drinks.

to create products that would otherwise be unviable. Glycerol, polymers and xanthan gum are often used for this purpose. Solidification of the continuous phase takes this effect to the limit and is used in a variety of products, perhaps the most common being bread making.

Approaches to and mechanisms of foam stabilization are dealt with in other chapters in this book. However, the selection and mixture of surfactant, protein or particle used is influenced by a combination of the desired final product structure, the processing route used, chemistry and interaction with other ingredients, regulation, price and consumer perception. A summary of the key factors is presented in Table 18.3.

Surfactant characteristics as a foaming agent can be broken down into: effectiveness at reducing surface tension, diffusion characteristics, disjoining pressure properties in films, elastic properties given to films [18]. Generally, foaming characteristics increase with concentration up to the critical micelle concentration (CMC). The essential function of surfactants is to modify the gas liquid interface; they create surface elasticity, which tends to counter the thinning process that ultimately leads to film rupture. Foams composed of larger bubbles have greater Laplace drainage pressures and so drain more rapidly from their films. They also have larger Plateau border cross-sectional areas (for the same wetness of foam), so also drain more rapidly under gravity down these channels. Likewise, higher surface tension tends to increase film drainage forces, so stability is enhanced if smaller bubbles can be used, or surfactants that further reduce surface tension.

Diffusion through lamellae is another phenomenon that can reduce the useful life of a foam. The rate of diffusion is dependent on the pressure gradient, which is caused by differences in bubble sizes and topology, and the permeability of the lamella to the gas [19]. Increased permeability can be achieved by careful selection of liquid and gas phases, but also surfactant type. Those surfactants that pack tightly at the interface will tend to reduce the permeability, such as those with a higher number of carbon atoms in the hydrophobic group or with lower molecular mass of the hydrophilic group [15].

The net rate of foam achieved in any process must equate to the rate of production minus the rate of loss. The minimum power required to create foam is equal to the product of the surface tension and the rate of surface area creation. Therefore, in general the greater the reduction in surface tension achieved by a given surfactant, the greater the rate of foam production will tend to be. This tendency is enhanced further by the fact that the lower surface tension will make the foam more stable and thus the rate of foam loss in a process will tend to decrease too [18].

The size of a surfactant molecule affects its diffusivity in solution. While a larger molecule (for example, a protein) might be very surface active it may not diffuse quickly enough to stabilize a surface that only exists for a very short period of time. This can be significant when the objective is to create very small daughter bubbles by break-up. It is not sufficient to just make bubbles small enough, a surfactant layer must be adsorbed quickly enough to stabilize the bubble before it experiences a collision that risks coalescence [20].

Somewhat different considerations apply in consumer product applications where surfactant activity is desired but foaming levels want to be limited; for example, in machine laundry detergents. While the reduction in surface activity will always tend to promote stability, it can be counteracted in various ways. For instance, if the surfactant is very fast diffusing then the Gibbs–Marangoni stability mechanism will be mitigated. Moreover, surfactant molecules that display a large area on the surface will tend to be more loosely packed and therefore stabilize the interface less.

### **18.2.2 Creation**

Bubbles must originate by nucleation of a new bubble, by the introduction of gas into the liquid phase through entrainment or injection, or by the break-up of existing bubbles into a greater number of smaller bubbles. This range of creation modes is illustrated in Fig. 18.3.

Nucleation involves the creation of a supersaturated solution of a foaming gas in liquid until gas spontaneously comes out of solution to form a gas bubble. Often this is achieved by means of a very rapid pressure drop; for instance, the sudden passage of a starch melt through an extruder die or shaving foam flowing from a pressurized canister. If the bubbles nucleate randomly within a continuous liquid phase it is known as homogeneous nucleation. This can be effective at producing a very large number of small bubbles quickly, but there is little control over the process. There is a risk that, once formed, bubbles will grow rapidly, consuming the supersaturated gas from solution instead of propagating the growth of future bubbles. This leads to polydisperse bubble sizes and a reduction in the total number of bubbles [21].

Nucleating agents are used for the production of polymeric foams by continuous extrusion with a blowing agent. McClurg [22] identified four desirable attributes of a nucleating agent, all of which are essentially orientated towards creating a narrow size range of bubbles in the product by limiting the significance of homogeneous nucleation:

- Nucleation on the agent is energetically or kinetically favourable compared to homogeneous nucleation,
- The agent has uniform geometry and surface properties,
- The agent is easily dispersed,
- The agent is plentiful so that growth of heterogeneously nucleated bubbles overwhelms homogeneous nucleation.

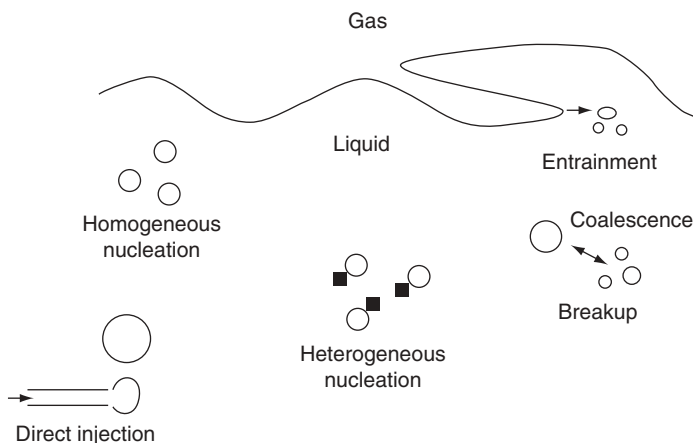


**Fig. 18.3** Modes of bubble creation.

For many years nucleation was thought to be the principal source of bubbles in bread crumb, with the yeast cells acting as a nucleating agent. Baker and Mize [23] showed for the first time that air bubbles that had been entrained and broken up during dough mixing and knocking back were, in fact, the only source of bubbles in the dough and consequently the final bread. This realisation opened up significant possibilities for bread making: if the bubbles are all created during processing, there must be methods to control them that can improve the process or product. Ultimately this led to the invention of the Chorleywood Bread Process (CBP), which revolutionized bread production in the UK and many other countries. The application of high headspace pressure in the CBP increases oxygen availability to the dough development and subsequent pulling of a vacuum in the headspace engineers the bubbles into an optimal size for growth into the final loaf crumb cells.

Entrainment of gas occlusions is essentially a process of bringing together of liquid surfaces that trap gas between them. Methods range from low agitation processes, which include massaging shampoo into hair with hands or laundry solution in a rotating drum, to high agitation processes, which include food whisking or rotor-stator structuring devices. The Ross-Miles (ASTM D1173) test has been developed as a standard method of assessing surfactant solution foamability in low-agitation conditions, and likewise using the Waring or Hamilton-Beach blenders to test high agitation conditions.

Any newly created bubbles are likely to undergo further changes once incorporated into the fluid, most significantly break-up during the processing stage. Despite this complication, measurement and modelling of the entrainment process is important because this is the foundation for all of the future foam structure development in these products. The challenge here is to find methods of separating entrainment from the simultaneous disentrainment or collapse processes that normally also occur and may themselves be linked to any bubble break-up that has occurred. The challenge is heightened because it is not normally possible to measure all the significant properties of the bubbles that may affect the break-up and disentrainment processes. Usually, only gas fraction (or a related parameter such as liquid hold up or overrun) can be measured.

Experimental studies normally start with a liquid with little entrained gas and show that entrained gas increases with time. The rate of disentrainment is typically a function of the quantity of gas entrained, and so plays a greater role with time. Eventually the disentrainment rate will balance with the entrainment rate and steady state aeration is reached. In some instances there may be an overshoot, either due to decreased effectiveness of surfactant (e.g. protein denaturation in whisking cream) [24] or due to the detailed mechanics of disentrainment [25].

In general it has been found for non-soluble gases that volumetric entrainment is largely independent of mixing pressure and that the rate of entrainment per impeller revolution is fairly constant at typical operating conditions. For systems using soluble gas (for example, CO<sub>2</sub> or NO), significant deviation from these trends can occur. If the liquid phase is saturated with the gas then the previous rules of thumb may hold true, but any change of pressure can lead to significant transport of gas from solution in the liquid to gas in the bubbles or vice versa.

The direct injection of gas into a liquid is the other main route of creating foams. These may act as seeds for future bubble growth or, more frequently, they constitute the final bubbles of the foam. It is used for drinks particularly, such as in beer can widgets, which release a burst of nitrogen when the can is opened, or sparklers on bar taps, which entrain small bubbles as a beer is pulled (the process of using a levered handle to pump beer from the barrel to the glass).

### **18.2.3 Growth**

For many products the final foam structure is a combination of a nucleation or entrainment break-up process followed by bubble growth. This has particular application for products where the foam is created by an action of the user at the point of use, but also finds application in a range of other production processes.

- Pressure change gas expansion. The bubble size in an aerated liquid will change proportionately with headspace pressure for an insoluble gas, albeit with some modification by the Laplace equation for surface tension effects. Substantial changes in foam structure are hard to create on this basis alone – although the effect is used to control final dough bubble size during industrial dough pressure vacuum mixing. However, dramatic changes are possible when a highly soluble gas is used under pressure. This is used in extrusion processing, carbonated drinks and pressurized cans such as shaving gels. For example, only sparkling wines where the bottle CO<sub>2</sub> pressure reaches at least 3.5 bar will form a foam when poured [26].
- Chemical gas creation. Again, this is popular where foam is to be created on demand; for example, cake raising agents are based on this approach.
- Biochemical gas creation. Fermentation processes mainly in the wine, beer and bread markets. The fermentation can have a significant role in taste creation as well as rheological development of the liquid phase.
- Heat. Rapid heating of a liquid material results in the creation of large volumes of vapour. This is normally generated on the surfaces of the liquid including the surfaces of bubbles, so baking and frying are both effective ways of inflating pre-existing bubbles in a liquid to create a foam product as the liquid phase sets.

### 18.2.4 Application of Structure

Underlying many of the applications of foams in consumer products is the ability to economically increase the volume of a product. It is serendipitous that this often also increases the product's appeal. The texture of foods can be greatly enhanced by the use of foams; making them softer, more palatable and also facilitating the release of flavour.

The structure of foams often gives them a yield stress. This is a very useful attribute since it means that the product will maintain its shape under the forces of gravity or handling once it is prepared. It is valuable for shaving foams, whipped cream, hair mousse, bubble bath and many others. The bulk rheology of the product is strongly dependent on the foam structure contained within it. Ice cream is appreciated for its complex multiphase structure and is produced and transported as a very wet foam before the final more solid structure is created by blast freezing in the tub [11].

Fundamental studies have yielded valuable insights into the relationship of foam structure and surfactant make-up to its bulk rheology [27]. This work has illustrated the difference in bulk rheological behaviour that occurs between low surface modulus and fast surface tension relaxation surfactants, such as typical synthetic surfactants, and those that have high surface modulus and slow relaxation, such as sodium and potassium salts of fatty acids. This second type has been shown to lead to significantly higher bulk viscosities and different flow curves.

### 18.2.5 Maintenance of Structure

The structure of the final consumer product foam is integral to its performance and appeal. However, the structure is also unstable and continuously changing. It is important to understand both of these together in order to design products with sufficiently long shelf lives or that deliver the required structure at the point of use. Furthermore, the structure of a foam product must be tolerant of its use. For instance, foaming is desired in hand washing laundry detergents and this foam should preferably withstand the agitation caused by washing [14].

Coarsening is the process of gas diffusing from small, high pressure bubbles, to larger, lower pressure bubbles. It is largely unwanted, since normally the desired structure is created during manufacture and so stability is desired after that point. Ripening tends to occur at time scales longer than the production, so is not a significant feature of the production process but then works detrimentally to the desired structure during product storage.

The introduction of novel biosurfactants, such as hydrophobin, has opened up the opportunity to create stable bubbles at the micron scale. These are exceptional surfactants, but also offer functionality such as forming surface networks at the interface that possess mechanical elasticity. Thus, they offer robust resistance to the effects of ripening, especially for very small bubbles with high Laplace pressures. They have application in frozen goods, for fat replacement with bubbles or for longer shelf lifes for aerated products such as mousse [28].

Bubble coalescence is a principal route to foam collapse. Bread is an example of this where volume increase is maximized before setting, and there is a risk of coalescence reducing final volume. A thin layer of surfactant solution in water is believed to line each bubble within the starch–gluten dough matrix. This layer provides a crucial extra degree of gas containment as the dough matrix ruptures between adjoining bubbles. The surfactant

solution layer forms a film bridging the ruptured dough matrix film, providing additional expansion capacity before the dough sets to retain its structure [29].

### 18.2.6 Summary

This section has followed the whole foam creation process as found in a range of consumer products. The breadth of technologies used to create, manipulate and maintain foams is too broad for a detailed analysis of each. The section has shown the basic principles that can be used and has shown that the process of the bubble creation and evolution is essentially the same in all products. The following section considers how these different foams are appreciated by users of the products and how this can be assessed.

## 18.3 Sensory Appeal

How can appeal be characterized and, then, how much can it be quantified? Appeal is a physiological state that is generally accessed by researchers and marketers through the use of sensory panels. Typically, a group of 10–20 people, trained to distinguish and articulate or score particular product attributes, is used in a series of randomised trials. Care is taken to normalize results; for example, by eating plain, dry biscuits between each sample in a tasting test.

Sensory panels provide valuable data, but results are hard to cross compare between groups or locations. They are also expensive to perform, and finding concrete relationships between panel preferences and product manufacturing route can be elusive. Figure 18.4 shows the results of a child's sensory perception of slices of white and brown bread, which was conducted at a museum engineering open day for schools. This result highlights the baker's challenge of producing brown bread (healthier with its higher whole grain content) that competes with the appeal of white bread (lighter and more aerated, as illustrated in the child's scores). A fundamental question is, are such preferences learned or innate?

An interesting example of this is given by Guinard *et al.* [30] in the context of a study of the sensory determinants of the thirst-quenching character of beer. A panel of ten men and two women assessed a total of 18 beers. The study rested on the notion that it is possible for someone to quantify their degree of thirst, and therefore it must be possible for them to quantify the thirst-quenching ability of a drink. A principal component analysis (PCA) study of the 21 assessed sensory attributes found a significant positive determinant for thirst-quenching only with carbonation and bubble density. However, it was ultimately concurred by the authors that this result was 'based on the past experiences of the judges involved' rather than on any actual quenching of thirst that took place within the time frame of the study. They speculated that these associations were likely to be cognitive but ultimately based on the physiological effects of their drinking experiences. In this context, only association is being detected and no real dependence on bubble size has been found on thirst-quenching. This test serves a purpose, particularly for marketing, but how can more fundamental sensory relationships be found?

Quantitative product tests are reliable, repeatable and portable and can be related to manufacturing process. Ultimately they must be related to the consumer response and

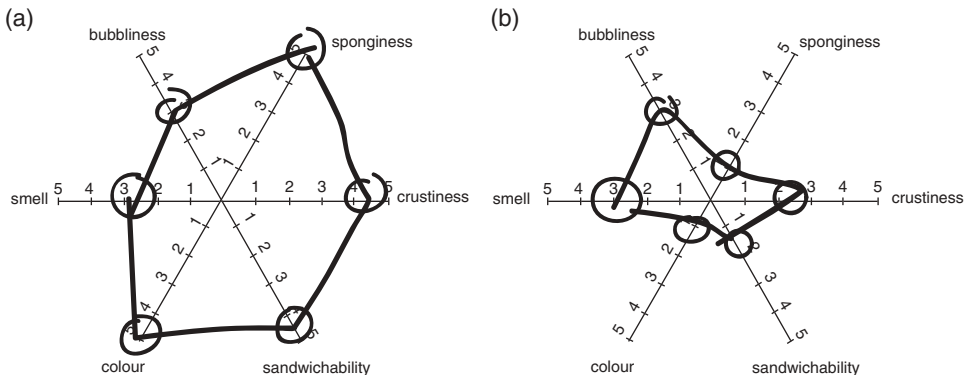


**Fig. 18.4** Example result of a child's product quality test from a school's engineering event.  
(a) Slice of white sandwich bread, (b) slice of brown sandwich bread.

normally this will be done by PCA with sensory panel data. Quantitative methods are particularly useful for establishing norms across locations. Once a method of quantitative measurement has been established and related to the consumer's preferred type, it can be used routinely across multiple sites at low cost and with high reliability. The removal of the subjective factor can be particularly beneficial, particularly in the business context.

The case of the UK family bread baker Warburtons illustrates this. Since a new generation of the family took control of the company in the early 1990s, they started expanding their business from a local operation in northern England to be the market leader over the entire UK [31]. By 2006 Warburtons was the second favourite brand at UK supermarkets, second only to Coca-Cola. Traditionally bakers have a well developed perception of the quality of the bread they produce. When there were only a few bakeries, interpersonal communication was sufficient to maintain desired standards across the business. However, the rapid expansion in number and location of bakeries limited the effectiveness of this approach.

Warburtons responded by developing the C-Cell bread slice imaging and analysis system in collaboration with Calibre Control and the Campden and Chorleywood Food Research Association (now Campden BRI). Illustrative images of a slice of sandwich bread from this system are shown in Fig. 18.5. The raw image (a) is analysed and software used to automatically and consistently identify features such as cell area (b) or contours of regions of cell similarity (c). The challenging task of relating the various outputs of this system to consumer preference had been completed within the company. However, once a consistent approach to product quality was achieved across the company the UK responded dramatically.

### 18.3.1 Visual

The high degree of light backscatter from foams makes them look bright and white, which is often associated with clean and high quality products. Foam is often the first attribute that consumers perceive and it has been shown that the appearance of beer influences the perception of its flavour [32]. The formation and stability of foam are the main characteristics

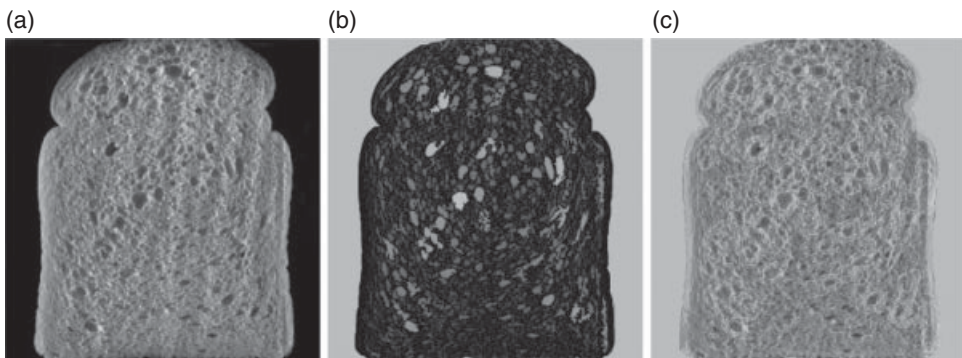


**Fig. 18.5** C-Cell images of a slice of white sandwich bread. (a) The original image, (b) analysed image distinguishing individual cells, (c) analysed image distinguishing regions of cell type.

of foam in drinks. Small bubbles rising slowly are appreciated and inform consumers' perception of bubble size. Bubbles also facilitate mass transfer of aroma molecules to the consumer. Sensory attributes considered important include: initial foam formed immediately after pouring, foam persistence, number of nucleation sites, bubble size, foam lace formed around beer surface and the perceived overall foam quality [33].

No scientific evidence correlates foam quality with desired perception of fineness of effervescence, but people often believe that smaller bubbles last longer on the surface and give the appearance of elegance in sparkling wines. Foamability in lab tests has been correlated with sensory analysis, which is of value because tests can then be performed on foamability of base wines before production into sparkling wines [26].

Alcohol free or low alcohol beer has become an increasingly large sector of the market, but foaming is one of the many properties of beer altered by the removal of alcohol. There are different routes of production, such as fermentation-free brewing, dilution or alcohol removal, but all of them experience this problem. Reduced foaming, in particular head retention, is a drawback associated with alcohol-free beers. The addition of glycerol and/or sugar alcohols can reinforce the foaming properties [34].

### 18.3.2 Auditory

The sound of bubbles bursting is a significant aspect of many products that entail transitory foams, perhaps conveying the foam's fleeting nature. This might be enjoyed as the sparkle of fizzy drinks and champagne, or even as bubble bath. Alternatively, the audible crunch of a snack product is intimately related to the solid foam structure.

Crispness is one of the most important sensory attributes of low-moisture solid food product quality, resulting from numerous failures that occur during mastication. Acoustic emission has been shown to correlate with crispness perception [35]. Products that are perceived as not being crispy have been found to emit sound waves with lower average amplitude, higher peaks and at low frequencies less than 3 kHz. On the contrary, the crispiest flakes emitted sounds with larger average amplitude, fewer high peaks and uniformly

distributed in the frequency domain. These qualities can be correlated with response to mechanical deformation, leading to convenient and reliable product testing methodologies.

### 18.3.3 Mouth Feel

Air bubbles lend themselves to pleasant mouth feel. It is thought that many of the mouth feel sensory aspects of food foams rely on bubble instabilities: coalescence, coarsening and creaming [36]. In principal, it might be thought that small stable air droplets should be perceived as creaminess – a sensation associated with small stable oil drops. This is not always found to be the case and the role of air bubbles in foam perception is still not elucidated, but foam has been shown to offer the potential to replace fats. At low air content (below 10%) foam perception is determined by matrix fluidity – aeration is not perceived and creaminess was not reported. At 80% gas matrix plays little role. Larger bubbles are more ‘airy’ possibly due to loss of gas when consumed, and less creamy, possibly due to lower firmness.

### 18.3.4 Summary

This section has given a short overview of some of the many ways in which users of consumer goods experience and appreciate foams. Some basic methodologies of quantifying these sensations have been described and it has been shown how, with care, these can often be related to directly measurable, quantifiable and repeatable product attributes.

## 18.4 Conclusions

This chapter has presented an overview of the use of foams in consumer products, including home care, personal care, foods and drinks. The range of foam type and application is broad, but a common theme of the need to stimulate the senses of the consumer using the product has been highlighted. The engineering challenge has been shown to be how to achieve the optimal foam and this has led to two broad strategies: foams created during production, which are then stabilized until use, or foams created at the point of use. The difficulty of establishing exactly what is appealing about foams has been studied. The contrast between what can be achieved with human testing panels and with analytical quality control equipment has illustrated the ethereal nature of optimal foam.

## References

- [1] J. Corstjens, M. Corstjens and R. Lal. Retail competition in the fast-moving consumer goods industry: the case of France and the UK. *Eur. Manag. J.*, **13**: 363–73, 1995.
- [2] A. Tennyson. *Maud and Other Poems*. Edward Moxon, London, 1855.
- [3] L. Brokaw. *Frommer's Montreal & Québec City 2009*. Wiley, New York, 2009.
- [4] D. Porter and D. Prince. *Frommer's Spain 2008*. Wiley, New York, 2008.

- [5] J.J.C. Browne. Birth and development of the widget, in *Bubbles in Food*, G.M. Campbell, C. Webb, S.S. Pandiella and K. Niranjan (eds). Eagan Press, MN, 1999.
- [6] NIIR Board and Associates. *The Complete Technology Book on Detergents*. National Institute of Industrial Research, Delhi, 2003.
- [7] M.W. Peng. *Global Strategy*. Cengage Learning, Ohio, 2009.
- [8] Bergeson and Campbell, <http://www.lawbc.com/news/2010/03/epa-planning-to-release-more-chemical-action-plans>, July 22, 2010.
- [9] D. Rust and S. Wildes. *Surfactants: A Market Opportunity Study Update*. Omni Tech Int., 2008.
- [10] S. Cohen-Addad, H. Hoballah and R. Höhler. Viscoelastic response of a coarsening foam. *Phys. Rev. E*, **57**: 6897–901, 1998.
- [11] A. Russell. Process innovation from research and development to production in a large company: development and commercialisation of a low temperature extrusion process. In *Case Studies in Food Product Development*, M. Earle and R. Earle (eds). CPL Press, Newbury, 2007.
- [12] S.H. Alavi, S.S.H. Rizvi and P. Harriot. Process dynamics of starch-based microcellular foams produced by supercritical fluid extrusion. I: Model development. *Food Res. Int.*, **36**: 309–19, 2003.
- [13] P.J. Martin, A. Tassell, R. Wiktorowicz, C.J. Morrant and G.M. Campbell. Mixing bread doughs under highly soluble gas atmospheres and the effects on bread crumb texture: experimental results and theoretical interpretation. In *Bubbles in Food 2: Novelty, Health and Luxury*, G.M. Campbell, M.G. Scanlon, D.L. Pyle and K. Niranjan (eds), Eagan Press, USA, 2008.
- [14] L. Ran, S.A. Jones, B. Embely, M.M. Tong, P.R. Garrett, S.J. Cox, P. Grassia and S.J. Neethling. Characterisation, modification and mathematically modelling of sudsing. *Coll. Surf. A: Physicochem. Eng. Aspects*, doi:10.1016/j.colsurfa.2010.11.028, 2010.
- [15] M.J. Rosen. *Surfactants and Interfacial Phenomena*, 3rd edn. Wiley, New York, 2004.
- [16] A. Namiki and M. Manga. Transition between fragmentation and permeable outgassing of low viscosity magmas. *J. Volcanol. Geotherm. Res.*, **169**: 48–60, 2008.
- [17] A.M. Trater, S. Alavi and S.S.H. Rizvi. Use of non-invasive X-ray microtomography for characterizing microstructure of extruded biopolymer foams. *Food Res. Int.*, **38**: 709–19, 2005.
- [18] D. Myers. *Surfactant Science and Technology*, 3rd edn. Wiley, New York, 2006.
- [19] S. Hilgenfeldt, A.M. Kraynik, D.A. Reinelt and J.M. Sullivan. The strucutre of foam cells: isotropic Plateau polyhedra. *Europhys. Lett.*, **67**: 484–90, 2004.
- [20] R. Pichot, F. Spyropoulos and I.T. Norton. Mixed-emulsifier stabilised emulsions: Investigation of the effect of monoolein and hydrophilic silica particle mixture on the stability against coalescence. *J. Coll. Int. Sci.*, **329**: 284–91, 2009.
- [21] M.A. Shafi, K. Joshi and R.W. Fumerfelt. Bubble size distributions in freely expanded polymer foams. *Chem. Eng. Sci.*, **52**: 635–44, 1997.
- [22] R.B. McClurg. Design criteria for ideal foam nucleating agents. *Chem. Eng. Sci.*, **59**: 5779–86, 2004.
- [23] J.C. Baker and M.D. Mize. The origin of the gas cell in bread dough. *Cereal Chem.*, **18**: 19–34, 1941.
- [24] K. Niranjan and S.F.J. Silva. Bubbles in foods: creating structure out of this air! In *Food Engineering: Integrated Approaches*, G.F. Gutiérrez-López, G.V. Barbosa-Cánovas, J. Welti-Chanes and E. Parada-Arias (eds). Springer, New York, 2008.
- [25] P.J. Martin, N.L. Chin and G.M. Campbell. Aeration during bread dough mixing. II. A population balance model of aeration. *Trans. IChemE Pt C: Food Bioprod. Process.*, **82**: 268–81, 2004.
- [26] M. Gallart, X. Tomás, G. Suberbiola, E. López-Tamames and S. Buxaderas. Relationship between foam parameters obtained by the gas-sparging method and sensory evaluation of sparkling wines. *J. Sci. Food Agric.*, **84**: 127–33, 2004.
- [27] N.D. Denkov, S. Tcholakova, K. Golemanov, K.P. Anathpadmanabhan and A. Lips. The role of surfactant type and bubble surface mobility in foam rheology. *Soft Mat.*, **5**: 3389–408, 2009.
- [28] A.R. Cox, D.L. Aldred and A.B. Russell. Exceptional stability of food foams using class II hydrophobin HFBII. *Food Hydrocol.*, **23**: 366–76, 2009.
- [29] E.N.C. Mills, P.J. Wilder, L.J. Salt and P. Skeggs. Bubble formation and stabilization in bread dough. *Trans. IChemE Pt C: Food Bioprod. Process.*, **81**: 189–93, 2003.

- [30] J.-X. Guinard, A. Souchard, M. Picot, M. Rogeaux and J.-M. Sieffermann. Sensory Determinant of the thirst-quenching character of beer. *Appetite*, **31**: 101–15, 1998.
- [31] L.G. Schiffman, H. Hansen and L.L. Kanuk. *Consumer Behaviour: A European Outlook*. Prentice Hall, Harlow, 2008.
- [32] J.E. Symthe, M.A. O'Mahony and C.W. Bamforth. The impact of beer on its perception. *J. Inst. Brewing*, **108**: 37–42, 2002.
- [33] A.P. Lobo, N.F. Tascón, R.R. Madrera and B.S. Valles. Sensory and foaming properties of sparkling cider. *J. Agric. Food Chem.*, **53**: 10051–6, 2005.
- [34] S. Sohrabvandia, S.M. Mousavia, S.H. Razavia, A.M. Mortazavianb and K. Rezaeia. Alcohol-free beer: methods of production, sensorial defects, and healthful effects. *Food Reviews Int.*, **26**: 335–52, 2010.
- [35] L. Chaunier, P. Courcoux, G. Della Valle and D. Lourdin. Physical and sensory evaluation of cornflakes crispness. *J. Texture Stud.*, **36**: 93–118, 2005.
- [36] M. Minor, M.H. Vingerhoeds, F.D. Zoet, R. de Wijk and G.A. van Aken. Preparation and sensory perception of fat-free foams: effect of matrix properties and level of aeration. *Int. J. Food Sci. Tech.*, **44**: 735–47, 2009.

# 19

## Foams for Blast Mitigation

*A. Britan, H. Shapiro and G. Ben-Dor*

### 19.1 Introduction

It is well established nowadays that blast wave mitigation in foams is a direct consequence of two interrelated features:

- High heat capacity of the liquid phase; and
- Strong compressibility of the gas phase.

The shattering of the foam cells actuates new processes of energy losses. As a result, acceleration and heating of the resulted droplets complement the friction between the gas and the liquid and the strong shear stress at the boundaries. Although in a qualitative fashion blast wave mitigation in foams has been well documented, the governing processes and even the boundary between the shattering and the non-destructive regimes have not been addressed yet. The interest in this area that emerged at least three decades ago still exists because of ever changing features of the foam structure. Even for cases in which the foam sustains the compression before and during the interaction of the blast wave with the foam, two different objects have to be dealt with. Initially, once prepared, it is an ensemble of the interconnected gas bubbles. As time goes on and the foam loses liquid it becomes non-homogeneous. This, in turn, can lead to polydispersity in the gas droplets mixture once it appears behind the shock wave due to the foam shattering. To quantify the relationship between the micro properties of the foam structure and the macroscopic features of shock wave/foam interaction, a great number of special tests have been conducted in the past. The main results of these efforts, as well as the state-of-the-knowledge of the theory which tried to explain the relevant physics, are reviewed in this paper.

## 19.2 Free Field Tests

### 19.2.1 Compressibility

To prevent severe damage to buildings, vehicles and personal, protection technology explores various engineering solutions in which the blast wave energy is transferred into less destructive forms. Granular filters, for example, reduce the blast overpressure due to strong viscous dissipation and/or dispersion of the blast wave within the bulk [1, 2]. Perforated solid or free-standing plates redistribute the energy within the moving gas due to complex fluid/structure interactions at large scale surfaces [3, 4]. Mechanical, piston/cylinder dampers mitigate quite well the peak overpressure while the impulse remains unchanged [5].

In contrast, water-based, multiphase protection reduces all the important characteristics of the blast wave. This was first observed when bubble screens reduced significantly the blast wave loading on underwater construction and biology objects. These behaviors have been well reviewed by Nigmatulin [6] and Nakoriakov *et al.* [7] and recently by Kedrinsky [8]. The focus here is mainly on the mitigation effects caused by aqueous foam barriers [9]. Generally, this phenomenon is ascribed to the high compressibility of the gas bubbles, which easily change their volume,  $V$ , as a response to the varied pressure,  $p$ . For the adiabatic process, for example, the compressibility,  $\beta_s$ , is:

$$\beta_s = -\frac{1}{V} \left( \frac{\partial V}{\partial p} \right)_s \quad (19.1)$$

where  $s$  is entropy. With the aid of the speed of sound,  $c^2 = \frac{\partial p}{\partial \rho} \Big|_s$ , it follows that  $\frac{\partial V}{\partial p} = -\frac{1}{(c\rho)^2}$ , and hence:

$$\beta_s = -\frac{1}{V} \left( \frac{\partial V}{\partial p} \right)_s = \frac{1}{c^2 \rho} \quad (19.2)$$

From Equation 19.2 it follows that the compressibility depends on the speed of sound,  $c$ , and the material density,  $\rho$ . The reflected pressure,  $P_R$ , registered at a distance 57 inches from the detonation of a one pound of TNT, versus the different material density,  $\rho$ , is shown in Fig. 19.1. The points appropriate to air, (1), and water, (2), fall on a single straight line, labeled (3). This line implies that the mitigation effect reduces when the density increases. The points appropriate to vacuum, (4), and polyurethane foam, (5), fall on a curved line, labeled (6). Notice that a peak pressure in water (2),  $P_R = 10^4$  psi, is much higher than the pressure peaks  $P_R \approx 10^3$  psi that is provided by vacuum (4) or  $P_R \approx 10^2$  psi that is recorded in air (1). The polyurethane foam (5) is ten times denser than air while has extremely low sound speed and thus its compressibility is high (Table 19.1). Unfortunately, whereas the peak pressure of about  $P_R \approx 30$  psi ensures maximal mitigation, solid foams are rare in use for protection, since they are easily knocked down by the blast wave without expending much energy. Moreover, due to the combustion extinguishing properties, solid foams are serious contributors to fire and toxic smoke generation. In contrast, the protective barriers of aqueous foam are safe to handle, could be quickly prepared at the site and demonstrate high mitigation characteristics.

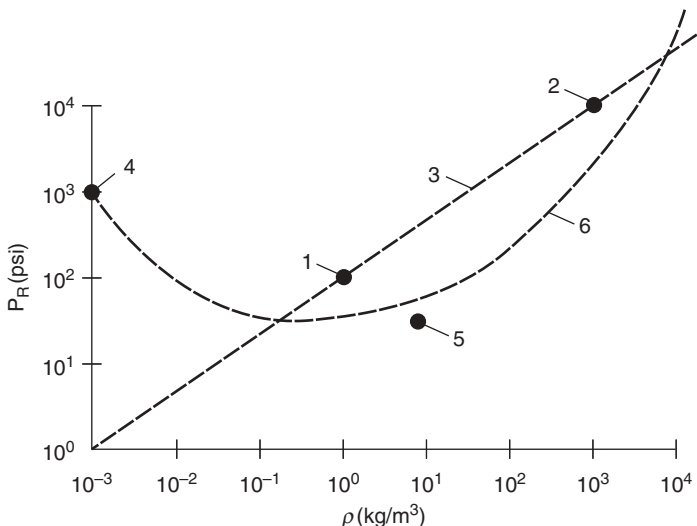


**Fig. 19.1** The reflected pressure,  $P_R$ , versus the material density [10].

**Table 19.1** Material characteristics of various protective barriers.

Protective material	Density ( $\text{kg}/\text{m}^3$ )	Sound speed (m/s)
Air	$10^0$	345
Vacuum	$10^{-3}$	345
Water	1000	1560
Polyurethane solid	1200	1780
Polyurethane foam	6	60

The density of the aqueous foam is usually defined as:  $\rho_f = (1 - \varepsilon)\rho_l + \varepsilon\rho_g$ , where  $\varepsilon = V_l/V_f$  is the volumetric liquid fraction,  $\rho_l$  and  $\rho_g$  are densities of water and the air, respectively. Since  $\rho_l > \rho_g$ , the sound speed in the air–liquid mixture,  $c_{gl}$ , is [7]:

$$c_{gl}^2 = \rho \left( \frac{\varphi}{\rho_g c_g^2} + \frac{1-\varphi}{\rho_l c_l^2} \right) \quad (19.3)$$

where  $\varphi = 1 - \varepsilon$  is a volume gas content. Relationship 19.3, shown in Fig. 19.2 by the solid curve, is separated by the two vertical dotted lines into the three domains:

- (1) Dry aqueous foam domain when  $\varepsilon < 0.05$ .
- (2) Wet aqueous foam domain when  $0.05 < \varepsilon < 0.36$ .
- (3) Bubbly liquid domain when  $\varepsilon > 0.36$ .

The speed of sound in standard air ( $\varepsilon = 0$ ), 345 m/s, decreases at  $\varepsilon = 0.5$  to about 24 m/s as it travels through either aqueous foams or bubbly liquids. An increase to  $\varepsilon > 0.9$  causes a gradual increase in the sound speed, to the limit of the sound speed in water. From the

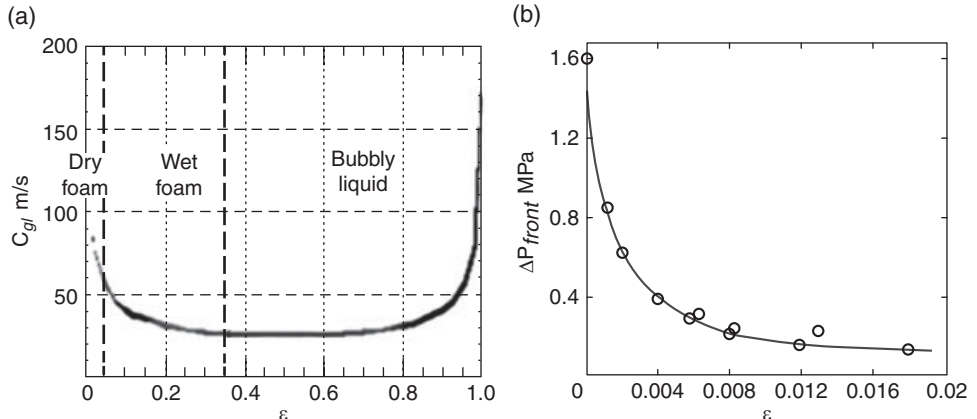


**Fig. 19.2** (a) The sound speed in water–air mixture; and (b) the blast wave peak overpressure vs. the liquid fraction,  $\epsilon$ .

other side, when the water content approaches zero, even small variations in  $\epsilon$  cause strong changes in the sound speed [11–13]. Fig. 19.2 also reveals a similar behavior with the peak overpressure,  $\Delta p_{front}$ , that was recorded by Palamarchuk and Postnov [14] at the front of the blast wave. As the liquid fraction,  $\epsilon$ , increases from zero, the value  $\Delta p_{front}$  quickly drops, while it remains unchanged when  $\epsilon$  approaches closer to the wet foam domain, that is,  $\epsilon > 0.05$ . Based on this evidence, the mitigation effect appears to depend strongly on the foam decay. When discussing the factors affecting the mitigation effect, an extensive literature survey by Gelfand and Silnikov [9] puts more emphasis on:

- (1) the arrangement of the barrier and its distance from the blast charge;
- (2) the type and the energy of the explosive;
- (3) the environment conditions; and
- (4) the foam density.

Whilst among these factors the non-homogeneity of the barrier is missed, the foam decay is actually an important reason of the high scattering (about 40%) of the data obtained in the free field tests. For the standard, free field blast in air this value does not exceed about 10%.

### 19.2.2 Typical Test Rigs

To mitigate a blast wave to a harmless level, the barrier arrangement has evidently to comply with the explosion type. When the charge is actuated inside the foam, this arrangement is referred to as *internal explosion* case. Quickly preparing and holding in place an aqueous foam barrier is not a simple task. As shown in Fig. 19.3a the foam that flows away can leave the explosive charge uncovered. To prevent this effect the foam material is usually enclosed inside a container of light plastic sheet, as is seen in Fig. 19.3b. To stop ejection of the solid

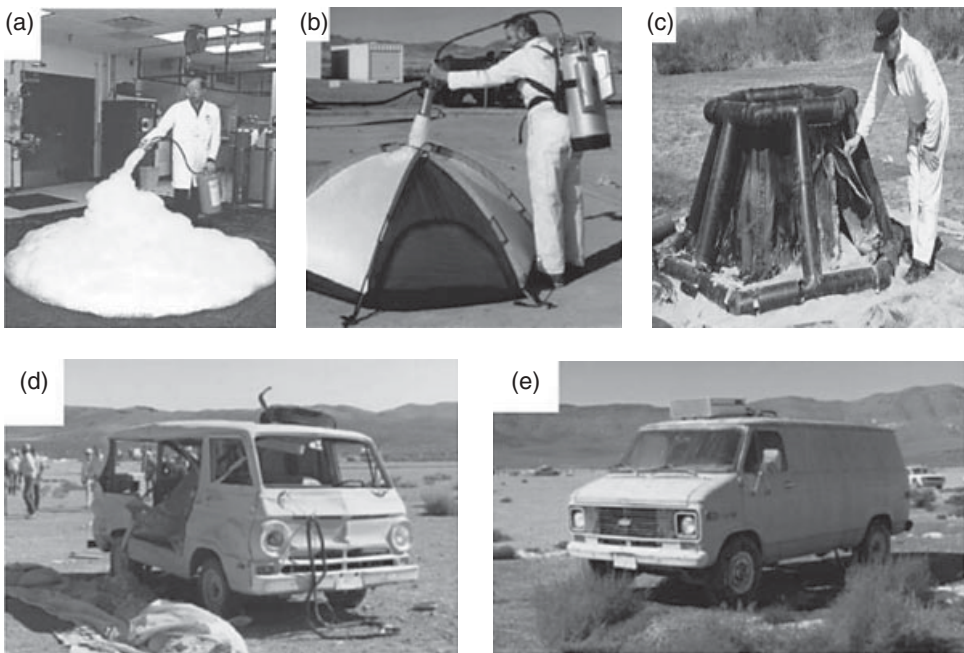


**Fig. 19.3** (a–c) Typical arrangements of the foam barrier for internal explosion case; (d and e) the effect on the van of a blast from an explosion of a 44 kg charge of C4 (d: not protected; e: protected). For a better understanding of the figure, please refer to the colour plate section.

fragments by bomb or mine explosion, the walls of container shown in Fig. 19.3c were produced of Kevlar [15, 16].

The two last pictures in Fig. 19.3 show that unprotected explosion destroys a van situated 10 m away from the charge (d), while foam protected explosion of a similar charge (e) causes negligible effect on the van [17].

To make the data analysis more reliable the test arrangement (the measuring instruments and the charge position) were designed so that the resulting features of the blast wave approach as close as possible to the standard conditions of the free explosion in air. This in turn, sets forth the following requirements for the test rig [18]:

- (1) The explosive material has to be placed on a special support at a height that prevents the formation of a crater at the ground.
- (2) The explosive material has to be spherical, with the detonator positioned close to the center of the sphere.
- (3) The gauges and the explosive charge have to be placed at the same height to exclude early arrival of the shock wave reflected from the ground.
- (4) The blast-generated shock has to be separated from the fireball to avoid electrical perturbations of the reading signals. To ensure this the first measuring point has to be placed far enough from the charge.

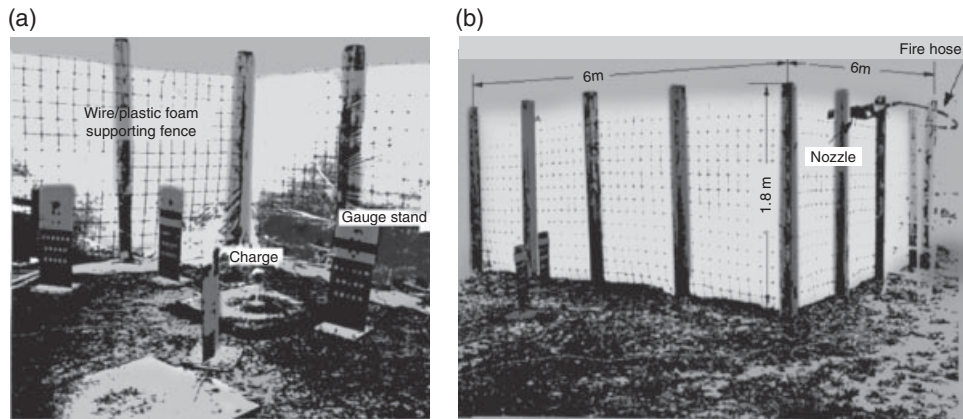


**Fig. 19.4** (a) Layout and (b) typical dimensions of a rig used for testing the close field of an internal explosion [19]. For a better understanding of the figure, please refer to colour plate section.

To ensure this the size of the typical rig, as shown in Fig. 19.4, has to be big, and hence it requires much foam to fill it. When the main objective is the emergence shock wave in air the test rig could be smaller and in turn the test is cheaper. The explosive, as shown in Fig. 19.5, is placed on the crushable plastic post centered inside the cubic enclosure of a thin polyethylene film. The blast wave pressure reduction (in dBs) is determined as the difference between the explosion of the charge exposed to air and the charge covered with foam. The pressures in such experiments are usually recorded by standard microphones (M1-M4) positioned far downstream from the charge.

The scenario of a so-called *external explosion* could be qualified as the head-on impact of the blast wave initiated in air with the aqueous foam barrier. Since the transient behaviors of this blast are well specified, an *external explosion* can be readily simulated in the laboratory using a foam bulk positioned against the end wall of a shock tube [20]. The main restrictions of these tests, as well as typical results, are discussed later.

### 19.2.3 Decay of the Foam Barrier

For the big test rig shown in Fig. 19.4, the foam is supplied using commercial fire-fighting equipment. The filling normally takes about ten minutes and the explosion is fired no earlier than about 15 minutes after the filling procedure has started. While during this time the foam inside the barrier decays, the resulting change of the foam conditions at the time instant of the blast are generally not controlled. Winfield and Hill [19], for example, tested the foam decay separately using a special  $0.3 \times 0.3 \times 0.3$  m container for these experiments. The results obtained are shown in Fig. 19.6 for three types of foam: Jet-X foam (tests Nos. 7, 10, 11 and 18); Chieftain XHX brand (tests Nos. 14 and 16); and protein-based Chieftain 6% concentrate (test No. 17).

Close inspection of Fig. 19.6 reveals that:

- (1) The data recorded in two subsequent tests with the same foam brand (Jet-X) scatter. This means that standard fire fighting equipment does not supply foam with repeatable properties.

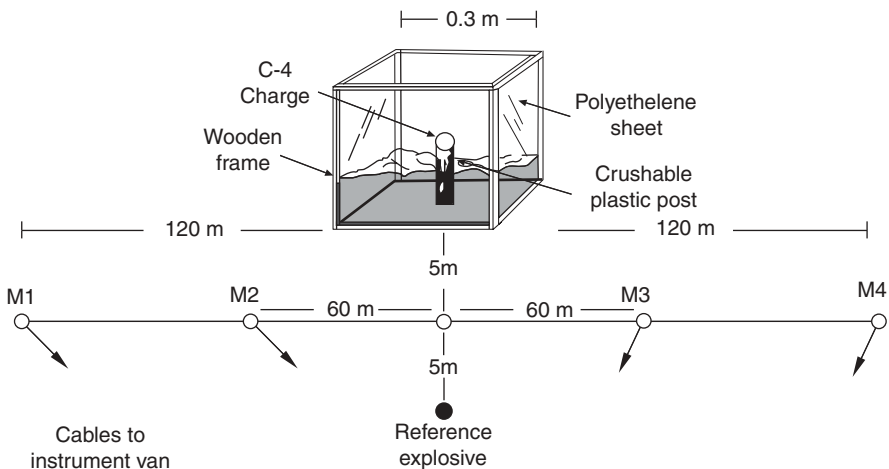
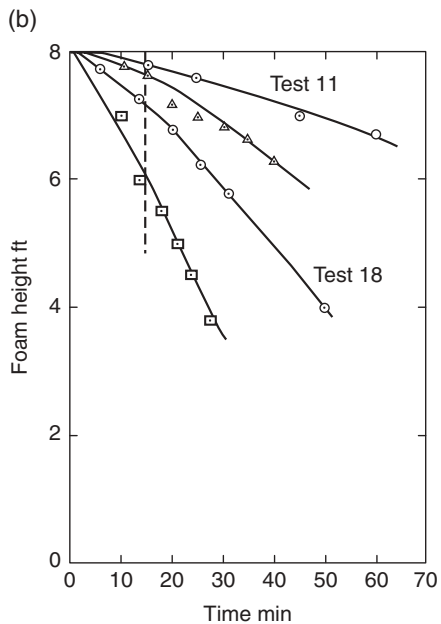
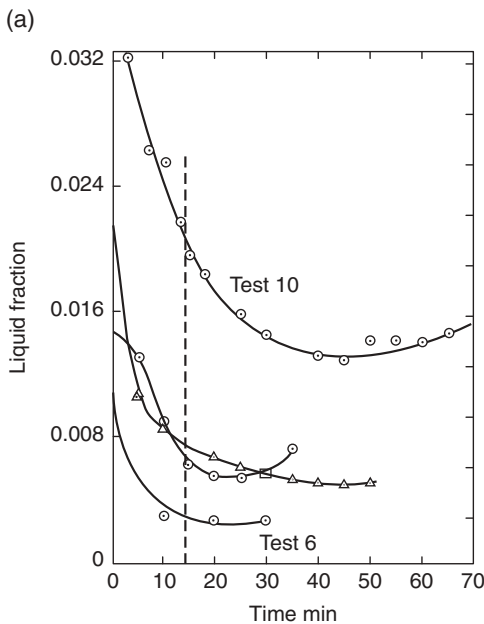


**Fig. 19.5** Typical rig for testing the reduction characteristics of the blast wave from an internal explosion in the far field [21].

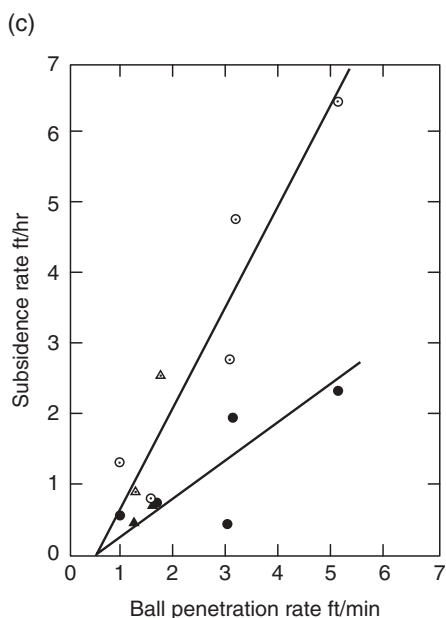
- (2) All foams quickly decay. At the instant of a blast marked in Fig. 19.6a by the dashed line, the actual liquid fraction,  $\varepsilon$ , in test No.10, for example, is about 30% lower and in test No.17 it is even halved.
- (3) The decaying foam barrier evidently subsides in time and reduces its height to about 13% (see, for example, the results of the test No. 17 in Fig. 19.6b).

When the foam decay test was repeated in a larger  $1.2 \times 1.2 \times 2.4$  m container, it was found that the larger foam bulk subsides slower. To measure the foam stiffness, a new series of the tests was conducted using a polystyrene ball that fell through the foam from a height of 2.4 m. The recorded penetration rate of the ball revealed high sensitivity to the foam decay. As can be seen in Fig. 19.6c, the effect of the foam subsidence on the ball penetration is stronger in the larger foam bulk. Notice that in the experiments of Larsen [22] the decay rate was higher in the smaller container. Generally, foam decay can be explained in the context of three interrelated effects: the gravity, the capillary, and the viscosity [12, 23]. While the role of viscous dissipation is not clear enough, foam drainage due to the gravity changes the macroscopic appearance of foam barrier significantly. When combined with capillarity, these changes are accomplished with a coarsening process, which can occur over the same timescale. Because of these couplings, predicting the resulted non-homogeneity of the foam barrier is not a simple task. Generally, drier foam coarsens more and coarsening foam drains more rapidly. However, additional flow of the liquid through the foam films complicates the issue, especially for wet foams [11, 23]. Despite its significance, the effect of the container walls on the flow through the films has found support only in recently published papers. Koehler *et al.* [24] were the first to show that the sidewall effect is significant when the number of wall films vs interstitial films is high. A similar consequence of the so-called *container effect* is demonstrated by the data in Fig. 19.6c. The major concern to be addressed is how the blast wave mitigation responds to the foam decay. To answer this question in the next section we discuss the role of the foam density for the pressure reduction in foam.

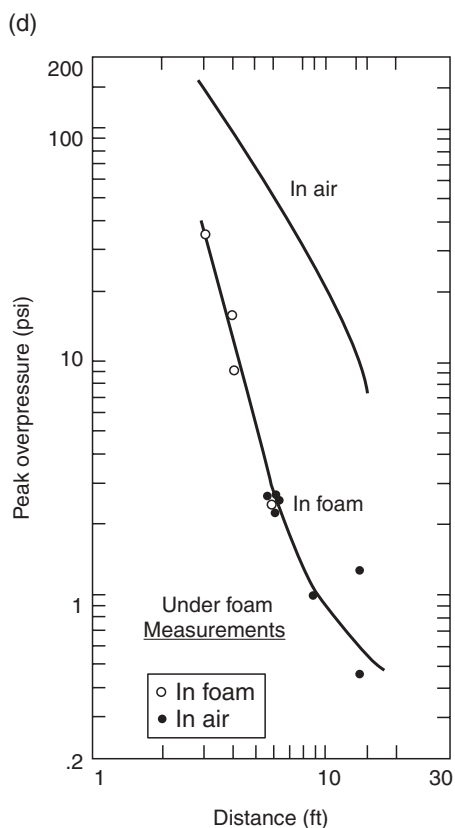


Foam	Test no.
○ JET-X	6.10
△ XHX	14
□ 6% protein	17

Foam	Test no.
○ JET-X	11.18
△ XHX	16
□ 6% protein	17



Foam	Container	
	8ft	1ft
JET-X	○	●
XHX	△	▲



(continued)

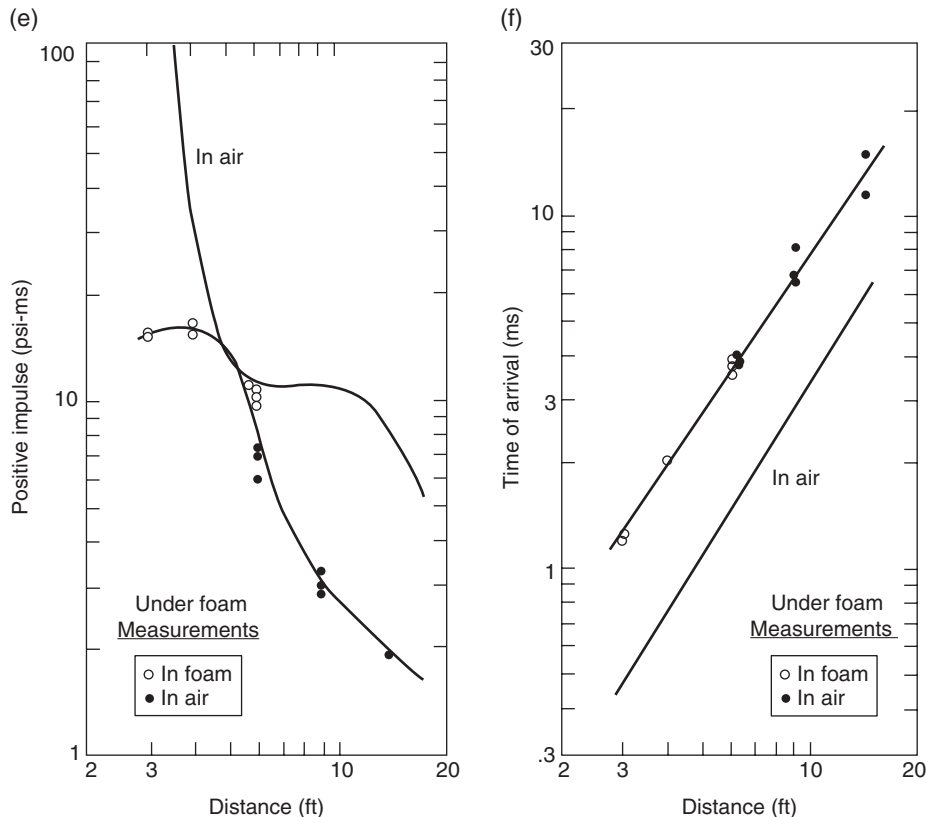


**Fig. 19.6** (a) Time variation of the foam density; (b) the rate of the foam subsidence; (c) the relationship between subsidence and ball penetration rates inside the foam filled container; and (d–f) characteristics of the close field mitigation of blast wave generated by the internal blast [19].

#### 19.2.4 Effect of Foam Density

Unfortunately, the limited evidence collected by Winfield and Hill [19] and shown in Figs 19.6d–19.6f gives no answer to the question on the role of the foam decay. These tests were not duplicated and the resulting characteristics of the blast look as equally altered by all foams. In contrast to this study, more comprehensive experiments by Raspet and Griffiths [21] revealed a clear relationship between the foam density and the resulting blast wave mitigation. Two foams, dry and wet, were tested and the thickness of the foam barrier,  $l$ , was changed from 0.31 to 2.4 m. Since the blast wave mitigation was recorded in air and the foam bulk, as shown in Fig. 19.5, was smaller, the explosion could be fired almost immediately, that is., about 30 s after foam generation. For dry foam having an initial density of  $\rho_f = 4 \text{ kg/m}^3$ , the analysis revealed that the bubble size (about 1 cm in diameter) and the liquid fraction ( $\varepsilon = 0.004$ ) at the instant of blast were within 20% of the nominal values. In a wet foam having an initial density of  $\rho_f = 33 \text{ kg/m}^3$ , the liquid fraction ( $\varepsilon = 0.03$ ) and bubble size (about 1 mm in diameter) remained unchanged during the first hour following generation. The recorded peak pressure reduction that is plotted in Fig. 19.7a is

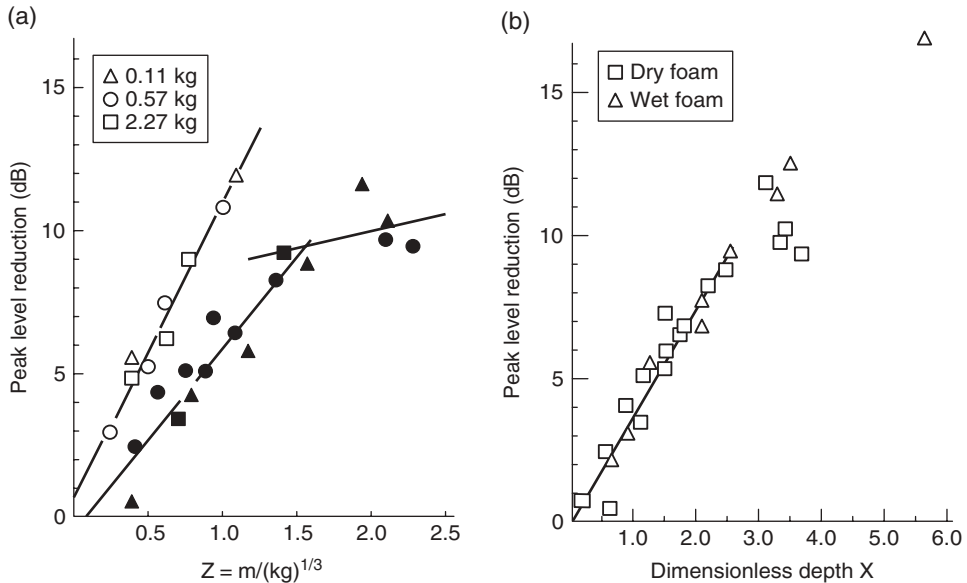


**Fig. 19.7** Blast noise reduction versus (a) scaled foam  $Z = l / (m_{ch})^{1/3}$  depth and (b) dimensionless depth  $X = (\rho_f^3 / m_{ch})^{1/3}$ . Data for the dry foam in Fig. 19.7a are shown by black points, for the wet foam by open points [21].

defined as  $20\log(p_{\max}/p_0)$ , where  $p_{\max}$  is the peak pressure and  $p_0 = 20 \mu\text{Pa}$  is a reference excessive noise level. The scaled distance  $Z = l / (m_{ch})^{1/3}$ , includes the thickness,  $l$  [m] scaled to the cubic root of the charge mass,  $m_{ch}$  [kg] in a TNT equivalent. In the dry foam case, the mitigation, shown in Fig. 19.7a, is seen to increase linearly until a certain “critical” scaled thickness,  $Z^*$ , after which it keeps on increasing with  $l$  for thicker barrier, but at much less rate. The position of the inflection point between these two linear functions was found to depend on the type of foam. Whereas for the dry foam  $Z^* \approx 1.5$  and pressure reduction is limited to about 10 dB, in the wet foam the inflection point does not exist at all. Based on the total mass of the foam barrier it can be concluded from the data in Fig. 19.7a that:

- (1) Wet foam provides stronger mitigation of sound waves than dry foam.
- (2) Increasing the foam density is more productive than the extension of the thickness of the barrier,  $l$ .
- (3) Increasing the foam thickness beyond the critical value,  $Z^*$ , is less productive for further mitigation.

Since the wet and dry foams are also structurally different, the density and the structural factors were separated. The data points for this purpose were re-plotted in Fig. 19.7b using a dimensionless scaled thickness,  $X$ . Since up to  $X \approx 2.5$  all the points fall on a common line for both dry and wet foams, this means that the foam density in this domain is the dominant factor. Raspet and Griffiths ascribed the systematic, about 25–30%, scattering between the points that appear at  $X \geq 2.5$  to the different bubble sizes that was clearly seen in the course of the sample analysis conducted before the tests.

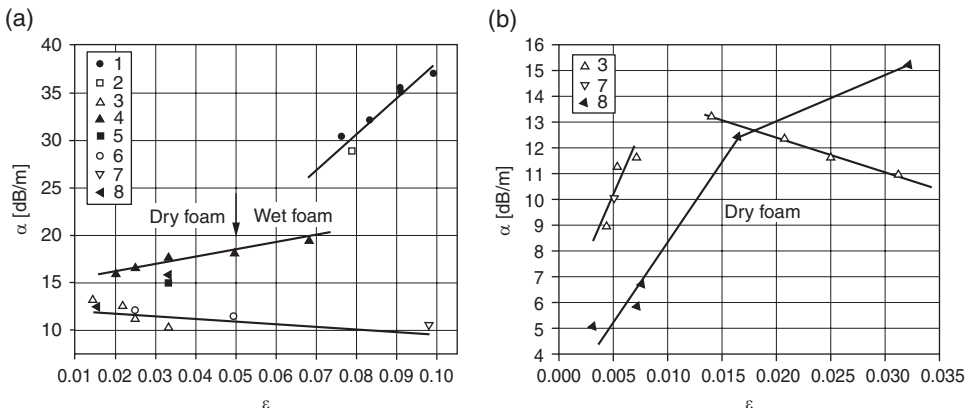


**Fig. 19.8** Attenuation coefficients vs. liquid fraction [25].

**Table 19.2** Summary of the test conditions used in the sound mitigation tests.

No.	Type of foam	Density ( $kg/m^3$ )	Bubble Diameter (mm)	Sample height (cm)	Method	Reference
1	Shaving	90	0.06	8	Sound tube	[25]
	Firefighting	200	0.09	8		
2	Shaving	71	0.02	25	Sound tube	[26]
	25% detergent	59	0.4	—		
3	2% Sulfanol	17–25	0.2	5	Sound tube	[27]
4	1.5% Sulfanol	40	0.1	10	Sound tube	[28]
		11	0.2	10		
5	National foam system	33	1	100	Blast explosion	[21]
		4	10	150	Far-field	
6	Sulfanol	20	0.07	25	Sound tube	[29]
		7	0.075	—		
7	Aqueous	100	—	76	Internal explosion	[30]
		5	—	152	Close-field	
8	Synthetic	67	—	6.35	Blast	[31]
		7	—	—		

To check whether the foam density is crucial also for other foams, similar data are shown in Fig. 19.8 for a wider range of test conditions [25]. The lines in this figure are least squares fits to the portions of the data and the test conditions are listed in Table 19.2. Although there is some scatter, a general trend that is demonstrated by points 3, 6, 7 and 8 correlates well with the expectations based on the data of Fig. 19.2. The reduction coefficient,  $\alpha$ , remains unchanged or decreases slowly if the liquid fraction is in the range  $0.01 < \epsilon < 0.07$ . However, within the same range, the reduction coefficient,  $\alpha$ , shown by points 4 and 5, initially increases slowly, while in the wet foam domain ( $\epsilon > 0.07$ ) starts to increase more quickly. A peak difference between the mitigation coefficients marked by points 1 and 2 and 6 and 7

finally reaches about 70%. Strong disagreement between the different points recorded in the dry foam limit is also observed in Fig. 19.8b. Initially, within the entire range of liquid fraction,  $0.0025 < \varepsilon < 0.007$ , points 3 and 7 from one side and point 8 show similar trends.

Thereafter, as the liquid fraction increases further, the increased hydrodynamic resistance of foam film resulted in an increase in the mitigation [32, 33]. However, as the liquid fraction, exceeds  $\varepsilon \approx 0.012$ , the common trend demonstrated by points 3, 7 and 8 is changed. Actually, points 3 in Fig. 19.8b start to decrease while points 8 continue to increase. This inconsistency could be attributed to the different methods and/or set-ups used by the authors in their tests. However, referring back to Table 19.2 ensures that this is not the case. The data obtained in the laboratory (points 1–4) show a different trend while correlating well with points 7 and 8 that were recorded in the course of the free field tests. In an attempt to separate between the relative importances of the various physical factors that affect this disagreement, a new series of the controlled tests and well specified foam conditions are required. Typical results of such tests were recently reported by Mujica and Fauve [34]. Unfortunately, their report was limited to short samples of shaving foam.

In contrast to sound waves, the situation with blast wave mitigation became clear in 2006 when the detailed report by Hartman *et al.* [30] was published. Since the reported free field tests were conducted in the early 1980s (by SANDIA), it seems reasonable to compare it with results of the same time period that were reported by Kudinov *et al.* [35]. This is done in va. For completeness the pressure reduction that was reported recently by Domergue *et al.* [18] is also added to this figure. It should be noted that all the data in this figure show evident sensitivity to the density,  $\rho_f$ , and even in Fig. 19.9b, which uses the dimensionless coordinate,  $X$ , this density dependence does not vanish. Based on these data it was adopted [30] that an optimal foam-based protection should have a density,  $\rho_f$ , in the range  $10 \leq \rho_f \leq 20 \text{ kg/m}^3$  (i.e.,  $0.01 \leq \varepsilon \leq 0.02$ ). When compared with denser foams, such barriers require less water and are thus cheaper. They also cause smaller loading on the container walls, which could then be produced from a thin plastic film. These requirements are among the major factors of a mobile protection against blast wave impact.

### **19.2.5 Foam Impedance and the Barrier Thickness**

When discussing density-related effects, the partial transmission of the blast wave at the foam boundary is of primary importance, since it depends on the impedance mismatch,  $\text{Im} = (\rho c)_f / (\rho c)_{\text{air}}$ . However, blast wave mitigation does not scale linearly with the impedance mismatch,  $\text{Im}$ , as it also depends on the barrier thickness,  $l$ . Neglecting in their simulations any energy losses, Ball and East [36] were the first to identify this beneficial mitigation of the blast wave caused by the foam thickness,  $l$ . Since, generally, blast pressure mitigates with distance as  $\sim 1/r_{\text{front}}^3$ , any additional reduce in the blast wave velocity,  $D$ , inside the foam enables the overpressure to mitigate further as the barrier thickness,  $l$ , increases. This effect becomes of importance at early stage when the blast wave only appears and its duration is much shorter than  $l/D$ . The interaction of the detonation products with foam and the heat transfer process are strongly sensitive at this stage to the polydispersity of the resulting droplets and other inclusions. Solid particles when specially added to foam also increase mitigation [37, 38] and make the foam more stable [39]. The simple formula which relates the resulting dampening effect to the barrier thickness,  $l$ , reads:

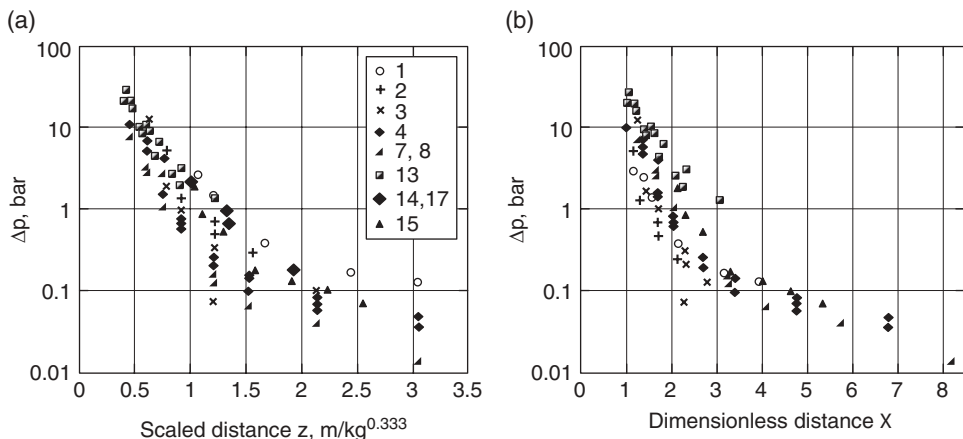


**Fig. 19.9** Blast wave peak overpressure as function of (a) the scaled distance from the charge; (b) and the dimensionless distances from the charge. The point's numbers correspond to the tests conditions of Table 19.3.

**Table 19.3** Summary of the test conditions within the close field of the internal explosion.

No	$\rho_i$ ( $kg/m^3$ )	$\rho_a$ ( $kg/m^3$ )	$\varepsilon_a$	Data	$m(lbs)$	Reference
1	1	1	0.0010	9/6/83	0.15	[30]
2	2.5	2.7	0.0027	3/28/83	1	[30]
3	5	5	0.0050	4/13/83	1	[30]
4	10	10	0.0100	11/18/82	1	[30]
5	10	10	0.0100	6/6/83	1	[30]
6	10	10	0.0100	8/9/83	1	[30]
7	16.7	18.5	0.0185	10/28/82	1	[30]
8	16.7	16.7	0.0170	4/28/83	50	[30]
9	16.7	10	0.0100	8/2/83	1	[30]
10	16.7	16.7	0.0170	3/1/9/84	1	[30]
11	50	37.04	0.0370	7/29/82	1	[30]
12	8	8	0.0125	—	18.5	[18]
13	15	—	0.015	—	1–6.2	[35]
13*	10–15	—	0.015	—	0.5–2.8	[41]
13**	10–15	—	0.01–0.015	—	1	[42]
14	32.3	28.6	0.029	—	2	[19]
15	22.2	8	0.008	—	2	[19]
16	16.13	8	0.008	—	2	[19]
17	8	4	0.004	—	2	[19]

$\rho_i$  – Intended foam density,  $\rho_a$  – Actual foam density,  $\varepsilon_a$  – Actual liquid fraction,  $m$  – charge mass

$$l = 1.24 \frac{d_p}{2F^{12}} \left( \frac{\rho_p}{\rho_a} \right)^{1/4} \left[ \ln \left( \frac{p_i}{p_{fin}} \right) \right]^{1/2} \quad (19.4)$$

where  $p_i$  is the initial overpressure at the blast wave front and  $p_{fin}$  the final pressure after mitigation,  $F = n/n_{max}$  is the “packing” factor,  $n$  is the number of particles in a specific volume,  $n_{max}$  is the maximum number of particles that could be dispersed in the same volume. For a water protection loaded by particles having a diameter  $d_p$  and a density  $\rho_p = 1 \text{ g/cm}^3$  Equation 19.4 yields:

$$l = 6.53 \frac{d_p}{2F^{12}} \left[ \ln \left( \frac{P_i}{P_f} \right) \right]^{1/2} \quad (19.5)$$

where the packing factor,  $F$ , is within the range 0.001–0.01 [38].

To determine the thickness,  $l$ , it is necessary firstly to estimate the blast threat. If, for example, a bomb detonates outside a building and raises the environment overpressure to about  $p_i \approx 100 \text{ kPa}$  (14.7 psi), the exterior windows will be broken since they sustain the overpressure  $p < 0.5 \text{ psi}$ . From this it follows that to prevent the breakage with a safety factor of two the protection has to reduce the final overpressure to about 0.25 psi. Once the blast threat and the safety factors are specified, the protective material and the barrier thickness,  $l$ , depend only on the initial overpressure,  $p_i$ . Fig. 19.10 illustrates the pressure reduction provided by barriers of sand, water droplets and polystyrene foam pellets having a similar particles diameter,  $d_p$ , and a packing factor,  $F$ .

Once the attenuation material is selected, the thickness,  $l$ , has to be adjusted according to the desired mitigation effect. To ensure that the blast overpressure  $p_i = 100 \text{ kPa}$  (= 14.7 psi) will not break the exterior windows, the final pressure has to be about  $p_f = 0.25 \text{ psi}$ . If a protective shield of water droplets having a diameter  $d_p = 0.1 \text{ mm}$  and a packing factor  $F = 0.001$  is selected, the thickness,  $l$ , of such a barrier should be about 75 cm. A close value of the pressure reduction can provide the barrier of larger droplets ( $d_p = 1 \text{ mm}$ ), while for this case the packing factor should be increased. In similar, the packing factor,  $F$ , or the thickness,  $l$ , have to be increased if the particles are denser than water. Since, generally, a

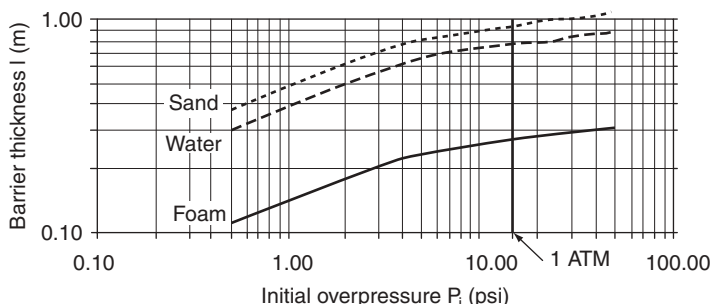


**Fig. 19.10** The blast reduction characteristics of particulate materials, which mitigate the blast pressure to 0.25 psi. Particles (droplets) diameter  $d_p = 0.2 \text{ mm}$ ,  $F = 0.001$  [38].

mitigation rate within the standard barrier is about 0.1 psi/cm, in order to reduce the blast overpressure from  $p_i > 100 \text{ kPa}$  to  $p_{final} \approx 14.7 \text{ psi}$  the barrier thickness has to be about  $l \approx 1 \text{ m}$ . A simple empirical relationship which is based on the large series of the experiments with aqueous foams is also available Palamarchyk and Postnov [14]:

$$\Psi(Y) = 20 \log \frac{\Delta p_{air}}{\Delta p_{foam}} = 3Y - 2 \quad (19.6)$$

Here the pressure reductions are related to the internal blast,  $\Delta p_{foam}$ , and to free blast in air,  $\Delta p_{air}$ . The factor  $Y = (m_f/m_{ch})^{1/3}$  is the mass ratio of foam barrier,  $m_f$ , and the spherical charge,  $m_{ch}$ , and is evidently akin to dimensionless coordinate  $X$  of Raspet and Griffiths. This equation works well at a distance  $r > 150$  charge radii,  $r_{ch}$ , and could be safely used in choosing the optimal thickness,  $l$ , if the foam density,  $\rho_f$ , the blast energy and the blast threat are known in advance Gelfand and Silnikov [9]. Using as an example of the blast threat the breakage of the windows, the final overpressure behind the protection must not to exceed about  $\Delta p_{foam}^* \approx 0.25 \text{ psi}$ . To define the pressure rise,  $\Delta p_{air}$ , the relationship of Smith and Hetherington [40] can be used:

$$\Delta p_{air} = \frac{0.975}{Z} + \frac{1.455}{Z^2} + \frac{5.85}{Z^3} - 0.019 \text{ bar} \quad (19.7)$$

The dimensionless curve  $l/r_{ch} = F(\rho_f/\rho_{ch})$ , shown as an insert in Fig. 19.11, was calculated using Equations 1.6 and 1.7. The dimensional curves,  $l(\rho_f)$ , in the main graph were calculated for standard value of the TNT density,  $\rho_{ch} = 1600 \text{ kg/m}^3$ . The mass of the spherical charge for

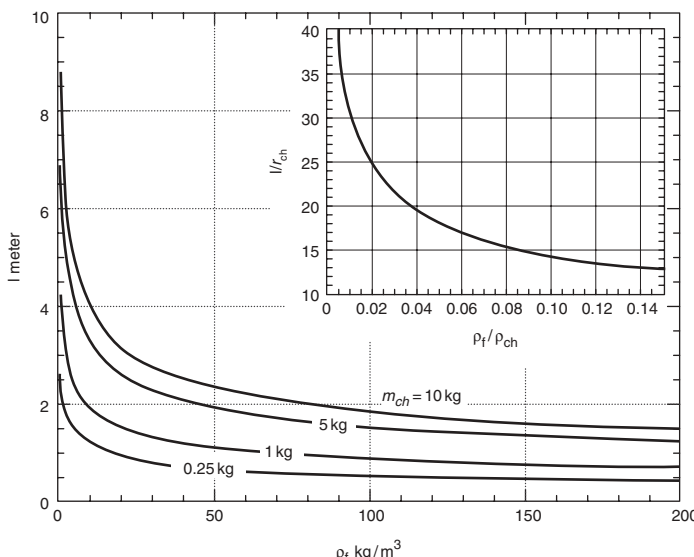


**Fig. 19.11** The thickness of the aqueous foam barrier as function of the aqueous foam density,  $\rho_f$ , and the charge mass,  $m_{ch}$ .

this case only depends on the radius,  $r_{ch}$ , and the barrier's thickness is a unique function of foam density,  $\rho_f$ . As expected, the barrier thickness,  $l$ , increases when the foam is drier and/or as the energy of the blast (mass  $m_{ch}$ ) increases. The requested pressure  $\Delta p_{foam}^* \approx 0.25$  psi at the distance  $r/r_{ch} \geq 150$  is seen to provide a foam barrier of 3 m long if foam density is  $\rho_f = 20\text{ kg/m}^3$  and the charge mass is about 1 kg. If the foam density is  $\rho_f = 50\text{ kg/m}^3$ , barrier thickness reduces to 2 m. If the charge mass increases to 10 kg a similar pressure reduction could be obtained using barriers of 4 m ( $\rho_f = 50\text{ kg/m}^3$ ) or 6 m ( $\rho_f = 20\text{ kg/m}^3$ ) in length.

In principle, the protective function of the foam barrier could be improved using solid additives which increase the reflectance at the barrier boundary. Unfortunately, this method has received only occasional attention in the current literature. Moxon *et al.* [37] were the first to measure the sound reduction caused by particulate foams and compared these data with other materials shown in Table 19.4. The Type I foam was produced by bubbling through the reagent Expandol. For Type II foam 6% water-Expandol solution was mixed in a mechanical blender. For the particulate foam a talc powder (maximal diameter 32  $\mu\text{m}$ ) was added to Type II foam. Polyurethane and polystyrene foams were obtained in the form of 8 mm beads, and vermiculite was also used for comparison. Actually, among the collected data that are presented in Table 19.4 the peak mitigation was provided by only Type II and

**Table 19.4** Performance of shock wave attenuating foam materials [37].

Material	$\varepsilon$	Bubble (beads) diameter $d_p$ mm	Pressure reduction, % ( $\Delta=8\text{ mm}$ )	Pressure reduction, % ( $\Delta=24\text{ mm}$ )
Particulate foam	0.025	0.5	72	78
Type II Foam	0.025	0.5	67	73
Vermiculite	—	—	42	61
Shaving Foam	0.1	0.02	37	56
Type I Foam	0.05	8	33	45
Polyurethane	—	—	30	39
Foam	—	—	—	—
Polystyrene Beads	—	8	—	36

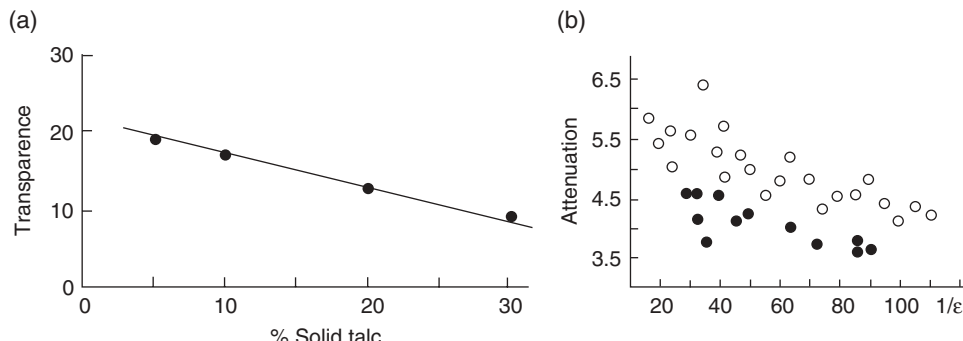


**Fig. 19.12** (a) Transparency of particulate foam barrier to sound wave vs. percentage of added talc particles [37]; (b) attenuation of sound wave vs. expansion factor,  $\text{Exp} = 1/\varepsilon$ , in conventional (open points) and particulate (close points) aqueous foams [28].

particulate foams. As to the role of the packing factor on the sound mitigation, the few papers on this subject contradict each other. While the data in Fig. 19.12a indicate that the added particles enhance the mitigation of sound, the recent results shown in Fig. 19.12b demonstrate that the sound wave mitigates less just inside the particulate foam.

### 19.3 Shock Tube Testing

#### 19.3.1 Main Restrictions

As an alternative to free field tests, shock tubes have been used in the past to simulate both the *internal* and the *external explosion* scenarios. Experiments of this type eliminate the fire ball and enable testing of the major details of the shock wave/foam interaction. When a foam barrier is positioned against the end wall of the test section, the resulting flow pattern, shown in Fig. 19.13, simulates the situation of an *external explosion*. The incident shock wave ( $In$ ) propagating in air reaches the barrier, compresses the foam and gives rise to the reflected shock wave ( $Rf$ ), which then interacts with the contact surface (CS). The air conditions at the barrier entrance are steady during the test time duration,  $\Delta t_s$ , until the arrival of the reflected shock ( $Rd$ ) [43]. In addition, since the time for the transmitted shock wave ( $Tr$ ) to reach the end wall is  $t_{Tr} > 2\Delta t_s$ , about half of its trajectory is disturbed by the arrival of the reflected shock ( $Rd$ ). To increase the test duration,  $\Delta t_s$ , it is necessary to increase the length of the channel,  $L$ . However, this does not improve the situation, since the rarefaction fan ( $RRw$ ) appears and causes the pressure to drop at the entrance and inside the barrier (its time of arrival is marked by (A):  $\Delta t_s < t_A < t_{Tr}$ ). In spite of the noted restrictions, a number of interesting features of the shock wave/foam interaction were first observed using shock tubes tests [9]. Fig. 19.14 demonstrates, as an example, the experimental relationships between the velocity,  $D$ , of the stepwise profiled shock wave and the

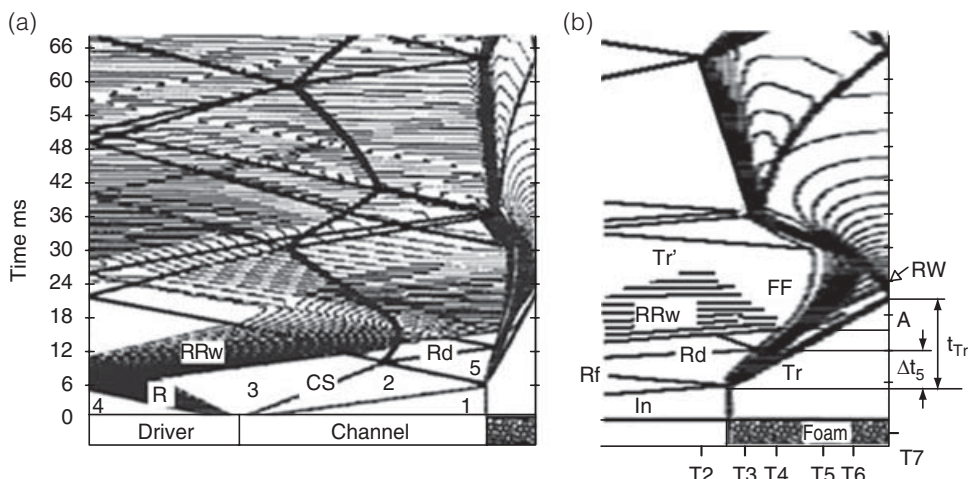


**Fig. 19.13** (a) A full-scale diagram of the shock tube flow and (b) zoomed fragment of the wave pattern inside a test section filled with wet aqueous foam,  $\alpha_0 \approx 0.2$ ,  $M_s = 1.3$ ,  $H = 0.597\text{ m}$ .

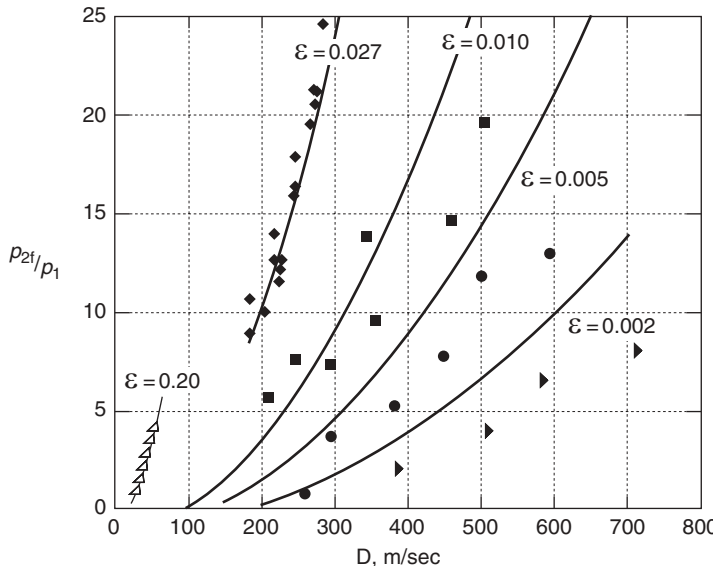


**Fig. 19.14** Pressure rise vs. velocity  $D$  of the transmitted shock wave propagating in foam columns of different liquid fraction,  $\epsilon$  [35, 43, 44].

post shock overpressure,  $\Delta p$ . Experiments with wet foam ( $\epsilon = 0.2$ ) were reported recently by Britan *et al.* [43], while the other data were published much earlier by Kudinov *et al.* [35, 44]. The shock wave velocity,  $D$ , in the drier foam, is seen to be larger while the pressure rise at the shock wave front,  $p_{2f}$ , becomes smaller. This trend correlates well also with the data recorded in a vertical shock tube by Britan *et al.* [43]. The marked stability of the shock wave propagation over the foam column was noted in the both studies. The last finding agrees well with the numerical predictions of Ball and East [36]. The disagreement between the experiments and the predictions and the pressure deficit that appears and increases when foam becomes dryer, is discussed later.

### 19.3.2 Foam Shattering

Most observations over steadily sheared foams indicate that the destructive stress within the foam is about two orders of magnitude lower than for an isolated bubble due to strong collective forces [45, 46]. This explains why the recorded value of the critical overpressure, which causes foam shattering, is only about several hundred kPa [21]. To observe the foam shattering little has been done, mainly because of the severity of the technical problems. The cheapest solution, which was explored in the 1980s is the “open shatter” technique [47–49]. A single picture per run was captured by a standard photographic camera in a dark room using a  $1\mu\text{s}$  spark. To facilitate further analysis, the time instant of the spark was synchronized with the shock wave arrival using a close positioned pressure transducer. The photographs on the top row in Fig. 19.15a show the bubbles’ structure (the mean diameter is about 2 mm) before the test, and the photographs on the bottom row were captured 20, 40, 60 and 200  $\mu\text{s}$  after the arrival of the shock wave. Each pair of the photographs of the vertical

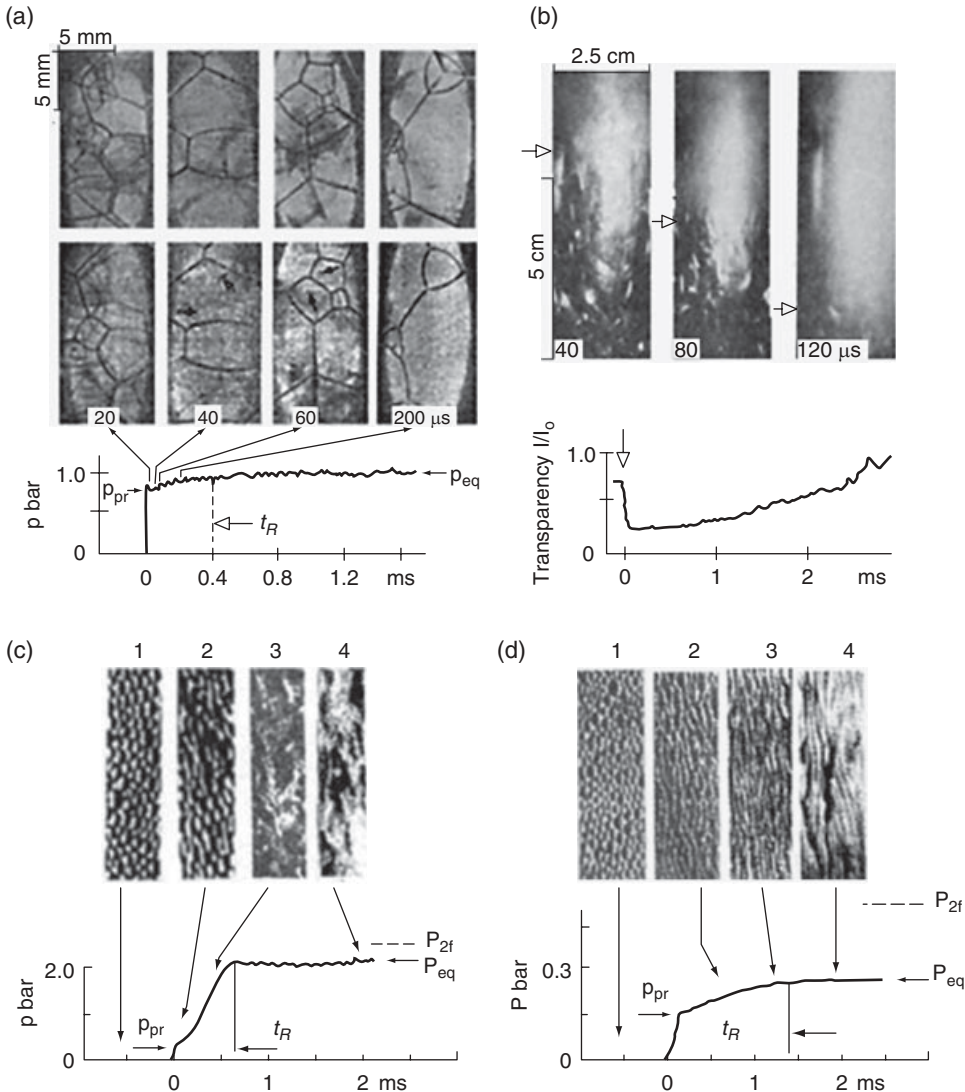


**Fig. 19.15** (a) and (b) Typical shock tube data demonstrating the dynamics of the post-shock wave pressure and the shattering of the polyhydric cells of dry foam adjacent to the shock tube wall. (Mach numbers of the air shock wave are: (a)  $M_s=1.22$ ; and (b)  $M_s=1.32$ . The initial foam density is  $P_f=4 \text{ kg/m}^3$ .) (c) and (d) Typical shock tube data demonstrating close relation between the dynamics of the post-shock wave pressure and the shattering of the wet foam cells by an air shock wave with Mach numbers. ((c)  $M_s=1.35$ ; and (d)  $M_s=1.12$ . Initial foam density is  $P_f=50 \text{ kg/m}^3$ .)

column is thus related to the specific test. The thin arrows mark the relevant amplitude of the sidewall pressure,  $p(t)$ , at the time instant the picture was captured.

An inspection of Fig. 19.15 reveals the following steps of the foam destruction phenomenon. Once the incident shock wave in air with a pressure rise,  $p_2$ , at the front first comes

into contact with the foam, at  $t=0$ , the reflected wave ( $R_w$ ) appears, which moves backward. The transmitted shock that enters the foam leaves behind the pressure,  $p_{2f}$ , which generally has to be equal to the pressure,  $p_{Rw}$ , in the air domain compressed by the reflected shock ( $R_f$ ). The foam bubbles that follow the front of the transmitted shock wave, rotate and stretch. Once passing a distance nearly equal to the size of the Plateau borders (in these tests it is about 2 mm) the foam films and the Plateau borders start to break. The droplets that appear at this stage are small and quickly picked up by the gas flow. The next portion of the liquid enters the air flow after the nodes shattering, which manifests itself as the small torches and jets marked in the pictures by the thick, black pointers. The network of Plateau borders and nodes initially adjacent to the window are ruptured later and generate large droplets. This multistage process modifies the profile of the sidewall pressure, which splits in Fig. 19.15a into a precursor of smaller amplitude,  $p_{pr}$ , and a main front of pressure,  $p_{eq}$ . Because the foam density is low ( $\rho_f = 4 \text{ kg/m}^3$ ), the impedance mismatch ( $Im$ ) at the air/foam boundary is close to unity and the reflected shock wave ( $R_f$ ) is weak. Due to this fact the pressure raised by the precursor differs slightly from the equilibrium value,  $p_{eq}$ , which however does not reach yet the final value,  $p_{2f} = p_{Rw}$ . The pressure deficit  $\Delta = p_{2f} - p_{eq}$  represents the energy losses within the relaxation zone.

The photographs in Fig. 19.15b ensure that when the impact is stronger the sequence of the processes, which has been discussed so far, breaks down. In fact, the front position marked by the arrows at the left side of each photograph ensures that the foam is destroyed immediately behind the shock wave. To resolve its' structure, the optical visualization was accomplished by measurement of the spectral transparency of the resulting mist [49]. A typical absorption curve that carries information on the optical transparency of the foam flow at the measurement point is shown in the bottom insert in Fig. 19.15b. The optical transparency reduces sharply once the transmitted shock wave appears (this time instant is marked by arrows) and then slowly increases with time until it finally reaches the value inherent to the gas flow.

The simple algorithm [47] converts the transient dynamics of this curve into the time history of the liquid fraction,  $\epsilon(t)$ , and/or the mean diameter of the water droplets,  $d_p(t)$ . More detailed numerical simulations revealed that the liquid fraction reduces in time due to evaporation of the droplets behind the shock wave [48]. Based on these findings, the shattering of the dry foam was described as a series of the subsequent events:

- (1) Deformation and rupture of the foam films, which generate the small (about  $2 \mu\text{m}$ ) drops whose initial volume concentration is  $c_v \approx 10^5$ .
- (2) Acceleration and mixing of the small droplets with air.
- (3) Evaporation of the small droplets, which causes a time reduction in the concentration,  $c_v$ .
- (4) Rupture of the Plateau borders and formation of the large drops, which then quickly accelerate and evaporate.

It should be noted that the first two events are responsible for the kinematic equilibrium and under the tested conditions terminate very quickly. In fact, the first event is completed after about  $\tau = 50 \mu\text{sec}$  and the second event after about  $\tau = 10 \mu\text{sec}$  following the arrival of the shock wave. The last two events, which continue much longer, about  $\tau > 500 \mu\text{sec}$ , are mainly responsible for the transient part of the pressure reading shown in Fig. 19.15a.

While considering the shattering phenomenon of the wet foam, it is readily seen that the pressure readings in Fig. 19.15c and Fig. 19.15d also split into a small leading precursor

and a main front. The cellular foam structure stretches within the relaxation zone and is finally replaced by the random fragments of the liquid on the surface of the window. As might be expected, the total duration of this process is sensitive to the impact intensity. For the case shown in Fig. 19.15c the transmitted shock wave is stronger and the duration,  $t_R$ , in this figure is twice as short as in Fig. 19.15d. Notice that in both cases the impedance mismatch ( $\text{Im}$ ) is larger than unity; however, the equilibrium pressure,  $p_{eq}$ , in Fig. 19.15c is really close to the value  $p_{2f} = p_s$ , while in Fig. 19.15d it is still much smaller than  $p_{2f}$ .

To identify the real process that follows the stretching, the shrink and further collapse of the foam structure, experiments of this type have to be accomplished with numerical simulations. Unfortunately, as to the theoretical efforts there is a limit to what can be done in these investigations.

## 19.4 Theoretical Approaches

### 19.4.1 Governing Processes

While the static and quasi-static properties of foam and its constituent parts could be well predicted by the SURFACE EVOLVER (SE) program, the dynamic effects remain as a considerable challenge, particularly for wet foams [50]. Using more simple phenomenological models the effect of the wall friction as the foam flows can also be taken into account [51]. However, even these simpler approaches are of little use without a fundamental knowledge of dissipation processes. The currently available evidence ensures that for an internal blast in foam the following processes are thought to be of important:

- (1) Detonation of the solid propellant.
- (2) High temperature effects at the fire ball/foam boundary.
- (3) Heat, mass and moment transfer behind the leading shock wave.
- (4) Foam rheology, bubbles rearrangement and possible shattering.
- (5) Viscous dissipation at the solid boundaries, dispersion and scattering at the bubbles.
- (6) Bubble pulsations, acoustic radiation and thermal conduction.

While the analysis of these processes has a long history, their interaction and contribution to the mitigation behavior of the resulting blast wave is not usually clear. In the early 1980s Schmidt and Kahl [52] argued, for example, that "... an aqueous foam acts to quench the strength of the blast through processes which *are not definitely established*". As another example Fig. 19.8 can again be referred to. Shea and Pater [31] qualified the trend demonstrated by the points marked 8 in the diagram as a "*typical for all foams*" even though it is presently seen that this trend contradicts the points marked 3.

The reason for this uncertainty is due to the fact that most of the first attempts were focused on a quick answer, rather than understanding the physics that is involved in the process. Moreover, as discussed so far, the information provided by free field experiments is usually limited. Along with the film that captures only the general view of the explosion, it usually involves several pressure gauges located either close or far from the explosive charge. Close to the charge the foam is quickly destroyed, the resultant flow equilibrates rapidly, and hence it can be easily represented as a single component fluid. Referring back

to the example shown in Fig. 19.7b, the related domain is located at  $X \leq 2.5$ , where all points fall on a common line for dry and for wet foams. It is clear that, within this domain, the effect of the foam structure on the pressure reduction is negligible, while the liquid fraction or foam density [21] plays the dominant role.

Far downstream, at  $X > 2.5$ , since the leading shock wave is much weaker, the foam sustains the impact and this dominates the processes from N4 to N6 (the processes listed above) acting on the “bubble scale.” The pressure traces enable the difference between these processes to be measured and evaluated. Due to dispersion, while the pressure traces spread in time, the impulse,  $\int_0^t pdt$ , remains constant. In contrast, since viscous dissipation reduces the peak pressure, the duration of positive phase remain unchanged. As a result the impulse has to reduce [26]. The series of processes N6 is mainly important for sound-wave mitigation [29, 53–56]. In wet foams, for example, the acoustic radiation is small, while the natural frequency of the bubble pulsations (compared to the acoustic frequency) is high. As the foam becomes drier or starts to move, the role of the bubble pulsation increases and viscous dissipation enhances the wave mitigation [26]. The different role of these processes in wet and in dry foams can explain the 25–30% shift between points that appears in Fig. 19.7b at  $X > 2.5$ . Due to the small temperature jump at the wave front the heat transfer is less effective and the droplets (if they appear) achieve equilibrium with the air flow later. As a result, the emerging shock wave in air is stronger and it mitigates slower.

#### 19.4.2 Hierarchy of the Process

Initially most authors did not assign a specific meaning to the hierarchy of the modeling issues. Since available experiments did not resolve the features on the bubble scale, the adopted philosophy was to construct the simplest possible model to describe the macro characteristics, namely, the pressure rise and the velocity of the blast wave. Neglecting dispersion and dissipation on the bubbles, the flow of the gas–droplet mixture is described by the following system of unsteady Euler equations:

$$\frac{\partial \rho}{\partial t} + u \frac{\partial \rho}{\partial r} + \frac{\rho}{r^{v-1}} \frac{\partial r^{v-1} u}{\partial r} = 0 \quad (19.8)$$

$$\rho \left( \frac{\partial u}{\partial t} + u \frac{\partial u}{\partial r} \right) + \frac{\partial p}{\partial r} = 0 \quad (19.9)$$

$$\rho \left( \frac{\partial e}{\partial t} + u \frac{\partial e}{\partial r} \right) + \frac{p}{r^{v-1}} \frac{\partial r^{v-1} u}{\partial r} = 0 \quad (19.10)$$

$$e = e(p, \rho) \quad (19.11)$$

Here  $p$ ,  $u$ ,  $\rho$ , and  $e$  are the average pressure, velocity, density and internal energy of the mixture, the values of  $v = 1, 2, 3$  are used for the cases of plane, cylindrical and spherical

symmetry of the problem. Historically, the first attempts at treating the foam flow as a gas–droplet mixture were associated with the Effective Gas Flow (EGF) equation of state [57]:

$$e = \frac{p(1 - \varepsilon_1)}{\rho(\Gamma_{foam} - 1)} \quad (19.12)$$

If the partial pressure of the liquid phase is neglected, the thermal and the kinematics equilibrium between the gas and the liquid phases are thought to be established, the effective adiabatic index of EGF,  $\Gamma_{foam}$ , is:

$$\Gamma_{foam} = \Gamma_{eq} = \gamma(1 + \eta\delta)(1 + \gamma\eta\delta)^{-1} \quad (19.13)$$

where  $\eta = \frac{\rho_w \varepsilon}{\rho_g(1 - \varepsilon)}$  is the ratio of the mass concentration of the liquid and the gas phases,

$\varepsilon$  is the condensed phase volume fraction,  $\delta = c_w/c_p$  is the ratio of the specific heat of the condensed phase to the specific heat of the gas (both at a constant pressure). The reduced number of key parameters makes this model convenient for simple calculations, which initially were focused on the pressure rise,  $p_{2f}/p_1$ , recorded in the shock tube tests [9, 44, 58–61]:

$$\frac{p_{2f}}{p_1} = \frac{p_{2f}}{p_1} = \frac{2\Gamma_{eq} M_{eq}^2 - (\Gamma_{eq} - 1)}{\Gamma_{eq} + 1} \quad (19.14)$$

where for the shock wave Mach number  $M_{eq} = D/c_{eq}$  the equilibrium speed of sound in the undisturbed foam is  $c_{eq}^2 = \Gamma_{eq} \frac{p_1}{\rho_{f1}(1 - \varepsilon_1)}$ . Notice that when  $p_{2f}/p_1 >> 1$ , Equation 19.14 is reduced to:

$$p_{front} = \frac{2\rho_{f1}D^2}{\Gamma_{eq} + 1} \quad (19.15)$$

It should be noted that the resulting predictions shown by solid curves in Fig. 19.14 make it clear that as the foam becomes drier and/or the shock wave velocity,  $D$ , increases, the recorded pressures tend to be smaller than calculated. This agrees well with the experimental findings in Fig. 19.15, which ensure that the initial pressure rise in the dry foam is usually smaller. Actually, to reach the equilibrium in these tests the shock tube has to be much longer [35].

Despite being neglected by this non-equilibrium behind the shock wave, the simple EGF model was used to predict the behaviors of a real blast in foam. These simulations assumed, that the energy,  $E_0$ , which is immediately transferred from the equivalent “point” explosion to the foam is:

$$E_0 = [2(\nu - 1)\pi + (\nu - 2)(\nu - 3)] \int_0^{r_{front}} \rho(e + 0.5u^2) r^{\nu-1} dr \quad (19.16)$$

The foam is treated as an ideal gas with an adiabatic index  $\Gamma_{foam} = \Gamma_{eq}$  and the solution of the problem was sought to be valid when: (i) the distance passed by the blast wave front was  $r_{front} >> r_{ch}$ ; (ii) the mass of the foam carried out by the blast wave exceeds the mass of

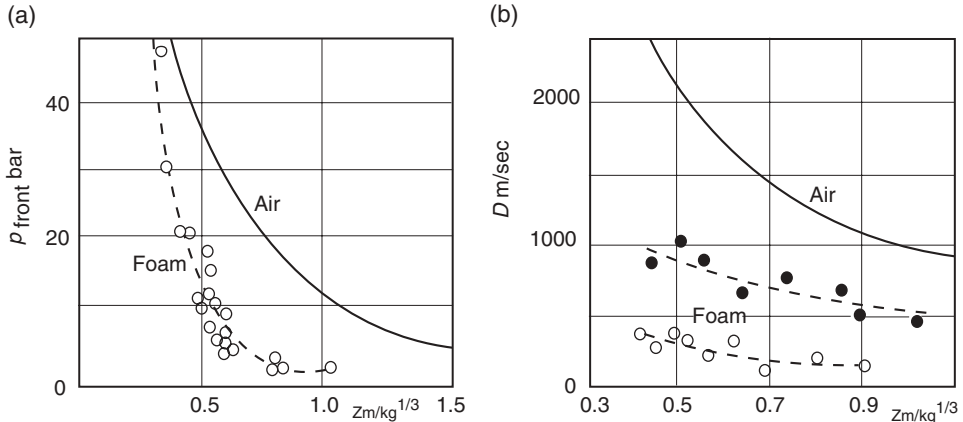


**Fig. 19.16** (a) Pressure jump and (b) propagating velocity of the blast wave as a function of distance  $Z$  [63]. ( $\varepsilon_i = 0.010$ ,  $\eta = 10$ ,  $\Gamma_{eq} = 1.008$ ). The mass of the explosive charges  $w$  (hexogen) was changed from 500 to 2800 g, (open points) and from 1 to 5 g (solid points).

the detonation products,  $m \approx m_{ch}$  (kg in TNT equivalent); (iii) the blast wave pressure is  $p_{front} > p_1$  and the energy of the blast,  $E_0$ , which is transferred to foam is:

$$E_0 = \frac{2(\nu-1)\pi + 0.5(\nu-2)(\nu-3)}{2\nu(\Gamma_{eq}-1)} r_{front}^\nu \rho_1 D^2 (1-\varepsilon_i)^2 \quad (19.17)$$

Similar to Equation 19.15 the pressure rise at the blast wave front is [62]:

$$p_{front} = \frac{3}{\pi} \frac{\Gamma_{eq}-1}{\Gamma_{eq}+1} \left( \frac{E_0}{1-\varepsilon_i} r_{front}^{-\nu} \right) \quad (19.18)$$

From Equation 19.18 it is readily seen that for the case of a spherical blast ( $\nu = 3$ ), the pressure rise reduces as  $\sim 1/r_{front}^3$  while since  $p_{front} \sim D^2$  the blast wave velocity mitigates as  $\sim 1/r_{front}^{1.5}$ .

Relating the pressure rise at the front of the air blast to that in the foam results in:

$$K = \frac{p_{air}}{p_{foam}} = (1-\varepsilon_i) \frac{\gamma-1}{\gamma+1} \left( \frac{\Gamma_{eq}+1}{\Gamma_{eq}-1} \right) \quad (19.19)$$

In terms of the reduced distance to the charge,  $Z = r_{front} / \sqrt[3]{m_{ch}}$ , the EGF model predicts a similar pressures rise,  $p_{front}$ , and a constant pressure reduction  $K$  for all foams having similar value of adiabatic indices,  $\Gamma_{eq}$ . It is interesting to note that the explosive type and the charge masses for these cases could be significantly different [62]. However, actually as can be seen in Fig. 19.16a, the pressure rise recorded in the foam, close to the charge, tends to exceed the values of the air blast while at a far distances from the charge, it

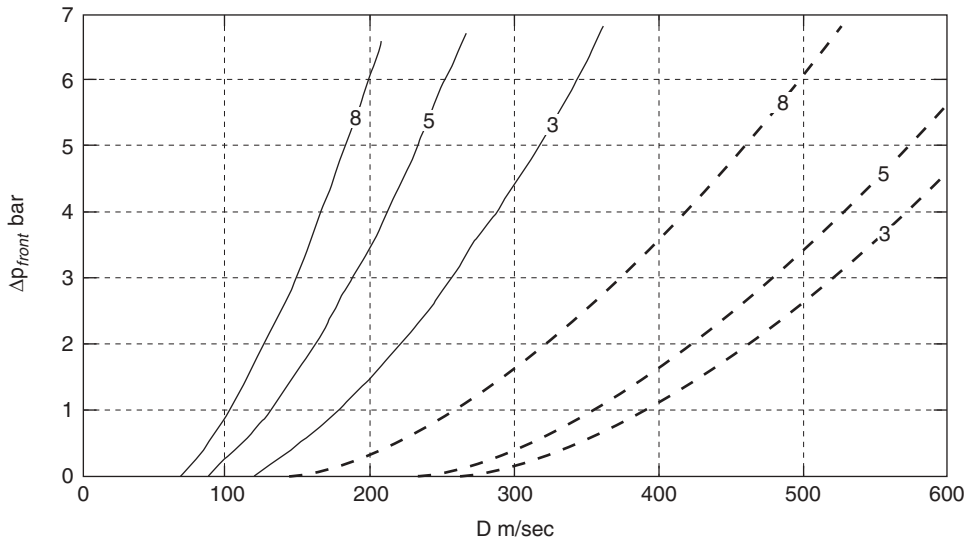


**Fig. 19.17** Blast wave pressure–velocity relationship as measured (dashed lines) and predicted (solid lines) based on the EGF model [30]. The numbers refer the curves to the tested conditions shown in Table 3.

becomes ten times smaller. Evident sensitivity to the charge mass,  $m_{ch}$ , illustrates the blast wave velocity,  $D$ , in Fig. 19.16b. These data together with the data presented in Fig. 19.17 clearly indicate that these key parameters of the blast could not be simulated correctly based on the EGF model. To improve the situation, Panczak and Krier [64] and later Zhdan [65] used more comprehensive models of the internal explosion. They both assumed that once the detonation enters the foam ( $x = r_{ch}$ ) the blast wave has a spherical shape with parameters typical for a self-similar detonation [66]. The foam was treated as a homogeneous pseudo-fluid having the average properties of air and water. To simulate the pressure reduction histories shown in Fig. 19.18, Panczak and Krier [64] resolved the system Equations 19.8–19.11, which was complemented with an equation accounting for the vaporization of the liquid.

The data in Fig. 19.18 show that close to the charge the pressure rise,  $\Delta p_{front}$ , in the foam is higher than in the air. A similar trend interpreted as a result of the high impedance mismatch,  $Im > 1$ , can be found also in Fig. 19.16a. As the blast wave recedes from the fire ball and moves further than  $r/r_{ch} \sim 10$ , the mitigation in the foam dominates while the role of the evaporation factor reduces. The liquid phase, which is left in the post-wave flow, causes the blast wave to mitigate more. Unfortunately, the experimental points which fill the gap between the SANDIA tests and the simulations at  $r/r_{ch} > 10$  are absent in the closer field. As a result, the predicted crucial importance of the water vaporization in the field close to the explosion still remains unproven by the experiment. It appears also surprising that the predicted pressure peak in the wetter foams is higher than that in the drier foams. Note that the approximations of the SANDIA tests illustrate the opposite trend.

To obtain the results represented in Fig. 19.18, Zhdan [65] complemented the system given by Equations 19.8 to 19.11 with the additional term responsible for the contact heat

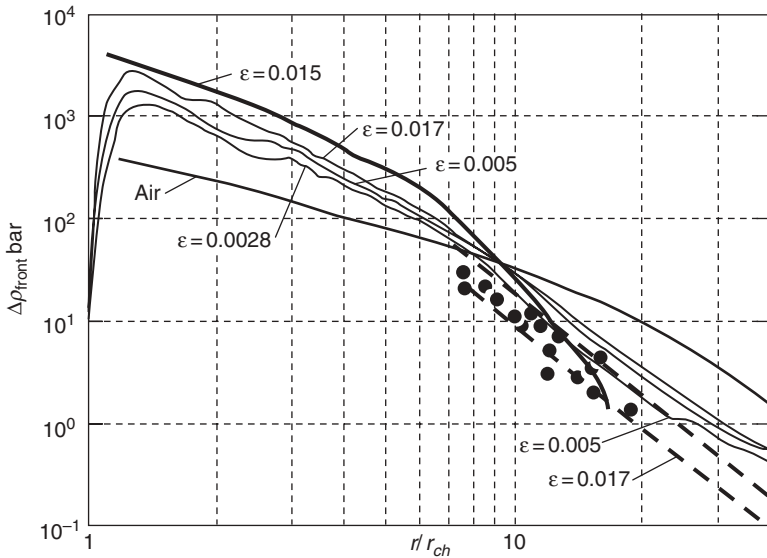


**Fig. 19.18** Pressure reduction vs. dimensionless distance from the charge. All but one solid lines show simulations of Panczak & Krier [64], the dashed lines are approximation of SANDIA, the solid line for  $\epsilon = 0.015$  is calculated by Zhdan [65], the points are experiments of Vachnenko et al. [41]. For the tested conditions see Table 3.

transfer between the liquid and the gas phases [63, 68]. The term responsible for the contact heat transfer between the liquid and the gas phases was introduced into the equation of energy:

$$\frac{\partial e_l}{\partial t} + u \frac{\partial e_l}{\partial r} = \frac{p}{\rho_l^2} \left( \frac{\partial \rho_l}{\partial t} + u \frac{\partial \rho_l}{\partial r} \right) + \frac{Q}{\beta_l \rho} \quad (19.20)$$

$$Q = \frac{12 \varphi_g \beta_l \rho \gamma_g r_{ch}}{\rho_l d^2 \text{Pr}(\gamma_g - 1) \mu_g} (T_g - T_l) \quad (19.21)$$

where  $\varphi$  is the viscosity,  $\mu$  is the molecular weight,  $T$  is the temperature,  $d = d_1 (\rho_l / \rho_g)^{1/3}$  is the local diameter of the droplets, and  $\text{Pr} = 4\gamma_g/(9\gamma_g - 5)$  is the Prandtl number; the indices  $g$  and  $l$  indicate the gas and the liquid phases, respectively. Since the mass concentration is an additive function:  $\beta_g + \beta_l = 1$ . Assuming that  $u_g = u_l = u$  the equations for the density and for the internal energy take the form:

$$\frac{1}{\rho} = \frac{\beta_g}{\rho_g} + \frac{\beta_l}{\rho_l}; \quad e = \beta_g e_g + \beta_l e_l$$

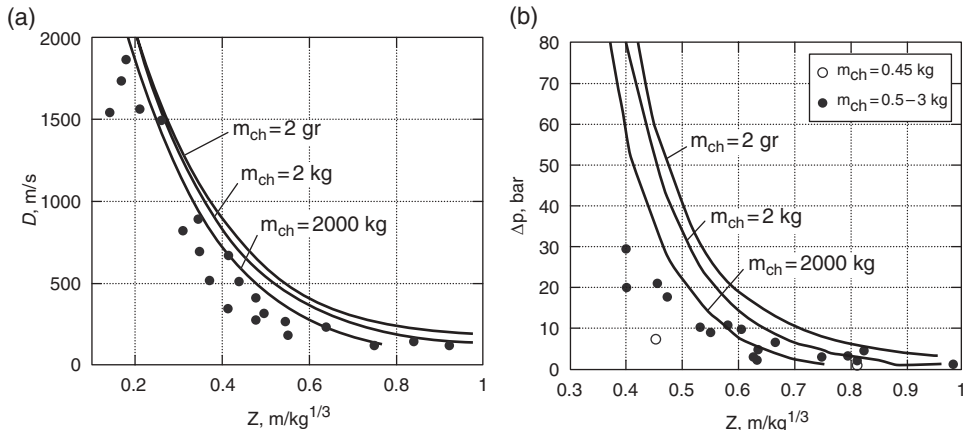


**Fig. 19.19** The blast wave velocity (a) and overpressure (b) as a function of distance  $Z$ . Numerical predictions for  $\varepsilon=0.015$  are shown by solid lines Zhidan [65], the points show the experimental data of SANDIA ( $m_{ch}=0.45 \text{ kg}$ ) and Kudinov et al. [35] ( $m_{ch}=0.5 \div 3 \text{ kg}$ ).

For the gas phase, the equation of state for an ideal gas, that is  $e_g = p/(\gamma_g - 1)\rho_g$ , was used. When the type and quantity of the explosive are known in advance, the transient dynamics of the heat transfer behind the blast wave is thus sensitive to: the foam liquid fraction,  $\varepsilon$ , the initial diameter of the droplets,  $d_c$ , and the size,  $r_{ch}$ , or mass,  $m_{ch}$ , of the charge. Moreover, if the relaxation length is about several cell diameters,  $d_c$  and  $r_{ch} > d_c$ , the kinematic equilibrium is established at  $r_{eq} > 10d_c$ . If, for example,  $d_c \approx 2 \text{ mm}$ , for most practical cases this requirement is met when  $m_{ch} \geq 0.05 \text{ kg}$ . Based on the Equation 19.21 the unsteady heat transfer has to depend on the droplet diameter,  $d$ , and on the charge mass,  $m_{ch}$ . Since  $Q \sim r_{ch}/d^2$ , increased energy,  $E_0$ , or mass of the charge,  $m_{ch}$ , intensify the heat transfer process and the gas-droplet flow reaches equilibrium more quickly. The presence of this feature illustrates the series of the simulated curves in Fig. 19.19, which ensures that the blast wave mitigates more quickly as the charge's mass,  $m_{ch}$ , increases. Unfortunately, due to the high scattering of the points in this figure this prediction remains unapproved by the experiment.

As to the role of the evaporation, it was found that close to the charge (at  $Z < 0.15$ ) where the temperature is high and the liquid is overheated, this effect is very small. Downstream from the charge, when  $Z > 0.35$  and the overpressure is reduced to about  $\Delta p_{front} < 90 \text{ bar}$  the evaporation is found to be impossible at all [65]. The highest contribution of this effect would thus be expected just within the range  $0.35 > Z > 0.15$  when the blast wave parameters were not registered.

Rather than including new processes into the model, which at this stage underestimates the recorded mitigation, a group of researchers led by Palamarchuk from Paton Institute of Electric Welding (Kiev, Ukraine) suggested a modified expression for the adiabatic index,  $\Gamma_{foam}$  [35]:

$$\Gamma_{foam} = \gamma \frac{1 + \eta \delta T_l / T_g}{1 + \gamma \eta \delta T_l / T_g} \quad (19.22)$$

As long as  $T_g \neq T_l$  this indicates that  $\Gamma_{foam} \neq \Gamma_{eq}$  and two limiting conditions are possible: (1) when the blast wave appears,  $T_l < T_g$ , and for these frozen conditions  $\Gamma_{foam} \approx \gamma = 1.4$ ; and later (2) when the thermal equilibrium is eventually reached,  $T_l = T_g$ , one gets  $\Gamma_{foam} = \Gamma_{eq} \approx 1.001$  ( $\varepsilon \approx 0.06$ ). Exploring this concept further, for  $v = 3$ ,  $\Gamma_{eq} - 1 = (\gamma - 1)/(1 + \gamma\delta\eta) \approx (\gamma - 1)/\gamma\delta\eta$  can be obtained. Thereafter, combining Equations 19.18 and 19.22 results in:

$$p_{front} \approx 0.5(\Gamma_{foam} - 1) \frac{E_0}{r_{front}^3} \sim \frac{0.5(\gamma - 1)}{\gamma\delta} \frac{T_g}{T_l} \frac{E_0}{\eta r_{front}^3}$$

or finally:

$$p_{front} \sim \frac{0.5(\gamma - 1)}{\gamma\delta} \frac{T_g}{T_l} \frac{m_{ch}}{\rho_{foam} r_{front}^3} \quad (19.23)$$

where the third multiplier in the right hand part is a well known dimensionless coordinate,  $X = \frac{m_{ch}}{\rho_{foam} r_{front}^3}$  introduced by Raspert and Griffiths [21]. If so, rewriting Equation 19.23 gives:

$$p_{front} \sim \frac{0.5(\gamma - 1)}{\gamma\delta} \frac{T_g}{T_l} X \quad (19.24)$$

Based on this simple analysis, it seems reasonable that the pressure rise,  $p_{front}$ , is largely governed by the foam density only when  $T_g/T_l \sim 1$ , while it has to depend also on the unsteady heat transfer when  $T_g/T_l > 1$ . To validate this conjecture the values of  $p_{front}$  are reproduced in Fig. 19.20 while separating the available data into two categories: recorded inside (a and b) and outside (c and d) the foam barrier. Interestingly, is that representing,  $\Delta p_{front}$ , versus the dimensionless length,  $X$ , in Fig. 19.20b does not reduce, as expected, the high scatterings of the points. However, on second thought it is not surprising, since the irreversible or waste work lost by the blast wave inside the foam as discussed so far depends on a number of complex processes. The slip, the inter-phase heat transfer and the refraction of the blast wave at the foam/air interface can eventually change the pressure reduction [21]. If so, any disagreement or scattering between the different points in Figs. 19.20a and 19.20b is a clear response illustrating how these processes proceed with time and distance [21, 63]. In contrast, for the emerging shock wave in air, the resulting points presented in Fig. 19.20d scale much better than in Fig. 19.20c. This indicates that using the dimensionless length,  $X$ , for this case provides unification of the data quite well. These give further support to the common knowledge that the unsteady process affecting the blast wave mitigation in air quickly decays. Moreover, this ensures that the final pressure reduction behind the emerging shock is mainly governed by the barrier's density,  $\rho_f$ , which agrees well with the main idea expressed by Equation 19.24.

To gain some insight into the contribution of each process to the final mitigation, several simulated curves,  $\Delta p_{front}(r/r_{ch})$ , illustrating different approaches to this problem are compared in Fig. 19.21 with the experiments of Palamarchuk and Malakhov [42]. To consider the internal explosion of 1 kg TNT in foam whose liquid fraction is in the range  $0.01 \leq \varepsilon \leq 0.015$ , the system of Equations 19.8 to 19.11 was complemented with equations accounting

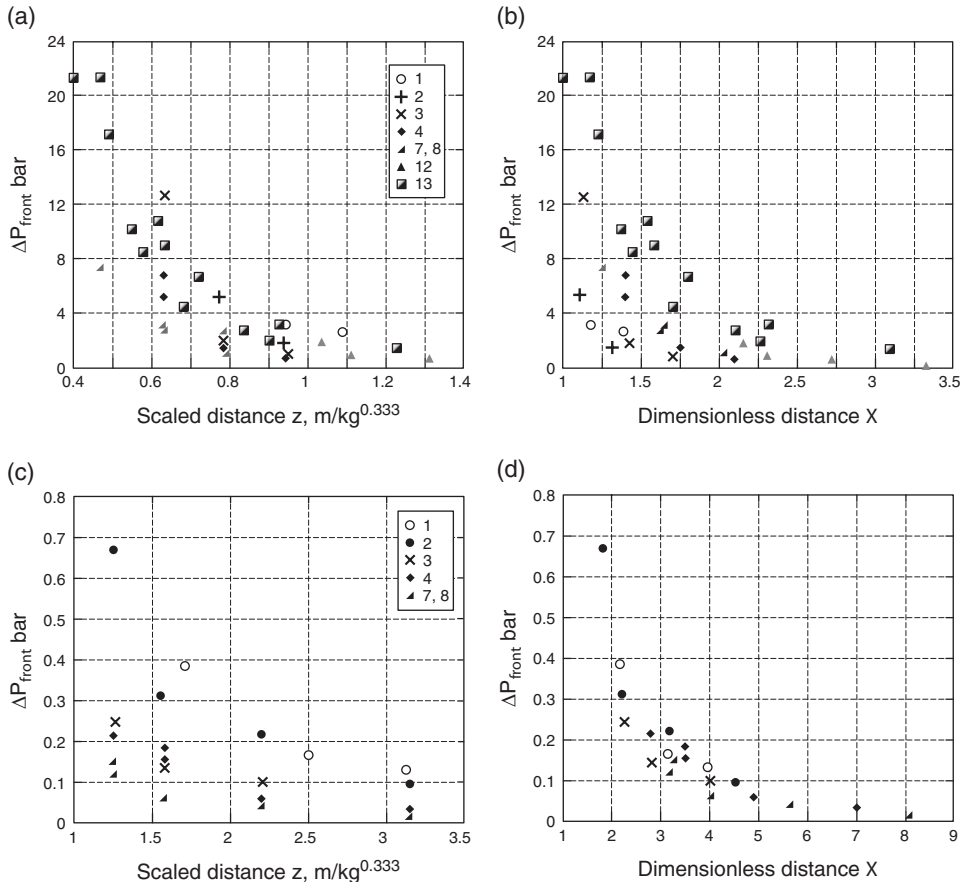


**Fig. 19.20** Blast wave peak overpressure recorded inside the foam (a & b) and in air downstream of the foam/air boundary (c & d). The points are plotted as function of the scaled and dimensionless distances from the charge. The numbers of the point correspond to the test conditions of Table 19.3.

for the expansion of the detonation products. When the expansion is isentropic, the resulting pressure change is:

$$p = A \rho_{dp}^n + (k-1) \rho_{dp} E_{dp} \quad (19.25)$$

$$p = A \frac{n-1}{k-1} \rho_{dp}^n + B \rho_{dp}^k$$

where the density of the detonation products,  $\rho_{dp}$ , and the constants A, n and B depend on the initial parameters, that is, the velocity,  $D_{dp}$ , the pressure rise at the blast wave front in the solid,  $E_{pd}$ , is the internal energy, and  $k$  is the adiabatic index of the detonation products. The pressure reduction curves in foam are compared in Fig. 19.21 with the mitigation history

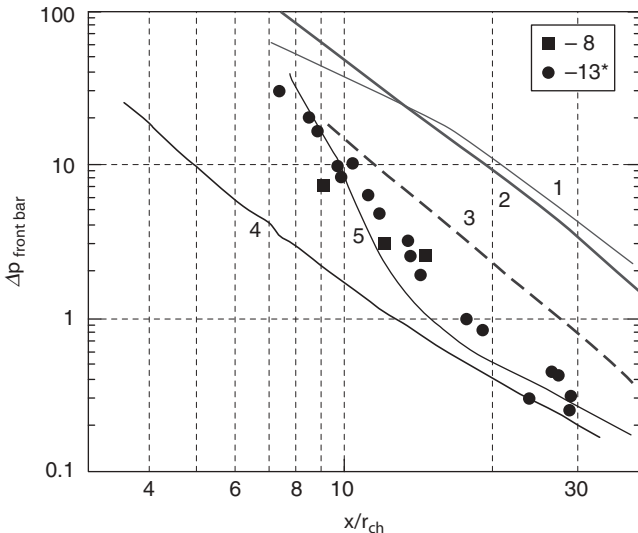


**Fig. 19.21** Pressure reduction vs. dimensionless distance from the charge. The numbers of the points correspond to the test conditions of Table 19.3.

(curve 1) for the blast wave generated by a free explosion in air. To be certain that this mitigation history is credible the simulations were repeated while replacing the real energy of the blast,  $E_0$ , by the energy of the equivalent point explosion,  $E_{pe} = \chi E_0$ , where the coefficient  $\chi$  reads:

$$\chi = 1 - \frac{p_1 V_{end}}{(k-1)E_0} + \frac{p_1 (V_{in} - V_{end})(1 - \varepsilon_1)}{(\Gamma - 1)E_0} \quad (19.26)$$

where the difference between the initial,  $V_{in}$ , and the final,  $V_{end}$ , volumes of the detonation products is a direct result of their isentropic expansion. After this correction, the final result shown by curve 1 was changed, however only slightly, because the internal energy of the detonation products is much higher than that of air and  $\chi \approx 1$ . Curve 2 corresponds to the blast wave mitigation in foam for the frozen conditions, when  $\Gamma_{foam} = \gamma$ . In the far field both curves approach each other because the related equations of state for these two cases differed due to the term  $(1 - \varepsilon_1)$ , which for dry foams ( $\varepsilon = 0.01 \div 0.015$ ) causes negligible effect on the pressure rise,  $p_{front}$ .

Simulations based on the equilibrium approach,  $\Gamma_{foam} = \Gamma_{eq}$ , shown by curve 3 fall below curves 1 and 2 and above the experimental points. This is probably due to one or more of the following effects: the liquid compressibility, the evaporation effect and the heat exchange between the explosive products and foam [42, 68] (Palamarchuk and Malakhov). Based on serial calculations it was found that the water compressibility has no effect on the resulting data, while due to evaporation the pressure rise in the close field has to increase by up to 40%. This is evidently suspicious since it will cause a much higher disagreement with the experiments. The most plausible reason is the neglect of a twofold effect inherent in the initial stage of the blast wave formation:

- The first is the hot fragments of the solid explosive, which leave behind the explosive products and thus remove partly the energy of the blast.
- The second is the non-adiabatic expansion of the explosive products, which has already been discussed.

As a result, the boundary between the blast products and foam becomes unstable [65], the heat transfer with foam is more effective and the driving force that pushes the foam away mitigates more quickly. Beyond this stage, when the blast wave and the detonation products already move separately, the “dynamic scale” of the explosive products,  $L$ , is changed with distance,  $r_{front}$  [69]:

$$\left(\frac{r_{front}}{L}\right)^3 = \frac{e_1 m_1(r_{front})}{E_0} = \frac{E'}{E_0} = R'$$

where  $m_1(r_{front})$  is the total mass and  $e_1$  is the specific internal energy of the medium entrapped by the shock wave,  $E' = e_1 m_1(r_{front})$ . For the pressure rise caused by the blast wave far from the explosion field, the refined solution gives the following analytical formulas for the Mach number of the blast wave [68]:

$$M_s^2 = 1 + \left[ \sqrt{1 + (1 + 2\Gamma_{eq} R')} \right] / \Gamma_{eq} R'$$

and for the overpressure:

$$\frac{p_{front} - p_1}{p_1} = \frac{2}{\Gamma_{eq} + 1} \frac{1}{R'} \left( 1 + \sqrt{1 + 2\Gamma_{eq} R'} \right) \quad (19.27)$$

Curve 4 in Fig. 19.21, which is based on these solutions, correlates well with the experiment at  $r/r_{ch} > 13$ , and it over-predicts the recorded mitigation in the close field when the flow is approaching the frozen conditions and  $\Gamma_{foam} \rightarrow \gamma$ .

To predict the mitigation behavior in the wide range of the tested conditions, the better solution is to combine the system Equations 19.8 to 19.11 with Equation 19.22. Since the ratio  $T_g/T_l$  is usually unknown in advance Palamarchuk and Malakhov [42] suggested using instead the relaxation equation:

$$\Gamma_{foam} = \Gamma_{eq} + (\gamma - \Gamma_{eq}) \exp(-\theta/t^*) \quad (19.28)$$

where  $\theta$  is the residence time, that is, the time that it takes for the specific volume of the liquid to pass over the relaxation zone of duration,  $t_R$ , and  $t^*$  is the characteristic time of the heat transfer process, which can be found as the solution of the following differential equation:

$$\frac{\partial \theta}{\partial t} + u \frac{\partial \theta}{\partial r} = 1 \quad (19.29)$$

for  $t = 0$  and  $r = r_{front}$ ,  $\theta = 0$ . During the blast wave formation, when  $\theta < < t^*$ , it can be read that  $\Gamma_{foam} = \gamma$  while at the final stage of the blast wave propagation, when  $\theta > > t^*$ ,

$\Gamma_{foam} = \Gamma_{eq}$ . The lacking value,  $t^*$ , could be found from the optimal matching between the recorded and the predicted rate of reduction of the pressure,  $dp/dr$  [35]. A simpler way is to use for  $t^*$  the following expression:

$$t^* \approx \frac{\rho_0 d^2 c_w}{12 \lambda_a} \quad (19.30)$$

where  $c_w$  is the specific heat of the liquid,  $\lambda_a$  is the heat transfer coefficient for air and the droplet diameter,  $d$ , is used as a scaling factor for a film's thickness. When  $d = 20\text{--}30\mu\text{m}$ ,  $t^* = 130\text{--}300\mu\text{s}$  is obtained, which agrees well with the estimation reported by Kudinov *et al.* [35]. With this knowledge in hand, it was revealed that the final result is very sensitive to the type of the detonation, the expansion rate and the real energy of the blast [42]. To account for the last factor it was suggested to use, instead of Equation 19.26, the following expression:

$$\chi = 1 + \frac{2 - \Gamma_{eq}}{\Gamma_{eq} - 1} \frac{E(r_{ch})}{E_0} \quad (19.31)$$

The resulting curve 5 in Fig. 19.21, which correlates much better with the experiments in a wide range of the tested conditions, was calculated based on the system of Equations 19.8 to 19.11 complimented with Equations 19.28 to 19.31.

Among the other attempts to simulate *the internal explosion* in foam the most recent calculations were made by Crepeau *et al.* [70] who used the SHAMRC code. Unfortunately, the code itself, the results and their comparison with the SANDIA tests are reported very briefly and this complicates the discussion. Similar investigations, based on shock tube tests, were reported in more details even in early 1980s by Britan *et al.* [20] and Vasiliev *et al.* [61]. The presented Dusty-Gas-Droplets (DGD) model neglected the fire ball but accounted for the transient processes in the gas–droplet flow that followed the foam shattering. The energy losses responsible for the acceleration of the droplets, heat transfer, evaporation and condensation of the water vapor are included as source terms in the right hand side of the Equations 19.8 to 19.11. Unfortunately, to date to validate this model the authors used only a restricted number of laboratory tests with weak shock waves that were conducted in shock tubes. The present model has not yet been applied to predict the parameters of real explosions that are realized in free field tests.

## 19.5 Conclusions

Since nowadays improved numerical schemes are starting to mature, the combined contribution of simulations and recorded blast wave mitigation in foam can help in better clarifying the physical pattern. In this context the knowledge reviewed in this paper brings additional challenges, both theoretical and experimental. The reasons stem from the fact that the foam has an unstable bubble structure. It is initially prone to decay, then passes into a non-homogeneous gas–droplets mixture behind the shock and only finally tends to reach equilibrium. These ever changing features of the mitigation material have to be considered by modern simulations. However, this is not the case and even the most comprehensive

codes in their present form fail to predict the main process that follows the foam collapse. Little has been done also to account for the role of the foam decay on these phenomena. However, as a direct consequence of the resulting non-homogeneity of the foam barrier at the instant of impact, the droplets behind the blast wave becomes polydisperse. Without specifying their transient features, the blast wave origin and its propagation history inside the protective barrier cannot be simulated correctly. Different phenomenological approaches discussed in this paper are rather complex and have to be examined in the wider range of the materials and the impact conditions. On the other side, the experimental evidence illustrating the foam's behaviors before and after the collapse as well as heating and evaporation of the liquid phase are also restricted. Novel promises in this field demonstrated by the particulate foams have only just begun and require more experiments. As to the test rigs, the controlling shock tube tests in the laboratories will continue in order to make significant progress in the kinetic analysis of the post-blast conditions in foam because they are superior. The optical control and the time history of static and dynamic pressure fields can give enough information on the relaxation and/or redistribution of the impact energy in freshly prepared or decaying foam samples. This information is of prime important to simulate correctly the experimental findings observed in shock tube tests. Much more expensive free field explosions are also important. While the techniques used in these tests are still restricted the recorded pressure readings carry information on the processes inherent only to real explosions. As shown in this review paper, to improve the available physical models they have to include the consequences of the fire ball, the expansion of the blast products and the strong heat transfer at the blast/foam boundaries registered in these tests.

## Acknowledgements

The authors are grateful to Mr Michael Liverts for his help. Appreciation is also expressed to Professor Boris Palamarchuk for fruitful discussions and for sharing with us his publications which were not easily accessible.

## References

- [1] A. Britan and A. Levy. Weak shock wave interaction with inert granular media. In *Handbook on Shock Waves*, G. Ben-Dor, O. Igra and T. Elperin (eds). Academic Press, Boston, MA (2001).
- [2] A. Britan, H. Shapiro and G. Ben-Dor. The contribution of shock tubes to simplified analysis of gas filtration through granular media. *J. Fluid Mech.*, **586**: 147–176, (2007a).
- [3] A. Britan, A.V. Karpov, E.I. Vasilev, O. Igra, G. Ben-Dor and E. Shapiro. Experimental and Numerical Study of Shock Wave Interaction With Perforated Plates. *ASME J. Fluids Eng.*, **126**: 399–409, (2004).
- [4] N. Kambouchev, L. Noels and R. Radovitzky. Numerical simulation of the fluid–structure interaction between air blast waves and free-standing plates, *Comp. and Struct.*, **85**: 923–931, (2007).
- [5] Z. Su, W. Peng, Z. Zhang, *et al.* Experimental investigation of a novel blast wave mitigation device. *Shock and Vibration*, **16**(6): 543–553, (2009).
- [6] R.I. Nigmatulin. *Dynamics of Multi-Phase System*. Volumes 1 and 2. Nauka, Russia (in Russian), 1987.
- [7] V.E. Nakoryakov, B.G. Pokusaev and I.R. Shreiber, *Wave Propagation in Gas-Liquid Media*. Boca Raton: CRC Press, NY, 1993.

- [8] V.K. Kedrinsky. *Hydrodynamics of explosion: experiment and models*. SO RAS, Novosibirsk, 2000 (in Russian).
- [9] B.E. Gelfand and M.V. Silnikov. *Explosions and blast control*. Asterion, St. Petersburg, (2004).
- [10] K.J. Graham and R.G.S. Sewell. US Patent 4,543,872, (1985).
- [11] A. Saint-Jalmes, M.U. Vera and D.J. Durian. Free drainage of aqueous foams: Container shape effects on capillarity and vertical gradients. *Europys. Lett.*, **50**(5): 695–701, (2000).
- [12] A. Saint-Jalmes, Y. Zhang and D. Langevin. Quantitative description of foam drainage: transitions with surface mobility. *European Phys. J. E*, **15**: 53–60, (2004).
- [13] S.A. Magrabi, B.Z. Dlugogorski and G.J. Jameson. A comparative study of drainage characteristics in AFFF and FFFP compressed-air fire-fighting foams. *Fire Safety J.*, **37**: 21–52, (2002).
- [14] B.I. Palamarchuk and A.B. Postnov, Shock waves attenuation at condensed HE detonations placed in gas contained envelopes// The use of explosion energy in welding technique// E.O. Paton's Institute of Electric Welding, Kiev, 39–41, (1989) (in Russian).
- [15] P.J. Peregrino, D. Bowman, R. Maulbetsch, D. Saunders and L. Vande Kieft. Blast and fragmentation suppression with aqueous foam and a Kevlar tent. 28th Dep. Def. Exp. Saf. Sem., Orlando, FL, 1998.
- [16] L.R. Payne and D.L. Cole. Fragment capture device, US Patent 7,685,923,B1 (2010).
- [17] L.A. Klennert. Aqueous foam for explosive containment SANDDOC2004-4516P. Sandia, Sandia Corporation, Albuquerque, NM, (2004).
- [18] L. Domergue, R. Nicolas, J.-C. Marle, et al. Shock wave attenuation in aqueous foam. In *Safety and Security Eng. III – WIT Transactions on the Built Environment No. 108*, M. Guarascio, C.A. Brebbia and F. Garzia (eds). WIT Press, Southampton, UK, (2009).
- [19] F.H. Winfield and D.A. Hill. Preliminary research on the physical properties of aqueous foams and their blast attenuation characteristics. Suffield Tech. Note 389, Def. Res. Est. Ralston, Alberta, Canada (1977).
- [20] A.B. Britan, E.I. Vasilev and B.A. Kulikovsky. Modeling the process of shock-wave attenuation by a foam screen. *Combustion, Explosion, and Shock Waves*, **30**(3): 389–396, (1994).
- [21] R. Raspet and S.K. Griffiths. The reduction of blast noise with aqueous foam. *J. Acoust. Soc. Amer.*, **74**(6): 1757–1763, (1983).
- [22] M.E. Larsen. Aqueous foam mitigation of confined blast. *Int. J. Mech. Sc.*, **34**: 409–418, (1992).
- [23] S. Hutzler, D. Weaire, A. Saugey, S. Cox and N. Peron. The physics of foam drainage. 52nd SEPAWA Congress, 12–14 October 2005, Wurzburg Congress Center, Germany, (2005).
- [24] S.A. Koehler, S. Hilgenfeldt, E.R. Weeks and H.A. Stone. Foam drainage on the microscale: II. Imaging flow through single Plateau borders. *J. Colloid and Interface Science*, **276**: 439–449, (2004).
- [25] A. Britan, M. Liverts and G. Ben-Dor. Mitigation of sound waves by wet aqueous foams. *Colloids and Surfaces A: Physicochem. Eng. Aspects*, **344**: 48–55, (2009a).
- [26] J.S. Krasinski. Some aspects of the fluid dynamics of liquid-air foams of high dryness fraction. *Prog. Aero. Sci.*, **29**: 125–163, (1992).
- [27] K.B. Kann. Sound waves in foams. *Colloids Surface A: Physicochem. Eng. Aspects*, **263**: 315–319, (2005).
- [28] I. Shreiber, G. Ben-Dor, A. Britan and V. Feklistov. Foam self-clarification phenomenon: An experimental investigation. *Shock Waves*, **15**: 199–204, (2006).
- [29] I. Goldfarb, I. Shreiber and F. Vafina. Heat transfer effect on sound propagation in foam. *J. Acoust. Soc. America*, **92**: 2756–2769, (1992).
- [30] W.E. Hartman, B.A. Boughton and M.E. Larsen. Blast mitigation capabilities of aqueous foam. Report SAND2006-0533, Sandia, Sandia Corporation, Albuquerque, NM, (2006).
- [31] J.W. Shea and L.L. Pater. Foam filled muzzle blast reducing device. US Patent 4,454,798 1984.
- [32] K.B. Kann and A.A. Kislitsyn. A film model of sound propagation in gas-liquid foams: 1. The sound velocity. *Colloid J.*, **65**: 26–30, (2003a).
- [33] K.B. Kann and A.A. Kislitsyn. A film model of sound propagation in gas-liquid foams: 2. The sound absorption. *Colloid J.*, **65**: 31–34, (2003b).
- [34] N. Mujica and S. Fauve. Sound velocity and absorption in a coarsening foam, *Phys. Rev. E*, **66**: 021404-1- 021404-13 (2002).

- [35] V.M. Kudinov, B.I. Palamarchuk, V.A. Vakhnenko, A.V. Cherkashin, S.D. Lebed and A.T. Malakhov. Relaxation phenomena in foamy structure. Proceedings 8th ICOGER, Minsk, pp. 96–118, 1981.
- [36] G.J. Ball and R.A. East, Shock and blast attenuation by aqueous foam barriers: influence of barrier geometry. *Shock Waves*, **9**(1): 37–47, (1999).
- [37] N.T. Moxon, A.C. Torrance and S.B. Richardson. Sound attenuation with foam. US Patent 4,964,329 (1990).
- [38] D.L. Edberg and S. Schneider. Blast attenuation device and method, US Patent 6,901,839B2, (2005).
- [39] A. Britan, M. Liverts, G. Ben-Dor, S.A. Koehler and N. Bennani. The effect of fine particles on the drainage and coarsening of foam. *Colloids and Surfaces A: Physicochem. Eng. Aspects*, **344**: 1–3, 15–23, (2009b).
- [40] P.D. Smith and J.G. Hetherington. *Blast and Ballistic Loading of Structures*. Butterworth-Heinemann Ltd, Oxford UK, 1994.
- [41] V. Vakhnenko, V. Kudinov and B. Palamaecuk. Damping of Strong Shocks in Relaxing Media. *Combustion, Explosion, and Shock Waves*, **20**(1): 97–103, (1984).
- [42] B.I. Palamarchuk and A.T. Malakhov. Zatuxanie udarnix voln v pene pri vzriva kondensirovannogo VV. *Fizika Gorenia I Vzriva*, **6**: 135–143, (1990) (in Russian).
- [43] A. Britan, G. Ben-Dor, H. Shapiro, M. Liverts and I. Shreiber. Drainage effects on shock wave propagating through aqueous foams. *Colloids and Surfaces A: Physicochem. Eng. Aspects*, **309**: 137–150, (2007b).
- [44] V.M. Kudinov, B.I. Palamarchuk, B.E. Gelfand and S.A. Gubin. Shock waves in gas-liquid foams. *Appl. Mech.*, **13**(3): 279–283, (1977).
- [45] N.D. Denkov, S. Tcholakova, K. Golemanov, K.P. Ananthapadmanabhan and A. Lips. Viscous friction in foams and concentrated emulsions under steady shear. *Phys. Rev. Lett.*, **100**: 138301, (2008).
- [46] G. Katgert, M E., Mobius and M. van Hecke. Rate dependence and role of disorder in linearly sheared two-dimensional foams. *Phys. Rev. Lett.*, **101**: 058301–4, (2008).
- [47] A.B. Britan, I.N. Zinovik and V.A. Levin, Breaking up foam with shock waves. *Combustion, Explosion, and Shock Waves*, **28**(5): 550–557, (1992).
- [48] A.B. Britan and N.M. Kortsenstein, Drop evaporation behind shock waves in dry foam *J. App. Mech. and Tech. Phys.*, **3**(44): 480–485, (1993a).
- [49] A.B. Britan, I.N. Zinovik and V.A. Levin, Measurement of gas suspension parameters behind a shock wave in foam. *Fluid Dyn.*, **28**(3): 400–405, (1993b).
- [50] D. Weaire, S. Cox and K. Brake. Liquid Foams. In *Cellular Ceramics*, P. Colombo and M. Scheffler (Eds). Wiley-VCH, Weinheim, Germany, 2005.
- [51] S.C. Joshi, Y.C. Lam, F.Y.C. Boey and A.I.Y. Tok. Power law fluids and Bingham plastics flow models for ceramic tape casting. *J. Materials Proc. Tech.*, **120**(1): 215–225, (2002).
- [52] E.M. Schmidt and G.D. Kahl. Gaseous blast reducer. US Patent N4, 392412, (1983).
- [53] G.K. Batchelor, *An Introduction to Fluid Dynamics*, Cambridge University Press, Cambridge, UK (1968).
- [54] L. Van Wijngaarden. One dimensional flow of liquids containing small gas bubbles. *Ann. Rev. Fluid Mech.*, **4**, 369–396, (1972).
- [55] I. Goldfarb, I. Shreiber and F. Vafina. On one experiment of determining the sound speed in a foam. *Acoustica*, **80**: 583–586, (1994).
- [56] I. Goldfarb, Z. Orenbach, I. Shreiber and F. Vafina. Sound and weak shock wave propagation in gas-liquid foams. *Shock Waves*, **7**: 77–88, (1997).
- [57] G. Rudinger. Some effects of finite particle volume of the dynamics of gas-particle mixture. *AIAA J.*, **3**: 1217–1222, (1965).
- [58] A.A. Borisov, B.E. Gelfand, V.M. Kudinov, et al. Shock waves in water foams. *Acta Astronautica*, **5**: 1027–1033, (1978).
- [59] A.A. Borisov, B.E. Gelfand and E.I. Timofeev, Shock waves in liquids containing gas bubbles. *Int. J. Multiphase Flow*, **9**(5): 531–543, (1983).
- [60] P.M. Weaver and N.H. Pratt. An experimental investigation of the mechanisms of shock wave-aqueous foam interactions. 12th Int. Symp. Shock Tubes and Waves. VCH, Aachen, Germany (1988).

- [61] E. Vasilev, S. Mitichkin, V. Testov and H. Haybo. Pressure dynamics in the shock loading of the gas-liquid foams. *J. Tech. Phys.*, **68**(7): 19–23, (1998).
- [62] V.M. Kudinov, B.I. Palamarchuk and V.A. Vakhnenko. Attenuation of a strong shock wave in a two-phase medium. *Sov. Phys. Dokl.*, **28**(10): 842–842, (1983).
- [63] B.I. Palamarchik, B.A. Vakhnenko, A.V Cherkashin and S.G Lebed. Vlania relaxacion procesov na zatuxanie udarnix voln v vodnix penax// Svarka i Rezka Vzrivom// E.O. Paton's Institute of Electric Welding, Kiev, 97–110, (1979) (in Russian).
- [64] T.D. Panczak and H. Krier. Shock propagation and blast attenuation through aqueous foams. *J. Hazardous Mat.*, **14**: 321–336, (1987).
- [65] C.A. Zhdan. Numerical modeling of the explosion of a high explosive charge (HE) in foam. *Combustion, Explosion, and Shock Waves*, **26**(2): 221–227, (1990).
- [66] G.I. Taylor. The dynamics of the combustion products behind plane and spherical detonation fronts in explosives. *Proc. Roy. Soc. London, Ser. A*, 200–235, (1950).
- [67] V.A. Vakhnenko, V.M. Kudiniv and B.I. Palamarchuk. Effect of thermal relaxation of attenuation of shock waves in two-phase medium. *Prikladnaya Mekhanika*, **18**(12): 91–97, (1982) (in Russian).
- [68] B.I. Palamarchuk and A.T. Malakhov. The effect of medium properties and energy source characteristics on shock waves attenuation// The use of explosion energy for manufacturing of metal materials with new properties: Proc. 4th Int. Symp. Gotvaldov, 535–544, (1985) (in Russian).
- [69] B.I. Palamarchuk. Ob energeticheskem podobi zatuxania udarnix voln // Primenenie energii vzriva v svarochnoy texnike// E.O. Paton's Institute of Electric Welding, Kiev, 158–167, (1985) (in Russian).
- [70] J. Crepeau, C. Needham, T. Caipen, D. Grady and F. Harper. First principles of the interaction of the blast waves with aqueous foams. In *Shock Compression of Condensed Matter*, M.D. Furnish, L.C. Chabildas and R.S. Hixson (eds). American Institute of Physics, Melville, New York. pp. 779–782, (1999).

# Index

Note: page numbers in italics refer to figures; page numbers in bold refer to tables.

- Aboav–Weaire law 218  
Abrikosov vortices 209  
acidizin foams 288  
acoustic activity 80, 472–3  
acrylic tubes 159, 160  
adsorption processes  
  foam fraction columns 310–15  
    dynamic interfaces 314–15  
    enhancement methods 319–22  
    equilibrium state 312  
    within the foam bed 315  
aerobic autothermal thermophilic aerobic  
  digestion (ATAD) 340  
aerobic bioreactors 332  
AES (ammonium alkyl ether sulfate) **434**  
AFFF *see* aqueous film-forming foams  
  (AFFFs)  
ageing of foam *see* coarsening  
agitation (foam generation) 163, 230, 243  
air entrainment 163, 467–8  
air recovery, flotation columns 232  
air stones 162  
alcohol resistant (AR) foam 413, 415  
alkyl aryl sulfonates 297  
alkyl phenol ethoxylate (APE) **435**  
alkyl polyglycoside (APG) 433, **434**, 436  
alpha olefin sulfonate (AOS) **435**  
ALS (ammonium lauryl sulfate) **434**  
aluminosilicate glass 355–6  
ammonium alkyl ether sulfate (AES)  
  **434**  
ammonium lauryl sulfate (ALS) **434**  
amphiphilic particles 123  
animal waste processing 340–1  
AOS (alpha olefin sulfonate) **435**  
APE (alkyl phenol ethoxylate) **435**  
APG (alkyl polyglycoside) 433, **434**, 436  
aqueous film-forming foams (AFFFs)  
  413  
  alcohol resistant 413, 415  
  composition **430**, 433, 436, **448**  
  expansion ratio 430  
  foam boosters 432  
  market 415  
  polymers in 445  
  salt concentration 446–7  
  spreading coefficient (SC) 425  
  viscosity 450–1  
  water deluge resistance 429, 443  
AR (alcohol resistant) foam 413, 415  
asphaltenes 272  
ATAD (aerobic autothermal thermophilic  
  aerobic digestion) 340  
atmosphere composition and pressure,  
  effect on glass foaming 382–3, 399  
auditory sensation 472–3  
axial curvature, film channels 32  
axial flow, film channels 37, 37, 42, 47  
  
Bardeen–Cooper–Schrieffer (BCS)  
  theory 208  
Basset force 237  
BCS (Bardeen–Cooper–Schrieffer)  
  theory 208

- beer foams 470  
 alcohol-free 472  
 creation 468  
 foam drainage 28  
 protein-based nanoparticles 123  
 sensory appeal 470  
 surfactant enrichment ratio 309
- Bikerman foamability test 154–5, 233–4
- binary glasses 383
- biological cells 22–3
- bioreactors 332
- bitumen 252
- bituminous froths 259–78  
 bubble size **271**, 272  
 deaeration 274–5  
 emulsified water formation 267, 270  
 froth formation 261, 262–3, 266–7  
 froth structure 265–72  
 froth treatment 274–8  
 mean droplet and bubble diameters **271**  
 physical properties **271**, 272–4
- black film states 77
- blast mitigation 115, 423, 477  
 free field tests 478–92  
 shock tube testing 493–7  
 theory 497–508
- bomb foams 115, 423
- borosilicate glass **372**, 379, 395
- boundary conditions 53–4  
 draining foams 44, 53, 55  
 foam-wall slip 113–14
- Boycott effect 162
- Brakke's Surface Evolver 10, 11, 497
- bread production 467, 469–70, 471
- Bretherton problem 112
- Brookfield viscosity test 450
- brown glass 370, **372**
- bubble bursting *see* coalescence
- bubble coarsening *see* coarsening
- bubble compressibility 31, 34–5
- bubble gas pressure 31, 34, 51, 60, 62
- bubble growth  
 consumer products 468  
 controlling 69–72  
 dry foams 61–5
- gas solubility 69  
 wet foams 59–60, 65–9
- bubble model 95, 110
- bubble nucleation  
 consumer products 466–7  
 glass foams 360, 363, 364, 370
- bubble packing *see* foam morphology
- bubble polydispersivity 8, 20, 53, 79  
 pneumatic foam columns 153  
 rheological studies 96, 97
- bubble rafts 14, 79–80, 110
- bubble size  
 bituminous froths **271**, 272  
 and coalescence 83–5, 86, 87  
 consumer products **464**  
 foam fractionation 318  
 foam morphology 8  
 glass foams 367–8  
 versus liquid fraction 343–4  
 versus mass transfer coefficient 350  
 and yield stress 105
- bubble size distribution 66–7, 79–80, 84  
 froth flotation columns 231  
 measurement 153  
 pneumatic foam columns 150, 153  
*see also* bubble polydispersivity
- bulk modulus 71–2
- C-Cell imaging and analysis 471, 472
- calcium carbonate precipitation 336
- capillary forces 34, 40, 41  
 pneumatic foam columns 149–50  
 thin-film balance 76
- capillary number 107  
 and foam-wall friction stress 112, *113*
- capillary pressure 71, 104, 107  
 particle stabilized foams 132–4, 135, 137
- carbon dioxide capture  
 gas–liquid mass transfer 333–4, 334, 336, 337  
 gas reservoirs 294
- carbon dioxide flooding 294
- Carman–Kozeny equation 50
- casein foam 67, 70
- cavitation 163–4, 342

- cavitation tubes 164  
 cellular structure *see* foam morphology  
 ceramic foams 123, **124**  
 cetyltrimethylammonium bromide (CTAB) 323  
 channel dominated model 41–3  
 channel flow 33, 36–8  
     mobile channel model 43–6  
     network model 48–50  
     node-dominated model 46–8  
     rigid channel model 41–3  
     *see also* foam drainage  
 channels 15, 18, 29–30  
     aspect ratio 31, 33  
     blockage 53  
     cross-sectional area 32, 38, 158  
     curvature 10  
         and gas pressure 31  
         and liquid fraction 32, 33  
     edge length 30, 31, 32, 33  
     *see also* nodes; Plateau borders  
 charged nanoparticles 123  
 chemical degradation, surfactants 28  
 Chorleywood Bread Process (CBP) 467  
 Class A foams 422  
 Class B foams 422–30  
 cleaning zone, flotation columns 229, 230  
 CMC *see* critical micelle concentration (CMC)  
 coal processing, froth flotation  
     columns 242, 244–6  
 coalescence 75–90, 233  
     and bubble size 83–5, 86, 87  
     consumer products 469  
     critical liquid fraction 85–8  
     experiments 79–80  
     flotation froths 231, 232, 233, 237  
     key parameters 81–6  
     phases 79  
     pneumatic foam columns 150, *151*  
     structure and dynamics 78–81  
     thin film stability 76–8  
 coarsening 28, 59–73  
     consumer products 469  
     controlling 69–72  
     dry limit 61–5  
     effect of bulk modulus 71–2  
     effect of gas permeation resistance 70  
     effect of gas solubility 69  
     effect of shell mechanical strength 70–1  
     foam fraction columns 316–17  
     linear relaxations 101  
     magnetic froths 207–8  
     pneumatic foam columns 150, 152  
     resistance to 70  
     reversibility 216–19  
     superconducting froths 215–19  
     wet foams 65–9  
     wet limit 59–60, 61  
 collectors (flotation columns) 229, 230  
 colloid classes **124**  
 colloidal armour 123  
 colloidal gas aphrons 287  
 colloidal particles 54, 123, 171  
     *see also* particle stabilized foams (PSFs)  
 column flotation *see* froth flotation  
     columns  
     combustible materials 412–13, **414**  
     Common Black Film state 77  
     completion foams 287–8  
     compressibility, bubble 31, 34–5  
     compression modulus 97–8  
     condensation energy 209  
     cone-plate geometry 93  
     confocal microscopy 27, 28, 38, 39  
     consumer products 459–75  
         bubble growth 468  
         bubble size and density **464**  
         foam coarsening 469  
         foam creation 463–4, 466–8  
         markets 460, **461**  
         regulatory framework 461–2  
         sensory appeal 470–3  
         stabilization strategies **465**  
         structure of foams 469  
         surfactants 464–6  
     contact angles  
         fire-fighting foams 422, 423, 425–7  
         foam stabilization 129–34, 201  
     contaminant stripping 335, 343  
     continuity equation 35–6  
     Cooper pairs 208

- Couette cylinders 93  
 creep behaviour 99, 100, 101  
 critical liquid fraction 85–8  
 critical micelle concentration (CMC) 427, 429, 433, 437–9  
 measurement 451  
 CTAB (cetyltrimethylammonium bromide) 323
- d'Alembert force 237  
 Darcy's law 28  
 DB (diethylene glycol monobutyl ether) 432  
 Decoration Theorem 14  
 deformation *see* rheological properties  
 density measurement 450  
 Denver Flotation Cell 340  
 depressants (flotation columns) 230  
 Derjaguin–Landau–Verwey–Overbeek (DLVO) theory 76, 78  
 detergents  
     consumer products 461, 462–3, **462**  
     foam drainage 42, 43  
     synthetic foam (S) 413  
 dewatering, flotation columns 243  
 diethylene glycol monobutyl ether (DB) 432  
 diffusing wave spectroscopy (DWS) 94  
 diffusion, bubble gas *see* coarsening  
 diffusion-controlled adsorption 311, 312  
 diglycerol fatty acid esters 172–203  
     molecular structure 172  
     phase behaviour 173–4, 189  
 diglycerol fatty acid esters/hexadecane system  
     effect of temperature 189, 191  
     effect of water addition 191–2, 196  
 diglycerol fatty acid esters/olive oil system  
     effect of surfactant concentration 177–81, 201  
     effect of water addition 192, 193, 196–200, 202  
     equilibrium surface tension 181, 185–6, 203  
     foam stability 183–4  
     foamability 182–3  
     phase behaviour 203  
     rheological properties 179–81, 185, 199–200  
 diglycerol fatty acid esters/paraffin system  
     effect of solvent molecular structure 174–7  
     foam stability 182  
     phase behaviour 173  
 diglycerol fatty acid esters/squalane system  
     effect of solvent molecular structure 174–7  
     effect of temperature 189, 191  
     effect of water addition 191–6  
     foam stability 182  
     particle shape and size 194–6  
     phase behaviour 173  
 diglycerol fatty acid esters/squalene system 172  
     effect of solvent molecular structure 174–7  
     foam stability 182  
 dilatancy 115  
 diphenyl ether disulfonate 295  
 discrete microfluidics 15  
 disjoining pressures 31–2, 76, 86–7  
 disordered foams 19–20  
     *see also* polydisperse foams  
 dispersion coefficient 239–40  
 DLVO (Derjaguin–Landau–Verwey–Overbeek) theory 76, 78  
 dodecahedron 31, 32  
 DOH (dodecanol) 28  
     conversion of SDS 28  
     foam drainage 42, 43, 45, 46, 49, 50  
 draft tubes 322, 323  
 Drave's wetting rate 452  
 drilling foams 287–8  
 drink products **461, 465, 468**  
     *see also* beer foams  
 dry foams 7–8  
     channel length 32  
     drainage velocity 41  
     geometrical considerations 29–30, 32  
     geometry 29, 32  
     idealised geometry 29

- number of contact per cell 11, 13  
 three dimensional foams 16  
 visco-elasticity 95–6  
 dry limit 9–11  
   foam ripening 61–5  
   two-dimensional foams 11, 12  
 dry powders (fire-fighting) 418  
 DWS (diffusing wave spectroscopy) 94  
 dynamic foaming 123, 163, 230, 243
- e-glasses 355, **372**  
   transient foaming experiments 375–83  
 edge length 30, 31, 32, 33  
 edge-seal 429, 440  
 EDHA 159  
 EDL (electric double layer) 313  
 effective viscosity 91  
 elastic deformation 92–3  
 elastic modulus 70, 71  
   non-aqueous foams 179–80, **186**  
     *see also* shear modulus  
 electric double layer (EDL) 313  
 electric glass melters 359, 379  
 electrical conductivity 68  
 electroflootation  
 electronic froth *see* suprafroth  
 electrostatic forces 76  
 emulsification, fuel 428, 429  
 emulsions 22, 23, 32, 105  
   oil sand bitumen 275, 276  
   stability 121, 123, 193, 194  
 energy dissipation 99, 101–2, 108–9  
   *see also* viscous dissipation  
 energy efficiency, glass manufacturing 362  
 enrichment ratio, foam fraction  
   columns 308–9, 318, 319  
 entrainment 163, 467–8  
 equilibrium liquid fraction 148, 149, 236  
 equilibrium surface tension 181, **181**, 185–6, **186**, 203  
 equivalent diameter, bubble 31  
 Euler's equation 498  
 Euler's theorem 11  
 evaporation from surface 155, 234
- expansion ratio 1, 7  
 fire-fighting foams 412, 419, 430, 432, 433, 436  
   tests 449–50
- fermentation 338–40, 468  
 ferrofluids 208  
 ferromagnetic garnets 208  
 FFR (foam flow resistance) factor 285  
 Fick's second law 59–60  
 film formation (fire-fighting) *see* spreading coefficient (SC)  
 film stretching 98  
 film thickness  
   bituminous froths 270  
   disjoining pressure 76–7  
   and drainage rate 32  
   fire-fighting foams 424–5  
   and foam ripening 68  
   and geometrical length 31  
   thermal fluctuations 77  
 films, inter-bubble 29–30, 43, 54  
   gas diffusion 61  
   stretching 87, 98  
 finite yield stress 2  
 fire-fighting foams 411–57  
   applications 415–16  
   chemical properties 430–47  
   Class A foams 422, **448**  
   Class B foams 422–30, **448**  
   edge-seal 429, 440  
   expansion ratio 419  
   film-forming 424–5  
   foam concentrate 412–13  
   fluorosurfactants 439–44, **441–2**  
   hydrocarbon surfactants 433–9, **434–5**  
   market 415, **416**  
   performance enhancers 446–7  
   polymer additives 444–7  
   proportioning rate 411–12, 451  
   sample recipes 447, **448**  
   solvents 431–2  
   stabilizers 446–7  
   storage 416, 419, 431

- fire-fighting foams (*cont'd*)  
 foam generation 412, 416, 417, 418,  
   420  
 future directions 453  
 hardware 415–16  
 history 413  
 ingredients and purpose 430–47  
 mechanism of action 416–30  
 for polar fuels 413, **414**, 427, 428, 444,  
   **449**  
 properties of selected fuels and  
   solvents **414**  
 spreading coefficient (SC) 424–5, 429,  
   451  
 standards 452–3  
 testing 448–53  
 flammable liquids *see* combustible  
   materials  
 flooding, pneumatic foam columns 155–7  
 flotation columns *see* froth flotation  
   columns  
 flow channels *see* channels  
 flow cross-sectional area 32, 38, 158  
   changes in 158, 324  
 flow junctions *see* nodes  
 flow resistance 37–8  
   mobile channel model 44, 45  
   network model 48  
   pipe geometries **38**  
   steam foams 297  
 flow resistance (FFR) factor 285  
 flow velocity  
   draining foams 35–6  
     forced drainage 36, 51–2  
     mobile interface model 45  
     rigid channel model 41, 42  
   flotation columns 241  
     horizontal flow 113–14, 159–61  
 fluorescence micrography 275  
 fluorine-free foams 423  
 fluorocarbon surfactants *see*  
   fluorosurfactants  
 fluoropolymer surfactants 440  
 fluoroprotein (FP) foam 413  
 fluorosurfactants 439–44  
   manufacture 453  
   mixtures 437  
 products **441–2**  
 retention in foam 440, 443, 452  
 surface tension 439, 440, 444  
 foam barriers 480–482, 482  
   decay 482–4  
   density 485–8  
   impedance 488–93  
   properties **479**  
 foam boosters 432, 438  
 foam coarsening *see* coarsening  
 foam contactors 331–4  
 foam drainage 27–58  
   Carman–Kozeny approach 50–1  
   continuity equation 35–6  
   drainage enhancement methods 322–4  
   fire-fighting foams 427, 430  
   foam fraction columns 315–16, 322–4  
   forced drainage *see* forced drainage  
   gas–liquid mass transfer 344  
   history 54–5  
   mobile channel model 43–6  
   network model 48–50  
   node-dominated model 46–8  
   non-aqueous foams 170, 176–7, 179,  
    183, 187  
   pneumatic foam columns 148, 152  
   rigid channel model 41–3  
   unconfined drained foam 33–5  
     *see also* channel flow  
   foam drilling fluids 287–8  
   foam flow resistance (FFR) factor 285  
   foam formation capacity *see* foamability  
   foam fraction columns 146, 307–30  
     adsorption enhancement methods  
       319–22  
     adsorption processes 310–15  
       dynamic interfaces 314–15  
       equilibrium state 312  
       within the foam bed 315  
     coarsening 316–17  
     draft tubes 322, 323  
     enrichment ratio 308–9, 318, 319  
     external reflux methods 321–2  
     foam drainage 315–16, 322–4  
     foam stability 316–17

- industrial scale applications 324–5  
 internal reflux 317  
 multistage foam fractionators 320–1,  
   321–2  
 nomenclature 325–6  
 operating modes 309, 317  
 parallel inclined channels (PIC) 322–3  
 recovery rate 317–18, 319  
 successive foam contraction and  
   expansion 324  
*see also* pneumatic foam
- foam generation  
 fire-fighting foams 416, 417, 418,  
   420  
 particle stabilized foams 123  
 petroleum recovery 288  
 pneumatic foams 162–4
- foam head 146
- foam life *see* stability of foams
- foam morphology 7–26  
 biological cells 22–3  
 disordered foams 19–20  
 dry limit 9–11  
 emulsions 22  
 glass foams 367–8  
 instabilities 21  
 number of contact per cell 11–14  
 ordered foams 15–18  
 solid foams 23, 24  
 statistics 20–1  
 topological changes 21  
 two-dimensional foams 11–14  
 wet limit 11
- foam quality 7, 449
- foam ripening *see* coarsening
- foam stability *see* stability of foams
- foam–wall friction stress 112, 113
- foam–wall shear stress  
 horizontal flow 158–9, 160  
 vertical columns 157–8
- foam–wall slip 91–2, 93, 112–14  
 horizontal flow 159–61
- foam–wall viscous friction 112–14
- foamability  
 Bikerman test 154–5, 233–4  
 non-aqueous foams 170
- effect of solvent molecular  
 structure 174–7
- effect of surfactant  
 concentration 177–81
- effect of surfactant molecular  
 structure 181–9
- effect of temperature 189, 191  
 effect of water addition 191–2
- foaming index 390
- foaming method  
 fire-fighting foams 416, 417, 418, 420  
 particle stabilized foams 123  
 petroleum recovery 288  
 pneumatic foams 162–4
- foaming temperature  
 glass foams 364  
*see also* temperature dependency
- foamy-oil production 293
- fodder yeast production 338–40
- food products 461, 465  
*see also* bread production
- food waste aeration 339
- forced drainage 38–40  
 coalescence 82  
 drainage velocity 36, 51–2  
 experiment 28, 29, 39–40  
 interpreting experiments 51–3  
 pneumatic foam columns 153  
 uncertainties 53–4
- form foams 293
- formation factor 68
- FP (fluoroprotein) foam 413
- fraction columns  
*see also* foam fraction columns
- fracturing fluid foams 288–9
- Frankel’s law 88
- freeze-protection 431–2
- froth flotation columns 145–6, 229–49  
 air recovery 232  
 cleaning zone 229, 230  
 collection zone 229, 230  
 detachment of particles from  
   bubbles 236–8  
 froth stability 233–4  
 frother-constrained plant 242–4  
 gangue recovery 238–41

- froth flotation columns (*cont'd*)  
 hydrodynamic condition of the  
   froth 235–6  
 newly proposed equipment 246  
 nomenclature 246–7  
 performance 229, 230, 232, 243,  
   244–5  
 plant experience 242–6  
 process accounting 244  
 process control 245–6  
 rheological properties 231  
 sampling 244–5  
 simulations 231–2  
 tailing stream 229, 230  
 velocity field of the froth bubbles 241  
 washwater 230  
 frother-constrained plant 242–4  
 frothers (flotation columns) 230, 242–4  
 FrothSim 232  
 fuel emulsification 428, 429  
 fuel-shedding foams 428  
 fuels (fire-fighting) 412–13, **414**  
 furnaces (glass melting) 362–3, 397
- galvanized steel pipes 159  
 gangue recovery 238–41  
 gas absorption devices 331–4  
   *see also* gas–liquid mass transfer  
 gas diffusion *see* coarsening  
 gas entrainment 163, 467–8  
 gas flowrate 152, 163  
   *see also* coarsening  
 gas fraction 7  
 gas injection 162–3  
   consumer products 468  
   glass foaming 384–6, 387–8  
 gas–liquid mass transfer 331–53  
   carbon dioxide capture 333–4  
   equilibrium considerations 345–7  
   foam drainage 344  
   future directions 350–1  
   gas–liquid equilibrium 345  
   horizontal foam contacting 341–2  
   hydrodynamics of pneumatic  
    foam 342–3, 348  
   induced air methods 339, 340–1  
 integrated model 347–9  
 mass transfer coefficients 332, 346–7,  
   349, 350  
 mass transfer rate 345–6  
 nomenclature 351  
 non-overflowing devices 334–6,  
   343–4  
 overflowing devices 333–4, 336–8  
 solid phase entrainment 336  
 specific surface area 342–3, 350  
 surfactant effect 346  
 vented underflow 335, 336  
 Waldhof fermentor 230, 338–40  
 gas solubility, and coarsening 69  
 gas strippers 335, 343, 348  
 gas volume fraction 91  
   rheological properties 96, 97  
   *see also* foam quality; liquid volume  
   fraction  
 gas wells, bottom-hole foam 289  
 gelling foams 287  
 geometric considerations 29–33, 53  
 Gibbs elastic modulus 70  
 Gibbs energy 126, 130, 131  
 glass composition 355–6, 380  
 glass cullets 379, 397  
 glass foams 356, 357, 358  
   bubble dynamics 371, 373  
   bubble gas composition 368, 370  
   bubble nucleation 370  
   compared with aqueous foams 366  
   in electric glass melters 359, 379  
   experimental studies **372**  
   film drainage 369  
   formation *see* glass foaming  
   interfacial surface tension 368  
   modeling 386–95  
   morphology 367–8  
   negative effects in glass  
     manufacturing 359, 362–3  
   primary foam 363, 377, 379  
   reboil 364  
   secondary foams 363–4, 376, 379  
   stability 369–70, 370–1  
   surface active agents in 368  
   types 363–4, 365

- glass foaming 361, 363–6  
 effect of atmosphere composition 382–3, 399  
 effect of atmosphere pressure 382–3  
 effect of batch compaction 380, 397  
 effect of batch composition 380, 396–7  
 effect of batch grain size, compaction, and cullets 380  
 effect of batch preheating 397  
 effect of glass composition 380  
 effect of glass cullets 379, 397  
 effect of redox state 359–60, 377–9, 397  
 effect of sulfate addition 381–2, 381, 386, 396  
 effect of sulfide addition 396  
 effect of temperature 360–1, 364, 369–70, 376–7, 385–6, 397  
 effect of water vapor 381–2  
 future research directions 401–2  
 by gas injection 384–6, 387–9  
 measures for reducing 396–401  
   atmosphere composition 399  
   batch composition 396–7  
   batch conditioning and heating 397  
   external and temporary actions 397–9  
   furnace temperature 397  
   luminесcent flame 399  
   by mechanical disturbance 398  
   reduced-pressure refining 400–1  
   spraying metal oxide powders 398  
   spraying  $\text{Na}_2\text{SO}_4$ ,  $\text{NaOH}$ , and  $\text{KOH}$  solutions 398  
   using pulsed laser 398  
 primary foaming 396  
 secondary foaming 396  
 steady-state foaming 384–6, 389–95  
   by thermal decomposition 387  
 glass frit 162  
 glass manufacturing 355–63  
   glass melting process 356  
   melting chemistry 360  
   redox state of glass 359–60, 377–9  
   reduced-pressure refining 362  
   refining chemistry 360–2  
 glass quality 362  
 glycerol fatty acid esters 172, 174–203  
 gravitational forces, draining foams 33–4, 36–7  
 Haagen–Poiseuille flow 37  
 headspace pressure, and bubble growth 468  
 height of a theoretical unit (HTU) 346  
 Henry's law 60, 69, 345  
 Herschel–Bulkley model 104, 106, 108  
 hexadecane 172  
   *see also* diglycerol fatty acid esters/hexadecane system  
 Hi-Ex (high-expansion) foams 419, 423  
 high surface modulus (HSM)  
   surfactants 108, 111, 113, 114  
 home care products 461, 465  
 horizontal flow  
   flow velocity 113–14, 159–61  
   foam–wall shear stress 158–9, 160  
   foam–wall slip 159–61  
   gas–liquid mass transfer 341–2  
   pneumatic foam 158–61  
   flow regimes 161  
   slip velocity 159, 160  
 HTU (height of a theoretical unit) 346  
 humidity *see* relative humidity  
 hydraulic resistance 37–8  
   flow resistance (FFR) factor 285  
   mobile channel model 44, 45  
   network model 48  
   pipe geometries 38  
   steam foams 297  
 hydrocarbon fuels 412–13, 414  
 hydrocarbon gas flooding 294–7  
 hydrocarbon surfactants 171, 433–9, 434–5  
 hydrodynamic cavitation 163–4  
 hydrodynamics  
   froth flotation columns 235–6  
   gas–liquid contactors 343–4  
   pneumatic foam columns 147–52  
 Hydrofloat Separator 230  
 hydrogel polymer threads 23  
 hydrolysate 413  
 hydrolyzed proteins 445–6

- hydrophilic particles 124  
 hydrophilic surfaces 159, 160  
 hydrophobic chain length 181–6  
 hydrophobic particles  
   adsorption 124, 201  
   bituminous froths 272  
   flotation columns 229, 233, 236–8  
 hydrophobins 70, 469
- IFT* *see* interfacial tension (IFT)  
 impellers 163  
*in situ* generated particles **124**  
 inclined channels, pneumatic foam 162  
 inertial effects, draining foams 36–7  
 integrated model, gas–liquid  
   contactors 346–7  
 inter-bubble gas diffusion *see* coarsening  
 interface curvature 10  
   and gas pressure 31  
   and liquid fraction 32, 33  
 interfacial area *see* specific surface area  
 interfacial dilatational viscosity 71  
 interfacial elasticity 70, 71  
 interfacial mobility 44  
 interfacial tension (IFT)  
   measurement 451  
   *see also* surface tension  
 internal reflux (foam fractionation) 317  
 interstitial flow *see* channel flow  
 ionic liquids 171  
 ionic surfactants  
   adsorption 312, 313  
   resistance to mass transfer 346
- Jameson Cell 230–1  
 Janus particles 123  
 JKSimFloat 232  
 junctions *see* nodes
- Kelvin bubble 29–30, 50  
 Kelvin foam 16, 32, 33, 95–6  
 kinetic controlled adsorption 311–12
- lamella settlers 276  
 lamellae *see* films, inter-bubble  
 Langmuir adsorption model 312, 319–20
- LAOS (large amplitude oscillatory experiments) 104  
 Laplace pressure 9, 31, 62, 69, 75  
   maximum capillary pressure 132  
 Laplace–Young law 9, 31  
 large amplitude oscillatory experiments (LAOS) 104  
 LAS (linear alkyl benzene sulfonate) **435**  
 lauryl betaine (LB) **435**  
 n-lauryl imino-dipropionate (LIDP) **434**  
 LB (lauryl betaine) **435**  
 lead crystals, suprafroth 211–15  
 Leonard and Lemlich model 43–6, 54  
 Lewis's law 220, 222  
 LIDP (n-lauryl imino-dipropionate) **434**  
 lime slurry carbonation 336  
 linear alkyl benzene sulfonate (LAS) **435**  
 linear elasticity 95–8  
 linear relaxations 99–102  
 liquid-aluminium alloy 123, 124  
 liquid crystalline phases 171, 172, 174,  
   183–4, 202–3  
 liquid films 76–8  
   *see also* films, inter-bubble  
 liquid flux  
   gas–liquid mass transfer 343–4, 348  
   pneumatic foam columns 146, 148,  
    150–2, 155, 235–6  
 liquid fraction *see* liquid volume fraction  
 liquid jet entrainment 163, 340  
 liquid-metal foams 122–3  
   particle stabilized 124–5  
   classification **124**  
   particle size 134, 136, 137  
   volume fraction 124–5  
 liquid tailings 146  
 liquid velocity *see* flow velocity; liquid  
   flux; superficial velocity  
 liquid volume fraction 7–8  
   versus bubble size 343–4  
   and channel length 32  
   and coalescence 82–8  
   drained foam 34, 35  
   edge length dependence 31  
   and flow velocity 55  
   foam fraction columns 316

- and foam ripening 68  
 and interface curvature 32  
 measurement 55  
 and number of edges 31  
 pneumatic foam columns 146–7,  
   148–51, 151, 152–3, 157  
 and rheological properties 96  
 spatiotemporal evolution 55  
 two-dimensional foams 13, 14  
 yield stress and strain 104–5  
*see also* dry limit; wet limit  
 low surface modulus (LSM) surfactants  
   foam–wall friction stress 113, 114  
   viscous dissipation in foams 108  
   viscous stress 111
- Mach number 499  
 magnetic froths 207–8  
*see also* suprafroth  
 magnetic resonance imaging (MRI) 94,  
   271  
 manganese sulfate 447  
 Marangoni forces 36, 44, 48, 54  
 mass transfer coefficients 332, 346–7,  
   349, 350  
 MEA (monoethanolamine) 333  
 mechanical agitation 163, 230, 243  
 mechanical disturbance, reduction of glass  
   foaming 398  
 mechanical flotation cells 163, 230,  
   243  
 mechanical impact 115  
 mechanical impellers 163  
 melted powder compacts 124  
 metal oxide powder spraying 398  
 metallic foams 122–3  
   particle stabilized 124–5  
     classification 124  
     particle size 134, 136, 137  
     volume fraction 124–5  
 micelle concentration *see* critical micelle  
   concentration (CMC)  
 micro-foam 287  
 microemulsions 22  
*see also* emulsions  
 minerals processing
- froth flotation columns 146, 164, 231,  
   236, 242  
 process accounting 244  
 process control 245–6  
 mist drilling 288  
 mobile interface model 43–6, 51  
 mobility reduction factor (MRF) 285, 295  
 modelling *see* simulations  
 monodisperse foams 15–18, 29  
 monoethanolamine (MEA) 333  
 monoglycerol fatty acid ester/oil  
   systems 187–9, 190  
 Mooney formulation 159  
 morphology of foams *see* foam  
   morphology  
 MRF (mobility reduction factor) 285,  
   295  
 MRI (magnetic resonance imaging) 94,  
   271  
 multistage foam fractionators 320–1,  
   321–2
- NADS (sodium decyl sulfate) 433, 434,  
   436  
 nano particles 123, 124  
 napthenic froth treatment 275  
 Navier–Stokes equation 36  
 neighbour-swapping event *see* T1 events  
 network model 48–50, 53  
 Newton Black Film state 77  
 Newtonian fluids 36  
 Nisin extraction 309–10, 325  
 node-dominated model 46–8  
 node-to-node separation 32  
 nodes 29–30  
*see also* channels; Plateau borders  
 nomenclature  
   flotation columns 247  
   foam fraction columns 325–6  
   gas–liquid mass transfer 351  
   pneumatic foam columns 164–5  
 non-aqueous foams 169–206  
   foam formation and structures 169–70  
   foam stability 170–2  
     stabilization mechanism 123, 201–3  
   foaming properties 174–203

- non-aqueous foams (*cont'd*)  
     effect of solvent molecular structure 174–7  
     effect of surfactant  
         concentration 177–81  
     effect of surfactant molecular structure 181–9  
     effect of temperature 189, 191  
     effect of water addition 191–2  
     phase behaviour 173–4  
     rheological properties 179–80, 185, 199–200  
         *see also* metallic foams  
     non-linear elasticity 98–9  
     non-Newtonian fluids 36  
         *see also* rheological properties  
     non-overflowing pneumatic foam devices 153–5, 334–6  
     NOS (sodium octyl sulfate) 434  
     nuclear waste vitrification 359, 379  
     nucleation  
         consumer products 466–7  
         glass foams 360, 363, 364, 370  
     oil agglomeration 164  
     oil-based foams 169–206  
         foam formation and structures 169–70  
         foam stability 170–2  
             stabilization mechanism 123, 201–3  
         foaming properties 174–203  
             effect of solvent molecular structure 174–7  
             effect of surfactant  
                 concentration 177–81  
             effect of surfactant molecular structure 181–9  
             effect of temperature 189, 191  
                 effect of water addition 191–2  
         phase behaviour 173–4  
         rheological properties 179–80, 185, 199–200  
         *see also* metallic foams  
     oil recovery *see* petroleum recovery  
     oil sands  
         composition 252–3  
         deposits 251–2  
     mining 253–5  
     slurries 255–65  
     water-based flotation process 255–65  
         *see also* bituminous froths  
     olive oil *see* diglycerol fatty acid esters/  
         olive oil system  
     optical observations 94  
     optical tomography 94  
     ordered foams 15–18, 16  
         columnar foams 18, 19  
         number of contact per cell 14, 15  
     ordered polymerized foam threads 24  
     organic solvents 431–2  
     oscillatory shear stress 93, 98, 99, 100, 104  
         large amplitude oscillatory experiments (LAOS) 103, 104  
     osmotic pressure 32, 115  
     osmotic stabilization 69  
     Ostwald ripening 28  
         *see also* coarsening  
     overflowing pneumatic foam devices, for  
         gas–liquid mass transfer 336–8  
     oxide remnants 124  
     oxygenation processes 332, 337, 338, 339  
     packed beds, compared with foam  
         compactors 331, 332  
     packing *see* foam morphology  
     paraffin 187–9, 190  
         *see also* diglycerol fatty acid esters/  
             paraffin system  
     paraffinic froth treatment 275  
     parallel inclined channels (PIC) 322–3  
     parallel plate geometry 93  
     particle adsorption  
         foam stability 176, 196, 201, 203  
         and foamability 177  
         and surface tension 181  
     particle entrainment  
         bitumen froths 263, 265, 267, 272  
         flotation columns 231, 236, 238, 238–41  
     particle stabilized foams (PSFs) 121–43  
         and capillary pressure 132–4  
         chemical composition 135

- classification 124  
 design rules 135–7  
 non-aqueous foams 171–2  
 particle shape 124, 172  
 particle size 124, 136, 172, 202  
 particle size distribution  
   effect of water addition 194–6,  
     198–9  
   versus surfactant concentration 179,  
     180, 183–4  
 stabilization mechanism 201–2  
 thermodynamic stability 125–31  
 particle volume fraction 123–4, 125, 134,  
     136–7  
 PCA (principal component analysis) 470  
 PDMS (polydimethylsiloxane) 370–1  
 PEG (polymer solutions) 36  
 penetration model 346  
 penicillin production 339  
 perfluoroalkyl chain 439  
 perfluorohexanoic acid (PFHA) 453  
 perfluorooctanoic acid (PFOA) 453  
 perfluorooctanyl sulfonate (PFOS)  
     453  
 perforated plates 162, 322, 323  
 permeability 29, 61, 70  
 personal care products 461, 465  
 Perspex tubes 159, 160  
 petroleum wells 287–9  
 petroleum recovery 272, 283–305  
   foam drilling and completion  
     fluids 287–8  
   foam generators 288  
   foamy-oil production 293  
   fracturing fluid foams 288–9  
   reservoir applications 292–8  
   surfactant loss 285, 286, 295  
   surfactant selection 284–7, 296–7  
   well applications 287–9  
 petroleum reservoirs  
   fluid injection processes 289–92  
     capillary trapping 291–2  
     sweep efficiency 290  
   foam applications 292–8  
 petroleum wells 287–9  
 PFG-NMR (pulsed-field gradient nuclear magnetic resonance) 153  
 PFHA (perfluorohexanoic acid) 453  
 PFOA (perfluorooctanoic acid) 453  
 PFOS (perfluorooctanyl sulfonate) 453  
 pH measurement 450  
 phase-trapping 285  
 physicochemical parameters 53–4, 68  
 PIC (parallel inclined channels) 322–3  
 Pickering emulsions *see* particle stabilized foams (PSFs)  
 pipe wall *see* foam-wall  
 plastic flow 105–6  
 plastic strain 93, 105  
 Plateau borders 11, 13, 14, 55  
   axial flow 37  
   flow resistance factors 38  
   *see also* channels  
 Plateau's rules of equilibrium 9, 11  
 platinum, flotation columns 234, 235  
 plug flow 114  
 plunging jet entrainment 163, 340  
 pneumatic foam  
   horizontal flow 158–61  
   flow regimes 161  
   slip velocity 159, 160  
   inclined channels 162  
   nomenclature 164–5  
   production methods 162–4  
   verticle columns 145–58  
     bubble coalescence 150, 151  
     bubble column regime 156–7  
     bubble size distribution 150, 153  
     capillary forces 149–50  
     coarsening 150, 152  
     cross-sectional area changes 158  
     flooding 155–7  
     foam phase 146  
     foam-wall shear stress 157–8  
     forced drainage 153  
     hydrodynamics 147–52  
     influence of humidity above  
       column 154–5  
     liquid flux 146, 148, 150–2, 155  
     liquid tailings 146

- pneumatic foam (*cont'd*)  
   liquid volume fraction 146–7,  
     148–51, 151, 152–3  
   non-overflowing 153–5, 334–6  
   pressure gradient 157  
   stability 154  
   superficial velocity 147, 148, 149,  
     150, 152, 235–6  
   viscous losses 155–7  
   washwater addition 151–2
- Poisson ratio 97
- polar fuels 413, **414**, 427, 428, 444, **449**
- pollutant emissions, glass  
   manufacturing 362
- polydimethylsiloxane (PDMS) 370–1
- polydisperse foams 8, 20, 53, 79  
   pneumatic foam columns 153  
   rheological studies 96, 97
- polyethylene glycol surfactant 81, 82, 83
- polymer-enhanced foams 123, 201–2,  
   286–7  
   fire-fighting foams 427, 428, 444–7  
   fluoropolymer surfactants 440
- polymer solutions (PEG) 36
- polysaccharide polymers 445, 450–1
- porous media  
   analogy 28–9, 50  
   oil reservoirs 285–6
- potassium hydroxide 398
- power-law index 107, 108, 110
- pressure drop  
   across nodes and channels 32, 37,  
     41, 47  
   bubble generation 288, 466
- principal component analysis (PCA) 470
- process accounting and control, froth  
   flotation 244–6
- productivity, glass manufacturing 362
- properties, gas–liquid foams 1–2
- proportioning rate, fire-fighting  
   foams 411–12, 451
- protein molecules, adsorption 310,  
   312–13, 313, 314–15
- protein skimmers 309
- protein-stabilized foams 70  
   beer foams 123
- bubble growth 67
- bubble stabilization 70–1
- consumer products 469
- drainage 42–3, 54
- fire-fighting 413
- physicochemical parameters 53–4
- surface viscosity 43
- PSF *see* particle stabilized foams (PSFs)
- pulsed-field gradient nuclear magnetic resonance (PFG-NMR) 153
- quarter drain time 449–50
- quasi-static behaviour 105
- rag layers 276–8
- reagent dosing, flotation columns 230,  
   243, 246
- reboil, glass foams 364
- recovery rate  
   foam fraction columns 317–18, 319  
   petroleum reservoirs 289
- redox state of glass 359–60, 377–9, 397
- reduced-pressure refining (glass) 400–1
- refractive index (RI) measurement 450
- relative density 54
- relative humidity, above foam  
   columns 154–5, 234, 317
- Reynolds number 36
- rheological properties 1–2, 91–120, 232  
   bituminous froths 274  
   consumer products 469  
   experimental studies 93–4  
   froth flotation columns 231  
   non-aqueous foams 179–80, **186**,  
     199–200  
   theoretical models 94–5  
   *see also* viscosity
- rhombic dodecahedral bubble 30
- rigid channel model 41–3
- Ross-Miles test 467
- rotational rheometers 93
- rupture of foams *see* coalescence
- SAG (surfactant-alternating-gas) 294
- salinity levels 285, 294, 295, 446–7
- sampling, flotation columns 244–5

- Sauter mean radius 96, 307  
 SC (spreading coefficient) 424–5, 429, 451  
 SDBS (sodium dodecylbenzenesulfonate) 81, 82, 83  
 SDS *see* sodium dodecyl sulfate (SDS)  
 seawater, foam formulation 446–7  
 sensory appeal, consumer products 470–3  
 sewage sludge digestion 337, 338  
 shear flow 92–3, 98  
     plastic flow 105–6, 107  
 shear modulus 71  
     and foam polydispersivity 96–7  
     and gas volume fraction 96–7  
     linear relaxations 99–102  
     particle-laden foams 102  
     static 95–6  
 shear start-up experiment 104  
 shear strain 95–6, 105  
 shear stress 44, 92–3, 98, 99, 105  
     *see also* yield stress  
 shear stress–strain relationship 95–8  
     plastic flow 105–6, 107  
     yielding 103–6  
 shear-thinning behaviour 107, 109, 159  
 shell mechanical strength 70–1  
 shock wave attenuating materials 507  
 Shubnikov state 209  
 silica particles, particle stabilized  
     foams 123, 171, 201–2  
 silicone oil in water 23  
 simulations  
     flotation columns 231–2  
     foam morphology 10, 11, 12  
     mobile channel model 45, 46  
     software 11, 232  
 sintered glass 162  
 slag foams 391, 398  
 slip velocity 1, 112  
     gas–liquid mass transfer 347, 350  
     pneumatic foam 157  
         horizontal flow 159, 160  
 sludge digestion 337, 338  
 slug injection 293  
 slurry foams 123  
 soap films 9–10  
 soap foam  
     coalescence 80  
     foam drainage 28, 47, 48  
     surface viscosity 43  
 sodium carbonate-bicarbonate solution 337, 338  
 sodium decyl sulfate (NADS) 433, **434**, 436  
 sodium dodecyl sulfate (SDS)  
     bubble growth 67  
     chemical degradation 28  
     confocal imaging 39  
     foam coarsening 69, 79, 316  
     forced drainage 40, 43, 44–5, 46  
     gas–liquid mass transfer 346  
     sodium dodecylbenzenesulfonate (SDBS) 81, 82, 83  
 sodium hydroxide 333, 337, 398  
 sodium lauryl sulfoacetate 294  
 sodium octyl sulfate (NOS) **434**  
 sodium sulfate 336, 381, 396, 398  
 soft disk mode 95  
 soft glassy rheology model 106  
 software, modelling 11, 232  
 solid foams 23, 24  
 solid particles *see* particle solvents  
     combustible materials 412–13, **414**  
     molecular structure  
         effect on foamability 174–7  
         non-aqueous foams 174–9  
         organic 431–2  
 sound propagation 115  
 sparging methods 162–3, 322  
 specific gravity (SG) measurement 450  
 specific surface area 50, 307  
     gas–liquid mass transfer 331, 332, 342–3  
     pneumatic foam 146  
 spray-controlled pneumatic foam 334–5, 338  
 spreading coefficient (SC) 424–5, 429, 451  
 sprinkler applications 429

- squalane 172, 187–9, 190  
*see also* diglycerol fatty acid esters/  
 squalane system
- squalene 172, 187–9, 190  
*see also* diglycerol fatty acid esters/  
 squalene system
- stability of foams 54, 76–8, 170–2  
 Bikerman foamability test 154–5  
 glass foams 369–70, 370–1  
 non-aqueous foams  
   effect of headgroup size of  
     surfactant 187–9  
   effect of solvent molecular  
     structure 174–7  
   effect of surfactant  
     concentration 177–81, 183–4,  
     187, 202  
   effect of surfactant molecular  
     structure 181–9  
   effect of temperature 189, 191  
   effect of water addition 192–200  
     stabilization mechanism 201–3
- particle stabilized foams 125–31  
 petroleum recovery 295  
 pneumatic foam columns 154  
   flotation columns 233–4  
   foam fraction columns 316–17  
*see also* coalescence; coarsening
- standards, fire-fighting foams 452–3  
 static foaming 123  
 statistics, foam morphology 20–1  
 steam flooding 297–8  
 Stern layer 313  
 Stokes's equations 55  
 storage, foam concentrate 416, 419, 431  
 sulfate addition, glass foaming 381–2,  
   381, 386, 396  
 sulfide addition, glass foaming 396  
 sulfobetaine (CAS) 435  
 superconducting froth *see* suprafroth  
 superficial velocity, pneumatic foam  
   columns 147, 148, 149, 150, 152,  
   235–6  
 suprafroth 208–25  
   cellular structure 215–23  
   coarsening 215–19  
   intermediate state patterns 211–15  
 surface active molecules  
 enrichment ratio 308–9  
 glass foams 368  
 interfacial adsorption 170, 310–15  
*see also* surfactants  
 surface energy 77, 95  
   pneumatic foam production 162  
   superconductors 209–10  
 Surface Evolver 10, 11, 32, 68  
   rheological studies 94, 96  
 surface modulus 108, 111, 113, 114  
 surface roughness 159  
 surface stability, flotation columns 233–4  
 surface stresses  
   coarsening 69  
   foam drainage 36, 44  
 surface tension 70  
   and elasticity 92, 98  
   fire-fighting foams 422, 423, 425–7  
   fluorosurfactants 439, 440, 444  
   glass foams 368  
   hydrocarbon surfactants 433, 437, 438  
   liquid-metal dispersions 124  
   measurement 451  
   non-aqueous foams 181, **186**, 201  
   particle stabilized foams 134  
   pneumatic foam 162  
   protein solution 313  
   versus surfactant concentration 181,  
   201, 438, 439, 440  
   and yield stress 105  
 surface viscosity, foam drainage 36, 43,  
   44, 45, 50  
 surfactants  
   characterisation 54  
   chemical degradation 28  
   consumer products 464–6  
   critical micelle concentration  
     (CMC) 427, 429, 433, 437  
   density fluctuations 78  
   disjoining pressures 31–2  
   drainage rates 44  
   effect of molecular structure 181–9  
   fire-fighting foams 433–9, **434–5**  
   foam stability optimization 28, 53–4

- non-aqueous foams 181–9
- oil tolerance 286
- petroleum reservoir applications 284–7, 296–7
- physicochemical properties 53–4
- surface modulus 108
- see also* particle stabilized foams (PSFs); protein-stabilized foams
- surfactant-alternating-gas (SAG) 294
- surfactant concentration
  - critical liquid fraction 85–6
  - non-aqueous foams 177–81, 202
  - particle detachment in flotation columns 237, 238
  - versus particle size distribution 179, 180, 183–4
  - phase diagrams 173
  - versus surface tension 181, 201, 438, 439, 440
- surfactant/oil systems *see* oil-based foams
- syneresis *see* foam drainage
- synthetic foam (S) 413
  
- T1 events 21, 22, 87–8, 105
- tailing stream 229, 230
- tar sands *see* oil sands
- temperature dependancy
  - bitumen froth formation 261
  - foam stability 189, 191
  - glass foaming 360–1, 364, 369–70, 376–7, 384–5, 397
  - non-aqueous foams 189, 191
  - suprafroth 208, 221–2
  - see also* phase behaviour
- tests
  - fire-fighting foams 448–53
  - foamability 154–5, 233–4
- tetradecyltrimethylammoniumbromide (TTAB) 42, 43, 45, 46, 49–50, 81, 85–6
- tetrakaidecahedron 29–30, 31
- thermal decomposition, glass foaming 387
- thermal stability 284–5, 295
  - see also* temperature dependancy
- thermodynamic critical field (superconductors) 208
  
- thermodynamic phases
  - (superconductors) 208–9
- thermodynamic stability, particle stabilized foams 125–31
- thickening, liquid Al alloys 123
- thin-film balance 76
- thin films
  - stability 76–8
  - see also* films, inter-bubble
- three-dimensional foams
  - characterisation 20–1
  - coarsening 64–5
  - dry foam 16
  - ideal 3D cell 21
  - mean number of faces 21
  - wet foam 17–18
- three-phase systems 126
- topological structures 21
- TTAB (tetradecyltrimethylammonium-bromide) 42, 43, 45, 46, 49–50, 81, 85–6
- tubular intermediate state patterns 210–15
- turbulent flow 156, 163, 345–6
- two-dimensional foams 11–16
  - dry cluster 15, 16
  - dry limit 11, 12, 62–4
  - honeycomb structure 14, 15
  - between the limits 11–14
  - number of contact per cell 11–14
  - wet limit 11, 12
- two-film theory 345
- type-I superconductors 208–15
- type-II superconductors 209
  
- unconfined drained foam 33–6
- uniform flow 37
- unit cell 30, 31
- unit of foaminess 390–1
  
- van der Waals forces 76–7
- vented underflow 146, 147
  - gas–liquid mass transfer 335, 336
- Verbist's foam drainage equation 41–2, 46
- vertical pneumatic foam 145–58
  - bubble coalescence 150, 151
  - bubble column regime 156–7

- vertical pneumatic foam (*cont'd*)  
     bubble size distribution 150, 153  
     capillary forces 149–50  
     coarsening 150, 152  
     cross-sectional area changes 158  
     flooding 155–7  
     foam phase 146  
     foam-wall shear stress 157–8  
     forced drainage 153  
     hydrodynamics 147–52  
     influence of humidity above  
         column 154–5  
     liquid flux 146, 148, 150–2, 155  
     liquid tailings 146  
     liquid volume fraction 146–7, 148–51,  
         151, 152–3  
     non-overflowing 153–5, 334–6  
     pressure gradient 157  
     stability 154  
     superficial velocity 147, 148, 149, 150,  
         152, 235–6  
     viscous losses 155–7  
     washwater addition 151–2
- visco-elasticity 95–102
- viscosity  
     aqueous film-forming foams  
         (AFFFs) 450–1  
     bitumen 252, 273  
     bituminous froths 271  
     bulk 71  
     and coalescence 84  
     and foam drainage 36, 43, 44, 45, 50  
     measurement 450–1
- viscous dissipation 46, 106–8, 114–15  
     pneumatic foam columns 155–7
- viscous drag 37, 40, 87, 237
- viscous friction 99, 108–14  
     foam-wall 112–14
- viscous froth model 95
- viscous modulus, non-aqueous  
     foams 179–80, 185
- viscous stress 71, 95, 107–8, 109, 111–12  
     foam-wall friction 114
- visual perception 471–2
- volume fraction  
     *see also* gas volume fraction; liquid  
         volume fraction  
     volume polydispersity *see* polydisperse  
         foams  
     volumetric flux *see* superficial velocity  
     von Neumann ripening *see* coarsening  
     von Neumann's law 221–2, 223
- WAG (water-alternating-gas) 294, 296
- Waldhof fermentor 230, 338–40
- wall slip *see* foam-wall slip
- Ward–Tordai equation 311
- washwater  
     addition to pneumatic foam 151–2  
     flotation columns 230, 232
- water addition, non-aqueous foams 192–200
- water-alternating-gas (WAG) 294, 296
- water deluge resistance 429, 440, 443, 451
- water vapor, effect on glass  
     foaming 381–2
- Weaire–Phelan structure 16, 17
- wet foams 7–8  
     foam ripening 65–9  
     geometrical considerations 29–33  
     idealised geometry 33  
     number of contact per cell 13, 14
- wet limit 11  
     foam ripening 59–60, 61  
     two-dimensional foams 12
- wettability  
     rock 286  
     wall surface 159, 160
- wetting rate measurement 452
- X-ray tomography 153
- yeast production 338–40
- yield strain 103–5
- yield stress 2, 91, 103–5  
     consumer products 469  
     foam-wall 112
- Young–Laplace law *see* Laplace–Young  
     law
- Zisman method 422, 423